

Université de Montréal

**Persistence of diverse
transcriptionally competent viral reservoirs
in people living with HIV-1**

Par

Gérémy Sannier

Département de microbiologie, infectiologie et immunologie

Faculté de médecine

Thèse présentée en vue de l'obtention du grade de
Philosophiae Doctor (Ph.D.) en Virologie et Immunologie

Juin 2023

© Gérémy Sannier, 2023

Université de Montréal
Faculté des études supérieures et postdoctorales
Département de Microbiologie, Infectiologie et Immunologie, Faculté de Médecine

Cette thèse intitulée

**Persistence of diverse
transcriptionally competent viral reservoirs
in people living with HIV-1**

Présentée par

Gérémy Sannier

A été évaluée par un jury composé des personnes suivantes

Dre. Naglaa H. Shoukry

Présidente-rapporteuse

Dr. Daniel E. Kaufmann

Directeur de recherche

Dr. Roger Lippé

Membre du jury

Dr. R. Brad Jones

Examineur externe

Dr. Guy Lemay

Représentant du doyen

Résumé

Malgré les améliorations significatives apportées par la thérapie antirétrovirale à la durée et à la qualité de vie des personnes vivant avec le VIH, elle ne permet pas de complètement éliminer le virus de l'organisme. La persistance du virus est due à l'existence de réservoirs viraux, des cellules infectées de manière latente par le VIH. Ces réservoirs nécessitent un traitement antirétroviral à vie, car le virus réapparaît en cas d'interruption du traitement, signifiant que l'immunité des cellules T spécifiques du VIH n'est pas restaurée. Bien que cela soit théoriquement possible, seule une fraction de personne vivant avec le VIH, appelée Contrôleurs Élites, parvient à contrôler le virus en absence de traitement. Pour la majorité des individus, l'infection par le VIH entraîne une évasion virologique ainsi qu'un épuisement et une altération des réponses cellulaires spécifiques au VIH.

À ce jour, les stratégies thérapeutiques visant à éliminer les réservoirs viraux ont échoué, en partie en raison de la présence de provirus principalement défectifs dans ces réservoirs. Dans cette thèse, nous avons identifié et caractérisé les provirus défectifs latents du VIH pouvant être transcrits et/ou traduits, ainsi que la relation entre ces réservoirs et les réponses immunitaires spécifique du virus.

Dans un premier temps, nous avons montré que bien que défectifs et potentiellement incapable de donner lieu à la réplication virale, ces provirus peuvent être transcrits et traduits soit par réactivation à l'aide d'agents de réversion de la latence, soit de manière spontanée. Ces réservoirs donnent lieu à plusieurs populations de réservoirs, en fonction de la présence ou de l'absence certains gènes viraux. Nous avons déterminé que ces différentes populations sont régies par le profil génomique des cellules infectées. Les

provirus identifiés étaient très rarement intacts, mais l'intégrité du génome était associée à la processivité de la transcription et de la traduction.

Dans un second objectif, nous avons caractérisé les réponses T CD4⁺ et CD8⁺ spécifiques du VIH avant et après le début du traitement antirétroviral. Nous avons observé que les réponses T CD4⁺ spécifiques étaient comparables pendant l'infection chronique et après le traitement. En revanche, les réponses T CD8⁺ diminuaient considérablement après l'initiation de la thérapie antirétrovirale. Nous avons également constaté que la taille du réservoir traductionnellement actif pendant le traitement antirétroviral était négativement associée aux réponses T CD8⁺ spécifiques avant le début de la thérapie, tandis que le réservoir incapable de traduire les protéines du VIH subsistait. Ces observations mettent en évidence le rôle des cellules T CD8⁺ dans le contrôle de l'infection par le VIH, comme nous l'avons observé chez les Contrôleurs Élites.

Nos travaux contribuent à une meilleure compréhension des réservoirs viraux du VIH, qui pourraient potentiellement être impliqués dans l'inflammation chronique et la dysfonction immunitaire associé à la pathogénèse du VIH.

Mots-clés : réservoirs du VIH, agent de réversion de latence, provirus défectifs, transcription et traduction virale, réponses spécifiques au VIH, Contrôleurs Élites, Pré/Post-thérapie antirétrovirale.

Abstract

Despite the significant improvement brought by antiretroviral therapy in the duration and quality of life for people living with HIV, it does not completely eliminate the virus from the body. The persistence of the virus is due to the existence of viral reservoirs, which are cells latently infected with HIV. These reservoirs require lifelong antiretroviral treatment because of the viral rebound reoccurring in case of treatment interruption. This suggests that HIV-specific T cell immunity is not restored. Although theoretically possible, only a fraction of people living with HIV, known as Elite Controllers, are able to control the virus in the absence of treatment. For the majority of individuals, HIV infection leads to virologic escape, as well as exhaustion and altered cellular responses to HIV.

To date, therapeutic strategies aimed at eliminating viral reservoirs have failed, partly due to the presence of predominantly defective proviruses in these reservoirs. In this thesis, we have identified and characterized latent defective proviruses of HIV that can be transcribed and/or translated. We also have characterized the relationship between these reservoirs and the specific immune responses to the virus.

Firstly, we have shown that although defective and potentially replication-incompetent, these proviruses can be transcribed and translated either through reactivation using latency reversal agents or spontaneously. These reservoirs give rise to several populations of reservoirs, depending on the presence or absence of certain viral genes. We have determined that these different populations are governed by the genomic profile of infected cells. The identified proviruses were rarely intact, and genome integrity was associated with the processivity of transcription and translation.

Then, we characterized the specific CD4⁺ and CD8⁺ T cell responses to HIV before and after the initiation of antiretroviral treatment. We observed that specific CD4⁺ T cell responses were comparable during chronic infection and after treatment. However, CD8⁺ T cell responses decreased significantly after the initiation of antiretroviral therapy. We also found that the size of the translationally active reservoir during antiretroviral treatment was negatively associated with the specific CD8⁺ T cell responses prior to treatment initiation, while the translation-incompetent cells persisted. These observations highlight the role of CD8⁺ T cells in the control of HIV infection, as observed in Elite Controllers.

Our work contributes to a better understanding of HIV viral reservoirs, which could potentially be involved in chronic inflammation and immune dysfunction associated with HIV pathogenesis.

Keywords: HIV reservoirs, latency reversal agent, defective proviruses, viral transcription and translation, HIV-specific responses, Elite Controllers, Pre/Post-antiretroviral therapy.

Table of contents

<i>Résumé</i>	<i>I</i>
<i>Abstract</i>	<i>III</i>
<i>Table of contents</i>	<i>V</i>
<i>List of figures</i>	<i>IX</i>
<i>Abbreviations</i>	<i>X</i>
<i>Remerciements</i>	<i>XVIII</i>
<i>Chapter 1 – Introduction</i>	<i>21</i>
HIV and AIDS – Generalities	23
Origins and epidemiology of HIV/AIDS.....	23
Taxonomy and structure of HIV	25
HIV-1 genome and proteins	26
Viral structural genes (gag, pol, and env).....	28
Essential regulatory genes (tat and rev).....	31
Accessory regulatory genes (nef, vpr, vif, and vpu)	32
Other HIV genes (vpx, asp, and fusion proteins).....	33
HIV replication cycle	34
Cellular tropism and viral entry.....	34
Reverse transcription and pre-integration events	35
Nuclear import and viral integration	38
Viral transcription and translation	39
Viral assembly and budding	42
Viral maturation	42
Stages of HIV-1 infection	44
Early/Acute phase	45
Chronic phase	47

AIDS	49
Antiretroviral therapy.....	50
HIV reservoirs.....	54
HIV latency	54
Pre-integrational latency	55
Post-integrational latency	56
Transcriptional “latency”	56
Non-epigenetic mechanisms	56
Epigenetic mechanisms.....	57
Viral latency.....	59
“Leaky latency”	61
Viral reservoir.....	64
“Total HIV DNA”	64
Replication-competent reservoir	65
Proviral integrity	66
Transcription- and translation-competent reservoir.....	67
Cellular reservoirs	68
CD4 ⁺ T lymphocytes	68
Monocytes and macrophages	70
Other cellular reservoirs	71
Anatomical reservoirs	72
Viral reservoir persistence	75
Viral reservoir stability	75
Mechanisms involved in the viral persistence	76
Clonal expansion	76
Ongoing replication.....	80
Immune responses and therapeutic strategies	81

Immune responses during HIV infection	81
Innate immunity	81
Adaptive immunity	82
HIV-specific CD8 ⁺ T cells	82
HIV-specific CD4 ⁺ T cells	84
HIV therapeutic strategies and cure	85
HIV vaccine strategies	86
Genome editing strategy	88
Broadly Neutralizing antibodies (bNAbs) strategy	89
Chimeric Antigen Receptor (CAR)-T cells strategy	91
“Block and Lock” strategy	92
“Shock/Kick and Kill” strategy	94
<i>Chapter 2 – Hypotheses and Objectives</i>	<i>97</i>
<i>Chapter 3 – Manuscript 1: Combined single-cell transcriptional, translational, and genomic profiling reveals HIV-1 reservoir diversity</i>	<i>100</i>
<i>Chapter 4 – Manuscript 2: Single-Cell Relationships Between HIV-1-Specific Immune Responses in Untreated Individuals and Viral Transcription and Translation.....</i>	<i>157</i>
<i>Chapter 5 – Discussion</i>	<i>214</i>
General conclusion.....	215
Use of RNAflow-FISH assay to study the viral reservoir cells	217
Proportion of the transcription-competent viral reservoir	219
Viral integrity of the transcriptionally competent HIV-infected cells during ART.....	221
Relationships between HIV-specific T cells responses and viral reservoirs.....	224
Possible impact of the defective proviruses on the HIV-specific T responses	226
Possible role of the HIV-specific T responses on the persistence of defective proviruses	228
<i>Chapter 6 – Limitations and perspectives.....</i>	<i>232</i>

Blood versus tissue	233
Perspectives for future treatment approaches	234
RNAflow-FISH requirements	235
The HIV-infected cohort	236
<i>Chapter 7 – Significance</i>	237
<i>Chapter 8 – References</i>	239
<i>Chapter 9 – Appendices</i>	cclxxii
<i>Appendix I: Author’s contribution to additional manuscripts</i>	cclxxiii
<i>Appendix II: Additional manuscripts</i>	cclxxvi
Appendix II.i: A Third SARS-CoV-2 mRNA Vaccine Dose in People Receiving Hemodialysis Overcomes B Cell Defects but Elicits a Skewed CD4 ⁺ T Cell Profile	cclxxvi
Appendix II.ii: An Extended SARS-CoV-2 mRNA Vaccine Prime-Boost Interval Enhances B Cell Immunity with Limited Impact on T Cells	cccxvi
Appendix II.iii: Spontaneous HIV Expression During Suppressive ART is Associated with the Magnitude and Function of HIV-Specific CD4 ⁺ and CD8 ⁺ T Cells	cccxlvi
Appendix II.iv: Temporal Associations of B and T Cell Immunity with Robust Vaccine Responsiveness in a 16-Week Interval BNT162b2 Regimen	ccclxxxv
Appendix II.iv: Single-Cell Technologies Applied to HIV-1 Research: Reaching Maturity	cdxxi
<i>Curriculum Vitae</i>	cdxxxv

List of figures

Figure 1. – HIV particle structure	26
Figure 2. – HIV-1 genome and proteins	29
Figure 3. – Conversion of the single-stranded RNA into double-stranded DNA.....	37
Figure 4. – Alternative splicing of HIV-1 gene expression.....	41
Figure 5. – HIV-1 replication cycle in CD4 ⁺ T cells	43
Figure 6. – Stages of HIV-1 infection.....	45
Figure 7. – Subclassification of early/acute HIV infection into Fiebig stages.	47
Figure 8. – Classes of current ART regimens and mechanisms of action.....	52
Figure 9. – Cellular models of latency establishment into CD4 ⁺ T cells	62
Figure 10. – Venn diagram comparison of each different viral genome subtypes	65
Figure 11. – Mechanisms contributing to clonal expansion of HIV-infected cells	79
Figure 12. – “Shock/Kick and Kill” strategy and Latency Reversal Agents classes ...	96
Figure 13. – Relationship between HIV-specific responses and viral reservoirs	226

Abbreviations

ADCC: Antibody-Dependent Cellular Cytotoxicity

ADCP: Antibody-Dependent Cellular Phagocytosis

AIDS: Acquired Immunodeficiency Syndrome

AML: Acute Myeloid Leukemia

APC: Antigen-Presenting Cells

APOBEC3G: Apolipoprotein B mRNA editing Enzyme, Catalytic subunit 3G

ART: Antiretroviral Therapy

ARV: Antiretrovirals

Asp: Antisense protein

ATI: Analytical Treatment Interruption

AZT: Azidothymidine (also known as Zidovudine)

BCL-2: B Cell Lymphoma 2

bNAb: broadly Neutralizing Antibody

BST-2: Bone marrow stromal antigen 2 (also known as Tetherin)

CA: Capsid (p24) protein

Cas9: CRISPR-Associated Protein 9

CCL: Chemokine (C-C motif) ligand or β -chemokines

CCR, CXCR: Chemokine (C-C, CXC motif) receptor

CD: Cluster of Differentiation

CD4bs: CD4 binding site

CDC: Center for Disease Control and Prevention

CNS: Central Nervous System

CPSF6: Cleavage and Polyadenylation Specific Factor 6

CRF: Circulating Recombinant Form

CRISPR: Cluster Regularity Interspaced Short Palindromic Repeat

CROI: Conference on Retroviruses and Opportunistic Infections

CSF: Cerebrospinal Fluid

CTL: Cytotoxic T cells

DAMP: Damage-Associated Molecular Patterns

DC: Dendritic Cells

dCA: Didehydro-Cortistatin A

DC-SIGN: Dendritic Cell-specific C-type lectin

DIS: Site of dimerization

DNA: Deoxyribonucleic Acid

cDNA: Complementary DNA

dsDNA: Double strand(ed) DNA

EC: Elite Controller

ELISA: Enzyme-Linked Immunosorbent Assay

Env: Envelope

ESCRT: Endosomal Sorting Complexes Required for Transport

FasL: Fas Ligand

FDA: Food and Drug Administration

FLIPS: Full-Length Individual Proviral Sequencing

Gag: Group-specific antigen

GALT: Gut-Associated Lymphoid Tissue

Gp: Glycoprotein

HAART: Highly Active Antiretroviral Therapy

HAT: Histone Acetyltransferase

HDAC: Histone Deacetylase

HDACi: Histone Deacetylase inhibitor

HIV: Human Immunodeficiency Virus

HLA: Human Leukocyte Antigen

HMT: Histone Methyltransferase

aHSCT: Allogeneic Hematopoietic Stem Cell Transplantation

HSP: Heat Shock Protein

IFN: Interferon

IL: Interleukin

IN: Integrase

INS: Instability elements

INSTI: Integrase Nuclear Strand Transfer Inhibitor

IRES: Internal Ribosome Entry Sequence

KIR: Killer-cell Immunoglobulin-like Receptor

LEDGF: Lens Epithelium-Derived Growth Factor

LAA: Long-Acting injectable ART

LN: Lymph Node

LPA: Latency-Promoting Agent

LPS: Lipopolysaccharides

LRA: Latency Reversal Agent

LTNP: Long-Term Non-Progressor

LTR: Long Terminal Repeat

MA: Matrix (p17) protein

MBD2: Methyl-CpG Binding Domain protein 2

M-CSF: Macrophage Colony-Stimulating Factor

MHC: Major Histocompatibility Complex

MPER: Membrane-Proximal External Region

MSD: Major Splice Donor

MSM: Men who have Sex with Men

mTOR: mammalian Target of Rapamycin

NC: Nucleocapsid (p7) protein

Nef: Negative Regulatory Factor

NEAT1: Nuclear Enriched Abundant Transcript 1

NFAT: Nuclear Factor of Activated T cell

NF κ B: Nuclear Factor-kappa B

NHP: Non-Human Primate

NK: Natural Killer cells

NNRTI: Non-Nucleoside Reverse Transcriptase Inhibitor

NPC: Nuclear Pore Complex

NRON: Non-coding Repressor of NFAT

N(t)RTI: Nucleoside/nucleotide-analog Reverse Transcriptase Inhibitor

NUP: Nucleoporin

ORF: Open Reading Frame

PAMP: Pathogen-Associated Molecular Patterns

PBMC: Peripheral Blood Mononuclear Cell

PBS: Primer Binding Site

PCR: Polymerase Chain Reaction

PI: Protease Inhibitor

PI3K/Akt: Phosphoinositide 3-kinases, Protein kinase B

PIC: Pre-Integration Complex

PKCa: Protein Kinase C Agonist

PLWHIV: People Living With HIV

Pol: Polymerase

PPT: Polypurine Tract

PR: Protease

PRR: Pattern Recognition Receptor

PTC: Post-Treatment Controller

P-TEFb: Positive Transcription Elongation Factor b

Rev: Regulator of Expression of Viral proteins

RNA: Ribonucleic Acid

RNAflow-FISH: Flow Cytometric Fluorescent *In Situ* RNA Hybridization

gRNA: Genomic RNA

lncRNA: Long non-coding RNA

mRNA: Messenger RNA

miRNA: Micro-RNA

snRNA: Small nuclear RNA

ssRNA: Single strand RNA

tRNA: Transfer RNA

RNase H: Ribonuclease H

vRNP: Viral Ribonucleoprotein Complex

RRE: Rev Responsive Element

RT: Reverse Transcriptase

RTC: Reverse Transcription Complex

RTI: Reverse Transcriptase Inhibitor

SAMHD1: Sterile Alpha Motif Domain and Histidine-Aspartic domain-containing protein 1

SCID: Severe Combined Immunodeficient

SD: Splice Donor site

SIV: Simian Immunodeficiency Virus

SL: Stem-Loop

SP: Spacer Peptides (SP1 and SP2)

SU: Surface envelope protein (gp120)

T_H: T Helper

cT_{FH}: Circulating T Follicular Helper

T_{CM}: Central Memory T cell

T_{EM}: Effector Memory T cell

T_{TM}: Transitional Memory T cell

T_{SCM}: Stem-Cell Memory T cell

T_N: Naïve T cell

T/F: Transmitter/Founder

TAF: TBP-Associated Factors

TAR: Trans-Activation Response element

Tat: Trans-Activator of Transcription protein

TBP: TATA-Binding Protein

TF: Transframe protein

TLR: Toll-Like Receptor

TM: Transmembrane envelope protein (gp41)

TNF: Tumor Necrosis Factor

TNPO3: Transportin-3

TRAIL: Tumor necrosis factor-Related Apoptosis-Inducing Ligand

TSG101: Tumor Susceptibility Gene 101

TSS: Transcription Start Site

Vif: Viral Infectivity Factor

VOA: Viral Outgrowth Assay

Vpr: Viral Protein R

Vpu: Viral Protein U

Vpx: Viral Protein X

*“We are not making science for science.
We are making science for the benefit of humanity.”*

Dre. Françoise Barré-Sinoussi

Remerciements

Une seule section afin de remercier toutes les personnes présentes durant ma thèse, de près comme de loin, ne peut pas être suffisante et ne saurait montrer toute ma gratitude.

Premièrement, je voudrais remercier les membres qui ont siégé sur mon comité de pré-doctorat pour leur précieux conseils qui m'ont permis d'avancer sur mes projets : Dre. Pétronela Ancuta, Dr. Éric A. Cohen et Dre. Anne Gatignol. Merci également à tous les membres de mon jury de thèse qui ont accepté de prendre le temps d'évaluer mon travail doctoral : Dre. Naglaa Shoukry, Dr. R. Brad Jones, Dr. Roger Lippé, et Dr. Guy Lemay.

Je souhaite aussi remercier le Dr. Daniel E. Kaufmann, pour sa supervision. Je te suis reconnaissant des collaborations avec d'incroyables scientifiques, ainsi que des conférences où tu m'as envoyé présenter mes travaux de thèse. Travailler sous ta supervision m'a permis de grandir scientifiquement, mais surtout humainement. Pour cela je ne te remercierai jamais assez.

Je voudrais également remercier Mathieu pour sa supervision, sa confiance et ses conseils. Tout n'a pas toujours été simple durant ces cinq années, avec beaucoup de conflits durant les premières années qui se sont transformés en précieuses discussions par la suite. J'ai conscience que travailler avec moi n'était pas une partie de plaisir au début, mais j'espère que ça l'est devenu ensuite.

Je tiens à remercier tous les membres présents comme passés du labo Kaufmann, et tout particulièrement Elsa et Julia. Elsa, tu as été la première personne à m'intégrer au Canada, m'invitant à une soirée chez toi après seulement 3 semaines à Montréal. Tu as également été un soutien incroyable pendant les 4 années ensemble dans le laboratoire.

Je pense que nous avons passé un peu trop de temps au Brewskey à pleurer nos conditions de pauvres étudiants au doctorat. Julia, tu auras été pour moi un modèle durant toutes ces années. Tes connaissances scientifiques m'ont toujours poussé à donner le meilleur de moi-même pour ne pas paraître stupide face à toi. Tu as aussi toujours fait preuve d'une extrême gentillesse, ce qui m'a permis de tenir maintes fois durant mon doctorat. Je voudrais aussi remercier Alexandre, qui a fait de mes dernières années de doctorat une souffrance absolue. Je n'avais jamais rencontré quelqu'un se posant autant de questions sur tous les aspects de la science que toi. Tu es cependant quelqu'un avec un grand cœur et c'est toujours un plaisir de discuter avec toi, quand le temps le permet ! Merci également à Manon pour tes conseils scientifiques, ton énergie et ces discussions à rallonge durant ces quelques années. Avec toi, j'étais certain de me perdre dans l'espace-temps. Merci à Audrée, Tayma et Marc pour les discussions scientifiques ou non, ainsi que pour votre amitié. Enfin un grand merci à Gloria, Nathalie, Mélanie, Rose, Roxanne et Mélina pour votre aide précieuse, ce fut apprécié à juste titre !

Merci à mes amis à l'étage qui se sont régulièrement arrêtés à mon bureau pour discuter, parfois pendant des heures. Je tiens particulièrement à remercier Alexandra, Alessandro, Augustine, Camille, Hélène, Jérémie, Sai Priya, Sana et Victoria pour votre soutien et les moments de plaisirs partagés en chemin ! Merci de m'avoir aidé à préserver ma santé mentale pendant mon doctorat. J'ai souvent râlé comme le français que je suis, mais vous m'avez toujours écouté et soutenu !

Même s'ils ne comprennent pas ce que je fais, ni même à quel point un doctorat peut être éprouvant, je voudrais remercier mes amis Camille, Caroline, Geoffrey, Margot et Sarah. Avec vous c'est « loin des yeux près du cœur ». Même si on peut passer plusieurs

semaines/mois sans parler, je sais que je peux toujours compter sur vous à n'importe quel moment ! Les visios le 31 décembre, pour me souhaiter la nouvelle année à 18h sont un concept qu'il faut garder. Guillaume, je n'allais pas oublier de te remercier. Tu es l'un de mes premiers amis ici à Montréal, et ce petit rituel du quiz tous les lundis pendant 5 ans aura aussi contribué à me changer les idées régulièrement. Tout ceci est en partie grâce à Mme Bille-en-Tête !

Je dédie cette section à la personne la plus intelligente et attentionnée que j'ai la chance de connaître et qui est entrée dans ma vie pile au bon moment. Clara, j'aurais énormément de choses à dire sur tout ce que tu as fait pour moi durant la fin de mon doctorat. Tu n'imagines pas à quel point ta présence m'a aidé à terminer cette thèse de la manière la plus saine qu'il soit. Chaque moment passé en ta compagnie m'a permis de penser à autre chose que le stress que je m'infligeais. Tu m'as offert la possibilité de garder la tête hors de l'eau. Tu m'as aidé à relativiser mes craintes et tu m'as soutenu et surtout supporté pendant toute cette période (et encore plus maintenant). Merci pour ta patience. Merci de m'avoir rassuré quand je stressais, quand je n'y arrivais pas. Merci de toujours croire en moi, même quand je ne crois pas en moi. Merci pour tous tes conseils. Juste merci d'être là. Maintenant que c'est terminé, je serai là pour te rendre la pareille. Je serai là pour te permettre de terminer ton PhD le plus sereinement possible.

Enfin, je finirai par remercier ma famille, mon frère, ma sœur, mes grands-parents qui m'ont aidé à devenir l'homme que je suis maintenant. Mais surtout merci à mes parents qui m'ont toujours donné les moyens nécessaires pour pousser mes études le plus loin possible. Vous avez toujours cru en moi et soutenu même dans les pires moments. Sans vous, rien de tout ça n'aurait été possible. Maman, papa, merci pour tout. Je vous aime.

Chapter 1 – Introduction

Parts of this introduction were used in the review article

“Sannier, Dubé et *al.*, Single-Cell Technologies Applied to HIV-1 Research:

Reaching Maturity,

Frontiers in Microbiology, 2020”

This article is included in Chapter 9 – Appendices

Since its discovery, the Human Immunodeficiency Virus (HIV) has persisted and continues to pose a significant global public health challenge. One of the main reasons for this is the absence of a long-term and effective curative treatment.

To date, almost no treatment exists to cure HIV infection. While some individuals have achieved HIV-free status through stem cell transplants with receptor mutations, this approach is not scalable for widespread treatment. It is medically intensive and primarily recommended for life-threatening cancer cases.

This thesis focuses on studying HIV-infected cells and the role of the virus. We characterized the profiles of infected CD4⁺ T cells at transcriptional, translational, and genomic levels in people living with HIV (PLWHIV) under suppressive antiretroviral therapy (ART), as well as in PLWHIV who were not receiving ART.

Additionally, we conducted a separate study to investigate the relationships between specific T cell responses prior to ART initiation and transcription and translation of HIV over time. This project involves a longitudinal investigation of T cell immune responses taking place during chronic infection and perduring under ART.

This introduction aims to provide a comprehensive overview of the current understanding of HIV-infected CD4⁺ T cells and the characteristics of the HIV profile itself. Furthermore, it explores existing treatment strategies and their development.

HIV and AIDS – Generalities

Origins and epidemiology of HIV/AIDS

In 1981, several cases of opportunistic infections in men who have sex with men (MSM) were reported to the Center for Disease Control and Prevention (CDC) in New York. Initially, infections by *Pneumocystis pneumonia* were observed, followed by an increasing number of MSM patients also being diagnosed with Kaposi's sarcoma. These opportunistic diseases were commonly found in immunosuppressed individuals. The existence of a new virus affecting the immune system was suspected. As the death toll rose rapidly, every patient exhibited a depletion of CD4⁺ T cells and severe immunodeficiency. In 1982, the epidemic was officially named Acquired Immune Deficiency Syndrome (AIDS) by the CDC for the first time. While initially limited to the United States of America, many cases were subsequently discovered in Africa, Europe, South America, and Asia. Furthermore, although AIDS was initially associated with MSM, the disease was also found in other populations. Individuals engaging in heterosexual intercourse, drug users (specifically heroin), hemophiliacs who received blood transfusions, and infants born to infected mothers were also diagnosed with AIDS. This led researchers to suggest that the virus was not only sexually transmitted but also spread through blood-to-blood contact and vertical transmission (from mother to child).

In 1983, the virus was isolated for the first time from a lymph node (LN) of a Caucasian patient showing signs and symptoms preceding AIDS [1]. Many teams worldwide also successfully isolated the virus from individuals with AIDS, confirming the link between the virus and the disease [2, 3]. This newly identified virus causing AIDS was later named the Human Immunodeficiency Virus (HIV).

HIV's sudden emergence, epidemic spread, and unique pathogenicity raised questions. Other viruses causing immunodeficiency were found in different primates, such as green monkeys, macaques, sooty mangabeys, and chimpanzees, and were collectively termed Simian Immunodeficiency Virus (SIV) [4, 5]. In 1986, a morphologically similar but antigenically and phylogenetically different virus was found to cause AIDS in patients in western Africa [6]. This newly identified virus, named Human Immunodeficiency Virus type 2 (HIV-2 to distinguish from the virus isolated in 1983 by Drs. Barré-Sinoussi, Chermann, and Montagnier, termed HIV-1), was found to be related to an SIV from sooty mangabeys (*Cercocebus atys*) and rhesus macaques (*Macaca mulatta*), known as SIVsm and SIVmac, respectively [7-9]. Another virus, closely related to HIV-1, was discovered in central chimpanzees (*Pan troglodytes troglodytes*) and named SIVcpz [8], suggesting that HIV was introduced into the human population through multiple zoonotic transmissions, evolving from SIV [8, 10].

Since the beginning of the epidemic in 1981, approximately 84.2 million [64.0 – 113.0 million] people have been infected with HIV, and about 40.1 million [33.6 – 48.6 million] people have died from HIV or related opportunistic diseases. By the end of 2021, an estimated 1.5 million [1.1 – 2.0 million] people became newly infected with HIV over the year, bringing the number of PLWHIV to 38.4 million [33.9 – 43.8 million]. In 2021, approximately 650 000 [510 000 – 860 000] people worldwide died from HIV-related illnesses [11]. However, the burden of HIV varies across different regions. In Western and Central Europe, as well as North America, it is estimated that 2.3 million [1.9 – 2.6 million] people are living with HIV, while in Eastern and Southern Africa, the number is approximately 20.6 million [18.9 – 23.0 million] [12].

Taxonomy and structure of HIV

HIV is a lentivirus within the *Retroviridae* family, specifically belonging to the subfamily *Orthoretrovirinae*. Its DNA can integrate into the host genome. The virion has a diameter of around 100-145 nm and is enveloped by a bilayered membrane derived from the host cell. The surface of the virion contains few trimeric spikes (between 7 and 14) consisting of the non-covalently bound surface glycoprotein (gp) gp120 which specifically binds to its receptor CD4, and the fusogenic transmembrane glycoprotein gp41 [13, 14] (Figure 1).

Both HIV-1 and HIV-2 have been classified into distinct phylogenetic groups. HIV-1 encompasses four phylogenetic groups (M, N, O, and P), with group M being the most predominant. Group M further comprises 12 subtypes or clades (A through L) and over 70 circulating recombinant forms (CRFs), which arise from recombination events in individuals co-infected with multiple clades [15]. Each of these groups represents an independent zoonotic transmission of SIV into humans (unlike subtypes) [10]. However, these different strains exhibit distinct geographical distributions. Clade B is prevalent in the Americas, Western Europe, and Australia [16], while clade C accounts for over 50% of current HIV infections, mostly found in Southern Africa and Southeast Asia. Nevertheless, the newest findings demonstrate the increase in HIV genetic diversity and prevalence of CRFs in recent years [16]. On the other hand, HIV-2 is composed of eight distinct groups (A through G), but only groups A and B have spread among humans, with groups C to G identified in only single individuals [17, 18].

Henceforward this thesis will focus on HIV-1 as it is the most prevalent type in North America. However, it is important to note that HIV-1 and HIV-2 are morphologically indistinguishable.

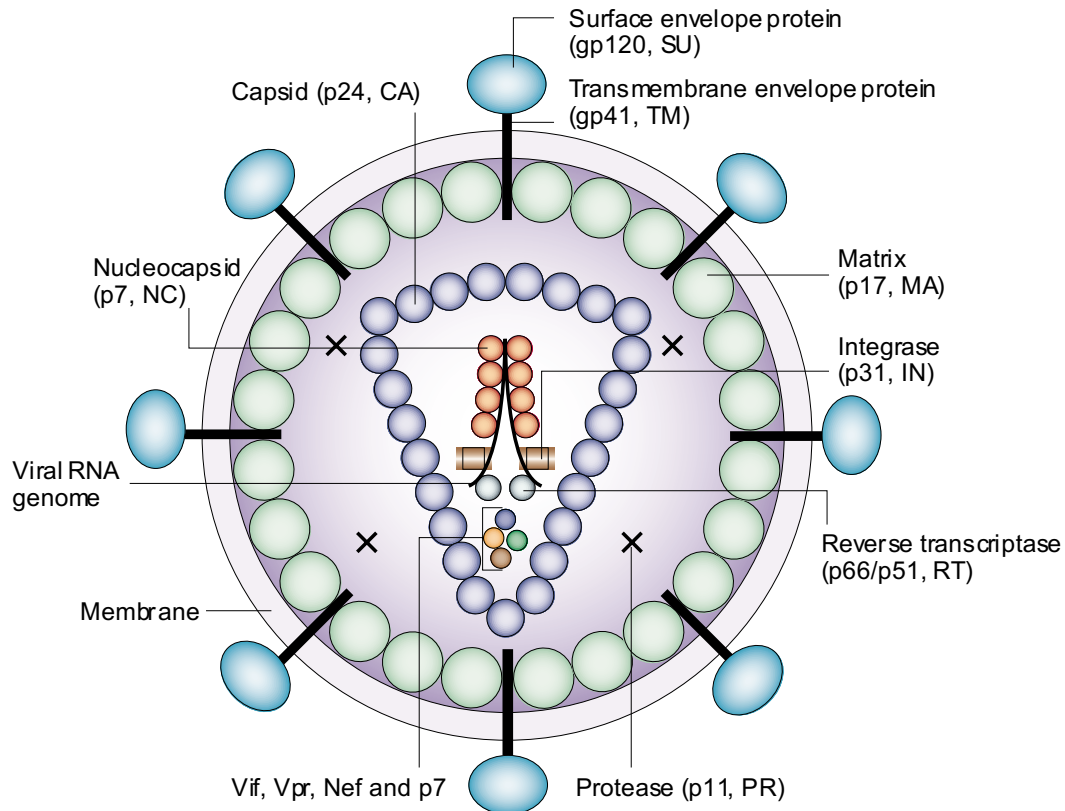


Figure 1. – HIV particle structure

HIV consists of a bilayered membrane incorporating the glycoproteins 120 (gp120) and gp41, derived from the precursor envelope (Env) polyprotein gp160. Both gp120 and gp41 form heterotrimeric structures on the surface of the HIV particle, triggering binding and entry into the host cell. The polyprotein Gag undergoes processing to generate several structural proteins: matrix (MA), capsid (CA), and nucleocapsid (NC). MA proteins surround the inner layer of the membrane, CA proteins form the cone-shaped viral capsid that encloses the viral ribonucleoprotein complex (vRNP). The vRNP consists of two positive-strand HIV RNA copies, covered by NC proteins, along with viral enzymes (reverse transcriptase, integrase, and protease), as well as other viral and cellular proteins. MA: Matrix, CA: Capsid, NC: Nucleocapsid. Figure adapted from [19] with permission from *Nature Springer*.

HIV-1 genome and proteins

The HIV genome consists of two identical positive single-strand RNA copies, each ranging from 9.2 to 9.6 kb in length (9.8 kb in the case of HIV-2), encapsulated within the capsid [20]. Both copies possess a 5' cap [21] and are polyadenylated at the 3' end [22].

Following reverse transcription of the HIV RNA, the ends of the resulting genomic DNA are flanked by long terminal repeat (LTR) sequences. These LTR regions play a vital role in viral DNA integration into the host genome and transcriptional regulation [23].

The 5' LTR functions as a robust promoter, hijacking the host cell's transcriptional machinery to regulate the transcription of the viral genome. It encompasses the HIV promoter, which includes a TATAbox, binding sites for the Sp family of transcription factors, and various binding sites for cellular transcription factors such as NF κ b, facilitating interaction with a multitude of transcription factors [24]. Both the TATAbox and Sp sites are critical for transcription initiation [25] and Tat-mediated transactivation. The 5' LTR also contains the primer binding site, which possesses a specific sequence that binds to the tRNA^{Lys} (transfer RNA) primer required for reverse transcription initiation [26]. Additionally, it comprises four stem-loops (SL): SL1, housing the dimerization initiation site (DIS) of the viral RNA [26]; SL2, containing the splice donor site (SD); SL3, hosting the retroviral Psi (ψ) packaging element necessary for encapsidation of the viral genome [27]; and SL4, containing the AUG start codon for translation. Finally, the 5' LTR encodes the hairpin-like RNA trans-activation response (TAR) element. The TAR element is a short RNA transcript that includes the N-terminal segment of the Tat reading frame, serving as a binding site for Tat [28, 29].

At the opposite end of the RNA is the 3' LTR, which shares the same sequence arrangement as the 5' LTR. Both LTRs are capable of initiating transcription, but the 5' LTR exerts dominant control over the 3' LTR [30]. While the 3' LTR typically does not function as a promoter, it is involved in transcriptional termination and polyadenylation.

Due to differential RNA splicing, the HIV-1 genome can give rise to nine different genes, along with several non-coding RNA regulators derived from its three different open reading frames (ORF) (Figure 2). These nine genes are located between the 5' LTR and the 3' LTR and can be categorized as follows:

- Structural genes (*gag*, *pol*, and *env*)
- Essential regulatory genes (*tat* and *rev*)
- Accessory regulatory genes (*nef*, *vpr*, *vif*, and *vpu*).

The unspliced full-length messenger RNA (mRNA) genomic transcripts are packaged into virions or used as a template for the translation of both Gag and Pol polyproteins. The partially spliced mRNAs encode for Env and the accessory proteins Vif, Vpr, and Vpu (or Vpx in the case of HIV-2). Finally, the multiply spliced mRNAs encode for Rev, Tat, and Nef, which are essential regulatory proteins.

Viral structural genes (gag, pol, and env)

Like all retroviruses, HIV-1 contains the *gag* (group-specific antigen) gene. It encodes the precursor Gag polyprotein (Pr55^{Gag}) and the Gag-Pol fusion protein (Pr160^{Gag-Pol} coding for viral enzymes protease, reverse transcriptase, and integrase; see after). Upon virus budding from the host cell, the HIV-1 protease (PR) cleaves Pr55^{Gag} into four mature structural Gag proteins: p17 matrix (MA), p24 capsid (CA), p7 nucleocapsid (NC), p6, and two small spacer peptides 1 and 2 (SP1 and SP2), which aid in virion formation [31]. MA lines the inner surface of the virion lipid bilayer and facilitates the formation of new particles by targeting Pr55^{Gag} [32] and Env to the plasma membrane [33, 34]. It also plays a role in reverse transcription and pre-integration complex (PIC) during the early stages

of replication [35]. CA forms a protective shell around the virus' RNA and core-associated proteins (Figure 1), forming a spherical lattice that encloses the viral ribonucleoprotein complex (vRNP) [36]. NC packages the two copies of the viral RNA into newly formed virions, stabilizes the RNA and the DNA conformations (Figure 1) [37], and contributes to the conversion of the genomic RNA into viral double-stranded DNA (dsDNA) [38]. The packaging of the viral genome depends on the interaction between NC and the RNA packaging signal ψ segment in the 5' LTR [27, 39]. The p6 protein recruits the ESCRT complex, which is necessary for the budding of newly assembled virions at the cell surface [40, 41]. Finally, SP1 and SP2, which separate CA and NC, and NC and p6 (Figure 2), play a crucial role in immature particle assembly and virus infectivity, respectively [42, 43].

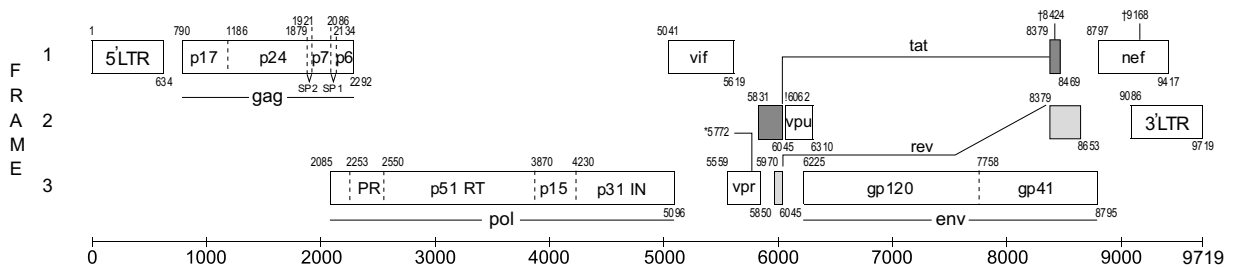


Figure 2. – HIV-1 genome and proteins

The HIV-1 genome sequence of the reference strain HXB2 is represented. The genome encodes for nine genes that themselves encode for 15 proteins. These include the structural proteins (p17, p24, p7, and p6) derived from the precursor Pr55^{Gag}, the viral enzyme proteins (PR, RT, and IN) derived from the precursor Pr160^{Gag-Pol}, and the accessory proteins Tat, Rev, Vif, Vpu, Vpr, and Nef, which are directly encoded by their respective genes. These proteins are generated from the viral mRNA, which can be multiply, partially, or unspliced. Figure adapted from [44] with permission from *Los Alamos National Library*.

The gene *pol* (polymerase) lacks an initiation codon and is only synthesized as part of Pr160^{Gag-Pol}. This precursor undergoes cleavage to generate MA, CA, SP2, NC, the transframe protein (TF or p6*), and the viral enzymes protease (PR), reverse transcriptase (RT, p51), ribonuclease H (RNase H, p15), and integrase (IN). Expression of the Gag-Pol polyprotein is made possible through programmed ribosomal -1 frameshift [45, 46]. The transframe protein p6* plays a regulatory role in PR activity [47]. Following virion budding from the plasma membrane, PR cleaves the Gag and Gag-Pol polyproteins [48, 49], resulting in significant structural rearrangements known as maturation [50]. After viral entry into the host cell, RT converts the viral single-strand (ss)RNA into dsDNA, which can then be integrated into the host genome. RT exists as a heterodimer p66/p51 and functions together with RNase H. It exhibits multiple enzymatic activities, including RNA-dependent and DNA-dependent DNA polymerase activities, as well as RNase H activity [51, 52]. The DNA polymerase can replicate either an RNA or a DNA template. During reverse transcription, RT can switch between the two co-package RNAs, utilizing segments from each RNA as templates. This process favors recombination and consequently increases the frequency of mutations caused by errors made by RT, which lacks proofreading functions [53]. IN, on the other hand, is responsible for integrating reverse transcripts into the cellular genome. IN is co-packaged with viral RNA, NC, and RT into the viral capsid, which forms the vRNP.

The gene *env* encodes for the gp160 polyprotein precursor, which is cleaved to yield the mature surface (SU) glycoprotein known as gp120, and the transmembrane (TM) glycoprotein called gp41. Trimeric spikes composed of gp120/gp41 complexes are incorporated into the lipid bilayer of newly assembled virions. Env, through its interaction

with CD4, downregulates the surface expression of CD4 molecules [54]. The gp120/gp41 complexes initiate the infection process by binding to receptors and co-receptors present on the surface of target cells. The trimeric gp120 SU glycoprotein directly binds three molecules of CD4 on the cell surface. This binding induces a conformational change, resulting in the formation of the coreceptor binding surface [55]. The variability of the gp120, particularly within its V1/V2 loop, facilitates evasion of immune responses and correlates with disease progression [56]. The gp41 TM glycoprotein facilitates the fusion of the envelope protein and the cell membrane. After the conformation change of the envelope protein upon binding of gp120 to CD4 and the coreceptor [55], the fusion peptide of gp41 becomes exposed and penetrates the target cell membrane, leading to the formation of the fusion pore [57].

Essential regulatory genes (tat and rev)

The *tat* and *rev* genes, along with *nef*, are amongst the earliest to be synthesized [58, 59]. Tat (trans-activator of transcription protein), and Rev (regulator of expression of viral proteins) are encoded by separate exons within their associated gene (Figure 2). Tat binds to the TAR hairpin structure present in the 5' LTR of the nascent RNA transcript and recruits the P-TEFb complex, which phosphorylates RNA polymerase II, thereby enhancing the transcription of the viral genome [60]. Tat also influences the HIV-1 RNA capping, splicing, translation, and reverse transcription [61]. It upregulates the expression of the co-receptor CCR5 and CXCR4 [62], as well as pro-inflammatory cytokines (such as TNF, CCL2, IL-2, IL-6, and IL-8) in both HIV-1-infected cells [63] and bystander cells, resulting in a pro-inflammatory environment [64].

Rev is indispensable for the regulation of viral transcription. It forms a complex with the Rev Responsive Element (RRE), a *cis*-acting RNA element located within the second intron of HIV-1, within *env* [65, 66]. This complex facilitates the export of partially spliced and unspliced viral mRNA from the nucleus to the cytoplasm through nuclear pores [65]. In the cytoplasm, the complex disassembles, releasing Rev, which is then capable of returning to the nucleus [67]. This continuous cycle of protein shuttling between the nucleus and cytoplasm ensures the export of HIV RNAs in the presence of a limited quantity of Rev proteins.

Accessory regulatory genes (nef, vpr, vif, and vpu)

The *nef*, *vpr*, *vif*, and *vpu* genes encode associated accessory proteins in HIV, meaning that they are not essential for viral replication. Nef (negative regulatory factor) is abundantly produced during the early phase of the viral replication cycle. This protein affects the cell surface expression of several proteins. Nef downregulates levels of CD4, CD8 β -chain, CD28, mature major histocompatibility complexes class I and II (MHC-I and MHC-II) [68-72], while upregulating CD74, the invariant chain of MHC-II, thereby increasing the levels of immature MHC-II [72].

Multiple effects have been attributed to Vpr (viral protein R). Vpr is involved in the nuclear import of the PIC presumably by facilitating its docking to nuclear pores [73, 74]. Additionally, this protein induces G2/M cell cycle arrest [75, 76], which may lead to host-cell apoptosis [77]. Vpr has been shown to regulate viral transcription either as an activator [78] or a repressor [79].

Vif (viral infectivity factor) is necessary for lentiviral replication in nonpermissive cells [80] and plays a critical role in viral infectivity. It inhibits the cellular protein APOBEC3G, which is responsible for potentially inhibiting the replication by cytidine deamination of the viral genome [81, 82].

Lastly, Vpu (viral protein U) prevents BST-2 (also known as tetherin) from retaining the virus at the plasma membrane [83]. This sequestration of BST-2 facilitates the release of the virion from the cell surface [84]. It is worth noting that HIV-2 and SIVs, which lack Vpu, use Env [85] and Nef [86] respectively, to counteract BST-2 by sequestering it intracellularly. Vpu also enhances the degradation of the CD4 molecule, reducing its accessibility at the cell surface [87].

Other HIV genes (vpx, asp, and fusion proteins)

Several other genes exist but are exclusive to specific HIV subtypes and recombinants, or their functions remain largely unknown. Vpx, present only in HIV-2 (and some SIVs), relieves the SAMHD1-mediated block to reverse transcription, making dendritic cells more susceptible to HIV-2 infection [88, 89], and enhances the virus' ability to infect resting T cells [90, 91]. Some studies revealed the presence of another gene, *asp* (antisense protein), in certain HIV-1 genomes, which is found in one of the negative sense ORFs overlapping the RRE and *env* regions [92]. However, the role of Asp remains largely unclear. Asp can be expressed on the surface of HIV-infected cells, co-localizing with gp120 [93], suggesting a role in viral entry. Additionally, within infected cells, Asp induces autophagy [94], which can increase viral production. Finally, many fusion proteins have been described over the years, mainly identified in laboratory strains [95]. While some of

these fusion proteins exert weaker activity compared to their parental proteins, no crucial role has been identified for any of them, indicating that their expression may be merely an epiphenomenon.

HIV replication cycle

The HIV-1 replication cycle has been studied for decades [96]. It can be broken down into six stages: i) viral entry [96, 97]; ii) reverse transcription [53, 96]; iii) viral integration [96, 98, 99]; iv) viral transcription and translation [96, 100]; v) viral assembly and budding [96, 101, 102]; and vi) viral maturation [96, 101, 102].

Cellular tropism and viral entry

The primary receptor for HIV-1 gp120 is the CD4 molecule expressed at the surface of CD4⁺ T lymphocytes, and myeloid cells such as macrophages or dendritic cells (DC). DC can sustain viral replication *in vitro* [103] but also internalize the virus and transmit it to CD4⁺ T cells [104]. This refers to trans-infection, the primary mode of HIV infection meaning infection through direct cell-to-cell contact. There are two types of trans-infection: one occurs via an immunological synapse between APCs and CD4⁺ T cells [105], while the other occurs via a virological synapse between two CD4⁺ T cells [106]. Contact between free infectious particles and the cell membrane can also occur, especially in the early stages of HIV infection when viral particles are largely present.

The process of viral entry can be divided into three steps. Firstly, the virion interacts with the cells through specific binding between gp120 and integrin $\alpha_4\beta_7$ [107, 108] or Dendritic Cell-specific C-type lectin (DC-SIGN) expressed on DC [105], or non-specific attachment

to heparan sulfate proteoglycans on macrophages [109, 110]. These interactions favor close interactions between gp120 and the surface CD4 molecules, as well as co-receptors CCR5 (or CXCR4, depending on the virus tropism), resulting in conformational changes of gp120 and gp41. The fusion peptide of gp41 translocates and inserts into the host cell membrane and triggers the gp41 to undergo a hairpin-like rearrangement. This conformational change leads to the fusion between the viral and host cell membranes. This fusion process releases the viral core into the cytoplasm [96, 97, 111]. However, the exact location of fusion, whether it occurs directly at the plasma membrane [112] or in the endosome following endocytosis [113], is still a topic of debate. Both mechanisms are thought to exist, but Miyauchi et al. presented evidence that plasma membrane-fusion events were dead-ends and proposed that only endosomal fusion is productive [96, 113].

Reverse transcription and pre-integration events

The reverse transcriptase complex (RTC) consists of the viral enzymes RT, PR, and IN, the viral proteins MA, CA, NC, Vif, Tat, Nef, and Vpr, as well as several cellular proteins [114, 115]. Within the RTC, RT synthesizes the first minus-strand DNA from the positive strand genomic RNA using the tRNA^{Lys3} previously incorporated into the viral particle during assembly. This tRNA^{Lys3} interacts with the primer binding site (PBS) located in the 5' LTR. Then, the U5 and R regions are reverse transcribed, and the RNA template is degraded by RNase H [53]. The newly synthesized short DNA is then transferred to the 3' end to transcribe the minus-strand DNA. The RNA template is degraded except for the purine-rich sequence (polypurine tract or PPT), which serves as the primer for initiating the synthesis of the positive-strand DNA [53]. The U3, R, and U5 regions from the 3' LTR

are then synthesized, and this DNA fragment is transferred to the 5' end to complete the transcription of the positive-strand DNA (Figure 3). Since the virions package two identical positive RNA copies [20], the RT can switch between the two copies, leading to recombination as well as mutations such as deletion, insertions, and duplications during reverse transcription [53]. Reverse transcription is facilitated by the interaction of the RTC with cellular cofactors [116]. The resulting viral DNA is also referred to as the provirus.

Simultaneously with the reverse transcription, the RTC traffics towards the nucleus using the microtubules network [117, 118]. It has been described that disrupting the microtubule-mediated trafficking inhibits HIV-1 infection [119], as well as core uncoating [96, 120, 121]. However, the precise localization (cytoplasm, nuclear surface, or inside the nucleus) and timing (early after viral entry or late before the viral integration) of capsid uncoating are still debated [122]. Some studies have shown that there is no viral capsid protein associated with the RTC, suggesting that uncoating occurs immediately after viral entry [96, 123, 124]. Others have described that some viral CA remains associated with the RTC, mediating nuclear import [96, 125, 126]. Finally, other studies have observed that the viral core remains intact until the RTC reaches the nuclear pore complex (NPC), where uncoating is completed in the vicinity of nuclear pores, thus protecting the viral genome from cytosolic sensors [127-129].

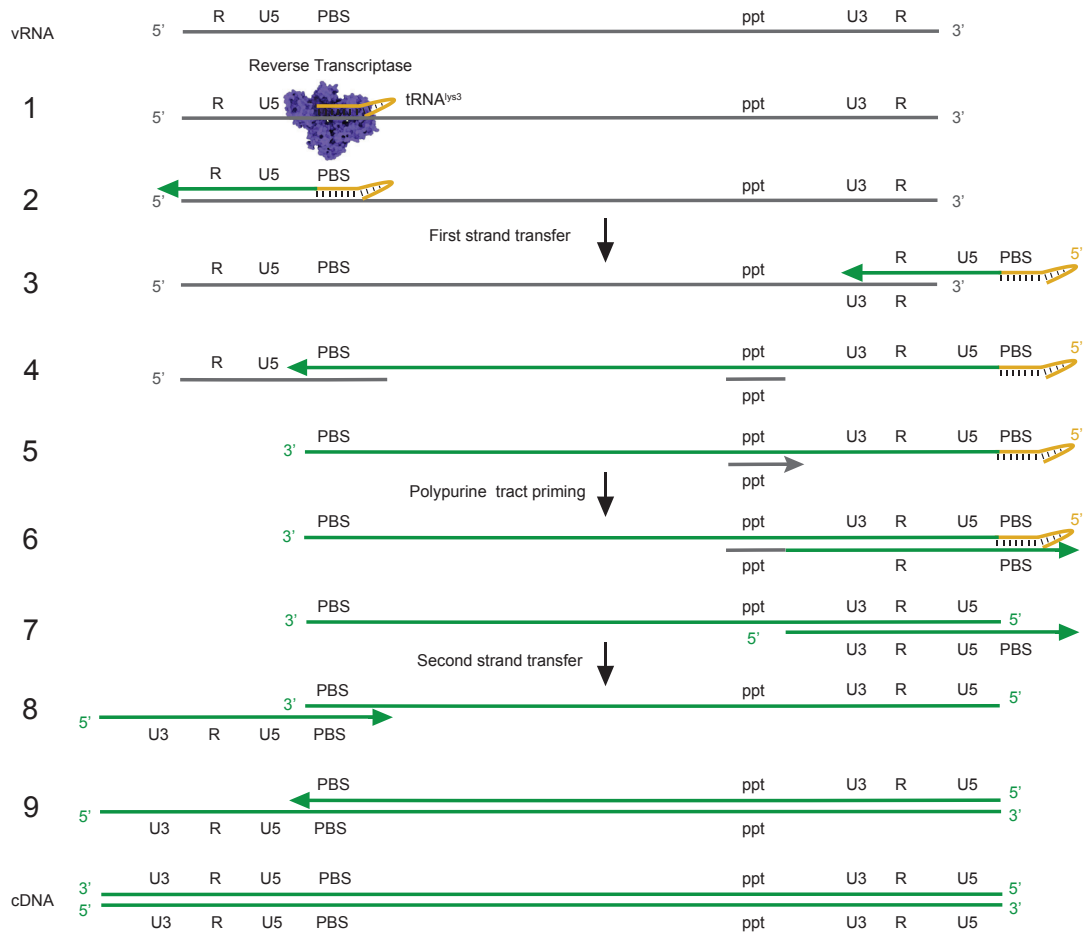


Figure 3. – Conversion of the single-stranded RNA into double-stranded DNA

The viral genomic RNA (in grey) serves as template, and the tRNA^{Lys3} acts as primer for the RT. 1) RT and tRNA^{Lys3} anneal near the 5' end of the vRNA template. 2) RT initiates the reverse transcription, generating the first minus-strand DNA until it reaches the repetitive region R at the 5' end. 3) The first transfer occurs, resulting in the extended primer annealed to the complementary repetitive R sequence at the 3' end. 4) RNase H activity degrades the RNA template, except for the PPT sequence, allowing complementary DNA (cDNA) synthesis to proceed further. 5) The PPT sequence serves as a primer for the synthesis of the positive-strand DNA, 6) The synthesis extends until it reaches the PBS region at the 3' end, at which point RNase H degrades the remaining RNA. 7) The complementary PBS sequence at the 5' end facilitates the second strand transfer. 8) Synthesis of the positive-strand cDNA continues. 9) The PBS region of the minus-strand is extended to copy the U3, R, and U5 regions, resulting in the formation of complete double-stranded DNA. Figure adapted from [130] with permission from *Current Opinion in Structural Biology*.

Nuclear import and viral integration

Upon arrival at the nuclear pore, the RTC transitions into a pre-integration complex (PIC) that is transported through the NPC. NPC are large multiproteic structures that enable passive and active exchanges between the nucleus and the cytoplasm. Due to its size, the PIC requires active trafficking into the nucleus through interactions between CA and nucleoporins (NUP) NUP153 and NUP358 [131, 132]. Two other cellular proteins, TNPO3 and CPSF6, which are not part of the NPC, also play roles in nuclear import [133]. CPSF6, in conjunction with TNPO3, binds CA to disengage the PIC from the NPC and move it toward the nuclear periphery. Subsequently, TNPO3 releases the CPSF6-PIC complex, which translocates through the nucleus to actively transcribed gene-producing RNAs requiring polyadenylation [98]. The remaining CA is then dissociated, and the interaction between viral IN and LEDGF/p75 mediates integration.

There are no specific integration sites or sequences that predict where the viral genome will be integrated. However, the integration site is associated with transcriptionally active regions of the host genome [134-136]. Viral IN performs a series of DNA cutting and joining reactions. Firstly, it hydrolyses and removes two nucleotides from each 3' end of the linear viral DNA [98, 137]. The resulting 3' ends of the viral DNA are terminated with a conserved CA sequence. Secondly, viral IN catalyzes the insertion of the viral DNA into the host chromosomal DNA. The 3' ends of the viral DNA open the cellular DNA and join with their respective opposite strands. Subsequently, cellular enzymes complete the integration process [98].

However, not all viral genomes will integrate into the host genome. Circular DNA can be observed due to autointegration, resulting in the formation of 1-LTR circles or 2-LTR

circles mostly observed during the active replication of HIV. 1-LTR circles are exclusively formed through homologous recombination between two LTR, while 2-LTR circles arise from non-homologous end-joining DNA repair events [138]. It has also been described that DNA can remain linear and non-integrated in the host cell nucleus [139].

Viral transcription and translation

Following integration, the viral genome undergoes transcription in two phases. The initial phase is Tat-independent and relies on the interaction between the 5' LTR and host cell transcription factors. The LTR contains several regulatory elements, including Sp1 binding sites and a TATA box that recruits TATA-binding protein (TBP). TBP facilitates the recruitment of TBP-associated factors (TAFs), forming the general transcription factor TFIID at the transcription start site (TSS), along with RNA polymerase II. TBP binding to the LTR is crucial for the formation of the preinitiation complex and subsequent HIV transcription. Additionally, the LTR contains binding sites for NF- κ B and the nuclear factor of activated T cells (NFAT), which promote transcription [23]. Activation of this step requires a basal transcriptional activity to initiate viral transcription.

The preinitiation complex initiates the basal transcription of the provirus, resulting in the production of a long viral RNA similar to genomic RNA (gRNA). Similar to cellular RNA, this RNA undergoes post-transcriptional modifications (capping, polyadenylation, splicing) before being exported into the cytoplasm. HIV-1 harbors four different splice donor sites and eight acceptor splice sites, resulting in the generation of over 40 different spliced mRNA species (Figure 4) [140]. During the early phase of infection, only short multiply spliced mRNAs (≤ 2 kb) encoding Tat, Rev, and Nef are produced. As the infection

progresses, more partially spliced mRNAs (ranging from 4.3 to 5.5 kb) are generated, encoding for Env and the accessory proteins Vif, Vpr, and Vpu. The latest products are full-length unspliced transcripts, which give rise to mRNAs encoding the Gag-Pol polyprotein, as well as the gRNA that will be encapsidated into newly formed virions [96].

Firstly, the multiply spliced mRNAs are exported into the cytoplasm through an endogenous cellular pathway and translated into Tat, Rev, and Nef proteins. Nef, by downregulating CD4, inhibits the superinfection of the cell by other virions that could lead to cell death. Then, the second phase of HIV transcription is Tat-dependent. Tat binds to TAR, which is located before the TSS in the LTR, and recruits P-TEFb, which phosphorylates and releases RNA Pol II from the promoter, thereby increasing proviral transcription [140]. On the other hand, Rev is a key regulator of alternative splicing. By interacting with the RRE sequence located in *env* of partially and unspliced mRNAs [65], Rev facilitates their export through nuclear pores into the cytoplasm via the CRM1 pathway and protects them from degradation.

Once in the cytoplasm, the viral transcripts can be translated into viral proteins. Usually, translation initiation is cap-dependent and involves scanning from the 5' end until an initiator AUG in a Kozak consensus sequence is recognized. However, HIV-1 possesses RNA structural elements that hinder the conventional ribosomal scanning mechanism. The use of cap-independent initiation through an internal ribosome entry sequence (IRES) circumvents the inhibition of scanning ribosomes [141, 142]. Slippery sequences and RNA elements called frameshift stimulatory signal (FSS) control ribosomal frameshift, enabling the translation of the genes from other ORFs [45, 46]. Elongation continues until ribosomes encounter a stop codon, triggering translation termination.

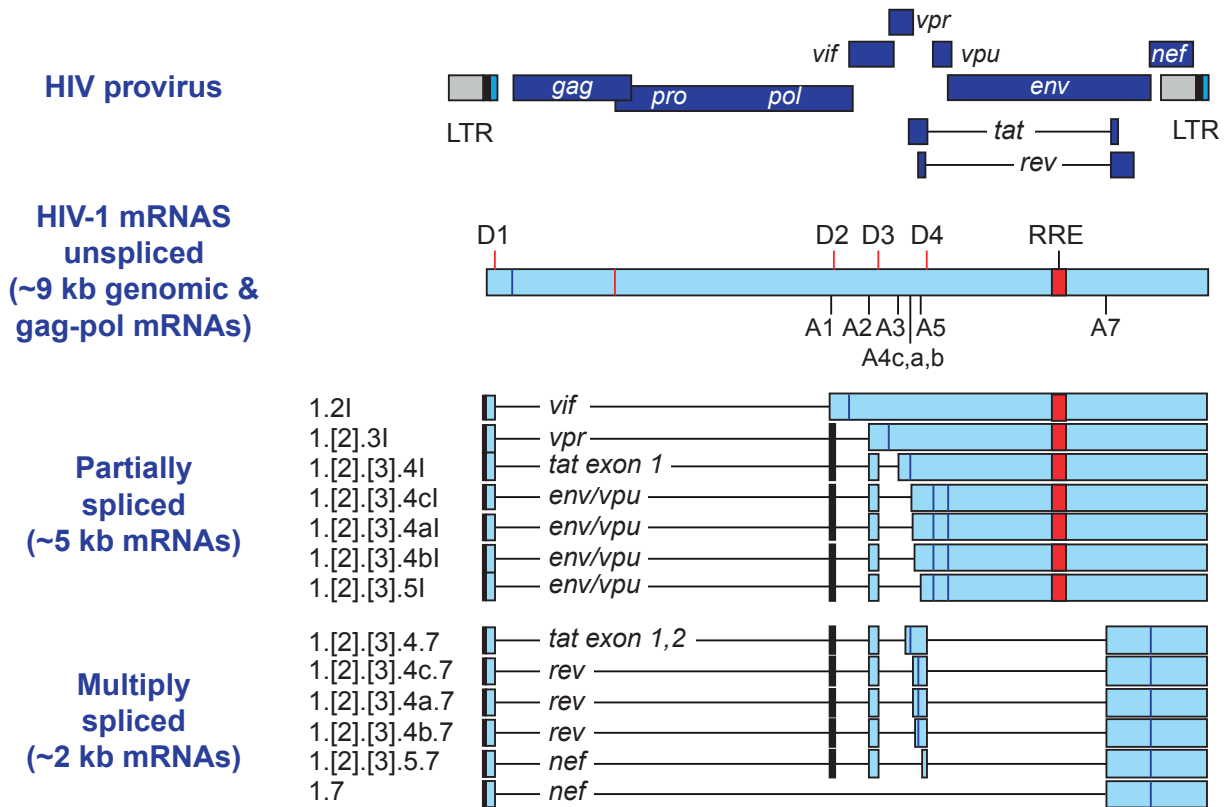


Figure 4. – Alternative splicing of HIV-1 gene expression

The HIV-1 provirus contains multiple donor (D) and acceptor (A) splicing sites that allow for alternative splicing during HIV-1 transcription. In the early stages of transcription, in the absence of Tat and Rev, the mRNAs are multiply spliced encoding for Tat, Rev, and Nef. Once translated in the cytoplasm, Tat returns to the nucleus, where it binds to the TAR element located in the 5' LTR, enhancing HIV-1 transcription. Subsequently, Rev binds to the RRE element (in red), facilitating the export of partially and unspliced transcripts to the cytoplasm. This export process enables the production of the Env glycoprotein and accessory proteins Vif, Vpr, and Vpu from the partially spliced transcripts, as well as the polyprotein Gag-Pol from the unspliced mRNAs. The unspliced transcripts also serve as genomic RNA to produce new virions. The non-coding exon 1 is present in all mRNA species, while one or both non-coding exons 2 and 3 may be included in some species. The figure illustrates exon compositions of the RNA species, with "1" indicating partially spliced species. The brackets indicate species that lack exon 2, lack exon 3, or lack both exons 2 and 3, or possess both exons 2 and 3. The blue bars indicate the locations of AUG codons used for protein synthesis initiation. Figure adapted from [140], originally adapted from [143] with permission from *Elsevier*.

Viral assembly and budding

For new HIV-1 virions to be infectious, several components, both viral and cellular, are required. These include two copies of the viral gRNA, the viral enzyme PR, RT, and IN, the Gag and Gag-Pol polyproteins, Vpr, the Env glycoproteins, and the cellular tRNA^{Lys3}. Low levels of Vif and Nef can also be present in the virions. Assembly at the plasma membrane is mainly coordinated by the Gag polyproteins. MA is responsible for binding the Gag protein to the plasma membrane and concentrating Env proteins. NC binds the full-length HIV genome by interacting with the ψ locus, thereby incorporating it into the virus particle. Gag/Gag-Pol multimerization is mediated by the CA domain of Gag, resulting in the formation of a lattice composed of radially oriented Gag proteins, forming the immature virion [144, 145]. Then, interactions between the p6 domain and the TSG101 subunit hijack the ESCRT complex to the budding site. The p6 domain also recruits the VSP4 protein to specific membrane sites where the assembly of immature virions and fission events occur [102, 146].

Viral maturation

The final step of the replication cycle is viral maturation. This step occurs concomitantly with (or directly follows) budding and relies on the cleavage of Gag and Gag-Pol polyproteins by the viral PR. Maturation is responsible for the formation of single structural particles necessary to form CA, MA, NC, and p6, as well as the viral enzymes. Cleavage of Gag also separates the immature capsid from the viral gRNA, allowing the rearrangement of the capsid into the mature spherical lattice structure. Then the nucleocapsid binds to the viral gRNA, protecting it from degradation once the virus infects a new cell [102, 147].

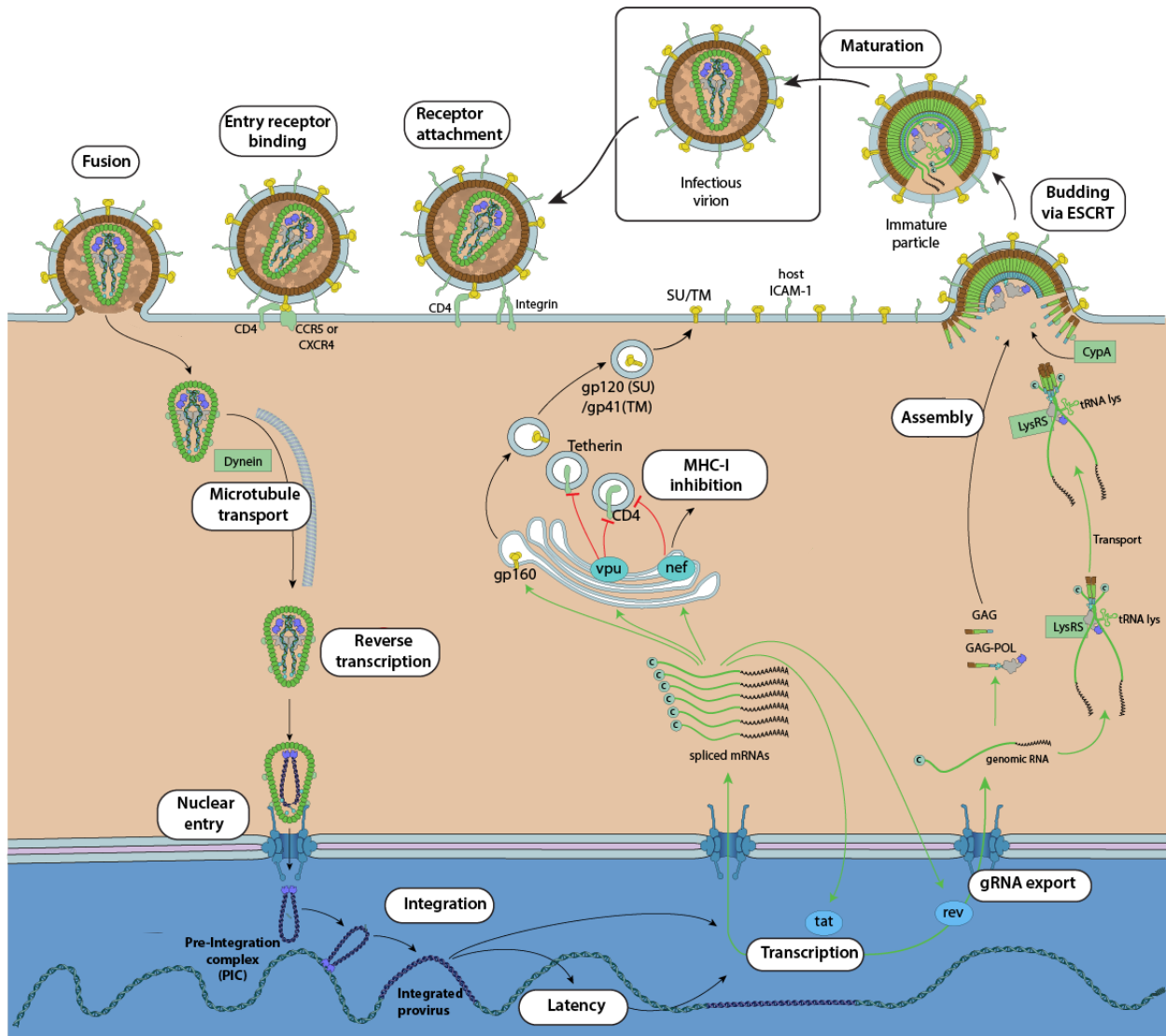


Figure 5. – HIV-1 replication cycle in CD4⁺ T cells

The interaction between gp120 and its receptor CD4, along with the coreceptor CCR5 (or CXCR4), allows virus attachment to the cell surface. It remains unclear whether the virus fuses with the cell membrane or is endocytosed via a clathrin-dependent mechanism. Following attachment, the viral capsid is released into the cytoplasm, and viral gRNA is reverse transcribed concomitantly with the RTC traffics towards the nucleus via the microtubule network. Uncoating takes place during nuclear entry, allowing the release of the PIC into the nucleus, where the viral DNA integrates into the host genome. The provirus can either be transcribed or methylated by host factors, leading to viral latency. Viral mRNA and gRNA are transcribed, exported into the cytoplasm, and translated into viral proteins enabling the assembly and budding of immature viral particles. Newly released virions undergo viral maturation, resulting in the formation of infectious particles. Figure adapted with permission from ViralZone, SIB Swiss Institute of Bioinformatics.

Stages of HIV-1 infection

The clinical course of HIV-1 infection can be divided into three stages: early/acute, chronic, and progression to AIDS (Figure 6). The early/acute phase typically occurs within the first few weeks of infection. The asymptomatic chronic phase in PLWHIV can last around 7-10 years without treatment. However, some cases have shown rapid disease progression, lasting only 3-5 years, and these people are referred to as “rapid progressors”. Conversely, there are cases of slow progression, taking up to 10-20 years with no disease progression and these people are referred to as “Long-Term Non-Progressors” (LTNPs) [148]. LTNPs maintain a CD4⁺ T cell count greater than 500 cells/ μ L of blood and have a plasma viral load lower than 10'000 copies/mL of blood. However, LNTNs eventually progress to AIDS without treatment as they are unable to control the viral load. Nevertheless, there is a group of PLWHIV referred to as “Elite Controllers” (EC) who can maintain CD4⁺ T cell counts and undetectable viremia without treatment [149]. AIDS represents the final stage of HIV infection, where the immune system breaks down completely, leading to the development of opportunistic infections and, ultimately, death in HIV-infected individuals.

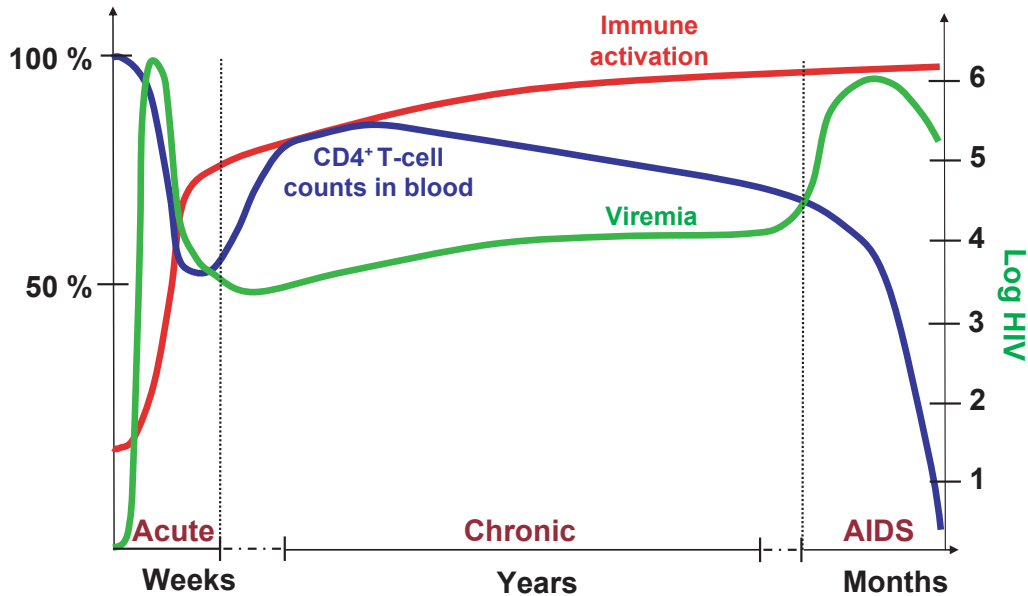


Figure 6. – Stages of HIV-1 infection

HIV-1 infection can be divided into three clinical phases: early/acute, chronic, and AIDS. In the early/acute phase, HIV viremia reaches its peak, accompanied by significant loss of CD4⁺ T cells in the blood. During the chronic phase, which can last for years, the viral load decreases to a stable set point. CD4⁺ T cell counts in the blood show partial recovery but gradually decline, while immune activation increases. Without ART, the infection progresses to AIDS, characterized by an accelerated loss of CD4⁺ T cells and increased viremia. Figure adapted from [150] with authorization by the *Nature Publishing Group*.

Early/Acute phase

During this period, the disease progression is influenced by both immune responses and the establishment of the viral reservoir. The primary mode of transmission for most individuals occurs through sexual contact with PLWHIV, with the viruses being transmitted via the genital tract or rectal mucosa [151]. Additional modes of transmission include the sharing of needles/syringes among drugs' users, mother-to-child transmission, as well as blood transfusion. The initial viral inoculum consists of a diverse mixture of HIV quasi-species, however, only a small proportion of viruses, known as transmitter/founder (T/F)

viruses, can establish an infection [152]. Compared to viruses isolated during chronic HIV infection, T/F viruses show a preferential utilization of CCR5, increased infectivity and replication capacity, resistance to type I IFN, and specific Env glycosylation patterns. The local inflammation at the site of infection triggers the recruitment of additional target cells. Furthermore, DC and myeloid cells can capture the virus, which then reaches the LN through infected CD4⁺ T cells and antigen-presenting cells (APCs) [152]. Subsequently, the virus further spreads to additional CD4⁺ T cells within the LN. This initial phase, known as the “eclipse phase”, is characterized by the absence of detectable viral RNA.

From the mucosa-draining LN, the virus disseminates to secondary lymphoid organs, particularly gut-associated lymphoid tissue (GALT). During this period, plasma levels of viral RNAs peak, reaching several million copies per mL of blood, while the number of CD4⁺ T cells drastically decreases both in the blood and the GALT [153]. In SIV models, vaginal infections resulted in increased levels of pro-inflammatory cytokines that parallel the levels of viral RNA [154, 155]. Some of these cytokines exhibit antiviral activity, such as type I interferons (IFNs), and enhance both innate and adaptive immune responses to HIV-1 infection. This overall activation also leads to an increased T cell turnover, promoting viral replication and subsequent cell death of most effector cells. However, even in the absence of ART, the peak of plasmatic HIV RNA decreases to a constant steady-state level during the chronic phase of infection, and the CD4⁺ T cell count in the blood partially recovers, albeit not in the GALT [153]. The extent of viremia control and the magnitude of the viral set point depend on the primary HIV-specific T cell responses to the T/F virus [156].

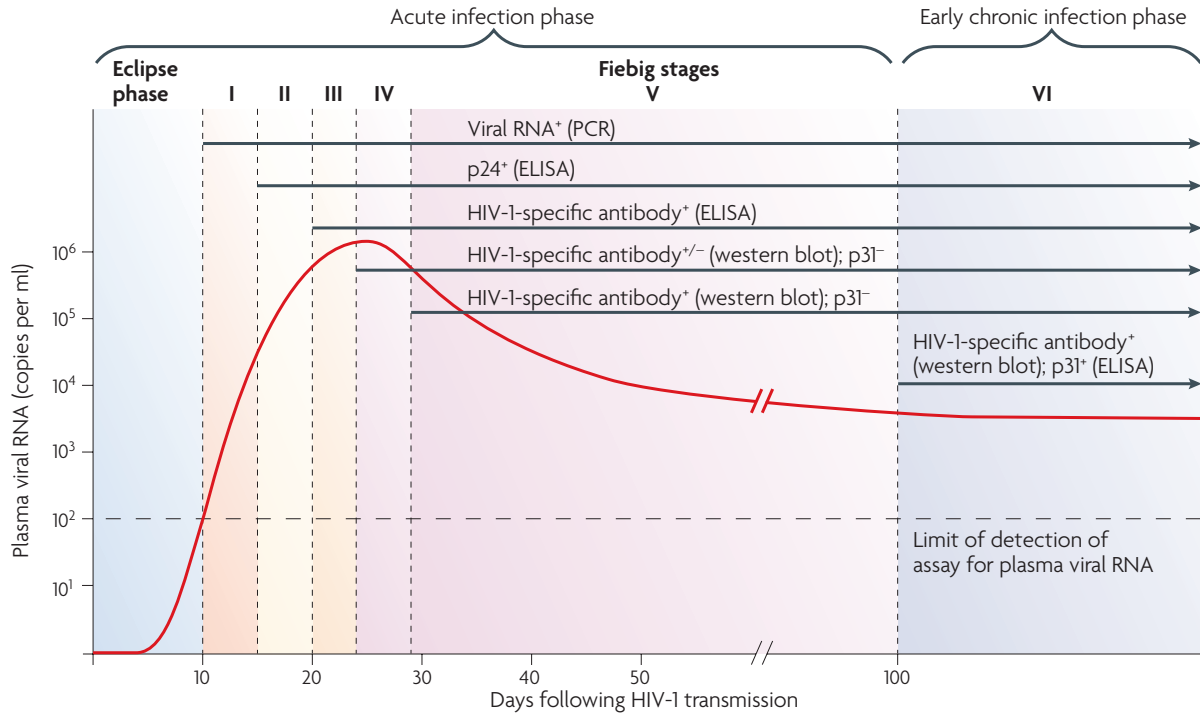


Figure 7. – Subclassification of early/acute HIV infection into Fiebig stages.

PLWHIV progress through different Fiebig stages during the early/acute phase of infection [157]. These stages are defined by the sequential detection of HIV infection using different clinical diagnostic tests (PCR for vRNA, ELISA for p24 antigens, western blots and ELISA for HIV-specific antibodies). The final Fiebig stage VI corresponds to the early chronic phase of HIV infection and is characterized by the establishment of a stable HIV plasma viremia (red line). Figure from [158] with authorization by *Nature Springer*.

The early/acute phase of HIV infection can be subdivided into Fiebig stages I-VI, named after Dr. Eberhard W. Fiebig. These stages are determined by the sequential detection of HIV using different clinical diagnostic assays (Figure 7) [157].

Chronic phase

During the chronic phase of HIV infection, the plasma viremia remains relatively stable (Figure 6). While this phase is generally asymptomatic, the virus continues to replicate,

and the high turnover of CD4⁺ T cells leads to their gradual depletion. Multiple mechanisms contribute to the loss of CD4⁺ T cells. The death of productively infected, which concerns approximately 5% of the total CD4⁺ T cells, implies caspase-3-dependent apoptosis [159]. When the virus infects resting and non-permissive cells, it leads to abortive infection, triggering the accumulation of cytosolic viral DNA detected by DNA sensors, components of the innate immune system, and resulting in cell death via caspase-1-dependent pyroptosis [160]. Caspase-3 activation induces apoptosis without inflammation, whereas pyroptosis creates a highly inflammatory environment as dead cells release their cytoplasmic contents into the extracellular space [161]. Thus, pyroptosis establishes a pathogenic cycle of CD4⁺ T cell depletion and chronic inflammation. Dying CD4⁺ T cells release inflammatory signals that attract more cells, which subsequently become infected, contributing to disease progression and tissue damage [162]. However, cell death is not limited to infected cells alone. Viral proteins may also be released into circulation and induce apoptosis in non-infected bystander cells. For instance, gp120 activates the CD95/CD95L pathway, Nef-expressing T cells coexpress CD95L, making them capable of killing CD95-expressing cells, and Tat upregulates CD95/CD95L expression on bystander cells, increasing their susceptibility to CD95-induced apoptosis. Moreover, Vpr expression plays a role in the death of non-infected cells by permeabilizing the mitochondrial membrane, releasing cytochrome c, and triggering cellular apoptosis [163].

Natural Killers (NK) and HIV-specific CD8⁺ T cells are associated with controlling plasma viremia during the chronic phase [156, 164]. However, despite their antiviral functions, these cells are unable to clear the infection completely, resulting in persistent plasma

viremia. Indeed, prolonged exposure to antigens leads to progressive dysfunctions of HIV-specific T cells [165, 166]. This exhaustion is characterized by impaired proliferation, loss of polyfunctionality, upregulation of activation and inhibitory markers, and ultimately, apoptosis of HIV-specific CD8⁺ T cells [167, 168]. This concept will be further detailed later in the introduction. In addition to CD8⁺ T cell exhaustion, the virus has the ability to acquire mutations. Cytotoxic T lymphocyte (CTL) responses during the acute phase temporarily reduce plasma viremia by exerting immune pressure. However, these mutations render the virus unrecognizable to CD8⁺ T cells, allowing it to escape immune responses [169, 170].

AIDS

The progressive, but inevitable, depletion of CD4⁺ T cells, coupled with the loss of HIV control by CTLs, lies at the core of AIDS. During this stage, the regenerative capacity of the immune system is ultimately compromised, leading to a significant decline in peripheral CD4⁺ T cell blood count to levels below the minimum threshold (<200 cells/ μ L of blood). The appearance of AIDS-related conditions may define this stage, irrespective of the CD4⁺ T cell count. These conditions encompass various infections such as *Pneumocystis jirovecii*, *Candidiasis*, *Cytomegalovirus retinitis*, *Mycobacterium tuberculosis*, *Cryptococcosis*, and certain cancers that are less common in immunocompetent individuals, including Kaposi's sarcoma, non-Hodgkin's lymphoma (such as diffuse large B cell lymphoma and Burkitt lymphoma), as well as HIV-related encephalopathy due to neurocognitive dysfunctions. The uncontrolled nature of these

conditions, driven by the depletion of CD4⁺ T cells, contributes to the mortality of individuals infected with HIV.

Antiretroviral therapy

Just a few years after the identification of HIV, the first antiretroviral (ARV) drugs were approved for HIV treatment. Prior to that, PLWHIV received palliative care to alleviate symptoms and treat opportunistic infections. In 1987, Zidovudine (also known as Azidothymidine or AZT), a nucleoside-analog reverse transcriptase inhibitor (NRTI), was introduced to the market [171]. However, the emergence of drug-resistant viral strains, resulting from mutations during reverse transcription or mediated by APOBEC3G, hindered the effectiveness of AZT as a monotherapy [172]. As a result, the combination of two or more classes of antiretroviral drugs, initially dual and later triple combination, became the gold standard for treating HIV-infected individuals. This therapeutic approach, known as Highly Active Antiretroviral Therapy (HAART), enables better viral load control, immune system restoration, reduction in AIDS-related morbidity and mortality, and impedes the development of resistance against drugs targeting multiple stages of the viral replication cycle [173] (Figure 8). Consequently, ART has transformed HIV from a fatal condition to a manageable chronic infection. However, not all PLWHIV have access to ART, with only 75% of all PLWHIV estimated to be receiving treatment in 2021 [12]. Access to ART varies significantly across regions, with the highest percentage in Western and Central Europe and North America (85%), and the lowest in the Middle East and North Africa (50%) [12].

Current combined ART regimens are classified based on the specific phase of the viral replication cycle they target. The Food and Drug Administration (FDA) has approved seven classes of antiretroviral drugs: nucleoside/nucleotide-analog reverse-transcriptase inhibitors (NRTIs and NtRTIs), non-nucleoside reverse-transcriptase inhibitors (NNRTIs), integrase nuclear strand transfer inhibitors (INSTIs), protease inhibitors (PIs) and entry/fusion inhibitors, CCR5 antagonist, and post-attachment inhibitors. Most combinations consist of two NRTIs with either a NNRTI, PI, or INSTI.

Reverse-transcriptase inhibitors (RTIs) block the viral RT (Figure 8). NRTIs and NtRTIs function in a similar manner. They are analogs of deoxynucleotides and compete with them by incorporating into the viral DNA during reverse transcription. The absence of a hydroxyl group at the 3' position acts as a chain terminator, halting DNA elongation [174]. However, NRTIs/NtRTIs also compete as substrates for host DNA synthesis, leading to serious toxicities associated with their impact on mitochondrial DNA [175]. NNRTIs differ from NRTIs/NtRTIs as they are noncompetitive inhibitors of reverse transcriptase. They bind to the reverse transcriptase enzyme, inducing a conformational change that reduces its catalytic activity [175].

INSTIs inhibit the viral IN, preventing the strand transfer step by removing the 3'-processed DNA from the active site. This action blocks the incorporation of viral DNA into the host genome (Figure 8). This inhibition of IN leads to the accumulation of 1 and 2-LTR circles as well as linear DNA forms [176].

PIs bind to the HIV PR, impeding the cleavage of the Gag-Pol polyprotein and consequently hindering the maturation of new virions [175] (Figure 8). Virus particles produced in the presence of PIs are defective and mostly non-infectious.

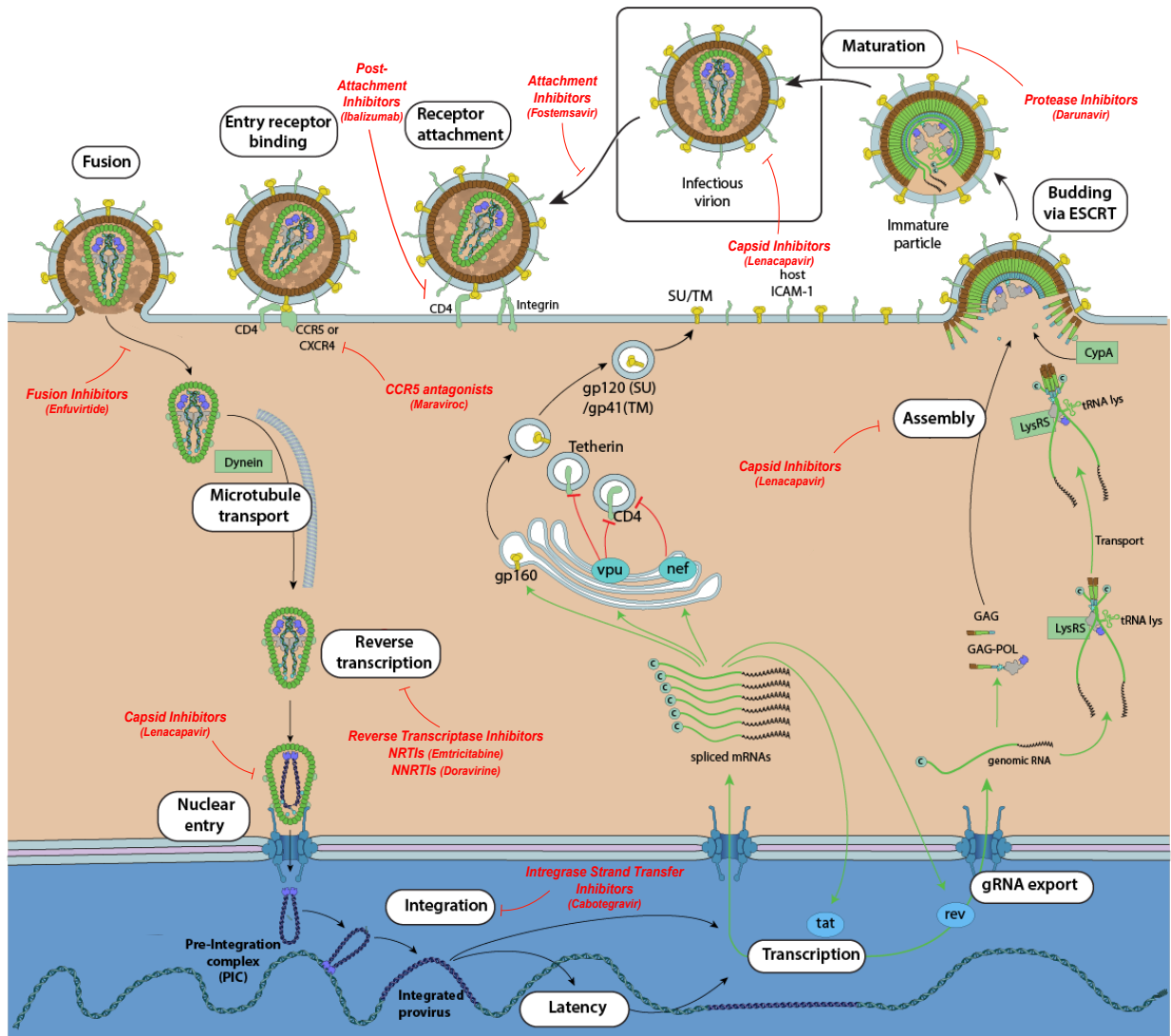


Figure 8. – Classes of current ART regimens and mechanisms of action

HIV replication can be inhibited at multiple steps by different classes of antiretrovirals (red lines). The latest antiretroviral approved by the FDA is mentioned as an example. Figure adapted with permission from ViralZone, SIB Swiss Institute of Bioinformatics.

Entry/fusion inhibitors are designed to block the initial steps of HIV infection and encompass the last three classes of FDA-approved drugs (Figure 8). Enfuvirtide, the only fusion inhibitor available, binds to the gp41 protein on the surface of the virus particle, maintaining the molecule in a pre-fusion conformation [175]. This inhibits the close proximity required for fusion between the virus and cell membranes. Maraviroc, a CCR5

antagonist, binds to the HIV coreceptor, preventing its interaction with HIV gp120 [175]. However, HIV can undergo a tropism shift, allowing it to target CXCR4, which is associated with disease progression [177]. Currently, no CXCR4 antagonists have been approved for clinical use, although many have been discovered and are under development [178]. Lastly, the post-attachment inhibitor Ibalizumab is a humanized monoclonal antibody that binds to CD4 on the cell surface, impeding the conformational change in the CD4-gp120 complex required for viral entry [179].

In addition to the seven classes of antiretroviral drugs, the FDA has recently approved two additional drugs. Fostemsavir, an attachment inhibitor, was approved in July 2020. Similar to Ibalizumab, Fostemsavir has been developed for individuals with multiple-drug-resistant HIV infections. Fostemsavir directly binds to gp120 and locks it into a closed state, preventing the conformational change necessary for the initial interaction between the virus and CD4 on the cell surface. As a result, it inhibits attachment and subsequent entry into the cells [180] (Figure 8). Furthermore, recent studies have shown that Fostemsavir can block the immunomodulatory activities of HIV-1 soluble gp120 by reducing its shedding, thereby protecting bystander cells from antibody-dependent cellular cytotoxicity (ADCC) [181].

Finally, Lenacapavir, a capsid inhibitor was approved on December 22, 2022. Similar to Fostemsavir, Lenacapavir is particularly useful in individuals with multiple-drug-resistant HIV infections. It interferes with the capsid-mediated nuclear uptake of the PIC and binds to and stabilizes curved capsid assemblies, inhibiting the functional disassembly of virus cores. This indicates that Lenacapavir acts at both early and late stages of the viral cycle [182, 183] (Figure 8).

HIV reservoirs

In the early 90s, the use of combined ART regimens raised hope for PLWHIV and researchers. Indeed, the first results demonstrated a decrease in plasma viremia, which became undetectable with prolonged therapy [184, 185]. These findings led the community to believe that HIV-1 infection could be eradicated within 3 years of continuous ART treatment [185]. Unfortunately, a few weeks after ART cessation, viral rebounds occur indicating that the virus is not cleared from the body. In some cases, the reemergence of HIV-infected cells is observed after a few months of interruption. These people, known as “Post-Treatment Controllers” (PTC), appear to prevent viral rebound through different mechanisms compared to EC. Indeed, PTC do not exhibit greater HIV-specific CD8⁺ T cell responses than those observed in EC. Additionally, while ECs often possess the protective class I human leukocyte antigen (HLA)-B*27 and HLA-B*57 alleles, PTC express HLA-B*07 and HLA-B*35, which are associated with rapid progression to AIDS and poor clinical outcomes [186]. The existence of a viral rebound despite prolonged ART therapy confirms the presence of persisting infected cells. Studies have shown that after HIV exposure and integration into the host genome, some viruses remain transcriptionally silent [187, 188] and these proviruses resume production upon reactivation of the T cell by its cognate antigen.

HIV latency

A significant hurdle in achieving an HIV cure is the persistence of latent viral reservoirs. Among these reservoirs, long-lived, resting, memory CD4⁺ T cells contribute the most to the HIV viral reservoirs [188, 189]. For years, it was believed that these reservoirs were

transcriptionally silent and had little immunological impact [190]. However, our studies and others suggest a different reality. The presence of spliced and unspliced viral RNA in HIV-infected cells indicates that complete silencing is rare [190, 191]. While these viral transcripts may be abortive [191], they have been associated with pro-inflammatory signaling *in vitro* [192, 193], and could therefore contribute to chronic inflammation during ART. HIV latency exists in two forms: pre-integrational and post-integrational latency, depending on whether the virus has integrated into the host genome or not [194].

Pre-integrational latency

Pre-integrational latency may occur as a result of failed steps or blocks during HIV infection. Unintegrated linear viral DNAs, which are capable of integration and can persist in infected cells, are necessary for pre-integrational latency. Activation of quiescent CD4⁺ T cells after infection increases the amount of integrated DNA [195, 196]. In resting CD4⁺ T cells, the capsid, viral DNA, and centrosome colocalize more than 21 days post-infection, and activation of these cells also enhances the integration of viral DNA, leading to viral production [197]. In PLWHIV receiving ART therapy, the majority of unintegrated DNA exists in circular forms (1- and 2-LTR circles). Recent studies have shown that these circular DNAs can serve as substrates for the HIV IN, meaning that they could lead to proviral integration and therefore contribute to the pre-integration latency [198]. However, the half-life of unintegrated linear viral DNAs in CD4⁺ T cells appears to be short, lasting approximately 11 days [199]. Although macrophages and brain tissues retain unintegrated linear DNA for a longer period of time [194], this suggests that the pre-integrational latency plays a minor role in the viral reservoir.

Post-integrational latency

Post-integrational latency represents the primary form of HIV latency, occurring when the cellular transcription machinery is blocked. In resting CD4⁺ T cells, both NFAT and NF-κB remain in the cytoplasm limiting transcriptional activity [200]. Post-transcriptional latency is also influenced by the integration site of the viral genome and the chromatin organization. The provirus preferentially integrates into chromatin regions near the nuclear membrane, characterized by active transcription chromatin marks [135, 201]. Integration into active genes facilitates the basal expression of the viral genome, which is necessary for subsequent Tat-mediated transactivation [202]. Sometimes, HIV can integrate into non-genic or pseudogenic genomic regions, which have been associated with a deeper level of viral latency [203]. Furthermore, integration near genes involved in cell growth and division can drive clonal expansion and persistence of HIV-infected cells, potentially contributing to the development of malignancies [204].

Transcriptional “latency”

Non-epigenetic mechanisms

In addition to pre- and post-integrational latency, transcriptional regulation by cellular factors can induce HIV latency. For instance, the involvement of long non-coding RNAs (lncRNA) regulating HIV transcription has been described. LncRNAs function in *cis*, *trans*, or both and are known to modulate gene expression. They can act as key regulators at the transcriptional and post-transcriptional levels by influencing polymerase functions and altering protein functions through changes in phosphorylation states [205-207]. In HIV infection, lncRNAs have been implicated in both maintaining viral latency and facilitating

viral replication in host cells [208, 209]. Two lncRNAs, NEAT1 (Nuclear Enriched Abundant Transcript 1) and NRON (Non-coding Repressor of NFAT) have been found to be upregulated in HIV-infected cells. NEAT1 regulates and maintains nuclear paraspeckle bodies, which serve as a reservoir for unspliced and partially spliced HIV transcripts containing cis-acting instability elements (INS) before their nuclear export [209]. NRON regulates NFAT activity by either enabling or inhibiting its nuclear transport. During the early stages of infection, Nef inhibits NRON, thereby promoting NFAT activity and upregulating HIV transcription. On the other hand, Vpu induces NRON expression, leading to the inhibition of viral transcription [210]. NRON, which is highly expressed in resting CD4⁺ T cells, facilitates Tat degradation by the proteasome [211]. However, most of these studies have been done in *in vitro* models utilizing cell lines, and the involvement of lncRNAs as modulators of the latency must be determined *in vivo*.

Epigenetic mechanisms

Post-translational modifications can regulate Tat activity, such as its acetylation/deacetylation by cellular proteins. While P/CAF, GCN5, and CBP activate Tat through acetylation [212], deacetylation by STIR1 or HDAC6 inactivates the Tat protein inhibiting viral gene expression [213]. Active P-TEFb, which consists of Cyclin T1 and CDK9 and is associated with Brd4 [214] is required during elongation. Its inactive form is regulated by the 7SK RNP complex, which inhibits CDK9 activity. This complex is composed of the 7SK small nuclear RNA (snRNA), HEXIM1/2, LARP7, and MePCE [215]. Then, CTIP2 another cellular protein, is also known to interfere with P-TEFb by repressing CDK9 activity through its direct association with 7SK snRNA and HEXIM1 [215].

Viral expression is also regulated by other epigenetic marks, such as DNA methylation and histone modifications (methylation, acetylation, ubiquitylation, crotonylation, *etc.*). In latently infected CD4⁺ T cells, two methylated CpG islands flanking the HIV TSS have been described. Moreover, the transcriptional repressor methyl-CpG binding domain protein 2 (MBD2) has been identified at these CpG islands, suggesting its involvement in HIV latency [216]. However, the levels of CpG methylation seem associated with the duration of ART treatment: low levels of CpG methylation have been observed with short treatment duration (<3 years), while these levels increase with the duration of ART [217]. Of note, the integration of HIV into the host genome means that its expression is mediated by chromatin organization. Heterochromatin, the condensed conformation of chromatin (in contrast to euchromatin), is modulated by post-translational modifications of histones such as acetylation and methylation. Acetylation and deacetylation are respectively mediated by histone acetyltransferases (HAT) and histone deacetylases (HDAC). Acetylation releases the chromatin, promoting active transcription, while deacetylation by HDAC renders the DNA inaccessible and is associated with latency. During viral latency, HDACs are recruited to the 5' LTR by transcription factors (NF- κ B, c-Myc, Sp1) resulting in chromatin compaction and preventing RNA pol II binding [218]. Histone methylation and demethylation are catalyzed by histone methyltransferases (HMT) and histone demethylases. Histone methylation can either enhance or repress transcription, depending on the methylated residue and whether it is mono-, di-, or tri-methylated. In HIV latency, methylation of histone H3 at lysine 9 (H3K9) is responsible for chromatin-mediated transcriptional silencing [219]. In addition to its interaction with the inactive form of P-TEFb, CTIP2 can silence viral transcription by recruiting HDAC1 and HDAC2 to promote local histone H3 deacetylation at the HIV-1 promoter region, along with

SUV39H1, which increases H3 methylation. These two actions lead to the formation of local heterochromatin, silencing HIV-1 transcription [215].

Therefore, it is evident that HIV latency is a multifactorial process mediated by various mechanisms that both establish and maintain the viral latent state. However, these modifications are closely linked to the activation state of the host cell. Once integrated, the proviruses remain unaffected by the treatments, and in the absence of viral protein production, infected cells remain undetectable by the immune system. As a result, proviruses can perdure within resting CD4⁺ T cells unless a stimulus induces the expression of viral genes, or the infected cells undergo cell death.

Viral latency

As mentioned earlier, the infection of CD4⁺ T cells depends on the activation and differentiation status of the targeted cell. *In vivo*, the infection of resting CD4⁺ T cells is unlikely due to the low level of CCR5 expression on the cell surface [220]. Furthermore, unlike activated cells, resting CD4⁺ T cells have high levels of SAMHD1, which interferes with reverse transcription by degrading nucleotides [90]. *In vitro*, HIV infection of resting CD4⁺ T cells is possible but with reduced efficiency in naïve compared to memory CD4⁺ T cells, as memory T cells express more CCR5 than their naïve counterparts [220]. Another possible scenario leading to latency in naïve CD4⁺ T cells (T_N) involves infection during thymopoiesis (Figure 9). This phenomenon has been studied in severe combined immunodeficient (SCID) humanized mice [221]. During thymopoiesis, transcriptionally active CD4⁺CD8⁺ thymocytes enter a quiescent state upon maturation into T_N [222]. Additionally, in PLWHIV receiving ART, HIV DNA has been detected in recent thymic

emigrants, suggesting infection of thymocytes [223, 224]. Although the infected T_N population appears to expand during ART, it contributes to only 2% of the viral reservoir [225].

Therefore, it is more plausible that latency occurs in activated (or previously activated) cells that transition into a resting state (Figure 9) [222]. Indeed, HIV replication appears to be most efficient in activated $CD4^+$ T cells, and the viral reservoir is predominantly established within memory $CD4^+$ T cells [225]. In response to an antigen, T_N undergo a burst of cellular proliferation and differentiation, increasing the pool of effector cells. Although the majority of these cells die, a subset survives and reverts to a resting state, persisting as memory cells. A similar process takes place during HIV infection. In the presence of HIV antigens, T_N proliferate and differentiate into effector cells. These activated antigen-specific $CD4^+$ T cells are highly susceptible to HIV infection. Two *scenarii* of infection of antigen-specific T cells exist [226]. First, the infection could occur early in the clonal burst, resulting in a large TCR-clone of HIV-infected cells. Alternatively, if the infection occurs later, only a fraction of the T cell clone would harbor the provirus. Usually, these activated infected cells undergo rapid death due to productive infection. However, some cells transition back to a resting state. Recently, it has been demonstrated that latently HIV-infected $CD4^+$ T cells express gene patterns that promote HIV silencing, cell survival, and cell proliferation [227, 228]. In the absence of a TCR activation, transcription is silenced through the recruitment of cellular factors that alter the chromatin structure, thereby reducing cellular transcriptional activity.

Finally, a third hypothesis suggests that infection does not take place when the cell is in a fully active state but rather during its transition to a resting state. However, if the provirus

integrates too early before quiescence is initiated, the transcription of Tat by the cellular machinery will result in viral expression despite the hypoactivation of the cells. In such cases, the cells may be recognized by the immune system or undergo viral cytotoxicity, leading to their destruction [229]. Given that activated cells are more permissive to HIV, it is more likely that latency occurs in activated infected cells that subsequently revert to a resting memory state, or that the infection occurs during the transition.

“Leaky latency”

The majority of cells within the viral reservoir are latent and, therefore, thought to be transcriptionally inactive. Activation of these cells requires a stimulus that induces viral gene expression and production. However, cells harboring the HIV genome may exhibit the ability to transcribe low levels of short and elongated viral RNA, potentially leading to the production of limited quantities of viral proteins during ART [230, 231]. These observations have given rise to the term “leaky latency”, which describes this state of incomplete transcriptional latency [232]. Indeed, studies have measured low levels of transcriptional initiation and elongation in latently infected resting CD4⁺ T cells from PLWHIV under ART treatment. The presence of abortive transcripts indicates the occurrence of certain blocks during viral transcription [191], although these blocks are not complete, as multiply-spliced and full-length transcripts can also be detected in resting CD4⁺T cells, alongside the production of viral proteins [230, 231].

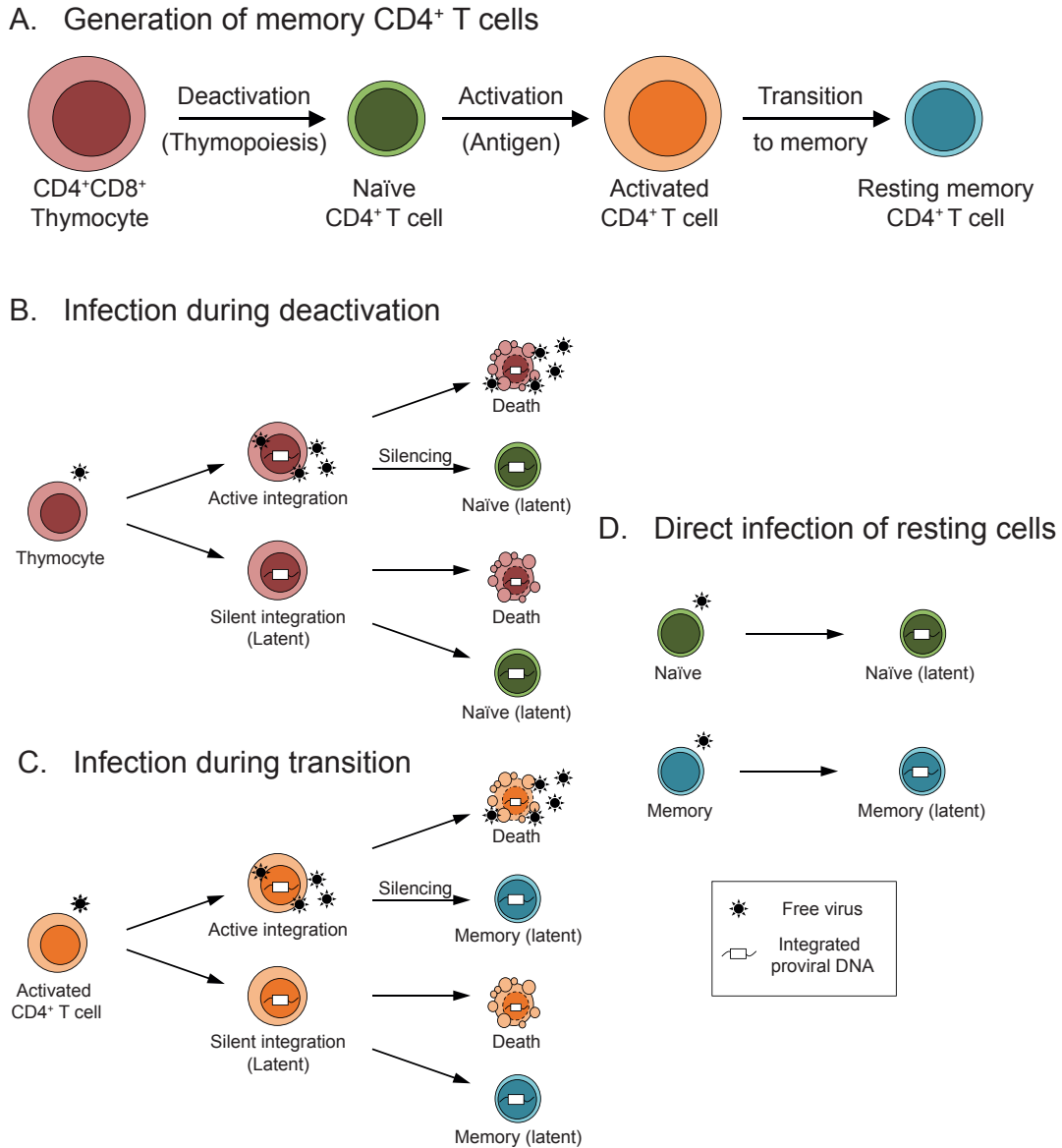


Figure 9. – Cellular models of latency establishment into CD4⁺ T cells

(A) Transcriptionally active thymocytes (CD4⁺CD8⁺) undergo deactivation to become T_N once thymopoiesis is completed. Upon activation by antigens presented by APCs, T_N undergo proliferation and differentiation into activated effector CD4⁺ T cells. A subset of activated CD4⁺ T cells then transitions back to a resting state, becoming memory T cells. Two non-exclusive mechanisms may explain HIV latency: (B) and (C) infection occurs when the cells are in an active state or transitioning to a resting state, either during thymopoiesis (B) or after antigen-driven activation (C); or, rarely, by direct infection of naïve/resting CD4⁺ T cells. Adapted from [222] with permission from *Springer Nature*.

Recently, our group and others have characterized the spontaneously transcriptionally active viral reservoir in peripheral infected CD4⁺ T cells from PLWHIV on ART [233]. Although the majority of these cells are transcription-competent but do not express the Gag protein, the persistence of HIV-specific CD4⁺, and CD8⁺ T cell responses has been observed. Notably, these responses were more pronounced when the protein was produced [233]. These findings suggest that immune responses might be sustained due to persistent antigen production during ART. Additionally, we have described that these spontaneously transcriptionally active infected resting cells are not restricted to a single CD4⁺ T cell subset but are predominantly enriched in central memory T cells (T_{CM}), as well as in markers of activation such as HLA-DR, ICOS, Ki67, and PD-1 [233]. This enrichment is consistent with homeostatic and antigen-driven proliferations, which will be further discussed in the introduction. The enrichments of chemokine receptors may reflect preferential HIV replication in specific anatomical compartments, such as the intestinal mucosa (CCR6 enrichment) and germinal centers of LN (CXCR5). This may explain why some cells are capable of “leaking” virus particles or viral transcripts. Certain environments have been identified to be more conducive to viral transcription and may be reflected in the periphery. Another possibility arises from the suboptimal distribution of antiviral drugs into tissues. In SIV-infected monkeys, ART partially reduced levels of both DNA and RNA in lymphoid tissues, which correlated with low drug concentrations in these tissues compared to peripheral blood [234].

Unfortunately, although this phenomenon seems to occur at a very low level, it can contribute to drug resistance, and lead to persistent immune activation and inflammation constitutive of immune dysfunction, even in PLWHIV undergoing prolonged therapy [235].

Therefore, therapeutic strategies are needed to eradicate the virus from the body (*i.e.*, sterilizing cure) or to achieve long-term control of HIV replication without the need for ART (*i.e.*, functional cure).

Viral reservoir

The term “reservoir” initially referred to the proviruses that persist in cells despite ART-treatment. However, over time, the term has evolved to encompass not only the cells harboring the provirus but also the organs where the virus persists and the various viral genomes. Each method used to measure the reservoir is important in understanding how and why proviruses persist despite ART. Also, it is important to note that each assay has its limitations, making precise measurements of the viral reservoir challenging (Figure 10).

“Total HIV DNA”

Overall, the HIV genome persisting within infected cells despite ART treatment can be considered as the reservoir, which includes 1- and 2-LTR circles, linear integrated as well as non-integrated DNA. Total HIV DNA levels are measured by PCR and allow for the early detection of infection as early as Fiebig I (Figure 7) and are predictive of the progression toward AIDS [236]. As mentioned previously, HIV DNA decrease in a two-step decay after initiating ART. The first step corresponds to the reduction of non-integrated DNA and productively infected cells. Subsequently, the second phase of viral decay is attributed to the decline of infected long-lived resting cells, which are part of the HIV reservoir [237]. However, total HIV DNA measurement does not distinguish the different DNA forms (1- and 2-LTR circles, linear non-integrated and integrated) that do

not contribute similarly to the reservoir establishment. Also, it has been shown that the majority of integrated DNA was defective and unable to produce new infectious viral particles, thus not replication-competent [238, 239].

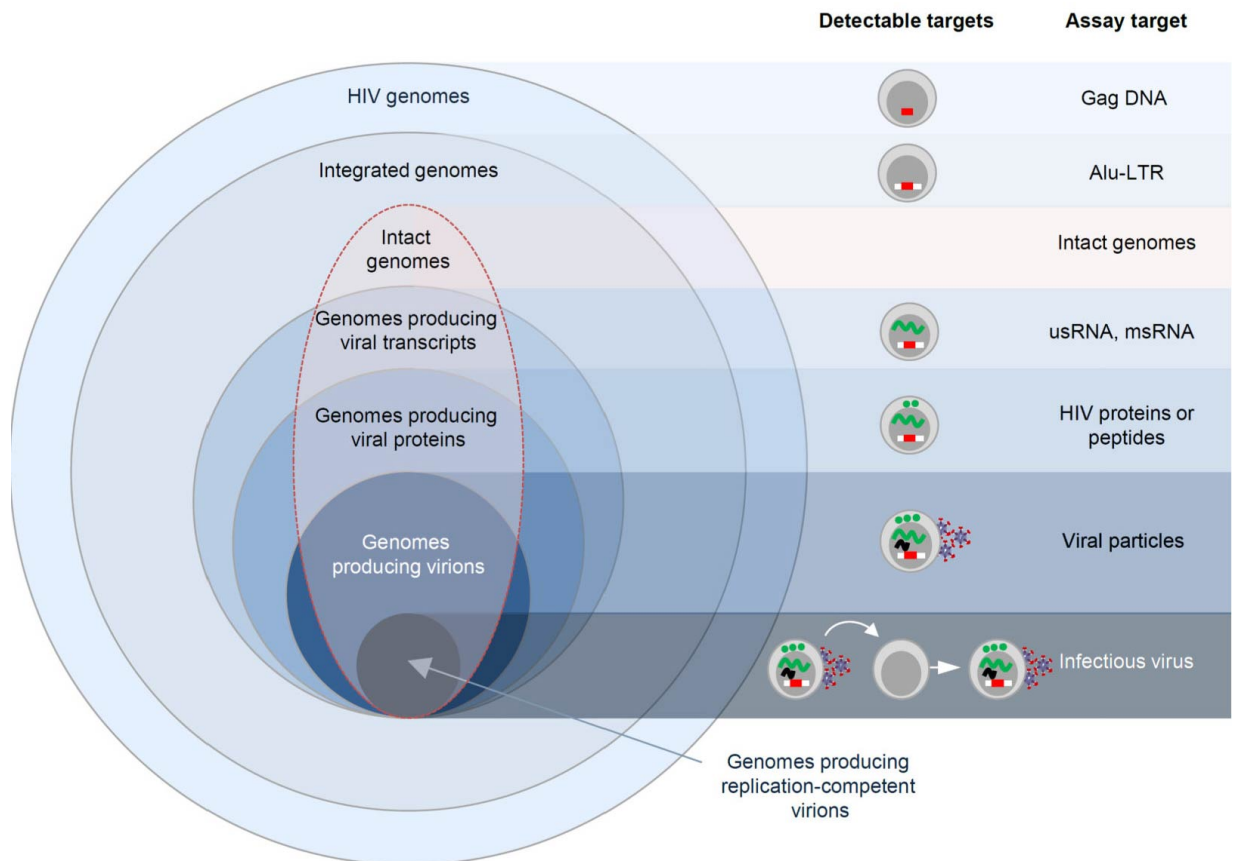


Figure 10. – Venn diagram comparison of each different viral genome subtypes

Each circle represents a fraction of the viral reservoir. The majority of total HIV DNA is integrated, but only a tiny portion is replication-competent [239]. However, even this small fraction is sufficient to cause viral rebound after ART interruption and poses a challenge for achieving a cure for HIV. Adapted from [240] with permission from *Springer Nature*.

Replication-competent reservoir

As mentioned previously, this term refers to proviruses capable of producing new infectious viral particles. This reservoir is likely involved in the viral rebound that occurs

after ART interruption. The viral outgrowth assay (VOA) is the standard method used to quantify the rare replication-competent and inducible proviruses [241]. HIV-infected cells are sorted and reactivated using latency reversal agents (LRAs) in co-culture with non-infected autologous CD4⁺ T cells to measure viral infection. Recent estimations place the size of the viral reservoir in PLWHIV upon ART at approximately 300 per 10⁶ CD4⁺ T cells containing total HIV DNA, with only 1 provirus per 10⁶ CD4⁺ T cells being replication-competent from a single stimulation [242, 243]. Multiple rounds of reactivation can lead to viral expression from additional proviruses, suggesting that some proviruses are more prone to reactivation than others [239]. Unlike measurements of total HIV DNAs, VOA tends to underestimate the true size of the viral reservoir as it overlooks active viral reservoirs – other than resting memory CD4⁺ T cells – that may be biologically relevant.

Proviral integrity

The differences between total HIV DNA and the replication-competent reservoir have prompted further qualitative analyses of the viral reservoir. Studies have revealed that the vast majority of the HIV reservoir consists of defective proviruses [238, 239]. Multiple mechanisms contributing to their generation have been proposed. As mentioned earlier, the RT lacks proofreading functions, resulting in roughly one mutation every 10'000 base pairs, or about one mutation per genome per cycle) [53, 244]. Another mechanism involves host cell restriction factors like ABOPEC3G. This factor restricts and hinders proviruses replication by inducing guanine-to-adenine changes during the RT, but also leads to HIV-1 hypermutations observed in defective proviruses [172, 244, 245]. The proportion of intact genomes has been estimated at 5% and 35% of the integrated DNA

in ART-treated and in viremic individuals, respectively [238, 246]. While the number of replication-competent proviruses is 300-fold lower than the number of CD4⁺ T cells that harbor HIV DNA detectable by PCR, in ART-treated individuals, this frequency represents only a fraction of the intact proviruses are reactivated by VOAs [247]. These frequencies have been determined by sequencing the complete viral genome in cells from PLWHIV. The observed defects mostly involve large deletions along the provirus but can also include hypermutations or defects into the ψ domain [238, 239, 247]. These defects are detrimental to the virus as they preclude the production of new infectious viral particles. Although the frequencies of cells harboring intact and defective proviruses decrease during ART, the latter decay to a lesser degree than intact proviruses over time [238].

Transcription- and translation-competent reservoir

Studies which focus on intact proviruses preclude the potential impact of defective proviruses on chronic inflammation and immune dysfunction. It has been revealed that defective proviruses can produce viral transcripts and proteins, thereby possibly contributing to HIV pathogenesis [248, 249]. Such proviruses are referred to as transcription- and translation-competent reservoirs. Of note these two categories are interconnected, as translation-competent reservoirs are inherently capable of producing viral transcripts. Measurements of multiply-spliced vRNAs provide estimates of the transcription-competent reservoirs that are 20 to 50 times higher than those of the replication-competent reservoirs [250, 251]. However, these assays do not capture the heterogeneity of the viral reservoir. To, address this, our team and others have used flow-cytometry-based methods to assess the reservoirs at a single-cell resolution. These

methods detect viral protein [252, 253] and viral RNA through flow cytometric fluorescent *in situ* RNA hybridization (RNAflow-FISH or RNA FISH-flow) [254-256]. Using these assays, we have determined the frequencies of CD4⁺ T cells capable of producing viral RNAs and Gag protein, which represents the translation-competent reservoir. We found that this reservoir was about 160 to 200 times smaller than the reservoir harboring integrated DNA. This technique has narrowed down the estimate of the translation-competent reservoir to approximately 4.7 HIV⁺ cells/10⁶ CD4⁺ T cells, yet higher than the replication-competent reservoirs measured by VOA [254, 256].

Flow cytometry also offers the opportunity to assess the contribution of specific cellular subtypes to the viral reservoir and allows for a more comprehensive characterization of HIV-infected cells, which is crucial for potential eradication strategies.

Cellular reservoirs

As mentioned earlier, HIV DNA integrates into the cellular genome, where it can be transcribed to produce new viral particles. However, even with ART treatment, a small fraction of the virus can remain transcriptionally silent. This viral genome is primarily integrated into CD4⁺ T cells, which constitute the majority of the viral reservoir.

CD4⁺ T lymphocytes

The majority of latently infected CD4⁺ cells during ART exhibit a resting memory phenotype, characterized by limited viral transcription due to epigenetic gene silencing

mechanisms as described earlier. These long-lasting, self-renewing cells are considered the primary contributor to the viral reservoir.

At the cellular level, integrated DNA persists in T_{CM} , T_{EM} , T_{TM} , and T_{SCM} (stem-cell memory T cells), as well as in T_N [223, 225]. Despite the abundance of T_N , the frequency of HIV-infected T_N is low [225]. However, some studies have indicated their role in the establishment and maintenance of the viral reservoir, as T_N may contain proportionally more intact HIV genomes than other subsets [246, 257, 258]. On the other hand, T_{EM} and T_{CM} represent the subsets in which the virus is mainly detected. Through homeostatic proliferation, T_{CM} favors the clonal expansion of the proviruses [225]. This concept will be further elaborated later in this manuscript. However, it has been described that T_{CM} predominantly harbor defective proviruses [246]. Conversely, T_{EM} , despite their limited proliferative capacity, harbor the largest pool of intact DNA [246]. Moreover, translation-competent cells are enriched in this subset, suggesting that T_{EM} provide a cellular context conducive to viral translation [253, 254, 259].

Memory $CD4^+$ T cells can exhibit polarization based on their pro- or anti-inflammatory functions, each making distinct contributions to the viral reservoir [260]. Similar to T_{CM} , T_{H9} cells harbor high levels of viral DNA, but the proviruses within them are mostly defective, unlike T_{H1} , which are less likely to be infected but harbor proportionally more intact genomes [261]. T_{H17} cells are also known as preferential targets for HIV infection, possibly due to their high plasticity, self-renewal capacity, and long-lasting characteristics, rather than their homing potential to the gut [260]. The suboptimal distribution of antiretroviral into tissues may favor the expression of HIV antigens. In turn, this expression can lead to antigen-driven proliferation, thereby promoting infection of T cells with homing capacity.

This phenomenon is also observed for T_{FH} cells, which reside in the germinal center of LN and constitute a major compartment for HIV persistence and viral production, despite ART [260].

Therefore, studying the contribution of different subsets of CD4⁺ T cells to the viral reservoir is of great importance for a potential therapeutic cure of HIV. Recently, there has been interest in exploring the possibility of reducing the size of the reservoir by inducing cellular differentiation and replenishing the pool of T_N cells. This strategy aims to “rinse and replace” the viral reservoir through homeostasis and T cell turnover of HIV-infected cells [262]. However, the generation of novel T_N cells relies on thymic functions, which peak at puberty and decline thereafter. This principle of immune aging is exacerbated in PLWHIV due to the *inflammaging* process, where HIV infection leads to immune dysfunction. Therefore, the “rinse and replace” strategy may necessitate the use of growth hormones to enhance thymic functions.

Monocytes and macrophages

While the presence of HIV DNA in monocytes isolated from peripheral blood mononuclear cells (PBMCs) can be detected [263, 264], their susceptibility to HIV infection is hindered by the expression of restriction factors such as SAMHD1, APOBEC3G, and various micro-RNAs (miRNAs) [265]. Recently, it has been shown that the HIV DNA detected in the small fraction of monocytes was not integrated [266].

Conversely, the differentiation of monocytes into macrophages is associated with an increased permissiveness to HIV infection. Therefore, *in vivo* reports of macrophage infection largely depend on the anatomical compartment with which they are associated

[267-269]. The persistence of the viral reservoir is associated with the long lifespan and self-renewal capacities of macrophages, as well as their resistance to HIV-mediated apoptosis and cell death caused by CTLs [270, 271]. Moreover, it has been described that HIV infection itself favors the survival of infected macrophages. For instance, the envelope glycoprotein induces the expression of anti-apoptotic genes Bfl-1 and Mcl-1, as well as the expression of macrophage colony-stimulating factor (M-CSF), which downregulates the tumor necrosis factor-related apoptosis-inducing ligand (TRAIL) receptor associated with apoptosis [272]. The capacity of macrophages to sustain HIV replication in the absence of CD4⁺ T cells has been demonstrated [273], making them an important reservoir for HIV persistence during ART treatment. However, evidence of phagocytosis of HIV-infected CD4⁺ T cells may also suggest that the presence of HIV DNA in macrophages could be attributed to phagocytosis rather than active infection [274, 275].

Other cellular reservoirs

Other non-conventional cellular HIV reservoirs have been described. Among them, these include megakaryocytes [276], and by extension platelets, where HIV particles can potentially hide [277].

Megakaryocytes and platelets (also known as thrombocytes) are abundant in the bloodstream. First evidence of HIV internalization into megakaryocytes and platelets was described *in vitro* [276, 278]. Platelets, produced by megakaryocytes, play a crucial role in hemostasis and thrombosis. They interact with signals from pathogens and damaged cells (pathogen-associated and damage-associated molecular patterns; PAMPs and DAMPS) resulting in aggregate formations that can lead to their depletion, potentially

causing thrombocytopenia in cases of inflammation [279]. PLWHIV are at a relatively higher risk of thrombocytopenia due to reduced platelet lifespan, splenic sequestration, and impaired platelet production by HIV-infected megakaryocytes [280]. Indeed, megakaryocytes express both CD4 and CXCR4, rendering these bone marrow cells susceptible to HIV infection. As a result, intact HIV particles can be present in platelets from ART treated individuals [277]. However, platelets also express various receptors, such as CCR1, 3, and 4, CXCR1, 2, and 4, and DC-SIGN, which can directly bind to HIV [279]. Importantly, studies have shown that the HIV particles internalized into platelets are replication-competent and that platelets can transfer the virus to macrophages after phagocytosis, leading to their infection [277]. Therefore, platelets serve as a carrier for internalized HIV particles, providing an alternative pathway for viral dissemination throughout the body. Additionally, higher frequencies of HIV-containing platelets have been associated with poor immune restoration despite ART treatment, suggesting a link to disease progression [277].

Unlike CD4⁺ T cells and macrophages, these cells have been less studied, and the mechanisms involved in the infection of such subsets, their roles, and contributions to the viral reservoir remain unclear. Although they are not primary actors, they undoubtedly assist the virus in persisting despite ART, thereby complicating the eradication of HIV.

Anatomical reservoirs

While peripheral blood CD4⁺ T cells represent the most extensively studied HIV reservoir, they only represent the tip of the iceberg. Major anatomical sites, such as lymphoid organs (LN, bone marrow, spleen, thymus), as well as the gut, liver, lungs, central nervous system

(CNS), reproductive system, adipose tissue, and others, also serve as reservoirs [281]. These compartments are physically separated from the immune circulation by barriers providing obstacles to effective ARV penetration. This low drug penetrance, associated with limited cellular trafficking permeability may represent a challenge for both immune responses and pharmacological intervention, and potentially result in viral replication in the anatomical sites [234]. These sites with limited trafficking of immune cells are therefore referred to as “sanctuaries”

Lymphoid tissues have been identified as major sites of viral replication, with germinal center T_{FH} cells being highly permissive to HIV infection [260]. In non-human primate (NHP) models, persistent SIV replication in B cell follicles has been observed, and the survival of infected T_{FH} has been attributed to the exclusion of CTLs within LN follicles [260]. Additionally, HIV-infected T_{CM} are found in LN, underscoring the role of this compartment in HIV persistence [260, 281].

A second significant anatomical reservoir is the gut, where T_{H17} cells are preferentially infected by HIV, potentially due to higher CCR5 expression and T cell activation in the gut mucosa [260, 281]. This sanctuary represents the highest frequency of HIV-infected cells and ongoing replication, even in individuals undergoing ART [281]. Moreover, this compartment is where a substantial proportion of infected myeloid cells is detected [260, 266, 273, 275, 281].

As early as the infection occurs, HIV can be detected in the cerebrospinal fluid (CSF) and brain tissues [281, 282]. Unlike the CSF, the rest of the CNS does not contain $CD4^+$ T cells, and other cell subtypes such as macrophages and microglial cells are infected by HIV [268, 281, 282]. However, astrocytes, which are susceptible to HIV infection *in vitro*,

do not harbor HIV DNA in the brain of ART-treated individuals, suggesting that they are not involved in the ongoing replication observed in the brain [268]. The limited penetration of ARV in the CNS facilitates viral rebound, contributing to the development of neurocognitive disorders [268, 281, 282].

Not surprisingly, the main entry portal for sexual transmission, namely the genital mucosal tissue, contains a significant proportion of urethral macrophages harboring replication-competent proviruses in penile tissue from ART-treated individuals [267]. This reservoir is particularly susceptible to activation by lipopolysaccharides (LPS), which can be associated with other sexually transmitted infections that result in LPS production. This LPS-mediated activation poses a potential risk factor for HIV shedding into semen and potentiating HIV infection [267, 283].

Primarily, tissue-resident CD4⁺ T cells (T_{RM}) and macrophages serve as the main HIV reservoirs within these compartments, although other cell subtypes can also be infected and contribute to the persistence of HIV. For instance, microglial cells [268] and Langerhans cells in the skin and foreskin mucosa [284, 285] are known to be infected. Moreover, the combination of limited penetration of ARV and certain cellular trafficking permeability pose significant barriers to therapeutic strategies, which, importantly, favor the ongoing replication of HIV within these sanctuary sites.

Viral reservoir persistence

Viral reservoir stability

Latently infected cells are relatively invisible to the immune system, allowing the virus to persist throughout the lifespan of these cells. Longitudinal analyses of the HIV reservoirs have revealed a half-life of approximately 44 months for those cells, suggesting potential eradication of the viral reservoirs after about 70 years on ART [188, 286]. These findings highlight the stability of the viral reservoir over time. Some studies indicated that the stability of the viral reservoir may be linked to its resistance to cell death [227, 287, 288]. During the active replication state, HIV-infected cells are typically eliminated through cell-mediated killing by CTL or die from the cytopathic effects induced by the virus. However, despite efficient CD8⁺ T cells, latently infected cells persist. Several mechanisms have been proposed. Notably, an increased expression of the pro-survival protein BCL-2 has been observed in reactivated viral reservoirs obtained from ART-treated individuals. This overexpression was not observed in chronic progressors [288]. The upregulation of BCL-2 has been associated with impaired CTL-mediated killing, potentially attributed to the inhibition of both the perforin/granzyme B and FasL/Fas pathways, thus regulating the apoptosis of the HIV-infected cells [288].

While the duration of ART treatment does not appear to impact the size of the viral reservoir, the time prior to treatment initiation does. An example is the case of the “Mississippi baby”, who was born to a mother living with HIV. ART was initiated only 30 hours after the baby’s birth, resulting in undetectable viral load for 12 months and stable CD4⁺ and CD8⁺ T cell counts, similar to individuals on ART. However, when the treatment was interrupted, the viral load remained undetectable for an additional 27 months in the

plasma but then reoccurred along with a drop in CD4⁺ T cells [289]. These findings suggest that early initiation of ARV restricts the establishment of the HIV viral reservoirs and may be associated with better virologic control. Several studies have indicated that the seeding of the HIV reservoir occurs prior to the detection of viremia in plasma, with proviruses already integrated in LNs and the gastrointestinal tract, rather than in the periphery [290, 291].

Mechanisms involved in the viral persistence

Despite ART, the viral reservoir persists. Initially, it was suggested that infected cells could persist over time due to their long half-life. It is now widely accepted the viral reservoir is not maintained solely by the long-term survival of infected cells but also through homeostatic proliferation of infected cells and antigen-driven proliferation [225, 226, 292]. Some studies suggest that the viral reservoir might also persist through residual ongoing replication, particularly in tissues where the penetrance of the ARVs is limited [189, 234]. However, this phenomenon is still debated as no direct proof has been given.

Clonal expansion

Clonal expansion allows for the replenishment of the viral reservoir without inducing viral replication and is supported by the increasing frequency of cells containing identical viral sequences observed during ART [292]. The presence of proviruses located within the same integration site in different cells, which is extraordinarily to occur from two distinct integration events, confirms that a significant fraction of infected cells proliferates through

clonal expansion [292]. Three mechanisms have been described to be involved in the clonal expansion of the viral reservoir (Figure 11).

The HIV reservoir is mainly found in memory cells, which appear to be maintained through homeostatic proliferation (Figure 11) [225, 292]. The increased expression of IL-7 in response to CD4⁺ T cell loss during HIV infection has been linked to the proliferation of HIV-infected cells in the absence of viral production [292]. Moreover, clonally expanded sequences are underrepresented in the T_{CM} subset, while they are more abundant in T_{TM} and T_{EM}. Interestingly, clonally expanded sequences within the T_{TM} and T_{EM} subsets can also be found in T_{CM} [225, 293]. These findings suggest that the clonally expanded reservoir derived from the T_{CM} fuels the T_{TM}/T_{EM} reservoirs without being eliminated, indicating that clonal expansion occurs in the absence of viral production or due to immune escape mechanisms [225, 293]. However, the observed contraction of certain HIV-infected T cell subsets implies the involvement of mechanisms other than homeostatic proliferation.

Despite adherence to ART treatment, there are instances where the plasma viral load becomes transiently detectable, albeit at levels lower than 200 copies/mL. This low-level viremia, known as viral blips, is not caused by drug-resistant viruses but is mainly derived from genetically identical clones [292]. It is suggested that this T cell activation is antigen-mediated, which may explain the contraction of some T cell subsets harboring clonally expanded sequences after their activation and differentiation into more effector subtypes (Figure 11) [292, 293]. These antigen-specific CD4⁺ T cells undergo viral expression and clonal expansion, leading to viral blips and subsequent elimination of infected and activated cells by the immune system [292]. Recent TCR sequencing studies of HIV-

infected cells producing viral protein upon reactivation have revealed that most translation-competent cells share the same TCR and harbor clonally expanded sequences [293]. Some clonal populations remain detectable in longitudinal samples, even 6 years after the initial visit, with transient clonal expansions followed by contractions, highlighting the role of antigen-driven clonal expansion in the persistence of the HIV reservoir [293].

Finally, the duplication of proviral integration sites represents another mechanism of clonal expansion (Figure 11). During HIV infection, proviruses integrate into intronic regions of transcriptionally active genes, either in the same or opposite direction as the host gene. *In vivo* studies have shown that integration of the HIV genome is enriched in cancer-related genes compared to their frequency in the human genome [134, 292, 294]. Moreover, HIV integration into these oncogenes *in vivo* consistently occurs in the same orientation as the genes. As a result, HIV transcription mediated by the LTR can also transcribe these cancer-related genes, triggering cellular proliferation and promoting clonal expansion of the viral reservoir. However, it should be noted that the majority of the HIV genomes are defective, and there is no observed difference in intactness between proviruses integrated into cancer-related genes and those integrated elsewhere [134, 294, 295]. Nonetheless, intact sequences appear to be enriched in non-genic regions, often found in the opposite orientation to host genes or within/close proximity to the centromere [294, 295]. These observations suggest that HIV persistence may be mediated by deeply latent proviruses, which could account for the discrepancy between the size of the intact reservoir and the size of the replication-competent reservoir detected by VOAs.

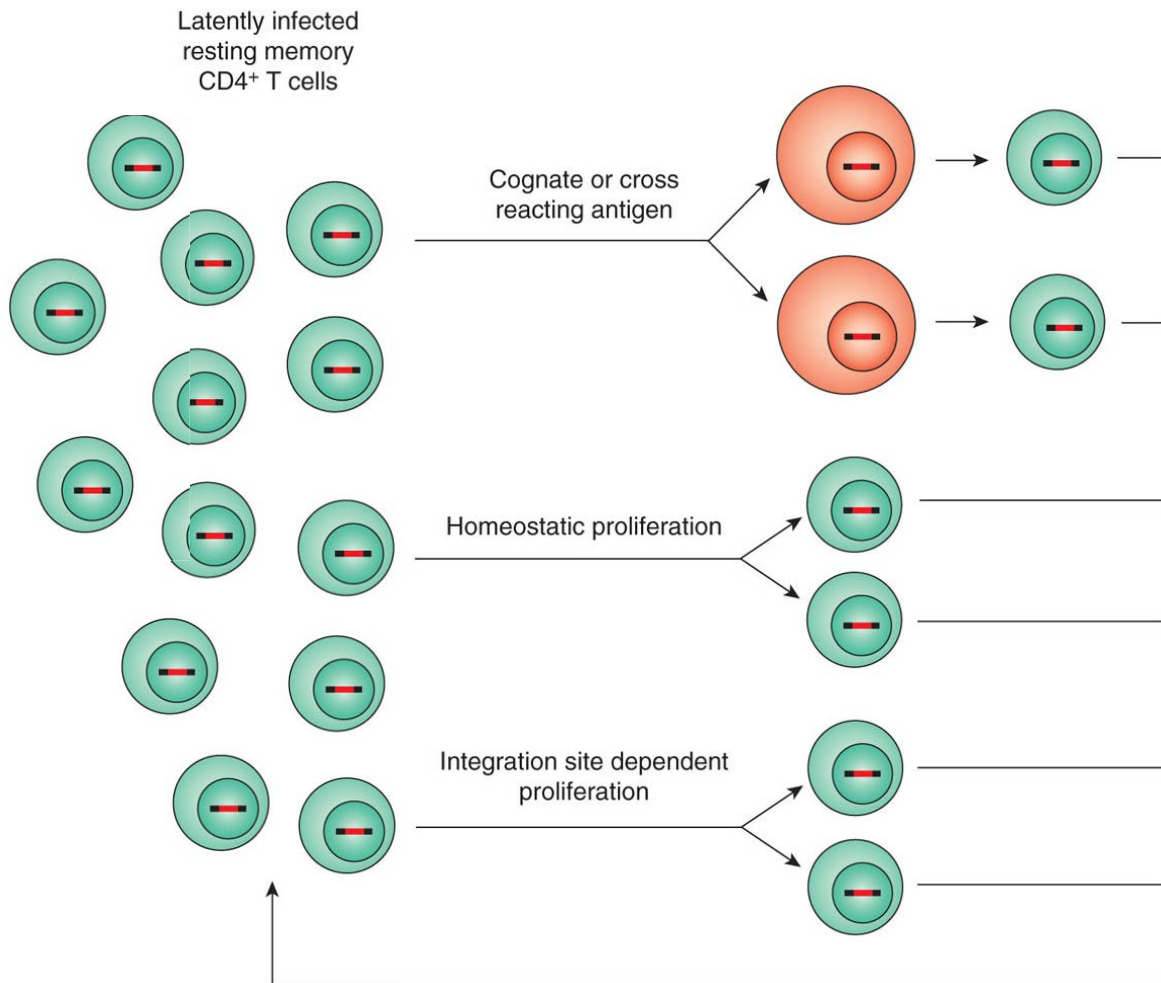


Figure 11. – Mechanisms contributing to clonal expansion of HIV-infected cells

Three cellular mechanisms are known to be involved in the clonal expansion. First, the interaction between a latently infected memory CD4⁺ T cell and its specific antigen triggers the activation and subsequent proliferation of the cell. A fraction of the proliferated cells will die while the other part will transition into a quiescent memory phenotype. Secondly, homeostatic proliferation maintains a constant pool of HIV-infected CD4⁺ T cells without reactivation of viral expression. Lastly, integration of the proviruses into oncogenes may also result in cell proliferation. Adapted from [296] with permission from *Journal of Immunology*.

Ongoing replication

In some studies, and despite long-term ART-treatment, HIV proteins can still be detected. These occurrences are predominantly observed in anatomical reservoirs where the penetration of ARVs is limited [189, 234]. The question of whether this phenomenon occurs in ART-treated individuals remains controversial, as certain studies have found no evidence of genetic evolution during ART, suggesting that HIV persistence may not be driven by low-level ongoing replication of the virus [297].

These observations have been made in the blood, while others have demonstrated viral evolution in tissues, as well as perturbation of the reservoir following treatment intensification [298, 299], implying the persistence of active replication despite ART. In germinal centers of LNs, the exclusion of CD8⁺ T cells from the replication sites [299] could also play a role. However, it is important to note that the samples were taken after only 3 and 6 months of therapy, which introduce a bias to the observations. Indeed, during the first months of therapy, the viral reservoir is not stable, as both productively infected cells and short-lived cells die rapidly. This sharp decline of infected cells alters the proviral diversity, making it challenging to compare with pretherapy sequences. On the other hand, several groups have reported that in some tissues (such as the GALT), despite high levels of immune activation, the diversity of HIV sequences does not increase even after 1 year of ART initiation. Moreover, there is no compartmentalization observed between the periphery and the tissue, suggesting the absence of *de novo* replication [297].

While these observations suggest that residual replication may occur, this phenomenon is largely debated, and it is widely accepted that clonal expansion represents the main mechanism of viral persistence.

Immune responses and therapeutic strategies

Immune responses during HIV infection

Innate immunity

Early after infection, PRR (Pattern Recognition Receptors) sense PAMPs present in HIV products, triggering a diverse array of innate immune responses [300]. Among these responses are the actions of intracellular HIV restriction factors such as APOBECs, TRIM5 α , SAMHD1, or BST-2, which inhibit various stages of the HIV replication cycle [300]. In addition, other factors, including type I and type III IFNs and proinflammatory cytokines, are secreted, creating a feedback loop that activates innate immune cells. Some Interferon-stimulated genes (ISGs) enhance antigen presentation, playing an important role in the recruitment and priming of adaptive immune cells [300]. Together, these mechanisms limit HIV replication and control the spread of the virus. However, HIV has developed strategies to counteract these antiviral immune mechanisms through the activities of its accessory proteins. These proteins can inhibit the functions of the restriction factors or downregulate surface receptors that are involved in the recognition and elimination of HIV-infected cells by NK cells [300].

The persistence of HIV during chronic infection perpetuates a proinflammatory environment, affecting both innate and adaptive responses [301]. For example, prolonged and high expression of type I IFNs leads to desensitization, reduced expression of antiviral ISGs, impaired development of DCs, limited proliferation and loss of CD4⁺ T cells, along with promoting apoptosis of bystander cells and increasing the size of the viral reservoir [301]. While type I IFNs signaling is crucial for inhibiting the spread of infection during chronic infection, persistent activation of these signals appears to contribute to the

depletion of CD4⁺ T cells, particularly in the gut, where the proinflammatory state is further fueled by the translocation of gut bacteria into the bloodstream. It is important to note that chronic immune activation is commonly observed in PLWHIV receiving ART and is generally associated with a poor prognosis of HIV infection.

Adaptive immunity

HIV-specific CD8⁺ T cells

Strong HIV-specific T cell responses are observed in almost all individuals infected with HIV during the early phase of infection. These T cell responses mediate the first viral control, explaining the sharp decrease in viral load during acute infection, even without ART [156, 164]. The abundance of Nef and Env epitopes, observed early during the acute phase of HIV infection, leads to their preferential targeting by the CD8⁺ T cells contributing to the decline of HIV viremia. However, both Nef and Env regions are among the most variable in the virus [302], meaning that early T cell responses shape the outcome of HIV infection. As the infection progresses, the virus undergoes genetic mutations, resulting in an increased diversity of epitopes targeted by CD8⁺ T cells but also favoring the selection of escape variants in HIV [169, 303]. Furthermore, individuals who maintain a high viral load tend to experience selective loss of high-avidity CD8⁺ T cell or potent cytolytic specific CD4⁺ T cell responses during early infection [302]. On the other hand, individuals achieving better control of viremia, such as elite controllers, show better HIV-specific CD8⁺ T cell responses.

During chronic HIV infection, T cells undergo repetitive stimulation by antigens, ultimately resulting in the exhaustion or dysfunction of HIV-specific T cell immunity [165]. Exhausted

cells are characterized by the loss of their functions and an increased expression of inhibitory receptors [169, 304, 305]. Importantly, continuous TCR signaling is required for the maintenance of exhausted T cells as they are unable to transition into a long-lived quiescent state. Moreover, HIV-specific CD8⁺ T cells retain an epigenetic program poised for PD-1 upregulation specific of nonfunctional antigen-specific responses, which persists even after successful ART [306]. However, in elite controllers who effectively control viremia, T cells exhibit a higher degree of polyfunctional CTLs capable of producing cytokines and chemokines in addition to their cytolytic capacity, as compared to viremic or ART-treated individuals [307]. It is now widely acknowledged that potent CD8⁺ T cell responses differ between ECs and HIV progressors. Although it was previously shown that certain HLA alleles (such as B*57 and B*27) were associated with better control of HIV infection [186], it has been found that while these HLA phenotypes are enriched in two-third of elite controllers, the targeted epitopes in ECs who do not bear these alleles do not overlap with those targeted in HLA-B*57⁺ individuals. Moreover, these protective alleles are also present in many PLWHIV. Whole human genome sequencing identified a single variant between ECs and viremic individuals, present in the Killer-cell Immunoglobulin-like Receptor KIR3DL1 affecting the interactions with HLA-B [308]. Also, it has been shown in ECs without protective HLA alleles, that HIV-specific CD8⁺ T cells were able to kill as effectively as the specific CTL cells in those with protective alleles [309], probably due to the restricted specificity of these CTL to HLA epitopes that do not tolerate escape mutations [310]. These findings suggest that the role of the protective HLA alleles is not the only contributor to viremia control.

HIV-specific CD4⁺ T cells

HIV-specific CD4⁺ T cells in long-term progressors also exhibit exhaustion and limited proliferation. This exhaustion is characterized by the upregulation of inhibitory receptors such as PD-1, CTLA-4, TIGIT, and CD200 [311-313]. Recent findings from our group have demonstrated that in chronic HIV infection, HIV-specific CD4⁺ T cells are predominantly exhausted cT_{FH} cells with skewed functions toward a T_{H1}-like phenotype and functions [313]. These cells undergo expansion in lymphoid tissues due to continuous stimulation of HIV-specific T_{FH} in germinal centers. Although the immune responses against opportunistic infections are improved with ART, the treatment does not fully restore an effective HIV-specific T cell pool capable of controlling HIV infection. As for CD8⁺ T cell functions, ECs possess less exhausted and more polyfunctional CD4⁺ T cells, especially in the mucosa, compared to viremic individuals with progressive disease [309]. Their HIV-specific CD4⁺ T cell responses exhibit enrichment in T_{H1} and T_{H17} signatures, along with high levels of granzymes, IFN γ , and IL-17 [314].

The precise relationship between these phenotypes and their impact on controlling viremia remains unclear. It is uncertain whether these phenotypes actively contribute to the control of infection or if they are merely a consequence of such control. Although the immune system is capable of controlling HIV infection, durable control in the absence of ART is seen only in a minority of individuals. In most cases, the capacity of HIV to develop escape mutations at its T cell epitopes leads to progression toward AIDS.

HIV therapeutic strategies and cure

Despite the tremendous success of ART therapy in controlling viremia and immune system reconstitution, ARV do not cure HIV infection. Therefore, lifelong therapy is needed, but it requires strict adherence. Skipping HIV medication increases the risk of drug resistance, drug side effects, and places a high economic burden. Previous studies, along with a few individuals who have been cured of HIV, have fueled hope for a potential cure. However, to date, only five individuals have been considered cured of HIV. All five underwent HIV-resistant stem cell transplantation.

In 2007, Timothy Ray Brown, formerly known as the “Berlin patient”, received two stem cell transplants from a donor who had a rare mutation known as CCR5 Δ 32. This mutation leads to the absence of CCR5 co-receptors. Timothy Ray Brown received the transplants to treat his acute myeloid leukemia (AML). It was described at the Conference on Retroviruses and Opportunistic Infections (CROI) in 2008 that HIV did not rebound even after analytical treatment interruption (ATI), both in the blood and tissues [315, 316]. Unfortunately, Timothy Ray Brown died in September 2020 due to a recurrence of leukemia, but he remained HIV-free for 13 years.

In 2019, Adam Castillejo (the “London patient”) became the second person to achieve an HIV cure after a bone marrow transplant to treat his Hodgkin lymphoma [317]. A 53-year old person, referred to as the “Dusseldorf patient”, was confirmed as cured early this year, even though he had stopped his treatment 4 years ago. The “Dusseldorf patient” received an allogeneic hematopoietic stem cell transplantation (aHSCT) in 2014 for AML [318].

Additionally, two more individuals, Paul Edmonds (formerly known as the “City of Hope patient”) [319] and a woman referred to as the “New York City patient”, both received AML

stem cell transplants from donors with the CCR5 Δ 32 mutation. However, the “New-York City patient”, underwent a haplo-cord transplant, which involved combining cord blood cells with haploidentical stem cells from an adult. This was due to the complexity of finding a match for someone of being of mixed race [320]. Moreover, unlike aHSCT, a graft-versus-host disease is less common with haplo-cord transplantation, presenting a potential HIV cure for PLWHIV who require a stem cell transplantation.

Notwithstanding the hope that these five cases represent, many other attempts have failed. Some infected cells appear to be partially resistant to chemotherapy regimens used for aHSCT and can cause viral rebound even with homozygous CCR5 Δ 32 stem cells [321]. In that study, Verheyen *et al.* revealed that the viral rebound was associated with a replicative CXCR4-tropic variant that had already been detected prior to the aHSCT [321]. Additionally, this procedure is not scalable for the treatment of millions of PLWHIV worldwide and is medically intensive, therefore, it is only recommended for the treatment of life-threatening cancer.

HIV vaccine strategies

Unfortunately, there is still no effective and widely available HIV vaccine to prevent or treat HIV infection. To date, six vaccine candidates have undergone efficacy trials out of which only one (RV144 trial) showed a modest efficacy. The initial two trials, VAX003 and VAX004, aimed to induce antibodies against gp120, but they failed given that no difference in the rate of infection or disease progression, no effects on CD4⁺ T cell counts or viral load levels, and more importantly, no neutralizing antibodies against different HIV variants were observed between vaccinated and non-vaccinated individuals [322]. On the

other hand, the STEP and Phambili trials tested recombinant adenovirus vectors encoding viral proteins Gag, Pol, and Nef. The objective was to elicit cellular immunity, but no overall protection against HIV was observed. In the STEP trial, individuals with pre-existing immunity to adenovirus experienced worsened HIV infection outcomes [323-326].

The RV144 “Thai trial” utilized a recombinant canarypox vector expressing the *env*, *gag*, and *pol* genes, which were further boosted with a recombinant gp120 from clade AE. Initial clinical evidence demonstrated an efficacy of 60.5% in the first year, but this effectiveness declined to 31.2% after 3.5 years from the first immunization [325]. The protection observed in the trial was attributed to non-neutralizing V1/V2-specific immunoglobulin (Ig)G antibodies, which triggered ADCC activity and antibody-dependent cellular phagocytosis (ADCP), along with decreased IgA responses [325]. However, the trial raised controversies due to the exclusion of some participants, and the results pertaining to those individuals were not disclosed. Subsequent analysis showed that the vaccine might only be 26% effective, but this result did not reach statistical significance [327]. The HIV Vaccine Trials Network 702 (HVTN 702) “Uhambo trial” was designed based on the RV144 trial, utilizing a recombinant gp120 from clade C instead of AE. In 2020, an interim analysis revealed no prevention of infection, leading to the termination of this trial.

Recently, two trials, namely HVTN 702 “Imbokodo trial” and HVTN 706 “Mosaico trial”, were halted due to a lack of efficacy in HIV protection. Both trials utilized an adenovirus 26 (Ad26)-vectored tetravalent vaccine, encoding for two distinct mosaic Gag-Pol Ad26 vectors and two Env Ad26, followed by gp140 protein boosts. Mosaic antigens involve computationally recombining HIV sequences to optimize the coverage of the diverse protein sequences that characterize HIV. This intricate procedure aims to generate a

mosaic antigen that encompasses a broader range of genetic variants, thereby enhancing immunogenicity and efficacy.

A novel platform has showcased its success in humans during the CoVID-19 pandemic. mRNA vaccines leverage host cells to produce protein immunogens capable of eliciting potent antibody and cellular responses. Our team and others have assessed the potential of mRNA vaccines in at-risk populations [328, 329], making them a promising avenue for further exploration in vaccination strategies. While no mRNA vaccines have been developed for HIV yet, RNA vaccines based on the Env protein have demonstrated the ability to generate robust specific responses in animal models [330].

Genome editing strategy

The use of CRISPR-Cas9 (Cluster Regularity Interspaced Short Palindromic Repeat Associated Protein 9) has been proposed as an approach for cure strategy. This system has proved its efficacy in precise insertion, deletion, and replacement of target dsDNA [331]. It has been extensively utilized for genome modification in various living organisms.

In line with the five individuals who have previously been cured of HIV, research has focused on studying the CCR5 Δ 32 mutation, which provides protection against HIV. Studies have shown that CCR5 knockout confers a selective advantage on CD4⁺ T cells in PLWHIV and has been proven safe [332]. The other HIV coreceptor, CXCR4, has also been a target of investigation. While CXCR4-modified cells have exhibited resistance to HIV infection [333], severe side effects may occur during thymic differentiation and hematopoietic cell development that require CXCR4. Therefore, targeting HIV coreceptors using gene editing machinery necessitates caution in the context of a cure strategy. Direct

elimination of integrated DNA by Cas9 is another possible approach. Several studies have demonstrated the effectiveness of CRISPR-Cas9 in targeting the HIV genome, including the LTR region [334, 335]. These promising results have led to the approval of the first trials by the FDA, which will test EBT-101, an *in vivo* CRISPR-Cas9 gene editing system delivered through an adenovirus-associated virus vector designed to excise HIV-1 proviral DNA [336].

Broadly Neutralizing antibodies (bNAbs) strategy

In addition to HIV prevention, broadly neutralizing antibodies (bNAbs) have been tested in both animal models and clinical trials as therapy during chronic untreated infection or after ART interruption. Neutralizing antibodies possess the ability to block viral entry by either preventing receptor/coreceptor binding or inhibiting conformational changes in the envelope glycoproteins. bNAbs, on their side, are capable of neutralizing a majority of strains from diverse clades and can be categorized into six groups based on the epitopes they target on the Env trimer: the CD4 binding site (CD4bs), the V2 apex, the V3 glycan region, the silent face, the membrane-proximal external region (MPER), and the interface between gp120 and gp41 [337].

Antibody monotherapy in mice and NHPs (non-human primates) using bNAbs resulted in a temporary reduction of the plasma viral load for two weeks before the viral rebound occurred. Similar results were observed in viremic PLWHIV using antibodies such as 3BNC117, VRC01, or 10-1074. The rapid viral rebound within a few weeks was mainly attributed to the development of escape mutation. Similar to ART regimens, a combination of multiple bNAbs targeting nonoverlapping epitopes on the envelope protein has been

employed to extend the period of viral load reduction [338]. However, prior testing of the virus is necessary to determine the efficacy of bNAbs therapy. The combination of ART and bNAbs therapy was tested in PLWHIV who had achieved successful viral suppression with ART [339]. Following ATI, bNAbs were able to control the viral load to undetectable levels. One possibility is that bNAbs directly bind to the virus, forming complexes that inhibit viral entry and prevent conformational changes in the envelope, thereby reducing infectivity.

Our team conducted a study on the specific-CD4⁺ and -CD8⁺ T cell responses to HIV peptides in individuals undergoing bNAbs therapy [340]. While escape mutations to 10-1074 were observed in rebound viruses, attributed to the shorter half-life of 3BNC117, almost all participants displayed higher levels of specific-CD4⁺ and -CD8⁺ T cells. It was suggested that this increase in T cell reactivity to HIV Gag epitopes might have played a role in controlling viral replication [340]. Notably, the expansion of HIV-specific T cell responses was unlikely to be driven by viral replication, as it was measured during a period of sustained viral suppression. It has been shown that the presence of bNAbs leads to the formation of immune complexes that activate DCs, thereby enhancing their antigen-presenting capacities and eliciting a vaccine-like effect [341].

To date, several ongoing clinical trials are testing different combinations of bNAbs or modified versions thereof, aiming to extend their half-life and achieve long-term viral suppression of HIV after ATI. Additionally, other clinical trials are investigating the impact of combining immunomodulators with bNAbs after ATI, with the goal of reactivating and reducing the viral reservoir or triggering antiviral immune responses. Consequently,

bNAbs can serve as an alternative strategy to ART in maintaining suppressed viral load in PLWHIV.

Chimeric Antigen Receptor (CAR)-T cells strategy

The CAR-T cell strategy has been successfully implemented in the treatment of hematologic cancers. It involves the use of autologous T cells that are engineered to recognize and bind to specific foreign antigens, thereby inducing immune system activation. The first CAR-T cell therapy was developed in the early 2000s, employing a fusion of the CD4 extracellular domain with the CD3 ζ signaling domain [342]. Utilizing CD4 was advantageous due to its recognition by Env proteins, ensuring broad targeting of all HIV isolates. Moreover, CD4 binding sites on the envelope protein exhibit relative stability, and mutations in these sites lead to decreased viral fitness, making CD4 an effective and consistent targeting molecule for anti-HIV CAR design. However, clinical trials have demonstrated that CD4-based CARs did not achieve long-lasting control of viral replication. This outcome has been associated with the susceptibility of CAR-T cells to HIV infection and the elimination of activated cells, inadequate activation signaling from costimulatory signals, suboptimal T cell expansion, and insufficient viral antigen stimulation [342]. Notwithstanding the lack of protection against HIV, initial CAR-T cell therapies have been proven safe and feasible *in vivo*.

Recently, a new approach incorporating bNAbs into CAR-T cells has been developed. These bNAb-based CARs consist of a single-chain variable fragment derived from bNAbs that target conserved sites within the Env protein. This modification enables CD8⁺ T cells to proliferate, eliminate infected cells, and suppress viral replication [343]. Given the high

potential for antigen escape, a combination of multiple bNAbs-based CAR-T cells would likely be necessary to achieve greater suppression.

Furthermore, CAR-modified NK cells have also been considered as a potential antiviral therapy against HIV. Typically, NK cells can target and eliminate infected cells that downregulate the MHC-I, or infected cells that increase the expression of ligands such as unique long-binding proteins ULBP-1 and -2. Moreover, NK cells can engage in ADCC against infected cells [344]. Currently, there are no CAR-modified NK cell therapies for HIV, as the first two clinical trials for cancer immunotherapies have only been completed earlier this year.

“Block and Lock” strategy

As its name suggests, this strategy aims to block viral reactivation, even after treatment interruption, using latency-promoting agents (LPAs). As described earlier, numerous viral and cellular proteins are involved in HIV latency and transcription and have been identified as potential targets for LPAs to permanently silence proviruses. LPAs can: 1) inhibit Tat, IN, or cellular factors that play a role during viral transcription; 2) inhibit cellular pathways involved in viral reactivation; 3) induce epigenetic modifications to establish a repressive chromatin environment at the LTR promoter [345].

The most extensively studied LPA thus far is didehydro-cortistatin A (dCA), which inhibits Tat [346]. dCA has been associated with a reduction in viral reactivation in CD4⁺ T cells from HIV-infected individuals, and a delay in viral rebound has been observed in HIV-infected humanized mice following ATI [347]. This delay has been attributed to increased

nucleosomal occupancy of the viral DNA mediated by dCA, thereby limiting the recruitment of RNA pol II to the HIV promoter [347].

The “Block and Lock” strategy can be mediated by various molecules, including LEDGINS. These molecules hinder the interaction between LEDGF/p75 and IN, thereby preventing viral integration into the host genome during the early phase of HIV infection [348]. Additionally, LEDGINS can inhibit the late stages of infection by modulating IN multimerization in the virions, resulting in the production of non-infectious viral particles [349]. Depletion of LEDGF/p75 by LEDGINS reduces integration into transcriptionally silent regions, promoting the establishment of deep latency for the provirus [350].

Targeting the Jak-STAT pathway to reduce homeostatic proliferation has also been investigated. Inhibiting Jak is associated with a decrease in the size of the viral reservoir. By blocking downstream events following the binding of various cytokines to their receptors, Jak inhibitors impede the activation and cellular division of cells. Thus, targeting this pathway could potentially reduce immune activation, inflammation, and the susceptibility of the cells to infection, as well as mitigate progressive immune system dysfunction [351].

Other molecules are being studied in the context of the “Block and Lock” strategy. For example, the anticancer compound curaxins inhibit the FACT complex (facilitates chromatin transcription complex), which usually acts as a histone chaperone destabilizing the nucleosomal structure for the RNA pol II-driven transcription [352]. AUY922 and 17-AAG, two other anticancer compounds, target heat shock protein 90 (HSP90). Inhibition of HSP90 suppresses Tat-mediated transcription and NF- κ B, NFAT, and STAT5 signaling [353]. Another target is the mammalian target of Rapamycin (mTOR). Inhibition of mTOR

reduces viral reactivation in CD4⁺ T cells by downregulating the phosphorylation of CDK9, which impedes phosphorylation of RNA pol II. The PI3K/Akt pathway (Phosphoinositide 3-kinases, Protein kinase B) lies upstream of mTOR. Activation of PI3K induces Akt, resulting in the activation of mTOR. PI3K and Akt inhibitors have been developed as anticancer drugs. The use of such inhibitors hampers the anti-apoptosis effects mediated by Akt and could induce the clearance of HIV-infected cells [354].

Despite limiting the viral transcription, these molecules are “only” capable of delaying viral rebound and cannot completely silence viremia in the absence of ART. Furthermore, the “Block and Lock” strategy does not eradicate the virus, necessitating regular intake to prevent viral transcription. Additionally, this strategy is relatively new, and only a few studies have investigated the effects of these molecules in animal models.

“Shock/Kick and Kill” strategy

The “Shock/Kick and Kill” strategy is one of the most extensively studied approaches and aimed at purging the viral reservoir and eradicating HIV from the body. It involves the use of LRAs to activate latently HIV-infected cells, thereby inducing viral expression [355]. Subsequently, CTLs are expected to eliminate the reactivated cells that display viral antigens on their surface, while new infections are inhibited by ARVs (Figure 12). This strategy implies that the viral reservoir remains completely hidden from the immune system in the absence of viral transcription. Many LRAs have been developed over the years, and they are classified based on their respective targets (Figure 12).

None of the molecules tested alone efficiently reduced the size of the viral reservoir, even after multiple doses of the same LRA. Our group and others have demonstrated potent *ex vivo* reactivation of HIV transcription and translation from latency mediated by various

LRAs [253, 254, 355]. Combinations of LRAs from different classes have also been studied, yielding diverse results in terms of reactivating latently infected cells. In the majority of studies, PKCa have been combined with LRAs that trigger non-T-cell activating mechanisms. Combination of PKCa with bromodomain domain inhibitor, HDACi, P-TEFb enhancers, or TLR agonists have demonstrated synergistic reactivation *in vitro* and *ex vivo* [355].

However, combining reactivation mediated by LRA with the killing of the infected cells is essential. The immune system can be supported by molecules that aid in the killing process. Studies have shown that the use of LRAs alone is insufficient in reducing the size of the reactivated viral reservoir. This is because the immune system in PLWHIV on ART is unable to effectively control viremia. Chronic HIV infection is associated with immune dysfunction, particularly in CD8⁺ T cells, which exhibit increased expression of inhibitory signals leading to their exhaustion [169, 304, 305], resulting in reduced HIV control. HIV also possesses the ability to evade CTL responses through mutations in its T cell epitopes [303]. Despite the initiation of ART, the number, and functions of HIV-specific CD8⁺ T cells are not fully restored due to decreased antigen concentrations [356]. Additionally, it has been described that the use of HDACi, in the context of shock is associated with impaired CTL functions in eliminating HIV-infected cells [357]. While HDACi can reactivate latently infected cells, they have a negative impact on the eradication of such cells within the “Shock/Kick and Kill” strategy. Enhancing CTL responses appears to be crucial for both reducing the size of the viral reservoir and improving viral control [358].

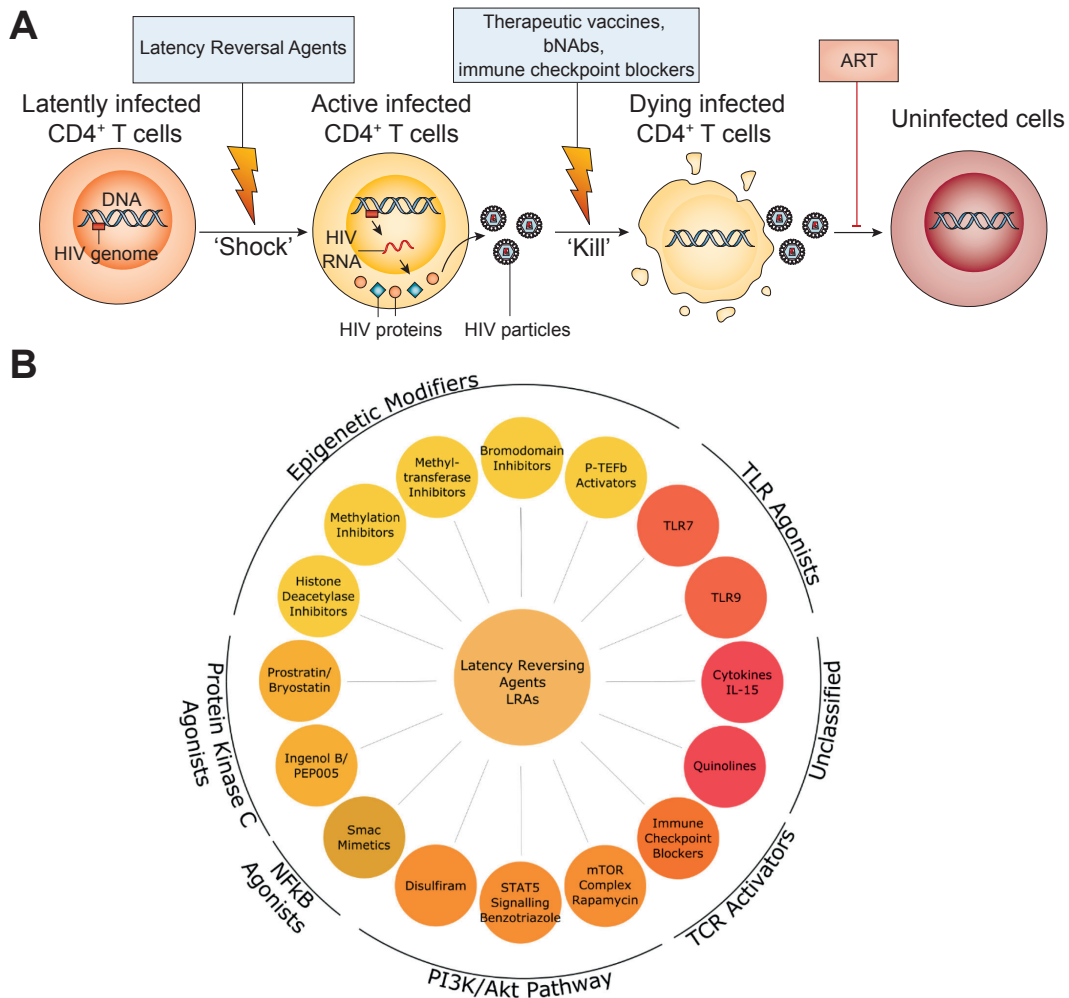


Figure 12. – “Shock/Kick and Kill” strategy and Latency Reversal Agents classes

(A) “Shock/Kick and Kill” strategy is based on the reactivation of latently HIV-infected cells using LRAs combined with therapeutics strategies aimed at eliminating the reactivated cells. Simultaneous administration of ARV prevents *de novo* infection by newly produced virions. (B) LRAs can target different pathways, leading to the reactivation of HIV transcription and, in some cases, viral production. However, clinical evidence demonstrating the effectiveness of the “shock/kick and kill” strategy *in vivo* is yet to be determined. Adapted from [359] and [355] with permission from *Nature Springer* and *Elsevier Publishing Group*.

Chapter 2 – Hypotheses and Objectives

Despite advances in ART, a cure for HIV remains elusive due to the persistence of viral reservoirs. These reservoirs consist of latently infected cells that can reactivate and produce new virus particles, leading to viral rebound if ART is interrupted or discontinued. Numerous assays have been employed to assess the size and characteristics of viral reservoirs. However, none of these assays comprehensively capture the translational, transcriptional, and phenotypic heterogeneity of the viral reservoirs. Notably, CD4⁺ T cells bearing HIV genomes are ten times more abundant than the transcription-competent cells [251], which, in turn, are ten times more frequent than cells competent for viral translation [253, 254, 259]. These discrepancies have been attributed to successive stages of blocks in viral transcription and translation [191].

Furthermore, HIV infection profoundly influences immune responses. The presence of a vast quantity of antigens leads to the exhaustion of HIV-specific T cell responses in individuals with detectable viremia [165, 169]. Paradoxically, these responses remain elevated after initiation of ART. Our group had recently demonstrated the existence of spontaneously active viral reservoirs in ART-treated PLWHIV which were associated with higher magnitudes of both HIV-specific CD4⁺ and CD8⁺ T cell responses [233]. Moreover, we have observed that, in contrast to CD8⁺ T cells, HIV-specific CD4⁺ T cell responses exhibit skewed phenotypes and functions [313, 314].

Based on previous results, **we hypothesized** that i) the stimulation of latent HIV-infected cells in ART-suppressed individuals can reactivate transcription-competent cells unable to express viral proteins, associated with the phenotypic and genomic profiles of the

infected cells; and that ii) the immune responses observed prior to initiating ART determine the establishment of viral reservoirs subsequent to treatment.

For the first project, our objective was therefore to first measure the viral reservoir cells in a cohort of ART-treated individuals, and secondly to phenotype and sequence these cells. We i) compared the frequency of HIV viral RNA-positive (vRNA⁺) cells between ART-treated individuals and untreated participants; ii) analyzed the cellular and viral characteristics of the inducible vRNA⁺ cells in both ART-treated and untreated individuals using diverse LRAs; and iii) investigated the association between the viral transcription profile and viral genome integrity of inducible vRNA⁺ in PLWHIV receiving ART.

For the second project, the primary objective was to examine how pre-ART HIV-specific immune responses affect the viral reservoir on ART. We also investigated if the transcriptional state of the infected cells pre-ART defines the decline post-ART or was associated with preferential persistence of viral subpopulations. Specifically, we aimed to: i) assess the presence of vRNA⁺ cells longitudinally before and after initiating ART; ii) determine the magnitude of HIV-specific CD4⁺ and CD8⁺ and antibody responses in both ART-treated individuals and untreated participants comparing them of ECs who naturally control viremia; and iii) investigate the persistence of preexisting proviruses following ART.

In summary, my research endeavors were driven by the aim of elucidating the relationship between latent HIV-infected cells, immune responses pre-ART, and the establishment of such viral reservoirs post-ART, with the intention of advancing our understanding of HIV pathogenesis and treatment outcomes.

Chapter 3 – Manuscript 1: Combined single-cell transcriptional, translational, and genomic profiling reveals HIV-1 reservoir diversity

Status: This research article was published in *Cell Reports*, August 31, 2021;

<https://doi.org/10.1016/j.celrep.2021.109643>

Author contribution: G er my Sannier, Mathieu Dub , and Daniel E. Kaufmann designed the study. Amy E. Baxter, Julia Niessl, Elsa Brunet-Ratnasingham, R mi Fromentin, and Nicolas Chomont provided assistance with assay protocols and experimental design. G er my Sannier, Caroline Dufour, Nathalie Brassard, Gloria Gabrielle Delgado, Am lie Pagliuzza and Roxanne Charlebois performed experiments. G er my Sannier, Mathieu Dub , Caroline Dufour, and Corentin Richard analyzed the data. Bertrand Routy and Jean-Pierre Routy contributed to recruitment and clinical assessments. G er my Sannier, Mathieu Dub , Caroline Dufour, R mi Fromentin, Nicolas Chomont, and Daniel E. Kaufmann interpreted the data. G er my Sannier wrote the initial draft of the manuscript with edits from Mathieu Dub  and Daniel E. Kaufmann. All co-authors reviewed and edited the manuscript. Daniel E. Kaufmann provided supervision.

Combined single-cell transcriptional, translational, and genomic profiling reveals HIV-1 reservoir diversity

Gérémy Sannier^{1,2,6}, Mathieu Dubé^{1,6}, Caroline Dufour^{1,2}, Corentin Richard¹, Nathalie Brassard¹, Gloria-Gabrielle Delgado¹, Amélie Pagliuzza¹, Amy E. Baxter^{1,2,7}, Julia Niessl^{1,2,8}, Elsa Brunet-Ratnasingham^{1,2}, Roxanne Charlebois¹, Bertrand Routy^{1,2}, Jean-Pierre Routy^{3,4}, Rémi Fromentin¹, Nicolas Chomont^{1,2}, and Daniel E. Kaufmann^{1,2,5,*}

¹Research Centre of the Centre Hospitalier de l'Université de Montréal (CRCHUM)

²Université de Montréal Montreal, Quebec, Canada

³Chronic Viral Illnesses Service and Division of Hematology, McGill University Health Centre, Montreal, QC H4A 3J1, Canada

⁴Infectious Diseases and Immunity in Global Health Program, Research Institute, McGill University Health Centre, Montreal, Quebec, Canada

⁵Lead contact

⁶These authors contributed equally

⁷Present address: Perelman School of Medicine, University of Pennsylvania, Philadelphia, PA, USA.

⁸Present address: Current affiliation: Center for Infectious Medicine, Department of Medicine Huddinge, Karolinska Institutet, Stockholm, Sweden.

*Correspondence: daniel.kaufmann@umontreal.ca

IN BRIEF

Sannier et al. describe diverse viral transcriptional and translational profiles of inducible HIV-1 reservoirs in antiretroviral-therapy (ART)-suppressed individuals, with class specificity of latency reversal agents. They reveal that reactivated proviruses are mostly defective, even in cells which express HIV-1 proteins, and that identical sequences can adopt diverse transcriptional patterns.

HIGHLIGHTS

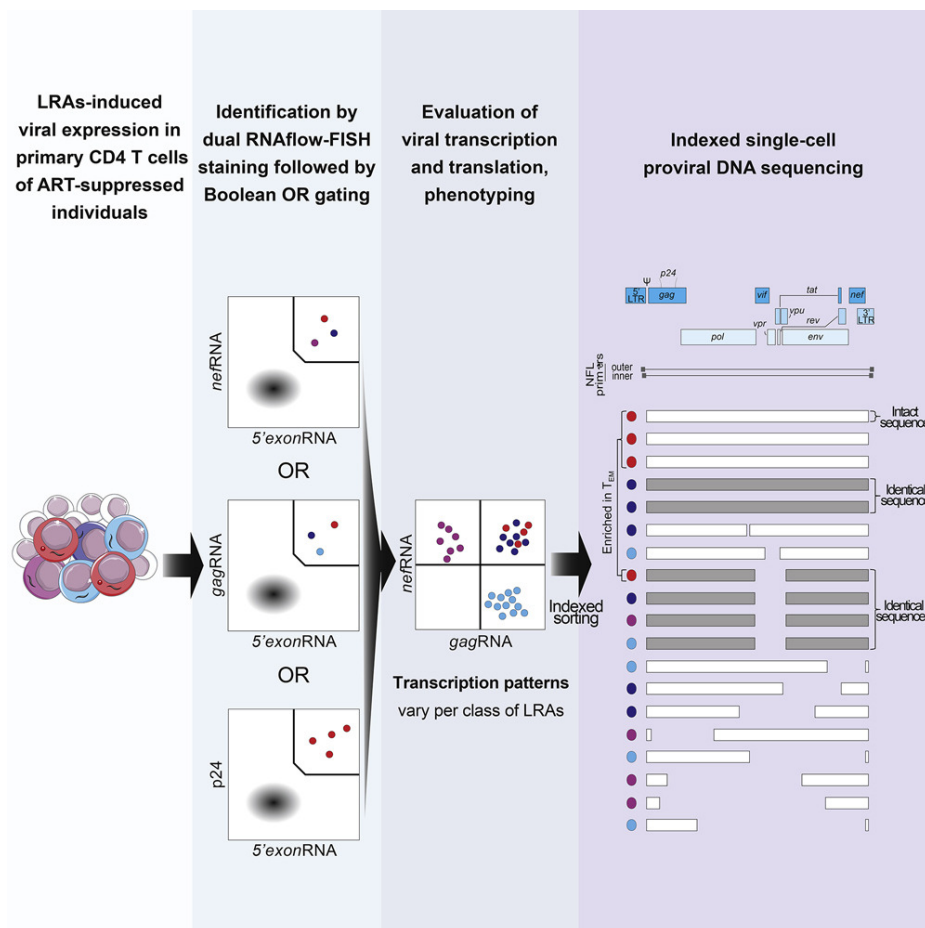
- Expression of p24 protein in induced vRNA⁺ cells is rare during ART suppression
- LRAs induce class-specific viral gene transcription and translation patterns
- Induced transcriptionally active proviruses are mostly defective, even in p24⁺ cells
- Identical HIV-1 clones can adopt diverse transcriptional and translational states

SUMMARY

Although understanding the diversity of HIV-1 reservoirs is key to achieving a cure, their study at the single-cell level in primary samples remains challenging. We combine flow cytometric multiplexed fluorescent in situ RNA hybridization for different viral genes with HIV-1 p24 protein detection, cell phenotyping, and downstream near-full-length single-cell vDNA sequencing. Stimulation-induced viral RNA-positive (vRNA⁺) cells from viremic and antiretroviral-therapy (ART)-suppressed individuals differ in their ability to produce p24. In participants on ART, latency-reversing agents (LRAs) induce a wide variety of viral gene transcription and translation patterns with LRA class-specific differences in reactivation potency. Reactivated proviruses, including in p24⁺ cells, are mostly defective. Although LRAs efficiently induce transcription in all memory cell subsets, we observe induction of

translation mostly in effector memory cells, rather than in the long-lived central memory pool. We identify HIV-1 clones with diverse transcriptional and translational patterns between individual cells, and this finding suggests that cell-intrinsic factors influence reservoir persistence and heterogeneity.

GRAPHICAL ABSTRACT



KEYWORDS

HIV-1, viral reservoirs, CD4 T cells, multiplexed fluorescent in situ RNA hybridization, single-cell analysis, multiparameter flow cytometry, viral sequencing, viral transcription, viral translation, latency-reversing agents

INTRODUCTION

A major obstacle to achieving HIV cure is the persistence of latent viral reservoirs because they are not cleared even after prolonged therapy. Upon stimulation, latently infected cells can revert to a state of transcriptional activity and fuel viral rebound when antiretroviral therapy (ART) is interrupted (Davey et al., 1999). Long-lived resting memory CD4+ T cells are the main component of the viral reservoir (Siliciano et al., 2003). Several assays have been used to evaluate the size and characteristics of viral reservoirs (Fromentin and Chomont, 2020). Recent iterations of DNA-based methods measure “intact” proviruses likely to support viral replication, rather than the predominant defective proviruses detected by traditional methods (Bruner et al., 2019; Gaebler et al., 2019). Conversely, viral growth assays (VOAs) quantify the rare replication-competent and inducible proviruses (Laird et al., 2013), but overlook other active viral reservoirs that may be of biological relevance. Measures of multiply spliced viral RNA (vRNA) (Pasternak and Berkhout, 2018; Procopio et al., 2015) provide good estimates of the size of the transcriptionally competent viral reservoir, but do not capture the heterogeneity of the viral reservoir. Flow-cytometry-based methods provide single-cell resolution, but to date have relied on protein detection (p24 (Pardons et al., 2019) or gp120 (Cohn et al., 2018)), single vRNA detection by flow cytometric fluorescent in situ RNA hybridization (RNAflow-FISH) (Grau-Expósito et al., 2017, 2019), or a combination of both (Baxter et al., 2016, 2017). Viral reservoir identification based on p24 expression limits the analysis to translation-competent viral reservoirs (Baxter et al., 2016; Grau-Expósito et al., 2019; Pardons et al., 2019).

Although important, none of these assays can individually provide an integrated comprehension of the viral reservoir's translational, transcriptional, and phenotypic heterogeneity. Differences in the range of detection of these assays can be attributed to the nature of their readouts. CD4⁺ T cells carrying HIV genomes are one order of magnitude more abundant than those with the ability to transcribe multiply spliced RNA (Procopio et al., 2015), which are another order of magnitude more frequent than those producing p24 (Baxter et al., 2016; Pardons et al., 2019). These differences may reflect successive stages of blocks in viral transcription and translation (Mohammadi et al., 2014; Yukl et al., 2018). The type of cells harboring viral genomes, and the latency-reversing agents (LRAs) used, influence how these blocks are alleviated, adding to the complexity of viral reservoirs (Baxter et al., 2016; Bullen et al., 2014; Grau-Expósito et al., 2019; Pardons et al., 2019; Yukl et al., 2018). How all these blocks intertwine in vivo to shape the translational and transcriptional heterogeneity of viral reservoirs remains unclear. Another critical bottleneck is the limited ability to link, at the single-cell level, a proviral DNA sequence with its capacity to produce viral transcripts and proteins. Such analyses require experimental approaches accommodating single-cell measurements of viral transcription, translation, and downstream proviral DNA sequencing (Brandt et al., 2020). Here, we characterized the viral reservoirs in the peripheral blood mononuclear cells (PBMCs) from people living with HIV (PLWHs). To define their heterogeneity and responsiveness to latency reversal, we performed combined single-cell analyses of viral gene co-expression, viral protein translation, cellular phenotypic features, and downstream near-full-length sequencing conducted on indexed single-sorted cells.

RESULTS

Multiplexed RNAflow-FISH enables robust detection of HIV viral RNA-positive (vRNA⁺) cells

RNAflow-FISH enables single-cell detection of viral reservoirs in primary human samples. However, its accuracy depends on dual viral products detection, as done previously using *gagpol* vRNA and p24 protein co-detection (Baxter et al., 2016, 2017). Consequently, only translation-competent cells could be reliably identified. To inclusively study transcriptionally active HIV-1-infected cells independently of viral protein translation, we elaborated a two-layer multiplexed vRNA detection strategy (Figure 1A). The purpose of the first layer was to provide the most inclusive detection of viral transcripts. To that end, we designed a *5'exon*RNA probe set targeting exon sequences (the 5' specification is a reminder; it covers all but the most distal exon in *nef*, see below) present on all viral transcripts (Karn and Stoltzfus, 2012). The second layer of detection ensured specificity. Two complementary probes were generated for that goal. First, a *nef*RNA probe set covered the exon sequence in *nef* before the 3' LTR. This probe targeted fully elongated transcripts. Second was a *gag*RNA probe set, detecting full-length genomic transcripts but also short *nef*RNA⁻ abortive transcripts previously reported in viral reservoirs (Yukl et al., 2018). Although the goal of our approach was not to specifically study splicing, *gag*RNA could also discriminate between cells enriched in elongated unspliced (*5'exon*RNA⁺ *gag*RNA⁺ *nef*RNA⁺) versus spliced (*5'exon*RNA⁺ *gag*RNA⁻ *nef*RNA⁺) transcripts. In a spiking experiment with HIV-1-infected ACH-2 cells, multiplexing the detection of vRNA⁺ cells decreased the threshold of detection down to 6/10⁶ cells (Figure S1A). We also stained for p24 as a measure of viral translation competence.

To test detection of vRNA⁺ in primary CD4⁺ T cells with this platform, we used CD4⁺ T cells isolated from PBMCs of 11 PLWHs sampled before ART initiation (untreated [UNT]) (Figures S1B and S1C) who displayed a range of viral loads and total and integrated HIV DNA levels per 10⁶ CD4⁺ T cells (Table S1). By design, 5' *exon*RNA was expected to provide an inclusive detection of vRNA⁺ cells. Cells co-expressing *gag*RNA, *nef*RNA, or p24 were found only in the 5' *exon*RNA⁺ population (Figure S1D). Therefore, we selected 5' *exon*RNA as the primary criterion for HIV⁺ cell identification. To increase the specificity of vRNA⁺ cells identification, we supplemented the 5' *exon*RNA probe set with *nef*RNA, *gag*RNA, or p24. vRNA⁺ cells were defined by a Boolean OR gate strategy in which vRNA⁺ cells were necessarily expressing 5' *exon*RNA, along with either *nef*RNA, *gag*RNA, or p24 (Figure 1B). As explained above, we privileged this OR gate strategy over a more standard triple-positive approach (5' *exon*RNA⁺ *gag*RNA⁺ *nef*RNA⁺) to include spliced transcript (theoretically 5' *exon*RNA⁺ *gag*RNA⁻ *nef*RNA⁺) and short abortive transcripts (theoretically 5' *exon*RNA⁺ *gag*RNA⁺ *nef*RNA⁻). Cells positive for (1) 5' *exon*RNA and (2) *gag*RNA, *nef*RNA, or p24 are henceforth termed vRNA⁺. Our approach quantified a median of 82 vRNA⁺ cells/10⁶ CD4⁺ T cells in UNT PLWHs (Figure 1C) with excellent interexperimental reproducibility (Figure S1E). We observed a median of two false-positive events per million cells in uninfected donors (UDs; Figure 1C). The threshold of detection (mean in UD + 2 SD) was set at 6/10⁶ CD4⁺ T cells, in line with the limit of accurate detection observed in the spiking experiment. The measure of vRNA⁺ cells/10⁶ CD4⁺ T cells strongly correlated with viral load (Figure 1D), indicating that the frequency of vRNA⁺ cells reflects the level of circulating vRNA in plasma. Overall, these data demonstrate that multiplexed RNAflow-FISH analyzed with a combined Boolean gating strategy provides a robust measure of vRNA⁺ cells in viremic PLWHs.

Stimulation-induced vRNA⁺ cells have much lower p24 translation propensity in ART compared with UNT participants

We next sought to quantify induced transcriptionally active viral reservoirs in 16 ART-treated and 9 UNT PLWHs. CD4⁺ T cells were stimulated for 12 h with phorbol 12-myristate 13-acetate (PMA)/ionomycin to induce latency reversal and viral gene expression. The multiplexed OR gate analysis strategy also resulted in specific detection of vRNA⁺ cells in ART samples (Figures S2A and S2B). In UNT samples, PMA/ionomycin induction led to a consistent 2-fold median increase in vRNA⁺ cell detection, suggesting that both latently infected and replication-competent cells are observed in viremic conditions (Figure 2A). In ART samples, stimulation significantly increased vRNA⁺ detection by 11-fold, to a median of 97 vRNA⁺ cells/10⁶ CD4⁺ T cells (Figure 2A). This measure was less than the measurements of integrated DNA (7-fold) and total DNA (16-fold), yet 20-fold greater than that of p24⁺ gagRNA⁺ cells (Figure S2C), thus providing intermediate measurements between DNA and p24-based detection methods (Figure 2B). Therefore, multiplexed RNAflow-FISH allows broad detection of transcriptionally and/or translationally inducible viral reservoirs.

Next, we examined the links between viral translation and transcription within individual cells. In UNT samples, most vRNA⁺ cells expressed p24, whereas it was comparatively infrequent among vRNA⁺ cells in ART (Figures 2C and 2D). This suggests a block to p24 translation in induced viral reservoirs. To assess viral transcription, we analyzed *gag*RNA and *nef*RNA co-expression in p24⁺ and p24⁻ vRNA⁺ cells (Figure 2E). Combined with p24 translation, this layered analysis created eight theoretical subpopulations of viral reservoirs (Figure 2F). Among these, single 5'*exon*RNA⁺ cells could not be interpreted

because of the insufficient specificity of single-parameter detection (see Figure 1). The prevalence of the remaining seven theoretical populations is summarized in Figure 2G. Although there was inter-donor variability in UNT samples (Figure S2D), we observed an overall consistent hierarchy of the different populations in absence of stimulation: $p24^+ gagRNA^+ nefRNA^+$ (fully elongated transcripts sustaining translation, termed $p24^+$) > $p24^- gagRNA^+ nefRNA^-$ (short abortive or deleted transcripts, termed $gagRNA^+$) > $p24^- gagRNA^+ nefRNA^+$ (fully elongated transcripts not sustaining translation, termed $vRNA_{DP}$ for “double $gagRNA^+ nefRNA^+$ positive”) > $p24^- gagRNA^- nefRNA^+$ (spliced or deleted transcripts, termed $nefRNA^+$). The hierarchy in ART samples was strikingly different: $gagRNA^+ \cong nefRNA^+ > vRNA_{DP} > p24^+$ cells. This difference in hierarchy compared with UNT samples suggested that the transcription process is suboptimal in induced viral reservoirs.

Cytometric fluorescent intensities (FIs) give a semiquantitative assessment of RNA copies per cell in RNAflow-FISH (Porichis et al., 2014) that can be used to assess the levels of transcription and translation per infected cell. We used this metric to determine if the level of viral transcription could define the success of viral translation. To avoid biases caused by low number of viral reservoir cells per participant, we concatenated all events from PMA/ionomycin-stimulated ART samples. Single-cell FI from PMA/ionomycin-induced $p24^+$ UNT cells were used as a benchmark of productively infected cells. $p24^+$ cells induced by PMA/ionomycin from ART and UNT individuals presented a similar median single-cell $p24$ FI, compatible with potential for replication (Figure 2H). Because $5'exonRNA$ is expressed in all $vRNA^+$ cells, we used it as a surrogate of global transcriptional activity. $5'exonRNA$ expression was equivalent in $p24^+$, $vRNA_{DP}$, and

*nef*RNA⁺ cells but significantly lower by 1 order of magnitude in *gag*RNA⁺ cells (Figure 2I). This can be explained either because elongation is inefficient in these cells, limiting the amount of probes that can hybridize with target vRNA, or there is a lower transcriptional rate. Expression levels of *nef*RNA were equivalent in all populations except for the *gag*RNA⁺ population (Figure 2J). The expression of *gag*RNA proved more variable: high in p24⁺ cells, low in vRNA_{DP} and *gag*RNA⁺ cells, and by definition null in *nef*RNA⁺ cells (Figure 2K). Globally, *gag*RNA⁺ cells showed consistent signs of poor transcriptional activity compared with all the other vRNA⁺ subpopulations, in line with poor transcriptional elongation of the HIV genome. Therefore, the level of *gag* transcripts may indicate key limitations for full viral gene expression.

Finally, we examined the expression of surface CD4 protein as a surrogate of Nef protein expression, because Nef downregulates surface CD4 in infected T cells (Lindwasser et al., 2007). Unfortunately, PMA/ionomycin induction severely downregulates surface CD4, thus precluding such analysis on ART samples. We therefore focused on the UNT cohort to compare CD4 expression at the single-cell level between vRNA⁺ cells and vRNA⁻ CD4⁺ T cells concatenated across multiple donors (Figure 2L). Compared with uninfected vRNA⁻ cells, CD4 was strongly downregulated on p24⁺ cells, and to a lesser extent on vRNA_{DP} cells. CD4 level on *nef*RNA⁺ cells followed a bimodal distribution: consistent with adequate Nef protein expression, most *nef*RNA⁺ cells displayed low CD4 levels. A smaller fraction was comparable with vRNA⁻ controls, suggesting inadequate Nef protein expression in these *nef*RNA⁺ cells. CD4^{high} cells were much more frequent in *gag*RNA⁺ cells. A minority of *gag*RNA⁺ cells expressed low levels of surface CD4, perhaps because of Vpu-mediated CD4 downregulation in the absence of Nef (Willey et al., 1992). These

results suggest a partial disconnect between Gag and Nef protein translation in viral reservoirs, adding to the heterogeneity of HIV-1-infected cells.

Near-full-length single-cell vDNA sequencing of induced, transcriptionally active viral reservoirs identify underlying proviral defects

To establish a link between the detection of viral transcripts and the integrity of the proviral genes that encode them within a given cell, we performed near-full-length sequencing of inducible proviruses using a modified FLIPS assay (Bruner et al., 2016, 2019; Hiener et al., 2017, 2018; Lee et al., 2017). Reactivated viral reservoirs identified by multiplexed RNAflow-FISH were indexed single-cell sorted based on *5'exon*RNA, *gag*RNA, *nef*RNA, and p24 expression patterns (Figure S3A). Individual cells were lysed and near-full-length proviral DNA amplified by nested PCR. The resulting ≤ 9 -kb fragments were subjected to PacBio Single Molecule Real-Time (SMRT) sequencing. We obtained a total of 196 sequences from three ART-treated participants across four subsets of transcriptionally induced cells, representing a recovery of 29% of all the single-sorted vRNA⁺ cells (Figures 3A and 3B). *nef*RNA⁺ cells, which did not express *gag*RNA, frequently displayed large internal deletions (>100 bp) in *gag* (Figure 3C). Conversely, large deletions in *nef* were restricted to *gag*RNA⁺ cells (Figure 3D). Deletion in *gag* and *nef* were rare in p24⁺ and vRNA_{DP} cells. We analyzed the sequences for previously described defects known to abrogate viral replication, as inversions, hypermutations, large internal deletions, premature stop codons, and frameshift (except in *nef* (Hiener et al., 2017), because it was reported dispensable for virus replication (Foster and Garcia, 2007)), ψ packaging motif, and alterations of the major splice donor (MSD) site (Bruner et al., 2016, 2019; Hiener et al., 2017; Ho et al., 2013; Lee et al., 2017; Lu et al., 2018) (Figure 3E). In most

transcriptionally active cells, we found packaging signal and MSD site mutations and stop codons/ frameshift defects, whereas large internal deletions were less common. Nevertheless, we did detect few occurrences of large deletions in viral genomes harbored by p24⁺ cells, indicating that protein production can occur even in cells bearing damaged proviruses (Figure 3E). This is consistent with a recent study showing the presence of defects in translation-competent proviruses (Cole et al., 2021). We found few hypermutated or inverted sequences, probably because most corresponding proviruses are not recognized by our probe sets or were not induced.

A previously reported sequential elimination process was used to infer proviral intactness (Hiener et al., 2017, 2018). In this approach, proviral sequences are considered intact if devoid of any of the defects listed above. We adapted this approach to verify if intact proviruses were enriched in any of the identified viral subpopulations. Proviral sequences were screened for the presence of defects following the hierarchy presented in Figure 3F. The integrity statuses summarized in Figure 3G are established based on highest defect found following this elimination process (Figure 3F), and therefore do not exclude the other defects listed beneath. Only two sequences were thus inferred intact (Figure 3G); one was found in a p24⁺ cell, and the other one was found in a vRNA_{DP} cell. All the other sequences harbored defects of various severities. Large deletions anywhere along the provirus were frequent in *nef*RNA⁺, and to a lesser extent in *gag*RNA⁺ and vRNA_{DP} cells. This is consistent with previous studies showing the dominance of large deletions among cells carrying proviral DNA (Bruner et al., 2016, 2019; Hiener et al., 2017; Ho et al., 2013; Lee et al., 2017) (Figure 3G). Proviruses bearing defects exclusively defined by ψ /MSD alterations were found almost exclusively in p24⁺ cells. We found that premature stop

codon/frameshift was the most prevalent defect status, especially in p24⁺ cells (Figure 3G). The premature stop codons from all the viral subpopulations were mapped mostly in *nef* and *tat* (Figure 3H). Given that *nef* was excluded in our sequential elimination workflow, it suggested that the presence of defects in the gene *tat* is an important characteristic of reactivated viral reservoirs. This may be because PMA/ionomycin can bypass *tat*-mediated transactivation, thus allowing Tat-independent transcriptional activity (Luznik et al., 1995). Overall, these data demonstrate that many defective proviruses maintain the ability to produce viral transcripts and even protein upon latency reversal.

Proviral clones display transcriptional and translational heterogeneity

Next, we verified if the heterogeneity of the inducible reservoirs' transcriptional profiles was due to identical proviral sequences with specific defects. Phylogenetic trees were generated for each participant (Figure 4A). It was previously postulated that two identical sequences from donors with a high proviral diversity can be considered proviral clones (Patro et al., 2019). Based on this report, we found evidence of 16 proviral clonal sequences (≥ 2 identical sequences) from all three participants, including 3 large clones in subjects ART3 and ART14, encompassing $>51\%$ of all sequenced proviruses. Clonal proviruses were not restricted to a specific transcriptional or translational profile (Figures 4A and 4B). Of all proviral clones, 11 adopted a single viral gene expression profile, whereas 5 were heterogeneous (2–4 different viral subpopulations). All four viral subpopulations were found in the largest clone (ART3 IV, 59 sequences) (Figures 4A and 4B). Based on the elimination process previously described (Figure 3F), all clones were defective because of premature stop/frameshifts ($n = 4$), large deletions ($n = 9$), ψ /MSD

defects (n = 2), or hypermutations (n = 1). Consequently, no clone was intact (Figure 4B). The high clonality of defective clones compared with intact clones and the rarity of the latter are consistent with previous reports (Bruner et al., 2016, 2019; Hiener et al., 2017, 2018). Globally, these analyses indicate that the clonality of inducible viral reservoirs is not restricted to a specific type of viral defect or vRNA expression. A single proviral clone can adopt different viral transcriptional and translational profiles in different cells, suggestive of non-viral determinants of HIV-1 gene expression.

Compared with protein kinase C agonist (PKCa), histone deacetylases inhibitor (HDACi) induces a low-grade transcriptional activity enriched in *gag*RNA transcripts

LRAs diverge in their capacity to promote HIV-1 transcription and translation (Yukl et al., 2018). We compared the transcriptional and translational effects of ingenol-3-angelate (ingenol; PKCa) and panobinostat (HDACi) at the single-cell level. Both allowed the specific detection of vRNA⁺ cells in samples from ART-treated participants (Figure S4A). Ingenol and panobinostat induced similar levels of vRNA⁺ cells, while combining these two LRAs induced levels insignificantly different from PMA/ionomycin (Figure 5A). Induction of viral translation as measured by p24⁺ cell frequencies reached levels similar to PMA/ionomycin or Ingenol alone. By comparison, panobinostat induced only weak p24 translation (Figure 5B). In all conditions tested, however, the frequencies of reactivated p24⁺ reservoirs were much smaller than those observed for induced vRNA⁺ cells. Co-expression profiles of *nef*RNA, *gag*RNA, and p24 expression in LRA-reactivated viral reservoirs (Figures 5C and S4B) revealed two different patterns (Figure 5D). Ingenol-

treated cells recapitulated the pattern observed with PMA/ionomycin: $gagRNA^+ > nefRNA^+ > vRNA_{DP} > p24^+$ cells, and both induced heterogeneous subpopulation distributions between samples (Figures 5D and S4C). Panobinostat induced much more homogeneous populations (Figures 5D and S4D) with an exacerbated representation of the $gagRNA^+$ and rare $p24^+$ cells (Figure 5E). This profile was recapitulated by the combination of LRAs (Figures 5D, 5E, and S4E). The distinct patterns of viral subpopulations were consistent among LRAs of the same class, because bryostatin-1 recapitulated expression profiles induced by ingenol (Figure S4G), and suberanilohydroxamic acid (SAHA, also called vorinostat) and romidepsin paralleled panobinostat (Figure S4H). These data are consistent with the notion of abortive transcription upon latency reversal with HDACi. Moreover, the combination of LRAs cannot rescue elongation of transcripts, suggesting a dominant and maybe antagonistic effect of panobinostat over ingenol.

We next compared at the single-cell level the transcriptional activity induced by the various LRAs, using $5'exonRNA$ signal intensity as a surrogate marker. We found that $vRNA^+$ cells stimulated by PMA/ionomycin were the most transcriptionally active, followed by those reactivated by the PKCa class of LRAs, ingenol, and bryostatin-1 (Figure 5F). HDACi had a modest pro-transcriptional activity, consistent with abortive elongation. Combination with ingenol slightly increased the transcriptional activity of the $vRNA^+$ cells compared with panobinostat alone but remained lower than ingenol alone. These data show that within $vRNA^+$ cells, PKCa induces a more robust viral transcription, and subsequent translation, than HDACi.

HIV-1 protein translation in viral reservoirs is associated with an effector memory phenotype

The robust and broad detection of inducible viral reservoirs provided an opportunity to determine their differentiation status. However, stimulation by LRAs can significantly alter expression of some surface markers on CD4⁺ T cells (Figure S5A). Because the combination of ingenol and panobinostat had no impact on CD45RA and CD27 (Figure S5B), we used this stimulation to evaluate the memory phenotype of induced viral reservoirs (Figure 6A). To avoid biased phenotyping, we included only samples with >5 vRNA⁺ events for each viral subpopulation (n = 5/11). All viral subpopulations predominantly displayed a memory phenotype (CD45RA⁻) (Figures 6B and 6C). p24⁺ cells were skewed toward an effector memory subset (T_{EM}, CD45RA⁻CD27⁻) (Figures 6B and 6C). In contrast, p24⁻ vRNA⁺ displayed both central memory (T_{CM}, CD45⁻CD27⁺) and T_{EM} phenotypes. Ingenol-induced gagRNA⁺ cells were also balanced, while nefRNA⁺ cells were overrepresented in the T_{EM} subset compared with total CD4⁺ T cells (Figures 6D and S5C). Panobinostat-induced gagRNA⁺ cells were mostly T_{CM} cells, similarly to total CD4⁺ T cells (Figures 6E and S5D). The phenotypes obtained with PMA/ionomycin were similar, although CD27⁻ phenotypes tended to be overrepresented (Figures S5E and S5F), in line with loss of CD27 surface expression on total CD4⁺ T cells following stimulation (Figure S5A). We conclude that, although p24⁺-producing cells are skewed toward T_{EM} cells, p24⁻ vRNA⁺ cells are equally distributed between T_{EM} and T_{CM} in a manner comparable with total CD4⁺ T cells.

DISCUSSION

We devised a combined approach allowing in-depth single-cell profiling of viral reservoirs in terms of viral transcription and translation, cell phenotype, and provirus integrity. This strategy provides a broad viral reservoir metric without compromising specificity or sensitivity. Transcriptionally active viral reservoirs were diverse in expression of vRNAs. Expression of p24 defined only a rare subpopulation of translationally competent cells. The hierarchy of frequencies of these populations remained globally similar for all LRAs tested, with an exacerbated predominance of the *gagRNA*⁺ population for HDACi. Near-full-length sequencing on indexed sorted cells revealed a myriad of defects among the transcriptionally active proviruses, including large deletions, stop codons, and ψ packaging alterations. The latter two defects were also present in translation-competent cells. Clonal sequences were found in all viral subpopulations, with evidence of various viral transcription and translation states within the same clone. Phenotypic analysis showed that translation-competent cells were enriched in T_{EM} cells, whereas representation of translation-incompetent viral reservoirs was balanced between T_{EM} and T_{CM} CD4⁺ T cells.

Targeting exon sequences, which are present on every viral transcript, ensured broad detection. Consequently, the multiplexed RNAflow-FISH bridged the gap between p24⁺ cells (20-fold higher) and HIV-DNA (7-fold lower) quantifications. Consistent with a previous study (Grau-Expósito et al., 2019), we found viral transcription is more easily reactivated by LRA than translation. The reasons underlying this lack of translation after latency reversal appear to be diverse. Some cells simply did not express *gag*-encoding transcripts, while other, more frequent cells expressed an aberrant *gag*-encoding

transcript lacking the proper 3' end, reminiscent of abortive transcription previously reported (Yukl et al., 2018). Consistent with this interpretation, *gagRNA*⁺ cells were dominant with HDACi, a class of LRA that fails to elevate blocks to transcriptional elongation (Yukl et al., 2018). These cells appeared to have low vRNA signal per cell. This is likely due to failed elongation, although we cannot exclude that the rate of transcriptional is also diminished. The translation-incompetent population co-expressing both *gagRNA* and *nefRNA* may highlight a block of viral protein translation. This emphasizes the need for new drugs that may synergize with HDACi by unblocking protein translation. By comparison, PKCa appeared partially capable to bypass such a block. Combination of an HDACi with a PKCa did not increase the proportion of vRNA_{DP} or p24⁺ cells in the vRNA⁺ population. Although it increased modestly the transcriptional activity per cell compared with panobinostat alone, elongation did not appear to be improved. Globally, our data suggest that the benefit of combining LRA resides in reactivating a more diverse pool of viral reservoirs rather than any real synergistic effect. It remains to be determined if other LRAs may prove more successful in complementing HDACi.

Intact proviral sequences were rare in transcriptionally active viral cells. Among the three subjects examined, intact sequences were found only twice out of 196 proviruses, and within the same subject (one within a p24⁺ cell and one in a vRNA_{DP} cell). This may reflect the extreme rarity of replication-competent proviruses in vivo (Ho et al., 2013; Hosmane et al., 2017). Alternatively, intact proviruses may preferentially reside in deeply latent cells (Einkauf et al., 2019). Recently, it has been shown that within the translation-competent reservoirs, only a fraction harbored a putatively intact provirus. Half of these proviruses had intact open reading frames but displayed mostly ψ /MSD mutations (Cole et al., 2021).

Most transcriptionally inducible viral reservoirs bore diverse genetic defects. Inversions and hypermutations, described in bulk sequencing studies (Bruner et al., 2016, 2019; Hiener et al., 2017; Lee et al., 2017), were rare in transcriptionally reactivated viral reservoirs. These severe defects may preclude viral gene reactivation or hinder their recognition by the RNA probe sets. Large deletions were found in every transcriptionally reactivated viral subpopulation, although less frequently than reported in studies assessing total integrated proviruses (Bruner et al., 2016, 2019; Hiener et al., 2017; Ho et al., 2013; Hosmane et al., 2017; Lee et al., 2017). This could be because of the abrogation of transcription or large deletions spanning over *gag* and *nef*, which would not be detected by our probe sets. Stop codons in *tat* were very frequent, more than in any other gene except for *nef*. It may suggest that *tat* defects contribute to establish and/or maintain latency during ART (Khoury et al., 2018). Although alterations in the ψ packaging motif were common, they were often overshadowed by more drastic defects. All these defects are expected to impede productive latency reversal in a physiological context. We believe that leveraging indexed single-cell sorting, followed by near-full-length provirus sequencing, this downstream of multiplexed RNAflow-FISH characterization, is a major asset of our approach. It could be next used to address other key gaps of knowledge concerning the transcriptional activity of viral reservoirs, such as the link between the proviral integration sites and viral gene expression, and mapping the TCR landscape of inducible viral reservoirs. Indeed, CD4⁺ T cell clonal expansion contributes to the persistence of the HIV reservoir (Gantner et al., 2020; Simonetti et al., 2021) and represents a probable explanation for the viral clones we detected.

We found transcriptionally active *gag*RNA⁺ cells with proper elongation still failing to translate p24. Conversely, we found p24⁺ cells with large deletions. The underlying determinants of translation competence are still obscure but do not appear to be only proviral in nature because a clonal provirus led to different transcriptional outcome in different cells. This indicates that viral gene expression, from transcription to translation, is not solely dictated by proviral integrity but also cellular mechanisms. As observed by others (Baxter et al., 2016; Grau-Expósito et al., 2017; Kulpa et al., 2019; Neidleman et al., 2020; Pardons et al., 2019), p24⁺ cells were enriched in T_{EM} cells. In contrast, p24⁻ transcriptionally active viral reservoirs had no preference between T_{CM} or T_{EM}. T_{EM} cells may provide a cellular context more compatible with p24 translation. Transcriptionally active viral reservoirs were rarely T_N (or T_{SCM}), consistent with the rarity of integrated vDNA in these cells (Buzon et al., 2014; Chomont et al., 2009) and potentially a higher threshold of reactivation (Grau-Expósito et al., 2017).

Although we believe that the approach described here represents an important advance for flow cytometric methods applied to the study of HIV reservoirs, it also has some limitations. The size of the inducible reservoir may still be underestimated, because our multiplexed strategy likely could not detect cells bearing a provirus with deletions spanning the region from *gag* to *nef*. In addition, our study relied on a single round of latency reversal reportedly insufficient for the most refractory viral reservoirs in deep latency (Ho et al., 2013; Hosmane et al., 2017). The phenotyping of the inducible viral reservoirs was limited by the inherent pleiotropic effects of the LRAs on cellular markers. Interestingly, this caveat could be minimized by a precursor predicting method (Neidleman et al., 2020). Finally, our RNAflow-FISH assay, optimized to maximize detection, does not preserve

cellular RNAs for downstream transcriptomic analyses. However, such studies proved possible using a milder in situ RNA hybridization assay that compromised on vRNA detection (Liu et al., 2020).

The biological impact of this large pool of transcriptionally active viral reservoirs remains unknown, although recent studies now provide evidence supporting pro-inflammatory sensing of HIV vRNA transcripts (Akiyama et al., 2018; McCauley et al., 2018; Vermeire et al., 2016). These observations are important, given that chronic inflammation is a problem persisting even during long-term ART (Lederman et al., 2013), and that sustained viral gene expression may shape anti-HIV responses (Imamichi et al., 2016, 2020; Pollack et al., 2017). The versatility, sensibility, and reproducibility of multiplexed RNAflow-FISH will provide a new in-depth perspective on viral transcription and translation in the context of LRA clinical trials.

STAR METHODS

KEY RESOURCES TABLE

REAGENT or RESOURCE	SOURCE	IDENTIFIER
Antibodies		
Mouse monoclonal anti-human CD45RA	BD Biosciences	Cat# 564442, RRID: AB_2738810
Mouse monoclonal anti-human CD45RA	BD Biosciences	Cat# 742249, RRID:AB_2871441
Mouse monoclonal anti-human CD4	BD Biosciences	Cat# 564651, RRID: AB_2744422
Mouse monoclonal anti-human CD4	BD Biosciences	Cat# 560649, RRID:AB_1727475
Mouse monoclonal anti-human CD27	BD Biosciences	Cat# 562655, RRID:AB_2744351
Mouse monoclonal anti-human CD3	BD Biosciences	Cat# 742207, RRID:AB_2871428
Mouse monoclonal anti-human CD8	Biologend	Cat# 344732, RRID:AB_2564624
Mouse monoclonal anti-human CD14	Biologend	Cat# 301842, RRID:AB_2561946
Mouse monoclonal anti-human CD16	BD Biosciences	Cat# 563829, RRID:AB_2744296
Mouse monoclonal anti-human CD19	Biologend	Cat# 302242, RRID:AB_2561668
Mouse monoclonal anti-human CD56	BD Biosciences	Cat# 563041, RRID:AB_2732786
Mouse monoclonal HIV-1 core antigen human	Beckman Coulter	Cat# 6604667, RRID:AB_1575989)
Chemicals, peptides, and recombinant proteins		
RPMI 1640	Gibco by Life Technologies	Cat# 11875-119
Heat-inactivated FCS	Seradigm	Cat# 97068-091
HEPES	Invitrogen	Cat# 15630-080
Penicillin-Streptomycin	Gibco by Life Technologies	Cat# 15140-122
Nuclease S7 from Staphylococcus aureus	Roche Diagnostics	Cat# 12344000
Phorbol 12-myristate 13-acetate (PMA)	Sigma-Aldrich	Cat# P1585
Ionomycin	Sigma-Aldrich	Cat# I9657-1mg
Panobinostat	Selleck Chem	Cat# S1030
Ingenol-3-angelate	Sigma-Aldrich	Cat# SML1318-1MG
Bryostatin-1	Enzo Life Sciences	Cat# BML-ST103-0010
Romidepsin	Selleck Chem	Cat# S3020
Vorinostat (SAHA)	NIH AIDS Reagent Program	Cat# 12130
Enfuvirtide	NIH AIDS Reagent Program	Cat# 12732
Zidovudine	NIH AIDS Reagent Program	Cat# 3485
FVD eFluor® 506	eBiosciences	Cat# 65-0866-14

Proteinase K	Life Technologies	Cat# 255530-015
Ultrapure 1M tris-HCl buffer pH 8.0	ThermoFisher	Cat# 15568025
Critical commercial assays		
EasySep™ Human CD4+ T Cell Enrichment Kit	StemCell	Cat# 19052
PrimeFlow™ RNA Assay Kit	Affymetrix	Cat# 88-18005-210
DirectPCR Lysis Reagent	Viagen Biotech	Cat# 301-C
Platinum™ SuperFi II PCR Master Mix	Invitrogen	Cat# 12368250
Deposited data		
DNA Sequencing	This paper	
Experimental models: Cell lines		
ACH-2		ACH-2 RRID: CVCL_0138
Oligonucleotides		
HIV-1 5'exons	Affymetrix	Custom Cat# VF1-6000978
HIV-1 <i>gag</i> RNA	Affymetrix	Custom Cat# VF6-6000975
HIV-1 <i>nef</i> RNA	Affymetrix	Custom Cat# VF4-6000647
Pre-amplification HIV-1 primer: Fwd : 5' GCGCCCGAACAGGGACYTGAAARCGAAAG 3' ; Rev: 5' GAGGGATCTCTAGTTACCAGAGTC 3'	Invitrogen	[261] [246]
Amplification HIV-1 primer : Fwd : 5' GACCTGAAAGCGAAAGGGAAAC 3' Rev: 5' CTAGTTACCAGAGTCACACAACAGACG 3'	Invitrogen	[238] [246]
Software and algorithms		
FlowJo V10.7.0	FlowJo LLC	https://www.flowjo.com
GraphPad Prism V8.4.3	GraphPad Software	https://www.graphpad.com
PacBio Sequel II	PacBio System	https://www.pacb.com/products-and-services/sequel-system/latest-system-release/
Geneious Prime v 2021.1.1	Geneious Prime	https://www.geneious.com/prime/
FigTree v1.4.4	FigTree	http://tree.bio.ed.ac.uk/software/figtree/
HIVDatabase QCtool	Los Alamos National Laboratory	https://www.hiv.lanl.gov/content/sequenc/QC/index.html
ProseqIT	NIH	https://psd.cancer.gov/tools/pvs_annot.php

RESOURCE AVAILABILITY

Lead contact

Additional information and request for resources should be directed to and will be made available by the Lead Contact, Daniel E. Kaufmann (daniel.kaufmann@umontreal.ca).

Materials availability

This study did not generate new unique reagents.

Data and code availability

- All 196 sequences for this study have been deposited in the GenBank Nucleotide database with the accession codes BankIt2483701: MZ662560 - MZ662755.
- This paper does not report original code.
- Any additional information required to reanalyze the data reported in this paper is available from the lead contact upon request.

EXPERIMENTAL MODEL AND SUBJECT DETAILS

Participants and samples

Leukaphereses were obtained from study participants at the McGill University Health Centre, Montreal, Quebec Canada and at Centre Hospitalier de l'Université de Montréal (CHUM), Quebec, Canada. The study was approved by the respective IRBs and written informed consent obtained from all participants prior to enrolment. Uninfected donors (UD) are free of HIV-1 infection. Untreated participants (UNT) were either naive for treatment

or off treatment for at least 6 months. Treated subjects (ART) were on antiretrovirals for over 3 years with controlled viremia (< 40 vRNA copies/mL). The donors included both sex and were older than 18 years. Participants' characteristics are summarized in Table S1. PBMCs were isolated by the Ficoll density gradient method and stored in liquid nitrogen until use.

METHOD DETAILS

Total and integrated DNA measurements

Quantifications of total and integrated HIV-1 DNA were determined as previously described (Vandergeeten et al., 2014).

HIV-1-infected cells stimulation

Frozen PBMCs were thawed in cold heat-inactivated Fetal Calf Serum (FCS; Seradigm) before CD4⁺ T cells isolation. CD4⁺ T cells were isolated by negative magnetic bead selection (StemCell). Purified CD4⁺ T cells were resuspended at 2×10^6 /mL in RPMI (GIBCO by Life Technologies) supplemented with penicillin/streptomycin (GIBCO by Life Technologies), 10% heat inactivated FCS and ARV (Enfuvirtide [7.5mg/mL] + Zidovudine [1mM]) and seeded into 24-well plates. Enfuvirtide and Zidovudine were obtained through the NIH AIDS Reagent Program. After a rest of 2h at 37°C, 5% CO₂, the cells were either left unstimulated or stimulated with PMA/ionomycin (162nM PMA, 705nM Ionomycin, Sigma) for 12h. Alternatively, for testing of pKCa and/or HDACi, cells were either left unstimulated or stimulated with LRA for 18h with the following concentrations: 30nM

panobinostat (Selleck Chem) or 25nM ingenol-3-angelate (Sigma) or 10nM bryostatin-1 (Enzo Life Sciences) or 500nM SAHA (NIH AIDS Reagent Program) or 10nM romidepsin, (Selleck Chem). Where indicated, 30nM panobinostat and 25nM ingenol-3-angelate were combined. A total of $10\text{-}15 \times 10^6$ purified CD4⁺ T cells were used per condition.

HIV-1 RNAflow-FISH assay

All buffers and fixation reagents were provided with the kit, with the exception of flow cytometry staining (2% FCS/PBS). The HIV-1 RNAflow-FISH assay was performed as previously described and as per manufacturer's instructions (Baxter et al., 2016; Baxter et al., 2017; Sannier et al., 2020). Briefly, cells were harvested after stimulation and stained first with Fixable Viability Dye (20 min, 4°C, Fixable LiveDead, eBioscience) next with a mix containing a brilliant stain buffer (BD Biosciences) and the surface markers for memory (CD45RA and CD27) phenotype as well as for CD4⁺ T cells detection (CD3 and CD4) and CD8/NK/B cells and macrophages exclusions (CD8, CD56, CD19, CD16) (30 min, 4°C). Samples were fixed, permeabilized with buffers provided by the manufacturer, and labeled intracellularly for the structural HIV-1 p24 protein with the anti-p24 clone KC57 antibody (30 min RT followed by 30 min 4°C, Beckman Coulter). HIV-1 RNA probing was performed using the PrimeFlow RNA Assay (ThermoFisher). HIV-1 RNA were labeled using HIV-1 *gag*RNA (20 pairs of "ZZ" probes), HIV-1 *5'exon*RNA (21 pairs of "ZZ" probes) and HIV-1 *nef*RNA (6 pairs of "ZZ" probes) probe sets, all designed based on a consensus B HIV sequence. Each tag sequence allows the hybridization of specific complementary branched DNA nanostructure with different excitation/emission spectra. The probes were diluted 1:5 in diluent and hybridized to the target mRNAs for 2 h at 40°C.

Samples were washed to remove excess probes and stored overnight in the presence of RNAsin. Signal amplification was achieved by performing sequential hybridization with DNA branches (i.e., Pre-Amplifier and Amplifier) The first DNA branch in the Pre-Amplifier Mix was added at a 1:1 ratio and was allowed to hybridize for 1.5 h at 40°C. Then the second DNA branch in the Amplifier Mix was added and hybridized for 1.5 h at 40°C (Baxter et al., 2016; Baxter et al., 2017; Porichis et al., 2014). Amplified mRNAs were labeled with fluorescently tagged probes allowing hybridization for 1 h at 40°C. The complete list of antibodies used is presented in Table S2 for panel. Samples were acquired on an LSRFortessa (BD Biosciences) and analyzed using FlowJo (BD, V10.7.0). Unspecific binding of the fluorescent labeled branched probe in the multiplex kit can lead to a low level of false-positive background noise, which, if present, is detected across all the four channels corresponding to the types of labeled probes (AF488, AF594, AF647, AF750). To decrease background noise, we thus left the AF594 channel vacant and excluded false-positive events based on fluorescence in this channel before further gating. Gates were set on the HIV-uninfected donor control, or unstimulated control where appropriate (See gating strategy, Figure S1).

Spiking experiment

HIV-1-latently infected ACH-2 cells, and uninfected CEMx174 cells were grown in separate flasks at a concentration of 0.5×10^6 cells per mL in RPMI 1640 medium (GIBCO, Life Technologies) supplemented with penicillin/streptomycin (GIBCO, Life Technologies), 10% heat inactivated FCS (Seradigm) and ARV (Enfuvirtide [7.5mg/mL] + Zidovudine [1mM]) (NIH AIDS Reagent Program). ACH-2 cells were stimulated for 24h

with PMA (50ng/mL, Sigma-Aldrich) and ionomycin (0.5mg/mL, Sigma-Aldrich). ACH-2 were spiked into uninfected CEMx174 cells for a concentration of 1,500 reactivated ACH-2 cells per million CEMx174 cells. These diluted ACH-2 cells were further serially diluted into uninfected CEMx174 cells down to 1 reactivated ACH-2 cell per million to generate a range of ACH-2 cells to be detected by RNAflow-FISH.

Single-cell near full-length PCR and sequencing

PMA/ionomycin-stimulated CD4⁺ T cells from 3 ART-treated donors were stained in HIV-1 RNAflow-FISH assays using anti-p24 antibodies and HIV-1 *gag*RNA, *5' exon*RNA, and *nef*RNA probes (Table S3). Single vRNA⁺ cells were sorted in 12-wells PCR strips containing 8 mL of DirectPCR Lysis Reagent (Viagen Biotech) with 0.4mg/mL proteinase K. The PCR strips were subsequently incubated at 55°C for 1h for cell lysis followed by 15 min at 85°C to inactivate proteinase K. Single sorted cells were subjected to near full-length amplification using a modified FLIPS assay (Hiener et al., 2017). HIV-1 genomes were pre-amplified using Invitrogen Platinum SuperFi II MasterMix with 0.2 mM of each primer (Table S4). 30 mL of PCR mix was added directly to the lysed cells for a 25 cycles 3-steps PCR protocol as recommended by the manufacturer. The pre-amplified products were diluted 1:3 with Tris-HCl 0.5 mM pH 8.0 and subjected to a nested PCR with 5 mL of pre-amplified product, 2X of Platinum SuperFi II PCR Mix and 0.2 mM of each primer (Table S4) in a 30 mL final volume. This second amplification consists in 30 cycles and follows the manufacturer's instructions. The length of the sequences obtained were verified on a 0.8% agarose gel and the amplicons were individually barcoded for PacBio Sequel II sequencing (Genome Quebec). ACH2 cells were single-sorted following

RNAflow-FISH fixation and standard fixation to control the impact of the RNAflow-FISH buffers on the recovery rate of the single-cell near full-length PCR. The recovery rates were similar for both conditions: 91% of the ACH2 sorted were amplified following the RNAflow-FISH fixation and 100% with the standard fixation. The demultiplex barcodes analysis was powered by the Lima PacBio software v2.0.0. High-quality phased consensus sequences representing near full HIV-1 genome sequences with high fidelity and without reconstruction have been generated with the LAA PacBio algorithm v2.4.2. For each individual, sequences obtained were aligned using Multiple Alignment using Fast Fourier Transform (MAFFT) with strategy E-INS-i and Scoring matrix for nucleotide sequences of 1PAM/ k = 2 (online <https://mafft.cbrc.jp/alignment/server/> or with Geneious Prime (v2021.1.1) plugging). Trees were built with iqtree2 using Maximum-Likelihood tree GTR+I+G model, with 1000 bootstraps, and then visualized with Figtree (v1.4.4). Clonality was evaluated with diversity of sequences in Geneious Prime, and sequences with 0 nucleotide difference were considered clonal. Integrity was assessed using both HIVDatabase QCtool (<https://www.hiv.lanl.gov/content/sequence/QC/index.html>) and ProseqIT (https://psd.cancer.gov/tools/pvs_annot.php). Finally, Psi defects were confirmed manually by visualization in Geneious Prime of this portion of the sequence.

QUANTIFICATION AND STATISTICAL ANALYSIS

Median values were used to generate donut charts. Each median value was normalized to obtain a total of 100%. All statistical analyses were performed using Prism (v8.4.3, GraphPad). Statistical tests were two-sided. For comparisons between groups, Mann-Whitney, Kruskal-Wallis or Friedman test with Dunn's post-test was used. Spearman's R

(Rs) correlation coefficient was used for correlations. For pairwise analysis of non-normally distributed data, Wilcoxon tests were used. $p < 0.05$ were considered significant.

ACKNOWLEDGEMENTS

We thank Josée Girouard, Angie Massicotte at the McGill University Health Centre in Montreal, and all study participants for their invaluable role in this project; Dr. Dominique Gauchat, Philippe St-Onge, and the CRCHUM Flow Cytometry Platform; and Dr. Olfa Debbeche and the CRCHUM BSL3 platform for technical assistance. We thank Dr. Sarah Palmer and Bonnie Hiener for their help in the analyses of the sequences. The following reagents were obtained through the NIH HIV Reagent Program, Division of AIDS, NIAID, NIH: Anti-Human Immunodeficiency Virus 1 (HIV-1) p24 Monoclonal Antibody (KC57)-PE Conjugate, ARP-13449, contributed by DAIDS/NIAID; T-20 (N-acetylated derivative; Enfuvirtide acetate salt), ARP-12732, contributed by DAIDS/NIAID (produced by RayBiotech, Inc.); Zidovudine, ARP-3485, contributed by DAIDS/NIAID; and Vorinostat (SAHA), ARP-12130, contributed by DAIDS/NIAID; ACH-2 cells, ARP-349, contributed by Dr. Thomas Folks. This study was supported by the Canadian Institutes for Health Research (CIHR grant 152977) and in part by the réseau Fonds de la recherche Québec-Santé (FRQ-S) SIDA and Maladies infectieuses and thérapies cellulaires. D.E.K. is a FRQS Merit Research Scholar. N.C. and B.R. are supported by FRQ-S Research Scholar Awards. G.S. is supported by a scholarship from the Department of Microbiology, Infectious Disease, and Immunology of the University of Montreal. C.D. is supported by a scholarship from CIHR. A.E.B. was supported by a CIHR fellowship. J.N. was supported by a FRQ-S doctoral scholarship. J.-P.R. is the holder of the Louis Lowenstein Chair at

McGill University. The graphical abstract was partly generated using Servier Medical Art, provided by Servier, licensed under a Creative Commons Attribution 3.0 unported license (available at <https://smart.servier.com>).

AUTHOR CONTRIBUTIONS

G.S., M.D., and D.E.K. designed the study; A.E.B., J.N., E.B.-R., R.F., and N.C. provided assistance with assay protocols and experimental design; G.S., C.D., N.B., G.G.D., A.P., and R.C. performed experiments; G.S., M.D., C.D., and C.R. analyzed data; B.R. and J.-P.R. contributed to recruitment and clinical assessments; G.S., M.D., C.D., R.F., N.C., and D.E.K. interpreted the data; G.S., M.D., and D.E.K. wrote the initial draft of the manuscript; all co-authors reviewed and edited the manuscript; and D.E.K. provided supervision.

DECLARATION OF INTERESTS

The authors declare no competing interests.

REFERENCES

- Akiyama, H., Miller, C.M., Ettinger, C.R., Belkina, A.C., Snyder-Cappione, J.E., and Gummuluru, S. (2018). HIV-1 intron-containing RNA expression induces innate immune activation and T cell dysfunction. *Nat. Commun.* 9, 3450.
- Baxter, A.E., Niessl, J., Fromentin, R., Richard, J., Porichis, F., Charlebois, R., Massanella, M., Brassard, N., Alshahfi, N., Delgado, G.G., et al. (2016). Single-Cell Characterization of Viral Translation-Competent Reservoirs in HIV-Infected Individuals. *Cell Host Microbe* 20, 368–380.
- Baxter, A.E., Niessl, J., Fromentin, R., Richard, J., Porichis, F., Massanella, M., Brassard, N., Alshahfi, N., Routy, J.P., Finzi, A., et al. (2017). Multiparametric characterization of rare HIV-infected cells using an RNA-flow FISH technique. *Nat. Protoc.* 12, 2029–2049.
- Brandt, L., Cristinelli, S., and Ciuffi, A. (2020). Single-Cell Analysis Reveals Heterogeneity of Virus Infection, Pathogenicity, and Host Responses: HIV as a Pioneering Example. *Annu. Rev. Virol.* 7, 333–350.
- Bruner, K.M., Murray, A.J., Pollack, R.A., Soliman, M.G., Laskey, S.B., Capoferri, A.A., Lai, J., Strain, M.C., Lada, S.M., Hoh, R., et al. (2016). Defective proviruses rapidly accumulate during acute HIV-1 infection. *Nat. Med.* 22, 1043–1049.
- Bruner, K.M., Wang, Z., Simonetti, F.R., Bender, A.M., Kwon, K.J., Sengupta, S., Fray, E.J., Beg, S.A., Antar, A.A.R., Jenike, K.M., et al. (2019). A quantitative approach for measuring the reservoir of latent HIV-1 proviruses. *Nature* 566, 120–125.
- Bullen, C.K., Laird, G.M., Durand, C.M., Siliciano, J.D., and Siliciano, R.F. (2014). New ex vivo approaches distinguish effective and ineffective single agents for reversing HIV-1 latency in vivo. *Nat. Med.* 20, 425–429.
- Buzon, M.J., Sun, H., Li, C., Shaw, A., Seiss, K., Ouyang, Z., Martin-Gayo, E., Leng, J., Henrich, T.J., Li, J.Z., et al. (2014). HIV-1 persistence in CD4⁺ T cells with stem cell-like properties. *Nat. Med.* 20, 139–142.

Chomont, N., El-Far, M., Ancuta, P., Trautmann, L., Procopio, F.A., Yassine-Diab, B., Boucher, G., Boulassel, M.R., Ghattas, G., Brenchley, J.M., et al. (2009). HIV reservoir size and persistence are driven by T cell survival and homeostatic proliferation. *Nat. Med.* 15, 893–900.

Cohn, L.B., da Silva, I.T., Valieris, R., Huang, A.S., Lorenzi, J.C.C., Cohen, Y.Z., Pai, J.A., Butler, A.L., Caskey, M., Jankovic, M., and Nussenzweig, M.C. (2018). Clonal CD4+ T cells in the HIV-1 latent reservoir display a distinct gene profile upon reactivation. *Nat. Med.* 24, 604–609.

Cole, B., Lambrechts, L., Gantner, P., Noppe, Y., Bonine, N., Witkowski, W., Chen, L., Palmer, S., Mullins, J.I., Chomont, N., et al. (2021). In-depth single-cell analysis of translation-competent HIV-1 reservoirs identifies cellular sources of plasma viremia. *bioRxiv*. <https://doi.org/10.1101/2021.02.15.431218>.

Davey, R.T., Jr., Bhat, N., Yoder, C., Chun, T.W., Metcalf, J.A., Dewar, R., Natarajan, V., Lempicki, R.A., Adelsberger, J.W., Miller, K.D., et al. (1999). HIV-1 and T cell dynamics after interruption of highly active antiretroviral therapy (HAART) in patients with a history of sustained viral suppression. *Proc. Natl. Acad. Sci. USA* 96, 15109–15114.

Einkauf, K.B., Lee, G.Q., Gao, C., Sharaf, R., Sun, X., Hua, S., Chen, S.M., Jiang, C., Lian, X., Chowdhury, F.Z., et al. (2019). Intact HIV-1 proviruses accumulate at distinct chromosomal positions during prolonged antiretroviral therapy. *J. Clin. Invest.* 129, 988–998.

Foster, J.L., and Garcia, J.V. (2007). Role of Nef in HIV-1 replication and pathogenesis. *Adv. Pharmacol.* 55, 389–409.

Fromentin, R., and Chomont, N. (2020). HIV persistence in subsets of CD4+ T cells: 50 shades of reservoirs. *Semin. Immunol.* 2020, 101438.

Gaebler, C., Lorenzi, J.C.C., Oliveira, T.Y., Nogueira, L., Ramos, V., Lu, C.L., Pai, J.A., Mendoza, P., Jankovic, M., Caskey, M., and Nussenzweig, M.C. (2019). Combination of quadruplex qPCR and next-generation sequencing for qualitative and quantitative analysis of the HIV-1 latent reservoir. *J. Exp. Med.* 216, 2253–2264.

Gantner, P., Pagliuzza, A., Pardons, M., Ramgopal, M., Routy, J.P., Fromentin, R., and Chomont, N. (2020). Single-cell TCR sequencing reveals phenotypically diverse clonally expanded cells harboring inducible HIV proviruses during ART. *Nat. Commun.* 11, 4089.

Grau-Expósito, J., Serra-Peinado, C., Miguel, L., Navarro, J., Curran, A., Burgos, J., Ocaña, I., Ribera, E., Torrella, A., Planas, B., et al. (2017). A Novel Single-Cell FISH-Flow Assay Identifies Effector Memory CD4⁺ T cells as a Major Niche for HIV-1 Transcription in HIV-Infected Patients. *MBio* 8, e00876-17.

Grau-Expósito, J., Luque-Ballesteros, L., Navarro, J., Curran, A., Burgos, J., Ribera, E., Torrella, A., Planas, B., Badía, R., Martín-Castillo, M., et al. (2019). Latency reversal agents affect differently the latent reservoir present in distinct CD4⁺ T subpopulations. *PLoS Pathog.* 15, e1007991.

Hiener, B., Horsburgh, B.A., Eden, J.S., Barton, K., Schlub, T.E., Lee, E., von Stockenstrom, S., Odevall, L., Milush, J.M., Liegler, T., et al. (2017). Identification of Genetically Intact HIV-1 Proviruses in Specific CD4⁺ T Cells from Effectively Treated Participants. *Cell Rep.* 21, 813–822.

Hiener, B., Eden, J.S., Horsburgh, B.A., and Palmer, S. (2018). Amplification of Near Full-length HIV-1 Proviruses for Next-Generation Sequencing. *J. Vis. Exp.* 2018, 58016.

Ho, Y.C., Shan, L., Hosmane, N.N., Wang, J., Laskey, S.B., Rosenbloom, D.I., Lai, J., Blankson, J.N., Siliciano, J.D., and Siliciano, R.F. (2013). Replication-competent noninduced proviruses in the latent reservoir increase barrier to HIV-1 cure. *Cell* 155, 540–551.

Hosmane, N.N., Kwon, K.J., Bruner, K.M., Capoferri, A.A., Beg, S., Rosenbloom, D.I., Keele, B.F., Ho, Y.C., Siliciano, J.D., and Siliciano, R.F. (2017). Proliferation of latently infected CD4⁺ T cells carrying replication-competent HIV-1: Potential role in latent reservoir dynamics. *J. Exp. Med.* 214, 959–972.

Imamichi, H., Dewar, R.L., Adelsberger, J.W., Rehm, C.A., O'Doherty, U., Paxinos, E.E., Fauci, A.S., and Lane, H.C. (2016). Defective HIV-1 proviruses produce novel protein-coding RNA species in HIV-infected patients on combination antiretroviral therapy. *Proc. Natl. Acad. Sci. USA* 113, 8783–8788.

Imamichi, H., Smith, M., Adelsberger, J.W., Izumi, T., Scrimieri, F., Sherman, B.T., Rehm, C.A., Imamichi, T., Pau, A., Catalfamo, M., et al. (2020). Defective HIV-1 proviruses produce viral proteins. *Proc. Natl. Acad. Sci. USA* 117, 3704–3710.

Karn, J., and Stoltzfus, C.M. (2012). Transcriptional and posttranscriptional regulation of HIV-1 gene expression. *Cold Spring Harb. Perspect. Med.* 2, a006916.

Khoury, G., Mota, T.M., Li, S., Tumpach, C., Lee, M.Y., Jacobson, J., Harty, L., Anderson, J.L., Lewin, S.R., and Purcell, D.F.J. (2018). HIV latency reversing agents act through Tat post translational modifications. *Retrovirology* 15, 36.

Kulpa, D.A., Talla, A., Brehm, J.H., Ribeiro, S.P., Yuan, S., Bebin-Blackwell, A.G., Miller, M., Barnard, R., Deeks, S.G., Hazuda, D., et al. (2019). Differentiation into an Effector Memory Phenotype Potentiates HIV-1 Latency Reversal in CD4+ T Cells. *J. Virol.* 93, e00969-19.

Laird, G.M., Eisele, E.E., Rabi, S.A., Lai, J., Chioma, S., Blankson, J.N., Siliciano, J.D., and Siliciano, R.F. (2013). Rapid quantification of the latent reservoir for HIV-1 using a viral outgrowth assay. *PLoS Pathog.* 9, e1003398.

Lederman, M.M., Funderburg, N.T., Sekaly, R.P., Klatt, N.R., and Hunt, P.W. (2013). Residual immune dysregulation syndrome in treated HIV infection. *Adv. Immunol.* 119, 51–83.

Lee, G.Q., Orlova-Fink, N., Einkauf, K., Chowdhury, F.Z., Sun, X., Harrington, S., Kuo, H.H., Hua, S., Chen, H.R., Ouyang, Z., et al. (2017). Clonal expansion of genome-intact HIV-1 in functionally polarized Th1 CD4+ T cells. *J. Clin. Invest.* 127, 2689–2696.

Lindwasser, O.W., Chaudhuri, R., and Bonifacino, J.S. (2007). Mechanisms of CD4 downregulation by the Nef and Vpu proteins of primate immunodeficiency viruses. *Curr. Mol. Med.* 7, 171–184.

Liu, R., Yeh, Y.J., Varabyou, A., Collora, J.A., Sherrill-Mix, S., Talbot, C.C., Jr., Mehta, S., Albrecht, K., Hao, H., Zhang, H., et al. (2020). Single-cell transcriptional landscapes reveal HIV-1-driven aberrant host gene transcription as a potential therapeutic target. *Sci. Transl. Med.* 12, eaaz0802.

Lu, C.L., Pai, J.A., Nogueira, L., Mendoza, P., Gruell, H., Oliveira, T.Y., Barton, J., Lorenzi, J.C.C., Cohen, Y.Z., Cohn, L.B., et al. (2018). Relationship between intact HIV-1 proviruses in circulating CD4⁺ T cells and rebound viruses emerging during treatment interruption. *Proc. Natl. Acad. Sci. USA* 115, E11341–E11348.

Luznik, L., Kraus, G., Guatelli, J., Richman, D., and Wong-Staal, F. (1995). Tat-independent replication of human immunodeficiency viruses. *J. Clin. Invest.* 95, 328–332.

McCauley, S.M., Kim, K., Nowosielska, A., Dauphin, A., Yurkovetskiy, L., Diehl, W.E., and Luban, J. (2018). Intron-containing RNA from the HIV-1 provirus activates type I interferon and inflammatory cytokines. *Nat. Commun.* 9, 5305.

Mohammadi, P., di Iulio, J., Muñoz, M., Martinez, R., Bartha, I., Cavassini, M., Thorball, C., Fellay, J., Beerewinkel, N., Ciuffi, A., and Telenti, A. (2014). Dynamics of HIV latency and reactivation in a primary CD4⁺ T cell model. *PLoS Pathog.* 10, e1004156.

Neidleman, J., Luo, X., Frouard, J., Xie, G., Hsiao, F., Ma, T., Morcilla, V., Lee, A., Telwatte, S., Thomas, R., et al. (2020). Phenotypic analysis of the unstimulated in vivo HIV CD4 T cell reservoir. *eLife* 9, e60933.

Pardons, M., Baxter, A.E., Massanella, M., Pagliuzza, A., Fromentin, R., Dufour, C., Leyre, L., Routy, J.P., Kaufmann, D.E., and Chomont, N. (2019). Single-cell characterization and quantification of translation-competent viral reservoirs in treated and untreated HIV infection. *PLoS Pathog.* 15, e1007619.

Pasternak, A.O., and Berkhout, B. (2018). What do we measure when we measure cell-associated HIV RNA. *Retrovirology* 15, 13.

Patro, S.C., Brandt, L.D., Bale, M.J., Halvas, E.K., Joseph, K.W., Shao, W., Wu, X., Guo, S., Murrell, B., Wiegand, A., et al. (2019). Combined HIV-1 sequence and integration site analysis informs viral dynamics and allows reconstruction of replicating viral ancestors. *Proc. Natl. Acad. Sci. USA* 116, 25891–25899.

Pollack, R.A., Jones, R.B., Perteza, M., Bruner, K.M., Martin, A.R., Thomas, A.S., Capoferri, A.A., Beg, S.A., Huang, S.H., Karandish, S., et al. (2017). Defective HIV-1

Provirus Are Expressed and Can Be Recognized by Cytotoxic T Lymphocytes, which Shape the Proviral Landscape. *Cell Host Microbe* 21, 494–506.e4.

Porichis, F., Hart, M.G., Griesbeck, M., Everett, H.L., Hassan, M., Baxter, A.E., Lindqvist, M., Miller, S.M., Soghoian, D.Z., Kavanagh, D.G., et al. (2014). High-throughput detection of miRNAs and gene-specific mRNA at the single-cell level by flow cytometry. *Nat. Commun.* 5, 5641.

Procopio, F.A., Fromentin, R., Kulpa, D.A., Brehm, J.H., Bebin, A.G., Strain, M.C., Richman, D.D., O'Doherty, U., Palmer, S., Hecht, F.M., et al. (2015). A Novel Assay to Measure the Magnitude of the Inducible Viral Reservoir in HIV-infected Individuals. *EBioMedicine* 2, 874–883.

Sannier, G., Dubé, M., and Kaufmann, D.E. (2020). Single-Cell Technologies Applied to HIV-1 Research: Reaching Maturity. *Front. Microbiol.* 11, 297. Siliciano, J.D., Kajdas, J., Finzi, D., Quinn, T.C., Chadwick, K., Margolick, J.B., Kovacs, C., Gange, S.J., and Siliciano, R.F. (2003). Long-term follow-up studies confirm the stability of the latent reservoir for HIV-1 in resting CD4+ T cells. *Nat. Med.* 9, 727–728.

Simonetti, F.R., Zhang, H., Soroosh, G.P., Duan, J., Rhodehouse, K., Hill, A.L., Beg, S.A., McCormick, K., Raymond, H.E., Nobles, C.L., et al. (2021). Antigen-driven clonal selection shapes the persistence of HIV-1-infected CD4+ T cells in vivo. *J. Clin. Invest.* 131, 145254.

Vandergeeten, C., Fromentin, R., Merlini, E., Lawani, M.B., DaFonseca, S., Bakeman, W., McNulty, A., Ramgopal, M., Michael, N., Kim, J.H., et al. (2014). Cross-clade ultrasensitive PCR-based assays to measure HIV persistence in large-cohort studies. *J. Virol.* 88, 12385–12396.

Vermeire, J., Roesch, F., Sauter, D., Rua, R., Hotter, D., Van Nuffel, A., Vanderstraeten, H., Naessens, E., Iannucci, V., Landi, A., et al. (2016). HIV Triggers a cGAS-Dependent, Vpu- and Vpr-Regulated Type I Interferon Response in CD4+ T Cells. *Cell Rep.* 17, 413–424.

Willey, R.L., Maldarelli, F., Martin, M.A., and Strebel, K. (1992). Human immunodeficiency virus type 1 Vpu protein regulates the formation of intracellular gp160-CD4 complexes. *J. Virol.* 66, 226–234.

Yukl, S.A., Kaiser, P., Kim, P., Telwatte, S., Joshi, S.K., Vu, M., Lampiris, H., and Wong, J.K. (2018). HIV latency in isolated patient CD4+ T cells may be due to blocks in HIV transcriptional elongation, completion, and splicing. *Sci. Transl. Med.* 10, eaap9927.

Figures

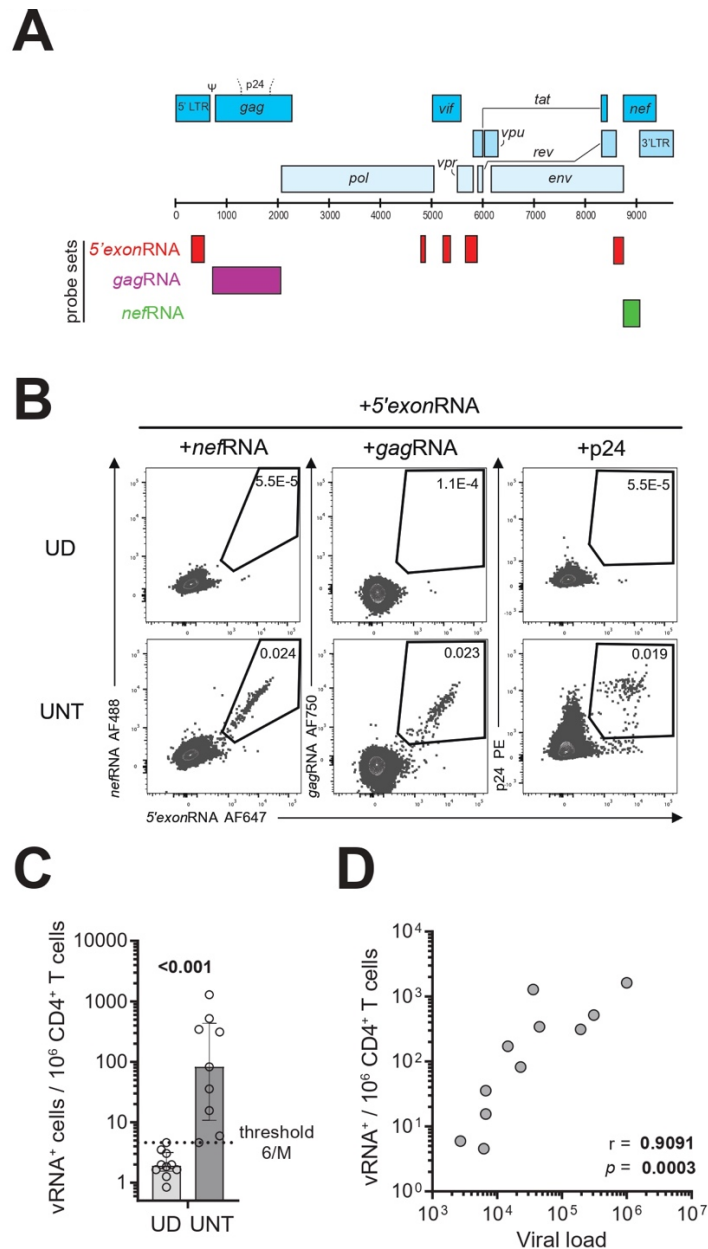


Figure 1. Multiplexed RNAflow-FISH enables robust detection of HIV vRNA⁺ cells

(A) Schematic representation of the regions of the HIV-1 genome targeted by the RNAflow-FISH probes. (B–D) CD4⁺ T cells isolated from UNT PBMCs were stained for p24 and RNA probes. (B) Co-detection of 5'exonRNA along with either nefRNA, gagRNA, or the structural p24 protein representing the core gating from which the OR gate strategy can be implemented. (C) Median quantification provided by the OR gate presented in (B). Cells positive for (1) 5'exonRNA and (2) gagRNA or nefRNA or p24 are termed vRNA⁺. The bars represent the interquartile range. The dotted line highlights the threshold of detection. (D) Correlation between vRNA⁺ cells/10⁶ CD4⁺ T cells and viral load. (C) Mann-Whitney test to compare the donor groups. (D) Spearman's correlation test. Data are from $n = 10$ UD and $n = 11$ UNT. UD, uninfected donor; UNT, untreated PLWHs.

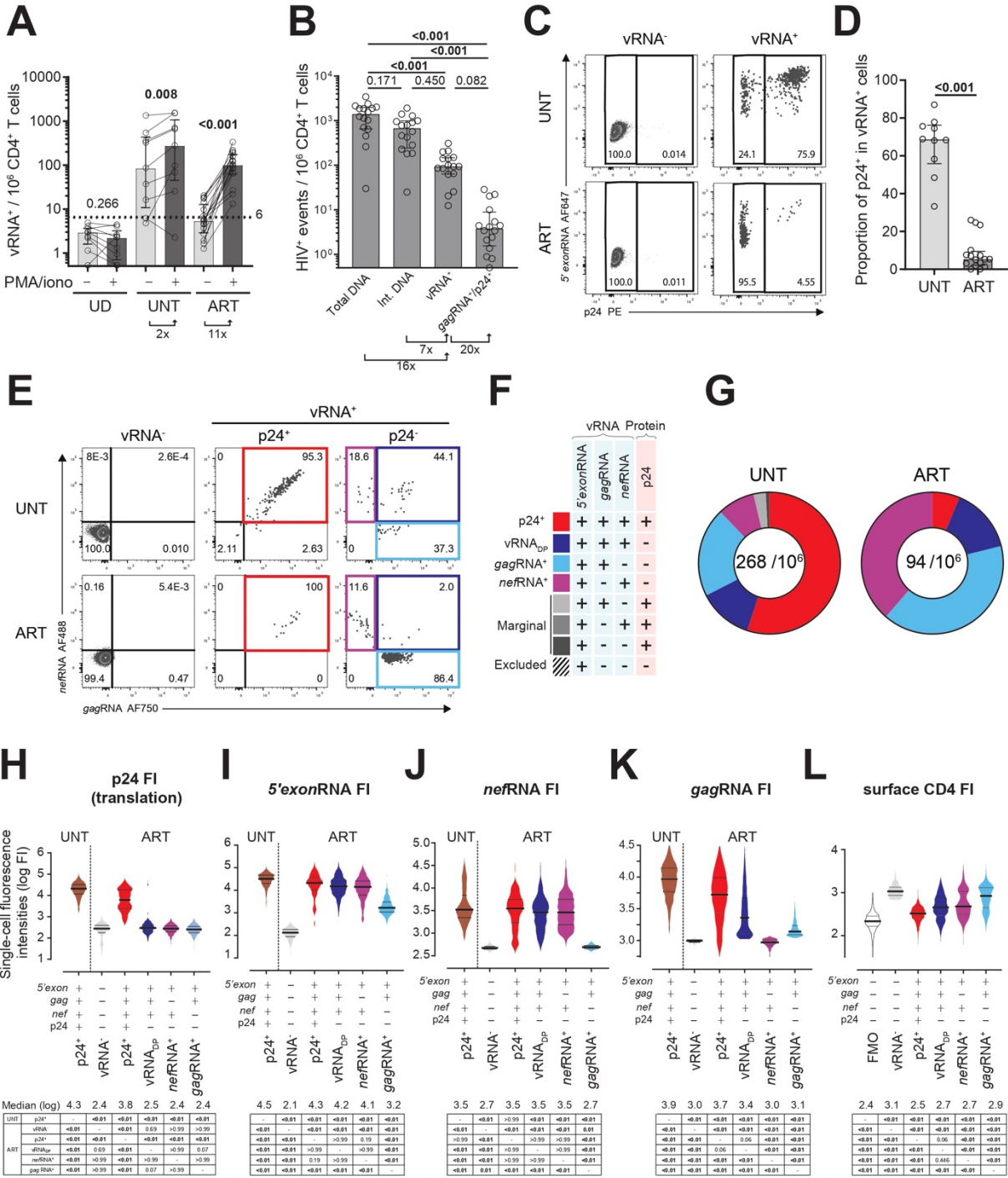


Figure 2. Stimulation-induced vRNA⁺ cells have much lower p24 translation propensity in ART compared with UNT participants

CD4⁺ T cells from 16 ART-treated and 9 UNT individuals were PMA/ionomycin stimulated (or not, as negative control) to induce viral transcription and reveal the inducible viral reservoirs. (A) Pairwise median quantification of vRNA⁺ cells in UD, UNT, and ART samples. The threshold of detection is indicated by the dotted line. Fold increases between induced and non-induced conditions are shown below. Wilcoxon test is performed for statistical analysis. (B) Median frequency of cells harboring total vDNA, integrated vDNA,

gagRNA⁺ p24⁺, and *vRNA*⁺ (HIV⁺ events per 10⁶ CD4⁺ T cells) in CD4⁺ T cells from 16 ART-treated people. The fold difference between *vRNA*⁺ and integrated DNA and p24⁺ *gagRNA*⁺ is shown below. The directionality of the fold increase is indicated by the arrow. Friedmann's test is performed for this panel. (C) Parental *vRNA*⁺ cells were subdivided into p24⁻ and p24⁺ subgroups for downstream analyses. (D) The frequency of *vRNA*⁺ cells expressing p24 upon PMA/ionomycin stimulation, as gated in (C). Mann-Whitney test is performed. In (A), (B), and (D), the bars indicate the interquartile range. (E) Representative dot plots representing the co-expression profile of *gagRNA* and *nefRNA* in the control *vRNA*⁻ populations compared with p24⁺ and p24⁻ *vRNA*⁺ cells. (F) Color-coded theoretical viral subpopulations. (G) Donut charts displaying the relative distribution of each viral subpopulation among parental *vRNA*⁺ cells. The median frequency of *vRNA*⁺ cells/10⁶ CD4⁺ T cells is shown in the middle of the donut. (H–L) Violin charts displaying single-cell fluorescence intensities on *vRNA*⁺ cells from concatenated PMA/ionomycin-reactivated ART samples. Median (thick line) and interquartile ranges (thin lines) are also shown. For the sake of comparison, p24⁺ cells from UNT are also shown on the left of each graph. For each viral subpopulation, (H) p24, (I) *5'exonRNA*, (J) *nefRNA*, (K) *gagRNA*, and (L) surface CD4 (UNT only) fluorescence intensities are shown. Fluorescence minus one (FMO) is represented in (L) to display an absence of CD4 fluorescence. (H–L) Kruskal-Wallis tests. The median values are shown below the graphs and the p values in the table.

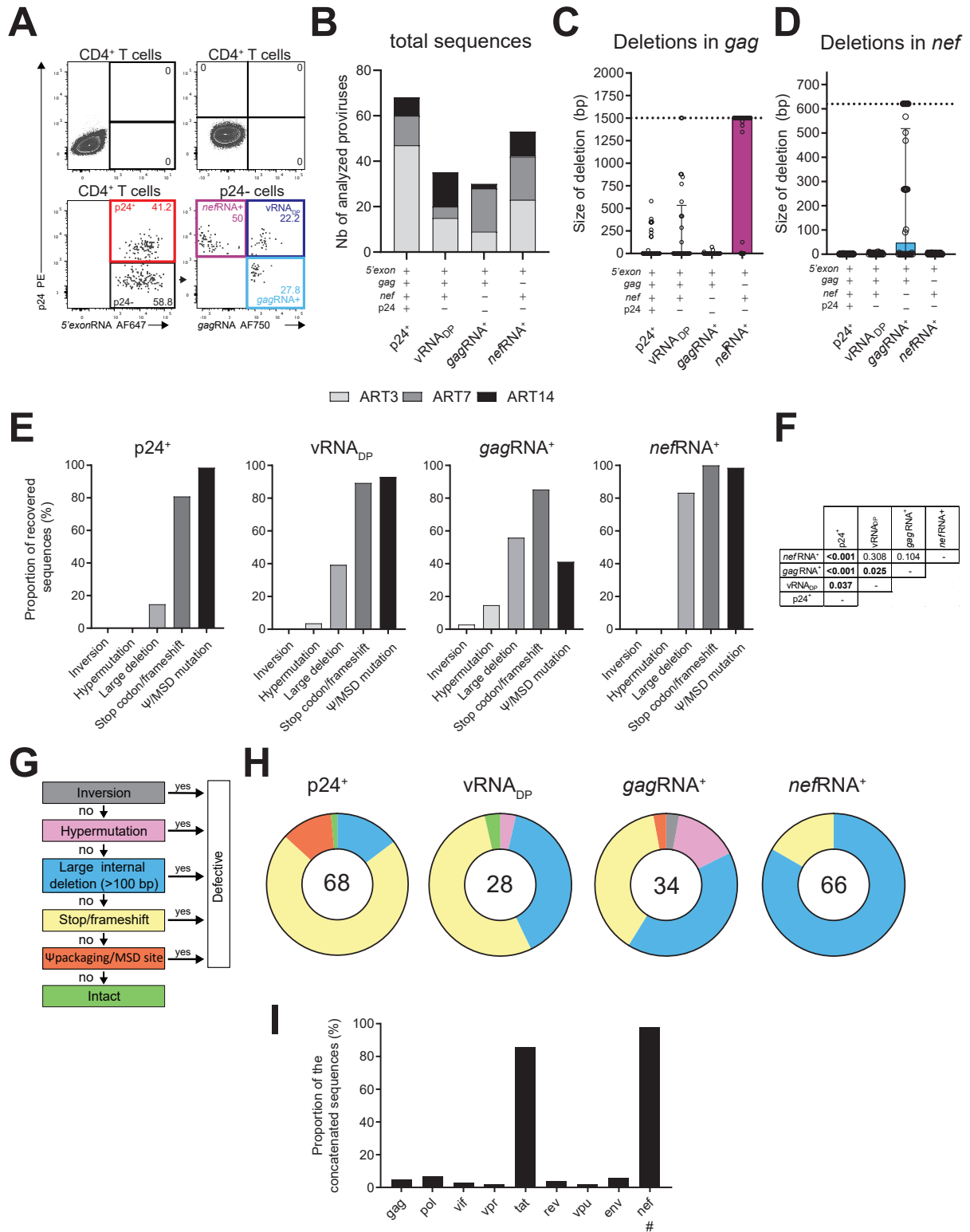


Figure 3. Near-full-length single-cell vDNA sequencing of induced, transcriptionally active viral reservoirs identifies underlying proviral defects

Purified CD4⁺ T cells from three ART-treated participants were co-stained by multiplexed HIV-1 RNAflow-FISH and p24 intracellular staining. vRNA⁺ cells were indexed and sorted individually for nested PCR amplification and near-full-length sequencing. (A) Gating strategy of the concatenated sorted vRNA⁺ cells from the three participants. (B) Total number of the 196 analyzed sequences from participants ART3, ART7, and ART14. (C and D) Size of deletions found in the gene (C) *gag* and (D) *nef* that are targeted by the probe sets of the multiplexed RNAflow-FISH method. The bars indicate interquartile ranges. (E) Proportion of the total proviral sequences analyzed bearing the indicated defects. (F) Result from chi-square tests on (E). To accommodate the test, we pooled the rare defects (inversion and hypermutations) with large deletions. The test was performed based on the absolute number of recovered sequences as depicted in (B). (G) Sequential elimination process to infer intact sequences. (H) Donut charts representing the relative proportions of each dominant proviral defect among indicated transcriptionally active viral subpopulations. The total number of sequences analyzed for each population is displayed in the donut holes. The proviral defects are color coded according to (G). (I) Localization of the frequency of stop/frameshift defects per coding regions. # indicates *nef*, not included in the sequential elimination process.

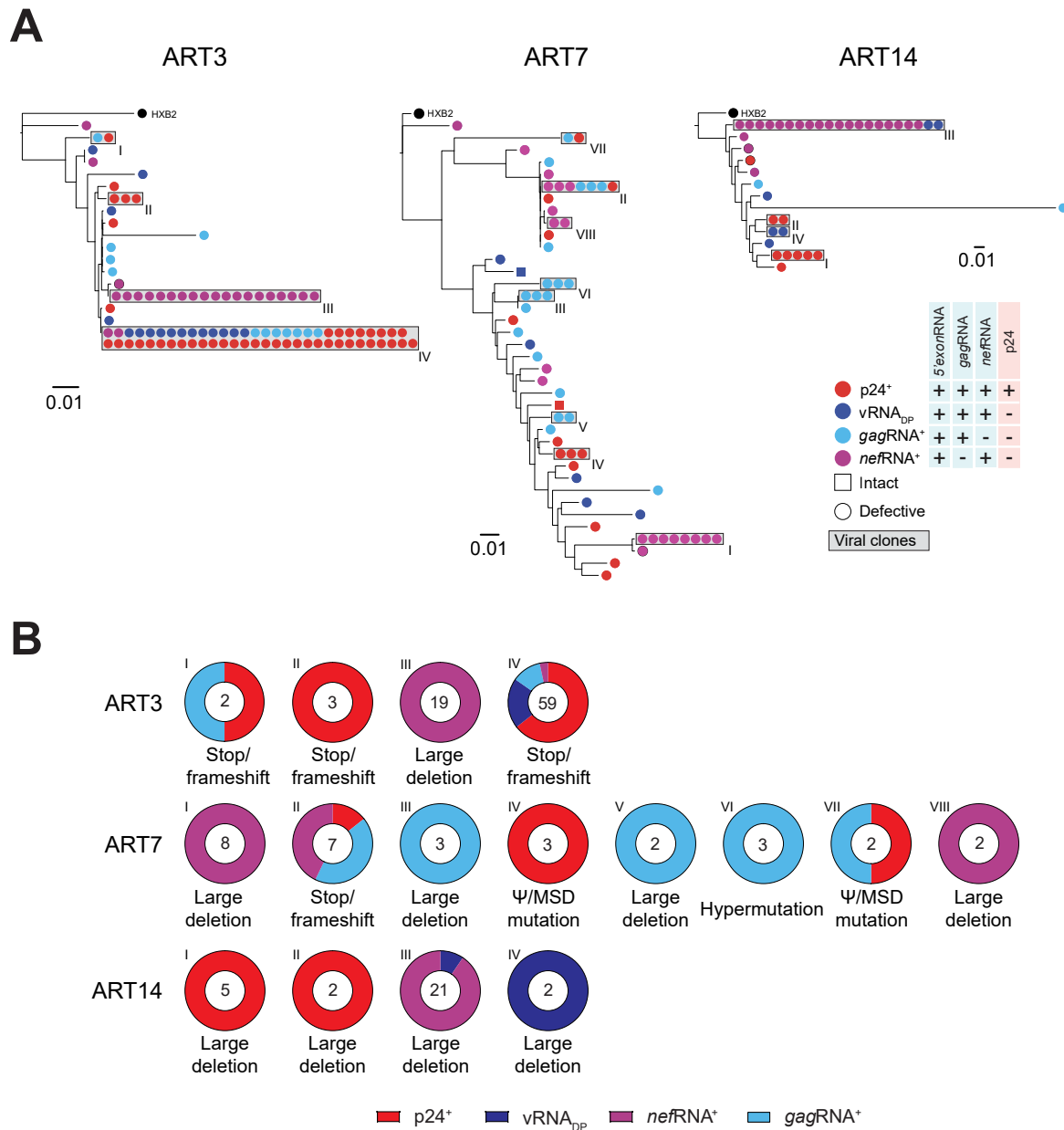


Figure 4. Proviral clones display single-cell-level transcriptional and translational heterogeneity

(A) Phylogenetic trees for the three participants ART3, ART7, and ART14 built from the entire amplified area sequenced based on maximum likelihood. Sequences with 100% identity are boxed in gray. Square: intact sequence; circle: defective sequence. Transcriptionally active viral subpopulations are color coded.

(B) Donut charts summarizing the transcriptional and translation profiles of clonal sequences. The proviral integrity status of each clone is indicated below. The colors in the donut charts represent the transcriptional and translational profiles. The total number of identical sequences for each population is displayed in the donut holes. For reference, roman numerals are attributed to each proviral clone.

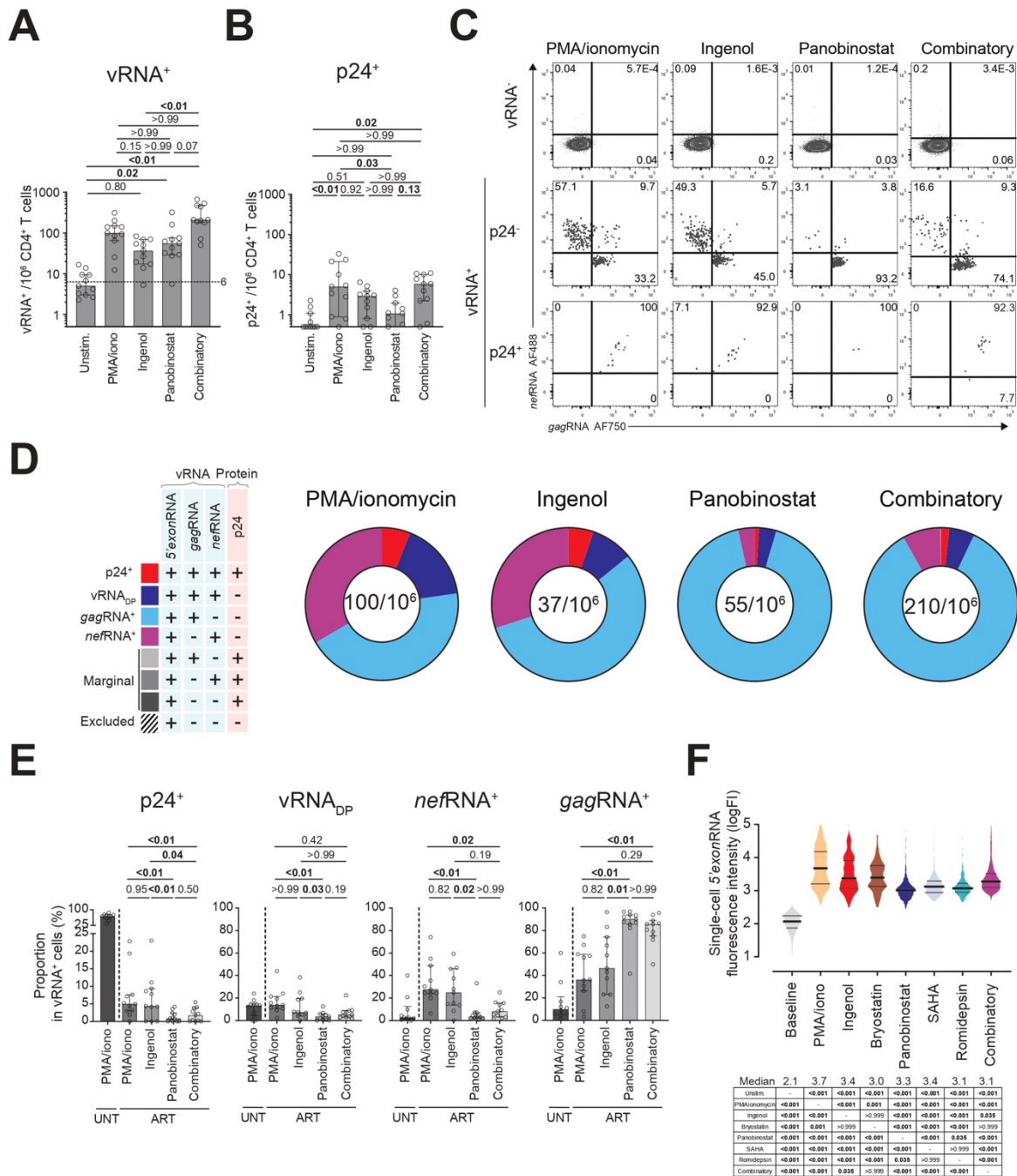


Figure 5. Compared with PKCas, HDACis induce a low-grade transcriptional activity enriched in gagRNA transcripts

CD4⁺ T cells from ART were LRA stimulated (or not, as negative control) to force viral gene expression and identify inducible viral reservoirs. Tested conditions included ingenol, panobinostat, and combinatory treatment, with unstimulated and PMA/ionomycin as negative and positive controls, respectively. (A and B) Comparative quantification of median (A) vRNA⁺ and (B) p24⁺ per 10⁶ CD4⁺ T cells. The dashed lines represent the threshold of positivity based on UD samples, as explained in the text. (C) Representative dot plots showing downstream co-expression profiles of gagRNA and nefRNA in the control vRNA⁻ compared with p24⁺ and p24⁻ vRNA⁺ populations, as defined in (A). (D) Donut charts displaying the relative distribution

of each viral subpopulation among parental vRNA⁺ cells. A legend of all theoretically possible populations is shown on the left. The median frequency of vRNA⁺ cells/10⁶ CD4⁺ T cells is shown in the middle of the donut. (E) Median proportions of each subpopulation are compared between LRA stimulations. (F) Violin chart of the single-cell fluorescence intensities of 5' *exon* RNA in all vRNA⁺ events. Data are from concatenated n = 11 ART donor samples. The solid lines represent the median, and the thin lines represent the quartiles. (A, B, and E) Friedman's test. (F) Kruskal-Wallis test. The median values are shown below the graphs and the p values in the table. In (A), (B), and (E), the bars display the interquartile ranges.

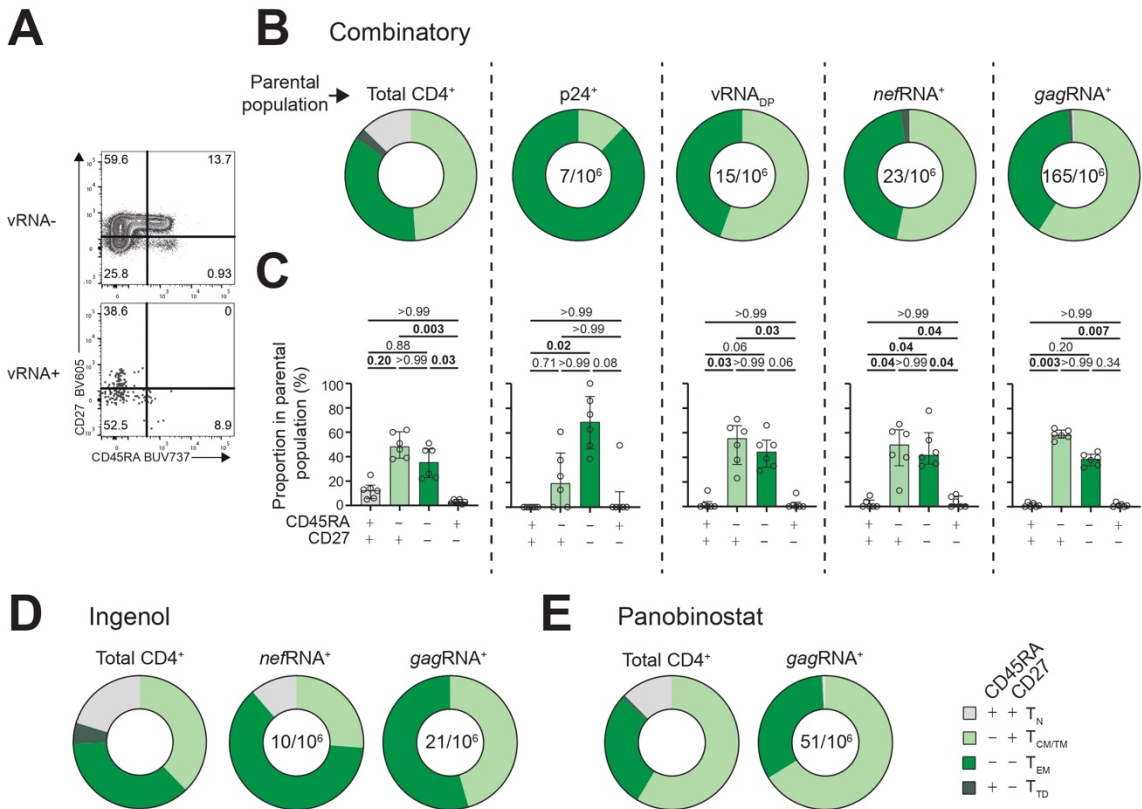
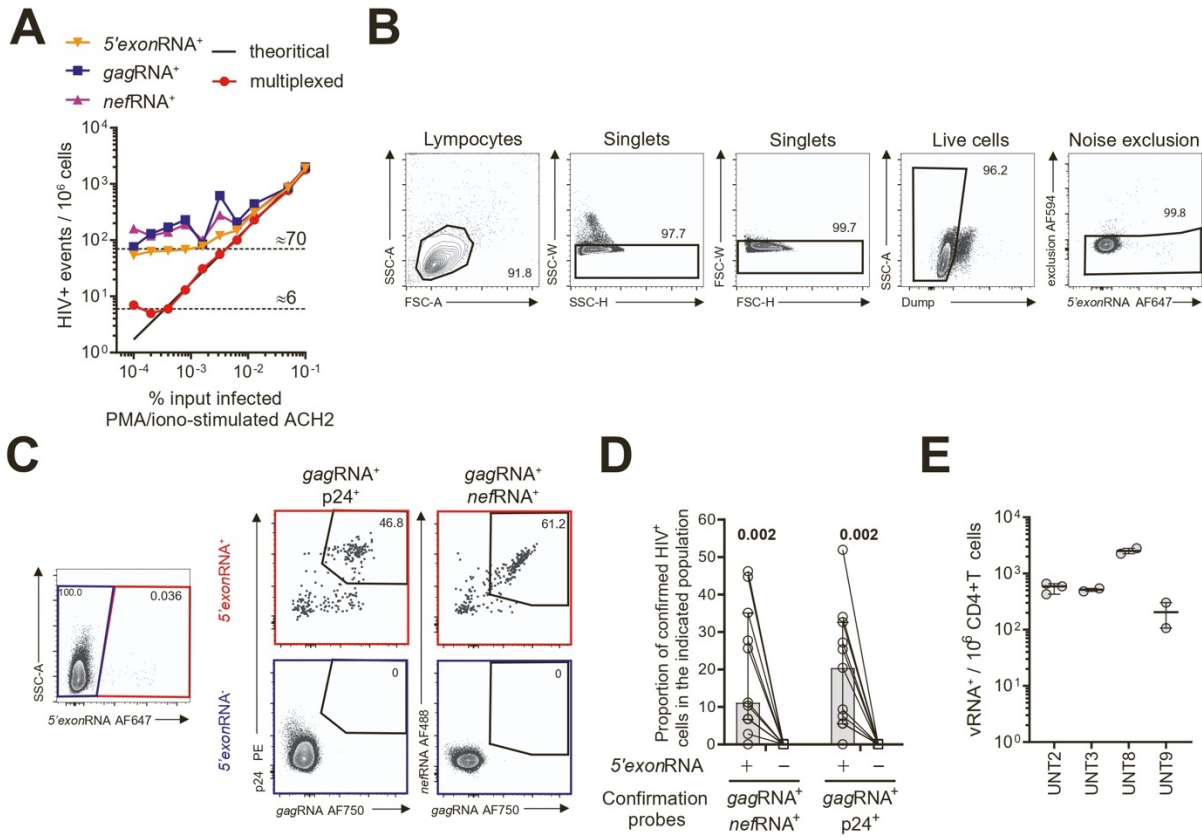


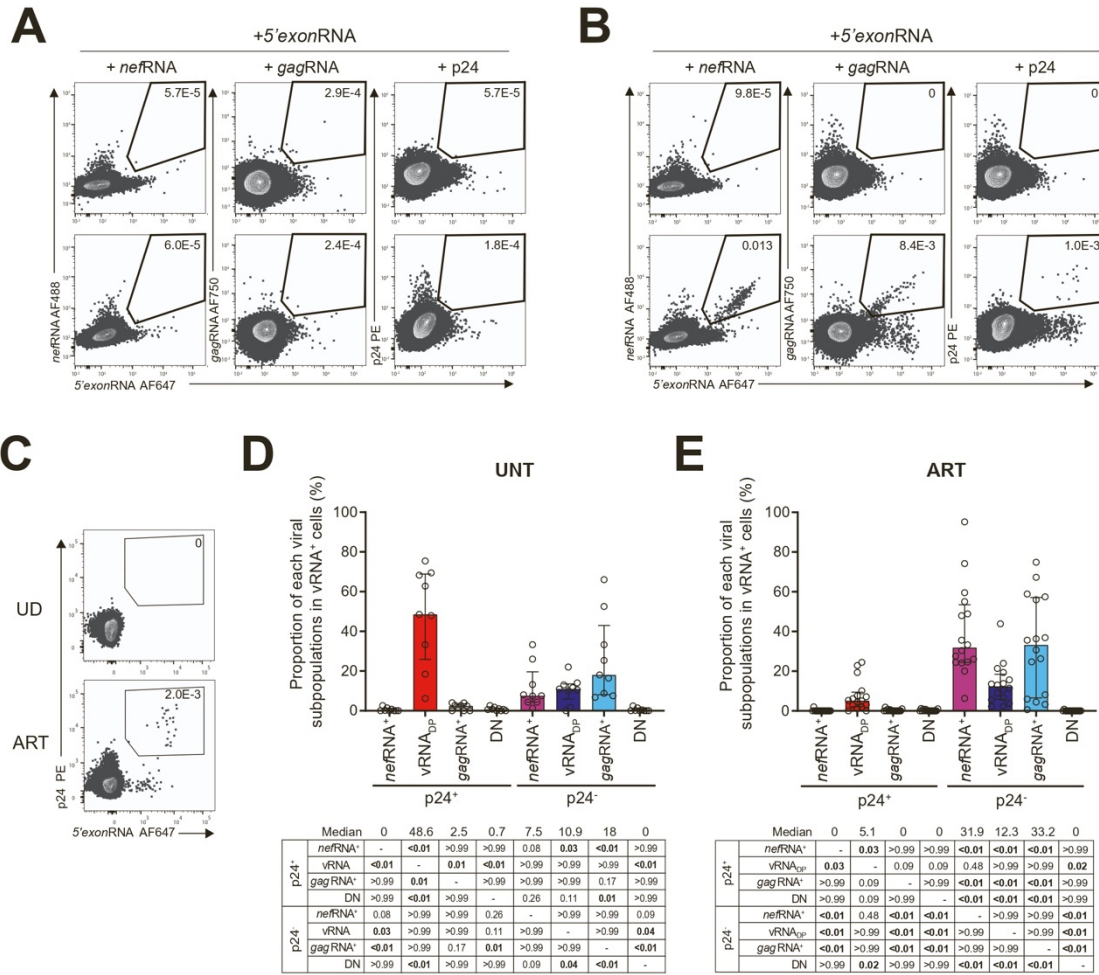
Figure 6. HIV-1 protein translation in viral reservoirs is associated with an effector memory phenotype

(A–C) CD4⁺ T cells from six ART stimulated with combined ingenol+panobinostat were analyzed for CD45RA and CD27 co-expression. (A) Dot plots displaying a representative example. (B) Donut charts summarizing the median distribution of the memory differentiation for each vRNA⁺ subpopulation. (C) Median frequencies of the memory phenotype for each subgroup with interquartile ranges depicted by the error bars. (D and E) Donut charts summarizing the memory differentiation of the indicated vRNA⁺ subpopulations in (D) ingenol- and (E) panobinostat-treated samples. For all analyses, the data on vRNA⁺ cells are paired to autologous total CD4⁺ T cells. In (B), (D), and (E), the median frequencies of vRNA⁺ cells/10⁶ CD4⁺ T cells are shown in the donut holes. Results from a Friedman’s test are shown in (C) (for inter-phenotypic comparisons).

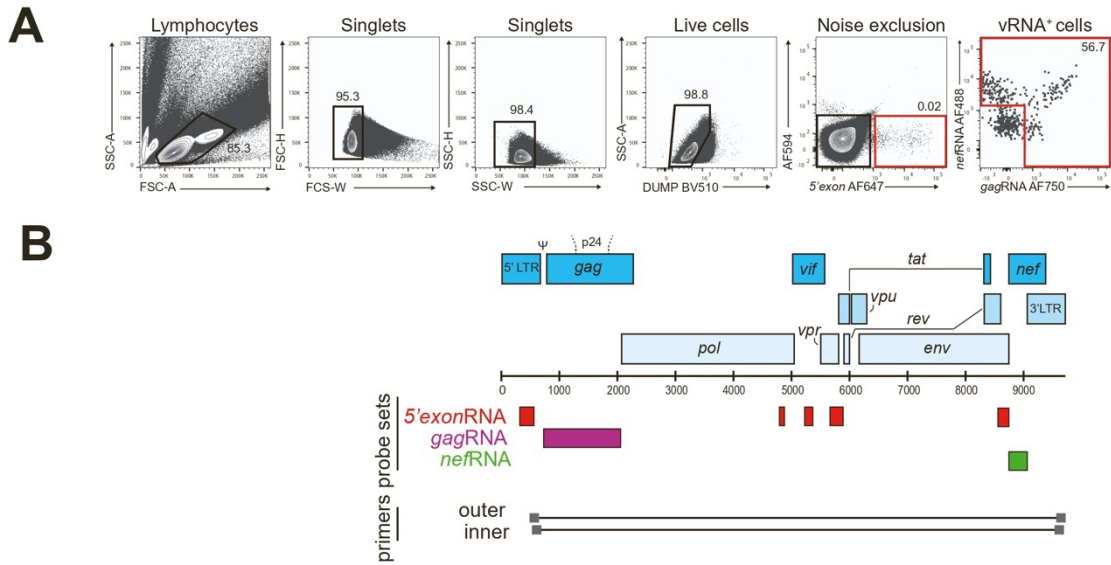
SUPPLEMENTAL INFORMATION



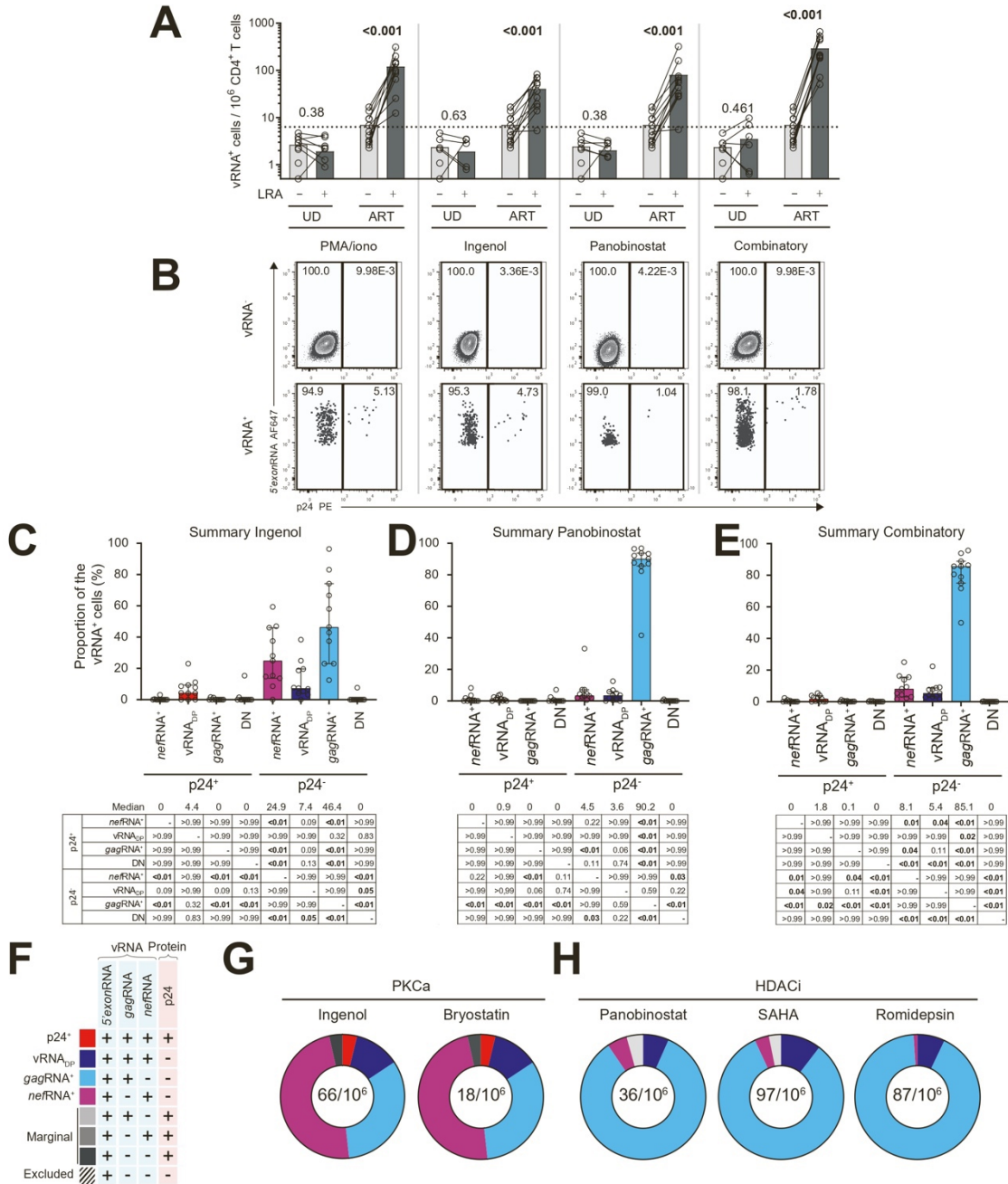
Supplemental Figure 1: Validation of the multiplexed HIV-1 RNAflow-FISH assay. Related to figure 1. (A) HIV-1 RNAflow-FISH spiking experiment. PMA/ionomycin-stimulated HIV-1⁺ ACH-2 cells were serially diluted in uninfected CEMx174. A theoretical regression based on the dilution factor of ACH-2 in CEMx174 cells is shown. Dashed lines represent the plateaus reached. (B) Gating strategy to detect the vRNA⁺ cells in primary samples from untreated, viremic participants. (C-D) Validation of 5'exonRNA as the primary criterion defining vRNA⁺ cells in unstimulated UNT samples. (C) Live CD4⁺ T-cells cleaned from noise, were grouped as 5'exonRNA⁺ (top) and 5'exonRNA⁻ (bottom), then analyzed for co-expression of gagRNA with either p24 or nefRNA and p24 co-expression. Proportion of co-expressing cells relative to the corresponding parental population is shown in the gate. (D) Median quantification derived from C with interquartile ranges depicted by the bars. (E) Independent quantification of vRNA⁺ cells to test the reproducibility of the multiplexed HIV-1 RNAflow-FISH.



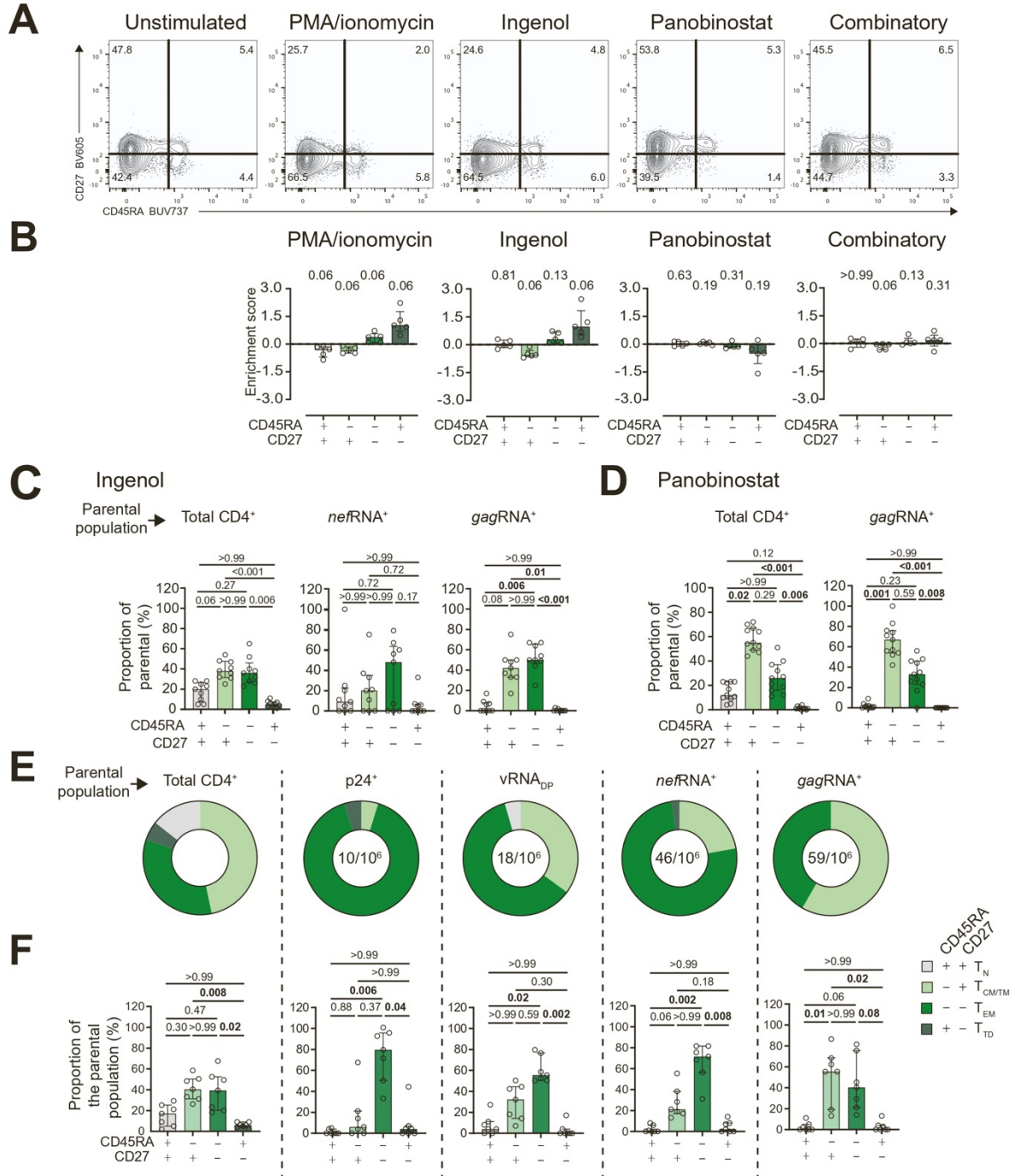
Supplemental Figure 2: Assessment of vRNA⁺ transcriptional and translational heterogeneity in UNT and ART samples. Related to figure 2. Analysis of the reactivated vRNA⁺ cells in samples from 16 ART-treated and 9 UNT PLWH. (A-B) Co-expression of *nef*RNA, *gag*RNA or p24 with 5'exonRNA in (A) Uninfected individuals (UD) and (B) ART-treated HIV infected individuals (ART) upon PMA/ionomycin stimulation or not. These dual gating served as the basis for the OR gating strategy. (C) p24⁺ *gag*RNA⁺ gating strategy on dump-negative cells. (D-E) Median viral subpopulation distribution among PMA/ionomycin-stimulated parental vRNA⁺ cells from (D) UNT and (E) ART samples, with bars representing the interquartile ranges. DN: double-negative. DP: double-positive. In support of the main Figure 2G. The table below shows the results from Kruskal-Wallis test. The median values are shown below the graphs and the *p* values, in the table.



Supplemental Figure 3: Near full-length sequencing on indexed sorted transcriptionally active viral reservoirs upon stimulation. Related to figure 3. Purified CD4⁺ T-cells from 3 ART participants were stained by multiplexed HIV-1 RNAflow-FISH with p24 staining. vRNA⁺ cells were indexed sorted individually for nested PCR amplification and near full-length sequencing. (A) Gating strategy for the index sorting. (B) Schematic representations depicting the targets of RNAflow-FISH probe sets and downstream primers for nested PCR.



Supplemental Figure 4: Deeper characterization of LRA-reactivated vRNA⁺ cells from ART. Related to figure 5. CD4⁺ T-cells from 11 ART were LRA-stimulated (or not, as negative control) to force viral gene expression and identification of inducible viral reservoirs. Tested conditions included Ingenol, Panobinostat and combinatory treatment, with unstimulated and PMA/ionomycin as negative and positive controls, respectively. (A) Histograms representing vRNA⁺ frequencies per 10⁶ CD4⁺ T-cells of LRA-reactivated samples all paired to unstimulated controls. Both UD and ART samples are shown to show the specificity of the signal. (B) Representative dot plot representing p24⁺ cells among LRA-reactivated vRNA⁺ cells. (C-E) Median viral subpopulation distribution in parental vRNA⁺ cells after (C) Ingenol, (D) Panobinostat or (E) combinatory Ingenol+Panobinostat stimulation, supporting the main Figure 3E. (F) Recapitulative legend of all theoretically possible viral subpopulations. (G-H) Donut charts displaying the relative distribution of each viral subpopulation among parental vRNA⁺ cells of the indicated (G) PKCa and (H) HDACi LRA. In A and C-E, the bars depict the interquartile ranges. The results from statistical tests are shown where applicable: (A) Wilcoxon and (C-E) Friedman tests. The median values are shown below the graphs and the *p* values, in the table.



Supplementary Figure 5: Support to the phenotyping of vRNA⁺ cells from ART samples. Related to figure 6. (A) A representative dot plot showing CD27 and CD45RA co-expression on total CD4⁺ T-cells from 5 ART samples is provided for each type of stimulation. (B) Median fold increases for each memory subsets versus the untreated conditions are shown. (C-F) Median proportion of memory subsets among total CD4⁺ T-cells and vRNA⁺ subgroups in 9 ART samples treated with (C) Ingenol (supporting Figure 4E), (D) Panobinostat (supporting Figure 4F) and (E-F) PMA/ionomycin (n = 7). The results from Friedman tests are shown in (C-D, F). The bars in B, C, D and F represent interquartile ranges. The results from Wilcoxon tests comparing the proportion of marker-positive vRNA⁺ versus autologous total CD4⁺ T-cells are provided above the bars in B.

Table S1. Clinical data for uninfected (UD), untreated (UNT) and treated (ART) participants

	Participant ID	Sex	Age (years)	VL (copies/mL)	Total DNA (copies/mL)	Int. DNA (copies/mL)	CD4 /CD8 Ratio	CD4 count (cells/ μ L)	Time on ARV (years)
U D	UD1	F	41	NA	NA	NA	2.10	1196	NA
	UD2	M	23	NA	NA	NA	2.29	465	NA
	UD3	M	50	NA	NA	NA	4.13	1758	NA
	UD4	M	64	NA	NA	NA	1.78	552	NA
	UD5	M	51	NA	NA	NA	2.18	532	NA
	UD6	F	39	NA	NA	NA	2.05	667	NA
	UD7	M	59	NA	NA	NA	2.25	811	NA
	UD8	F	41	NA	NA	NA	3.93	1273	NA
	UD9	F	60	NA	NA	NA	1.46	670	NA
	UD10	F	45	NA	NA	NA	2.31	632	NA
	UD11	M	57	NA	NA	NA	1.95	726	NA
	UD12	F	38	NA	NA	NA	1.65	529	NA
	UD13	M	63	NA	NA	NA	3.50	675	NA
U N T	UNT1	M	26	2700	6	11	1.11	597	NA
	UNT2	M	70	55260	51374	8083	0.29	321	NA
	UNT3	M	43	139220	7000	1015	0.31	356	NA
	UNT4	M	49	44848	12738	3664	0.36	281	NA
	UNT5	M	38	14614	9346	1560	0.35	138	NA
	UNT6	M	41	34229	1345	567	0.44	406	NA
	UNT7	M	40	3371	3353	458	0.75	571	NA
	UNT8	M	22	35859	24210	1300	0.31	597	NA
	UNT9	M	34	1000000	9876	619	0.07	300	NA
	UNT10	M	54	22959	3279	423	0.77	577	NA
	UNT11	M	38	6235	149	3	0.89	1036	NA
A R T	ART1	M	51	< 40	1856	425	1.28	533	15.1
	ART2	M	52	< 40	1858	1288	0.27	194	25.3
	ART3	M	60	< 40	1246	783	0.34	249	21.9
	ART4	M	63	< 40	1889	796	0.52	782	6.1
	ART5	M	54	< 40	1133	959	1.10	973	5.2
	ART6	M	43	< 40	639	181	1.39	793	4.1
	ART7	M	58	< 40	2020	997	0.56	278	26.9
	ART8	M	58	< 40	454	284	1.12	619	7.0
	ART9	M	26	< 40	1152	185	1.34	871	3.6
	ART10	M	59	< 40	1027	570	2.12	843	18.3
	ART11	M	52	< 40	30	25	0.33	333	25.3
	ART12	M	48	< 40	3431	912	0.37	531	5.4
	ART13	M	70	< 40	463	701	0.44	407	17.4
	ART14	M	67	< 40	2142	1404	0.68	602	16.8
	ART15	M	39	< 40	262	229	1.96	445	7.0
	ART16	M	57	< 40	2386	1913	1.04	911	20.1

VL : viral load; int. DNA : integrated DNA; NA : Not-Applicable

Table S2. Flow Cytometry panel for detection of HIV-1 vRNA⁺ cells by RNAflow-FISH related to Figures 1, 2, 5 and 6.

Target	Fluorochrome	Clone	Supplier	Detection	Catalogue n°	Volume per test (µL)
CD45RA	BUV737	H100	BD	Surface	564442	3
CD4	BUV496	SK3	BD	Surface	564651	4
CD27	BV605	L128	BD	Surface	562655	2
CD3	BB700	HIT3a	BD	Surface	742207	0.5
CD8	BV510	SK1	Biolegend	Surface	344732	3
CD14	BV510	M5E2	Biolegend	Surface	301842	3
CD16	BV510	3G8	BD	Surface	563830	3
CD19	BV510	H1B19	Biolegend	Surface	302242	3
CD56	BV510	NCAM16.2	BD	Surface	563041	0.5
Fixable Viability Dye	eFluor 506	-	ThermoFisher	Surface	65-0866-14	0.1
HIV core antigen	RD1	KC57	Beckman Coulter	Intracellular	6604667	2
HIV-1 5' exonRNA	Alexa Fluor 647	-	ThermoFisher	Intracellular	VF1-6000978	5
HIV-1 gagRNA	Alexa Fluor 750	-	ThermoFisher	Intracellular	VF6-6000975	5
HIV-1 nefRNA	Alexa Fluor 488	-	ThermoFisher	Intracellular	VF4-6000647	5

Table S3. Flow Cytometry panel for indexed single-cell sorting of HIV-1 vRNA⁺ cells detected by RNAflow-FISH related to Figures 3 and 4.

Target	Fluorochrome	Clone	Supplier	Detection	Catalogue n°	Volume per test (µL)
CD27	BV605	L128	BD	Surface	562655	2
CD45RA	BB700	5H9	BD	Surface	742249	0.5
CD4	PE-Cy7	RPA-T4	BD	Surface	560649	5
CD8	BV510	SK1	Biolegend	Surface	344732	3
CD14	BV510	M5E2	Biolegend	Surface	301842	3
CD16	BV510	3G8	BD	Surface	563830	3
CD19	BV510	H1B19	Biolegend	Surface	302242	3
CD56	BV510	NCAM16.2	BD	Surface	563041	0.5
Fixable Viability Dye	eFluor 506	-	ThermoFisher	Surface	65-0866-14	0.1
HIV core antigen	RD1	KC57	Beckman Coulter	Intracellular	6604667	2
HIV-1 5' exonRNA	Alexa Fluor 647	-	ThermoFisher	Intracellular	VF1-6000978	5
HIV-1 gagRNA	Alexa Fluor 750	-	ThermoFisher	Intracellular	VF6-6000975	5
HIV-1 nefRNA	Alexa Fluor 488	-	ThermoFisher	Intracellular	VF4-6000647	5

Table S4. Near Full-Length primers related to Figures 3 and 4

Step	Primer and probe name	Sequence (5' to 3')	HXB2 position	Reference
Pre-amplification	638F	GCG CCC GAA CAG GGA CYT GAA ARC GAA AG	638 - 665	(Lee <i>et al.</i> , 2017)
	BLOuterR	GAG GGA TCT CTA GTT ACC AGA GTC	9663 - 9686	(Hiener <i>et al.</i> , 2017)
Amplification	263F	GAC CTG AAA GCG AAA GGG AAA C	651 - 672	(Bruner <i>et al.</i> , 2016)
	280R	CTA GTT ACC AGA GTC ACA CAA CAG ACG	9650 - 9676	(Hiener <i>et al.</i> , 2017)

Chapter 4 – Manuscript 2: Single-Cell Relationships Between HIV-1-Specific Immune Responses in Untreated Individuals and Viral Transcription and Translation

Status: This research article is in preparation for a submission in Cell Reports

Author contribution: Gérémy Sannier and Daniel E. Kaufmann designed the study. Nicolas Chomont, Andrés Finzi, and Mathieu Dubé provided assistance with assay protocols and experimental design. Gérémy Sannier, Gloria Gabrielle Delgado, Rose Cloutier, Mehdi Benlarbi, Amélie Pagliuzza, Mélina Duchesne, Catherine Bourassa, and Gabrielle Gendron-Lepage performed experiments. Gérémy Sannier analyzed the data. Jean-Pierre Routy contributed to recruitment. Gérémy Sannier, Nicolas Chomont, Andrés Finzi, Mathieu Dubé, and Daniel E. Kaufmann interpreted the data. Gérémy Sannier wrote the initial draft of the manuscript with edits from Mathieu Dubé and Daniel E. Kaufmann. All co-authors reviewed and edited the manuscript. Mathieu Dubé and Daniel E. Kaufmann provided supervision.

Single-Cell Relationships Between HIV-1-Specific Immune Responses in Untreated Individuals and Viral Transcription and Translation

Gérémy Sannier^{1,2}, Gloria-Gabrielle Delgado¹, Rose Cloutier¹, Mehdi Benlarbi^{1,2}, Amélie Pagliuzza¹, Mélina Duchesne¹, Catherine Bourassa¹, Gabrielle Gendron-Lepage¹, Nathalie Brassard¹, Jean-Pierre Routy^{3,4}, Nicolas Chomont^{1,2}, Andrés Finzi^{1,2}, Mathieu Dubé^{1,#,*}, Daniel E. Kaufmann^{1,2,5,6,#,*}

¹Research Centre of the Centre Hospitalier de l'Université de Montréal (CRCHUM)

²Université de Montréal Montreal, Quebec, Canada

³Chronic Viral Illnesses Service and Division of Hematology, McGill University Health Centre, Montreal, Quebec, Canada

⁴Infectious Diseases and Immunity in Global Health Program, Research Institute, McGill University Health Centre, Montreal, Quebec, Canada

⁵Division of Infectious Diseases, Department of Medicine, University Hospital of Lausanne and University of Lausanne, Lausanne, Switzerland

⁶Lead Contact

#These authors contributed equally

*Correspondence: mathieu.dube.chum@ssss.gouv.qc.ca and daniel.kaufmann@chuv.ch

ABSTRACT

The persistence and impact of diverse transcriptionally HIV-infected CD4⁺ T cells on immune responses from chronic to controlled infection remain unclear. Using RNAflow-FISH, we detected inducible HIV transcription in ART-treated and untreated individuals, including Elite Controllers (EC) who control the infection. HIV-specific CD4⁺ T cell levels were similar across groups, while specific CD8⁺ T cell responses were lower in ART-treated individuals. In EC, these responses negatively correlated with the size of the transcriptionally active reservoir, contrasting with positive associations observed in ART-treated individuals. No contemporary correlations were found in untreated individuals with uncontrolled HIV infection, although T cell responses appeared associated with a reduction in p24-expressing cells after ART initiation. The decline of short abortive transcripts, more abundant during ART, showed no correlation with the immune responses. Our findings suggest that pre-ART HIV immune responses effectively reduce translation-competent reservoirs but also highlight the resistance of transcriptionally active reservoirs to immune responses.

INTRODUCTION

Despite the remarkable success of ART, a significant obstacle to achieving a cure for HIV remains in the form of a latent viral reservoir^{1,2}. This reservoir consists of dormant HIV-infected cells that persist in the body even during ART, and they can reactivate and fuel viral rebound if ART is interrupted³.

Some studies have shown that some reservoir cells remain capable of transcription during ART but fail to effectively translate the p24 protein^{4,5}. The majority of these reservoir cells harbor defective proviruses that probably hinder viral replication by initiating short abortive transcription, while only a minority arise from intact viral genomes^{5,6}. These reservoirs are susceptible to reactivation by external stimuli, as demonstrated by their detection using latency reversal agents (LRA). Recently, our group has observed that short and abortive transcription can occur spontaneously during ART⁷ suggesting that reservoirs carrying transcription-competent defective proviruses may be less susceptible to cell death^{8,9}. These findings may also reflect a series of successive stages of blockage during viral transcription and translation processes¹⁰⁻¹², which can be overcome by reactivation.

T cells, as key components of the immune system, actively engage in recognizing and eliminating HIV-infected cells¹³⁻¹⁶. The existence of T cell immunity prior to initiating ART has emerged as a potentially crucial determinant of the viral reservoir size. Pre-ART, the presence of HIV-specific CD4⁺ and CD8⁺ T cell responses has been associated with smaller reservoir sizes based on DNA measurements^{17,18}. Early initiation of ART after seroconversion has been associated with a smaller viral reservoir¹⁹⁻²¹ and enhanced functionality of HIV-specific CD4⁺ and CD8⁺ T cells^{22,23}. During ART, the magnitudes, and functions of HIV-specific CD4⁺ and CD8⁺ T cells vary significantly among individuals^{24,25}.

Reports indicated that ART initiation is linked with diminished T cell responses, possibly due to the scarcity of HIV antigens^{26,27}. However, we recently showed the persistence of low levels of viremia during ART shaping antiviral immunity^{7,27}. This persistent presence of antigen sustains HIV-specific T cell responses in a chronically expanded, activated, and exhausted state during ART.

Within the untreated people living with HIV (PLWHIV), a minute fraction ($\leq 1\%$) demonstrates the remarkable ability to naturally suppress viral replication to levels that plunge below the detectable limit of standard viral load assays (<40 copies/mL of blood)²⁸. These individuals, commonly known as elite controllers (EC), provide valuable insights into the potential for naturally controlling HIV infection.

This study endeavors to utilize a longitudinal approach that incorporates both pre- and post-ART samples, enabling a comprehensive investigation into how immune responses prior to ART initiation influence the viral reservoir during the treatment. By harnessing the power of cutting-edge single-cell techniques, our aim is to unravel the intricate dynamics of the viral reservoir and shed light on the immune responses that contribute to its control.

RESULTS

Reactivation induces vRNA expression in Elite Controllers

We measured viral reservoirs in 24 untreated PLWHIV including EC (17 Chronic Progressors; CP + 7 EC) living with HIV for a median of 6 and 16 years, respectively (Table S1). Additionally, we analyzed 33 PLWHIV receiving antiretroviral treatment (ART) for an average of 6.3 years (Table S1). The size of the reservoirs measured by total and integrated DNA showed that the frequency of CD4⁺ T cells harboring total HIV DNA was lower in ART and even lower in EC compared to CP, but no difference between ART and CP was observed for cells bearing integrated DNA (Fig. 1A,B) suggesting that following ART, non-integrated DNA are significantly reduced.

To identify and characterize transcriptionally competent viral reservoir, we utilized a previously described multiplexed HIV RNAflow-FISH assay⁵. This assay detects viral reservoirs based on either viral RNA (vRNA) or protein (p24) expression. Recently, we optimized this version to detect spontaneously active infected cells, which proved more sensitive than the previous iterations⁷. In this approach, the primary *5'exons*RNA probe set targets all viral transcripts, allowing inclusive detection, whereas the *gag*RNA probe set ensures stringency. We also add the *pol*RNA probe set to identify viral transcripts elongating beyond *gag* (Fig. 1C, S1A,B). Viral translation was assessed by intracellular staining of the p24 protein (Fig. S1A,B, Table 2). Negative controls consisted of CD4⁺ T cells from 17 uninfected donors (UD). This group allowed the determination of a threshold of detection (Median+2xSD = 7 events/10⁶ CD4⁺ T cells). Spontaneously active viral reservoirs were detected in 82% of CP, 64% of ART, and 14% of EC, with median detections of 100, 22, and 2.2 vRNA⁺ cells /10⁶ CD4⁺, respectively (Fig. 1D, S1C). To

reveal inducible reservoirs, CD4⁺ T cells from PBMCs were treated with a combination of PMA/Ionomycin or a combination of ingenol-3-angelate (PEP005) and Panobinostat (PNB) for 16h. PMA/Ionomycin-inducible were found in 94% of CP, 92% of ART, and 71% of EC with significantly higher median detection (280, 65.7, and 10.6 vRNA⁺ cells /10⁶ CD4⁺, respectively). PEP005/PNB reactivation showed greater potency in ART⁵, and inducible viral reservoirs were detected in all ART with a higher median size (300 vRNA⁺ /10⁴ CD4⁺ T cells), to a similar level than CP (180 vRNA⁺ /10⁴ CD4⁺ T cells) (Fig. 1D, S1C). However, we demonstrated that this combination mostly reactivated viral transcription, PMA/Ionomycin remaining the most potent to trigger p24 production.

We compared vRNA expression and integrated DNA to determine the transcriptional activity of the cell (Fig. 1DF, S1D). Spontaneously, CP demonstrated a higher transcriptional activity than ART-treated and EC (Fig. 1D). As expected, both reactivations increased transcriptional activity in ART and EC closer to the one of CP (Fig. 1F, S1C). Because spontaneously active reservoirs are difficult to assess in EC, we would rely on inducible reservoirs. To that extent, we observed that the size of the spontaneously active viral reservoirs correlated better with the inducible reservoirs in EC (Fig. S1F,G) as observed in ART⁷.

Globally, these highlighted the strong inhibition of spontaneous vRNA⁺ reservoirs in EC compared to CP or ART-treated PLWHIV. However, using potent LRA allows the reactivation of inducible reservoirs that are associated with stronger transcriptional activity.

vRNA-expressing cells in EC are phenotypically similar to those in ART-treated individuals

Next, we analyzed the vRNA⁺ profile in the 3 cohorts. Initially, we identified translation-competent cells by their ability to produce the protein Gag (p24) (Fig. 2A)^{5,30}. Subsequently, the RNA profile was determined based on *gag* and *pol* transcript expressions (Fig. 2B). In CP, we observed that more than half of the vRNA⁺ cells were p24⁺ (57.2% of the vRNA⁺ cells) (Fig. 2C) with the exception of PEP005/PNB-inducible cells, reminiscent of the role of the combination on transcription⁵. In both ART-treated and EC individuals, only a few vRNA-expressing cells were p24⁺ (Fig. 2C), indicating effective control of HIV. We also observed higher proportions of *gag*RNA⁺ *pol*RNA⁻ transcripts (termed *gag*RNA⁺) among spontaneously and inducible vRNA⁺ cells that do not translate p24. These reservoirs represent short abortive transcript⁷ or deleted transcripts (Fig. 2D, S2A)⁵. Additionally, we detected a smaller proportion of p24⁻ double positive *gag*RNA⁺ *pol*RNA⁺ transcripts, although at lower levels compared to the *gag*RNA⁺ population (Fig. 2D, S2A). These transcripts encompass a more processive population of reservoirs (elongated transcripts not sustaining translation, termed vRNA_{DP} for “double *gag*RNA⁺ *pol*RNA⁺ positive”).

Subsequently, we asked whether the cellular phenotype of the cells could be associated with better control of the viral reservoir in EC. We aimed to characterize the HIV-infected cells identified within the three cohorts focusing on populations previously identified as enriched in HIV-infected cells. CD4⁺ T cells encompass diverse subpopulations, including naïve (T_N), central (T_{CM}), effector (T_{EM}), transitional memory (T_{TM}), and effector memory expressing CD45RA (T_{EMRA}), based on the expression patterns of CD45RA, CCR7, and

CD27 (Fig. S2B). Due to the limited number of spontaneously active vRNA⁺ cells and alteration of cellular markers by PMA/Ionomycin, we phenotyped the reservoir cells following PEP005/PNB reactivation⁵. To minimize noise, we focused our analysis on individuals with ≥ 5 vRNA⁺ cells detected after PEP005/PNB reactivation. Consistent with previous findings, our analysis revealed that the majority of vRNA⁺ cells in both CP and ART exhibited a T_{CM} and, although at lower levels, a T_{EM} phenotype (Fig. S2C). EC showed a similar pattern, with a predominance of T_{CM} and T_{EM} among the vRNA-expressing cells (Fig. S2C).

Overall, these data highlight close similarities between the vRNA-expressing cells in ART-treated and EC at the phenotypical level. Thus, these findings cannot explain why ART-treated individuals are unable to control HIV infection while EC can, implying that factors other than cellular and viral differentiation play a crucial role.

High levels of T cell responses and functions in EC are associated with fewer vRNA-expressing cells

Both CD4⁺ and CD8⁺ T cell responses play a crucial role in the control of HIV infection. Therefore, we investigated the impact of HIV infection on immune responses in the 3 cohorts of PLWHIV. Using a TCR-dependent activation-induced marker (AIM) assay^{25,31,32}, we evaluated antigen-specific T cell responses and functions (Fig. S3A, Table S3,S4). We employed an OR Boolean combination gating strategy that involved analyzing the upregulation of CD69, CD40L, 4-1BB, and OX-40 following a 15h stimulation with peptide pools spanning the coding sequences of either Gag, Pol, Nef, or

Env (Fig. S3B)³²⁻³⁴. For CD8⁺ responses, we measured the upregulation of CD69 and 4-1BB (Fig. S3C). Cells expressing at least one pair of AIM were considered HIV-specific. The specificity of the assay was confirmed by significant increases compared to unstimulated conditions (Fig. S3D,E).

We observed detectable Gag, Pol, Nef, and, to a lesser extent, Env CD4⁺ (Fig. 3A) and CD8⁺ T cell responses (Fig. 3B). To quantify the overall HIV responses, we summed the net responses across peptide pools, as described previously⁷. No significant differences were found in the total HIV-specific CD4⁺ T cell responses amongst the 3 cohorts (Fig. 3C). However, ART-treated individuals exhibited lower specific CD8⁺ T cell responses compared to CP and EC, whereas CP and EC had equivalent magnitudes of CD8⁺ responses (Fig. 3D). ART-treated individuals were characterized by a loss of the specific CD8⁺ T cells responses oriented toward predominant CD4⁺ responses (Fig. 3E).

To evaluate the HIV-specific T cell functions, we measured the expression of IFN γ , IL-2, and TNF α after a 6h stimulation with the same peptide pools used in the AIM assays. Total cytokine⁺ CD4⁺ and CD8⁺ T cells were determined using a similar OR Boolean combination gating strategy (Fig. S3F). In most participants cytokine⁺ CD4⁺ and CD8⁺ T cell responses were detected (Fig. S3G,H). Cytokine⁺ CD4⁺ and CD8⁺ T cell responses were also detectable in all 3 cohorts (Fig. 3E,F). Similarly to the AIM assay, no statistical differences were observed in the ICS⁺ CD4⁺ T cell responses between CP, ART, and EC (Fig. 3G), while effector CD8⁺ T cell functions were significantly greater in CP compared to ART individuals, akin to measurements in EC (Fig. 3H). However, we observed in all three groups that the cytokine⁺ T cell responses were skewed toward specific CD8⁺ T cell functions, with no significant differences between cohorts (Fig. 3I).

We then examined the correlations between HIV responses and inducible vRNA⁺ cells, and spontaneously active vRNA⁺ cells (Fig. 3J,K). In CP, no significant correlation between HIV-specific T cell responses and functions was observed with either inducible or spontaneously active vRNA⁺ cells (Fig. 3J,K). In ART, induced and spontaneously active reservoirs displayed strong positive associations with the frequencies of HIV-specific CD4⁺ and CD8⁺ T cell responses, as well as specific CD4⁺ effector functions (Fig. 3J,K) but no significant correlation with CD8⁺ T cell functions was observed. We observed in EC, negative associations between specific T cell responses, CD8⁺ T cell functions, and inducible viral reservoirs (Fig. 3J, S3I), whereas HIV-specific CD4⁺ T cell functions were negatively associated with spontaneously active reservoir cells (Fig. 3K). Finally, no significant correlation between inducible p24⁺ cells and T cell immunity was observed in the three cohorts (Fig. S3J), nor with the inducible p24⁺ cells in CP (Fig. S3K). Positive associations with specific CD4⁺ and CD8⁺ T cell responses were observed for ART-treated individuals (Fig. S3K) consistent with another study⁷.

Overall, these results suggest that despite comparable levels of HIV-specific T cell responses, and functions when compared to EC, CP face a significant impediment to achieving control of viral transcription and translation.

CD4-induced antibodies are associated with high levels of viral reservoirs in CP but with lower inducible vRNA-expressing cells in EC

Antibodies, in addition to T cells, play a role in viremia control. Accordingly, we assessed the levels of anti-p24 (Fig. 4A) and CD4-induced antibodies (Fig. 4B). Anti-p24 antibodies,

produced by the B cells in response to the p24 antigen, form immune complexes upon recognition and binding. All 3 cohorts displayed higher levels of anti-p24 antibodies compared to the control participants, with no significant difference observed between CP and ART, while EC exhibited the highest levels (Fig. 4A). CD4-induced antibodies, generated through the interaction between Env and the CD4 molecule, target specific epitopes on the Env accessible upon viral engagement with the CD4 receptor. Although the levels of CD4-induced antibodies were elevated in all the 3 groups compared to UD, no significant differences were observed among the cohorts (Fig. 4B).

In EC, we observed a positive association between inducible vRNA⁺ cells and anti-p24 antibodies and a negative trend with CD4-induced antibodies (Fig. 4C, S4A,B). In CP, we detected strong positive associations between inducible or spontaneously active vRNA⁺ cells (Fig. 4C,D). as well as p24⁺ cells (Fig. S4C,D). However, no significant correlations were observed for ART-treated individuals between vRNA⁺ or p24⁺ cells and antibodies (Fig. 4D, S4C,D).

The decline in vRNA-expressing cells is more severe in translation-competent cells following ART initiation

To investigate whether the immune responses prior to ART correlated with lower levels of transcriptionally active reservoirs, we studied the immune-viral relationships in a longitudinal subcohort of 12 participants before and after ART initiation. Pre-ART participants were treatment-naïve for an average of 1.4 years, while post-ART samples were collected at a median of 2.4 years after treatment initiation (Fig. 6A, Table S5).

Firstly, we assessed the size of viral DNA reservoirs. Following ART initiation, we observed a decrease in the total viral DNA in all individuals, whereas no significant decrease was detected for integrated DNA (Fig. 5B,C). Both spontaneously active and inducible viral transcription decreased after ART initiation (Fig. 5D). Prior to ART, 75% of participants had spontaneously active vRNA⁺ cells higher than the threshold of 7 vRNA⁺ cells/10⁶ CD4⁺ T cells, with an overall detection rate of 110 vRNA⁺ cells/10⁶ CD4⁺ T cells (Fig. 5D). ART significantly reduced both the prevalence of spontaneously active vRNA-expressing cells (25% of individuals), and its size (2.7 vRNA⁺ cells /10⁶ CD4⁺ T cells) (Fig. 5D). Consistent with Figure 1A, both PEP005/PNB and PMA/Ionomycin reactivation robustly reactivated viral reservoirs in post-ART samples, (90 and 30.9 vRNA⁺/10⁶ CD4⁺ T cells, respectively) (Fig. 5D). We observed that ART initiation preferentially reduced the size of the spontaneously active vRNA-expressing cells (Fig. 5E). However, we did not observe associations between spontaneously active vRNA⁺ cells prior to and after ART initiation (Fig. 5F) whereas induced viral reservoirs correlated pre- and post-ART (Fig. 5F, S5A).

Next, we wondered if the decline of vRNA-expressing cells was associated with their transcriptional and translational potential. Consistent with previous findings, pre-ART samples contained a higher proportion of cells competent for p24 translation, whereas post-ART samples exhibited an enrichment of cells competent for abortive transcription (Fig. 5G, S5B,C). We calculated the frequency of residual viral reservoirs after ART relative to the magnitude of infected cells before treatment, which gave us the viral subpopulations persistence under ART (Fig. 5H, S5D). Following ART initiation, all subpopulations were significantly reduced in both spontaneously active and inducible

vRNA⁺ cells (Fig. 5H, S5D). Cells competent for p24 translation were strongly reduced followed by the vRNA_{DP} and to a lesser extent *gag*RNA⁺ cells, in post-ART samples (Fig. 5H, S5D). However, the latter population was enriched in all vRNA-expressing cells following ART initiation (Fig. 5H, S5D).

Globally, these data highlight that the decline of vRNA-expressing cells following ART is more severe in some viral subpopulations, with short abortive transcripts being more persistent.

vRNA-expressing cells are maintained after ART irrespective of immune responses elicited before ART

The differential decrease in viral subpopulations after ART raises questions about the impact of the immune response prior to ART initiation. We examined the trajectory of HIV-specific T cell responses adopted after ART compared to pre-ART. We found similar levels of HIV-specific CD4⁺ T cell responses after therapy compared to pre-ART (Fig. 6A), while HIV-specific CD8⁺ T cell responses were reduced under treatment (Fig. 6B). Consistent with this, CD4⁺ T effector functions remained unchanged despite ART (Fig. S6A), while CD8⁺ T effector functions decreased (Fig. S6B). We also observed positive correlations between HIV-specific CD4⁺ and CD8⁺ T cell responses both before (Fig. S6C) and after ART (Fig. S6D) suggesting that immune responses persisted during ART. We next wonder if the immune responses post-ART tend to be determined by the size of the vRNA-expressing cells during the chronic infection. We observed that the size of vRNA-

expressing cells and the size of translation-competent p24⁺ reservoirs during chronic infection were associated with HIV-specific CD4⁺ T cell responses under ART (Fig. 6C,D).

To determine if the decline of HIV-infected cells under ART could be attributed to pre-ART immune responses, we calculated a “reduction score”. This score corresponded to the fold decrease of each viral component analyzed post-ART compared to pre-ART samples (Fig. 6E). Higher scores indicate a greater contraction of the population under ART. As expected, all components decreased after ART initiation, with the most severe decline observed for p24⁺ cells (Fig. S6E). We found that the frequencies of HIV-specific CD4⁺ T cells correlated with the contraction of the cells carrying integrated DNA and the total inducible vRNA⁺ cells (Fig. 6F), while HIV-specific CD4⁺ T cell functions tend to be associated with the decline of spontaneously active vRNA⁺ cells and inducible p24⁺ reservoirs. HIV-specific CD8⁺ T cell responses correlated strongly with the decrease of integrated DNA, spontaneously active and inducible translation-competent reservoirs (Fig. 6F), while CD8⁺ T cell functions were associated with the last two (Fig. 6F).

These findings suggest the potential impact of the vRNA-expressing cells in the process of establishing viral reservoirs. Moreover, these cells demonstrate a remarkable level of resistance to the immune responses mediated by both CD4⁺ and CD8⁺ T cells.

DISCUSSION

In this study, we examined the relationship between vRNA-expressing cells and HIV-specific T cell responses. Inducible viral reservoirs were detected in both ART-treated individuals and untreated PLWHIV, with similarities observed in their vRNA profile between EC and ART individuals, albeit at lower levels. Most HIV-infected cells displayed short abortive or deleted transcripts enriched in central memory (T_{CM}). We detected HIV-specific $CD4^+$ and $CD8^+$ T cell responses in all groups, but ART individuals had lower specific $CD8^+$ T cell responses compared to CP and EC. The correlations between immune responses and viral reservoirs differed between the cohorts, indicating differences in immune control. In a longitudinal analysis before and after ART initiation, we observed a reduction in spontaneously active viral reservoirs and a shift in the viral profile following ART initiation, due to the differential decline of the viral subpopulations upon treatment.

We previously demonstrated the utility of the multiplexed RNAflow-FISH assay in identifying inducible viral reservoirs⁵ and spontaneously active viral reservoirs⁷ at the single-cell level. We detected viral reservoirs in both chronic progressors and ART-treated individuals, even without *ex vivo* latency reversal. However, in EC, vRNA-expressing cells required potent stimuli for detection. Despite lower levels of integrated DNA in EC, reactivation with PEP005/PNB led to vRNA expression in the majority of individuals. One possible explanation for this potent reactivation of HIV-infected cells in EC could be the absence of $CD8^+$ T cells, which effectively suppress viral expression³⁵⁻³⁷. One crucial factor to consider is the impact of the combination of latency-reversal agents used. While Panobinostat initiates viral transcription^{38,39}, PEP005 induces elongation^{11,40}. Our

previous findings indicated that the combination of PEP005/PNB exhibited greater potency compared to the control PMA/Ionomycin, but primarily resulted in short abortive transcripts⁵.

The RNAflow-FISH enables viral profiling of the HIV-infected cells^{5,30,41,42}. The vast majority of HIV-infected cells were detected in memory cells, yet some differences can be noted between cohorts⁴³. Consistently with other findings, we have observed enrichment of HIV-infected cells in T_{CM} in both untreated and ART-treated individuals⁴³. Also, while the majority of the vRNA-expressing cells were capable of translating p24 in CP, we observed a similar viral profile of mostly short abortive transcripts in both ART and EC, albeit at lower levels. We attributed this profile to the predominance of defective proviruses induced as observed in ART individuals⁵. However, recent studies have indicated that HIV-infected cells in EC harbor a greater proportion of intact integrated DNA compared to CP and ART-treated PLWHIV⁴⁴. The low frequency of fully transcribed vRNAs in EC may be attributed to the deeply silent state of the integrated DNA in these individuals⁴⁵⁻⁴⁷.

Untreated (CP and EC) and ART-treated individuals have comparable magnitudes of HIV-specific CD4⁺ T cell responses while HIV-specific CD8⁺ T cell responses are diminished during ART. However, there is a strong association between HIV-specific T cell responses and the size of both the inducible and spontaneously active viral reservoirs in individuals receiving ART. In Elite Controllers, the size of inducible vRNA-expressing cells correlated with lower HIV-specific CD8⁺ T cell immunity while no association was found in chronic progressors. These results suggest that while CP show similar magnitudes of HIV-specific immune responses to EC, the persistence of high levels of vRNA-expressing cells hinders control of HIV infection, likely due to active replication leading to immune dysfunction and

exhaustion. This might be due to the altered differentiation of HIV-specific T cell responses in CP who are characterized by exacerbated cT_{FH} functions, away from the T_{H17} functions elicited in EC^{25,31}.

CD4-induced antibodies were high in all three groups, although non-neutralizing, seem associated with better control of HIV infection in EC in comparison to CP. These antibodies target the Env accessible upon viral engagement with the CD4 receptor. It is possible that impaired Nef protein in Elite Controllers inhibiting CD4 downregulation^{48,49} allows high levels of CD4-induced antibodies to eliminate HIV-infected cells through ADCC. We also detected anti-p24 antibodies in CP and ART-treated individuals indicating an active replication state or spontaneously active viral reservoir⁷, as well as in EC, suggesting that despite the smaller size of viral reservoirs, viral protein expression happens.

As EC represent the goal to reach in viremia control, we studied both viral and immune characteristics in a longitudinal pre/post ART cohort. Initiation of ART was accompanied by a reduction of the spontaneously active and inducible vRNA-expressing cells. Also, ART induced the decline of all viral subpopulations, the decline appeared more severe in the p24-translation competent cells leading to an enrichment of short abortive transcripts. This is consistent with the observation in the ART-treated cohorts and previous report⁵. The inducible cells bearing short abortive transcripts on ART were also observed prior to ART initiation, suggesting that these cells were not caused by the treatment but were already pre-existent. One possibility might involve the error rate of the RNA pol II during the reverse transcription which leads to an aberrant HIV genome.

Although the HIV-specific CD8⁺ T cell responses on ART are significantly reduced, they tend to be determined by the size of the HIV reservoir prior to ART initiation. Moreover, we observed that the T cell immunity established during the chronic infection was associated with a greater reduction of the size of both the spontaneously active and inducible translation-competent cells upon ART. However, the absence of correlation between the vRNA-expressing cells and the HIV-specific T cell responses suggests that the reservoirs enriched in short abortive transcripts might be less detectable by the immune cells as they may produce little to no, or cryptic⁸, viral protein or be more resistant to the immune killing^{8,9,50}.

Although we believe that the results described here represent an important advance for understanding the underlying mechanisms driving HIV pathogenesis, it also has some limitations. Firstly, EC represent less than 1% of the total PLWHIV and therefore, we had access to a limited number of participants^{51,52}. Also, the size of the spontaneously active reservoir in EC is limited and restricts our analysis to only inducible reservoirs in that group. This precludes deeper phenotyping of the viral reservoirs because of the inherent pleiotropic effects of the LRAs on cellular markers. Finally, our RNAflow-FISH assay, optimized to maximize detection, does not preserve cellular RNAs for downstream transcriptomic analyses.

In summary, our study provides a comprehensive characterization of inducible vRNA-expressing cells in different HIV infection contexts, shedding light on the composition and dynamics of viral reservoirs. The distinct features observed in CP, ART individuals, and EC highlight the heterogeneous nature of HIV infection and its impact on viral persistence and immune responses. These findings contribute to our understanding of the underlying

mechanisms driving HIV pathogenesis and may guide the development of novel therapeutic approaches aimed at achieving a functional cure.

METHODS

RESSOURCE AVAILABILITY

Lead contact

Further information and requests for resources and reagents should be directed to and will be fulfilled by the lead contact, Daniel E. Kaufmann (daniel.kaufmann@chuv.ch).

Material availability

This study did not generate new unique reagents.

Data and code availability

This paper does not report original code.

EXPERIMENTAL MODEL AND SUBJECT DETAILS

Ethics Statement

All work was conducted following the Declaration of Helsinki regarding informed consent and approval by an appropriate institutional board. Blood samples were obtained from donors who consented to participate in this research project at CHUM (CE13.019).

Subject characteristics

Subject characteristics are summarized in Table S1. Leukaphereses were obtained from study participants at the McGill University Health Centre, Montreal, Quebec Canada and at Centre Hospitalier de l'Université de Montréal (CHUM), Quebec, Canada. The study was approved by the respective IRBs and written informed consent obtained from all participants prior to enrolment. Uninfected donors (UD) are free of HIV-1 infection. Untreated participants (UNT, EC, Pre-ART) were naive for treatment. Treated subjects (ART, Post-ART) were on antiretrovirals with controlled viremia (< 40 vRNA copies/mL). The donors included both sex and were older than 18 years.

METHOD DETAILS

PBMCs and plasma isolation

Peripheral blood mononuclear cells (PBMCs) were isolated from blood samples by Ficoll density gradient centrifugation and cryopreserved in liquid nitrogen until use. Plasma was stored at -80°C . For antibody assays, plasma was heat-inactivated for 1 h at 56°C prior to experiments. Plasma from uninfected donors were used as negative controls and used to calculate the threshold in our ELISA assay.

HIV-1-infected cells stimulation.

Frozen PBMCs were thawed in cold heat-inactivated Fetal Calf Serum (FCS; Seradigm) before CD4^{+} T-cells isolation. CD4^{+} T cells were isolated by adverse magnetic bead selection (StemCell). Purified CD4^{+} T cells were resuspended at $2 \times 10^6/\text{mL}$ in RPMI (Gibco by Life Technologies) supplemented with penicillin/streptomycin (Gibco by Life

Technologies), 10% heat-inactivated FCS, and ARV (Entricitabine [10 μ M] + Maraviroc [10 μ M] + Raltegravir [0.2 μ M] + Tenofovir [5 μ M]) and seeded into 24-well plates. All ARV were obtained through the NIH AIDS Reagent Program. After a rest of 2h at 37°C, 5% CO₂, the cells were either left unstimulated or stimulated with stimulated with 30nM panobinostat (Selleck Chem) complemented with 25nM ingenol-3-angelate (Sigma). For 16h. Alternatively, cells were either left unstimulated or stimulated with 162nM PMA (Sigma) complemented with 705nM Ionomycin (Sigma)⁵ (Dubé et al., in preparation). 10-15 x 10⁶ purified CD4⁺ T cells were used per condition.

HIV-1 RNAflow-FISH assay

All buffers and fixation reagents were provided with the kit, apart from flow cytometry staining (2% FCS/PBS). The HIV-1 RNAflow-FISH assay was performed as previously described and as per manufacturer's instructions^{5,7,30,41,42}. Briefly, cells were harvested after stimulation and stained first with Fixable Viability Dye (20 min, 4°C, Fixable LiveDead, eBioscience) next with a mix containing a brilliant stain buffer (BD Biosciences) and the surface markers for memory (CD45RA, CCR7, and CD27) phenotype as well as for CD4⁺ T cells detection (CD3 and CD4) and CD8/NK/B cells and macrophages exclusions (CD8, CD56, CD14, CD16, CD19) (30 min, 4°C). Samples were fixed, permeabilized with buffers provided by the manufacturer, and labeled intracellularly for the structural HIV-1 p24 protein with the anti-p24 clone KC57 antibody (30 min 4°C, Beckman Coulter). HIV-1 RNA probing was performed using the PrimeFlow RNA Assay (ThermoFisher). HIV-1 RNA were labeled using HIV-1 *gag*RNA (20 pairs of "ZZ" probes), HIV-1 *exons*RNA (21 pairs of "ZZ" probes) and HIV-1 *pol*RNA (6 pairs of "ZZ" probes)

probe sets, all designed based on a consensus B HIV sequence. Each tag sequence allows the hybridization of specific complementary branched DNA nanostructure with different excitation/emission spectra. The probes were diluted 1:5 in diluent and hybridized to the target mRNAs for 2h at 40°C. Samples were washed to remove excess probes and stored overnight in the presence of RNAsin. Signal amplification was achieved by performing sequential hybridization with DNA branches (*i.e.*, Pre-Amplifier and Amplifier). The first DNA branch in the Pre-Amplifier Mix was added at a 1:1 ratio and was allowed to hybridize for 1.5 h at 40°C. Then the second DNA branch in the Amplifier Mix was added and hybridized for 1.5 h at 40°C^{5,7,30,41,42}. Amplified mRNAs were labeled with fluorescently tagged probes allowing hybridization for 1h at 40°C. The complete list of antibodies used is presented in Table S2 for panel. Samples were acquired on the flow cytometer (FACSymphony A5 Cell Analyzer; BD Biosciences) and analyzed using FlowJo (BD, v10.8.1). Unspecific binding of the fluorescent labeled branched probe in the multiplex kit can lead to a low level of false-positive background noise, which, if present, is detected across all the four channels corresponding to the types of labeled probes (AF488, AF594, AF647, AF750). To decrease background noise, we thus left the AF594 channel vacant and excluded false-positive events based on fluorescence in this channel before further gating. Gates were set on the HIV-uninfected donor control, or unstimulated control where appropriate (See gating strategy, Figure S1).

Total and integrated DNA measurements

Quantifications of total and integrated HIV-1 DNA were determined as previously described⁵³.

Activation-induced markers (AIM) assay

PBMCs were plated in a 96-wells flat bottom plate, at 10×10^6 cells/mL RPMI (Gibco by Life Technologies) supplemented with penicillin/streptomycin (Gibco by Life Technologies), 10% heat inactivated FCS and incubated at 37°C, 5% CO₂. After a rest of 3h, a CD40 blocking antibody (Miltenyi) was added to the culture to prevent the interaction of CD40L with CD40 and its subsequent downregulation. In addition, antibodies for chemokine receptors CXCR6, CXCR3, CXCR5, and CCR6 were added in culture. After 15 min incubation at 37°C, 5% CO₂, cells were stimulated with 0.5 mg/mL staphylococcal enterotoxin B (SEB) or 0.5 mg/mL of overlapping peptide pools for Gag, Pol, Nef and Env (JPT) for 15h at 37°C, 5% CO₂. An unstimulated condition with 0.4mL of DMSO served as a negative control.

Cells were stained for viability dye (Aquavidin, Thermofisher, 20 min, 4°C), surface markers (30 min, 4°C) (see Table S3 for antibodies) and fixed using 2% paraformaldehyde (Sigma-Aldrich, 15 min, RT) before acquisition on the flow cytometer (FACSymphony A5 Cell Analyzer; BD Biosciences) and analyzed using FlowJo (BD, v10.8.1). For analysis of antigen-specific CD4⁺ T cell subsets as percentage of total CD4⁺ T cells, background-subtracted net values were used, which did not require excluding responses.

Intracellular cytokines staining (ICS) assay

PBMCs were resuspended at 10×10^6 cells/mL RPMI (Gibco by Life Technologies) supplemented with penicillin/streptomycin (Gibco by Life Technologies), 10% heat

inactivated FCS, and incubated at 37°C, 5% CO₂. After a rest of 2h, cells were stimulated with 0.5 mg/mL staphylococcal enterotoxin B (SEB) or 0.5 mg/mL of overlapping peptide pools for Gag, Pol, Nef and Env (JPT) for 6h at 37°C, 5% CO₂. An unstimulated condition with 0.4mL of DMSO served as a negative control.

Brefeldin A (BD Biosciences) and Monensin-1 (BD Biosciences) were added for the remaining 5hrs.

Cells were stained for viability dye (Aquavidin, Thermofisher, 20min, 4°C), surface markers (30 min, 4°C), and intracellularly for cytokines (30 min, RT) using the IC Fixation/Permeabilization kit (eBioscience) (see Table S4 for antibodies) before acquisition on the flow cytometer (FACSymphony A5 Cell Analyzer, BD Biosciences) and analyzed using FlowJo (BD, v10.8.1).

Measurement of CD4-induced and p24-specific antibodies by ELISA

For measurement of CD4-induced antibodies, stabilized gp120 inner domain (ID2)⁵⁴ (0.1 µg/mL), or bovine serum albumin (BSA) (0.1 µg/mL) as a negative control, were prepared in PBS and were adsorbed to plates (MaxiSorp; Nunc) overnight at 4°C. Coated wells were subsequently blocked with blocking buffer (Tris-buffered saline [TBS] containing 0.1% Tween20 and 2% BSA) for 1h at room temperature. Wells were then washed four times with washing buffer (Tris-buffered saline [TBS] containing 0.1% Tween20). A32 mAb (1 µg/mL) or diluted plasma (1:1000) from HIV-infected or uninfected individuals were incubated with the coated wells for 1h30 at room temperature. Plates were washed four times with washing buffer followed by incubation with HRP-conjugated goat-anti-

human IgG (Invitrogen) (1:3000) for 1h at room temperature, followed by four washes. HRP enzyme activity was determined after the addition of a 1:1 mix of Western Lightning oxidizing and luminol reagents (Perkin Elmer Life Sciences). Signal obtained with BSA was subtracted for each plasma and was then normalized to the signal obtained with A32 mAb present in each plate.

For measurement of anti-p24 antibodies³¹, wells were coated with recombinant p24 protein (NIH #12028) (0.1 µg/mL), in parallel with BSA (0.1 µg/mL). After blocking for 1h30, Rabbit anti-HIV p24 antiserum (NIH #4250) (1:5000) or diluted plasma (1:1000) from HIV-infected or uninfected individuals were added to the well for 2h. Detection of plasma antibodies was performed using HRP-conjugated goat-anti-human IgG or HRP-conjugated goat-anti rabbit IgG (Invitrogen) (1:3000) for 1h30. The signal was measured as described above and signal obtained with BSA was subtracted for each plasma and was then normalized to the signal obtained with rabbit anti-HIV p24 antiserum present in each plate.

ACKNOWLEDGMENT

We thank Josée Girouard, Angie Massicotte at the McGill University Health Centre in Montreal, and all study participants for their invaluable role in this project; Dr. Gaël Dulude, Philippe St-Onge, and the CRCHUM Flow Cytometry Platform; and Dr. Olfa Debbeche and the CRCHUM BSL3 platform for technical assistance. The following reagents were obtained through the NIH HIV Reagent Program, Division of AIDS, NIAID, NIH: Emtricitabine HRP-10071, Maraviroc HRP-11580, Raltegravir HRP-11680, Tenofovir HRP-10199, contributed by DAIDS/NIAID.

AUTHORS CONTRIBUTION

G.S, and D.E.K. designed the study; G.S., G.G.D., R.C., M.B., A.M., M.D., C.B., G.G.L., N.B. performed the experiments. G.S. analyzed data; J.P.R. ensured recruitment and clinical assessments; G.S., M.D., A.P., D.E.K. interpreted the data; G.S. wrote the initial draft of the manuscript; all co-authors reviewed and edited the manuscript, and M.D. and D.E.K. provided supervision.

DECLARATION OF INTERESTS

The authors declare no conflict of interests.

FUNDINGS

This study was supported by the Canadian Institutes for Health Research (CIHR grant #152977) and in part by the réseau Fonds de la recherche Québec-Santé (FRQ-S) SIDA and Maladies infectieuses and thérapies cellulaires. D.E.K. is a FRQS Merit Research Scholar. N.C. is supported by FRQ-S Research Scholar Awards. G.S. is supported by an FRQS doctoral fellowship and by a scholarship from the Department of Microbiology, Infectious Disease, and Immunology of the University of Montreal. M.B. is the recipient of a CIHR master's scholarship award. J-P.R. is the holder of the Louis Lowenstein Chair at McGill University. The funders had no role in the study design, data collection, analysis, decision to publish, or preparation of the manuscript.

REFERENCES

1. Finzi, D., Hermankova, M., Pierson, T., Carruth, L.M., Buck, C., Chaisson, R.E., Quinn, T.C., Chadwick, K., Margolick, J., Brookmeyer, R., et al. (1997). Identification of a reservoir for HIV-1 in patients on highly active antiretroviral therapy. *Science* 278, 1295-1300. [10.1126/science.278.5341.1295](https://doi.org/10.1126/science.278.5341.1295).
2. Wong, J.K., Hezareh, M., Gunthard, H.F., Havlir, D.V., Ignacio, C.C., Spina, C.A., and Richman, D.D. (1997). Recovery of replication-competent HIV despite prolonged suppression of plasma viremia. *Science* 278, 1291-1295. [10.1126/science.278.5341.1291](https://doi.org/10.1126/science.278.5341.1291).
3. Davey, R.T., Jr., Bhat, N., Yoder, C., Chun, T.W., Metcalf, J.A., Dewar, R., Natarajan, V., Lempicki, R.A., Adelsberger, J.W., Miller, K.D., et al. (1999). HIV-1 and T cell dynamics after interruption of highly active antiretroviral therapy (HAART) in patients with a history of sustained viral suppression. *Proc Natl Acad Sci U S A* 96, 15109-15114. [10.1073/pnas.96.26.15109](https://doi.org/10.1073/pnas.96.26.15109).
4. Grau-Exposito, J., Serra-Peinado, C., Miguel, L., Navarro, J., Curran, A., Burgos, J., Ocana, I., Ribera, E., Torrella, A., Planas, B., et al. (2017). A Novel Single-Cell FISH-Flow Assay Identifies Effector Memory CD4(+) T cells as a Major Niche for HIV-1 Transcription in HIV-Infected Patients. *mBio* 8. [10.1128/mBio.00876-17](https://doi.org/10.1128/mBio.00876-17).
5. Sannier, G., Dube, M., Dufour, C., Richard, C., Brassard, N., Delgado, G.G., Pagliuzza, A., Baxter, A.E., Niessl, J., Brunet-Ratnasingham, E., et al. (2021). Combined single-cell transcriptional, translational, and genomic profiling reveals HIV-1 reservoir diversity. *Cell Rep* 36, 109643. [10.1016/j.celrep.2021.109643](https://doi.org/10.1016/j.celrep.2021.109643).
6. Dufour, C., Richard, C., Pardons, M., Massanella, M., Ackaoui, A., Murrell, B., Routy, B., Thomas, R., Routy, J.P., Fromentin, R., and Chomont, N. (2023). Phenotypic characterization of single CD4+ T cells harboring genetically intact and inducible HIV genomes. *Nat Commun* 14, 1115. [10.1038/s41467-023-36772-x](https://doi.org/10.1038/s41467-023-36772-x).
7. Dube, M., Tastet, O., Dufour, C., Sannier, G., Brassard, N., Delgado, G.G., Pagliuzza, A., Richard, C., Nayrac, M., Routy, J.P., et al. (2023). Spontaneous HIV expression during suppressive ART is associated with the magnitude and function of HIV-specific CD4(+) and CD8(+) T cells. *Cell Host Microbe* 31, 1507-1522 e1505. [10.1016/j.chom.2023.08.006](https://doi.org/10.1016/j.chom.2023.08.006).

8. Imamichi, H., Dewar, R.L., Adelsberger, J.W., Rehm, C.A., O'Doherty, U., Paxinos, E.E., Fauci, A.S., and Lane, H.C. (2016). Defective HIV-1 proviruses produce novel protein-coding RNA species in HIV-infected patients on combination antiretroviral therapy. *Proc Natl Acad Sci U S A* 113, 8783-8788. 10.1073/pnas.1609057113.
9. Pollack, R.A., Jones, R.B., Perteza, M., Bruner, K.M., Martin, A.R., Thomas, A.S., Capoferri, A.A., Beg, S.A., Huang, S.H., Karandish, S., et al. (2017). Defective HIV-1 Proviruses Are Expressed and Can Be Recognized by Cytotoxic T Lymphocytes, which Shape the Proviral Landscape. *Cell Host Microbe* 21, 494-506 e494. 10.1016/j.chom.2017.03.008.
10. Clark, I.C., Mudvari, P., Thaploo, S., Smith, S., Abu-Laban, M., Hamouda, M., Theberge, M., Shah, S., Ko, S.H., Perez, L., et al. (2023). HIV silencing and cell survival signatures in infected T cell reservoirs. *Nature* 614, 318-325. 10.1038/s41586-022-05556-6.
11. Telwatte, S., Kim, P., Chen, T.H., Milush, J.M., Somsouk, M., Deeks, S.G., Hunt, P.W., Wong, J.K., and Yukl, S.A. (2020). Mechanistic differences underlying HIV latency in the gut and blood contribute to differential responses to latency-reversing agents. *AIDS* 34, 2013-2024. 10.1097/QAD.0000000000002684.
12. Yukl, S.A., Kaiser, P., Kim, P., Telwatte, S., Joshi, S.K., Vu, M., Lampiris, H., and Wong, J.K. (2018). HIV latency in isolated patient CD4(+) T cells may be due to blocks in HIV transcriptional elongation, completion, and splicing. *Sci Transl Med* 10. 10.1126/scitranslmed.aap9927.
13. Cartwright, E.K., Spicer, L., Smith, S.A., Lee, D., Fast, R., Paganini, S., Lawson, B.O., Nega, M., Easley, K., Schmitz, J.E., et al. (2016). CD8(+) Lymphocytes Are Required for Maintaining Viral Suppression in SIV-Infected Macaques Treated with Short-Term Antiretroviral Therapy. *Immunity* 45, 656-668. 10.1016/j.immuni.2016.08.018.
14. Chevalier, M.F., Julg, B., Pyo, A., Flanders, M., Ranasinghe, S., Soghoian, D.Z., Kwon, D.S., Rychert, J., Lian, J., Muller, M.I., et al. (2011). HIV-1-specific interleukin-21+ CD4+ T cell responses contribute to durable viral control through the modulation of HIV-specific CD8+ T cell function. *J Virol* 85, 733-741. 10.1128/JVI.02030-10.
15. International, H.I.V.C.S., Pereyra, F., Jia, X., McLaren, P.J., Telenti, A., de Bakker, P.I., Walker, B.D., Ripke, S., Brumme, C.J., Pulit, S.L., et al. (2010). The major genetic

determinants of HIV-1 control affect HLA class I peptide presentation. *Science* 330, 1551-1557. [10.1126/science.1195271](https://doi.org/10.1126/science.1195271).

16. Walker, B., and McMichael, A. (2012). The T-cell response to HIV. *Cold Spring Harb Perspect Med* 2. [10.1101/cshperspect.a007054](https://doi.org/10.1101/cshperspect.a007054).

17. Hurst, J., Hoffmann, M., Pace, M., Williams, J.P., Thornhill, J., Hamlyn, E., Meyerowitz, J., Willberg, C., Koelsch, K.K., Robinson, N., et al. (2015). Immunological biomarkers predict HIV-1 viral rebound after treatment interruption. *Nat Commun* 6, 8495. [10.1038/ncomms9495](https://doi.org/10.1038/ncomms9495).

18. Takata, H., Buranapraditkun, S., Kessing, C., Fletcher, J.L., Muir, R., Tardif, V., Cartwright, P., Vandergeeten, C., Bakeman, W., Nichols, C.N., et al. (2017). Delayed differentiation of potent effector CD8(+) T cells reducing viremia and reservoir seeding in acute HIV infection. *Sci Transl Med* 9. [10.1126/scitranslmed.aag1809](https://doi.org/10.1126/scitranslmed.aag1809).

19. Ananworanich, J., Chomont, N., Eller, L.A., Kroon, E., Tovanabutra, S., Bose, M., Nau, M., Fletcher, J.L.K., Tipsuk, S., Vandergeeten, C., et al. (2016). HIV DNA Set Point is Rapidly Established in Acute HIV Infection and Dramatically Reduced by Early ART. *EBioMedicine* 11, 68-72. [10.1016/j.ebiom.2016.07.024](https://doi.org/10.1016/j.ebiom.2016.07.024).

20. Leyre, L., Kroon, E., Vandergeeten, C., Sacdalan, C., Colby, D.J., Buranapraditkun, S., Schuetz, A., Chomchey, N., de Souza, M., Bakeman, W., et al. (2020). Abundant HIV-infected cells in blood and tissues are rapidly cleared upon ART initiation during acute HIV infection. *Sci Transl Med* 12. [10.1126/scitranslmed.aav3491](https://doi.org/10.1126/scitranslmed.aav3491).

21. Strain, M.C., Little, S.J., Daar, E.S., Havlir, D.V., Gunthard, H.F., Lam, R.Y., Daly, O.A., Nguyen, J., Ignacio, C.C., Spina, C.A., et al. (2005). Effect of treatment, during primary infection, on establishment and clearance of cellular reservoirs of HIV-1. *J Infect Dis* 191, 1410-1418. [10.1086/428777](https://doi.org/10.1086/428777).

22. Trautmann, L., Mbitikon-Kobo, F.M., Goulet, J.P., Peretz, Y., Shi, Y., Van Grevenynghe, J., Procopio, F.A., Boulassel, M.R., Routy, J.P., Chomont, N., et al. (2012). Profound metabolic, functional, and cytolytic differences characterize HIV-specific CD8 T cells in primary and chronic HIV infection. *Blood* 120, 3466-3477. [10.1182/blood-2012-04-422550](https://doi.org/10.1182/blood-2012-04-422550).

23. Ndhlovu, Z.M., Kazer, S.W., Nkosi, T., Ogunshola, F., Muema, D.M., Anmole, G., Swann, S.A., Moodley, A., Dong, K., Reddy, T., et al. (2019). Augmentation of HIV-specific

T cell function by immediate treatment of hyperacute HIV-1 infection. *Sci Transl Med* 11. 10.1126/scitranslmed.aau0528.

24. Reiss, S., Baxter, A.E., Cirelli, K.M., Dan, J.M., Morou, A., Daigneault, A., Brassard, N., Silvestri, G., Routy, J.P., Havenar-Daughton, C., et al. (2017). Comparative analysis of activation induced marker (AIM) assays for sensitive identification of antigen-specific CD4 T cells. *PLoS One* 12, e0186998. 10.1371/journal.pone.0186998.

25. Niessl, J., Baxter, A.E., Morou, A., Brunet-Ratnasingham, E., Sannier, G., Gendron-Lepage, G., Richard, J., Delgado, G.G., Brassard, N., Turcotte, I., et al. (2020). Persistent expansion and Th1-like skewing of HIV-specific circulating T follicular helper cells during antiretroviral therapy. *EBioMedicine* 54, 102727. 10.1016/j.ebiom.2020.102727.

26. Kalams, S.A., Goulder, P.J., Shea, A.K., Jones, N.G., Trocha, A.K., Ogg, G.S., and Walker, B.D. (1999). Levels of human immunodeficiency virus type 1-specific cytotoxic T-lymphocyte effector and memory responses decline after suppression of viremia with highly active antiretroviral therapy. *J Virol* 73, 6721-6728. 10.1128/JVI.73.8.6721-6728.1999.

27. Jones, R.B., and Walker, B.D. (2016). HIV-specific CD8(+) T cells and HIV eradication. *J Clin Invest* 126, 455-463. 10.1172/JCI80566.

28. Stevenson, E.M., Ward, A.R., Truong, R., Thomas, A.S., Huang, S.H., Dilling, T.R., Terry, S., Bui, J.K., Mota, T.M., Danesh, A., et al. (2021). HIV-specific T cell responses reflect substantive in vivo interactions with antigen despite long-term therapy. *JCI Insight* 6. 10.1172/jci.insight.142640.

29. Deeks, S.G., and Walker, B.D. (2007). Human immunodeficiency virus controllers: mechanisms of durable virus control in the absence of antiretroviral therapy. *Immunity* 27, 406-416. 10.1016/j.immuni.2007.08.010.

30. Baxter, A.E., Niessl, J., Fromentin, R., Richard, J., Porichis, F., Charlebois, R., Massanella, M., Brassard, N., Alshahafi, N., Delgado, G.G., et al. (2016). Single-Cell Characterization of Viral Translation-Competent Reservoirs in HIV-Infected Individuals. *Cell Host Microbe* 20, 368-380. 10.1016/j.chom.2016.07.015.

31. Morou, A., Brunet-Ratnasingham, E., Dube, M., Charlebois, R., Mercier, E., Darko, S., Brassard, N., Nganou-Makamdop, K., Arumugam, S., Gendron-Lepage, G., et al.

(2019). Altered differentiation is central to HIV-specific CD4(+) T cell dysfunction in progressive disease. *Nat Immunol* 20, 1059-1070. 10.1038/s41590-019-0418-x.

32. Niessl, J., Baxter, A.E., Mendoza, P., Jankovic, M., Cohen, Y.Z., Butler, A.L., Lu, C.L., Dube, M., Shimeliovich, I., Gruell, H., et al. (2020). Combination anti-HIV-1 antibody therapy is associated with increased virus-specific T cell immunity. *Nat Med* 26, 222-227. 10.1038/s41591-019-0747-1.

33. Sannier, G., Nicolas, A., Dube, M., Marchitto, L., Nayrac, M., Tastet, O., Chatterjee, D., Tauzin, A., Lima-Barbosa, R., Laporte, M., et al. (2023). A third SARS-CoV-2 mRNA vaccine dose in people receiving hemodialysis overcomes B cell defects but elicits a skewed CD4(+) T cell profile. *Cell Rep Med* 4, 100955. 10.1016/j.xcrm.2023.100955.

34. Nicolas, A., Sannier, G., Dube, M., Nayrac, M., Tauzin, A., Painter, M.M., Goel, R.R., Laporte, M., Gendron-Lepage, G., Medjahed, H., et al. (2023). An extended SARS-CoV-2 mRNA vaccine prime-boost interval enhances B cell immunity with limited impact on T cells. *iScience* 26, 105904. 10.1016/j.isci.2022.105904.

35. Betts, M.R., Nason, M.C., West, S.M., De Rosa, S.C., Migueles, S.A., Abraham, J., Lederman, M.M., Benito, J.M., Goepfert, P.A., Connors, M., et al. (2006). HIV nonprogressors preferentially maintain highly functional HIV-specific CD8+ T cells. *Blood* 107, 4781-4789. 10.1182/blood-2005-12-4818.

36. Collins, D.R., Gaiha, G.D., and Walker, B.D. (2020). CD8(+) T cells in HIV control, cure and prevention. *Nat Rev Immunol* 20, 471-482. 10.1038/s41577-020-0274-9.

37. Ndhlovu, Z.M., Stampoulouglou, E., Cesa, K., Mavrothalassitis, O., Alvino, D.M., Li, J.Z., Wilton, S., Karel, D., Piechocka-Trocha, A., Chen, H., et al. (2015). The Breadth of Expandable Memory CD8+ T Cells Inversely Correlates with Residual Viral Loads in HIV Elite Controllers. *J Virol* 89, 10735-10747. 10.1128/JVI.01527-15.

38. Rasmussen, T.A., Tolstrup, M., Brinkmann, C.R., Olesen, R., Erikstrup, C., Solomon, A., Winckelmann, A., Palmer, S., Dinarello, C., Buzon, M., et al. (2014). Panobinostat, a histone deacetylase inhibitor, for latent-virus reactivation in HIV-infected patients on suppressive antiretroviral therapy: a phase 1/2, single group, clinical trial. *Lancet HIV* 1, e13-21. 10.1016/S2352-3018(14)70014-1.

39. Barton, K., Hiener, B., Winckelmann, A., Rasmussen, T.A., Shao, W., Byth, K., Lanfear, R., Solomon, A., McMahon, J., Harrington, S., et al. (2016). Broad activation of latent HIV-1 in vivo. *Nat Commun* 7, 12731. 10.1038/ncomms12731.
40. Jiang, G., Mendes, E.A., Kaiser, P., Wong, D.P., Tang, Y., Cai, I., Fenton, A., Melcher, G.P., Hildreth, J.E., Thompson, G.R., et al. (2015). Synergistic Reactivation of Latent HIV Expression by Ingenol-3-Angelate, PEP005, Targeted NF- κ B Signaling in Combination with JQ1 Induced p-TEFb Activation. *PLoS Pathog* 11, e1005066. 10.1371/journal.ppat.1005066.
41. Baxter, A.E., Niessl, J., Fromentin, R., Richard, J., Porichis, F., Massanella, M., Brassard, N., Alshafiq, N., Routy, J.P., Finzi, A., et al. (2017). Multiparametric characterization of rare HIV-infected cells using an RNA-flow FISH technique. *Nat Protoc* 12, 2029-2049. 10.1038/nprot.2017.079.
42. Sannier, G., Dube, M., and Kaufmann, D.E. (2020). Single-Cell Technologies Applied to HIV-1 Research: Reaching Maturity. *Front Microbiol* 11, 297. 10.3389/fmicb.2020.00297.
43. Chomont, N., El-Far, M., Ancuta, P., Trautmann, L., Procopio, F.A., Yassine-Diab, B., Boucher, G., Boulassel, M.R., Ghattas, G., Brenchley, J.M., et al. (2009). HIV reservoir size and persistence are driven by T cell survival and homeostatic proliferation. *Nat Med* 15, 893-900. 10.1038/nm.1972.
44. Lian, X., Seiger, K.W., Parsons, E.M., Gao, C., Sun, W., Gladkov, G.T., Roseto, I.C., Einkauf, K.B., Osborn, M.R., Chevalier, J.M., et al. (2023). Progressive transformation of the HIV-1 reservoir cell profile over two decades of antiviral therapy. *Cell Host Microbe* 31, 83-96 e85. 10.1016/j.chom.2022.12.002.
45. Jiang, C., Lian, X., Gao, C., Sun, X., Einkauf, K.B., Chevalier, J.M., Chen, S.M.Y., Hua, S., Rhee, B., Chang, K., et al. (2020). Distinct viral reservoirs in individuals with spontaneous control of HIV-1. *Nature* 585, 261-267. 10.1038/s41586-020-2651-8.
46. Lian, X., Gao, C., Sun, X., Jiang, C., Einkauf, K.B., Seiger, K.W., Chevalier, J.M., Yuki, Y., Martin, M., Hoh, R., et al. (2021). Signatures of immune selection in intact and defective proviruses distinguish HIV-1 elite controllers. *Sci Transl Med* 13, eabl4097. 10.1126/scitranslmed.abl4097.

47. Elsheikh, M.M., Tang, Y., Li, D., and Jiang, G. (2019). Deep latency: A new insight into a functional HIV cure. *EBioMedicine* 45, 624-629. 10.1016/j.ebiom.2019.06.020.
48. Alshafi, N., Ding, S., Richard, J., Markle, T., Brassard, N., Walker, B., Lewis, G.K., Kaufmann, D.E., Brockman, M.A., and Finzi, A. (2015). Nef Proteins from HIV-1 Elite Controllers Are Inefficient at Preventing Antibody-Dependent Cellular Cytotoxicity. *J Virol* 90, 2993-3002. 10.1128/JVI.02973-15.
49. Alshafi, N., Richard, J., Prevost, J., Coutu, M., Brassard, N., Parsons, M.S., Kaufmann, D.E., Brockman, M., and Finzi, A. (2017). Impaired Downregulation of NKG2D Ligands by Nef Proteins from Elite Controllers Sensitizes HIV-1-Infected Cells to Antibody-Dependent Cellular Cytotoxicity. *J Virol* 91. 10.1128/JVI.00109-17.
50. Anderson, E.M., Simonetti, F.R., Gorelick, R.J., Hill, S., Gouzoulis, M.A., Bell, J., Rehm, C., Perez, L., Boritz, E., Wu, X., et al. (2020). Dynamic Shifts in the HIV Proviral Landscape During Long Term Combination Antiretroviral Therapy: Implications for Persistence and Control of HIV Infections. *Viruses* 12. 10.3390/v12020136.
51. Lambotte, O., Boufassa, F., Madec, Y., Nguyen, A., Goujard, C., Meyer, L., Rouzioux, C., Venet, A., Delfraissy, J.F., and Group, S.-H.S. (2005). HIV controllers: a homogeneous group of HIV-1-infected patients with spontaneous control of viral replication. *Clin Infect Dis* 41, 1053-1056. 10.1086/433188.
52. Hubert, J.B., Burgard, M., Dussaix, E., Tamalet, C., Deveau, C., Le Chenadec, J., Chaix, M.L., Marchadier, E., Vilde, J.L., Delfraissy, J.F., et al. (2000). Natural history of serum HIV-1 RNA levels in 330 patients with a known date of infection. The SEROCO Study Group. *AIDS* 14, 123-131. 10.1097/00002030-200001280-00007.
53. Vandergeeten, C., Fromentin, R., Merlini, E., Lawani, M.B., DaFonseca, S., Bakeman, W., McNulty, A., Ramgopal, M., Michael, N., Kim, J.H., et al. (2014). Cross-clade ultrasensitive PCR-based assays to measure HIV persistence in large-cohort studies. *J Virol* 88, 12385-12396. 10.1128/JVI.00609-14.
54. Tolbert, W.D., Gohain, N., Veillette, M., Chapleau, J.P., Orlandi, C., Visciano, M.L., Ebadi, M., DeVico, A.L., Fouts, T.R., Finzi, A., et al. (2016). Paring Down HIV Env: Design and Crystal Structure of a Stabilized Inner Domain of HIV-1 gp120 Displaying a Major ADCC Target of the A32 Region. *Structure* 24, 697-709. 10.1016/j.str.2016.03.005.

 Uninfected Donors (UD)
  Chronic Progressors (CP)
  ART-treated individuals (ART)
  Elite Controllers (EC)

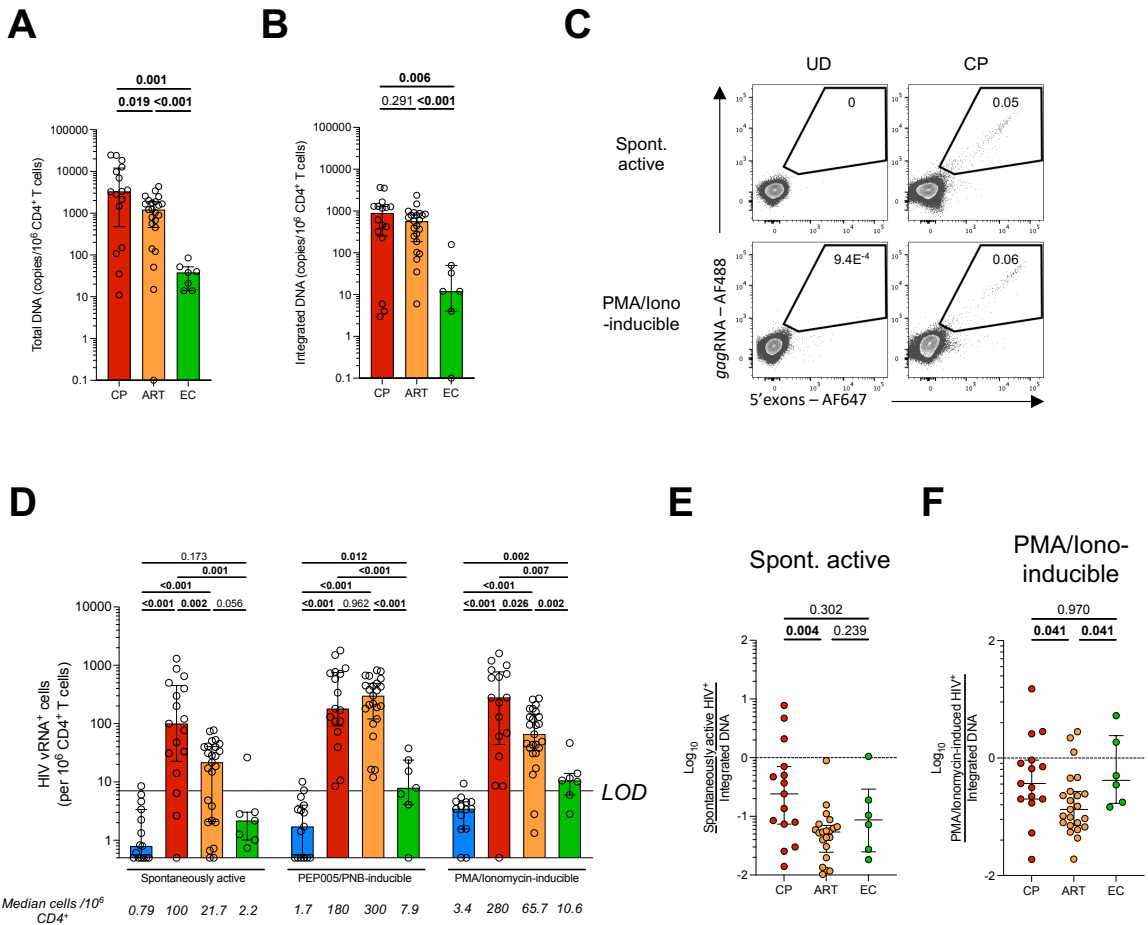
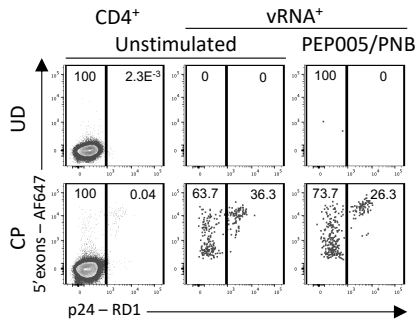


Figure 1. Reactivation induces vRNA expression in Elite Controllers

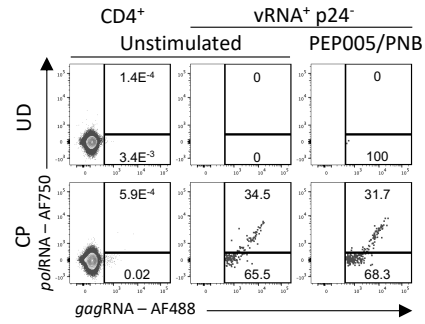
Uninfected (UD) are represented in blue, Chronic Progressors (CP) in red, ART-treated (ART) in orange, and Elite Controllers (EC) in green. (A) Quantification of total and (B) integrated DNA. (C) Gating strategy identifying vRNA⁺ cells in CP (right) either in unstimulated condition (top) or following reactivation (bottom). UD serve as a control for specificity. (D) Total quantifications of vRNA⁺ cells in all 4 groups. Numbers below indicate the median cells per million CD4⁺ T cells. Limit of detection (LOD) is set at 7 vRNA⁺ cells based on the median detection in UD + 2xSD. (E-F) Transcriptional activity of the (E) spontaneously active and (F) PMA/Ionomycin-inducible vRNA⁺ cells. The transcriptional activity is calculated as the log₁₀ transformation of the ratio between vRNA⁺ cells and the integrated DNA. (A-B; D-F) Statistical tests shown are Mann-Whitney for cohort comparisons. N=15 UD, n=17 CP, n=25 ART, and n=7 EC. The histograms indicate the median, and the error bars illustrate the interquartile range



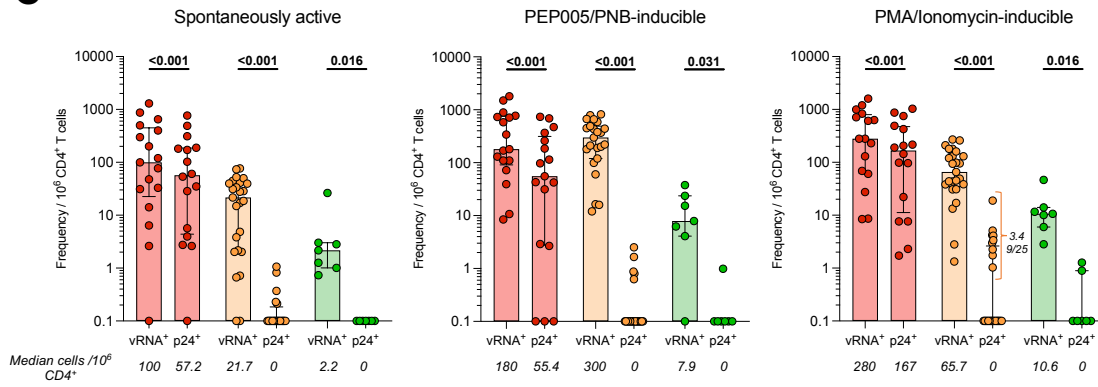
A



B



C



D

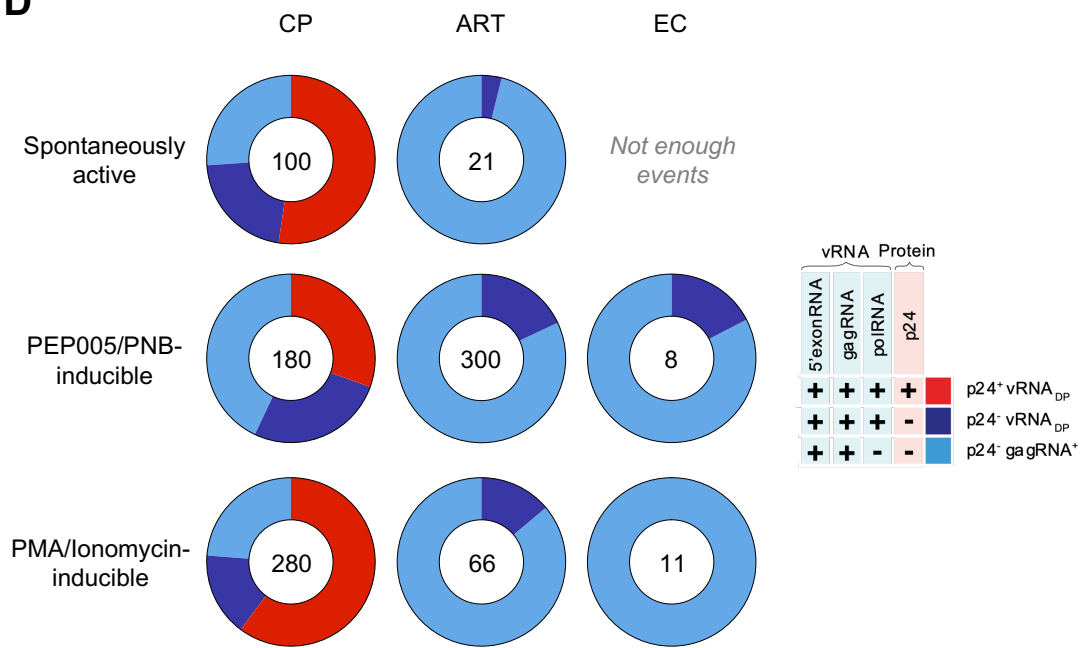


Figure 2. vRNA-expressing cells in EC are phenotypically similar to those in ART-treated individuals

(A-B) Gating strategy to assess: (A) p24 expression in vRNA⁺ cells, and (B) *gag*RNA and *pol*RNA co-expression in p24⁻ vRNA⁺ cells. (C) Compared frequencies of spontaneous (left), PEP005/PNB-inducible (middle), and PMA/Ionomycin-inducible (right) vRNA⁺ and p24⁺ cells. The medians are written below the histograms. The median of the 9 participants in which p24 was detected following PMA/Ionomycin stimulation is shown. The bars indicate the median, and the error bars illustrate the interquartile range. Results from Wilcoxon tests are shown above. for cohort comparisons (D) Donut charts presenting the median proportions of each vRNA⁺ subpopulations for spontaneous, PEP005/PNB-, or PMA/ionomycin-induced reservoirs. Numbers in the donut holes represent the median vRNA⁺ per 10⁶ CD4⁺ T cells. Legend of the vRNA⁺ populations is on the right. (C) N=17 CP, n=25 ART, and n=7 EC. (D) N=16 CP, n=25 ART, and n=5 EC as some donors did not reach at least 5 vRNA⁺ cells for phenotyping.

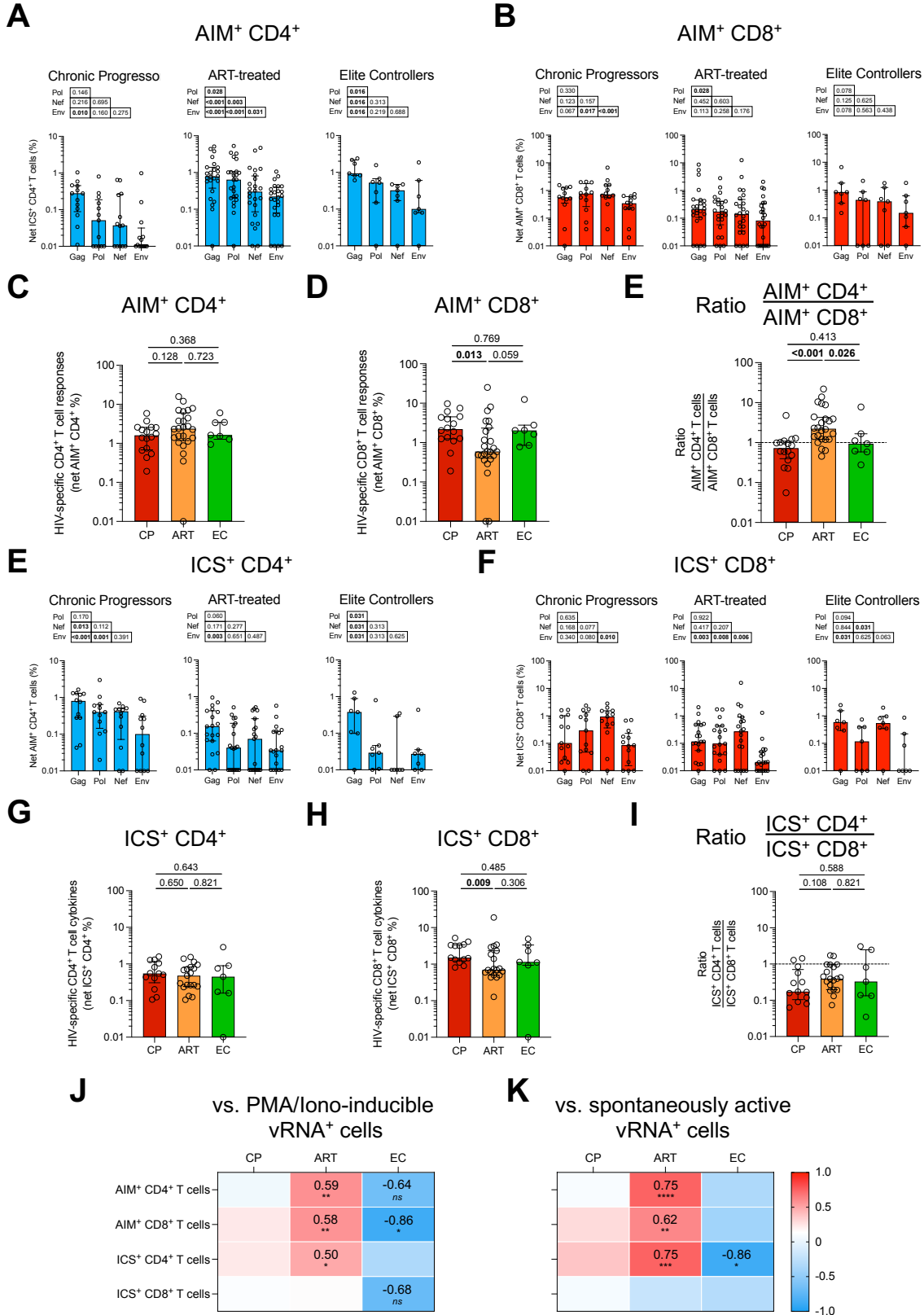


Figure 3. High levels of T cell responses and functions in EC are associated with fewer vRNA-expressing cells

Net magnitude of specific (A) CD4⁺ and (B) CD8⁺ T cell responses by AIM assay. Comparison of the total HIV-specific (C) CD4⁺ and (D) CD8⁺ T cell responses between the 3 groups. (E) Ratio of HIV-specific CD4⁺ T cell and CD8⁺ T cell responses between 3 groups. Net magnitude of specific (E) CD4⁺ and (F) CD8⁺ T cell functions by ICS assay. Comparison of the total HIV-specific (G) CD4⁺ and (H) CD8⁺ T cell functions between the 3 groups. (I) Ratio of HIV-specific CD4⁺ T cell and CD8⁺ T cell functions between 3 groups. Heat map reporting associations between (J) PMA/Ionomycin inducible and (K) spontaneously active vRNA⁺ cells and HIV-specific T cell responses and functions. (A,B,E,F) Peptide pools used to stimulate PMBCs are indicated. (C-E,G-I, J,K) "HIV" responses were inferred by the sum of Gag, Pol, Env, and Nef net responses. The bars indicate the median, and the error bars illustrate the interquartile range. In (A,B,E,F) the results from Wilcoxon tests are shown above the histograms. In (C-E,G-I) the results from Mann-Whitney tests are shown above the histograms. In (J-K) R and ρ (Spearman) values are shown. * $p < 0.05$, ** $p < 0.01$, *** $p < 0.001$. (A-I) N=17 CP, n=25 ART, and n=7 EC. (J-K) N=16 CP, n=25 ART, and n=5 EC as some donors did not reach at least 5 vRNA⁺ cells for phenotyping.

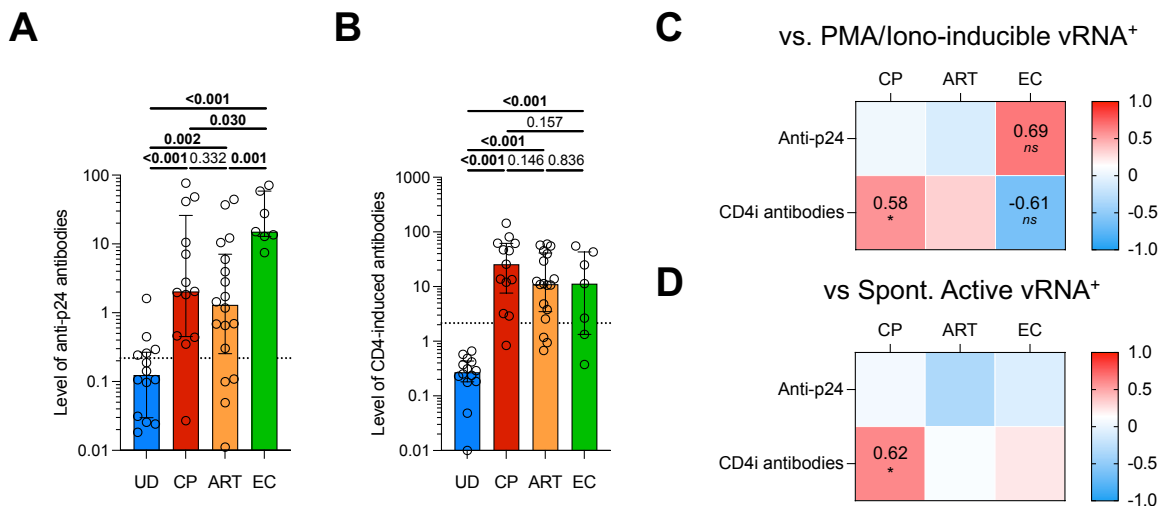


Figure 4. CD4-induced antibodies are associated with high levels of viral reservoirs in CP but with lower inducible vRNA-expressing cells in EC

Levels of (A) anti-p24 antibodies and (B) CD4-induced antibodies in UD, CP, ART, and EC. The bars indicate the median, and the error bars illustrate the interquartile range. The results from Mann-Whitney tests are shown above the histograms. Heat map reporting associations between (C) PMA/Ionomycin inducible and (D) spontaneously active vRNA⁺ cells and anti-p24 and CD4-induced antibodies. R and p (Spearman) values are shown. * p < 0.05, ** p < 0.01, *** p < 0.001. N=17 CP, n= 25 ART, and n= 7 EC.

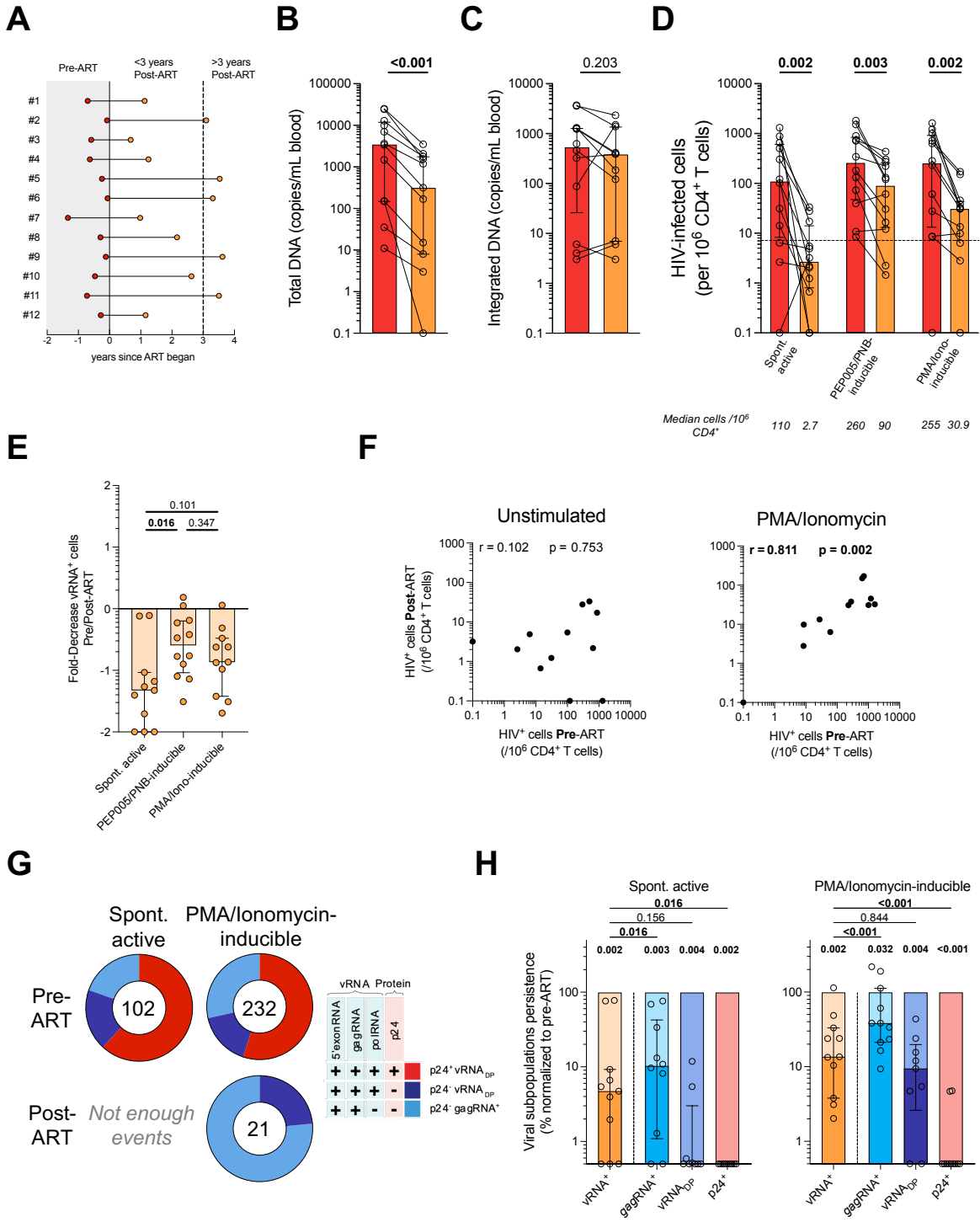


Figure 5. The decline in vRNA-expressing cells is more severe in translation-competent cells following ART initiation

(A) Schematic representing longitudinal pre-post ART individuals. Pre-ART are represented in red while post-ART individuals are in orange. Dashed line represents 3 years of treatment, considered for stable reservoirs. Comparison of (B) total and (C) integrated DNA. (D) Comparison of spontaneous, and inducible vRNA+ cells between pre- and post-ART treatment. (B-D) The results from Wilcoxon tests are shown above the histograms. (E) Fold-decrease of vRNA+ cells following ART initiation. The results from Man-Whitney tests between stimulations are shown above the histograms. (F) Correlations between the spontaneously active vRNA+ cells Pre-ART and Post-ART (left), and between the PMA/Ionomycin-inducible vRNA+ cells Pre-ART and Post-ART (right). R and p (Spearman) values are shown. (G) Donut charts presenting the median proportions of each vRNA+ subpopulations for spontaneous, and PMA/ionomycin-induced reservoirs. Numbers in the donut holes represent the median vRNA+ per 10⁶ CD4+ T cells. Legend of the vRNA+ populations is on the right (H) Frequency of residual spontaneously active (left) and PMA/Ionomycin-inducible (right) viral reservoirs after ART normalized to the infected cell before treatment. The light boxes represent 100% of the viral population pre-ART. Dark colors represent the frequency of residual population post-ART. The results from Wilcoxon tests between viral subpopulations and parental vRNA+ cells are shown above the lines. The results from Wilcoxon tests for the decline are shown above the histograms. (B-H) n=12.

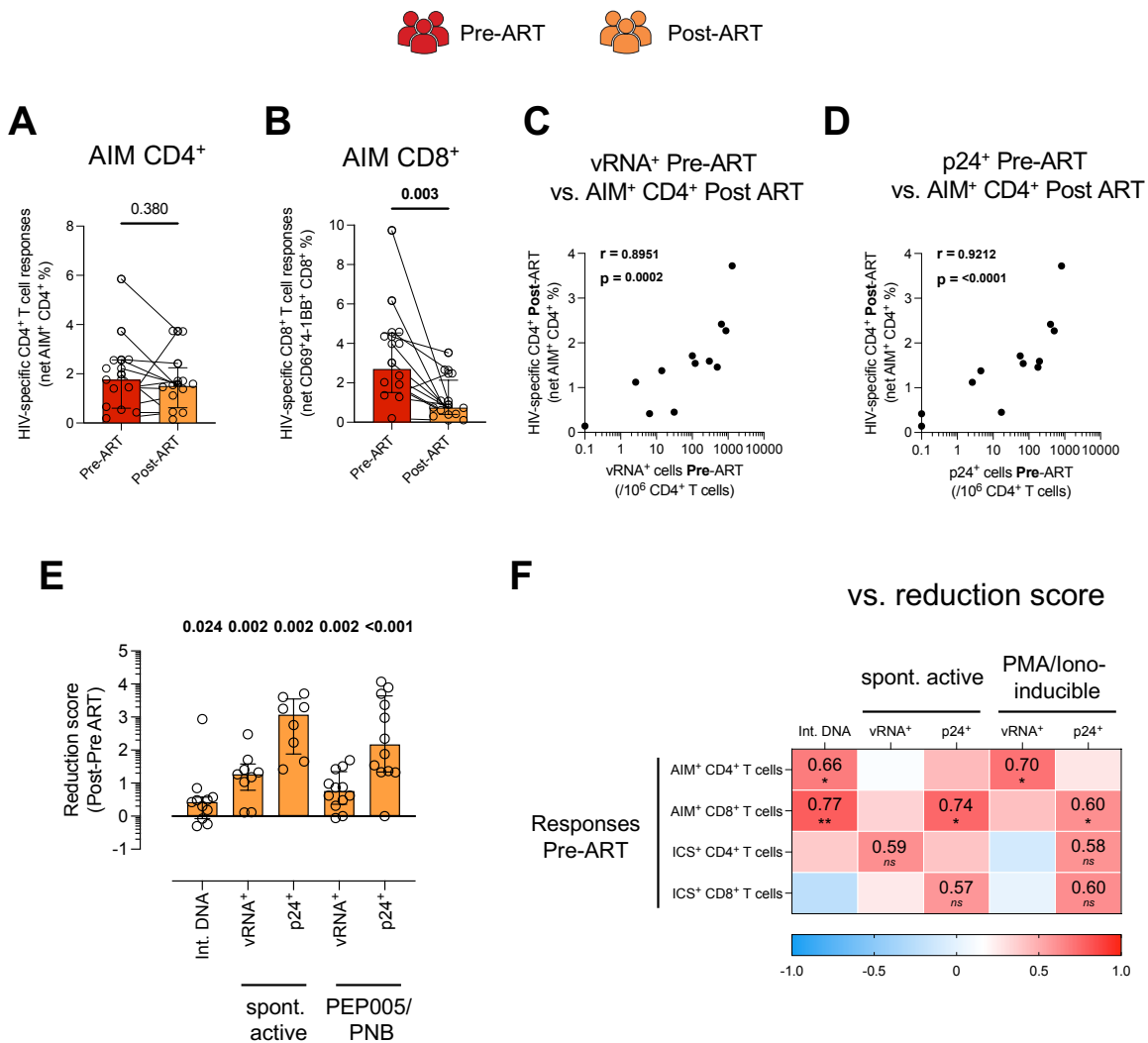
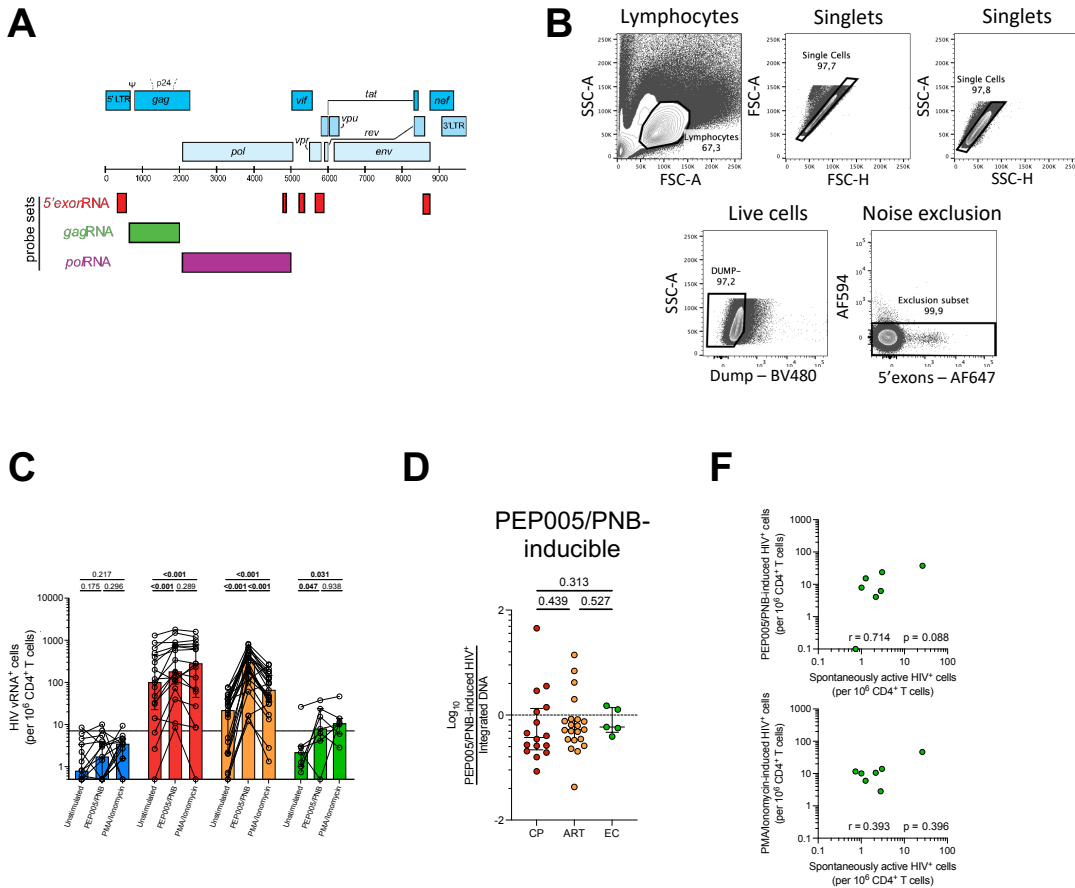
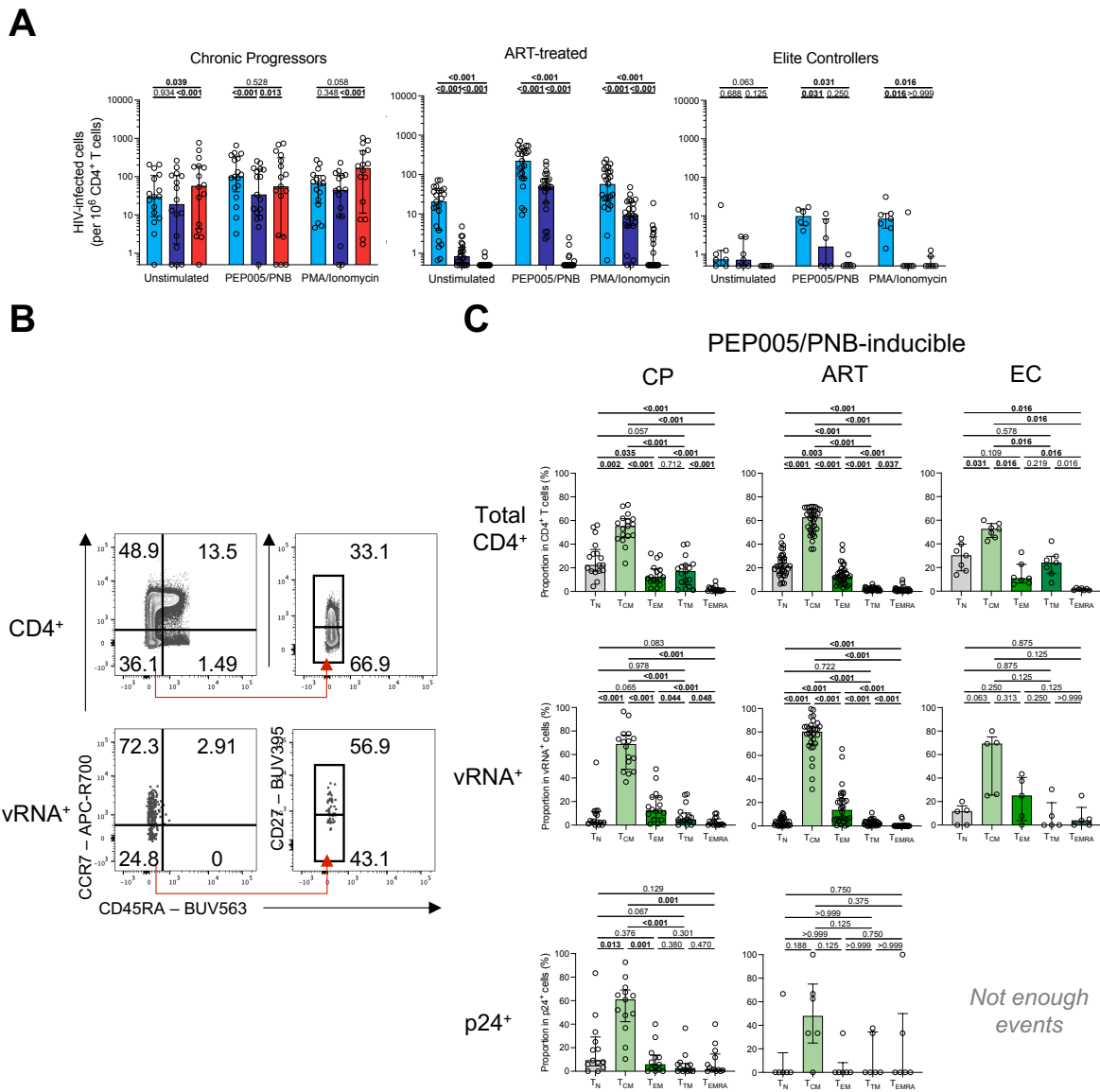


Figure 6. vRNA-expressing cells are maintained after ART irrespective of immune responses elicited before ART

Net magnitude of HIV-specific (A) CD4⁺ and (B) CD8⁺ T cell responses by AIM assay. (C) Correlations between the spontaneously active vRNA⁺ cells Pre-ART and the HIV-specific CD4⁺ T cell responses Post-ART. (D) Correlations between the spontaneously active p24⁺ cells Pre-ART and the HIV-specific CD4⁺ T cell responses Post-ART. (E) Reduction score of the different viral features. This score represents the fold decrease of each viral components analyzed post-ART compared to pre-ART samples. (F) Heat map reporting associations between the reduction score and the HIV-specific T cell responses and functions pre-ART. (A,B,E) The results from Wilcoxon tests are shown above the histograms. (C,D,F) R and p (Spearman) values are shown. (F) * p < 0.05, ** p < 0.01, *** p < 0.001. (A-F) n=12

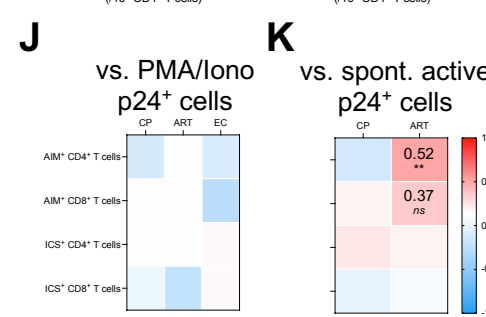
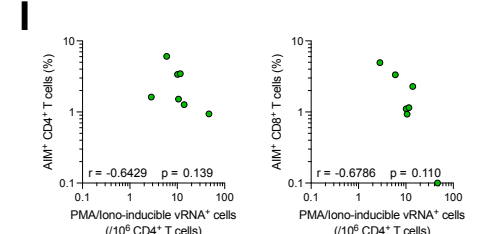
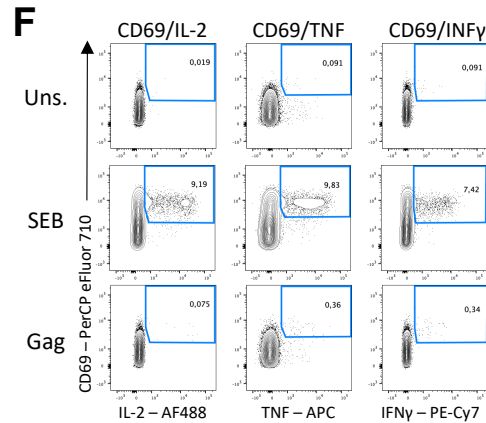
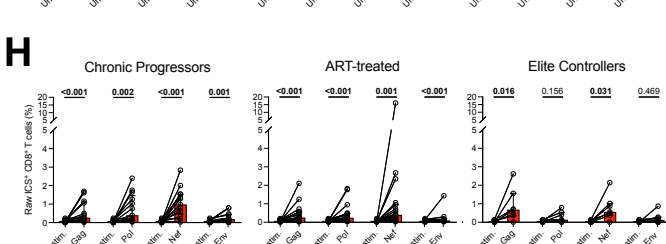
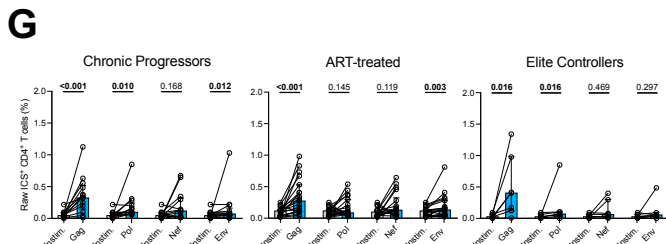
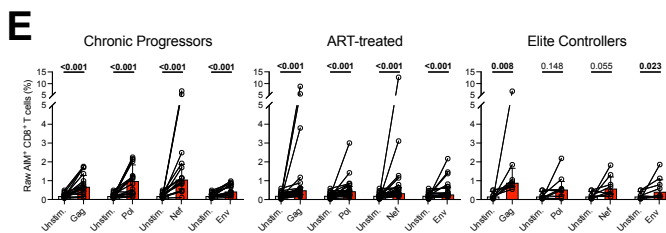
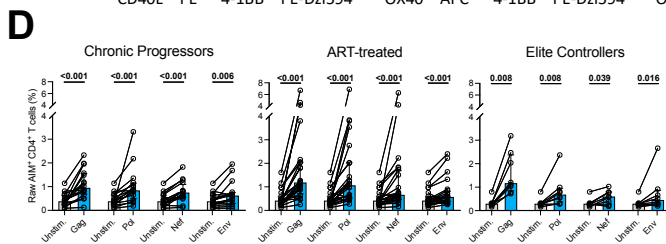
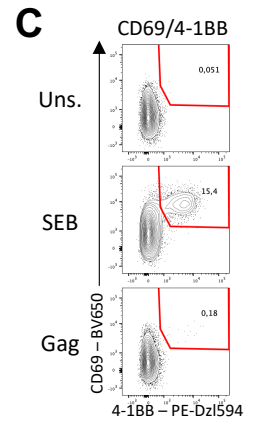
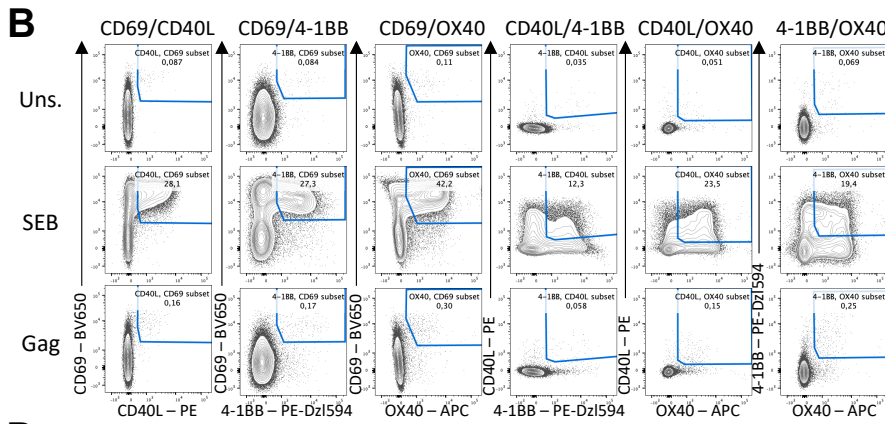
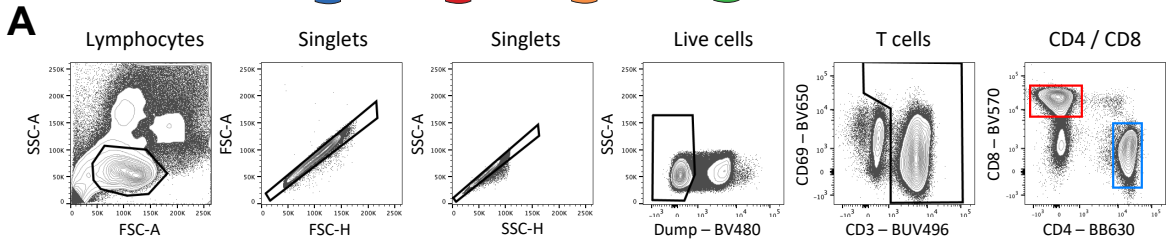


Supplemental Figure 1. **Detection of vRNA expression in CD4+ T cells. Related to Figure 1** (A) vRNA probe set designs. (B) Gating strategy identifying vRNA+ cells. (C) Total vRNA+ cells detection in UD (blue), CP (red), ART (orange), and EC (green). The histograms indicate the median, and the error bars illustrate the interquartile range. Statistical tests shown are Wilcoxon for stimulation comparisons. (D) Transcriptional activity of the PEP005/PNB-inducible vRNA+ cells. The results from Mann-Whitney tests are shown above the histograms. (E) Correlations between spontaneously active and PEP005/PNB inducible (top) or PMA/Ionomycin (bottom) vRNA+ cells in EC. R and p (Spearman) values are shown. (C-E) n=15 UD, n=17 CP, n=25 ART, and n=7 EC.



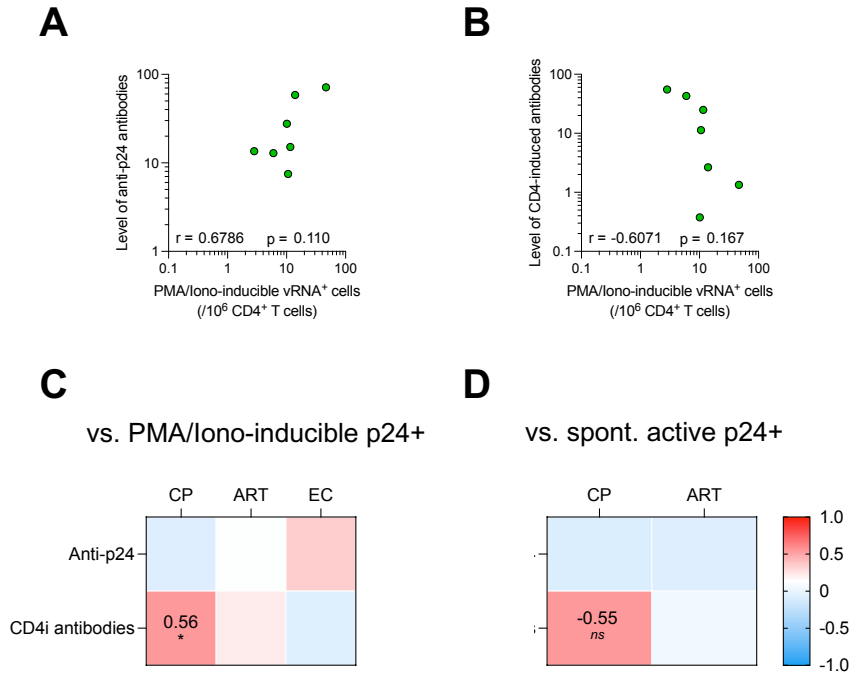
Supplemental Figure 2. Phenotypic characterization of the vRNA-expressing cells. Related to Figure 2

(A) The histograms report the proportions of each vRNA⁺ subpopulations for CP (left), ART-treated (middle), and EC (right) supporting Figure 2D. The bars represent median values. The results from Wilcoxon tests are shown above the histograms. (B) Representative gating strategy for memory phenotype. (C) Complete representation of the memory phenotype in total CD4⁺ T cells (top), vRNA⁺ cells (center), and p24⁺ cells (bottom) in CP (left), ART (middle), and EC (right). The results from Wilcoxon tests are shown above the histograms. (A) n=17 CP, n=25 ART, and n=7 EC. (C) N=16 CP, n=25 ART, and n=5 EC as some donors did not reach at least 5 vRNA⁺ cells for phenotyping.



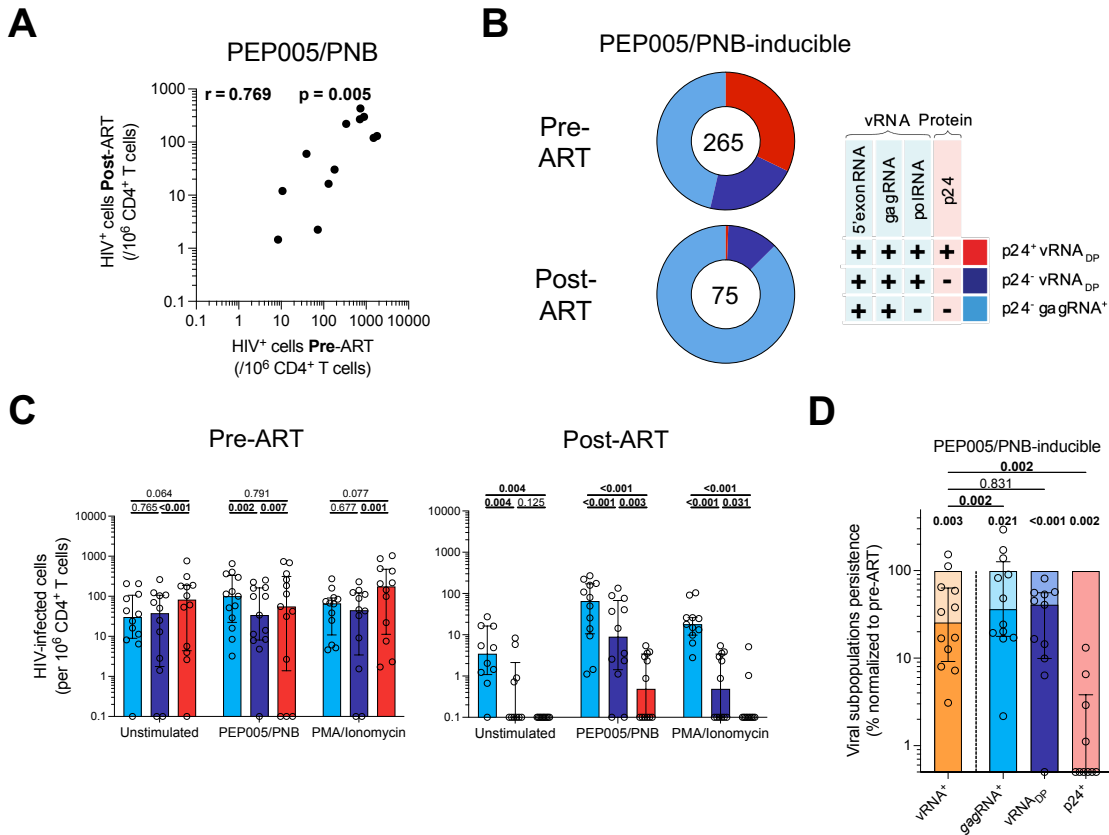
Supplemental Figure 3. **AIM and ICS assays. Related to Figure 3**

Representative gating strategy for AIM and ICS assays. (B) Representative gating of each AIM pair used for the ORgate analysis of Gag-specific CD4+ T cell responses. The same gating was applied for Pol, Nef, and Env-specific CD4+ T cells. (C) Representative gating of CD69+/-1BB+ for Gag-specific CD8+ T cell responses. The same gating was applied for Pol, Nef, and Env-specific CD4+ T cells. (D) Raw CD4+ and (E) raw CD8+ T cell responses, comparing the unstimulated vs. peptide-stimulated conditions. The bars indicate the median, and the error bars indicate the interquartile range. The results from Wilcoxon tests are shown above the histograms. (F) Representative gating of each cytokine used for the ORgate analysis of Gag-specific CD4+ T cell responses. The same gating was applied for Pol, Nef, and Env-specific CD4+ T cells and specific CD8+ T cells. (G) Raw CD4+ and (H) raw CD8+ T cell responses, comparing the unstimulated vs. peptide-stimulated conditions. The bars indicate the median, and the error bars indicate the interquartile range. The results from Wilcoxon tests are shown above the histograms. (I) Correlations between PMA/Ionomycin-inducible vRNA+ cells and HIV-specific CD4+ (left) and CD8+ (right) T cells. R and p (Spearman) values are shown. Heat map reporting associations between (J) PMA/Ionomycin inducible and (K) spontaneously active p24+ cells and HIV-specific T cell responses and functions. R and p (Spearman) values are shown. * p < 0.05, ** p < 0.01, *** p < 0.001. N=17 CP, (J) N=17 CP, n=25 ART, and n=7 EC. (K) EC are not represented as the correlation is null because no spontaneously active p24+ are detected.



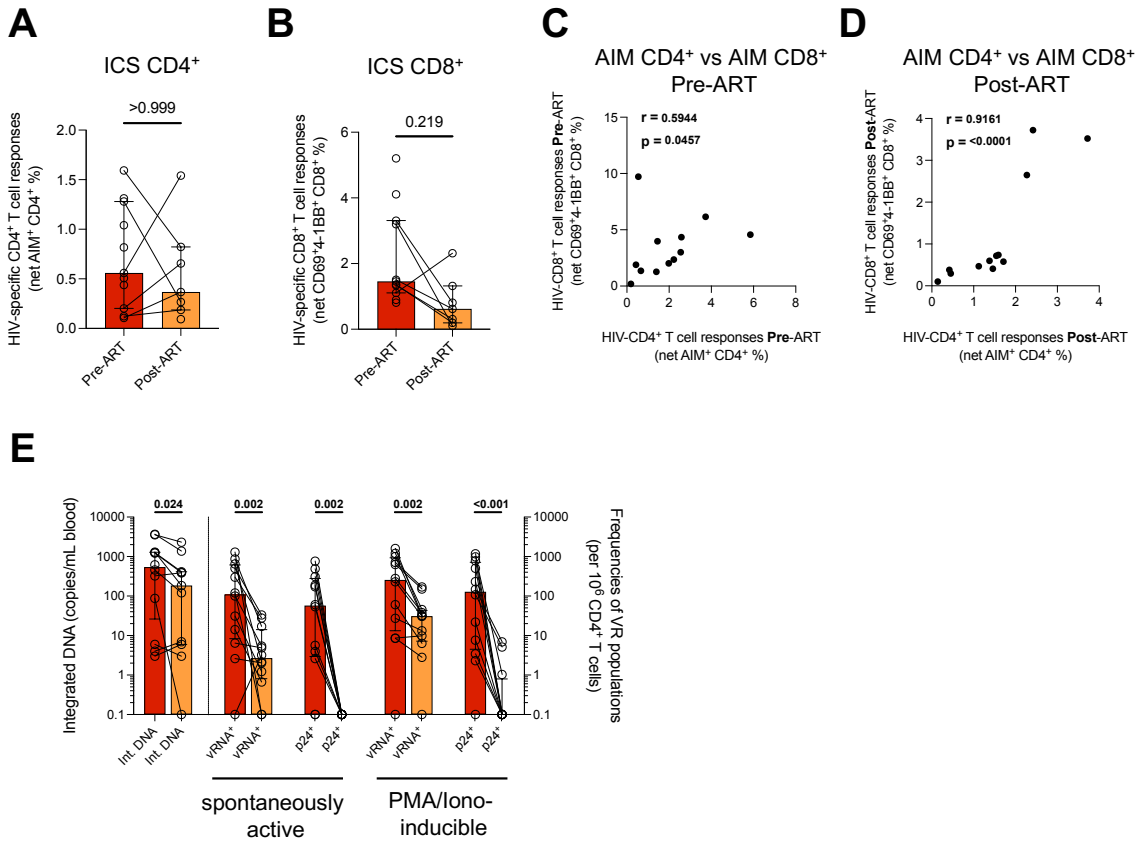
Supplemental Figure 4. Antibody correlations. Related to Figure 4

Correlations of PMA/Ionomycin vRNA⁺ cells in EC with (A) anti-p24 antibodies and (B) CD4-induced antibodies. R and p (Spearman) values are shown. Heat map reporting associations between (C) PMA/Ionomycin inducible and (D) spontaneously active p24⁺ cells and anti-p24 and CD4-induced antibodies. R and p (Spearman) values are shown. * $p < 0.05$, ** $p < 0.01$, *** $p < 0.001$. N=17 CP, n= 25 ART, and n= 7 EC. (D) EC are not represented as the correlation is null because no spontaneously active p24⁺ are detected.



Supplemental Figure 5. Characterization of the vRNA subpopulations in Pre/Post-ART individuals. Related to Figure 5

(A) Correlations between PEP005/PNB-inducible vRNA⁺ cells pre-ART vs. post-ART. R and p (Spearman) values are shown. (B) Donut charts presenting the median proportions of each vRNA⁺ subpopulations for PEP005/PNB-induced reservoirs. Numbers in the donut holes represent the median vRNA⁺ per 10⁶ CD4⁺ T cells. Legend of the vRNA⁺ populations is on the right. (C) The histograms report the proportions of each vRNA⁺ subpopulations for Pre-ART (left) and Post-ART (right) supporting Figure 5G and S5B. The bars represent median values. The results from Wilcoxon tests are shown above the histograms. (D) Frequency of residual PEP005/PNB-inducible viral reservoirs after ART normalized to the infected cell before treatment. The light boxes represent 100% of the viral population pre-ART. Dark colors represent the frequency of residual population post-ART. The results from Wilcoxon tests between viral subpopulations and parental vRNA⁺ cells are shown above the lines. The results from Wilcoxon tests for the decline are shown above the histograms. (A-D) n=12.



Supplemental Figure 6. **Immune and viral features in Pre/Post-ART individuals. Related to Figure 6**

Net magnitude of HIV-specific (A) CD4⁺ and (B) CD8⁺ T cell functions by ICS assay. The results from Wilcoxon tests are shown above the histograms. (C) Correlations between the HIV-specific CD4⁺ and CD8⁺ T cell responses before and (D) after ART. R and p (Spearman) values are shown. (E) Viral features before and after ART treatment utilized to calculate the reduction score. The results from Wilcoxon tests are shown above the histograms. (A-E) n=12.

Table S1. Clinical data for Uninfected (UD). Chronic Progressors (CP). Elite Controllers (EC). and Treated (ART) participants

Participant ID	Sex	Age (years)	VL (copies/mL)	Total DNA (copies/mL)	Int. DNA (copies/mL)	CD4 /CD8 Ratio	CD4 count (cells/ μ L)	Duration of infection (years)	Duration of ART (years)	
UD	UD1	F	41	NA	NA	NA	2.1	1196	NA	NA
	UD2	M	23	NA	NA	NA	2.29	465	NA	NA
	UD3	M	50	NA	NA	NA	4.13	1758	NA	NA
	UD4	M	64	NA	NA	NA	1.78	552	NA	NA
	UD5	M	51	NA	NA	NA	2.18	532	NA	NA
	UD6	F	39	NA	NA	NA	2.05	667	NA	NA
	UD7	M	66	NA	NA	NA	2.43	701	NA	NA
	UD8	M	59	NA	NA	NA	2.40	530	NA	NA
	UD9	F	41	NA	NA	NA	3.93	1273	NA	NA
	UD10	F	60	NA	NA	NA	1.46	670	NA	NA
	UD11	F	45	NA	NA	NA	2.31	632	NA	NA
	UD12	M	57	NA	NA	NA	1.95	726	NA	NA
	UD13	F	38	NA	NA	NA	1.65	529	NA	NA
	UD14	M	63	NA	NA	NA	3.50	675	NA	NA
	UD15	M	65	NA	NA	NA	2.61	310	NA	NA
CP	CP1	M	26	2700	11	6	1.11	597	5.6	NA
	CP2	F	23	7095	2135	230	0.27	172	23.9	NA
	CP3	M	55	3834	3316	894	0.3	184	22.9	NA
	CP4	M	38	7000	108	1169	1.63	962	0.1	NA
	CP5	M	47	39489	35	4	0.96	492	8.5	NA
	CP6	M	49	44848	12738	3664	0.36	281	7.3	NA
	CP7	M	25	9871	2836	1300	0.37	371	1.5	NA
	CP8	F	37	36715	1466	323	0.59	321	0.2	NA
	CP9	M	50	79043	18446	1658	0.23	383	12.4	NA
	CP10	M	51	96873	6933	1226	0.12	216	13.4	NA
	CP11	M	42	105130	3605	1256	0.45	320	23.8	NA
	CP12	M	40	6678	3353	458	0.75	571	0.2	NA
	CP13	M	22	35859	24210	1300	0.31	597	0.1	NA
	CP14	M	34	1000000	9876	619	0.07	300	1.1	NA
	CP15	M	54	22959	3279	423	0.33	434	11.6	NA
	CP16	M	38	6235	149	3	0.89	1036	0.4	NA
	CP17	M	38	132886	24641	3545	0.23	320	0.4	NA
EC	EC1	F	38	< 40	14	4	1.17	375	3.7	NA
	EC2	M	46	<40	40	0.1	0.7	591	10.4	NA
	EC3	M	62	< 40	38	12	0.96	695	22.4	NA
	EC4	F	52	< 40	85	50	1.01	500	18.9	NA
	EC5	F	47	< 40	52	12	2.73	744	16.4	NA
	EC6	M	33	< 40	21	158	0.47	642	6.5	NA
	EC7	M	59	< 20	14	33	1.12	663	19.6	NA
ART	ART1	M	42	<40	0.1	1481	2.3	509	3.3	3.1
	ART2	M	54	<40	1760	391	0.4	448	16.7	3.3
	ART3	F	37	<40	140	252	1.3	579	4	3.5
	ART4	M	42	<40	15	6	1.34	876	4.7	3.5
	ART5	M	26	<40	1552	185	1.34	871	3.9	3.6
	ART6	M	48	<40	3431	912	0.37	531	16	5.4
	ART7	M	63	< 40	1889	796	0.52	782	10.3	6.1
	ART8	M	57	<40	2489	849	0.43	786	20.5	6.5
	ART9	M	58	<40	454	284	1.12	619	9.9	7
	ART10	M	58	<40	1681	701	0.40	671	21.4	7.4
	ART11	M	56	<40	670	444	1.34	677	10.9	9.5

ART12	M	19	<40	121	70	1.01	708	19.6	10
ART13	M	50	<40	2564	884	0.60	1110	11.3	10.8
ART14	M	51	<40	797	610	1.63	941	26	10.8
ART15	M	46	<40	1666	789	0.74	503	17.3	13.8
ART16	M	55	74	564	103	0.31	398	16	15.8
ART17	M	55	<40	2704	1424	0.58	568	23.3	16.8
ART18	M	52	<40	898	368	0.22	271	20.2	18.1
ART19	M	57	<40	1213	95	0.43	431	18.4	18.3
ART20	M	55	<40	4365	2371	0.47	557	24.3	19.3
ART21	M	59	<40	1027	570	2.12	843	24.3	19.9
ART22	M	58	<40	1230	590	1.02	544	21.4	20.3
ART23	M	60	<40	1246	783	0.3	249	25.8	21.9
ART24	M	58	<40	2020	997	0.4	474	30.8	26.9
ART25	M	55	<40	51	35	0.55	411	31.2	28.5

UD: Uninfected Donor; CP: Chronic Progressor; EC: Elite Controllers; ART: ART-treated Individuals
F: Female; M: Male; VL: Viral load; Int.DNA: Integrated DNA; NA: Not Applicable

Table S2. Flow Cytometry panel for detection of HIV-1 vRNA⁺ cells by RNAflow-FISH related to Figures 1. 2. 4 and 5.

Target	Fluorochrome	Clone	Supplier	Detection	Catalogue n°	Volume per test (µL)
CD27	BUV395	L128	BD	Surface	563815	1
CD3	BUV496	UCHT1	BD	Surface	612941	4
CD45RA	BUV563	HI100	BD	Surface	741411	0.5
CD4	BB630	SK3	BD	Surface	CUSTOM	0.5
CCR7	APC-R700	2-L1-A	BD	Surface	566767	2
CD8	BV480	RPA-T8	BD	Surface	566121	0.5
CD14	BV480	M5E2	BD	Surface	746304	1
CD16	BV480	3G8	BD	Surface	566108	1
CD19	BV480	H1B19	BD	Surface	746457	0.5
CD56	BV480	NCM16.2	BD	Surface	566124	0.5
Fixable Viability Dye	eFluor 506	-	ThermoFisher	Surface	65-0866-14	0.1
HIV core antigen	RD1	KC57	Beckman Coulter	Intracellular	6604667	2
HIV-1 5'exonRNA	Alexa Fluor 647	-	ThermoFisher	Intracellular	VF1-6000978	5
HIV-1 gagRNA	Alexa Fluor 750	-	ThermoFisher	Intracellular	VF6-6000975	5
HIV-1 nefRNA	Alexa Fluor 488	-	ThermoFisher	Intracellular	VF4-6000647	5

Table S3. Flow Cytometry panel for detection of HIV-specific T cell responses by Activation Induced Markers (AIM) assays related to Figures 3 and 6.

Target	Fluorochrome	Clone	Supplier	Detection	Catalogue n°	Volume per test (µL)
CD3	BUV496	UCHT1	BD	Surface	612941	4
CD8	BV570	RPA-T8	BioLegend	Surface	301037	1
CD69	BV650	FN50	BioLegend	Surface	310934	2
CD4	BB630	SK3	BD	Surface	CUSTOM	0.5
CD40L	PE	TRAP1	BD	Surface	555700	5
4-1BB	PE-Dazzle 594	4B4-1	BioLegend	Surface	309826	2
OX40	APC	ACT35	BD	Surface	56473	2
Aquavid	-	-	Invitrogen	Surface	L34966	0.5
CD14	BV480	M5E2	BD	Surface	746304	1
CD16	BV480	3G8	BD	Surface	566108	1
CD19	BV480	H1B19	BD	Surface	746457	0.5
CD56	BV480	NCM16.2	BD	Surface	566124	0.5

Table S4. Flow Cytometry panel for detection of HIV-specific T cell functions by Intracellular Cytokines Staining (ICS) assays related to Figures 3 and 6.

Target	Fluorochrome	Clone	Supplier	Detection	Catalogue n°	Volume per test (µL)
CD3	BV605	OKT3	BioLegend	Surface	317322	1.5
CD4	BV650	OKT4	BioLegend	Surface	317435	2
CD8	APC-eFluor 780	SK1	eBioScience	Surface	47-0087-42	1
IL-2	Alexa Fluor 488	MQ1-17H12	BioLegend	Intracellular	500314	5
IFN γ	PE-Cy7	IA6-2	BD	Intracellular	561314	4
TNF	APC	Mab11	BD	Intracellular	562084	1.5
CD69	PerCP-eFluor710	FN50	eBioScience	Intracellular	46-0699-42	4
Aquavid	-	-	Invitrogen	Surface	L34966	0.5
CD14	V500	M5E2	BD	Surface	561391	1
CD19	V500	H1B19	BD	Surface	561121	1

Table S5. Clinical data for Pre-ART and Post-ART participants

	Participant ID	Sex	Age (years)	VL (copies/mL)	Total DNA (copies/mL)	Int. DNA (copies/mL)	CD4 /CD8 Ratio	CD4 count (cells/ μ L)	Duration of infection (years)	Duration of ART (years)
P r e - A R T	#1	M	26	2700	11	6	1.11	597	5.6	NA
	#2	M	38	7000	108	1169	1.63	962	0.1	NA
	#3	M	47	39489	35	4	0.96	492	8.5	NA
	#4	M	49	44848	12738	3664	0.36	281	7.3	NA
	#5	F	37	36715	1466	323	0.59	321	0.2	NA
	#6	M	51	96873	6933	1226	0.12	216	13.4	NA
	#7	M	42	105130	3605	1256	0.45	320	23.8	NA
	#8	M	40	6678	3353	458	0.75	571	0.2	NA
	#9	M	22	35859	24210	1300	0.31	597	0.1	NA
	#10	M	34	1000000	9876	619	0.07	300	1.1	NA
	#11	M	38	6235	149	3	0.89	1036	0.4	NA
	#12	M	38	132886	24641	3545	0.23	320	0.4	NA
P o s t - A R T	#1	M	28	<40	3	3	1.19	694	7.4	1.1
	#2	M	42	<40	0.1	1481	2.3	509	3.3	3.1
	#3	M	48	<40	8	7	1.72	640	9.8	0.7
	#4	M	50	<40	2062	1370	0.80	700	9.2	1.2
	#5	F	37	<40	140	252	1.3	579	4	3.5
	#6	M	54	<40	1760	391	0.4	448	16.7	3.3
	#7	M	43	<40	1179	411	0.61	482	24.9	1
	#8	M	42	<40	314	121	1.80	602	2.7	2.2
	#9	M	26	<40	1552	185	1.34	871	3.9	3.6
	#10	M	37	<40	1366	288	0.29	662	4.2	2.6
	#11	M	42	<40	15	6	1.34	876	4.7	3.5
	#12	M	40	<40	3488	2312	0.49	616	1.8	1.2

F: Female; M: Male; VL: Viral load; Int.DNA: Integrated DNA; NA: Not Applicable

Chapter 5 – Discussion

General conclusion

The viral reservoirs remain the principal barrier to cure the HIV infection. Despite the relatively low frequency of replication-competent cells, they are responsible for the viral rebound upon ART interruption [239]. However, these reservoirs account for only a small fraction of the total infected cells based on integrated DNA measurements [239]. While intact reservoir has been extensively studied [246, 261, 294], most integrated proviruses are defective [238, 246, 247, 261, 360] raising questions about their biological impact.

Here, we studied the inducible HIV reservoir in individuals treated or not with standard ART to better characterize viral heterogeneity and responsiveness to external stimuli (Manuscript 1). Additionally, we analyzed the relationship between the virus-specific T cell responses and the viral reservoir. We investigated how specific T cell responses emerging during HIV infection shape the viral reservoir profile (Manuscript 2).

In Manuscript 1, we examined a cohort of 16 ART-treated individuals recruited in Montreal to investigate the inducible viral reservoir. We compared the transcriptional, translational, genomic, and cellular profiles to a cohort of 11 untreated Chronic Progressors. To measure and characterize the reservoir cells in ART-treated individuals, we reactivated the latently infected cells using latency reversal agents. Using a multiplexed version of the RNAflow-FISH for single-cell mRNA detection via flow cytometry, we demonstrated distinct differences in the ability to produce p24 protein between vRNA-expressing cells from viremic individuals and those on ART. Additionally, we observed LRA-class-specific gene transcription and translation patterns. However, the majority of induced proviruses were defective, including those capable of viral translation. We also identified viral clones displaying diverse transcriptional, translational, and phenotypic patterns among individual

cells, suggesting the influence of cell-intrinsic factors on viral reservoir persistence and heterogeneity.

For Manuscript 2, we conducted a comprehensive study involving 25 ART-treated individuals and 24 untreated PLWHIV, including 17 Chronic Progressors and 7 Elite Controllers. Despite Elite Controllers being known for their viremia control, we detected inducible HIV-infected cells in their samples. Interestingly, the HIV-infected cells exhibited a transcriptional and translational profile similar to the viral reservoirs observed in ART-treated individuals, unlike Chronic Progressors. Although all three cohorts showed strong HIV-specific T cell responses, only those measured in Elite Controllers were associated with a reduced size of HIV-infected cells. To understand why the virus-specific T cells failed to clear the infected cells, we performed a focused analysis on Pre/Post-ART individuals. Our findings revealed that short abortive inducible transcripts detected during ART were already present prior to treatment initiation, and these reservoirs were not associated with the HIV-specific T cells that emerged during the infection, suggesting that these cells are less recognizable by the immune system, in contrast to p24-expressing cells.

Together, our findings emphasize the complex nature of viral reservoirs and the challenges they pose in achieving a cure for HIV. Firstly, they highlight the fact that viral transcription does not necessarily equate to antigen expression which is considered as a marker of efficient latency reversal. Our results also demonstrate that these short abortive transcripts, despite being replication-incompetent, respond to stimuli, but may also be detected in the absence of stimulation in ART-treated individuals. Furthermore, they suggest that the persistence of these cells may involve additional mechanisms beyond

HIV transcriptional silencing, including resistance to cell death. Future studies will be necessary to decipher whether the expression of these short abortive transcripts leads to immune dysfunction and exhaustion associated with HIV pathogenesis even in virally suppressed individuals. Indeed, these defective transcripts may drive sensing mechanisms activating IFN signaling and the production of inflammatory cytokines contributing to systemic inflammation [192, 244, 248].

Therefore, it is worth considering the implications of these findings on therapeutic interventions. Understanding the role of these short abortive transcripts could inform the development of targeted strategies. Furthermore, the interplay between these transcripts and the immune system could provide valuable insights into the dynamics of HIV pathogenesis. It may uncover novel targets for immunomodulatory therapies aimed at mitigating the persistent immune dysfunction seen in individuals living with HIV, even under successful viral suppression, and potentially moving us closer to a functional cure.

Use of RNAflow-FISH assay to study the viral reservoir cells

In both studies presented, we used fluorescent *in situ* hybridization (FISH) with gene-specific probes to identify HIV transcription in infected CD4⁺ T cells [254, 256]. This approach, known as RNAflow-FISH or RNA FISH-flow, utilizes multiple oligomeric probes and branched DNA signal amplification to enhance the sensitivity of detection [254-256]. Our group has previously developed and utilized RNAflow-FISH assay for identifying cells containing translation-competent viral reservoirs. In this technique, Baxter et al. co-detected the p24 protein along with probe sets targeting the *gag* and *pol* genes [254, 255], which have highly conserved sequences across different clinical isolates [361].

In the first manuscript, we multiplexed the previous iteration of the RNAflow-FISH assay to comprehensively investigate the transcriptionally active viral reservoir, irrespective of viral protein expression. For this purpose, we developed a two-layer multiplexed vRNA detection strategy (Manuscript 1, Figure 1). The first probe set, called “5′*exon*RNA”, targeted exon sequences present in all viral transcripts [140], providing detection of viral transcription except for the most distal exon in *nef*. To ensure specificity, we used two complementary probes. The *nef*RNA probe set covered the exon sequence in *nef* before the 3′ LTR to avoid recognition of the repeated sequence in the 5′ LTR and allowed the detection of fully elongated transcripts. Additionally, we developed a *gag*RNA probe set that targeted both full-length genomic transcripts and short *nef*RNA⁻ abortive transcripts [191]. Our observations revealed distinct characteristics in the viral profiles between CP and ART-treated individuals. CP exhibited a higher proportion of HIV-infected cells capable of p24 translation, indicating their competency for viral protein expression. In contrast, ART-treated individuals predominantly had translation-incompetent viral reservoirs characterized by the presence of *gag*-encoding transcripts (Manuscript 1, Figure 2). Building upon these findings, in Manuscript 2, we further optimized our multiplexed RNAflow-FISH assay to detect processive elongation beyond the *gag* gene. This was achieved by incorporating a *pol*RNA probe set [233]. This revised version enabled the identification of spontaneously active short transcripts in cells without the need for activation (Manuscript 2, Figure 1). By nature, inducible HIV-infected cells are susceptible to reactivating in the presence of external stimuli whereas spontaneously active reservoirs might sustain viral expression in the absence of stimulation. The latter may be reminiscent of what happens in anatomical sanctuaries that have been identified to be more conducive to viral transcription, possibly due to the suboptimal distribution of

antiviral drugs into tissues [234]. For instance, in SIV-infected monkeys, ART partially reduced levels of both DNA and RNA in lymphoid tissues, which correlated with low drug concentrations in these tissues compared to peripheral blood [234]. To validate the specificity of the RNAflow-FISH assay, we conducted a spiking experiment using HIV-infected ACH-2 cells, a cell line with a single copy of integrated HIV DNA in its genome. This experiment confirmed the multiplexed RNAflow-FISH assay's sensitivity, detecting as low as 6 HIV-infected cells per million CD4⁺ T cells (Manuscript 1, Supplemental Figure 1). Furthermore, the use of flow cytometry to measure viral reservoirs enables the phenotypic characterization of HIV-infected cells. Consistent with recent studies, we have observed that translation-competent cells in individuals receiving ART were found to be enriched in T_{TM} and T_{EM} CD4⁺ T cells, while proviruses harboring large deletions were enriched in T_{CM}. This enrichment of defective proviruses into T_{CM} might be explained by the differentiation of T_{CM} into T_{EM} which are then eliminated by the immune system. Overall, these results represent an important milestone in the HIV reservoir research. The utilization of the RNAflow-FISH technique enables a comprehensive characterization of the inducible viral reservoirs, revealing a substantial population of transcriptionally active cells that are typically undetectable by flow cytometry-based methods relying on p24 protein expression [253, 254, 256].

Proportion of the transcription-competent viral reservoir

The size of the HIV reservoir varies depending on the measurement method used. In both manuscripts presented, we measured the size of the transcription-competent viral reservoir. Our findings indicated that the pool of translation-competent cells, detected

through the presence of p24 protein, was approximately 20 times smaller than the transcription-competent reservoirs [253, 254]. Additionally, the transcription-competent reservoirs were approximately 7 times smaller than the quantification of HIV DNA [236] (Manuscript 1, Figure 2).

In Manuscript 1, we observed that the viral transcription was more dependent on latency reversal agents compared to translation [259]. Moreover, we discovered that different classes of LRA had specific effects on gene transcription and translation patterns (Manuscript 1, Figure 5). Histone deacetylase inhibitors, which initiate transcription, predominantly led to the production of aberrant *gag*-encoding short transcripts, suggesting abortive transcription as previously reported [191]. On the other hand, protein Kinase C agonists induced more elongated transcripts. However, combining both classes of LRA did not result in an increased proportion of full-length transcripts or translation-competent cells among the reactivated HIV⁺ cells. Contrary to expectations, the advantage of combining LRA did not yield a true synergistic effect but instead lies in its ability to reactivate a broader pool of viral reservoirs. In Manuscript 2, we compared spontaneously active viral reservoirs with induced reservoirs using a combination of PEP005 and Panobinostat (a PKCa and an HDACi, respectively) in different groups of people living with HIV. The profile of the vRNA-expressing cells in CP and ART-treated individuals aligned with the observations made in Manuscript 1. Interestingly, we observed that HIV-infected cells in EC displayed a profile more closely resembling that of ART-treated individuals rather than CP. Also, we observed a strong association between the two features of HIV reservoirs, which aligns with previous observations from our group (Manuscript 2, Figure 1) [233]. This led us to consider the combination of LRAs as a

surrogate for the spontaneously active transcription-competent reservoir. Moreover, our measurements revealed that the combination of PEP005 and Panobinostat induced viral transcription from the majority of the integrated DNA at a ratio close to 1:1. This suggests that the LRA combination is efficient in actively transcribing the majority of viral reservoirs in ART-treated and EC individuals, and that which contrast with a previous study [362]. In this study, the authors observed that the HIV-infected cells in EC individuals were associated with inefficient reactivation of the infected CD4⁺ T cells and with less efficient virion production. However, the authors assessed the viral reactivation of the cells by measuring either the virion or the viral RNA production in the supernatant, regardless of the intactness of the transcripts. We observed that the majority of inducible proviruses harbored large deletion spanning over *rev*. Therefore, it is possible that the majority of these transcripts are retained in the nucleus of the cells and thus cannot be detected in the supernatant. Overall, our findings suggest a convergence in the characteristics of vRNA-expressing cells between EC and ART-treated individuals, highlighting potential similarities in the viral reservoir dynamics and the influence of treatment on viral persistence.

Viral integrity of the transcriptionally competent HIV-infected cells during ART

Our studies revealed a diverse range of inducible proviruses in all individuals living with HIV, although the distribution varied depending on the infection status. In individuals with active replication, such as chronic progressors, approximately half of the HIV-infected cells expressed the p24 viral protein, followed by short abortive *gag*-encoding transcripts,

fully elongated transcripts, and transcripts lacking *gag*. In environments in which HIV replication is controlled, either through ART or in EC, only a small fraction of HIV-infected cells exhibited p24 translation, with the majority showing aberrant or short abortive transcripts (Manuscript 1, Figures 2 and 5, and Manuscript 2, Figure 1). These observations suggest a suboptimal transcriptional process reminiscent of abortive transcription [191]. The viral profile also reflects the reactivation of defective proviruses, which constitute a significant proportion of the integrated proviruses [238, 246, 261].

In order to investigate the relationship between the detection of viral transcripts and the integrity of proviral genes within a given cell, we employed a modified FLIPS assay (Full-Length Individual Proviral Sequencing) for near-full-length sequencing of inducible proviruses [238, 246, 261] (Manuscript 1, Figure 3). Our analyzes revealed that intact proviruses represent 1% of the reactivated cells, close to the 2-5% previously measured [238, 239]. These observations indicate that even translation-competent reservoirs harbor defective proviruses. It is worth noting that the low proportion of intact sequences could be attributed to their integration in regions with low transcriptional activity, such as those close to the centromeres of chromosomes [294, 295]. The nature of these defects varied among the transcriptionally active reservoirs. Consistent with another study, the translation-competent cells predominantly exhibited mutations in the packaging signal ψ or in the major splice donor (MSD) site [360, 363]. Mutations in the ψ locus hindered proper encapsidation of the viral genome [27, 39] but do not impede the production of virus-like particles that contain viral proteins [364]. MSD mutation site could impair the correct splicing of the viral transcripts, potentially affecting their subsequent translation into viral proteins [365, 366]. The detection of spliced RNA despite MSD defects suggests

that this mutation may be bypassed, possibly through the activation of an alternative splice donor site [249]. Similar defects were observed in the vRNA-expressing cells incapable of p24 translation, although they were often overshadowed by more severe defects. Large deletions spanning over either *gag* or *nef* regions were commonly detected, consistent with previous studies demonstrating the prevalence of large deletions among cells carrying proviral DNA [238, 246, 247, 261]. Premature stop codons, particularly in *nef* and *tat*, were also found across all viral subpopulations, although defects in *nef* do not hinder viral replication [367]. These findings raise the possibility that *tat* mutations contribute to establishing and/or maintaining latency during ART [368]. However, the premature stop codon did not impair the potent reactivation and transcription of proviruses, as the use of LRA, especially PKCa such as PMA or PEP005, overcomes the block by directly recruiting NF- κ B or P-TEFb, promoting transcription elongation in a Tat-independent manner [369]. Unlike analyzes of integrated DNA [238, 246, 247, 261], we observed minimal occurrences of inversions and hypermutations in transcriptionally active viral reservoirs. These defects have potentially either impeded productive transcription or affected their detection by the RNAflow-FISH probe sets.

Recent studies in EC have uncovered an intriguing finding: despite their lower frequency of integrated proviruses, these proviruses were, in fact, proportionally more intact compared to ART-treated individuals [370] and therefore to CP [238]. However, the profile of inducible HIV-infected cells in EC, resembling that of ART-treated individuals (Manuscript 2, Figure 1), suggests that inducible viral reservoirs in EC might be enriched in defective proviruses. Some studies have shown that the intact proviruses from EC were enriched in transcriptionally repressed regions, while the defective proviruses were

predominantly found in euchromatic regions [370, 371]. These findings suggest indeed that the inducible HIV-infected cells in EC are mostly defective and further investigations will be required to determine the inducible viral reservoir integrity in EC.

While it is acknowledged that defective proviruses carrying large deletions or inversions are incapable of generating replication-competent viruses, it is important to consider the potential implications of proviruses harboring milder defects. Among the majority of defective proviruses, which commonly exhibit stop codons or point mutations, there remains a possibility for reversion [372, 373], giving rise to fully intact HIV viruses that are capable of replication. This prospect raises questions about the role of these less severe defects in the persistence and evolution of the viral reservoir, as well as their potential contribution to viral rebound and disease progression. Therefore, further investigations are needed to determine if these defective proviruses can lead to the emergence of replication-competent viral variants.

Relationships between HIV-specific T cell responses and viral reservoirs

Thus far, two hypotheses have been proposed to explain the persistent immune activation, inflammation, and subsequent immune dysfunction observed in all individuals living with HIV, including those receiving ART and EC. The first, widely studied, implicates the viral reservoirs as the primary culprits [192, 193, 235, 374]. Recently, our group and others have also described spontaneous viral gene transcription and translation during ART [233, 375], suggesting that immune persistence might be driven by continuous

expression of viral antigens. The second, known as the “die is cast” hypothesis, posits that the pathogenic processes occurring prior to the initiation of ART are the main factors responsible for immune dysfunction after treatment [376-378]. Be that as it may, this immune persistence underscores its potential importance for future HIV cure strategies. These strategies should purge the viral reservoir, uphold immunosurveillance, and bolster the development of bNAbs [379, 380]. In this thesis, we unveiled an intriguing connection between the quantitative and qualitative features of the viral reservoirs and the HIV-specific immune responses, and how these dynamics influence one another.

Notably, in chronic progressors, the absence of a discernible association between the size of the viral reservoir and HIV-specific CD4⁺ and CD8⁺ T cell responses may be due to the coexistence of both positive and negative associations combining different features, which would mask any overt correlation (Figure 13). During ART, however, we show a positive correlation of the viral reservoirs with HIV-specific CD4⁺ and CD8⁺ T cell responses, implying that the reservoirs may play a role in sustaining these immune responses (Figure 13). Finally, elite controllers present a different scenario, with negative associations suggesting that the HIV-specific T cells control the infection (Figure 13). We also have shown that pre-ART HIV-specific CD4⁺ and CD8⁺ T cell responses exhibited a clear correlation with the clearance of both spontaneously and active viral reservoirs, highlighting the crucial role the immune responses play in controlling viral persistence.

This thesis also reveals that even defective proviruses are not biologically inert, as previously considered, and potentially influence the HIV-specific immune responses, affecting the efficacy of therapies reliant on such responses. These proviruses may still express viral genes, potentially impacting the immune system. The proportion of these

proviruses capable of expressing Env, spontaneously or not, may hold critical implications for therapy effectiveness, either by maintaining a reservoir of cells poised to control the viral rebound or by continuously stimulating HIV-specific cells, potentially leading to immune exhaustion.

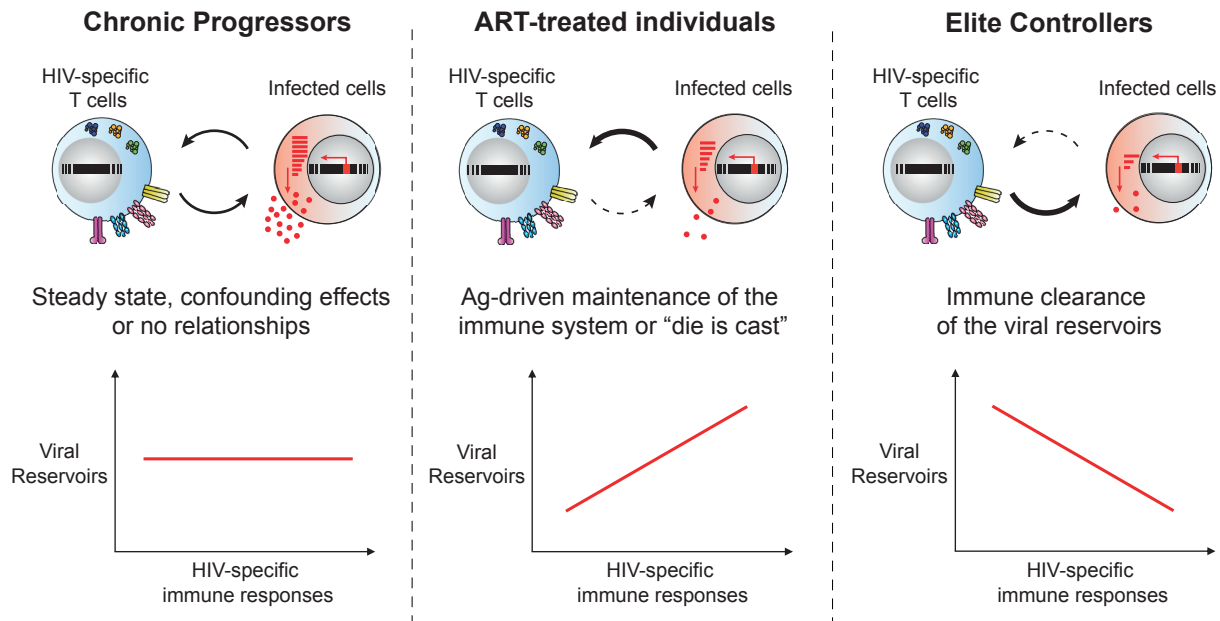


Figure 13. – Relationship between HIV-specific responses and viral reservoirs
 Viral reservoirs and HIV-specific immune responses share an intriguing association. In CP (left), there is an absence of associations between the HIV-specific immune responses and the infected cells. During ART (middle), either the spontaneous expression or the pathogenic processes that occurred prior to ART are responsible for the persistence of immune activation. In EC (right), the HIV-specific immune responses clear the viral reservoirs.

Possible impact of the defective proviruses on the HIV-specific T responses

To date, the prevailing understanding is that defective proviruses are incapable of replication, as no studies have demonstrated the production of infectious particles.

However, evidence suggests that these defective proviruses may still exert some influence on HIV pathogenesis [244]. For instance, HIV-infected cells generate MHC-I-associated peptides, including cryptic epitopes, that are recognized by CTL [249, 381, 382]. Our own investigations have indirectly shown that HIV-infected cells carrying defective proviruses downregulate the CD4 molecule on their cell surface, suggesting the potential production of viral proteins such as Nef or Vpu [87]. Moreover, some reports have indicated that defective proviruses have the ability to generate what is referred to as “zombie” viral proteins, possibly derived from cryptic or alternative RNA sequences allowing viral translation [244, 382]. These zombie proteins may trigger immune responses aimed at eliminating the HIV-infected cells harboring such proviruses [248, 249, 374]. Also, the defective RNA transcripts might be targets for immune sensors which can lead to the production of inflammatory cytokines, sustaining an inflammatory environment [192, 244]. These findings raise the possibility that defective proviruses could contribute to the complex interplay between the virus and the immune system.

The impact of defective proviruses on HIV-specific immune responses and pathogenesis is a subject of considerable interest. During HIV pathogenesis, there is a well-documented association between persistent antigen stimulation and the exhaustion and dysfunction of HIV-specific T cell responses. For example, HIV-specific CD8⁺ T cells express elevated levels of inhibitory molecules such as PD-1, TIGIT, and LAG-3, resulting in the reduction of anti-viral functions [165, 169]. Our findings, which demonstrate a negative correlation between the presence of vRNA-expressing cells and HIV-specific T cell responses in EC support the notion that high levels of vRNA-expressing cells contribute to compromised control of the HIV infection. This may explain why some cells are capable of “leaking” virus

particles or viral transcripts during ART. The existence of spontaneously active proviruses during ART [233] may perpetuate chronic inflammation and immune dysfunction. This study demonstrated an association between HIV-specific responses, their functional properties, and the magnitudes of spontaneously active viral reservoirs. These results suggest that the phenomenon of spontaneous viral expression plays a crucial role in driving and shaping immune responses during ART. These observations hold significant implications, particularly in the context of the “shock/kick and kill” strategy, which requires the involvement of potent HIV-specific CD4⁺ and CD8⁺ T cells. The presence of viral RNA, which serves as targets for cellular sensors, may lead to a persistent inflammatory environment that can contribute to diminished anti-viral functions of HIV-specific T cells due to exhaustion and dysfunction [169, 305, 306]. Consequently, this hindrance may impede the eradication of reactivated HIV-infected cells.

Further investigations are required to clarify the complex dynamics and potential immune implications associated with defective proviruses in the context of HIV infection and the “shock/kick and kill” strategy.

Possible role of the HIV-specific T responses on the persistence of defective proviruses

How the immune responses impact the persistence of the viral reservoirs and their associations with the spontaneously active viral reservoir is unclear. HIV infection correlates with elevated levels of pro-inflammatory cytokines and chemokines. This inflammatory environment is associated with the impairment of HIV-specific T cell

responses and the disruption of T cell homeostasis. For instance, TNF, a pro-inflammatory cytokine highly produced during HIV infection, appears to favor HIV transcription by activating NF- κ B signaling [383]. Therefore, this pro-inflammatory environment could potentially create a feedback loop, triggering the activation of defective proviruses and exacerbating immune activation. Following the initiation of ART, translation-competent cells, which are susceptible to recognition and elimination by CTL [302], are reduced in number. Consequently, there is an enrichment of HIV-infected cells harboring short abortive transcripts. These short transcripts were observed prior to ART initiation, suggesting that the cells carrying such abortive transcripts are pre-existent to ART initiation. By sequencing these short transcripts from the longitudinal individuals, it may be possible to ascertain whether they originate from the same clone or represent distinct events, providing valuable insights into their origin and persistence.

The lack of correlation observed between the vRNA-expressing cells carrying short abortive transcripts and the HIV-specific T cell responses suggests that these reservoirs might either evade detection by immune cells or exhibit increased resistance to immune clearance. It is also plausible that the immune system itself fails to eliminate these HIV-infected cells with defective proviruses, as immune dysfunction and exhaustion persist despite the initiation of ART [227, 287, 288, 307, 309]. Our group has identified distinct functional profiles of HIV-specific CD4⁺ T cells depending on the analyzed cohort. In chronic infection, HIV-specific CD4⁺ T cells exhibit a prominent cT_{FH} signature within non-cT_{FH} cells, while individuals who effectively control viral replication display T_{H17} functions [313, 314]. Although ART-treated individuals show some restoration of T_{H17} functions, there is a persistence of expanded and altered HIV-specific T cell populations expressing

CXCL13 and IL-21 [313]. The enrichment of cT_{FH}-like functions prior to and after ART initiation may play a role in shaping the viral reservoir. While cT_{FH} cells are critical for sustaining protective antibody responses for pathogen clearance, their heightened cytokine expression also contributes to the maintenance of non-specific antibodies. In the context of HIV infection, it is conceivable that B cells produce less specific antibodies, which may not confer a beneficial effect, allowing the defective proviruses that produce cryptic proteins to evade antibody responses [384]. Despite the presence of these alternative functions, we observed that pre-treatment HIV-specific CD4⁺ T cell responses in CP were associated with a reduction in HIV-infected cells following ART initiation. However, no such association was found between the cells carrying short abortive cells and HIV-specific T cell responses, suggesting that pre-ART HIV-specific T cell responses are more effective in clearing translation-competent infected cells rather than translation-incompetent for Gag. This preferential disappearance of translation-competent cells for the Gag protein could be attributed to the cytopathic effect of the virus or their preferential recognition by CTLs. It is also plausible that HIV-infected cells containing defective proviruses incompetent for Gag translation, exhibit increased resistance to cell death [385, 386]. Notably, studies have shown that CTL responses targeting epitopes from the protein Gag are more efficient in controlling viral replication compared to responses targeting other viral proteins [387-389]. The pro-inflammatory environment, sustained by HIV infection could play a role in the persistence of these proviruses. For instance, IL-7 signaling induced the expression of BCL-2 [390], which has been associated with the survival of T cells but also with the survival of HIV-infected cells and their resistance to cell death [288]. Additionally, the early initiation of ART following infection may have influenced the profile of the viral reservoir. In our study, the cohort of pre/post-ART

individuals is enriched in people who initiated the treatment early after infection. It is known that individuals who start ART early experience a significant reduction in viral reservoir size and maintain more potent HIV-specific immune responses [290, 391, 392]. These findings provide an explanation for the observed persistence of short abortive transcripts over time. Therefore, further investigations are necessary to ascertain whether the intricate relationship between viral reservoirs and HIV-specific immunity holds true for individuals who remained ART-naïve for a longer period of time.

Chapter 6 – Limitations and perspectives

Blood versus tissue

Due to challenges associated with working with large animals that can be infected with SIV, both manuscripts presented in this thesis focused solely on studying viral reservoir cells in *ex vivo* samples of peripheral blood. Lymphocytes constitute a mere 2% of circulating cells but comprise 98% of cells in lymphoid tissues [393]. The high concentration of lymphocytes in tissues facilitates the spread of HIV through cell-to-cell transmission within anatomical compartments [394], suggesting that the proportion of HIV reservoir cells is likely to be higher in tissues than in peripheral blood [395]. Moreover, the suboptimal distribution of ARVs within tissues may allow for replication escape, leading potentially to the independent evolution of proviruses and the emergence of drug resistance during ART [234]. Therefore, investigating tissues from HIV-infected individuals would be necessary to determine the viral profile of proviruses that are more likely to contribute to viral rebound during ART. Our group is collaborating with Dr. Jake D. Estes' team at Oregon Health & Science University in Portland, USA, to characterize tissue reservoirs in comparison to peripheral reservoir cells in SIV-infected NHP. Preliminary findings in viremic animals indicate no significant difference in the viral profile between tissue and blood compartments (data not shown). We are also planning to study the viral reservoir cells in treated monkeys, although the analysis has not yet started due to the recent completion of sample collection.

Perspectives for future treatment approaches

Undoubtedly, ART has revolutionized the management of HIV. However, this treatment does not represent a cure for individuals living with HIV as viral reservoirs exist. Moreover, we highlighted the continued presence of short abortive transcripts, even in individuals undergoing ART. These transcripts, though replication-incompetent, remain responsive to stimuli, and can also be expressed spontaneously, representing a reservoir of latent viral activity. This phenomenon poses a significant obstacle to achieving a cure and raises questions about the long-term efficacy of current treatment regimens. Indeed, ARV do not target the step of transcription.

Addressing this challenge requires a multifaceted approach. One avenue of exploration could involve the development of targeted LRAs that specifically trigger the reactivation of cells harboring short viral transcripts. Also, as described in Manuscript 1, exploring combinatorial approaches that synergistically target multiple aspects of the viral lifecycle could represent a promising avenue for future research. Reactivation of the viral reservoirs might render them susceptible to immune recognition and clearance. Furthermore, it might be worth investigating the signaling pathways and molecular interactions involved in viral latency. As observed for exhausted T cells during chronic infection [396-398], it is possible that HIV infection leads to epigenetic regulations, including DNA methylation, long-distance chromatin remodeling, or posttranslational histone modifications favoring viral latency. To do so, our group is planning to study these epigenetic hallmarks in HIV-infected CD4⁺ T cells from longitudinal individuals living with HIV pre-post ART initiation.

RNAflow-FISH requirements

While RNAflow-FISH provides valuable insight into the characteristics of the HIV-infected cells, it does have certain limitations. Firstly, the identification of latent viral reservoirs in primary samples is hindered by the scarcity of these cells in ART-treated individuals, with an estimated frequency of 1 HIV-infected cell per million CD4⁺ T cells. Therefore, the accuracy of the assay improves as more events are acquired, aligning with the Poisson distribution for detecting rare events. Typically, we acquire around 1.5-3 million CD4⁺ T cells per subject, per condition. To ensure sufficient cell numbers for flow cytometry, considering the cell loss associated with the RNAflow-FISH protocol, we start with at least 15-20 x 10⁶ CD4⁺ T cells in culture. It is also possible that the size of the measured reservoir using the multiplexed RNAflow-FISH strategy is underestimated. In both manuscripts, we utilized probe sets designed based on the consensus B HIV sequences, limiting our studies to Clade B only. While the majority of individuals in our cohort are infected with Clade B isolates, this approach restricts the characterization of viral reservoirs from other clades. Developing probes that target other strains would allow the characterization of viral reservoirs from diverse clades. The multiplexed RNAflow-FISH might also fail to detect cells carrying proviruses with deletions spanning the region targeted by our designed probe sets. In both manuscripts, inducible viral reservoir cells were identified through *ex vivo* stimulation using LRAs. However, this reactivation process limits the phenotyping of inducible viral reservoirs due to the pleiotropic effects of LRAs on cellular markers. Moreover, stimulation using LRAs only provides information on inducible reservoirs poised for reactivation. Nevertheless, in Manuscript 2, we used an optimized iteration of the multiplexed RNAflow-FISH [233] to identify cells that are primed

for spontaneous viral gene transcription and translation during ART without the need for stimulations. Finally, despite its ability to identify and characterize transcription- and translation-competent cells, the branched DNA amplification of a low amount of viral RNA can degrade RNA and thus hinder downstream transcriptomic analyzes.

The HIV-infected cohort

The majority of the participants included in both studies were males, reflecting the epidemiology of the HIV-infected population in Montreal. It is known that immune responses can vary based on sex, as biological factors such as hormonal differences contribute to distinct HIV infection patterns between males and females [399, 400]. For instance, estrogen has been associated with protective effects against SIV infection and lower HIV infection rates due to reduced lymphocyte migration to the site of infection [399]. Females also exhibit smaller reservoir sizes than men during ART [239, 400]. Moreover, women are overrepresented among elite controllers and post-treatment controllers [401]. In our cohort of EC, we observed a similar trend, with 43% of female participants compared to 11% and 4% in the CP and ART-treated individual cohorts, respectively. However, as EC comprise approximately 1% of the total HIV-infected individuals, our access to a limited number of individuals in Montreal restricted the extent of characterization we could achieve. Therefore, recruiting EC from other regions would provide reliable insights into the viral reservoir cells of individuals controlling viremia.

Chapter 7 – Significance

Our results contribute to a better understanding of the persistence and characteristics of viral reservoir cells during HIV infection. The results from both manuscripts shed light on a population of defective viral genomes that exhibit transcriptional and transcriptional activity.

Our studies demonstrate that the reactivation of intact proviruses through LRA stimulation represents only a minor fraction of the inducible reservoirs in individuals undergoing ART. Additionally, we show that while current LRAs effectively promote viral transcription, they fail to increase viral protein production which is crucial for antigen presentation and subsequent recognition by CTL. Therefore, these observations may have important implications for therapeutic strategies that aim to target viral reservoir cells.

Defective proviruses are considered replication-incompetent for HIV infection. Although our findings do not directly investigate this particular aspect of infected cells, they suggest the production of viral transcripts and proteins that could contribute to the pathophysiological significance of defective proviruses. The identification of these transcriptionally active reservoirs in EC suggests that they persist at low levels, potentially contributing to the loss of infection control and the deleterious impact of immune activation commonly observed in all HIV-infected individuals.

Chapter 8 – References

1. Barre-Sinoussi, F., et al., *Isolation of a T-lymphotropic retrovirus from a patient at risk for acquired immune deficiency syndrome (AIDS)*. Science, 1983. **220**(4599): p. 868-71.
2. Popovic, M., et al., *Detection, isolation, and continuous production of cytopathic retroviruses (HTLV-III) from patients with AIDS and pre-AIDS*. Science, 1984. **224**(4648): p. 497-500.
3. Gallo, R.C., et al., *Frequent detection and isolation of cytopathic retroviruses (HTLV-III) from patients with AIDS and at risk for AIDS*. Science, 1984. **224**(4648): p. 500-3.
4. Brinkworth, J.F. and K. Pechenkina, *Primates, pathogens, and evolution*. 2013: Springer.
5. Chahroudi, A., et al., *Natural SIV hosts: showing AIDS the door*. Science, 2012. **335**(6073): p. 1188-93.
6. Clavel, F., et al., *Isolation of a new human retrovirus from West African patients with AIDS*. Science, 1986. **233**(4761): p. 343-6.
7. Hirsch, V.M., et al., *An African primate lentivirus (SIVsm) closely related to HIV-2*. Nature, 1989. **339**(6223): p. 389-92.
8. Gao, F., et al., *Human infection by genetically diverse SIVSM-related HIV-2 in west Africa*. Nature, 1992. **358**(6386): p. 495-9.
9. Reeves, J.D. and R.W. Doms, *Human immunodeficiency virus type 2*. J Gen Virol, 2002. **83**(Pt 6): p. 1253-1265.
10. Hahn, B.H., et al., *AIDS as a zoonosis: scientific and public health implications*. Science, 2000. **287**(5453): p. 607-14.
11. WHO. *Key facts HIV & AIDS - 2022*. 2022; Available from: https://cdn.who.int/media/docs/default-source/hq-hiv-hepatitis-and-stis-library/key-facts-hiv-2021-26july2022.pdf?sfvrsn=8f4e7c93_5.
12. UNAIDS. *Global HIV & AIDS statistics - 2022 fact sheet*. 2022; Available from: https://www.unaids.org/sites/default/files/media_asset/UNAIDS_FactSheet_en.pdf.
13. Zhu, P., et al., *Distribution and three-dimensional structure of AIDS virus envelope spikes*. Nature, 2006. **441**(7095): p. 847-52.

14. Zhu, P., et al., *Electron tomography analysis of envelope glycoprotein trimers on HIV and simian immunodeficiency virus virions*. Proc Natl Acad Sci U S A, 2003. **100**(26): p. 15812-7.
15. Robertson, D.L., et al., *HIV-1 nomenclature proposal*. Science, 2000. **288**(5463): p. 55-6.
16. Bbosa, N., P. Kaleebu, and D. Ssemwanga, *HIV subtype diversity worldwide*. Curr Opin HIV AIDS, 2019. **14**(3): p. 153-160.
17. Santiago, M.L., et al., *Simian immunodeficiency virus infection in free-ranging sooty mangabeys (*Cercocebus atys atys*) from the Tai Forest, Cote d'Ivoire: implications for the origin of epidemic human immunodeficiency virus type 2*. J Virol, 2005. **79**(19): p. 12515-27.
18. Marx, P.A., P.G. Alcibes, and E. Drucker, *Serial human passage of simian immunodeficiency virus by unsterile injections and the emergence of epidemic human immunodeficiency virus in Africa*. Philos Trans R Soc Lond B Biol Sci, 2001. **356**(1410): p. 911-20.
19. Robinson, H.L., *New hope for an AIDS vaccine*. Nat Rev Immunol, 2002. **2**(4): p. 239-50.
20. German Advisory Committee Blood, S.A.o.P.T.b.B., *Human Immunodeficiency Virus (HIV)*. Transfus Med Hemother, 2016. **43**(3): p. 203-22.
21. Ding, P., et al., *5'-Cap sequestration is an essential determinant of HIV-1 genome packaging*. Proc Natl Acad Sci U S A, 2021. **118**(37).
22. Wilusz, J., *Putting an 'End' to HIV mRNAs: capping and polyadenylation as potential therapeutic targets*. AIDS Res Ther, 2013. **10**(1): p. 31.
23. Roebuck, K.A. and M. Saifuddin, *Regulation of HIV-1 transcription*. Gene Expr, 1999. **8**(2): p. 67-84.
24. Pereira, L.A., et al., *A compilation of cellular transcription factor interactions with the HIV-1 LTR promoter*. Nucleic Acids Res, 2000. **28**(3): p. 663-8.
25. Jones, K.A. and B.M. Peterlin, *Control of RNA initiation and elongation at the HIV-1 promoter*. Annu Rev Biochem, 1994. **63**: p. 717-43.

26. Gotte, M., X. Li, and M.A. Wainberg, *HIV-1 reverse transcription: a brief overview focused on structure-function relationships among molecules involved in initiation of the reaction*. Arch Biochem Biophys, 1999. **365**(2): p. 199-210.
27. Lever, A., et al., *Identification of a sequence required for efficient packaging of human immunodeficiency virus type 1 RNA into virions*. J Virol, 1989. **63**(9): p. 4085-7.
28. Berkhout, B., R.H. Silverman, and K.T. Jeang, *Tat trans-activates the human immunodeficiency virus through a nascent RNA target*. Cell, 1989. **59**(2): p. 273-82.
29. Kao, S.Y., et al., *Anti-termination of transcription within the long terminal repeat of HIV-1 by tat gene product*. Nature, 1987. **330**(6147): p. 489-93.
30. Cullen, B.R., P.T. Lomedico, and G. Ju, *Transcriptional interference in avian retroviruses-- implications for the promoter insertion model of leukaemogenesis*. Nature, 1984. **307**(5948): p. 241-5.
31. Freed, E.O., *HIV-1 gag proteins: diverse functions in the virus life cycle*. Virology, 1998. **251**(1): p. 1-15.
32. Boyd, P.S., et al., *NMR Studies of Retroviral Genome Packaging*. Viruses, 2020. **12**(10).
33. Freed, E.O. and M.A. Martin, *Domains of the human immunodeficiency virus type 1 matrix and gp41 cytoplasmic tail required for envelope incorporation into virions*. J Virol, 1996. **70**(1): p. 341-51.
34. Tedbury, P.R., et al., *Biochemical evidence of a role for matrix trimerization in HIV-1 envelope glycoprotein incorporation*. Proc Natl Acad Sci U S A, 2016. **113**(2): p. E182-90.
35. Kutluay, S.B., et al., *Global changes in the RNA binding specificity of HIV-1 gag regulate virion genesis*. Cell, 2014. **159**(5): p. 1096-1109.
36. Carlson, L.A., et al., *Three-dimensional analysis of budding sites and released virus suggests a revised model for HIV-1 morphogenesis*. Cell Host Microbe, 2008. **4**(6): p. 592-9.
37. Lu, K., X. Heng, and M.F. Summers, *Structural determinants and mechanism of HIV-1 genome packaging*. J Mol Biol, 2011. **410**(4): p. 609-33.
38. Darlix, J.L., et al., *Flexible nature and specific functions of the HIV-1 nucleocapsid protein*. J Mol Biol, 2011. **410**(4): p. 565-81.

39. Amarasinghe, G.K., et al., *Stem-loop SL4 of the HIV-1 psi RNA packaging signal exhibits weak affinity for the nucleocapsid protein. structural studies and implications for genome recognition.* J Mol Biol, 2001. **314**(5): p. 961-70.
40. Gottlinger, H.G., et al., *Effect of mutations affecting the p6 gag protein on human immunodeficiency virus particle release.* Proc Natl Acad Sci U S A, 1991. **88**(8): p. 3195-9.
41. Huang, M., et al., *p6Gag is required for particle production from full-length human immunodeficiency virus type 1 molecular clones expressing protease.* J Virol, 1995. **69**(11): p. 6810-8.
42. de Marco, A., et al., *Role of the SP2 domain and its proteolytic cleavage in HIV-1 structural maturation and infectivity.* J Virol, 2012. **86**(24): p. 13708-16.
43. Datta, S.A., et al., *On the role of the SP1 domain in HIV-1 particle assembly: a molecular switch?* J Virol, 2011. **85**(9): p. 4111-21.
44. Kuiken, C., et al., *HIV Sequence Compendium 2010.* 2010: United States. p. Medium: ED; Size: 442 p.
45. Biswas, P., et al., *The human immunodeficiency virus type 1 ribosomal frameshifting site is an invariant sequence determinant and an important target for antiviral therapy.* J Virol, 2004. **78**(4): p. 2082-7.
46. Jacks, T., et al., *Characterization of ribosomal frameshifting in HIV-1 gag-pol expression.* Nature, 1988. **331**(6153): p. 280-3.
47. Ludwig, C., A. Leiberer, and R. Wagner, *Importance of protease cleavage sites within and flanking human immunodeficiency virus type 1 transframe protein p6* for spatiotemporal regulation of protease activation.* J Virol, 2008. **82**(9): p. 4573-84.
48. Oroszlan, S. and R.B. Luftig, *Retroviral proteinases.* Curr Top Microbiol Immunol, 1990. **157**: p. 153-85.
49. Konvalinka, J., H.G. Krausslich, and B. Muller, *Retroviral proteases and their roles in virion maturation.* Virology, 2015. **479-480**: p. 403-17.
50. Swanstrom, R. and J.W. Wills, *Synthesis, Assembly, and Processing of Viral Proteins, in Retroviruses,* J.M. Coffin, S.H. Hughes, and H.E. Varmus, Editors. 1997: Cold Spring Harbor (NY).

51. di Marzo Veronese, F., et al., *Characterization of highly immunogenic p66/p51 as the reverse transcriptase of HTLV-III/LAV*. *Science*, 1986. **231**(4743): p. 1289-91.
52. Bjorling, E., et al., *Two highly antigenic sites in the human immunodeficiency virus type 1 reverse transcriptase*. *J Clin Microbiol*, 1993. **31**(3): p. 588-92.
53. Hu, W.S. and S.H. Hughes, *HIV-1 reverse transcription*. *Cold Spring Harb Perspect Med*, 2012. **2**(10).
54. Crise, B., L. Buonocore, and J.K. Rose, *CD4 is retained in the endoplasmic reticulum by the human immunodeficiency virus type 1 glycoprotein precursor*. *J Virol*, 1990. **64**(11): p. 5585-93.
55. Chen, B., et al., *Structure of an unliganded simian immunodeficiency virus gp120 core*. *Nature*, 2005. **433**(7028): p. 834-41.
56. Curlin, M.E., et al., *HIV-1 envelope subregion length variation during disease progression*. *PLoS Pathog*, 2010. **6**(12): p. e1001228.
57. Brasseur, R., et al., *Orientation into the lipid bilayer of an asymmetric amphipathic helical peptide located at the N-terminus of viral fusion proteins*. *Biochim Biophys Acta*, 1990. **1029**(2): p. 267-73.
58. Cochrane, A., et al., *The human immunodeficiency virus rev protein is a nuclear phosphoprotein*. *Virology*, 1989. **171**(1): p. 264-6.
59. Malim, M.H., et al., *Functional dissection of the HIV-1 Rev trans-activator--derivation of a trans-dominant repressor of Rev function*. *Cell*, 1989. **58**(1): p. 205-14.
60. Brady, J. and F. Kashanchi, *Tat gets the "green" light on transcription initiation*. *Retrovirology*, 2005. **2**: p. 69.
61. Romani, B., S. Engelbrecht, and R.H. Glashoff, *Functions of Tat: the versatile protein of human immunodeficiency virus type 1*. *J Gen Virol*, 2010. **91**(Pt 1): p. 1-12.
62. Huang, L., et al., *Tat protein induces human immunodeficiency virus type 1 (HIV-1) coreceptors and promotes infection with both macrophage-tropic and T-lymphotropic HIV-1 strains*. *J Virol*, 1998. **72**(11): p. 8952-60.
63. Albin, A., et al., *HIV-1 Tat protein mimicry of chemokines*. *Proc Natl Acad Sci U S A*, 1998. **95**(22): p. 13153-8.

64. Vogel, B.E., et al., *A novel integrin specificity exemplified by binding of the alpha v beta 5 integrin to the basic domain of the HIV Tat protein and vitronectin*. J Cell Biol, 1993. **121**(2): p. 461-8.
65. Malim, M.H., et al., *The HIV-1 rev trans-activator acts through a structured target sequence to activate nuclear export of unspliced viral mRNA*. Nature, 1989. **338**(6212): p. 254-7.
66. Cochrane, A.W., C.H. Chen, and C.A. Rosen, *Specific interaction of the human immunodeficiency virus Rev protein with a structured region in the env mRNA*. Proc Natl Acad Sci U S A, 1990. **87**(3): p. 1198-202.
67. Strebel, K., *Virus-host interactions: role of HIV proteins Vif, Tat, and Rev*. AIDS, 2003. **17 Suppl 4**: p. S25-34.
68. Garcia, J.V. and A.D. Miller, *Serine phosphorylation-independent downregulation of cell-surface CD4 by nef*. Nature, 1991. **350**(6318): p. 508-11.
69. Schwartz, O., et al., *Endocytosis of major histocompatibility complex class I molecules is induced by the HIV-1 Nef protein*. Nat Med, 1996. **2**(3): p. 338-42.
70. Stove, V., et al., *Human immunodeficiency virus Nef induces rapid internalization of the T-cell coreceptor CD8alpha*. J Virol, 2005. **79**(17): p. 11422-33.
71. Swigut, T., N. Shohdy, and J. Skowronski, *Mechanism for down-regulation of CD28 by Nef*. EMBO J, 2001. **20**(7): p. 1593-604.
72. Schindler, M., et al., *Down-modulation of mature major histocompatibility complex class II and up-regulation of invariant chain cell surface expression are well-conserved functions of human and simian immunodeficiency virus nef alleles*. J Virol, 2003. **77**(19): p. 10548-56.
73. Fouchier, R.A., et al., *Interaction of the human immunodeficiency virus type 1 Vpr protein with the nuclear pore complex*. J Virol, 1998. **72**(7): p. 6004-13.
74. Subramanian, R.A., et al., *Human immunodeficiency virus type 1 Vpr localization: nuclear transport of a viral protein modulated by a putative amphipathic helical structure and its relevance to biological activity*. J Mol Biol, 1998. **278**(1): p. 13-30.

75. Goh, W.C., et al., *HIV-1 Vpr increases viral expression by manipulation of the cell cycle: a mechanism for selection of Vpr in vivo*. *Nat Med*, 1998. **4**(1): p. 65-71.
76. Kewalramani, V.N., et al., *Protein stability influences human immunodeficiency virus type 2 Vpr virion incorporation and cell cycle effect*. *Virology*, 1996. **218**(2): p. 326-34.
77. Andersen, J.L., E. Le Rouzic, and V. Planelles, *HIV-1 Vpr: mechanisms of G2 arrest and apoptosis*. *Exp Mol Pathol*, 2008. **85**(1): p. 2-10.
78. Liu, R., et al., *HIV-1 Vpr stimulates NF-kappaB and AP-1 signaling by activating TAK1*. *Retrovirology*, 2014. **11**: p. 45.
79. Ayyavoo, V., et al., *HIV-1 Vpr suppresses immune activation and apoptosis through regulation of nuclear factor kappa B*. *Nat Med*, 1997. **3**(10): p. 1117-23.
80. Strebel, K., et al., *The HIV 'A' (sor) gene product is essential for virus infectivity*. *Nature*, 1987. **328**(6132): p. 728-30.
81. Mariani, R., et al., *Species-specific exclusion of APOBEC3G from HIV-1 virions by Vif*. *Cell*, 2003. **114**(1): p. 21-31.
82. Mangeat, B., et al., *Broad antiretroviral defence by human APOBEC3G through lethal editing of nascent reverse transcripts*. *Nature*, 2003. **424**(6944): p. 99-103.
83. Neil, S.J., T. Zang, and P.D. Bieniasz, *Tetherin inhibits retrovirus release and is antagonized by HIV-1 Vpu*. *Nature*, 2008. **451**(7177): p. 425-30.
84. Galao, R.P., et al., *Innate sensing of HIV-1 assembly by Tetherin induces NFkappaB-dependent proinflammatory responses*. *Cell Host Microbe*, 2012. **12**(5): p. 633-44.
85. Bour, S., et al., *The envelope glycoprotein of human immunodeficiency virus type 2 enhances viral particle release: a Vpu-like factor?* *J Virol*, 1996. **70**(2): p. 820-9.
86. Zhang, F., et al., *Nef proteins from simian immunodeficiency viruses are tetherin antagonists*. *Cell Host Microbe*, 2009. **6**(1): p. 54-67.
87. Willey, R.L., et al., *Human immunodeficiency virus type 1 Vpu protein regulates the formation of intracellular gp160-CD4 complexes*. *J Virol*, 1992. **66**(1): p. 226-34.
88. Tristem, M., et al., *Origin of vpx in lentiviruses*. *Nature*, 1990. **347**(6291): p. 341-2.
89. Guyader, M., et al., *VPX mutants of HIV-2 are infectious in established cell lines but display a severe defect in peripheral blood lymphocytes*. *EMBO J*, 1989. **8**(4): p. 1169-75.

90. Baldauf, H.M., et al., *SAMHD1 restricts HIV-1 infection in resting CD4(+) T cells*. Nat Med, 2012. **18**(11): p. 1682-7.
91. Descours, B., et al., *SAMHD1 restricts HIV-1 reverse transcription in quiescent CD4(+) T-cells*. Retrovirology, 2012. **9**: p. 87.
92. Miller, R.H., *Human immunodeficiency virus may encode a novel protein on the genomic DNA plus strand*. Science, 1988. **239**(4846): p. 1420-2.
93. Affram, Y., et al., *The HIV-1 Antisense Protein ASP Is a Transmembrane Protein of the Cell Surface and an Integral Protein of the Viral Envelope*. J Virol, 2019. **93**(21).
94. Torresilla, C., et al., *Detection of the HIV-1 minus-strand-encoded antisense protein and its association with autophagy*. J Virol, 2013. **87**(9): p. 5089-105.
95. Langer, S. and D. Sauter, *Unusual Fusion Proteins of HIV-1*. Front Microbiol, 2016. **7**: p. 2152.
96. Sannier, G., M. Dube, and D.E. Kaufmann, *Single-Cell Technologies Applied to HIV-1 Research: Reaching Maturity*. Front Microbiol, 2020. **11**: p. 297.
97. Wilen, C.B., J.C. Tilton, and R.W. Doms, *HIV: cell binding and entry*. Cold Spring Harb Perspect Med, 2012. **2**(8).
98. Craigie, R. and F.D. Bushman, *HIV DNA integration*. Cold Spring Harb Perspect Med, 2012. **2**(7): p. a006890.
99. Suzuki, Y. and R. Craigie, *The road to chromatin - nuclear entry of retroviruses*. Nat Rev Microbiol, 2007. **5**(3): p. 187-96.
100. Wu, Y. and J.W. Marsh, *Selective transcription and modulation of resting T cell activity by preintegrated HIV DNA*. Science, 2001. **293**(5534): p. 1503-6.
101. Freed, E.O., *HIV-1 assembly, release and maturation*. Nat Rev Microbiol, 2015. **13**(8): p. 484-96.
102. Sundquist, W.I. and H.G. Krausslich, *HIV-1 assembly, budding, and maturation*. Cold Spring Harb Perspect Med, 2012. **2**(7): p. a006924.
103. Nobile, C., et al., *Covert human immunodeficiency virus replication in dendritic cells and in DC-SIGN-expressing cells promotes long-term transmission to lymphocytes*. J Virol, 2005. **79**(9): p. 5386-99.

104. Arrighi, J.F., et al., *DC-SIGN-mediated infectious synapse formation enhances X4 HIV-1 transmission from dendritic cells to T cells*. J Exp Med, 2004. **200**(10): p. 1279-88.
105. Geijtenbeek, T.B., et al., *DC-SIGN, a dendritic cell-specific HIV-1-binding protein that enhances trans-infection of T cells*. Cell, 2000. **100**(5): p. 587-97.
106. Jolly, C., et al., *HIV-1 cell to cell transfer across an Env-induced, actin-dependent synapse*. J Exp Med, 2004. **199**(2): p. 283-93.
107. Arthos, J., et al., *HIV-1 envelope protein binds to and signals through integrin alpha4beta7, the gut mucosal homing receptor for peripheral T cells*. Nat Immunol, 2008. **9**(3): p. 301-9.
108. Cicala, C., et al., *The integrin alpha4beta7 forms a complex with cell-surface CD4 and defines a T-cell subset that is highly susceptible to infection by HIV-1*. Proc Natl Acad Sci U S A, 2009. **106**(49): p. 20877-82.
109. Roderiquez, G., et al., *Mediation of human immunodeficiency virus type 1 binding by interaction of cell surface heparan sulfate proteoglycans with the V3 region of envelope gp120-gp41*. J Virol, 1995. **69**(4): p. 2233-9.
110. Saphire, A.C., et al., *Syndecans serve as attachment receptors for human immunodeficiency virus type 1 on macrophages*. J Virol, 2001. **75**(19): p. 9187-200.
111. Klasse, P.J., *The molecular basis of HIV entry*. Cell Microbiol, 2012. **14**(8): p. 1183-92.
112. Marsh, M. and A. Helenius, *Virus entry: open sesame*. Cell, 2006. **124**(4): p. 729-40.
113. Miyachi, K., et al., *HIV enters cells via endocytosis and dynamin-dependent fusion with endosomes*. Cell, 2009. **137**(3): p. 433-44.
114. Fassati, A. and S.P. Goff, *Characterization of intracellular reverse transcription complexes of human immunodeficiency virus type 1*. J Virol, 2001. **75**(8): p. 3626-35.
115. Warrillow, D., G. Tachedjian, and D. Harrich, *Maturation of the HIV reverse transcription complex: putting the jigsaw together*. Rev Med Virol, 2009. **19**(6): p. 324-37.
116. Li, D., et al., *Specific Interaction between eEF1A and HIV RT Is Critical for HIV-1 Reverse Transcription and a Potential Anti-HIV Target*. PLoS Pathog, 2015. **11**(12): p. e1005289.
117. Bukrinskaya, A., et al., *Establishment of a functional human immunodeficiency virus type 1 (HIV-1) reverse transcription complex involves the cytoskeleton*. J Exp Med, 1998. **188**(11): p. 2113-25.

118. Arhel, N., et al., *Quantitative four-dimensional tracking of cytoplasmic and nuclear HIV-1 complexes*. Nat Methods, 2006. **3**(10): p. 817-24.
119. Sabo, Y., et al., *HIV-1 induces the formation of stable microtubules to enhance early infection*. Cell Host Microbe, 2013. **14**(5): p. 535-46.
120. Lukic, Z., et al., *HIV-1 uncoating is facilitated by dynein and kinesin 1*. J Virol, 2014. **88**(23): p. 13613-25.
121. Pawlica, P. and L. Berthoux, *Cytoplasmic dynein promotes HIV-1 uncoating*. Viruses, 2014. **6**(11): p. 4195-211.
122. Campbell, E.M. and T.J. Hope, *HIV-1 capsid: the multifaceted key player in HIV-1 infection*. Nat Rev Microbiol, 2015. **13**(8): p. 471-83.
123. Pante, N. and M. Kann, *Nuclear pore complex is able to transport macromolecules with diameters of about 39 nm*. Mol Biol Cell, 2002. **13**(2): p. 425-34.
124. Yang, R., et al., *Second-site suppressors of HIV-1 capsid mutations: restoration of intracellular activities without correction of intrinsic capsid stability defects*. Retrovirology, 2012. **9**: p. 30.
125. Hulme, A.E., O. Perez, and T.J. Hope, *Complementary assays reveal a relationship between HIV-1 uncoating and reverse transcription*. Proc Natl Acad Sci U S A, 2011. **108**(24): p. 9975-80.
126. Xu, H., et al., *Evidence for biphasic uncoating during HIV-1 infection from a novel imaging assay*. Retrovirology, 2013. **10**: p. 70.
127. Lahaye, X., et al., *The capsids of HIV-1 and HIV-2 determine immune detection of the viral cDNA by the innate sensor cGAS in dendritic cells*. Immunity, 2013. **39**(6): p. 1132-42.
128. Rasaiyaah, J., et al., *HIV-1 evades innate immune recognition through specific cofactor recruitment*. Nature, 2013. **503**(7476): p. 402-405.
129. Fernandez, J., et al., *Transportin-1 binds to the HIV-1 capsid via a nuclear localization signal and triggers uncoating*. Nat Microbiol, 2019. **4**(11): p. 1840-1850.
130. Krupkin, M., et al., *Advances in understanding the initiation of HIV-1 reverse transcription*. Curr Opin Struct Biol, 2020. **65**: p. 175-183.

131. Matreyek, K.A., et al., *Nucleoporin NUP153 phenylalanine-glycine motifs engage a common binding pocket within the HIV-1 capsid protein to mediate lentiviral infectivity*. PLoS Pathog, 2013. **9**(10): p. e1003693.
132. Schaller, T., et al., *HIV-1 capsid-cyclophilin interactions determine nuclear import pathway, integration targeting and replication efficiency*. PLoS Pathog, 2011. **7**(12): p. e1002439.
133. Lee, K., et al., *Flexible use of nuclear import pathways by HIV-1*. Cell Host Microbe, 2010. **7**(3): p. 221-33.
134. Cohn, L.B., et al., *HIV-1 integration landscape during latent and active infection*. Cell, 2015. **160**(3): p. 420-32.
135. Marini, B., et al., *Nuclear architecture dictates HIV-1 integration site selection*. Nature, 2015. **521**(7551): p. 227-31.
136. Schroder, A.R., et al., *HIV-1 integration in the human genome favors active genes and local hotspots*. Cell, 2002. **110**(4): p. 521-9.
137. Maertens, G.N., A.N. Engelman, and P. Cherepanov, *Structure and function of retroviral integrase*. Nat Rev Microbiol, 2022. **20**(1): p. 20-34.
138. Sloan, R.D. and M.A. Wainberg, *The role of unintegrated DNA in HIV infection*. Retrovirology, 2011. **8**: p. 52.
139. Hamid, F.B., J. Kim, and C.G. Shin, *Distribution and fate of HIV-1 unintegrated DNA species: a comprehensive update*. AIDS Res Ther, 2017. **14**(1): p. 9.
140. Karn, J. and C.M. Stoltzfus, *Transcriptional and posttranscriptional regulation of HIV-1 gene expression*. Cold Spring Harb Perspect Med, 2012. **2**(2): p. a006916.
141. Ohlmann, T., C. Mengardi, and M. Lopez-Lastra, *Translation initiation of the HIV-1 mRNA*. Translation (Austin), 2014. **2**(2): p. e960242.
142. Bolinger, C. and K. Boris-Lawrie, *Mechanisms employed by retroviruses to exploit host factors for translational control of a complicated proteome*. Retrovirology, 2009. **6**: p. 8.
143. Stoltzfus, C.M., *Chapter 1. Regulation of HIV-1 alternative RNA splicing and its role in virus replication*. Adv Virus Res, 2009. **74**: p. 1-40.
144. Wright, E.R., et al., *Electron cryotomography of immature HIV-1 virions reveals the structure of the CA and SP1 Gag shells*. EMBO J, 2007. **26**(8): p. 2218-26.

145. Briggs, J.A., et al., *Structure and assembly of immature HIV*. Proc Natl Acad Sci U S A, 2009. **106**(27): p. 11090-5.
146. Welker, L., J.C. Paillart, and S. Bernacchi, *Importance of Viral Late Domains in Budding and Release of Enveloped RNA Viruses*. Viruses, 2021. **13**(8).
147. Engelman, A. and P. Cherepanov, *The structural biology of HIV-1: mechanistic and therapeutic insights*. Nat Rev Microbiol, 2012. **10**(4): p. 279-90.
148. Poropatchik, K. and D.J. Sullivan, Jr., *Human immunodeficiency virus type 1 long-term non-progressors: the viral, genetic and immunological basis for disease non-progression*. J Gen Virol, 2011. **92**(Pt 2): p. 247-68.
149. Deeks, S.G. and B.D. Walker, *Human immunodeficiency virus controllers: mechanisms of durable virus control in the absence of antiretroviral therapy*. Immunity, 2007. **27**(3): p. 406-16.
150. Grossman, Z., et al., *Pathogenesis of HIV infection: what the virus spares is as important as what it destroys*. Nat Med, 2006. **12**(3): p. 289-95.
151. Boily, M.C., et al., *Heterosexual risk of HIV-1 infection per sexual act: systematic review and meta-analysis of observational studies*. Lancet Infect Dis, 2009. **9**(2): p. 118-29.
152. Joseph, S.B., et al., *Bottlenecks in HIV-1 transmission: insights from the study of founder viruses*. Nat Rev Microbiol, 2015. **13**(7): p. 414-25.
153. Mattapallil, J.J., et al., *Massive infection and loss of memory CD4+ T cells in multiple tissues during acute SIV infection*. Nature, 2005. **434**(7037): p. 1093-7.
154. Abel, K., et al., *Temporal and anatomic relationship between virus replication and cytokine gene expression after vaginal simian immunodeficiency virus infection*. J Virol, 2005. **79**(19): p. 12164-72.
155. Sandler, N.G., et al., *Type I interferon responses in rhesus macaques prevent SIV infection and slow disease progression*. Nature, 2014. **511**(7511): p. 601-5.
156. Borrow, P., et al., *Virus-specific CD8+ cytotoxic T-lymphocyte activity associated with control of viremia in primary human immunodeficiency virus type 1 infection*. J Virol, 1994. **68**(9): p. 6103-10.

157. Fiebig, E.W., et al., *Dynamics of HIV viremia and antibody seroconversion in plasma donors: implications for diagnosis and staging of primary HIV infection*. AIDS, 2003. **17**(13): p. 1871-9.
158. McMichael, A.J., et al., *The immune response during acute HIV-1 infection: clues for vaccine development*. Nat Rev Immunol, 2010. **10**(1): p. 11-23.
159. Finkel, T.H., et al., *Apoptosis occurs predominantly in bystander cells and not in productively infected cells of HIV- and SIV-infected lymph nodes*. Nat Med, 1995. **1**(2): p. 129-34.
160. Doitsh, G., et al., *Cell death by pyroptosis drives CD4 T-cell depletion in HIV-1 infection*. Nature, 2014. **505**(7484): p. 509-14.
161. Lamkanfi, M. and V.M. Dixit, *Manipulation of host cell death pathways during microbial infections*. Cell Host Microbe, 2010. **8**(1): p. 44-54.
162. Bergsbaken, T., S.L. Fink, and B.T. Cookson, *Pyroptosis: host cell death and inflammation*. Nat Rev Microbiol, 2009. **7**(2): p. 99-109.
163. Gougeon, M.L., *To kill or be killed: how HIV exhausts the immune system*. Cell Death Differ, 2005. **12 Suppl 1**: p. 845-54.
164. Ndhlovu, Z.M., et al., *Magnitude and Kinetics of CD8+ T Cell Activation during Hyperacute HIV Infection Impact Viral Set Point*. Immunity, 2015. **43**(3): p. 591-604.
165. Wherry, E.J., *T cell exhaustion*. Nat Immunol, 2011. **12**(6): p. 492-9.
166. Yi, J.S., M.A. Cox, and A.J. Zajac, *T-cell exhaustion: characteristics, causes and conversion*. Immunology, 2010. **129**(4): p. 474-81.
167. Day, C.L., et al., *PD-1 expression on HIV-specific T cells is associated with T-cell exhaustion and disease progression*. Nature, 2006. **443**(7109): p. 350-4.
168. Kaufmann, D.E., et al., *Upregulation of CTLA-4 by HIV-specific CD4+ T cells correlates with disease progression and defines a reversible immune dysfunction*. Nat Immunol, 2007. **8**(11): p. 1246-54.
169. Jones, R.B. and B.D. Walker, *HIV-specific CD8(+) T cells and HIV eradication*. J Clin Invest, 2016. **126**(2): p. 455-63.

170. Phillips, R.E., et al., *Human immunodeficiency virus genetic variation that can escape cytotoxic T cell recognition*. *Nature*, 1991. **354**(6353): p. 453-9.
171. Cmons, M., *U.S. Approves Sale of AZT to AIDS Patients*, in *Los Angeles Times*. 1987.
172. Rhee, S.Y., et al., *HIV-1 Protease, Reverse Transcriptase, and Integrase Variation*. *J Virol*, 2016. **90**(13): p. 6058-6070.
173. Arts, E.J. and D.J. Hazuda, *HIV-1 antiretroviral drug therapy*. *Cold Spring Harb Perspect Med*, 2012. **2**(4): p. a007161.
174. Cihlar, T. and A.S. Ray, *Nucleoside and nucleotide HIV reverse transcriptase inhibitors: 25 years after zidovudine*. *Antiviral Res*, 2010. **85**(1): p. 39-58.
175. Pau, A.K. and J.M. George, *Antiretroviral therapy: current drugs*. *Infect Dis Clin North Am*, 2014. **28**(3): p. 371-402.
176. Hazuda, D.J., et al., *Inhibitors of strand transfer that prevent integration and inhibit HIV-1 replication in cells*. *Science*, 2000. **287**(5453): p. 646-50.
177. Connor, R.I., et al., *Change in coreceptor use correlates with disease progression in HIV-1-infected individuals*. *J Exp Med*, 1997. **185**(4): p. 621-8.
178. Zhang, C., et al., *Discoveries and developments of CXCR4-targeted HIV-1 entry inhibitors*. *Exp Biol Med (Maywood)*, 2020. **245**(5): p. 477-485.
179. Jacobson, J.M., et al., *Safety, pharmacokinetics, and antiretroviral activity of multiple doses of ibalizumab (formerly TNX-355), an anti-CD4 monoclonal antibody, in human immunodeficiency virus type 1-infected adults*. *Antimicrob Agents Chemother*, 2009. **53**(2): p. 450-7.
180. Kozal, M., et al., *Fostemsavir in Adults with Multidrug-Resistant HIV-1 Infection*. *N Engl J Med*, 2020. **382**(13): p. 1232-1243.
181. Richard, J., et al., *Temsavir blocks the immunomodulatory activities of HIV-1 soluble gp120*. *Cell Chem Biol*, 2023.
182. Segal-Maurer, S., et al., *Capsid Inhibition with Lenacapavir in Multidrug-Resistant HIV-1 Infection*. *N Engl J Med*, 2022. **386**(19): p. 1793-1803.
183. Bester, S.M., et al., *Structural and mechanistic bases for a potent HIV-1 capsid inhibitor*. *Science*, 2020. **370**(6514): p. 360-364.

184. Perelson, A.S., et al., *HIV-1 dynamics in vivo: virion clearance rate, infected cell life-span, and viral generation time*. Science, 1996. **271**(5255): p. 1582-6.
185. Perelson, A.S., et al., *Decay characteristics of HIV-1-infected compartments during combination therapy*. Nature, 1997. **387**(6629): p. 188-91.
186. International, H.I.V.C.S., et al., *The major genetic determinants of HIV-1 control affect HLA class I peptide presentation*. Science, 2010. **330**(6010): p. 1551-7.
187. Finzi, D., et al., *Identification of a reservoir for HIV-1 in patients on highly active antiretroviral therapy*. Science, 1997. **278**(5341): p. 1295-300.
188. Finzi, D., et al., *Latent infection of CD4+ T cells provides a mechanism for lifelong persistence of HIV-1, even in patients on effective combination therapy*. Nat Med, 1999. **5**(5): p. 512-7.
189. Chun, T.W., et al., *Quantification of latent tissue reservoirs and total body viral load in HIV-1 infection*. Nature, 1997. **387**(6629): p. 183-8.
190. Hermankova, M., et al., *Analysis of human immunodeficiency virus type 1 gene expression in latently infected resting CD4+ T lymphocytes in vivo*. J Virol, 2003. **77**(13): p. 7383-92.
191. Yukl, S.A., et al., *HIV latency in isolated patient CD4(+) T cells may be due to blocks in HIV transcriptional elongation, completion, and splicing*. Sci Transl Med, 2018. **10**(430).
192. Akiyama, H., et al., *HIV-1 intron-containing RNA expression induces innate immune activation and T cell dysfunction*. Nat Commun, 2018. **9**(1): p. 3450.
193. McCauley, S.M., et al., *Intron-containing RNA from the HIV-1 provirus activates type I interferon and inflammatory cytokines*. Nat Commun, 2018. **9**(1): p. 5305.
194. Van Lint, C., S. Bouchat, and A. Marcello, *HIV-1 transcription and latency: an update*. Retrovirology, 2013. **10**: p. 67.
195. Stevenson, M., et al., *HIV-1 replication is controlled at the level of T cell activation and proviral integration*. EMBO J, 1990. **9**(5): p. 1551-60.
196. Zhou, Y., et al., *Kinetics of human immunodeficiency virus type 1 decay following entry into resting CD4+ T cells*. J Virol, 2005. **79**(4): p. 2199-210.

197. Petitjean, G., et al., *Unintegrated HIV-1 provides an inducible and functional reservoir in untreated and highly active antiretroviral therapy-treated patients*. *Retrovirology*, 2007. **4**: p. 60.
198. Richetta, C., et al., *Two-long terminal repeat (LTR) DNA circles are a substrate for HIV-1 integrase*. *J Biol Chem*, 2019. **294**(20): p. 8286-8295.
199. Roux, H.M., et al., *DNA ultra-sensitive quantification, a technology for studying HIV unintegrated linear DNA*. *Cell Reports Methods*, 2023. **3**(4): p. 100443.
200. Fisher, W.G., et al., *NFAT and NFkappaB activation in T lymphocytes: a model of differential activation of gene expression*. *Ann Biomed Eng*, 2006. **34**(11): p. 1712-28.
201. Di Primio, C., et al., *Single-cell imaging of HIV-1 provirus (SCIP)*. *Proc Natl Acad Sci U S A*, 2013. **110**(14): p. 5636-41.
202. Jordan, A., P. Defechereux, and E. Verdin, *The site of HIV-1 integration in the human genome determines basal transcriptional activity and response to Tat transactivation*. *EMBO J*, 2001. **20**(7): p. 1726-38.
203. Battivelli, E., et al., *Distinct chromatin functional states correlate with HIV latency reactivation in infected primary CD4(+) T cells*. *Elife*, 2018. **7**.
204. Maldarelli, F., et al., *HIV latency. Specific HIV integration sites are linked to clonal expansion and persistence of infected cells*. *Science*, 2014. **345**(6193): p. 179-83.
205. Kopp, F. and J.T. Mendell, *Functional Classification and Experimental Dissection of Long Noncoding RNAs*. *Cell*, 2018. **172**(3): p. 393-407.
206. Latos, P.A., et al., *Airn transcriptional overlap, but not its lncRNA products, induces imprinted Igf2r silencing*. *Science*, 2012. **338**(6113): p. 1469-72.
207. Gonzalez, I., et al., *A lncRNA regulates alternative splicing via establishment of a splicing-specific chromatin signature*. *Nat Struct Mol Biol*, 2015. **22**(5): p. 370-6.
208. Biswas, S., et al., *Differentially expressed host long intergenic noncoding RNA and mRNA in HIV-1 and HIV-2 infection*. *Sci Rep*, 2018. **8**(1): p. 2546.
209. Zhang, Q., et al., *NEAT1 long noncoding RNA and paraspeckle bodies modulate HIV-1 posttranscriptional expression*. *mBio*, 2013. **4**(1): p. e00596-12.

210. Willingham, A.T., et al., *A strategy for probing the function of noncoding RNAs finds a repressor of NFAT*. *Science*, 2005. **309**(5740): p. 1570-3.
211. Li, J., et al., *Long noncoding RNA NRON contributes to HIV-1 latency by specifically inducing tat protein degradation*. *Nat Commun*, 2016. **7**: p. 11730.
212. D'Orso, I. and A.D. Frankel, *Tat acetylation modulates assembly of a viral-host RNA-protein transcription complex*. *Proc Natl Acad Sci U S A*, 2009. **106**(9): p. 3101-6.
213. Pagans, S., et al., *SIRT1 regulates HIV transcription via Tat deacetylation*. *PLoS Biol*, 2005. **3**(2): p. e41.
214. Yang, Z., et al., *Recruitment of P-TEFb for stimulation of transcriptional elongation by the bromodomain protein Brd4*. *Mol Cell*, 2005. **19**(4): p. 535-45.
215. Cherrier, T., et al., *CTIP2 is a negative regulator of P-TEFb*. *Proc Natl Acad Sci U S A*, 2013. **110**(31): p. 12655-60.
216. Kauder, S.E., et al., *Epigenetic regulation of HIV-1 latency by cytosine methylation*. *PLoS Pathog*, 2009. **5**(6): p. e1000495.
217. Trejbalova, K., et al., *Development of 5' LTR DNA methylation of latent HIV-1 provirus in cell line models and in long-term-infected individuals*. *Clin Epigenetics*, 2016. **8**: p. 19.
218. Matalon, S., T.A. Rasmussen, and C.A. Dinarello, *Histone deacetylase inhibitors for purging HIV-1 from the latent reservoir*. *Mol Med*, 2011. **17**(5-6): p. 466-72.
219. du Chene, I., et al., *Suv39H1 and HP1gamma are responsible for chromatin-mediated HIV-1 transcriptional silencing and post-integration latency*. *EMBO J*, 2007. **26**(2): p. 424-35.
220. Bleul, C.C., et al., *The HIV coreceptors CXCR4 and CCR5 are differentially expressed and regulated on human T lymphocytes*. *Proc Natl Acad Sci U S A*, 1997. **94**(5): p. 1925-30.
221. Brooks, D.G., et al., *Generation of HIV latency during thymopoiesis*. *Nat Med*, 2001. **7**(4): p. 459-64.
222. Donahue, D.A. and M.A. Wainberg, *Cellular and molecular mechanisms involved in the establishment of HIV-1 latency*. *Retrovirology*, 2013. **10**: p. 11.
223. Wightman, F., et al., *Both CD31(+) and CD31(-) naive CD4(+) T cells are persistent HIV type 1-infected reservoirs in individuals receiving antiretroviral therapy*. *J Infect Dis*, 2010. **202**(11): p. 1738-48.

224. Fabre-Mersseman, V., et al., *CD4(+) recent thymic emigrants are infected by HIV in vivo, implication for pathogenesis*. AIDS, 2011. **25**(9): p. 1153-62.
225. Chomont, N., et al., *HIV reservoir size and persistence are driven by T cell survival and homeostatic proliferation*. Nat Med, 2009. **15**(8): p. 893-900.
226. Simonetti, F.R., et al., *Antigen-driven clonal selection shapes the persistence of HIV-1-infected CD4+ T cells in vivo*. J Clin Invest, 2021. **131**(3).
227. Clark, I.C., et al., *HIV silencing and cell survival signatures in infected T cell reservoirs*. Nature, 2023. **614**(7947): p. 318-325.
228. Sun, W., et al., *Phenotypic signatures of immune selection in HIV-1 reservoir cells*. Nature, 2023. **614**(7947): p. 309-317.
229. Shan, L., et al., *Transcriptional Reprogramming during Effector-to-Memory Transition Renders CD4(+) T Cells Permissive for Latent HIV-1 Infection*. Immunity, 2017. **47**(4): p. 766-775 e3.
230. Lassen, K.G., J.R. Bailey, and R.F. Siliciano, *Analysis of human immunodeficiency virus type 1 transcriptional elongation in resting CD4+ T cells in vivo*. J Virol, 2004. **78**(17): p. 9105-14.
231. DeMaster, L.K., et al., *A Subset of CD4/CD8 Double-Negative T Cells Expresses HIV Proteins in Patients on Antiretroviral Therapy*. J Virol, 2015. **90**(5): p. 2165-79.
232. Plantin, J., M. Massanella, and N. Chomont, *Inducible HIV RNA transcription assays to measure HIV persistence: pros and cons of a compromise*. Retrovirology, 2018. **15**(1): p. 9.
233. Dube, M., et al., *Spontaneous HIV expression during suppressive ART is associated with the magnitude and function of HIV-specific CD4(+) and CD8(+) T cells*. Cell Host Microbe, 2023. **31**(9): p. 1507-1522 e5.
234. Estes, J.D., et al., *Defining total-body AIDS-virus burden with implications for curative strategies*. Nat Med, 2017. **23**(11): p. 1271-1276.
235. Fenwick, C., et al., *T-cell exhaustion in HIV infection*. Immunol Rev, 2019. **292**(1): p. 149-163.
236. Avettand-Fenoel, V., et al., *Total HIV-1 DNA, a Marker of Viral Reservoir Dynamics with Clinical Implications*. Clin Microbiol Rev, 2016. **29**(4): p. 859-80.

237. Cardozo, E.F., et al., *Treatment with integrase inhibitor suggests a new interpretation of HIV RNA decay curves that reveals a subset of cells with slow integration*. PLoS Pathog, 2017. **13**(7): p. e1006478.
238. Bruner, K.M., et al., *Defective proviruses rapidly accumulate during acute HIV-1 infection*. Nat Med, 2016. **22**(9): p. 1043-9.
239. Ho, Y.C., et al., *Replication-competent noninduced proviruses in the latent reservoir increase barrier to HIV-1 cure*. Cell, 2013. **155**(3): p. 540-51.
240. Deeks, S.G., et al., *International AIDS Society global scientific strategy: towards an HIV cure 2016*. Nat Med, 2016. **22**(8): p. 839-50.
241. Laird, G.M., et al., *Rapid quantification of the latent reservoir for HIV-1 using a viral outgrowth assay*. PLoS Pathog, 2013. **9**(5): p. e1003398.
242. Bachmann, N., et al., *Determinants of HIV-1 reservoir size and long-term dynamics during suppressive ART*. Nat Commun, 2019. **10**(1): p. 3193.
243. Bruner, K.M., N.N. Hosmane, and R.F. Siliciano, *Towards an HIV-1 cure: measuring the latent reservoir*. Trends Microbiol, 2015. **23**(4): p. 192-203.
244. Kuniholm, J., C. Coote, and A.J. Henderson, *Defective HIV-1 genomes and their potential impact on HIV pathogenesis*. Retrovirology, 2022. **19**(1): p. 13.
245. Cuevas, J.M., et al., *Extremely High Mutation Rate of HIV-1 In Vivo*. PLoS Biol, 2015. **13**(9): p. e1002251.
246. Hiener, B., et al., *Identification of Genetically Intact HIV-1 Proviruses in Specific CD4(+) T Cells from Effectively Treated Participants*. Cell Rep, 2017. **21**(3): p. 813-822.
247. Bruner, K.M., et al., *A quantitative approach for measuring the reservoir of latent HIV-1 proviruses*. Nature, 2019. **566**(7742): p. 120-125.
248. Imamichi, H., et al., *Defective HIV-1 proviruses produce viral proteins*. Proc Natl Acad Sci U S A, 2020. **117**(7): p. 3704-3710.
249. Pollack, R.A., et al., *Defective HIV-1 Proviruses Are Expressed and Can Be Recognized by Cytotoxic T Lymphocytes, which Shape the Proviral Landscape*. Cell Host Microbe, 2017. **21**(4): p. 494-506 e4.

250. Pasternak, A.O. and B. Berkhout, *What do we measure when we measure cell-associated HIV RNA*. *Retrovirology*, 2018. **15**(1): p. 13.
251. Procopio, F.A., et al., *A Novel Assay to Measure the Magnitude of the Inducible Viral Reservoir in HIV-infected Individuals*. *EBioMedicine*, 2015. **2**(8): p. 874-83.
252. Cohn, L.B., et al., *Clonal CD4(+) T cells in the HIV-1 latent reservoir display a distinct gene profile upon reactivation*. *Nat Med*, 2018. **24**(5): p. 604-609.
253. Pardons, M., et al., *Latency-Reversing Agents Induce Differential Responses in Distinct Memory CD4 T Cell Subsets in Individuals on Antiretroviral Therapy*. *Cell Rep*, 2019. **29**(9): p. 2783-2795 e5.
254. Baxter, A.E., et al., *Single-Cell Characterization of Viral Translation-Competent Reservoirs in HIV-Infected Individuals*. *Cell Host Microbe*, 2016. **20**(3): p. 368-380.
255. Baxter, A.E., et al., *Multiparametric characterization of rare HIV-infected cells using an RNA-flow FISH technique*. *Nat Protoc*, 2017. **12**(10): p. 2029-2049.
256. Grau-Exposito, J., et al., *A Novel Single-Cell FISH-Flow Assay Identifies Effector Memory CD4(+) T cells as a Major Niche for HIV-1 Transcription in HIV-Infected Patients*. *mBio*, 2017. **8**(4).
257. Venanzi Rullo, E., et al., *Genetic Evidence That Naive T Cells Can Contribute Significantly to the Human Immunodeficiency Virus Intact Reservoir: Time to Re-evaluate Their Role*. *Clin Infect Dis*, 2019. **69**(12): p. 2236-2237.
258. Zerbato, J.M., et al., *Naive CD4+ T Cells Harbor a Large Inducible Reservoir of Latent, Replication-competent Human Immunodeficiency Virus Type 1*. *Clin Infect Dis*, 2019. **69**(11): p. 1919-1925.
259. Grau-Exposito, J., et al., *Latency reversal agents affect differently the latent reservoir present in distinct CD4+ T subpopulations*. *PLoS Pathog*, 2019. **15**(8): p. e1007991.
260. Kulpa, D.A. and N. Chomont, *HIV persistence in the setting of antiretroviral therapy: when, where and how does HIV hide?* *J Virus Erad*, 2015. **1**(2): p. 59-66.
261. Lee, G.Q., et al., *Clonal expansion of genome-intact HIV-1 in functionally polarized Th1 CD4+ T cells*. *J Clin Invest*, 2017. **127**(7): p. 2689-2696.

262. Grossman, Z., et al., *'Rinse and Replace': Boosting T Cell Turnover To Reduce HIV-1 Reservoirs*. Trends Immunol, 2020. **41**(6): p. 466-480.
263. Delobel, P., et al., *Persistence of distinct HIV-1 populations in blood monocytes and naive and memory CD4 T cells during prolonged suppressive HAART*. AIDS, 2005. **19**(16): p. 1739-50.
264. Lambotte, O., et al., *Detection of infectious HIV in circulating monocytes from patients on prolonged highly active antiretroviral therapy*. J Acquir Immune Defic Syndr, 2000. **23**(2): p. 114-9.
265. Triques, K. and M. Stevenson, *Characterization of restrictions to human immunodeficiency virus type 1 infection of monocytes*. J Virol, 2004. **78**(10): p. 5523-7.
266. Cattin, A., et al., *HIV-1 is rarely detected in blood and colon myeloid cells during viral-suppressive antiretroviral therapy*. AIDS, 2019. **33**(8): p. 1293-1306.
267. Ganor, Y., et al., *HIV-1 reservoirs in urethral macrophages of patients under suppressive antiretroviral therapy*. Nat Microbiol, 2019. **4**(4): p. 633-644.
268. Ko, A., et al., *Macrophages but not Astrocytes Harbor HIV DNA in the Brains of HIV-1-Infected Aviremic Individuals on Suppressing Antiretroviral Therapy*. J Neuroimmune Pharmacol, 2019. **14**(1): p. 110-119.
269. Cribbs, S.K., et al., *Healthy HIV-1-infected individuals on highly active antiretroviral therapy harbor HIV-1 in their alveolar macrophages*. AIDS Res Hum Retroviruses, 2015. **31**(1): p. 64-70.
270. Castellano, P., L. Prevedel, and E.A. Eugenin, *HIV-infected macrophages and microglia that survive acute infection become viral reservoirs by a mechanism involving Bim*. Sci Rep, 2017. **7**(1): p. 12866.
271. Clayton, K.L., et al., *Resistance of HIV-infected macrophages to CD8(+) T lymphocyte-mediated killing drives activation of the immune system*. Nat Immunol, 2018. **19**(5): p. 475-486.
272. Swingler, S., et al., *Apoptotic killing of HIV-1-infected macrophages is subverted by the viral envelope glycoprotein*. PLoS Pathog, 2007. **3**(9): p. 1281-90.

273. Honeycutt, J.B., et al., *HIV persistence in tissue macrophages of humanized myeloid-only mice during antiretroviral therapy*. Nat Med, 2017. **23**(5): p. 638-643.
274. Baxter, A.E., et al., *Macrophage infection via selective capture of HIV-1-infected CD4+ T cells*. Cell Host Microbe, 2014. **16**(6): p. 711-21.
275. Calantone, N., et al., *Tissue myeloid cells in SIV-infected primates acquire viral DNA through phagocytosis of infected T cells*. Immunity, 2014. **41**(3): p. 493-502.
276. Sato, T., et al., *HIV infection of megakaryocytic cell lines*. Leuk Lymphoma, 2000. **36**(3-4): p. 397-404.
277. Real, F., et al., *Platelets from HIV-infected individuals on antiretroviral drug therapy with poor CD4(+) T cell recovery can harbor replication-competent HIV despite viral suppression*. Sci Transl Med, 2020. **12**(535).
278. Zucker-Franklin, D., S. Seremetis, and Z.Y. Zheng, *Internalization of human immunodeficiency virus type I and other retroviruses by megakaryocytes and platelets*. Blood, 1990. **75**(10): p. 1920-3.
279. Pretorius, E., *Platelets in HIV: A Guardian of Host Defence or Transient Reservoir of the Virus?* Front Immunol, 2021. **12**: p. 649465.
280. Cole, J.L., et al., *Ineffective platelet production in thrombocytopenic human immunodeficiency virus-infected patients*. Blood, 1998. **91**(9): p. 3239-46.
281. Wong, J.K. and S.A. Yukl, *Tissue reservoirs of HIV*. Curr Opin HIV AIDS, 2016. **11**(4): p. 362-70.
282. Ho, D.D., et al., *Isolation of HTLV-III from cerebrospinal fluid and neural tissues of patients with neurologic syndromes related to the acquired immunodeficiency syndrome*. N Engl J Med, 1985. **313**(24): p. 1493-7.
283. Galvin, S.R. and M.S. Cohen, *The role of sexually transmitted diseases in HIV transmission*. Nat Rev Microbiol, 2004. **2**(1): p. 33-42.
284. Ganor, Y., et al., *Within 1 h, HIV-1 uses viral synapses to enter efficiently the inner, but not outer, foreskin mucosa and engages Langerhans-T cell conjugates*. Mucosal Immunol, 2010. **3**(5): p. 506-22.

285. Kalter, D.C., et al., *Epidermal Langerhans cells are not principal reservoirs of virus in HIV disease*. J Immunol, 1991. **146**(10): p. 3396-404.
286. Siliciano, J.D., et al., *Long-term follow-up studies confirm the stability of the latent reservoir for HIV-1 in resting CD4+ T cells*. Nat Med, 2003. **9**(6): p. 727-8.
287. Huang, S.H., et al., *Have Cells Harboring the HIV Reservoir Been Immunoedited?* Front Immunol, 2019. **10**: p. 1842.
288. Ren, Y., et al., *BCL-2 antagonism sensitizes cytotoxic T cell-resistant HIV reservoirs to elimination ex vivo*. J Clin Invest, 2020. **130**(5): p. 2542-2559.
289. Ledford, H., *HIV rebound dashes hope of 'Mississippi baby' cure*. Nature, 2014.
290. Leyre, L., et al., *Abundant HIV-infected cells in blood and tissues are rapidly cleared upon ART initiation during acute HIV infection*. Sci Transl Med, 2020. **12**(533).
291. Whitney, J.B., et al., *Rapid seeding of the viral reservoir prior to SIV viraemia in rhesus monkeys*. Nature, 2014. **512**(7512): p. 74-7.
292. Liu, R., F.R. Simonetti, and Y.C. Ho, *The forces driving clonal expansion of the HIV-1 latent reservoir*. Virol J, 2020. **17**(1): p. 4.
293. Gantner, P., et al., *Single-cell TCR sequencing reveals phenotypically diverse clonally expanded cells harboring inducible HIV proviruses during ART*. Nat Commun, 2020. **11**(1): p. 4089.
294. Einkauf, K.B., et al., *Intact HIV-1 proviruses accumulate at distinct chromosomal positions during prolonged antiretroviral therapy*. J Clin Invest, 2019. **129**(3): p. 988-998.
295. Lian, X., et al., *Progressive transformation of the HIV-1 reservoir cell profile over two decades of antiviral therapy*. Cell Host Microbe, 2023. **31**(1): p. 83-96 e5.
296. Murray, A.J., et al., *The Latent Reservoir for HIV-1: How Immunologic Memory and Clonal Expansion Contribute to HIV-1 Persistence*. J Immunol, 2016. **197**(2): p. 407-17.
297. Simonetti, F.R. and M.F. Kearney, *Review: Influence of ART on HIV genetics*. Curr Opin HIV AIDS, 2015. **10**(1): p. 49-54.
298. Buzon, M.J., et al., *HIV-1 replication and immune dynamics are affected by raltegravir intensification of HAART-suppressed subjects*. Nat Med, 2010. **16**(4): p. 460-5.

299. Lorenzo-Redondo, R., et al., *Persistent HIV-1 replication maintains the tissue reservoir during therapy*. *Nature*, 2016. **530**(7588): p. 51-56.
300. Altfeld, M. and M. Gale, Jr., *Innate immunity against HIV-1 infection*. *Nat Immunol*, 2015. **16**(6): p. 554-62.
301. Soper, A., et al., *Type I Interferon Responses by HIV-1 Infection: Association with Disease Progression and Control*. *Front Immunol*, 2017. **8**: p. 1823.
302. Walker, B. and A. McMichael, *The T-cell response to HIV*. *Cold Spring Harb Perspect Med*, 2012. **2**(11).
303. Ganusov, V.V., et al., *Fitness costs and diversity of the cytotoxic T lymphocyte (CTL) response determine the rate of CTL escape during acute and chronic phases of HIV infection*. *J Virol*, 2011. **85**(20): p. 10518-28.
304. Jones, R.B., et al., *Tim-3 expression defines a novel population of dysfunctional T cells with highly elevated frequencies in progressive HIV-1 infection*. *J Exp Med*, 2008. **205**(12): p. 2763-79.
305. Trautmann, L., et al., *Upregulation of PD-1 expression on HIV-specific CD8+ T cells leads to reversible immune dysfunction*. *Nat Med*, 2006. **12**(10): p. 1198-202.
306. Youngblood, B., et al., *Cutting edge: Prolonged exposure to HIV reinforces a poised epigenetic program for PD-1 expression in virus-specific CD8 T cells*. *J Immunol*, 2013. **191**(2): p. 540-4.
307. Migueles, S.A. and M. Connors, *Success and failure of the cellular immune response against HIV-1*. *Nat Immunol*, 2015. **16**(6): p. 563-70.
308. Martin, M.P., et al., *Killer cell immunoglobulin-like receptor 3DL1 variation modifies HLA-B*57 protection against HIV-1*. *J Clin Invest*, 2018. **128**(5): p. 1903-1912.
309. Migueles, S.A., et al., *Lytic granule loading of CD8+ T cells is required for HIV-infected cell elimination associated with immune control*. *Immunity*, 2008. **29**(6): p. 1009-21.
310. Gorin, A.M., et al., *HIV-1 epitopes presented by MHC class I types associated with superior immune containment of viremia have highly constrained fitness landscapes*. *PLoS Pathog*, 2017. **13**(8): p. e1006541.

311. Brunet-Ratnasingham, E., et al., *Immune checkpoint expression on HIV-specific CD4+ T cells and response to their blockade are dependent on lineage and function*. EBioMedicine, 2022. **84**: p. 104254.
312. Fromentin, R., et al., *CD4+ T Cells Expressing PD-1, TIGIT and LAG-3 Contribute to HIV Persistence during ART*. PLoS Pathog, 2016. **12**(7): p. e1005761.
313. Niessl, J., et al., *Persistent expansion and Th1-like skewing of HIV-specific circulating T follicular helper cells during antiretroviral therapy*. EBioMedicine, 2020. **54**: p. 102727.
314. Morou, A., et al., *Altered differentiation is central to HIV-specific CD4(+) T cell dysfunction in progressive disease*. Nat Immunol, 2019. **20**(8): p. 1059-1070.
315. Brown, T.R., *I am the Berlin patient: a personal reflection*. AIDS Res Hum Retroviruses, 2015. **31**(1): p. 2-3.
316. Hutter, G., et al., *Long-term control of HIV by CCR5 Delta32/Delta32 stem-cell transplantation*. N Engl J Med, 2009. **360**(7): p. 692-8.
317. Gupta, R.K., et al., *HIV-1 remission following CCR5Delta32/Delta32 haematopoietic stem-cell transplantation*. Nature, 2019. **568**(7751): p. 244-248.
318. Jensen, B.O., et al., *In-depth virological and immunological characterization of HIV-1 cure after CCR5Delta32/Delta32 allogeneic hematopoietic stem cell transplantation*. Nat Med, 2023. **29**(3): p. 583-587.
319. Dickter, J., *The "City of Hope" Patient: prolonged HIV-1 remission without antiretrovirals (ART) after allogeneic hematopoietic stem cell transplantation (aHCT) of CCR5Δ32/Δ32 donor cells for acute myelogenous leukemia (AML)*. 2022, The 24th International AIDS Conference.
320. Hsu, J., et al., *HIV-1 remission and possible cure in a woman after haplo-cord blood transplant*. Cell, 2023. **186**(6): p. 1115-1126 e8.
321. Verheyen, J., et al., *Rapid Rebound of a Preexisting CXCR4-tropic Human Immunodeficiency Virus Variant After Allogeneic Transplantation With CCR5 Delta32 Homozygous Stem Cells*. Clin Infect Dis, 2019. **68**(4): p. 684-687.
322. Benmira, S., V. Bhattacharya, and M.L. Schmid, *An effective HIV vaccine: A combination of humoral and cellular immunity?* Curr HIV Res, 2010. **8**(6): p. 441-9.

323. Buchbinder, S.P., et al., *Efficacy assessment of a cell-mediated immunity HIV-1 vaccine (the Step Study): a double-blind, randomised, placebo-controlled, test-of-concept trial*. Lancet, 2008. **372**(9653): p. 1881-1893.
324. Duerr, A., et al., *Extended follow-up confirms early vaccine-enhanced risk of HIV acquisition and demonstrates waning effect over time among participants in a randomized trial of recombinant adenovirus HIV vaccine (Step Study)*. J Infect Dis, 2012. **206**(2): p. 258-66.
325. Kim, J., et al., *Current approaches to HIV vaccine development: a narrative review*. J Int AIDS Soc, 2021. **24 Suppl 7**(Suppl 7): p. e25793.
326. Moodie, Z., et al., *Continued Follow-Up of Phambili Phase 2b Randomized HIV-1 Vaccine Trial Participants Supports Increased HIV-1 Acquisition among Vaccinated Men*. PLoS One, 2015. **10**(9): p. e0137666.
327. Lee, J.H. and S. Crotty, *HIV vaccinology: 2021 update*. Semin Immunol, 2021. **51**: p. 101470.
328. Lapointe, H.R., et al., *People With Human Immunodeficiency Virus Receiving Suppressive Antiretroviral Therapy Show Typical Antibody Durability After Dual Coronavirus Disease 2019 Vaccination and Strong Third Dose Responses*. J Infect Dis, 2023. **227**(7): p. 838-849.
329. Sannier, G., et al., *A third SARS-CoV-2 mRNA vaccine dose in people receiving hemodialysis overcomes B cell defects but elicits a skewed CD4(+) T cell profile*. Cell Rep Med, 2023. **4**(3): p. 100955.
330. Zhang, P., et al., *A multiclade env-gag VLP mRNA vaccine elicits tier-2 HIV-1-neutralizing antibodies and reduces the risk of heterologous SHIV infection in macaques*. Nat Med, 2021. **27**(12): p. 2234-2245.
331. Ta, T.M., et al., *Insights Into Persistent HIV-1 Infection and Functional Cure: Novel Capabilities and Strategies*. Front Microbiol, 2022. **13**: p. 862270.
332. Tebas, P., et al., *Gene editing of CCR5 in autologous CD4 T cells of persons infected with HIV*. N Engl J Med, 2014. **370**(10): p. 901-10.
333. Schumann, K., et al., *Generation of knock-in primary human T cells using Cas9 ribonucleoproteins*. Proc Natl Acad Sci U S A, 2015. **112**(33): p. 10437-42.

334. Hu, W., et al., *RNA-directed gene editing specifically eradicates latent and prevents new HIV-1 infection*. Proc Natl Acad Sci U S A, 2014. **111**(31): p. 11461-6.
335. Dash, P.K., et al., *Sequential LASER ART and CRISPR Treatments Eliminate HIV-1 in a Subset of Infected Humanized Mice*. Nat Commun, 2019. **10**(1): p. 2753.
336. *Study of EBT-101 in Aviremic HIV-1 Infected Adults on Stable ART*. <https://ClinicalTrials.gov/show/NCT05144386>.
337. Parker Miller, E., et al., *A Structural Update of Neutralizing Epitopes on the HIV Envelope, a Moving Target*. Viruses, 2021. **13**(9).
338. Bar-On, Y., et al., *Safety and antiviral activity of combination HIV-1 broadly neutralizing antibodies in viremic individuals*. Nat Med, 2018. **24**(11): p. 1701-1707.
339. Mendoza, P., et al., *Combination therapy with anti-HIV-1 antibodies maintains viral suppression*. Nature, 2018. **561**(7724): p. 479-484.
340. Niessl, J., et al., *Combination anti-HIV-1 antibody therapy is associated with increased virus-specific T cell immunity*. Nat Med, 2020. **26**(2): p. 222-227.
341. Caskey, M., F. Klein, and M.C. Nussenzweig, *Broadly neutralizing anti-HIV-1 monoclonal antibodies in the clinic*. Nat Med, 2019. **25**(4): p. 547-553.
342. Mitsuyasu, R.T., et al., *Prolonged survival and tissue trafficking following adoptive transfer of CD4zeta gene-modified autologous CD4(+) and CD8(+) T cells in human immunodeficiency virus-infected subjects*. Blood, 2000. **96**(3): p. 785-93.
343. Ali, A., et al., *HIV-1-Specific Chimeric Antigen Receptors Based on Broadly Neutralizing Antibodies*. J Virol, 2016. **90**(15): p. 6999-7006.
344. Mu, W., M.A. Carrillo, and S.G. Kitchen, *Engineering CAR T Cells to Target the HIV Reservoir*. Front Cell Infect Microbiol, 2020. **10**: p. 410.
345. Vansant, G., et al., *Block-And-Lock Strategies to Cure HIV Infection*. Viruses, 2020. **12**(1).
346. Mousseau, G., et al., *The Tat Inhibitor Didehydro-Cortistatin A Prevents HIV-1 Reactivation from Latency*. mBio, 2015. **6**(4): p. e00465.
347. Kessing, C.F., et al., *In Vivo Suppression of HIV Rebound by Didehydro-Cortistatin A, a "Block-and-Lock" Strategy for HIV-1 Treatment*. Cell Rep, 2017. **21**(3): p. 600-611.

348. Christ, F., et al., *Rational design of small-molecule inhibitors of the LEDGF/p75-integrase interaction and HIV replication*. Nat Chem Biol, 2010. **6**(6): p. 442-8.
349. Desimie, B.A., et al., *LEDGINs inhibit late stage HIV-1 replication by modulating integrase multimerization in the virions*. Retrovirology, 2013. **10**: p. 57.
350. Vranckx, L.S., et al., *LEDGIN-mediated Inhibition of Integrase-LEDGF/p75 Interaction Reduces Reactivation of Residual Latent HIV*. EBioMedicine, 2016. **8**: p. 248-264.
351. Gavegnano, C., et al., *Novel mechanisms to inhibit HIV reservoir seeding using Jak inhibitors*. PLoS Pathog, 2017. **13**(12): p. e1006740.
352. Gasparian, A.V., et al., *Curaxins: anticancer compounds that simultaneously suppress NF-kappaB and activate p53 by targeting FACT*. Sci Transl Med, 2011. **3**(95): p. 95ra74.
353. Joshi, P., E. Maidji, and C.A. Stoddart, *Inhibition of Heat Shock Protein 90 Prevents HIV Rebound*. J Biol Chem, 2016. **291**(19): p. 10332-46.
354. Pasquereau, S. and G. Herbein, *CounterAKTing HIV: Toward a "Block and Clear" Strategy?* Front Cell Infect Microbiol, 2022. **12**: p. 827717.
355. Kim, Y., J.L. Anderson, and S.R. Lewin, *Getting the "Kill" into "Shock and Kill": Strategies to Eliminate Latent HIV*. Cell Host Microbe, 2018. **23**(1): p. 14-26.
356. Migueles, S.A., et al., *Defective human immunodeficiency virus-specific CD8+ T-cell polyfunctionality, proliferation, and cytotoxicity are not restored by antiretroviral therapy*. J Virol, 2009. **83**(22): p. 11876-89.
357. Jones, R.B., et al., *Histone deacetylase inhibitors impair the elimination of HIV-infected cells by cytotoxic T-lymphocytes*. PLoS Pathog, 2014. **10**(8): p. e1004287.
358. Jones, R.B., et al., *A Subset of Latency-Reversing Agents Expose HIV-Infected Resting CD4+ T-Cells to Recognition by Cytotoxic T-Lymphocytes*. PLoS Pathog, 2016. **12**(4): p. e1005545.
359. Deeks, S.G., et al., *HIV infection*. Nat Rev Dis Primers, 2015. **1**: p. 15035.
360. Dufour, C., et al., *Phenotypic characterization of single CD4+ T cells harboring genetically intact and inducible HIV genomes*. Nat Commun, 2023. **14**(1): p. 1115.
361. Bagnarelli, P., et al., *Dynamics and modulation of human immunodeficiency virus type 1 transcripts in vitro and in vivo*. J Virol, 1996. **70**(11): p. 7603-13.

362. Noel, N., et al., *Long-Term Spontaneous Control of HIV-1 Is Related to Low Frequency of Infected Cells and Inefficient Viral Reactivation*. J Virol, 2016. **90**(13): p. 6148-6158.
363. Cole, B., et al., *In-depth single-cell analysis of translation-competent HIV-1 reservoirs identifies cellular sources of plasma viremia*. Nat Commun, 2021. **12**(1): p. 3727.
364. Aldovini, A. and R.A. Young, *Mutations of RNA and protein sequences involved in human immunodeficiency virus type 1 packaging result in production of noninfectious virus*. J Virol, 1990. **64**(5): p. 1920-6.
365. Das, A.T., A.O. Pasternak, and B. Berkhout, *On the generation of the MSD-Ψ class of defective HIV proviruses*. Retrovirology, 2019. **16**(1): p. 19.
366. Purcell, D.F. and M.A. Martin, *Alternative splicing of human immunodeficiency virus type 1 mRNA modulates viral protein expression, replication, and infectivity*. J Virol, 1993. **67**(11): p. 6365-78.
367. Foster, J.L. and J.V. Garcia, *Role of Nef in HIV-1 replication and pathogenesis*. Adv Pharmacol, 2007. **55**: p. 389-409.
368. Khoury, G., et al., *HIV latency reversing agents act through Tat post translational modifications*. Retrovirology, 2018. **15**(1): p. 36.
369. Luznik, L., et al., *Tat-independent replication of human immunodeficiency viruses*. J Clin Invest, 1995. **95**(1): p. 328-32.
370. Jiang, C., et al., *Distinct viral reservoirs in individuals with spontaneous control of HIV-1*. Nature, 2020. **585**(7824): p. 261-267.
371. Lian, X., et al., *Signatures of immune selection in intact and defective proviruses distinguish HIV-1 elite controllers*. Sci Transl Med, 2021. **13**(624): p. eabl4097.
372. Morris, J.F., et al., *Effect of a single amino acid substitution in the V3 domain of the human immunodeficiency virus type 1: generation of revertant viruses to overcome defects in infectivity in specific cell types*. J Virol, 1994. **68**(12): p. 8380-5.
373. Mitsuya, Y., et al., *Minority human immunodeficiency virus type 1 variants in antiretroviral-naive persons with reverse transcriptase codon 215 revertant mutations*. J Virol, 2008. **82**(21): p. 10747-55.

374. Olson, A., et al., *HIV-1 Transcription but Not Intact Provirus Levels are Associated With Systemic Inflammation*. J Infect Dis, 2021. **223**(11): p. 1934-1942.
375. Takata, H., et al., *An active HIV reservoir during ART is associated with maintenance of HIV-specific CD8(+) T cell magnitude and short-lived differentiation status*. Cell Host Microbe, 2023. **31**(9): p. 1494-1506 e4.
376. Ward, A.R., et al., *No evidence that circulating HIV-specific immune responses contribute to persistent inflammation and immune activation in persons on long-term ART*. AIDS, 2022. **36**(12): p. 1617-1628.
377. Centlivre, M., et al., *In HIV-1 pathogenesis the die is cast during primary infection*. AIDS, 2007. **21**(1): p. 1-11.
378. Gandhi, R.T., et al., *Levels of HIV-1 persistence on antiretroviral therapy are not associated with markers of inflammation or activation*. PLoS Pathog, 2017. **13**(4): p. e1006285.
379. Moysi, E., et al., *Altered immune cell follicular dynamics in HIV infection following influenza vaccination*. J Clin Invest, 2018. **128**(7): p. 3171-3185.
380. Trautmann, L., *Kill: boosting HIV-specific immune responses*. Curr Opin HIV AIDS, 2016. **11**(4): p. 409-16.
381. Bansal, A., et al., *CD8 T cell response and evolutionary pressure to HIV-1 cryptic epitopes derived from antisense transcription*. J Exp Med, 2010. **207**(1): p. 51-9.
382. Cardinaud, S., et al., *Identification of cryptic MHC I-restricted epitopes encoded by HIV-1 alternative reading frames*. J Exp Med, 2004. **199**(8): p. 1053-63.
383. Pasquereau, S., A. Kumar, and G. Herbein, *Targeting TNF and TNF Receptor Pathway in HIV-1 Infection: from Immune Activation to Viral Reservoirs*. Viruses, 2017. **9**(4).
384. Fahey, L.M., et al., *Viral persistence redirects CD4 T cell differentiation toward T follicular helper cells*. J Exp Med, 2011. **208**(5): p. 987-99.
385. Pinzone, M.R., et al., *Longitudinal HIV sequencing reveals reservoir expression leading to decay which is obscured by clonal expansion*. Nat Commun, 2019. **10**(1): p. 728.
386. Cho, A., et al., *Longitudinal clonal dynamics of HIV-1 latent reservoirs measured by combination quadruplex polymerase chain reaction and sequencing*. Proc Natl Acad Sci U S A, 2022. **119**(4).

387. Kiepiela, P., et al., *CD8+ T-cell responses to different HIV proteins have discordant associations with viral load*. Nat Med, 2007. **13**(1): p. 46-53.
388. Migueles, S.A., et al., *CD8(+) T-cell Cytotoxic Capacity Associated with Human Immunodeficiency Virus-1 Control Can Be Mediated through Various Epitopes and Human Leukocyte Antigen Types*. EBioMedicine, 2015. **2**(1): p. 46-58.
389. Zuniga, R., et al., *Relative dominance of Gag p24-specific cytotoxic T lymphocytes is associated with human immunodeficiency virus control*. J Virol, 2006. **80**(6): p. 3122-5.
390. Sprent, J. and C.D. Surh, *Normal T cell homeostasis: the conversion of naive cells into memory-phenotype cells*. Nat Immunol, 2011. **12**(6): p. 478-84.
391. Ndhlovu, Z.M., et al., *Augmentation of HIV-specific T cell function by immediate treatment of hyperacute HIV-1 infection*. Sci Transl Med, 2019. **11**(493).
392. Takata, H., et al., *Delayed differentiation of potent effector CD8(+) T cells reducing viremia and reservoir seeding in acute HIV infection*. Sci Transl Med, 2017. **9**(377).
393. Westermann, J. and R. Pabst, *Distribution of lymphocyte subsets and natural killer cells in the human body*. Clin Investig, 1992. **70**(7): p. 539-44.
394. Costiniuk, C.T. and M.A. Jenabian, *Cell-to-cell transfer of HIV infection: implications for HIV viral persistence*. J Gen Virol, 2014. **95**(Pt 11): p. 2346-2355.
395. Yukl, S.A., et al., *The distribution of HIV DNA and RNA in cell subsets differs in gut and blood of HIV-positive patients on ART: implications for viral persistence*. J Infect Dis, 2013. **208**(8): p. 1212-20.
396. Yates, K.B., et al., *Epigenetic scars of CD8(+) T cell exhaustion persist after cure of chronic infection in humans*. Nat Immunol, 2021. **22**(8): p. 1020-1029.
397. Wherry, E.J., et al., *Molecular signature of CD8+ T cell exhaustion during chronic viral infection*. Immunity, 2007. **27**(4): p. 670-84.
398. Sen, D.R., et al., *The epigenetic landscape of T cell exhaustion*. Science, 2016. **354**(6316): p. 1165-1169.
399. Straub, R.H., *The complex role of estrogens in inflammation*. Endocr Rev, 2007. **28**(5): p. 521-74.

400. Moran, J.A., S.R. Turner, and M.D. Marsden, *Contribution of Sex Differences to HIV Immunology, Pathogenesis, and Cure Approaches*. Front Immunol, 2022. **13**: p. 905773.
401. de Azevedo, S.S.D., et al., *Highly divergent patterns of genetic diversity and evolution in proviral quasispecies from HIV controllers*. Retrovirology, 2017. **14**(1): p. 29.

Chapter 9 – Appendices

Appendix I: Author's contribution to additional manuscripts

Author's contribution to the first additional manuscript "A Third SARS-CoV-2 mRNA Vaccine Dose in People Receiving Hemodialysis Overcomes B Cell Defects but Elicits a Skewed CD4⁺ T Cell Profile"

Conceptualization, G.S., A.N., M.D., A.F., R.S.S., and D.E.K.; methodology, G.S., A.N., M.D., M.N., J.N., A.F., and D.E.K.; software, O.T. and G.S.; formal analysis, J.B. and R.L.B.; investigation, G.S., A.N., L.M., M.N., M.L., D.C., A.T., M.B., S.Y.G., C.B., G.G.L., and H.M.; resources, M.L., R.C., A.M.S.F., C.B., G.G.L., H.M., N.B., G.G.D., L.G., C.M., P.A., C.T., V.M.L., G.G., and SD; writing – original draft, G.S., A.N., M.D., and D.E.K.; writing – review & editing, G.S., A.N., M.D., and D.E.K.; supervision, D.E.K., A.F., and R.S.S.; funding acquisition, D.E.K., A.F., and R.S.S.

Author's contribution to the second additional manuscript "An Extended SARS-CoV-2 mRNA Vaccine Prime-Boost Interval Enhances B Cell Immunity with Limited Impact on T Cells"

A.N., G.S., M.D., A.F., and D.E.K. designed the studies. A.N., G.S., M.N., N.B., and M.L. performed B cell and T cell assays. A.N., G.S., and M.D. performed and analyzed the B and T cell experiments. G.G.L. and A.T. performed RBD ELISA, RBD avidity index and OC43 staining. J.N. contributed to the T cell assay design. A.T., H.M., L.G., C.M., P.A., C.T., J.C.W., and V.M.L. secured and processed blood samples. M.M.P., R.R.G., A.R.G., and E.J.W. provided unique reagents. G.G. produced and purified proteins. A.N., G.S., M.D., and D.E.K. wrote the article. Every author has read, edited, and approved the final article.

Author's contribution to the third additional manuscript "Spontaneous HIV Expression During Suppressive ART is Associated with the Magnitude and Function of HIV-Specific CD4⁺ and CD8⁺ T Cells"

Conceptualization and supervision, M.D. and D.E.K.; methodology, M.D., G.S., and N.B.; software, O.T.; investigation and validation, G.-G.D., M.D., N.B., G.S., M.N., and A. Pa; formal analysis, M.D., O.T., C.D., C.R., and R.F. J.-P.R. ensured recruitment and clinical assessments. Data curation, C.R. and M.D.; interpretation, M.D., O.T., A. Pa, R.F., J.D.E., N.C., and D.E.K. J.D.E. and A. Prat provided intellectual input. Writing – original draft, M.D. and D.E.K.; review & editing, all co-authors; visualization, M.D., C.D., and O.T.; project administration, M.D.; funding acquisition, D.E.K., N.C., and J.D.E.

Author's contribution to the fourth additional manuscript "Temporal Associations of B and T Cell Immunity with Robust Vaccine Responsiveness in a 16-Week Interval BNT162b2 Regimen"

M.N., M.D., A.F., and D.E.K. designed the studies. M.N., G.S., A.N., N.B., and M.L. performed B cell and T cell assays. J.P. generated the B cell probes. M.N., M.D., G.S., A.N., and O.T. performed and analyzed the B and T cell experiments. J.N. contributed to the T cell assay design. O.T. performed unsupervised clustering analyses. L.M., A.T., G.B.-B., D.V., S.Y.G., M.B., R.G., J.P., C.B., G.G.-L., and J.R. performed ELISA, ADCC, flow cytometry, avidity, and neutralization assays. A.L., C.B., G.G.-L., H.M., L.G., C.M., P.A., G.-G.O.-D., C.T., and V.M.-L. secured and processed blood samples. G.G. produced and purified proteins. A.P. provided intellectual input. J.B. and R.L.-B. generated

and applied the linear mixed models for statistical comparison. M.N., M.D., and D.E.K. wrote the manuscript. Every author has read, edited, and approved the final manuscript.

Author's contribution to the review "Single-Cell Technologies Applied to HIV-1 Research: Reaching Maturity"

GS and MD performed the literature review and wrote the manuscript. DK edited the manuscript and provided supervision. All authors read and approved the final version of the manuscript.

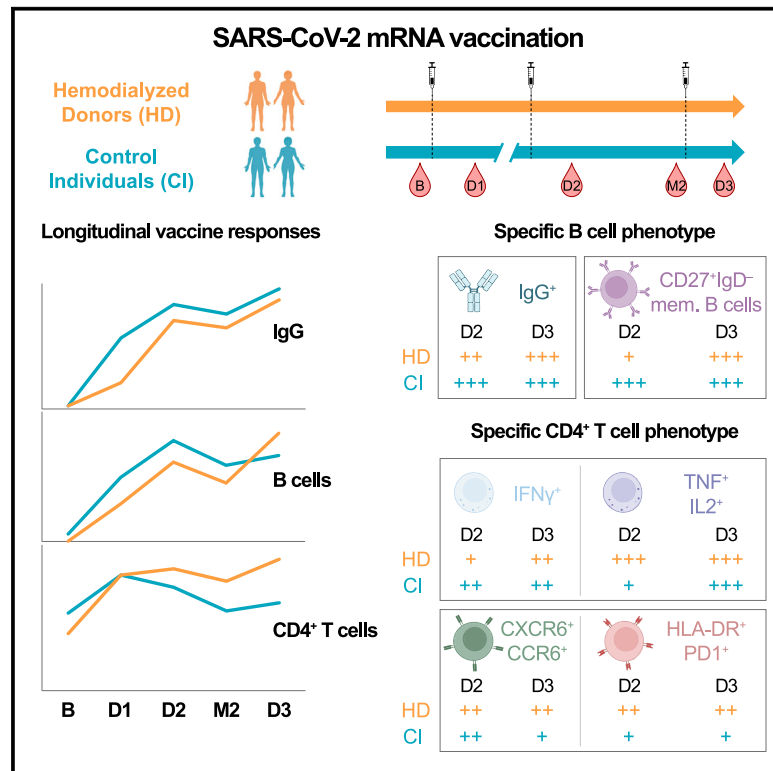
Appendix II: Additional manuscripts

Appendix II.i: A Third SARS-CoV-2 mRNA Vaccine Dose in People Receiving Hemodialysis Overcomes B Cell Defects but Elicits a Skewed CD4⁺ T Cell Profile

Cell Reports Medicine, 2023

A third SARS-CoV-2 mRNA vaccine dose in people receiving hemodialysis overcomes B cell defects but elicits a skewed CD4⁺ T cell profile

Graphical abstract



Authors

G r my Sannier, Alexandre Nicolas, Mathieu Dub , ..., Andr s Finzi, Rita S. Suri, Daniel E. Kaufmann

Correspondence

andres.finzi@umontreal.ca (A.F.), rita.suri@mcgill.ca (R.S.S.), daniel.kaufmann@chuv.ch (D.E.K.)

In brief

Sannier et al. describe specific humoral, B, and T cell responses in people on hemodialysis (HD) after mRNA vaccination against SARS-CoV-2. Three doses are critical to elicit robust antibody, B cell, and CD8⁺ T cell responses. CD4⁺ T cell profile is skewed toward TNF/IL-2, CCR6, CXCR6, PD-1, and HLA-DR expression.

Highlights

- Two doses of SARS-CoV-2 vaccine induce weak B cells in people on hemodialysis (HD)
- People on HD generate less mature B cells after two vaccine doses
- A third immunization in HD robustly boosts B and CD4⁺ T cell responses
- CD4⁺ T cell profile in HD is skewed toward CCR6, CXCR6, PD-1, HLA-DR, and TNF α /IL-2



Article

A third SARS-CoV-2 mRNA vaccine dose in people receiving hemodialysis overcomes B cell defects but elicits a skewed CD4⁺ T cell profile

Gérémy Sannier,^{1,2,15} Alexandre Nicolas,^{1,2,15} Mathieu Dubé,¹ Lorie Marchitto,^{1,2} Manon Nayrac,^{1,2} Olivier Tastet,¹ Debashree Chatterjee,^{1,2} Alexandra Tauzin,^{1,2} Raphaël Lima-Barbosa,^{2,13} Mélanie Laporte,¹ Rose Cloutier,¹ Alina M. Sreng Flores,¹ Marianne Boutin,^{1,2} Shang Yu Gong,^{1,3} Mehdi Benlarbi,^{1,2} Shilei Ding,¹ Catherine Bourassa,¹ Gabrielle Gendron-Lepage,¹ Halima Medjahed,¹ Guillaume Goyette,¹ Nathalie Brassard,¹ Gloria-Gabrielle Delgado,¹ Julia Niessl,^{1,2,14} Laurie Gokool,¹ Chantal Morrisseau,¹ Pascale Arlotto,¹ Norka Rios,⁴ Cécile Tremblay,^{1,2} Valérie Martel-Laferrrière,^{1,2} Alexandre Prat,^{1,5} Justin Bélair,^{2,13} William Beaubien-Souligny,^{1,6} Rémi Goupil,^{7,8} Annie-Claire Nadeau-Fredette,^{6,8,9} Caroline Lamarche,^{6,8,9} Andrés Finzi,^{1,2,3,*} Rita S. Suri,^{1,4,10,*} and Daniel E. Kaufmann^{1,11,12,16,*}

¹Centre de Recherche du Centre Hospitalier de l'Université de Montréal, Montreal, QC H2X 0A9, Canada

²Université de Montréal, Montreal, QC H3T 1J4, Canada

³Department of Microbiology and Immunology, McGill University, Montreal, QC H3A 2B4, Canada

⁴Research Institute of the McGill University Health Centre, Montreal, QC H3H 2L9, Canada

⁵Département de Neurosciences, Université de Montréal, Montreal, QC H3T 1J4, Canada

⁶Nephrology Division, Centre Hospitalier de l'Université de Montréal, Montreal, QC H3X 3E4, Canada

⁷Centre de Recherche of the Hôpital du Sacré-Cœur de Montréal, Montreal, QC H4J 1C5, Canada

⁸Faculty of Medicine, Université de Montréal, Montreal, QC H3T 1J4, Canada

⁹Centre de Recherche of the Hôpital Maisonneuve-Rosemont, Montreal, QC H1T 2M4, Canada

¹⁰Division of Nephrology, Department of Medicine, McGill University, Montreal, QC H3G 2M1, Canada

¹¹Département de Médecine, Université de Montréal, Montréal, QC H3T 1J4, Canada

¹²Division of Infectious Diseases, Department of Medicine, Lausanne University Hospital and University of Lausanne, Lausanne, Switzerland

¹³Present address: JB Consulting, Montréal, QC H3S1K8, Canada

¹⁴Present address: Center for Infectious Medicine, Department of Medicine Huddinge, Karolinska Institutet, 141 52 Huddinge, Stockholm, Sweden

¹⁵These authors contributed equally

¹⁶Lead contact

*Correspondence: andres.finzi@umontreal.ca (A.F.), rita.suri@mcgill.ca (R.S.S.), daniel.kaufmann@chuv.ch (D.E.K.)

<https://doi.org/10.1016/j.xcrm.2023.100955>

SUMMARY

Cellular immune defects associated with suboptimal responses to severe acute respiratory syndrome coronavirus 2 (SARS-CoV-2) mRNA vaccination in people receiving hemodialysis (HD) are poorly understood. We longitudinally analyze antibody, B cell, CD4⁺, and CD8⁺ T cell vaccine responses in 27 HD patients and 26 low-risk control individuals (CIs). The first two doses elicit weaker B cell and CD8⁺ T cell responses in HD than in CI, while CD4⁺ T cell responses are quantitatively similar. In HD, a third dose robustly boosts B cell responses, leads to convergent CD8⁺ T cell responses, and enhances comparatively more T helper (T_H) immunity. Unsupervised clustering of single-cell features reveals phenotypic and functional shifts over time and between cohorts. The third dose attenuates some features of T_H cells in HD (tumor necrosis factor alpha [TNF α]/interleukin [IL]-2 skewing), while others (CCR6, CXCR6, programmed cell death protein 1 [PD-1], and HLA-DR overexpression) persist. Therefore, a third vaccine dose is critical to achieving robust multifaceted immunity in hemodialysis patients, although some distinct T_H characteristics endure.

INTRODUCTION

Implementation of severe acute respiratory syndrome coronavirus 2 (SARS-CoV-2) vaccination has led to a sharp decrease in the severity of COVID-19 disease worldwide.^{1,2} In the general population, mRNA vaccines against SARS-CoV-2 induce robust responses of both humoral^{3–5} and cellular immunity, which is dominated by B cells and T helper (T_H) responses with a weaker

CD8⁺ T cell component.^{6,7} The initial series of mRNA vaccines comprised two doses. A third dose was recommended to offset waning immunity and improve recognition of variants of concern (VOCs), including Omicron.^{8–10} In low-risk populations, substantial protection is conferred by one dose,¹¹ with notable antigen-specific immunity.^{12–14} Some public health agencies delayed the recommended interval between doses to increase population coverage during initial vaccine scarcity.^{15,16} Studies in low-risk



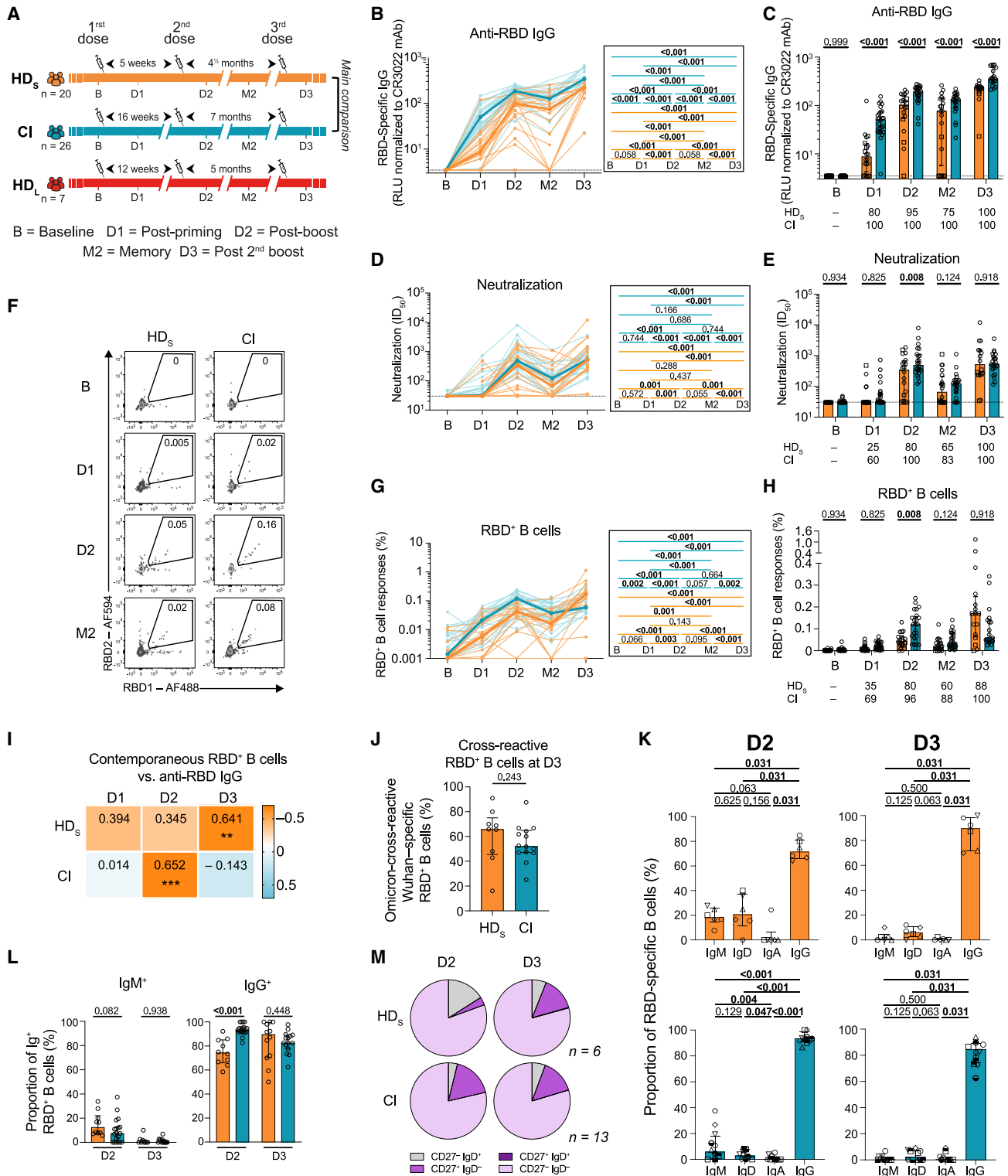


Figure 1. In HD patients, the initial two mRNA vaccine inoculations elicit poor B cell responses, which are reinvigorated by a third dose (A) Schematic representation of study design, visits, and vaccine dose administration (indicated by a syringe). Blood samples were collected at five time points: at baseline, B; 3–4 weeks after the first dose, D1 and the second dose, D2; 12–16 weeks after the second dose, M2; and 4 weeks after the third dose, D3. Following provincial vaccination guidelines, 20 HD participants (HD_s) received the two doses at 5-week intervals and 26 control individuals (CIs) received the two doses at

(legend continued on next page)

individuals subsequently showed that a longer interval between the first two doses enhanced humoral responses,^{5,17,18} and increased specific B cell responses and maturation, with little impact on T cells.^{18–20}

Patients with end-stage kidney disease receiving hemodialysis (HD) are susceptible to infections and demonstrate suboptimal responses to standard vaccinations against diphtheria, hepatitis B virus (HBV), or influenza.²¹ They display altered immune functions affecting B and T lymphocytes,²² monocytes,²³ dendritic cells, and neutrophils²⁴ due to uremia toxins²⁵ and blood-membrane interactions during the dialysis process.²⁶ However, multiple and/or higher vaccine doses proved to be an effective strategy, e.g., for HBV or influenza vaccination.²⁷

HD patients are vulnerable to SARS-CoV-2 infection, severe COVID-19,^{28,29} and breakthrough events.³⁰ Therefore, HD are considered a high-priority population for SARS-CoV-2 vaccination. Vaccination in HD generated anti-SARS-CoV-2 antibodies but at lower levels compared with the global population,^{31,32} and with earlier decline,³³ even after three doses.³⁴ While vaccine studies in HD have focused on humoral responses, a better understanding of specific B and T cell immunity is essential to identify underlying defects. CD4⁺ T cell help plays a critical role in the generation and maintenance of adaptive immunity, particularly of B cell responses,³⁵ and CD8⁺ T cells may play a direct protective role against the virus. Some studies have shown lower SARS-CoV-2-reactive interferon gamma (IFN γ)-producing T cell frequencies in HD,^{36,37} strengthening the need to understand this arm of the immune system. While studies suggest that long-interval vaccine regimens are not appropriate for HD, resulting in weaker antibody levels, the impact on cellular immunity remains to be defined.

Herein, we conducted a prospective longitudinal cohort study to define the quantitative and qualitative trajectories of vaccine-induced antibody, B, CD4⁺, and CD8⁺ T cell responses in SARS-CoV-2-naïve HD patients receiving three mRNA SARS-CoV-2

vaccine doses, compared with antigen-specific responses in low-risk CIs.

RESULTS

Study participants

We assessed cellular and antibody responses in blood samples from three cohorts of SARS-CoV-2-naïve participants who received three mRNA vaccine doses (Figure 1A, Table 1): (1) 20 people on HD (HD_S cohort) who received the first two doses with a 5-week interval (median, interquartile range [IQ] = 35 [33–35] days); (2) 26 low-risk health care workers with no major kidney disease or immunosuppressive condition (control individuals [CIs]) who received the first two doses at a 16-week interval (median [IQ] = 111 [109–112] days), in agreement with the Quebec Public Health guidelines at the time of the study; (3) seven HD who received a 12-week delayed second dose (median [IQ] = 83 [82–84] days) (HD_L long-interval HD cohort). The HD_S and CI cohorts were studied in detail, while we performed focused analyses on the HD_L cohort.

Blood was sampled at baseline (B) 1–12 days before the first dose; 3–4 weeks after the first dose (D1); 3–4 weeks after the second dose (D2); 3–4 months after the second dose (memory; M2), and 4 weeks after the third dose (D3). Donors with breakthrough COVID-19 events were excluded afterward. There were no significant differences between HD_S and HD_L in terms of gender, age, or time on HD. HD_S and HD_L were respectively 10 and 15 years older than the CI. The time of sampling before the first dose (B), between D1 and D2, between D1 and D3, between D2 and D3, and between injection and sampling were significantly different.

Hemodialyzed participants are a heterogeneous population.³⁸ Clinical details for our cohorts are provided in Table S1. The causes of end-stage renal disease (ESRD) were diverse (diabetes mellitus [DM], glomerulonephritis, hypertension, etc.), as were comorbidities other than DM. None were living with HIV.

16-week intervals. A second group of seven HD participants (HD_L) received a delayed second dose with an interval of 12 weeks. Actual times are summarized in Table 1.

(B and C) Kinetics of RBD⁺ IgG responses in HD_S participants (orange) or CI (blue) participants. HD_S on immunosuppressive drugs are represented by square symbols, and HD_S not on immunosuppressants are represented by circles. (B) Lines connect data points from the same donor. The bold lines represent the median values of each cohort. Right panel: statistical comparisons using a linear mixed model. (C) Comparisons between HD_S and CI participants. Bars represent median \pm interquartile range. Intercohort statistical comparisons using a linear mixed model are shown. Frequencies of responders are written below the histograms.

(D and E) Kinetics of antibody neutralizing activity measured with plasma from HD_S participants (orange) or CI (blue) participants. HD_S on immunosuppressive drugs are represented by square symbols; HD_S not on immunosuppressants are represented by circles. (D) Lines connect data points from the same donor. The bold lines represent the median values of each cohort. Right panel: statistical comparisons using a linear mixed model. (E) Comparisons between HD_S and CI participants. Bars represent medians \pm interquartile ranges. Intercohort statistical comparisons using a linear mixed model are shown. Frequencies of responders are written below the histograms.

(F–H) (F) Gating strategy to identify RBD⁺ B cells. (G and H) Kinetics of RBD⁺ B cell responses in HD_S participants (orange) or CI (blue) participants. HD_S on immunosuppressive drugs are represented by square symbols; HD_S not on immunosuppressants are represented by circles. (G) Lines connect data points from the same donor. The bold lines represent the median values of each cohort. Right panel: statistical comparisons using a linear mixed model. (H) Comparisons between HD_S and CI participants. Bars represent median \pm interquartile range. Intercohort statistical comparisons using a linear mixed model are shown. Frequencies of responders are written below the histograms.

(I) Contemporaneous correlations of RBD⁺ B cells and anti-RBD IgG. Values and colors represent Spearman *r*, asterisks indicate p values (**p* < 0.05, ***p* < 0.01, ****p* < 0.001).

(J) Comparison between HD_S and CI of the proportions of Omicron BA.1-RBD⁺ B cells among wild-type Wuhan-1-specific RBD⁺ B cells. Mann-Whitney tests are shown.

(K) Proportions of IgD⁻, IgM⁻, IgA⁻, and IgG⁻ cells in RBD⁺ B cells at D2 and D3 in HD_S and CI participants, with Wilcoxon tests.

(L) Comparison of IgM⁺ and IgG⁺ RBD⁺ B cells between HD_S and CI participants at D2 and D3. Mann-Whitney tests are shown.

(M) Proportion of IgD^{+/−} and CD27^{+/−} populations in RBD⁺ memory B cells in HD_S and CI participants at D2 and D3. In (B–E) and (G–I) *n* = 20 HD_S, *n* = 26 CI; in (J) *n* = 9 HD_S, *n* = 14 CI; in (K) and (M) *n* = 6 HD_S, *n* = 13 CI; in (L) *n* = 10 HD_S, *n* = 15 CI.

Table 1. Clinical characteristics of study participants

mRNA vaccine	CI _s ^a	HD ^a	
	Long delay ^b (16 weeks)	Short delay (HD _S) ^b (5 weeks)	Long delay (HD _L) ^b (12 weeks)
Variable	(n = 26)	(n = 20)	(n = 7)
Vaccine regimen			
Pfizer BNT162b2 vaccine (3 doses)	n = 25	n = 19	n = 7
Heterologous vaccine strategy (Moderna mRNA- 1273 and Pfizer BNT162b2)	n = 1	n = 1	n = 0
Age (years) ^c	51 (41–56)	61 (55–64)	66 (55–77)
Gender			
Male	11 (42%)	13 (65%)	4 (57%)
Female	15 (58%)	7 (35%)	3 (43%)
Vaccine dose spacing			
Days between doses 1 and 2 ^c	111 (109–112)	35 (33–35)	83 (82–84)
Days between doses 1 and 3 ^c	329 (323–334)	168 (166–168)	230 (229–231)
Days between doses 2 and 3 ^c	219 (211–222)	133 (133–133)	147 (147–147)
Visits for immunological profiling			
B, days before first dose ^c	1 (0–5)	12 (7–12)	1 (01–2)
D1, days after first dose	21 (19–26)	28 (28–30)	28 (28–29)
D1, days before second dose	90 (85–92)	5 (5–7)	54 (54–56)
D1, days before third dose ^c	306 (302–310)	138 (138–139)	203 (201–203)
D2, days after first dose ^c	133 (130–139)	63 (63–63)	111 (110–112)
D2, days after second dose	21 (20–27)	28 (28–29)	28 (28–28)
D2, days before third dose ^c	196 (193–197)	105 (103–105)	119 (119–119)
M2, days after first dose ^c	224 (222–228)	119 (117–119)	167 (167–168)
M2, days after second dose ^c	112 (110–119)	84 (84–84)	84 (84–84)
M2, days before third dose ^c	104 (101–112)	49 (49–49)	63 (63–63)
D3, days after first dose ^c	362 (355–364)	198 (198–198)	265 (264–266)
D3, days after second dose ^c	249 (245–252)	163 (163–163)	182 (182–182)
D3, days after third dose	29 (25–34)	30 (30–32)	35 (35–35)

^aValues displayed are medians, with interquartile range (IQR) in parentheses for continuous variables, or percentages for categorical variables.
^bCI, HD_S and HD_L HD participants cohorts were compared by: Mann-Whitney test for continuous variables, Fisher's test for categorical variables.
^cValues statistically different between the CI, HD_S, and/or HD_L cohorts (p < 0.05).

A few participants received immunosuppressive medications (prednisone, cyclosporine, tacrolimus). However, these patients did not behave as outliers in the different immunological analyses. These individuals are represented by different symbols—squares instead of circles—in the figure plots.

In HD patients, the initial two mRNA vaccine inoculations elicit poor B cell responses, which are reinvigorated by a third dose

We measured the levels of immunoglobulin (Ig) G targeting the receptor-binding domain (RBD). This domain is the major target for neutralization^{39,40} and is associated with vaccine efficacy.⁴¹ At baseline, anti-RBD IgG were undetectable in all participants, consistent with their SARS-CoV-2-naïve status (Figures 1B and 1C). Both cohorts developed anti-RBD IgG responses after each vaccine dose (D1, D2, and D3) with a small decline at a memory time point (M2) (Figure 1B). However, the antibody levels at D1 were lower in HD_S compared with CI, with a median-fold difference of 6. The antibody levels in HD_S remained significantly lower through all follow-up time points (Figure 1C).

Only 80% (16 out of 20) of HD_S seroconverted after the first dose compared with 100% (26 out of 26) of CIs. However, all HD_S experienced an increase in anti-RBD IgG responses after the third dose (Figure 1C). In the HD_L regimen, the levels of anti-RBD IgG were not significantly different compared with HD_S (Figure S1A). We also evaluated the capacity of plasma samples from donors to neutralize pseudoparticles bearing the SARS-CoV-2 spike (S) (D614G) glycoprotein, as previously described.^{14,42} Neutralizing activity was measured by the neutralization half-maximum inhibitory dilution (ID₅₀). None of the plasma samples collected at baseline was able to neutralize SARS-CoV-2 in HD_S and CIs (Figures 1D and 1E). The first dose had only a small impact on the neutralization capacity in most donors (Figures 1D and 1E) with only 25% (5 out of 20) of HD_S compared with 60% (15 out of 25) of CI exhibiting a neutralizing activity against the D614G S at D1 (Figure 1E). The second dose increased the neutralization capacity in the HD_S cohort but had significantly less activity than in the CI cohort. Strikingly, the third dose abrogated the differences between both groups (Figures 1D and 1E). In line with anti-RBD-IgG levels (Figure S1A),

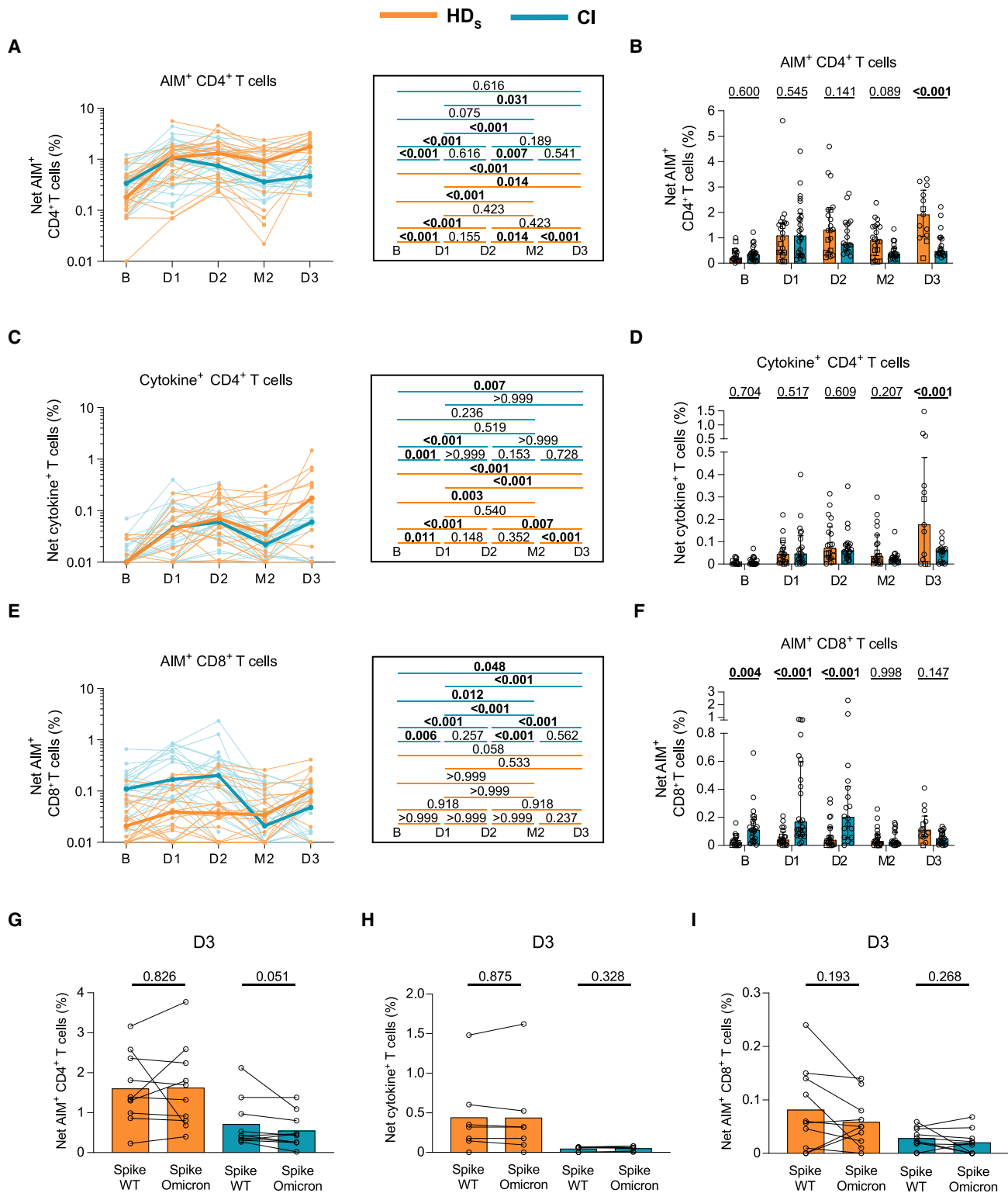


Figure 2. Vaccination induces strong CD4⁺ T cell responses but poor CD8⁺ T cell immunity in HD participants

Frequencies of SARS-CoV-2 S-specific CD4⁺ and CD8⁺ T cells in HD_s (orange) and CI (blue) who received three vaccine doses. HD_s on immunosuppressive drugs are represented by square symbols, HD_s not on immunosuppressants are represented by circles. PBMCs were stimulated *ex vivo* with a pool of overlapping S peptides.

(legend continued on next page)

the longer interval between the first two doses in HD_L did not lead to higher neutralizing activity against the S glycoprotein (Figure S1B).

We next measured RBD⁺ B cells using two fluorescently labeled recombinant RBD probes (Figures 1F and S1C).^{6,19} We observed differences in both magnitude and longitudinal trajectories of B cell responses between cohorts (Figures 1G and 1H). There was a trend for weaker priming of B cell responses (D1) in HD_S than in CI, which did not reach statistical significance after correction for multiple comparisons. At D2 and M2, the frequencies of RBD⁺ B cells in HD_S were lower and consistently trailed those in CIs, resulting in almost parallel curves (Figure 1G). In contrast, the responses to the third dose differed, with a more robust expansion of B cell responses in HD_S compared with CIs. Consequently, we observed stronger B cell responses at D3 in HD_S than in CIs (Figure 1H). Consistent with the antibodies (Figure S1A) and unlike CIs,¹⁹ a long interval in HD_L did not improve the generation of the RBD⁺ B cell pool (Figure S1D). The delayed kinetics of anti-RBD IgG responses in HD_S compared with CIs is illustrated by contemporaneous associations between B cell and antibody responses: while we observed in CIs a significant positive correlation between RBD⁺ B cells and anti-RBD IgG at D2, this correlation only appeared at D3 in HD_S (Figure 1I).

The rapid worldwide spread of the Omicron variant has decreased vaccine efficacy against infection.⁴³ However, protection against severe diseases remains good and is significantly increased by a third vaccine dose.¹⁰ To determine if HD treatment was associated with altered viral cross-recognition by B cells, we tested if HD_S immunized with wild-type (WT) Wuhan-1 strain S could elicit cross-reactive B cell responses against Omicron BA.1 RBD (Figure S1E). Among all the WT RBD⁺ B cells at D3, 65% co-stained for Omicron BA.1 RBD probes, indicating cross-reactivity (Figure 1J). No significant difference was observed between HD_S and CIs (Figure 1J).

We next assessed the differentiation of RBD⁺ B cells following vaccination. To avoid phenotyping bias, we only included donors in whom we detected ≥ 5 RBD⁺ B cells at every time point. As the rare RBD⁺ B cells in HD_S at D1 precluded reliable phenotyping, we focused on D2 and D3. We measured the expression of IgM, IgD, IgA, and IgG on RBD⁺ B cells (Figure S1F). While IgG⁺ cells were dominant in both cohorts at all time points (Figures 1K, 1L, and S1G), its fraction was lower in HD_S at D2, and those of IgM⁺ and IgD⁺ cells were higher (Figures 1L and S1H). The profiles converged between cohorts at D3. We next determined the memory differentiation profile of RBD⁺ B cells

using IgD and CD27 co-expression (Figure S1I). CD27 is expressed on memory B cells⁴⁴ and IgD is mostly found on unswitched B cells.⁴⁵ In both cohorts, RBD⁺ B cells were mainly IgD⁻CD27⁻ (Figure 1M). In HD_S, CD27⁻IgD⁺ cells represented 15% of RBD⁺ B cells at D2 and decreased at D3 in favor of mature CD27⁺IgD⁻ cells. Compared with HD_S, we measured in CIs a low fraction of immature CD27⁻IgD⁺ RBD⁺ B cells at D2, in favor of more mature cells. This phenotype was stable at D3. Quantitatively, the magnitude of memory B cell responses increased between M2 and D3 in both groups (Figure S1J).

Our data show that, compared with a CI cohort, HD_S elicit low RBD⁺ and mature B cell responses after two doses, consistent with lower antibody levels. A third immunization in HD_S is critical to achieving B cell responses of higher magnitudes than those observed in CIs and leads to convergent differentiation profiles.

Vaccination induces strong CD4⁺ T cell responses but poor CD8⁺ T cell immunity in HD participants

SARS-CoV-2-specific CD4⁺ T cells help is crucial to the development of B cell responses and correlates with long-term humoral responses and CD8⁺ T cell immunity.^{6,7,46,47} We measured Spike (S)-specific T cell responses (Figure S2A) using activation-induced marker (AIM)^{5,6,48,49} and intracellular cytokine staining (ICS) assays.⁶

S-specific CD4⁺ and CD8⁺ T cell responses were assessed by an AND/OR Boolean combination gating strategy of the upregulation of CD69, CD40L, 4-1BB, and OX-40 upon a 15-h stimulation with an overlapping peptide pool spanning the S coding sequence (Figure S2B). This strategy detected S-specific AIM⁺ CD4⁺ (Figure S2C) and CD8⁺ T cell responses (Figure S2D) at all time points. Baseline responses were reported in other studies to result from previous cross-reactive expositions to common coronaviruses,^{50,51} and possibly to pre-exposition to abortive infection without seroconversion.⁵² To assess the functionality of the specific T cells, we measured the expression of IFN γ , interleukin (IL)-2, tumor necrosis factor alpha (TNF α), IL-17A, IL-10, and CD107a following a 6-h stimulation with the S peptide pool. We determined total cytokine⁺ CD4⁺ T cell responses by a similar OR Boolean combination gating strategy applied to the ICS results (Figure S2E). Specific cytokine⁺ CD4⁺ T cell responses were detected at all time points (Figure S2F). In most participants, no significant CD8⁺ T cell functions were detected and this could not be further assessed (Figure S2G).

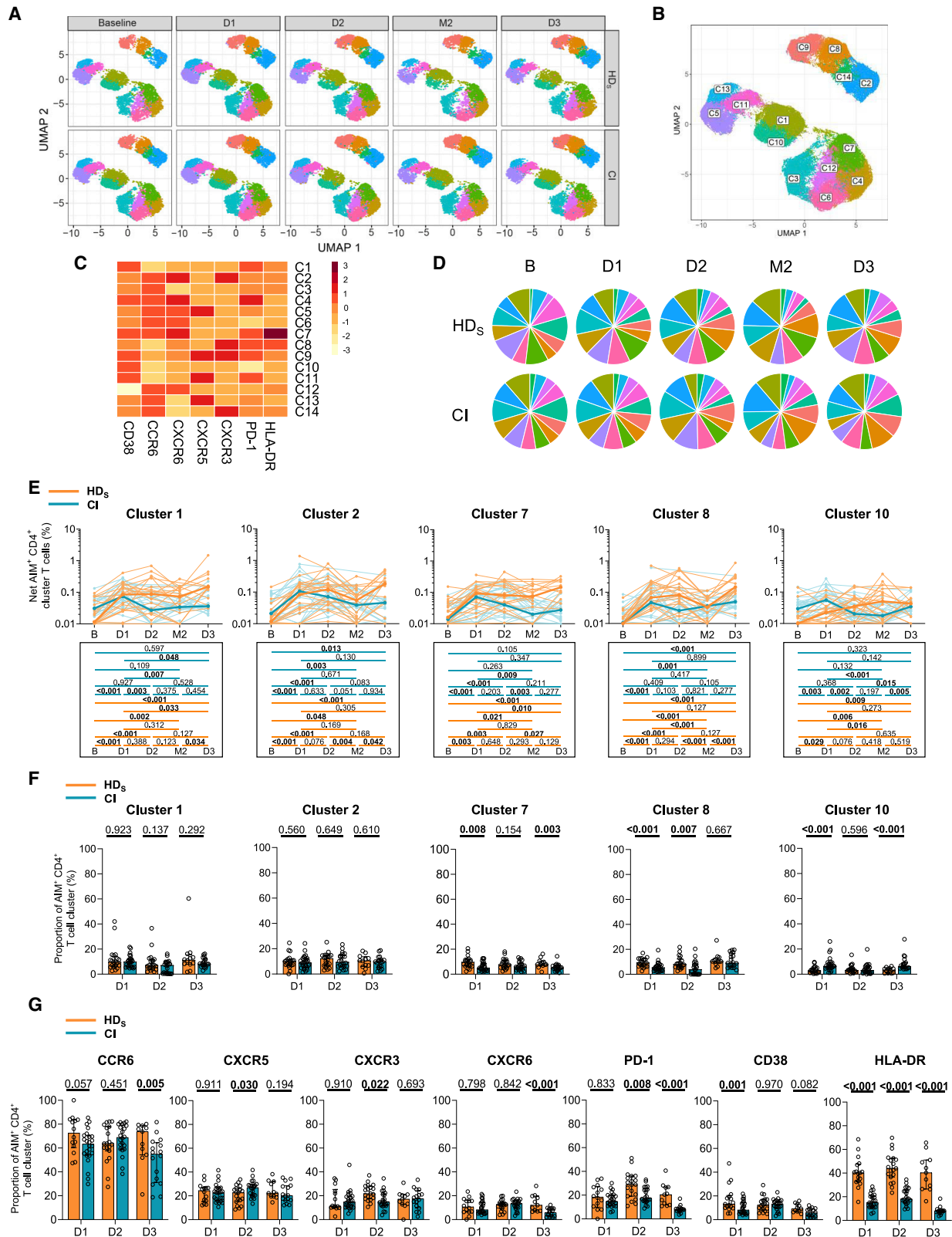
AIM⁺ CD4⁺ T cell responses in HD_S significantly increased after priming, plateaued at D2, waned slightly at M2, and further

(A and B) Net AIM⁺ CD4⁺ T cell responses. (A) Longitudinal analysis of S-specific AIM⁺ CD4⁺ T cell responses. Lines connect datapoints from the same donor. The bold lines represent the median values of each cohort. Right panel: statistical comparisons using a linear mixed model. (B) Comparisons between HD_S and CI participants. Bars represent median \pm interquartile range. Intercohort statistical comparisons using a linear mixed model are shown.

(C and D) Net cytokine⁺ CD4⁺ T cell responses measured by ICS. (C) Longitudinal analysis of the magnitude of cytokine⁺ CD4⁺ T cell responses. Lines connect datapoints from the same donor. The bold lines represent the median values of each cohort. Right panel: statistical comparisons using a linear mixed model. (D) Comparisons between HD_S and CI participants. Bars represent median \pm interquartile range. Intercohort statistical comparisons using a linear mixed model are shown.

(E and F) Net AIM⁺ CD8⁺ T cell responses. (E) Longitudinal analysis of S-specific AIM⁺ CD8⁺ T cell responses. Lines connect datapoints from the same donor. The bold lines represent the median values of each cohort. Right panel: statistical comparisons using a linear mixed model. (F) Comparisons between HD_S and CI participants. Bars represent median \pm interquartile range. Intercohort statistical comparisons using a linear mixed model are shown.

(G–I) Comparison of WT Wuhan-1-specific and Omicron BA.1-specific CD4⁺ and CD8⁺ T cell responses in HD_S (orange) and CI (blue) participants. Mann-Whitney tests are shown. (G) Net S-specific AIM⁺ CD4⁺ T cell responses, (H) Net S-specific cytokine⁺ CD4⁺ T cell responses, and (I) Net S-specific AIM⁺ CD8⁺ T cell responses. In (A–F) and (J) n = 20 HD_S, n = 26 CI participants; in (G) n = 10 HD_S, n = 10 CI; in (H) n = 7 HD_S, n = 7 CI; in (I) n = 9 HD_S, n = 10 CI participants.



(legend on next page)

increased to peak at D3 (Figure 2A). In CIs, the increase at D3 was more muted (Figure 2A). We observed a trend for stronger AIM⁺ CD4⁺ T cell responses in HD_S than in CIs at M2 and significantly higher magnitudes at D3 (Figure 2B). Cytokine⁺ CD4⁺ T cell responses in HD_S followed trajectories comparable with the AIM responses (Figures 2C and 2D), with stronger effector CD4⁺ T cell responses in HD_S compared with CI at D3 (Figure 2D). Unlike CD4⁺ T cells, AIM⁺ CD8⁺ T cell responses were lower in HD_S than CI at all time points except M2 and D3, at which they converged (Figures 2E and 2F). A trend for increased CD8⁺ T cell responses in HD_S at D3 compared with baseline was observed (Figures 2E and 2F). Of note, the CI cohort was characterized by sizable pre-existing CD8⁺ T cell responses at baseline, which likely affected the patterns observed (Figures 2E and 2F). Similar to the RBD⁺ B cell responses, a longer interval in HD_L did not show clear benefits for mRNA-vaccine-elicited cellular responses, for either CD4⁺ (Figure S2H and S2I) or CD8⁺ (Figure S2J) T cell responses.

We next assessed the presence of Omicron-reactive CD4⁺ and CD8⁺ T cell responses using an overlapping Omicron BA.1 S peptide pool on D3 samples. We detected Omicron BA.1-reactive AIM⁺ CD4⁺ (Figure 2G), cytokine⁺ CD4⁺ (Figure 2H), and AIM⁺ CD8⁺ (Figure 2I) T cell responses in both cohorts. The magnitude of WT and Omicron BA.1 S-specific CD4⁺ T cell responses did not differ between groups, suggesting cross-reactivity.

These data demonstrate the emergence of robust SARS-CoV-2-specific CD4⁺ T cell responses after the initial priming dose in HD_S, while a minimum of three doses was required to generate low CD8⁺ T cell responses.

mRNA vaccines elicit multifaceted AIM⁺ CD4⁺ T cell responses with qualitative features in HD distinct from CI participants

To qualitatively evaluate the S-specific AIM⁺ CD4⁺ T cell responses, we applied unsupervised analyses, as described.⁶ We studied chemokine receptors that are preferentially expressed by some lineages and involved in tissue homing (CXCR5 for T_{FH}; CXCR3 for T_{H1}; CCR6 for T_{H17}/T_{H22} and mucosal homing; CXCR6 for pulmonary mucosal homing, activation markers [Human Leukocyte Antigen-DR isotype (HLA-DR) and CD38], and an inhibitory checkpoint [programmed cell death protein 1 (PD-1)].

The distribution of clustered populations was represented by the uniform manifold approximation and projection (UMAP) algorithm. Cluster identity was performed using Phenograph,

resulting in the identification of 14 clusters (Figures 3A and 3B) based on distinct profiles of relative marker expression (Figures 3C and S3A). The 14 clusters were detectable at all time points (Figures 3A and 3D), most of them following frequency trajectories consistent with those observed for total AIM⁺ CD4⁺ T cells in both cohorts (Figures 3E and S3B). Some qualitative differences in relative proportions persisted after the third dose, in HD_S significant expansion of C4 and C7, two clusters enriched in CXCR6, CCR6, CD38, and PD-1 expression (Figures 3F and S3C). As shown in Figure 3C, C7 differed from C4 only by its enrichment in HLA-DR expression (Figure 3C). In univariate analyses, we observed at D3 in HD_S significant expansion of PD-1⁺, HLA-DR⁺, CXCR6⁺ cells, and, to a lesser extent, CD38⁺ cells both in absolute frequencies and as relative fractions of AIM⁺ CD4⁺ T cells (Figures 3G and S3D).

Therefore, mRNA vaccination elicits in both HD_S and CI a multifaceted response already observed after the first dose. After the full course of three vaccinations, T_H responses show some qualitative differences between cohorts, with higher expression in HD_S of chemokine receptors associated with mucosal immunity (CCR6, CXCR6), immune activation (HLA-DR), and the inhibitory immune checkpoint PD-1.

The first two vaccine inoculations elicit in HD_S a TNF α /IL-2 skewed T_H profile that is attenuated by the third dose

Given the qualitative differences observed with AIM assays, we used the same unsupervised approach to identify differences in CD4⁺ T cell effector functions. Expression of TNF α , CD107A, IL-10, IFN γ , IL-2, and IL-17A defined eight functional clusters, also detected at all time points (Figures 4A–4C and S4A) in both cohorts (Figure 4D). All clusters increased in magnitude after the first two doses, irrespective of clinical status (Figures 4E and S4B). Several qualitative differences were observed at D1 and D2 between cohorts, with the TNF α /IL-2-expressing C6 enriched in HD_S and C1, C2, and C8 overrepresented in CIs (Figure 4F). The third dose led to a partial convergence of the functional profiles, although the differences in C6 and C8 proportions remained significant at D3. In univariate analyses, TNF α and IL-2 expressions were also higher, and IFN γ and IL-10 were lower in HD_S compared with CIs during the initial vaccination series. Statistically significant differences were mostly abrogated by the third dose (Figures 4G and S4D).

These analyses show that HD_S are associated with a functional skewing upon mRNA vaccination. However, functional

Figure 3. mRNA vaccines elicit multifaceted AIM⁺ CD4⁺ T cell responses with qualitative features in HD distinct from CI participants

(A) Multiparametric UMAP representation of S-specific AIM⁺ CD4⁺ T cells based on CD38, HLA-DR, CCR6, CXCR6, CXCR5, CXCR3, and PD-1 expression at each time point, aggregated data for the HD_S and CI cohorts. The colors identify 14 populations clustered by unsupervised analysis using Phenograph.

(B) Each cluster is labeled on the global UMAP.

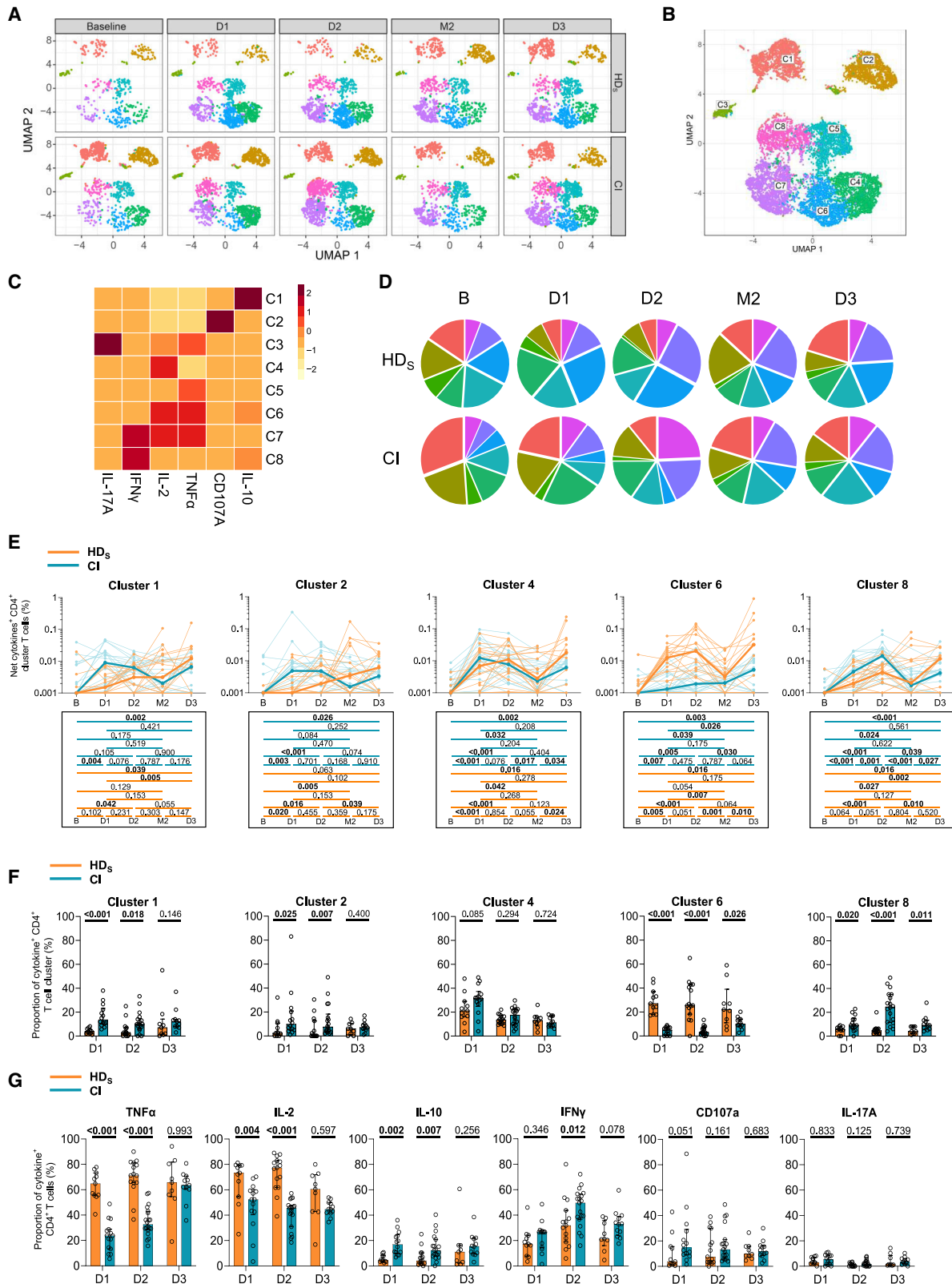
(C) Heatmap summarizing for each cluster the mean fluorescence intensity (MFI) of each loaded parameter.

(D) Pie charts depicting the representation of each identified cluster within total AIM⁺ CD4⁺ T cells.

(E) Longitudinal net frequencies of selected AIM⁺ CD4⁺ T cell clusters in HD_S (orange) and CI (blue) participants for clusters 1, 2, 7, 8, and 10. Lines connect data from the same donor. The bold lines represent the median values of each cohort. Wilcoxon tests for each pairwise comparison are shown below.

(F) Proportions of AIM⁺ clusters 1, 2, 7, 8, and 10 among AIM⁺ CD4⁺ T cells in HD_S and CI at D1, D2, and D3. Bars represent median \pm interquartile range. Mann-Whitney tests are shown.

(G) Cohort comparison of univariate analyses. Bars represent median \pm interquartile range. Statistical comparisons using a linear mixed model are shown. (A)–(G) n = 20 HD_S, n = 26 CI participants.



(legend on next page)

responses quantitatively and qualitatively converge between cohorts after the third dose.

Associations between RBD⁺ B cell and S-specific CD4⁺ T cell responses appear late in people on HD

We next examined temporal associations between B and CD4⁺ T cell responses. The net magnitudes of baseline, D1, and D2 responses for each AIM⁺ and cytokine⁺ cluster were correlated with post-boost RBD⁺ B cell responses at D2 (Figures 5A and S5A) or D3 (Figures 5B and S5B). No positive correlation between the two cellular compartments was found at D2 in HD_S (Figure 5A), in contrast to CIs (Figure S5A).⁶ Instead, several temporal associations were found in HD_S between T_H and RBD⁺ B cell responses at D3 (Figure 5B). Among the subsets with significant correlations, we found clusters enriched in CXCR3 and/or CXCR5 (AIM⁺ C8, C9, C11, and C14), and functional clusters enriched in IL-2 and TNF α (cytokine⁺ C4, C5, and C6) (Figure 5B).

We previously reported in a low-risk population of vaccinees that S-specific CXCR5⁺ AIM⁺ CD4⁺ T cells (cT_{FH}) after the first vaccine dose were predictive of RBD⁺ B cell responses after the second dose.⁶ We observed in HD_S an association between the cT_{FH} after the second dose and RBD⁺ B cell responses after the third dose (Figure 5C). In comparison, we only found a contemporary association between cT_{FH} and the RBD⁺ B cell responses after the third dose in CIs (Figure S5C). Narrowing our observations to PD-1⁺ cT_{FH} sub-populations, as they have been more strongly associated with B cell help,⁵³ we only observed temporal and contemporary correlations with the RBD-B⁺ cells at D3 in HD_S but not in CIs (Figure S5D).

These data demonstrate that there are temporal associations between CD4⁺ T cell help and B cell responses in HD_S participants. However, these correlations mostly emerge only after the third dose, consistent with the delayed kinetics of vaccine response in HD_S individuals.

Trajectories of vaccine features highlight the need for multiple boosts in people on HD

Our data reveal multiple immune features whose trajectories differed between cohorts. To compare these trajectories, we used a normalization strategy allowing comparisons between features irrespective of their magnitude. First, we calculated the average response per participant at all time points, for each feature. The ratio of the measured parameter at the time point to its averaged value defined its trajectory. Each ratio was then plotted on a heatmap, and clustered according to the normalized trajectory (Figures 6A and 6B). Three patterns were

observed among HD_S (Figure 6A): a first group of features peaked early after the priming (AIM⁺ C1, C12, and cytokine⁺ C3). A second group showed strong responses after different boosts. This group notably included humoral RBD⁺ IgG responses, CXCR3⁺ (C2, C8, C9, and C14) AIM clusters, and the TNF α ⁺ IL-2⁺-enriched C6 cluster. The third pattern corresponded to late response peaking at D3 and included RBD⁺ B cells, AIM⁺ CD8⁺ T cells, total AIM⁺ and cytokine⁺ CD4⁺ T cells, and several AIM⁺ and cytokine⁺ clusters.

Different trajectories were observed in CIs (Figure 6B). Unlike HD_S, total CD4 and CD8 responses, along with most AIM⁺ clusters, were mobilized early at D1 and were boosted at D2. The first boost enhanced total cytokine⁺ CD4⁺ T, B cell, and IgG responses and most cytokine⁺ clusters. The second boost further recalled these responses. In contrast, these immune features were delayed in HD_S and mobilized only at D3.

These results highlight the necessity for repeated boosting in HD_S to achieve peak immune responses for all immune features. This contrasts with overall earlier peak immune responses in CIs, for whom the immune parameters are robustly generated after the first or the second dose.

DISCUSSION

HD patients are at risk for severe infectious diseases, including COVID-19, and frequently respond poorly to standard vaccinations, including the initial two-dose series of SARS-CoV-2 mRNA vaccines. We show that the administration of a third vaccine dose is pivotal in stimulating B cell expansion and maturation to levels similar to controls. While previous studies reported reduced IFN γ -producing T cell responses, high-dimensional functional assays demonstrate that T_H responses in HD are phenotypically and functionally skewed, not quantitatively inferior. Our results on cellular immunity are consistent with vaccination strategies previously proved effective in HD: administration of multiple and/or higher injections can counterbalance their low responses to immunization.²⁷ We show that the optimal vaccine dosing interval is population dependent: in contrast to the general population,^{18–20} increasing the time between the first two doses resulted in weaker humoral and cellular immunity in HD.

The third dose led to partially converging antibody levels between cohorts, although they remained lower in HD than CIs at all time points. This is consistent with studies on HBV, hepatitis C virus (HCV), and influenza vaccines,²¹ and previous SARS-CoV-2 studies.^{32,54} Importantly, while the neutralization capacity was significantly lower after the second dose in HD_S than in

Figure 4. The first two vaccine inoculations elicit in HD_S a TNF α /IL-2 skewed T_H profile that is attenuated by the third dose

(A) Multiparametric UMAP representation of S-specific cytokine⁺ CD4⁺ T cells based on TNF α , CD107a, IL-10, IFN γ , IL-2, and IL-17A expression at each time point, aggregated data for the HD_S and CI cohorts. The colors identify eight populations clustered by unsupervised analysis using Phenograph. (B) Each cluster is labeled on the global UMAP. (C) Heatmap summarizing for each cluster the MFI of each loaded parameter. (D) Pie charts depicting the representation of each identified cluster within total cytokine⁺ CD4⁺ T cells. (E) Longitudinal frequencies of selected cytokine⁺ CD4⁺ T cell clusters 1, 2, 4, 6, and 8 in HD_S (orange) and CI (blue) participants. Lines connect data from the same donor. The bold lines represent the median values of each cohort. Wilcoxon tests for each pairwise comparisons are shown below the graphs. (F) Proportions of cytokine⁺ clusters 1, 2, 4, 6, and 8 among cytokine⁺ CD4⁺ T cells in HD_S and CI at D1, D2, and D3. Bars represent median \pm interquartile range. Mann-Whitney tests are shown. (G) Cohort comparison of univariate analyses. Bars represent median \pm interquartile range. Statistical comparisons using a linear mixed model are shown. In (A)–(G) n = 20 HD_S, n = 26 CI participants.

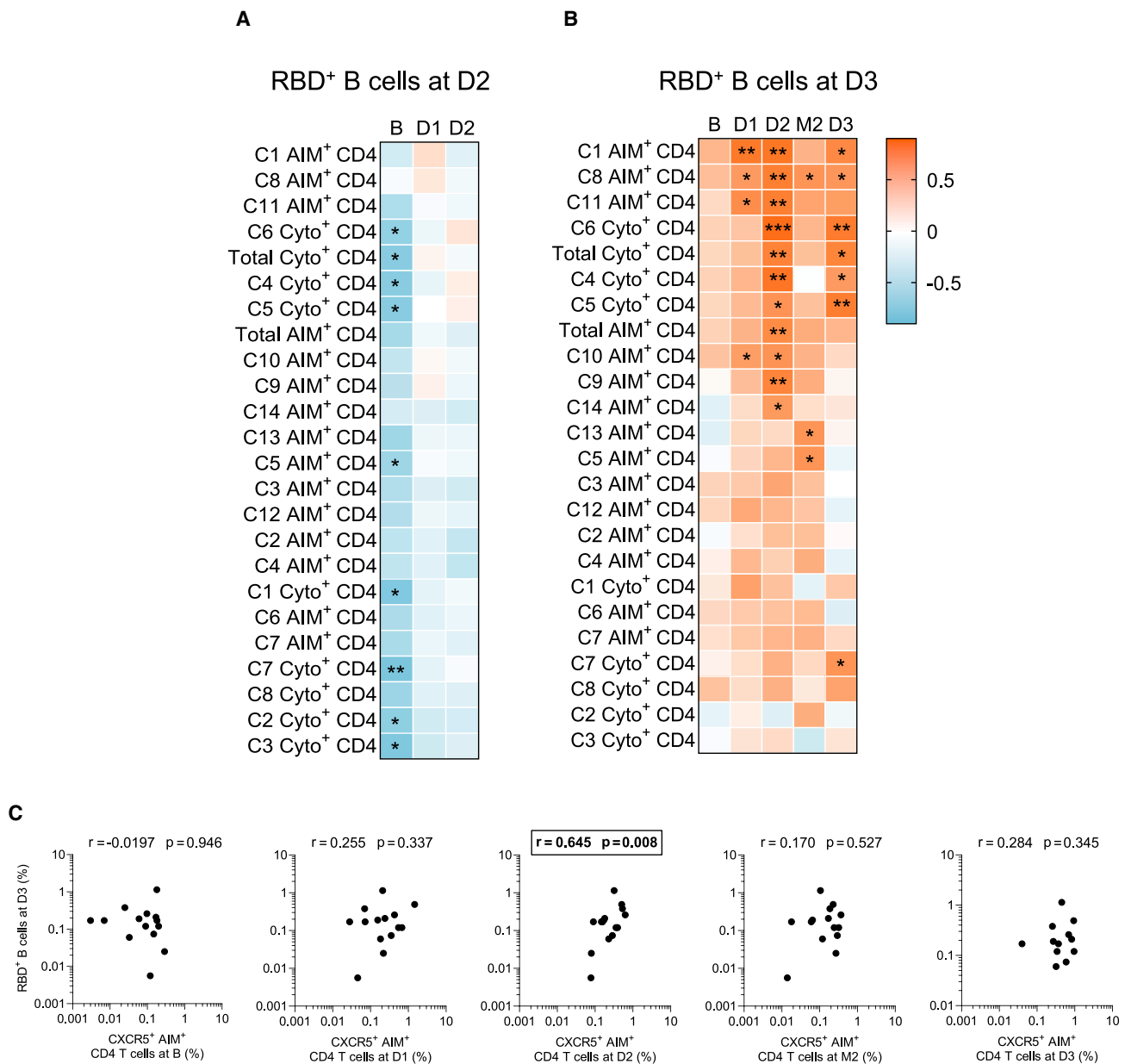


Figure 5. Associations between RBD⁺ B cell and S-specific CD4⁺ T cell responses appear late in people on HD

Temporal relationships between S-specific-CD4⁺ T cells and RBD⁺ B cells in HD_S.

(A) Correlation between total CD4⁺ T cell frequencies at B–D2 and RBD⁺ B cell frequencies at D2 in HD_S (n = 20).

(B) Correlation between total CD4⁺ T cell frequencies at B–D3 and RBD⁺ B cell frequencies at D3 in HD_S (n = 20). Asterisks indicate statistically significant p values from a Spearman test (*p < 0.05, **p < 0.01, ***p < 0.001). Colors indicate Spearman r.

(C) Correlations between frequencies of AIM⁺ CXCR5⁺ CD4⁺ T cells (for cT_{FH}) at the B–D3 visits and RBD⁺ B cell frequencies at D3 in HD_S. The r and p values from a Spearman test are indicated in each graph.

CI participants, the third dose significantly increased the neutralization responses in HD_S, bringing them to levels similar to those measured in CIs. The low frequencies of RBD⁺ B cell responses observed in HD after the first two doses are likely major contributors to these disparities, but their quality may play a role as well. There was a delay in the maturation of B cell responses with the persistence of immature and unswitched IgM⁺ and IgD⁺ RBD⁺

B cells in HD after two mRNA vaccine doses. These features were reported in kidney transplant recipients and dialysis patients^{55,56} and attributed to chronic inflammation caused by uremia toxins, along with defects of innate and T cell immunity.^{22,23,25} We also observed incomplete B cell maturation in a cohort of CI vaccinated with the standard 3-week short-interval regimen of mRNA vaccine,¹⁹ and thus we cannot univocally

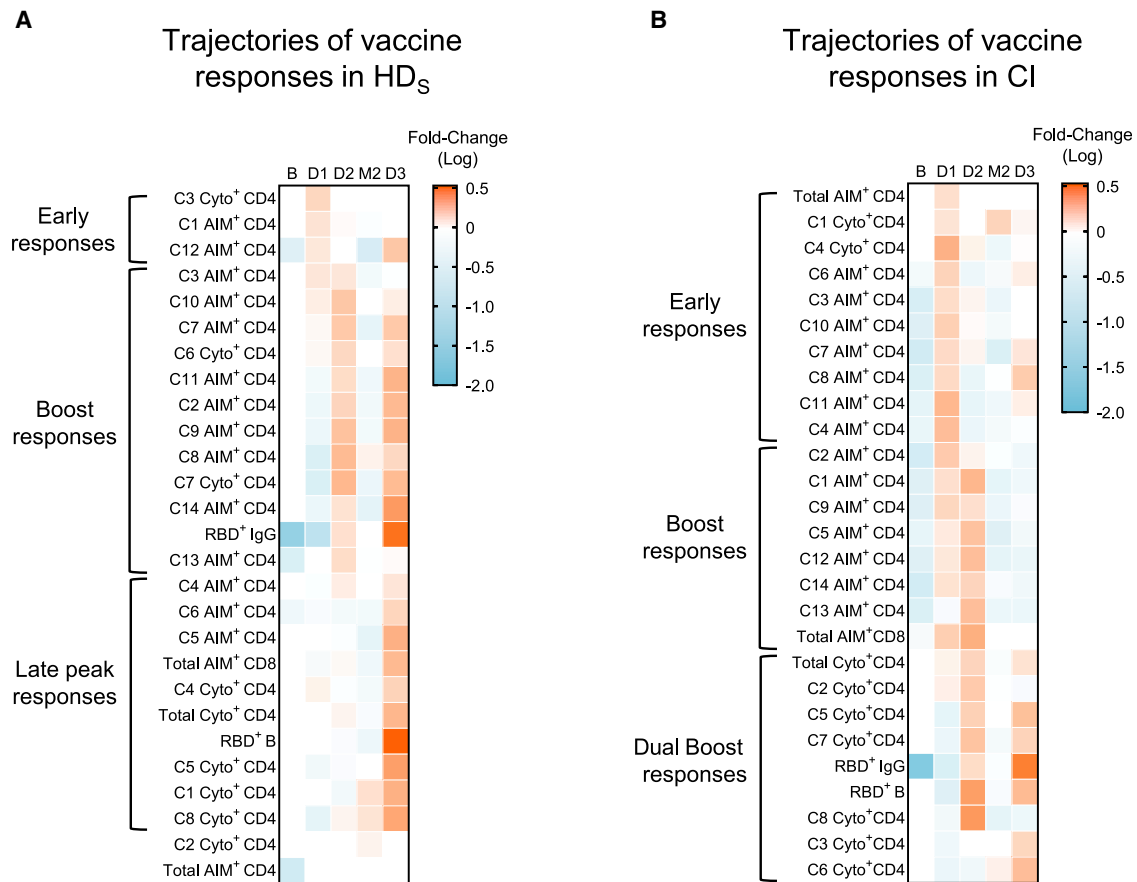


Figure 6. Trajectories of vaccine features highlight the need for multiple boosts in people on HD

(A and B) Trajectories of specific responses to mRNA vaccines in (A) HD_S and (B) CI. Trajectories are represented by the fold change of the response at each time point for a given feature, to the mean response of every time point for the same feature. Significant fold change is colored in either orange (if increased) or blue (if decreased) (mixed-effect analysis with Bonferroni correction for multiple comparisons, colors represent adjusted $p < 0.05$). White color represents fold changes that are not significantly different from the mean response. $n = 20$ HD_S and 26 CI.

delineate such defects in the 5-week-interval regimen applied to the HD_S cohort. The longer delay between the two first doses might contribute to this difference in maturation. Some vaccinal studies with a standard 21-day schedule reported that antigen-specific germinal center reactions were maintained after 6 months with an increase in somatic hypermutations over time.^{57,58}

Another key finding is that antigen-specific CD4⁺ T cell responses in HD were robust. As measured by multiplexed AIM and ICS, their magnitudes were comparable with or greater than those measured in controls, depending on the time point considered. These responses were as highly diverse in phenotype and function in HD_S as in CIs, but with qualitative differences that persisted throughout the longitudinal follow-up. We identified a pro-inflammatory/activated skewing of T_H responses in HD, with CCR6, CXCR6, and HLA-DR overexpression. Such CD4⁺ T cell populations have been described as preferentially recruited at sites of inflammation in autoimmune diseases, including inflammatory kidney disease.^{59,60} The simultaneous overexpression of the inhibitory checkpoint PD-1 by these cells may contribute to suboptimal help to other immune subsets.

PD-1 upregulation on both CD4⁺ and CD8⁺ T cell populations in HD was previously reported, indicating that this dysregulation is not unique to SARS-CoV-2-specific responses.⁶¹ While cT_{FH} cells are heterogeneous,⁶² with the PD-1⁺ fraction of cT_{FH} endowed with better helper capacity to B cells in direct *ex vivo* co-culture experiments than the quiescent PD-1⁻ fraction,^{53,63,64} the broad expression of PD-1 in HD complicates interpretation of this marker's upregulation on CXCR5⁺ CD4⁺ T cells in HD donors. As we draw a comparison with a control cohort, we therefore mostly used a conservative analysis on total CXCR5⁺ CD4⁺ T cells. However, analyses focusing on CXCR5⁺ PD-1⁺ cT_{FH} revealed some additional associations between T cell help and RBD⁺ B cells in the HD cohort.

CD4⁺ T cell responses in HD also presented functional skewing, with an overrepresentation of TNF α ⁺ and IL-2⁺, at the expense of IL-10⁺ and IFN γ ⁺ cells. These patterns raise questions about the impact of these cytokines in the establishment of vaccine responses. It has been shown that high levels of TNF α in COVID-19 could induce downstream activation of T_{H1} cells and block the final step of cT_{FH} differentiation.⁶⁵ This skewing may contribute to the delay observed in B cell responses to

SARS-CoV-2 vaccination due to insufficient feedback inhibition of pro-inflammatory cytokines.⁶⁶ The third dose was characterized in HD by the normalization of the effector function profile compared with the CI. Therefore, differences in the assays used (e.g., high-dimensional flow cytometry versus IFN γ Elispot) likely explain discrepancies between our data, in which we found robust CD4⁺ T cell responses in HD, and studies showing weaker T cell responses in this population.^{36,37}

CD8⁺ T cell responses tend to be generated in HD only after the third dose of vaccine, in light of previous results showing that people with ESRD have more exhausted and anergic CD8⁺ T cells than CIs.⁶¹ In both cohorts, CD8⁺ T cell responses remain low compared with their CD4⁺ T cell counterparts, consistent with the T_H-biased profile of responses elicited by SARS-CoV-2 mRNA vaccines.⁵⁷

Our results show that a long (12-week) interval between the first two doses is not beneficial for people receiving HD: both B cell and antibody responses in HD_L after the second dose tend to be weaker than those observed in the HD_S cohort. The optimal dosing interval in people receiving HD remains uncertain; another study suggests that a slightly longer interval (up to 45 days, compared with 35 days in our study) was associated with stronger humoral responses.⁶⁸

VOCs are an evolving challenge. After the third dose, HD developed B and CD4⁺ T cell responses specific to SARS-CoV-2 cross-reactive to Omicron BA.1 and at levels similar to CI. These findings complement previous reports showing that a third vaccine dose in HD enhanced neutralizing capacity of antibody responses against VOCs.⁹ Therefore, they might have protection against VOCs such as Omicron similar to CIs.^{8–10}

The global immune profiles observed longitudinally are consistent with a model in which HD respond more slowly to vaccination, with a third dose required to achieve B and T cell responses quantitatively and qualitatively close to those generated after two doses in CIs. Temporal associations between SARS-CoV-2-specific CD4⁺ T cell and RBD⁺ B cell responses are shifted by one dose in HD, with a delayed link between the two features compared with CIs. As cellular immune responses are comparatively less affected by the third dose in CIs than HD individuals, responses from both cohorts globally converged after the full vaccination course. Some studies have highlighted such convergence for anti-RBD IgG responses between HD and CIs after three mRNA vaccine doses.^{69,70} We believe that the finding that low cellular immunity responsiveness in HD can be overcome by repeat dosing is a major positive conclusion of our study and provides an immunological basis for previous findings on the antibody responses elicited by a third dose in this vulnerable population.

Determining whether the qualitative skewing of CD4⁺ T cell responses observed in HD can alter protection against breakthrough infection, how long cellular responses persist after the third dose, and how additional booster doses can further modulate the immune profiles identified will warrant further study.

Limitations of the study

Our study identified several alterations of adaptive immunity elicited by SARS-CoV-2 vaccines in HD patients, with a spectrum

of responsiveness in this population. Further studies are needed to better understand what individual factors may contribute to this heterogeneity. Mechanistic studies of related immune defects are very challenging, as no animal model for long-term chronic HD exists.

HD individuals are known to have frequent comorbidities and in our study were older than CIs. These factors might affect immune responses independently of HD. However, while the cohorts studied are too small to conduct multivariate analyses, chronic diseases are highly prevalent in HD patients, therefore distinguishing individual factors would have limited practical impact.

This study focuses on SARS-CoV-2 naive individuals. Additional studies are required to evaluate how prior infection shapes hybrid immunity in HD upon vaccination.

The size of the long-interval hemodialyzed cohort is small. It was not possible to recruit more suitable participants as the standard of care shifted to a short-interval regimen soon after the vaccination campaign began. The time points between D1 and D3, and D2 and D3, were not matched between cohorts. Therefore, this difference in timing might lead to potential quantitative differences in anti-SARS-CoV-2 antibodies due to the higher rate of RBD-B cell maturation in the short-delay cohort.

STAR★METHODS

Detailed methods are provided in the online version of this paper and include the following:

- KEY RESOURCES TABLE
- RESOURCE AVAILABILITY
 - Lead contact
 - Materials availability
 - Data and code availability
- EXPERIMENTAL MODEL AND SUBJECT DETAILS
 - Institutional permissions and oversight
 - Informed consent
 - Subject characteristics
- METHOD DETAILS
 - PBMCs and plasma isolation
 - Enzyme-linked immunosorbent assay
 - Virus neutralization assay
 - RBD-specific B cell staining
 - Activation-induced markers (AIM) assay
 - Intracellular cytokines staining (ICS) assay
- QUANTIFICATION AND STATISTICAL ANALYSIS
 - Statistics
 - Software scripts and visualization

SUPPLEMENTAL INFORMATION

Supplemental information can be found online at <https://doi.org/10.1016/j.xcrm.2023.100955>.

ACKNOWLEDGMENTS

The authors are grateful to the study participants. We thank the CRCHUM BSL3 and Flow Cytometry platforms for technical assistance and Dr. Johanne Poudrier for advice and discussions. This work was supported by an FRQS

Merit Research Scholar award #268471 (D.E.K.), the Réseau rénal Québécois, the Fondation du CHUM, le Ministère de l'Économie et de l'Innovation du Québec, Programme de soutien aux organismes de recherche et d'innovation (A.F.), a Canadian Institutes of Health Research (CIHR) operating grant #178344 (D.E.K. and A.F.), a CIHR Rapid Research COVID-19 funding opportunity grant #447760 (R.S.S.), a foundation grant #352417 (A.F.), a CIHR operating Pandemic and Health Emergencies Research grant #177958 (A.F.), and an Exceptional Fund COVID-19 from the Canada Foundation for Innovation (CFI) #41027 to A.F. and D.E.K. The Symphony flow cytometer was funded by a John R. Evans Leaders Fund from the Canada Foundation for Innovation (#37521 to D.E.K.) and the Fondation Sclérodémie Québec. A.F. is the recipient of Canada Research Chair on Retroviral Entry no. RCHS0235 950-232424. A.P. holds a Canada Research Chair in Multiple Sclerosis and the Power Corporation of Canada Chair of Université de Montréal. C.T. holds the Pfizer/Université de Montréal Chair on HIV translational research. V.M.L. is supported by an FRQS Junior 1 salary award. G.S. is supported by an FRQS doctoral fellowship and by a scholarship from the Department of Microbiology, Infectious Disease, and Immunology of the University of Montreal. M.B. was supported by a CIHR fellowship. A.T. was supported by a Mitacs Accélération postdoctoral fellowship. The funders had no role in the study design, data collection, analysis, decision to publish, or preparation of the manuscript.

AUTHOR CONTRIBUTIONS

Conceptualization, G.S., A.N., M.D., A.F., R.S.S., and D.E.K.; methodology, G.S., A.N., M.D., M.N., J.N., A.F., and D.E.K.; software, O.T. and G.S.; formal analysis, J.B. and R.L.B.; investigation, G.S., A.N., L.M., M.N., M.L., D.C., A.T., M.B., S.Y.G., C.B., G.G.L., and H.M.; resources, M.L., R.C., A.M.S.F., C.B., G.G.L., H.M., N.B., G.G.D., L.G., C.M., P.A., C.T., V.M.L., G.G., and S.D.; writing – original draft, G.S., A.N., M.D., and D.E.K.; writing – review & editing, G.S., A.N., M.D., and D.E.K.; supervision, D.E.K., A.F., and R.S.S.; funding acquisition, D.E.K., A.F., and R.S.S.

DECLARATION OF INTERESTS

C.T. serves as a consultant for Merck, Gilead, GSK, AstraZeneca, and Medicago.

Received: August 8, 2022

Revised: December 27, 2022

Accepted: February 2, 2023

Published: March 21, 2023

REFERENCES

- Haas, E.J., Angulo, F.J., McLaughlin, J.M., Anis, E., Singer, S.R., Khan, F., Brooks, N., Smaja, M., Mircus, G., Pan, K., et al. (2021). Impact and effectiveness of mRNA BNT162b2 vaccine against SARS-CoV-2 infections and COVID-19 cases, hospitalisations, and deaths following a nationwide vaccination campaign in Israel: an observational study using national surveillance data. *Lancet* 397, 1819–1829. [https://doi.org/10.1016/S0140-6736\(21\)00947-8](https://doi.org/10.1016/S0140-6736(21)00947-8).
- Tenforde, M.W., Self, W.H., Adams, K., Gaglani, M., Ginde, A.A., McNeal, T., Ghamande, S., Douin, D.J., Talbot, H.K., Casey, J.D., et al. (2021). Association between mRNA vaccination and COVID-19 hospitalization and disease severity. *JAMA* 326, 2043–2054. <https://doi.org/10.1001/jama.2021.19499>.
- Earle, K.A., Ambrosino, D.M., Fiore-Gartland, A., Goldblatt, D., Gilbert, P.B., Siber, G.R., Dull, P., and Plotkin, S.A. (2021). Evidence for antibody as a protective correlate for COVID-19 vaccines. *Vaccine* 39, 4423–4428. <https://doi.org/10.1016/j.vaccine.2021.05.063>.
- Gilbert, P.B., Montefiori, D.C., McDermott, A.B., Fong, Y., Benkeser, D., Deng, W., Zhou, H., Houchens, C.R., Martins, K., Jayashankar, L., et al. (2022). Immune correlates analysis of the mRNA-1273 COVID-19 vaccine efficacy clinical trial. *Science* 375, 43–50. <https://doi.org/10.1126/science.abm3425>.
- Tauzin, A., Gong, S.Y., Beaudoin-Bussièrès, G., Vézina, D., Gasser, R., Nault, L., Marchitto, L., Benlarbi, M., Chatterjee, D., Nayrac, M., et al. (2022). Strong humoral immune responses against SARS-CoV-2 Spike after BNT162b2 mRNA vaccination with a 16-week interval between doses. *Cell Host Microbe* 30, 97–109.e5. <https://doi.org/10.1016/j.chom.2021.12.004>.
- Nayrac, M., Dubé, M., Sannier, G., Nicolas, A., Marchitto, L., Tastet, O., Tauzin, A., Brassard, N., Lima-Barbosa, R., Beaudoin-Bussièrès, G., et al. (2022). Temporal associations of B and T cell immunity with robust vaccine responsiveness in a 16-week interval BNT162b2 regimen. *Cell Rep.* 39, 111013. <https://doi.org/10.1016/j.celrep.2022.111013>.
- Painter, M.M., Mathew, D., Goel, R.R., Apostolidis, S.A., Pattekar, A., Kuthuru, O., Baxter, A.E., Herati, R.S., Oldridge, D.A., Gouma, S., et al. (2021). Rapid induction of antigen-specific CD4(+) T cells is associated with coordinated humoral and cellular immunity to SARS-CoV-2 mRNA vaccination. *Immunity* 54, 2133–2142.e3. <https://doi.org/10.1016/j.immuni.2021.08.001>.
- Liu, J., Chandrashekar, A., Sellers, D., Barrett, J., Jacob-Dolan, C., Lifton, M., McMahan, K., Sciacca, M., VanWyk, H., Wu, C., et al. (2022). Vaccines elicit highly conserved cellular immunity to SARS-CoV-2 Omicron. *Nature* 603, 493–496. <https://doi.org/10.1038/s41586-022-04465-y>.
- Schmidt, F., Muecksch, F., Weisblum, Y., Da Silva, J., Bednarski, E., Cho, A., Wang, Z., Gaebler, C., Caskey, M., Nussenzweig, M.C., et al. (2022). Plasma neutralization of the SARS-CoV-2 Omicron variant. *N. Engl. J. Med.* 386, 599–601. <https://doi.org/10.1056/NEJMc2119641>.
- Tauzin, A., Gong, S.Y., Chatterjee, D., Ding, S., Painter, M.M., Goel, R.R., Beaudoin-Bussièrès, G., Marchitto, L., Boutin, M., Laumaea, A., et al. (2022). A boost with SARS-CoV-2 BNT162b2 mRNA vaccine elicits strong humoral responses independently of the interval between the first two doses. *Cell Rep.* 47, 111554. <https://doi.org/10.1016/j.celrep.2022.111554>.
- Polack, F.P., Thomas, S.J., Kitchin, N., Absalon, J., Gurtman, A., Lockhart, S., Perez, J.L., Pérez Marc, G., Moreira, E.D., Zerbini, C., et al. (2020). Safety and efficacy of the BNT162b2 mRNA covid-19 vaccine. *N. Engl. J. Med.* 383, 2603–2615. <https://doi.org/10.1056/NEJMoa2034577>.
- Baden, L.R., El Sahly, H.M., Essink, B., Kotloff, K., Frey, S., Novak, R., Diekmert, D., Spector, S.A., Rouphael, N., Creech, C.B., et al. (2021). Efficacy and safety of the mRNA-1273 SARS-CoV-2 vaccine. *N. Engl. J. Med. Overseas*. Ed. 384, 403–416. <https://doi.org/10.1056/NEJMoa2035389>.
- Absalon, J., Koury, K., and Gruber, W.C. (2021). Safety and efficacy of the BNT162b2 mRNA covid-19 vaccine. *N. Engl. J. Med.* 384, 1578–1577. <https://doi.org/10.1056/NEJMc2036242>.
- Tauzin, A., Nayrac, M., Benlarbi, M., Gong, S.Y., Gasser, R., Beaudoin-Bussièrès, G., Brassard, N., Laumaea, A., Vézina, D., Prévost, J., et al. (2021). A single dose of the SARS-CoV-2 vaccine BNT162b2 elicits Fc-mediated antibody effector functions and T cell responses. *Cell Host Microbe* 29, 1137–1150.e6. <https://doi.org/10.1016/j.chom.2021.06.001>.
- Paltiel, A.D., Zheng, A., and Schwartz, J.L. (2021). Speed versus efficacy: quantifying potential tradeoffs in COVID-19 vaccine deployment. *Ann. Intern. Med.* 174, 568–570. <https://doi.org/10.7326/M20-7866>.
- Tuite, A.R., Zhu, L., Fisman, D.N., and Salomon, J.A. (2021). Alternative dose allocation strategies to increase benefits from constrained COVID-19 vaccine supply. *Ann. Intern. Med.* 174, 570–572. <https://doi.org/10.7326/M20-8137>.
- Grunau, B., Goldfarb, D.M., Asamoah-Boaheng, M., Golding, L., Kirkham, T.L., Demers, P.A., and Lavoie, P.M. (2022). Immunogenicity of extended mRNA SARS-CoV-2 vaccine dosing intervals. *JAMA* 327, 279–281. <https://doi.org/10.1001/jama.2021.21921>.
- Hall, V.G., Ferreira, V.H., Wood, H., Ilerullo, M., Majchrzak-Kita, B., Manguiat, K., Robinson, A., Kulasingam, V., Humar, A., and Kumar, D. (2022). Delayed-interval BNT162b2 mRNA COVID-19 vaccination enhances humoral immunity and induces robust T cell responses. *Nat. Immunol.* 23, 380–385. <https://doi.org/10.1038/s41590-021-01126-6>.
- Nicolas, A., Sannier, G., Dubé, M., Nayrac, M., Tauzin, A., Painter, M.M., Goel, R.R., Laporte, M., Gendron-Lepage, G., Medjahed, H., et al.

- (2023). An extended SARS-CoV-2 mRNA vaccine prime-boost interval enhances B cell immunity with limited impact on T cells. *iScience* 26, 105904. <https://doi.org/10.1016/j.isci.2022.105904>.
20. Payne, R.P., Longet, S., Austin, J.A., Skelly, D.T., Dejnirattaisai, W., Adele, S., Meardon, N., Faustini, S., Al-Taei, S., Moore, S.C., et al. (2021). Immunogenicity of standard and extended dosing intervals of BNT162b2 mRNA vaccine. *Cell* 184, 5699–5714.e11. <https://doi.org/10.1016/j.cell.2021.10.011>.
 21. Zimmermann, P., and Curtis, N. (2019). Factors that influence the immune response to vaccination. *Clin. Microbiol. Rev.* 32, 000844-18. <https://doi.org/10.1128/CMR.00084-18>.
 22. Betjes, M.G. (2020). Uremia-associated ageing of the thymus and adaptive immune responses. *Toxins* 12, 224. <https://doi.org/10.3390/toxins12040224>.
 23. Girndt, M., Trojanowicz, B., and Ulrich, C. (2020). Monocytes in uremia. *Toxins* 12, 340. <https://doi.org/10.3390/toxins12050340>.
 24. Kim, J.K., Hong, C.W., Park, M.J., Song, Y.R., Kim, H.J., and Kim, S.G. (2017). Increased neutrophil extracellular trap formation in uremia is associated with chronic inflammation and prevalent coronary artery disease. *J. Immunol. Res.* 2017, 8415179. <https://doi.org/10.1155/2017/8415179>.
 25. Cohen, G. (2020). Immune dysfunction in uremia 2020. *Toxins* 12, 439. <https://doi.org/10.3390/toxins12070439>.
 26. Abdelrasoul, A., Westphalen, H., Saadati, S., and Shoker, A. (2021). Hemodialysis biocompatibility mathematical models to predict the inflammatory biomarkers released in dialysis patients based on hemodialysis membrane characteristics and clinical practices. *Sci. Rep.* 11, 23080. <https://doi.org/10.1038/s41598-021-01660-1>.
 27. Krueger, K.M., Ison, M.G., and Ghossein, C. (2020). Practical guide to vaccination in all stages of CKD, including patients treated by dialysis or kidney transplantation. *Am. J. Kidney Dis.* 75, 417–425. <https://doi.org/10.1053/j.ajkd.2019.06.014>.
 28. Clark, A., Jit, M., Warren-Gash, C., Guthrie, B., Wang, H.H.X., Mercer, S.W., Sanderson, C., McKee, M., Troeger, C., Ong, K.L., et al. (2020). Global, regional, and national estimates of the population at increased risk of severe COVID-19 due to underlying health conditions in 2020: a modelling study. *Lancet Global Health* 8, e1003–e1017. [https://doi.org/10.1016/S2214-109X\(20\)30264-3](https://doi.org/10.1016/S2214-109X(20)30264-3).
 29. Hsu, C.M., Weiner, D.E., Aweh, G., Miskulin, D.C., Manley, H.J., Stewart, C., Ladik, V., Hosford, J., Lacson, E.C., Johnson, D.S., and Lacson, E., Jr. (2021). COVID-19 among US dialysis patients: risk factors and outcomes from a national dialysis provider. *Am. J. Kidney Dis.* 77, 748–756.e1. <https://doi.org/10.1053/j.ajkd.2021.01.003>.
 30. Anand, S., Montez-Rath, M.E., Han, J., Garcia, P., Cadden, L., Hunsader, P., Morgan, C., Kerschmann, R., Beyer, P., Dittrich, M., et al. (2021). SARS-CoV-2 vaccine antibody response and breakthrough infection in patients receiving dialysis. *Ann. Intern. Med.* 175, 371–378. <https://doi.org/10.7326/M21-4176>.
 31. Goupil, R., Benlarbi, M., Beaubien-Souigny, W., Nadeau-Fredette, A.C., Chatterjee, D., Goyette, G., Gunaratnam, L., Lamarche, C., Tom, A., Finzi, A., et al. (2021). Short-term antibody response after 1 dose of BNT162b2 vaccine in patients receiving hemodialysis. *CMAJ (Can. Med. Assoc. J.)* 193, E793–E800. <https://doi.org/10.1503/cmaj.210673>.
 32. Grupper, A., Sharon, N., Finn, T., Cohen, R., Israel, M., Agbaria, A., Rechavi, Y., Schwartz, I.F., Schwartz, D., Lellouch, Y., and Shashar, M. (2021). Humoral response to the pfizer BNT162b2 vaccine in patients undergoing maintenance hemodialysis. *Clin. J. Am. Soc. Nephrol.* 16, 1037–1042. <https://doi.org/10.2215/CJN.03500321>.
 33. Alcázar-Arroyo, R., Portolés, J., López-Sánchez, P., Zalamea, F., Furaz, K., Méndez, Á., Nieto, L., Sánchez-Hernández, R., Pizarro, S., García, A., et al. (2021). Rapid decline of anti-SARS-CoV-2 antibodies in patients on haemodialysis: the COVID-FRIAT study. *Clin. Kidney J.* 14, 1835–1844. <https://doi.org/10.1093/ckj/sfab048>.
 34. Ducloux, D., Colladant, M., Chabannes, M., Yannarakis, M., and Courivaud, C. (2021). Humoral response after 3 doses of the BNT162b2 mRNA COVID-19 vaccine in patients on hemodialysis. *Kidney Int.* 100, 702–704. <https://doi.org/10.1016/j.kint.2021.06.025>.
 35. Crotty, S. (2019). T follicular helper cell biology: a decade of discovery and diseases. *Immunity* 50, 1132–1148. <https://doi.org/10.1016/j.immuni.2019.04.011>.
 36. Broseta, J.J., Rodríguez-Espinosa, D., Rodríguez, N., Mosquera, M.D.M., Marcos, M.Á., Egri, N., Pascal, M., Soruco, E., Bedini, J.L., Bayés, B., and Maduell, F. (2021). Humoral and cellular responses to mRNA-1273 and BNT162b2 SARS-CoV-2 vaccines administered to hemodialysis patients. *Am. J. Kidney Dis.* 78, 571–581. <https://doi.org/10.1053/j.ajkd.2021.06.002>.
 37. Melin, J., Svensson, M.K., Albinsson, B., Winqvist, O., and Pauksens, K. (2021). Humoral and cellular response to SARS-CoV-2 BNT162b2 mRNA vaccine in hemodialysis patients. *BMC Immunol.* 22, 70. <https://doi.org/10.1186/s12865-021-00458-0>.
 38. Webster, A.C., Nagler, E.V., Morton, R.L., and Masson, P. (2017). Chronic kidney disease. *Lancet* 389, 1238–1252. [https://doi.org/10.1016/S0140-6736\(16\)32064-5](https://doi.org/10.1016/S0140-6736(16)32064-5).
 39. Piccoli, L., Park, Y.J., Tortorici, M.A., Czudnochowski, N., Walls, A.C., Beltramello, M., Silacci-Fregni, C., Pinto, D., Rosen, L.E., Bowen, J.E., et al. (2020). Mapping neutralizing and immunodominant sites on the SARS-CoV-2 spike receptor-binding domain by structure-guided high-resolution serology. *Cell* 183, 1024–1042.e21. <https://doi.org/10.1016/j.cell.2020.09.037>.
 40. Shi, R., Shan, C., Duan, X., Chen, Z., Liu, P., Song, J., Song, T., Bi, X., Han, C., Wu, L., et al. (2020). A human neutralizing antibody targets the receptor-binding site of SARS-CoV-2. *Nature* 584, 120–124. <https://doi.org/10.1038/s41586-020-2381-y>.
 41. Barin, B., Kasap, U., Selçuk, F., Volkan, E., and Uluçkan, Ö. (2022). Comparison of SARS-CoV-2 anti-spike receptor binding domain IgG antibody responses after CoronaVac, BNT162b2, ChAdOx1 COVID-19 vaccines, and a single booster dose: a prospective, longitudinal population-based study. *Lancet. Microbe* 3, e274–e283. [https://doi.org/10.1016/S2666-5247\(21\)00305-0](https://doi.org/10.1016/S2666-5247(21)00305-0).
 42. Prévost, J., Gasser, R., Beaudoin-Bussièrès, G., Richard, J., Duerr, R., Laumaea, A., Anand, S.P., Goyette, G., Benlarbi, M., Ding, S., et al. (2020). Cross-sectional evaluation of humoral responses against SARS-CoV-2 spike. *Cell Rep. Med.* 1, 100126. <https://doi.org/10.1016/j.xcrm.2020.100126>.
 43. Hacisuleyman, E., Hale, C., Saito, Y., Blachere, N.E., Bergh, M., Conlon, E.G., Schaefer-Babajew, D.J., DaSilva, J., Muecksch, F., Gaebler, C., et al. (2021). Vaccine breakthrough infections with SARS-CoV-2 variants. *N. Engl. J. Med.* 384, 2212–2218. <https://doi.org/10.1056/NEJMoa2105000>.
 44. Macallan, D.C., Wallace, D.L., Zhang, Y., Ghattas, H., Asquith, B., de Lara, C., Worth, A., Panayiotakopoulos, G., Griffin, G.E., Tough, D.F., and Beverley, P.C.L. (2005). B-cell kinetics in humans: rapid turnover of peripheral blood memory cells. *Blood* 105, 3633–3640. <https://doi.org/10.1182/blood-2004-09-3740>.
 45. Kaminski, D.A., Wei, C., Qian, Y., Rosenberg, A.F., and Sanz, I. (2012). Advances in human B cell phenotypic profiling. *Front. Immunol.* 3, 302. <https://doi.org/10.3389/fimmu.2012.00302>.
 46. Goel, R.R., Apostolidis, S.A., Painter, M.M., Mathew, D., Pattekar, A., Kuthuru, O., Gouma, S., Hicks, P., Meng, W., Rosenfeld, A.M., et al. (2021). Distinct antibody and memory B cell responses in SARS-CoV-2 naive and recovered individuals following mRNA vaccination. *Sci. Immunol.* 6, eabi6950. <https://doi.org/10.1126/sciimmunol.abi6950>.
 47. Sette, A., and Crotty, S. (2021). Adaptive immunity to SARS-CoV-2 and COVID-19. *Cell* 184, 861–880. <https://doi.org/10.1016/j.cell.2021.01.007>.
 48. Morou, A., Brunet-Ratnasingham, E., Dubé, M., Charlebois, R., Mercier, E., Darko, S., Brassard, N., Nganou-Makamdop, K., Arumugam, S., Gendron-Lepage, G., et al. (2019). Altered differentiation is central to HIV-specific CD4(+) T cell dysfunction in progressive disease. *Nat. Immunol.* 20, 1059–1070. <https://doi.org/10.1038/s41590-019-0418-x>.

49. Niessl, J., Baxter, A.E., Morou, A., Brunet-Ratnasingham, E., Sannier, G., Gendron-Lepage, G., Richard, J., Delgado, G.G., Brassard, N., Turcotte, I., et al. (2020). Persistent expansion and Th1-like skewing of HIV-specific circulating T follicular helper cells during antiretroviral therapy. *EBioMedicine* 54, 102727. <https://doi.org/10.1016/j.ebiom.2020.102727>.
50. Braun, J., Loyal, L., Frentsch, M., Wendisch, D., Georg, P., Kurth, F., Hippenstiel, S., Dingeldey, M., Kruse, B., Fauchere, F., et al. (2020). SARS-CoV-2-reactive T cells in healthy donors and patients with COVID-19. *Nature* 587, 270–274. <https://doi.org/10.1038/s41586-020-2598-9>.
51. Grifoni, A., Weiskopf, D., Ramirez, S.I., Mateus, J., Dan, J.M., Moderbacher, C.R., Rawlings, S.A., Sutherland, A., Premkumar, L., Jadi, R.S., et al. (2020). Targets of T Cell responses to SARS-CoV-2 coronavirus in humans with COVID-19 disease and unexposed individuals. *Cell* 181, 1489–1501.e15. <https://doi.org/10.1016/j.cell.2020.05.015>.
52. Swadling, L., Diniz, M.O., Schmidt, N.M., Amin, O.E., Chandran, A., Shaw, E., Pade, C., Gibbons, J.M., Le Bert, N., Tan, A.T., et al. (2022). Pre-existing polymerase-specific T cells expand in abortive seronegative SARS-CoV-2. *Nature* 601, 110–117. <https://doi.org/10.1038/s41586-021-04186-8>.
53. Locci, M., Havenar-Daughton, C., Landais, E., Wu, J., Kroenke, M.A., Arlehamn, C.L., Su, L.F., Cubas, R., Davis, M.M., Sette, A., et al. (2013). Human circulating PD-1+CXCR3-CXCR5+ memory Tfh cells are highly functional and correlate with broadly neutralizing HIV antibody responses. *Immunity* 39, 758–769. <https://doi.org/10.1016/j.immuni.2013.08.031>.
54. Stumpf, J., Siepmann, T., Lindner, T., Karger, C., Schwöbel, J., Anders, L., Faulhaber-Walter, R., Schewe, J., Martin, H., Schirutschke, H., et al. (2021). Humoral and cellular immunity to SARS-CoV-2 vaccination in renal transplant versus dialysis patients: a prospective, multicenter observational study using mRNA-1273 or BNT162b2 mRNA vaccine. *Lancet Reg. Health. Eur.* 9, 100178. <https://doi.org/10.1016/j.lanepe.2021.100178>.
55. Rincon-Arevalo, H., Choi, M., Stefanski, A.L., Halleck, F., Weber, U., Szeleinski, F., Jahrsdörfer, B., Schrezenmeier, H., Ludwig, C., Sattler, A., et al. (2021). Impaired humoral immunity to SARS-CoV-2 BNT162b2 vaccine in kidney transplant recipients and dialysis patients. *Sci. Immunol.* 6, eabj1031. <https://doi.org/10.1126/sciimmunol.abj1031>.
56. Lederer, K., Bettini, E., Parvathaneni, K., Painter, M.M., Agarwal, D., Lundgreen, K.A., Weirick, M., Muralidharan, K., Castaño, D., Goel, R.R., et al. (2022). Germinal center responses to SARS-CoV-2 mRNA vaccines in healthy and immunocompromised individuals. *Cell* 185, 1008–1024.e15. <https://doi.org/10.1016/j.cell.2022.01.027>.
57. Cho, A., Muecksch, F., Wang, Z., Ben Tanfous, T., DaSilva, J., Raspe, R., Johnson, B., Bednarski, E., Ramos, V., Schaefer-Babajew, D., et al. (2022). Antibody evolution to SARS-CoV-2 after single-dose Ad26-COV2.S vaccine in humans. *J. Exp. Med.* 219, e20220732. <https://doi.org/10.1084/jem.20220732>.
58. Kim, W., Zhou, J.Q., Horvath, S.C., Schmitz, A.J., Sturtz, A.J., Lei, T., Liu, Z., Kalaidina, E., Thapa, M., Alsoussi, W.B., et al. (2022). Germinal centre-driven maturation of B cell response to mRNA vaccination. *Nature* 604, 141–145. <https://doi.org/10.1038/s41586-022-04527-1>.
59. Hou, L., and Yuki, K. (2022). CCR6 and CXCR6 identify the Th17 cells with cytotoxicity in experimental autoimmune encephalomyelitis. *Front. Immunol.* 13, 819224. <https://doi.org/10.3389/fimmu.2022.819224>.
60. Linke, A., Tiegs, G., and Neumann, K. (2022). Pathogenic T-cell responses in immune-mediated glomerulonephritis. *Cells* 11, 1625. <https://doi.org/10.3390/cells11101625>.
61. Hartzell, S., Bin, S., Cantarelli, C., Haverly, M., Manrique, J., Angeletti, A., Manna, G.L., Murphy, B., Zhang, W., Levitsky, J., et al. (2020). Kidney failure associates with T cell exhaustion and imbalanced follicular helper T cells. *Front. Immunol.* 11, 583702. <https://doi.org/10.3389/fimmu.2020.583702>.
62. Schmitt, N., and Ueno, H. (2013). Blood Tfh cells come with colors. *Immunity* 39, 629–630. <https://doi.org/10.1016/j.immuni.2013.09.011>.
63. Crotty, S. (2014). T follicular helper cell differentiation, function, and roles in disease. *Immunity* 41, 529–542. <https://doi.org/10.1016/j.immuni.2014.10.004>.
64. He, J., Tsai, L.M., Leong, Y.A., Hu, X., Ma, C.S., Chevalier, N., Sun, X., Vandenberg, K., Rockman, S., Ding, Y., et al. (2013). Circulating precursor CCR7(lo)PD-1(hi) CXCR5(+) CD4(+) T cells indicate Tfh cell activity and promote antibody responses upon antigen reexposure. *Immunity* 39, 770–781. <https://doi.org/10.1016/j.immuni.2013.09.007>.
65. Kaneko, N., Kuo, H.H., Boucau, J., Farmer, J.R., Allard-Chamard, H., Mahajan, V.S., Piechocka-Trocha, A., Lefteri, K., Osborn, M., Bals, J., et al. (2020). Loss of bcl-6-expressing T follicular helper cells and germinal centers in COVID-19. *Cell* 183, 143–157.e13. <https://doi.org/10.1016/j.cell.2020.08.025>.
66. Ulrich, C., Wilke, A., Schleicher, N., Girndt, M., and Fiedler, R. (2020). Hypervolemia-induced immune disturbances do not involve IL-1ss but IL-6 and IL-10 activation in haemodialysis patients. *Toxins* 12, 159. <https://doi.org/10.3390/toxins12030159>.
67. Corbett, K.S., Edwards, D.K., Leist, S.R., Abiona, O.M., Boyoglu-Barnum, S., Gillespie, R.A., Himansu, S., Schäfer, A., Ziwawo, C.T., DiPiazza, A.T., et al. (2020). SARS-CoV-2 mRNA vaccine design enabled by prototype pathogen preparedness. *Nature* 586, 567–571. <https://doi.org/10.1038/s41586-020-2622-0>.
68. Haarhaus, M., Duhanes, M., Leševic, N., Matej, B., Ramsauer, B., Da Silva Rodrigues, R., Su, J., Haase, M., Santos-Araújo, C., and Macario, F. (2022). Improved immunologic response to COVID-19 vaccine with prolonged dosing interval in haemodialysis patients. *Scand. J. Immunol.* 95, e13152. <https://doi.org/10.1111/sji.13152>.
69. Shashar, M., Nacasch, N., Grupper, A., Benchetrit, S., Halperin, T., Erez, D., Rozenberg, I., Shitrit, P., Sela, Y., Wand, O., and Cohen-Hagai, K. (2022). Humoral response to pfizer BNT162b2 vaccine booster in maintenance hemodialysis patients. *Am. J. Nephrol.* 53, 207–214. <https://doi.org/10.1159/000521676>.
70. Verdier, J.F., Boyer, S., Chalmin, F., Jeribi, A., Egasse, C., Maggi, M.F., Auvray, P., and Yalaoui, T. (2022). Response to three doses of the Pfizer/BioNTech BNT162b2 COVID-19 vaccine: a retrospective study of a cohort of haemodialysis patients in France. *BMC Nephrol.* 23, 189. <https://doi.org/10.1186/s12882-022-02751-5>.
71. Beaudoin-Bussièrès, G., Laumaea, A., Anand, S.P., Prévost, J., Gasser, R., Goyette, G., Medjahed, H., Perreault, J., Tremblay, T., Lewin, A., et al. (2020). Decline of humoral responses against SARS-CoV-2 spike in convalescent individuals. *mBio* 11, 025900-20. <https://doi.org/10.1128/mBio.02590-20>.
72. Quintelier, K., Couckuyt, A., Emmaneel, A., Aerts, J., Saeys, Y., and Van Gassen, S. (2021). Analyzing high-dimensional cytometry data using FlowSOM. *Nat. Protoc.* 16, 3775–3801. <https://doi.org/10.1038/s41596-021-00550-0>.

STAR★METHODS

KEY RESOURCES TABLE

REAGENT or RESOURCE	SOURCE	IDENTIFIER
Antibodies		
UCHT1 (BUV395) [Human anti-CD3]	BD Biosciences	Cat#563546; Lot:9,058,566; RRID:AB_2744387
1B5 (BUV 395) [Human anti-CCR10]	BD Biosciences	Cat# 565322; Lot:1,198,884; RRID:AB_2739181
IA6-2 (BUV 563) [Human anti-IgD]	BD Biosciences	Cat# 741394; Lot:2,048,494; RRID:AB_2870889
MI15 (BUV 661) [Human anti-CD138]	BD Biosciences	Cat# 749873; Lot:1,140,733; RRID:AB_2874113
UCH-B1 (BUV 737) [Human anti-IgM]	BD Biosciences	Cat# 748928; Lot:1,154,015; RRID:AB_2873331
ML5 (BUV 805) [Human anti-CD24]	BD Biosciences	Cat# 742010; Lot:1,154,017; RRID:AB_2871308
G18-145 (BV421) [Human anti-IgG]	BD Biosciences	Cat# 562581; Lot:1,033,053; RRID:AB_2737665
SJ25C1 (BV650) [Human anti-CD19]	Biolegend	Cat# 363026; Lot:B328293; RRID:AB_2564255
2H7 (BV711) [Human anti-CD20]	BD Biosciences	Cat# 563126; Lot:2,032,072; RRID:AB_2313579
B-LY4 (BV786) [Human anti-CD21]	BD Biosciences	Cat# 740969; Lot:1,167,364; RRID:AB_2740594
G46-6 (BB700) [Human anti-HLADR]	BD Biosciences	Cat# 566480; Lot:1,053,189; RRID:AB_2744477
HIT2 (BB790) [Human anti-CD38]	BD Biosciences	Cat#624296; Lot:9,119,974; CUSTOM
IS11-8E10 (PE) [Human anti-IgA]	Miltenyi	Cat# 130-113-476; Lot:5,210,405,486; RRID:AB_2733861
M-T271 (APC-R700) [Human anti-CD27]	BD Biosciences	Cat# 565116; Lot:0,262,146; RRID:AB_2739074
UCHT1 (BUV496) [Human anti-CD3]	BD Biosciences	Cat#612941; Lot:1,022,424; RRID:AB_2870222
L200 (BV711) [Human anti-CD4]	BD Biosciences	Cat#563913; Lot:03,000,025; RRID:AB_2738484

(Continued on next page)

Continued

REAGENT or RESOURCE	SOURCE	IDENTIFIER
SK3 (BB630) [Human anti-CD4]	BD Biosciences	Cat#624294; Lot:0,289,566; CUSTOM
RPA-T8 (BV570) [Human anti-CD8]	Biologend	Cat#301037; Lot:B281322; RRID:AB_10933259
M5E2 (BUV805) [Human anti-CD14]	BD Biosciences	Cat#612902; Lot:0,262,150; RRID:AB_2870189
M5E2 (BV480) [Human anti-CD14]	BD Biosciences	Cat#746304; Lot:9,133,961; RRID:AB_2743629
3G8 (BV650) [Human anti-CD16]	Biologend	Cat#302042; Lot:B323847; RRID:AB_2563801
HIB19 (APC-eFluor780) [Human anti-CD19]	Thermo Fisher Scientific	Cat#47-0199; Lot:2,145,095; RRID:AB_1582231
HIB19 (BV480) [Human anti-CD19]	BD Biosciences	Cat#746457; Lot:1,021,649; RRID:AB_2743759
HI100 (PerCP Cy5.5) [Human anti-CD45RA]	BD Biosciences	Cat#563429; Lot:8,332,746; RRID:AB_2738199
NCAM16.2 (BUV737) [Human anti-CD56]	BD Biosciences	Cat#564448; Lot:8,288,818; RRID:AB_2744432
FN50 (PerCP-eFluor710) [Human anti-CD69]	Thermo Fisher Scientific	Cat#46-0699-42; Lot:1,920,361; RRID:AB_2573694
FN50 (BV650) [Human anti-CD69]	Biologend	Cat# 310934; Lot:B303462; RRID:AB_2563158
H4A3 (BV786) [Human anti-CD107A]	BD Biosciences	Cat#563869; Lot:8,144,866; RRID:AB_2738458
ACT35 (APC) [Human anti-CD134 (OX40)]	BD Biosciences	Cat#563473; Lot:1,015,537; RRID:AB_2738230
4B4-1 (PE-Dazzle 594) [Human anti-CD137 (4-1BB)]	Biologend	Cat# 309826; Lot:B253152; RRID:AB_2566260
TRAP1 (BV421) [Human anti-CD154 (CD40L)]	BD Biosciences	Cat#563886; Lot:9,037,850; RRID:AB_2738466
TRAP1 (PE) [Human anti-CD154 (CD40L)]	BD Biosciences	Cat#555700; Lot:7,086,896; RRID:AB_396050
J25D4 (BV421) [Human anti-CD185 (CXCR5)]	Biologend	Cat# 356920; Lot:B325837; RRID:AB_2562303
B27 (PECy7) [Human anti-IFN- γ]	BD Biosciences	Cat#557643; Lot:8,256,597; RRID:AB_396760

(Continued on next page)

Continued

REAGENT or RESOURCE	SOURCE	IDENTIFIER
MQ1-17H12 (PE-Dazzle594) [Human anti-IL-2]	Biologend	Cat#500344; Lot:B2261476; RRID:AB_2564091
JES3-9D7 (PE) [Human anti-IL-10]	BD Biosciences	Cat#554498; Lot:8,198,773; RRID:AB_395434
eBio64CAP17 (eFluor660) [Human anti-IL-17A]	Thermo Fisher Scientific	Cat#50-7179-42; Lot:2,151,998; RRID:AB_11149126
Mab11 (Alexa Fluor 488) [Human anti-TNF- α]	Biologend	Cat#502915; Lot:B285221; RRID:AB_493121
LIVE/DEAD Fixable dead cell	Thermo Fisher Scientific	L34960
Cell lines		
HEK293T cells	ATCC	Cat#CRL-3216 RRID:CVCL_0063
293T-ACE2 cells	Ref. ⁴²	N/A
Chemicals, peptides, recombinant proteins, and DNA		
RBD1 probe (Alexa Fluor 488)	<i>In house</i>	N/A
RBD2 probe (Alexa Fluor 594)	<i>In house</i>	N/A
RBD Omicron (Alexa Fluor 647)	<i>In house</i>	N/A
PepMix™ SARS-CoV-2 (Spike Glycoprotein)	JPT	Cat#PM-WCPV-S-1
Staphylococcal Enterotoxin B (SEB)	Toxin technology	Cat#BT202
PepMix™ SARS-CoV-2 (Spike B.1.1.529/Omicron Glycoprotein)	JPT	Cat#PM-SARS2-SMUT08-1
SARS-CoV-2 Spike RBD, His Tag (B.1.1.529/Omicron)	Acrobiosystems	Cat#SPD-C522e-100ug
pNL4.3 R-E– Luc	NIH AIDS Reagent program	Cat#3418
pCG1-SARS-CoV-2 Spike D614G	Ref. ⁷¹	N/A
Software and algorithms		
Flow Jo v10.8.0	Flow Jo	https://www.flowjo.com
GraphPad Prism v8.4.1	GraphPad	https://www.graphpad.com
R studio v4.1.0	R studio	https://rstudio.com
R codes scripted	Github	https://github.com/otastet/Nayrac_et_al

RESOURCE AVAILABILITY

Lead contact

Further information and requests for resources and reagents should be directed to and will be fulfilled by the lead contact, Daniel E. Kaufmann (daniel.kaufmann@chuv.ch or daniel.kaufmann@umontreal.ca).

Materials availability

All unique reagents generated during this study are available from the [lead contact](#) upon a material transfer agreement (MTA).

Data and code availability

- The published article includes all datasets generated and analyzed for this study. Further information and requests for resources and reagents should be directed to and will be fulfilled by the [lead contact](#) Author (daniel.kaufmann@chuv.ch).
- We adapted previously submitted⁶ R codes scripted to perform unsupervised analyzes on B and T cells from hemodialyzed donors and controls individuals. All original codes have been deposited on Github and are publicly available as of the date of publication. URL link is listed in the [key resources table](#).

EXPERIMENTAL MODEL AND SUBJECT DETAILS

Institutional permissions and oversight

All work was conducted in accordance with the Declaration of Helsinki and approved by the institutional boards of the participating institutions (Quebec Renal Network³¹ multicentric protocol MP-02-2021-9006; and CHUM protocols 19.381 and 20.065).

Informed consent

All work was conducted in accordance with the Declaration of Helsinki and written informed consent obtained before enrollment into the study.

Subject characteristics

Subject characteristics are summarized in [Table 1](#). Patients with end-stage renal disease receiving hemodialysis (HD) were enrolled into the Quebec Renal Network (QRN) COVID-19 Study as previously described³¹ and followed every 2-3 days at the *Center Universitaire de Santé McGill* (CUSM), the *Center Hospitalier de l'Université de Montréal* (CHUM), and the *Hôpital du Sacré-Coeur de Montréal* (HSCM). Participants from this cohort were followed and sampled before and after vaccination. Blood draws were performed at baseline (B) 12 days before the first dose of vaccine with mRNA vaccine, 4 weeks after the first dose (D1), 4 weeks post second dose (D2), 12 weeks after the second dose (M2) and 4-5 weeks post third dose (D3). Hemodialyzed participants were divided into two cohorts: a short interval cohort for which the first two vaccine doses were administered 5 weeks apart (HD_S, n = 20); and a long interval cohort (HD_L, n = 7) for which the first two doses were given 12 weeks apart when vaccine scarcity was limiting.

The cohort of control individuals (CI, n = 26) consisted of healthcare workers who did not have a major medical precondition qualifying for a short interval schedule (e.g, immunosuppression) and who received the first two vaccine doses 16 weeks apart per Quebec public health guidelines early in the vaccination campaign in Canada. The third inoculation was given 7 months after the second dose. Blood draws were performed at baseline (B) 1 day before the first dose of mRNA vaccine, 3 weeks after the first dose (D1), 3 weeks following the second dose (D2), 16 weeks after the second dose (M2), and 4 weeks after the third dose (D3).

Median age and interquartile range for the HD_S cohort was 61 [55-64], and 13 individuals were males (65%). Median age and interquartile range for the CI cohort were younger (median = 51 [41-56], p < 0.001), and 11 individuals were males (42%). The HD_L cohort was not significantly older (median = 66 [55-77]) and 4 individuals were males (57%). Time on hemodialysis between each cohort was comparable (See [Table 1](#)).

METHOD DETAILS

PBMCs and plasma isolation

Peripheral blood mononuclear cells (PBMCs) were isolated from blood samples by Ficoll density gradient centrifugation and cryopreserved in liquid nitrogen until use. Plasma was stored at -80°C . For antibody assays, plasma was heat-inactivated for 1 h at 56°C prior to experiments. Plasma from uninfected donors collected before the pandemic were used as negative controls and used to calculate the seropositivity threshold in our ELISA assay.

Enzyme-linked immunosorbent assay

The SARS-CoV-2 RBD ELISA assay used was previously described.⁴² Briefly, recombinant SARS-CoV-2 RBD proteins or BSA (2.5 $\mu\text{g}/\text{mL}$) as negative control were prepared in PBS and adsorbed to plates overnight at 4°C . Coated wells were subsequently blocked with blocking buffer and then washed. CR3022 mAb (50 ng/ml) or a $1/50$ dilution of plasma from HD, or CI donors were prepared in a diluted solution of blocking buffer and incubated with the RBD-coated wells. Plates were washed followed by incubation with the respective secondary Abs. The binding of CR3022 IgG was quantified with HRP-conjugated antibodies specific for the Fc region of human IgG and used to normalize the RLU from each plate. HRP enzyme activity was determined after the addition of a 1:1 mix of Western Lightning oxidizing and luminol reagents (Perkin Elmer Life Sciences). Light emission was measured with an LB942 Tri-Star luminometer (Berthold Technologies). Signal obtained with BSA was subtracted for each plasma and was then normalized to the signal obtained with CR3022 present in each plate. The seropositivity threshold was established using the following formula: mean of pre-pandemic SARS-CoV-2 negative plasma + (3 SD of the mean of pre-pandemic SARS-CoV-2 negative plasma).

Virus neutralization assay

The SARS-CoV-2 virus neutralization assay was used previously.⁴² Briefly, 293T cells were transfected with the lentiviral vector pNL4.3 R-E- Luc plasmid (NIH AIDS Reagent Program) and a plasmid encoding for the full-length SARS-CoV-2 Spike D614G glycoprotein^{42,71} at a ratio of 10:1. Two days post-transfection, cell supernatants were harvested and stored at -80°C until use. Pseudoviral particles were incubated with the indicated plasma dilutions (1/50; 1/250; 1/1250; 1/6250; $1/3$ 1/31,250) for 1 h at 37°C and were then added to the 293T-ACE2 target cells followed by incubation for 48 h at 37°C . Then, cells were lysed and followed

by one freeze-thaw cycle. An LB942 Tri-Star luminometer (Berthold Technologies) was used to measure the luciferase activity. The neutralization half-maximal inhibitory dilution (ID₅₀) represents the plasma dilution to inhibit 50% of the infection of 293T-ACE2 cells by SARS-CoV-2 pseudoviruses.

RBD-specific B cell staining

PBMCs were resuspended at 4×10^6 cells/mL in RPMI (Gibco by Life Technologies) supplemented with penicillin/streptomycin (Gibco by Life Technologies), 10% heat inactivated FCS and incubated at 37°C, 5% CO₂ for 2hrs in the presence of fluorescently labeled CCR10 antibody.

For surface stain, PBMCs were first stained for viability dye (Aquavidin, ThermoFisher, 20min, 4°C) next with a mix containing a brilliant stain buffer (BD Biosciences), the surface markers for B cells detection (CD19, CD20, CD21, IgM and IgD), B cells memory phenotype (CD24, CD27, IgG and IgA), plasmablasts and plasma cells (CD38 and CD138) phenotypes, T-cells and monocytes exclusion (CD3, CD56, CD14, and CD16) (30min, 4°C) (see [Table S2](#) for antibodies), as well as fluorescently-labeled probes for RBD⁺ B cells detection targeting two different epitopes of the RBD (RBD1-AF488 and RBD2 AF594). Omicron BA.1-RBD peptide (Accrobiosystem) was labeled, and the Omicron BA.1-RBD probe was also added into the mix where appropriate (RBD Omicron BA.1 AF647). Cells were fixed with 1% paraformaldehyde (Sigma-Aldrich) for 15 min at room temperature before filtration for acquisition on a FACSymphony A5 Cell Analyzer (BD Biosciences) and analyzed using FlowJo (BD, v10.6.2).

Activation-induced markers (AIM) assay

PBMCs were plated in a 96-wells flat bottom plate, at 10×10^6 cells/mL RPMI (Gibco by Life Technologies) supplemented with penicillin/streptomycin (Gibco by Life Technologies), 10% heat inactivated FCS and incubated at 37°C, 5% CO₂. After a rest of 3hrs, a CD40 blocking antibody (Miltenyi) was added to the culture to prevent the interaction of CD40L with CD40 and its subsequent downregulation. In addition, antibodies for chemokine receptors CXCR6, CXCR3, CXCR5, and CCR6 were added in culture. After 15min incubation at 37°C, 5% CO₂, cells were stimulated with 0.5 μg/mL staphylococcal enterotoxin B (SEB) or 0.5 μg/mL of overlapping peptide pools for Wuhan-1 or Omicron BA.1 variants SARS-CoV-2 Spike (JPT) for 15 hrs at 37°C, 5% CO₂. An unstimulated condition with 0.4 μL of DMSO served as a negative control.

Cells were stained for viability dye (Aquavidin, ThermoFisher, 20min, 4°C), surface markers (30min, 4°C) (see [Table S3](#) for antibodies) and fixed using 2% paraformaldehyde (Sigma-Aldrich, 15min, RT) before filtration for acquisition on the flow cytometer (FACSymphony A5 Cell Analyzer; BD Biosciences) and analyzed using FlowJo (BD, v10.6.2). For phenotypic analysis of antigen-specific CD4⁺ T cells, only responses that were >2-fold over unstimulated condition were included to limit the impact of background staining. In contrast, for analysis of antigen-specific CD4⁺ T cell subsets as percentage of total CD4⁺ T cells, background-subtracted net values were used, which did not require excluding responses.

Intracellular cytokines staining (ICS) assay

PBMCs were resuspended at 10×10^6 cells/mL RPMI (Gibco by Life Technologies) supplemented with penicillin/streptomycin (Gibco by Life Technologies), 10% heat inactivated FCS, and incubated at 37°C, 5% CO₂. After a rest of 2hrs, cells were stimulated with 0.5 μg/mL staphylococcal enterotoxin B (SEB) or 0.5 μg/mL of overlapping peptide pools for Wuhan-1 or Omicron BA.1 variants SARS-CoV-2 Spike (JPT) for 6 hrs at 37°C, 5% CO₂. An unstimulated condition with 0.4 μL of DMSO served as a negative control. Brefeldin A (BD Biosciences), Monensin-1 (BD Biosciences), and a fluorescently labeled CD107a antibody were added for the remaining 5hrs.

Cells were stained for viability dye (Aquavidin, ThermoFisher, 20min, 4°C), surface markers (30min, 4°C), and intracellularly for cytokines (30min, room temperature) using the IC Fixation/Permeabilization kit (eBioscience) (see [Table S4](#) for antibodies) and filtrated before acquisition on the flow cytometer (FACSymphony A5 Cell Analyzer, BD Biosciences) and analyzed using FlowJo (BD, v10.6.2).

QUANTIFICATION AND STATISTICAL ANALYSIS

Statistics

Symbols represent biologically independent samples from HD and CI donors. Lines connect data from the same donor. Thick lines represent median values. Linear mixed models fitting cell frequencies in terms of cohort, time point, and their interaction were run using R and the package “nlme”. Model diagnostics were performed, checking for heteroscedasticity and normality among residuals. All retained models used a square-root transform on the response variable, which helped in reducing the impact of outliers. Post-hoc contrasts across all pairwise comparisons of factor levels were obtained with the package “emmeans”, correcting the p values by the method of Holm-Bonferroni where applicable. An important caveat of the square-root transform is that the reported contrast estimates and their confidence intervals remain on this scale, making their interpretation tricky. This was not deemed too great an obstacle, as qualitative statements on significant contrasts could be made based on p values. Thirty-five linear mixed models were retained, those being anti-RBD IgG, RBD B, AIM CD4, ICS CD4, AIM CD8, CXCR3, CXCR5, CXCR6, CCR6, PD-1, CD38, HLA-DR, IFN_γ, IL-2, TNF_α, IL-10, CD107a and IL-17A being compared between HD_S, CI and HD_L cohorts. There were also comparisons of HD_S, HD_L, and CI for anti-RBD IgG, RBD B, AIM CD4, ICS CD4, and AIM CD8. Models without satisfactory diagnostics were abandoned in favor of non-parametric methods. Differences in responses for the same patient before and after

vaccination were performed using Wilcoxon matched pair tests. Differences in responses between HD_S and CI were measured by Mann-Whitney tests. Wilcoxon and Mann-Whitney tests were generated using GraphPad Prism (version 9.2.0). *p* values < 0.05 were considered significant. *p* values are indicated for each comparison assessed. For descriptive correlations, Spearman's R correlation coefficient was applied. For graphical representation on a log scale (but not for statistical tests), null values were arbitrarily set at the minimal values for each assay.

Software scripts and visualization

Graphics and pie charts were generated using GraphPad PRISM (v9.2.0) and ggplot2 (v3.3.3) in R (v4.1.0). Heat maps were generated in R (v4.1.0) using the *pheatmap* package (v1.0.12). Principal component analyses were performed with the *prcomp* function (R). Uniform manifold approximation and projection (UMAP) was performed using package M3C (v1.14.0) on gated FCS files loaded through the flowCore package (v2.4.0). Samples were downsampled to a comparable number of events (300 cells for AIM, 100 cells for ICS). Scaling and logical transformation of the flow cytometry data were applied using the FlowSOM⁷² R package (v2.0.0). All samples at all time points were loaded. Clustering was achieved using Phenograph (v0.99.1) with the hyperparameter *k* (number of nearest neighbors) set to 150). We previously provided all R codes scripted for this paper in another study.⁶ We obtained an initial 14 AIM⁺ and 8 ICS⁺ clusters. For B and CD4⁺ T cell phenotyping, only participants with ≥ 5 events across all depicted time points were analyzed.

Supplemental information

**A third SARS-CoV-2 mRNA vaccine dose in people
receiving hemodialysis overcomes B cell defects
but elicits a skewed CD4⁺ T cell profile**

G r my Sannier, Alexandre Nicolas, Mathieu Dub , Lorie Marchitto, Manon Nayrac, Olivier Tastet, Debashree Chatterjee, Alexandra Tauzin, Rapha l Lima-Barbosa, M lanie Laporte, Rose Cloutier, Alina M. Sreng Flores, Marianne Boutin, Shang Yu Gong, Mehdi Benlarbi, Shilei Ding, Catherine Bourassa, Gabrielle Gendron-Lepage, Halima Medjahed, Guillaume Goyette, Nathalie Brassard, Gloria-Gabrielle Delgado, Julia Niessl, Laurie Gokool, Chantal Morrissette, Pascale Arlotto, Norka Rios, C cile Tremblay, Val rie Martel-Laferr re, Alexandre Prat, Justin B lair, William Beaubien-Souigny, R mi Goupil, Annie-Claire Nadeau-Fredette, Caroline Lamarche, Andr s Finzi, Rita S. Suri, and Daniel E. Kaufmann

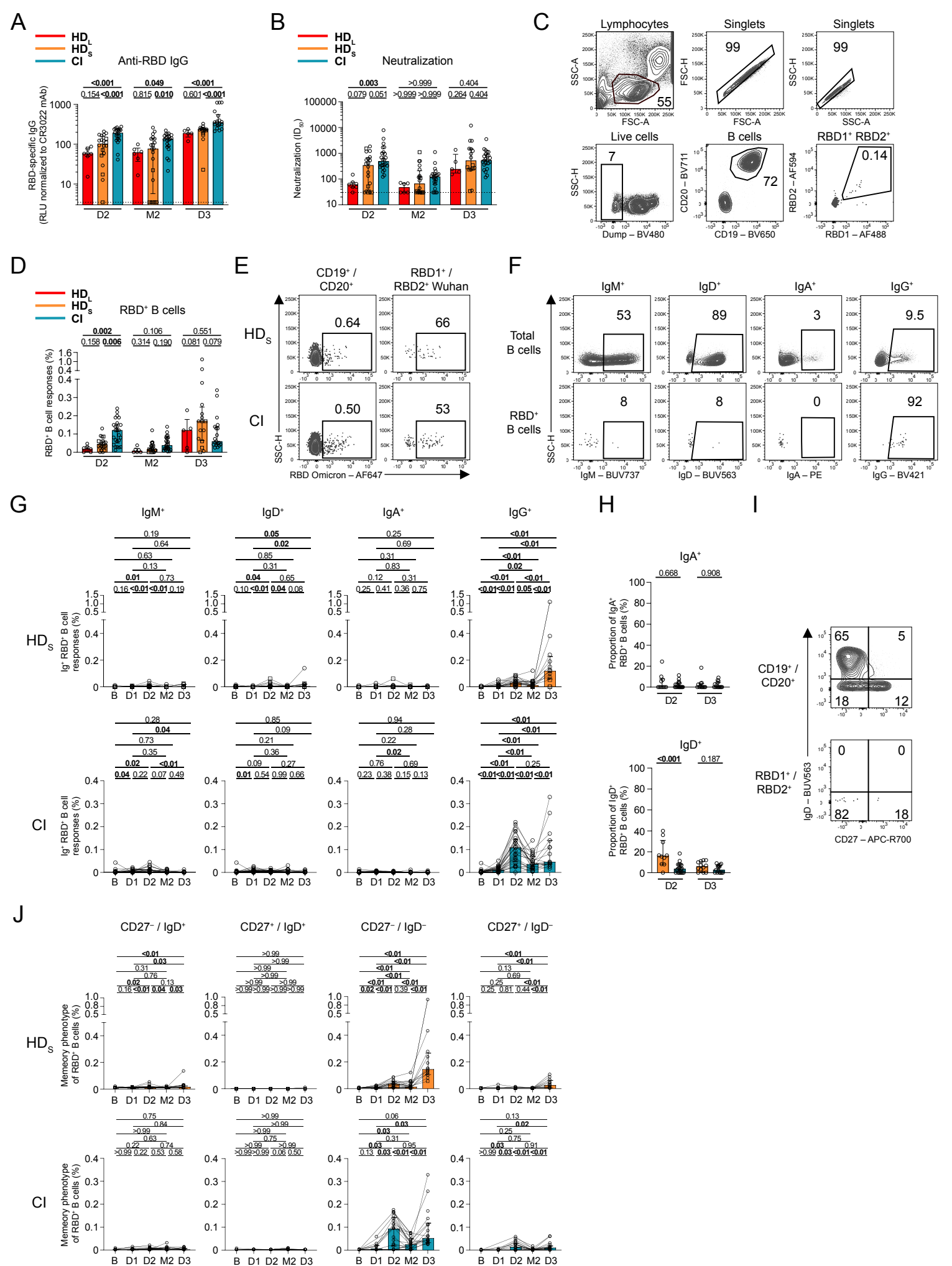


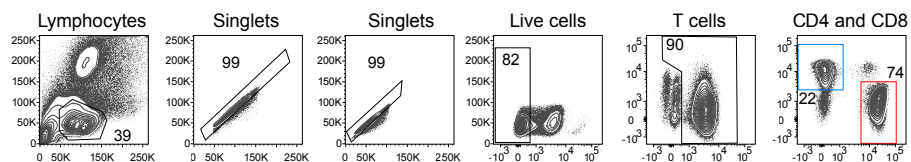
Figure S1

Figure S1. Antibody and SARS-CoV-2-specific B cell responses in hemodialysis patients.

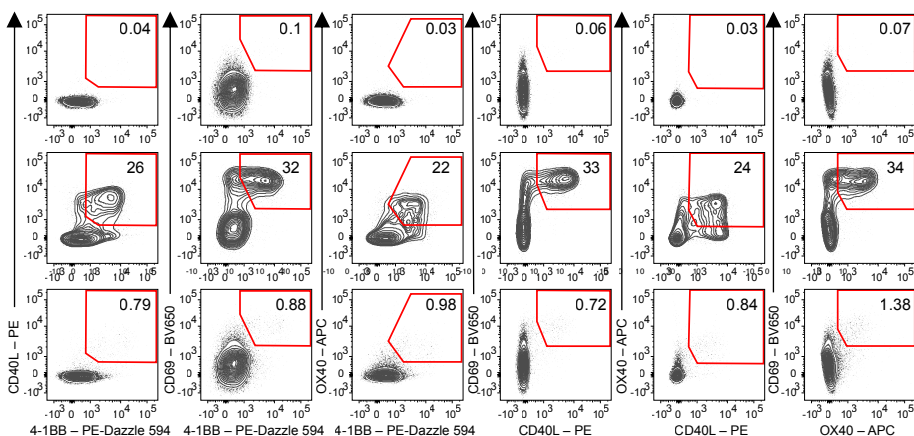
Related to Figure 1. (A) Comparison of RBD-specific IgG responses between HD_L (red), HD_S (orange) and CI (blue) participants at D2, M2 and D3. HD_S on immunosuppressive drugs are represented by square symbols, and HD_S not on immunosuppressants are represented by circles. Bars represent medians ± interquartile ranges. Intercohort statistical comparisons using a linear mixed model are shown. **(B)** Comparison of neutralizing activity between HD_L (red), HD_S (orange) and CI (blue) participants at D2, M2 and D3. HD_S on immunosuppressive drugs are represented by square symbols, and HD_S not on immunosuppressants are represented by circles. Bars represent medians ± interquartile ranges. Intercohort statistical comparisons using a linear mixed model are shown. **(C)** Gating strategy to identify RBD⁺ B cells. **(D)** Comparison of RBD⁺ B cell responses between HD_L (red), HD_S (orange) and CI (blue) participants at D2, M2 and D3. HD_S on immunosuppressive drugs are represented by square symbols, and HD_S not on immunosuppressants are represented by circles. Bars represent medians ± interquartile ranges. Intercohort statistical comparisons using a linear mixed model are shown. **(E)** Gating strategy of Omicron RBD⁺ B cells among total B cells (left) and among Wuhan-1-RBD⁺ B cells (right). **(F)** Examples of gatings for IgD, IgM, IgA and IgG expression on total CD19⁺CD20⁺ B cells (left) or RBD⁺ B cells (right). **(G)** Histograms reporting the longitudinal frequency of isotype expression in HD_S (orange) and CI (blue) participants. Lines connect data points for individual participants. Wilcoxon tests are shown above each panel. **(H)** Comparison of IgD⁺ and IgA⁺ RBD⁺ B cells between HD_S and CI participants at D2 and D3. Mann-Whitney tests are shown. **(I)** Gating strategy of IgD^{+/-} and CD27^{+/-} of total (left) and RBD⁺ memory B cells (right). **(J)** Histograms reporting the longitudinal frequency of each IgD and CD27 RBD-B phenotypes in CD19⁺CD20⁺ B cells for HD_S (orange) and CI (blue) participants. In support of the pie charts displayed in Figure 1K. Wilcoxon tests are shown above. In ABD) n=7 HD_L, n=20 HD_S, n=26 CI. GJ) n=20 HD_S, n=26 CI. H) n=16 HD_S, n=23 CI.

Figure S2

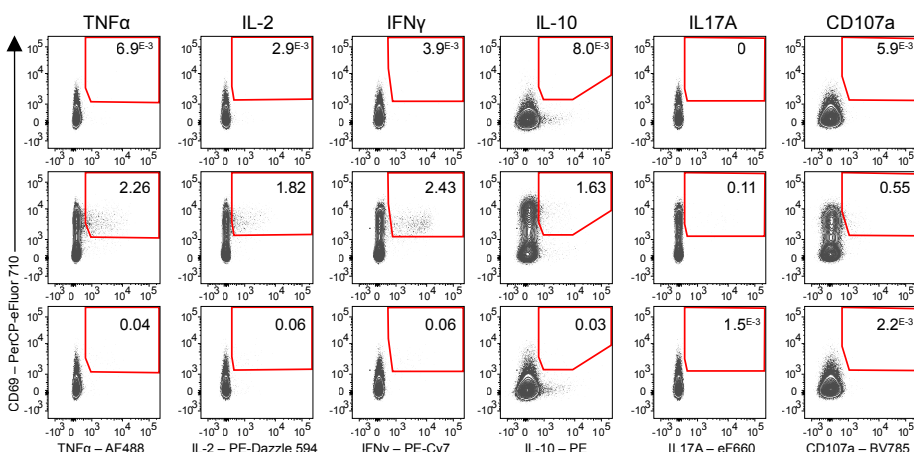
A



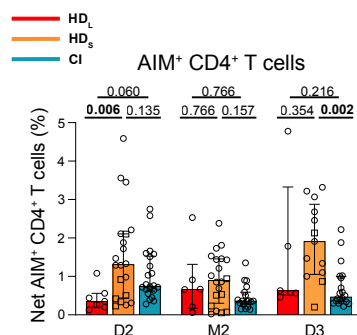
B



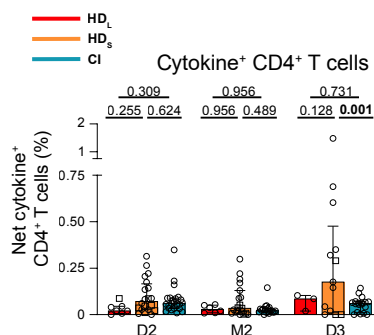
E



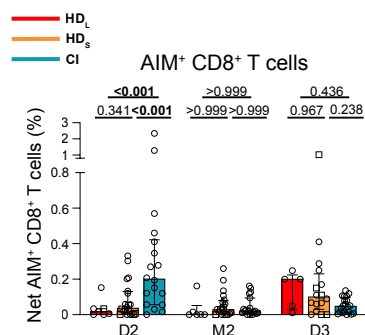
H



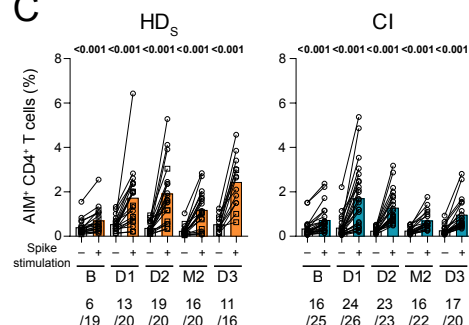
I



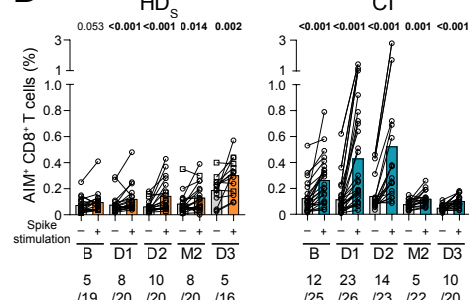
J



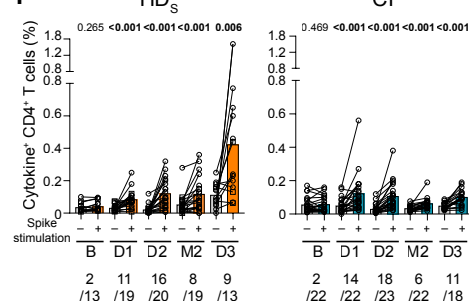
C



D



F



G

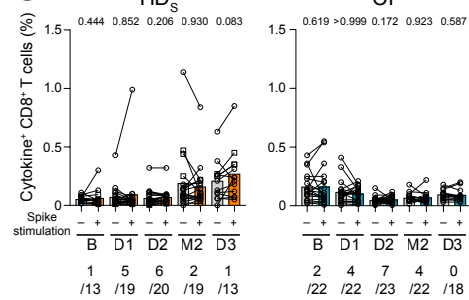


Figure S2. SARS-CoV-2-specific T cell responses in hemodialysis patients. Related to Figure 2. (A) Representative upstream generic gating and (B) ORgate strategy to identify SARS-CoV-2-specific AIM⁺ T cells. For simplicity, the example focuses on CD4⁺ T cells. (C) Raw frequencies of AIM⁺ CD4⁺ and (D) CD8⁺ T cells following ex vivo stimulation of PBMCs with a pool of SARS-CoV-2 Spike peptides (colored). HD_s are represented on the left and CI on the right for each panel. As a control, PBMCs cells were left unstimulated (grey bars). HD_s on immunosuppressive drugs are represented by square symbols, and HD_s not on immunosuppressants are represented by circles. The bars represent median values. Wilcoxon tests are shown. The numbers of responders at least two times over unstimulated conditions are written below the histograms for each timepoint. (E) Representative ORgate strategy to identify SARS-CoV-2-specific cytokine-expressing T cells. For simplicity, the example focuses on CD4⁺ T cells. (F) Raw frequencies of cytokine-expressing CD4⁺ T cells and (G) CD8⁺ T cells following ex vivo stimulation of PBMCs with a pool of SARS-CoV-2 Spike peptides (colored). HD_s are represented on the left and CI on the right for each panel. As a control, PBMCs cells were left unstimulated (grey bars). HD_s on immunosuppressive drugs are represented by square symbols, and HD_s not on immunosuppressants are represented by circles. The bars represent median values. Wilcoxon tests are shown. The numbers of responders at least two times over unstimulated conditions are written below the histograms for each timepoint. (H-I-J) Comparison at D2, M2 and D3 of (H) net AIM⁺ CD4⁺ T cell responses, (I) net cytokines⁺ CD4⁺ responses and (J) net AIM⁺ CD8⁺ responses between HD_L (red), HD_s (orange) and CI (blue) participants. HD_s on immunosuppressive drugs are represented by square symbols, and HD_s not on immunosuppressants are represented by circles. The bars represent median and interquartile ranges. Intercohort statistical comparisons using a linear mixed model. In A-G) n=20 HD_s, n=26 CI participants, in H-J) n=20 HD_s, n=26 CI, n=7 HD_L participants.

Figure S3

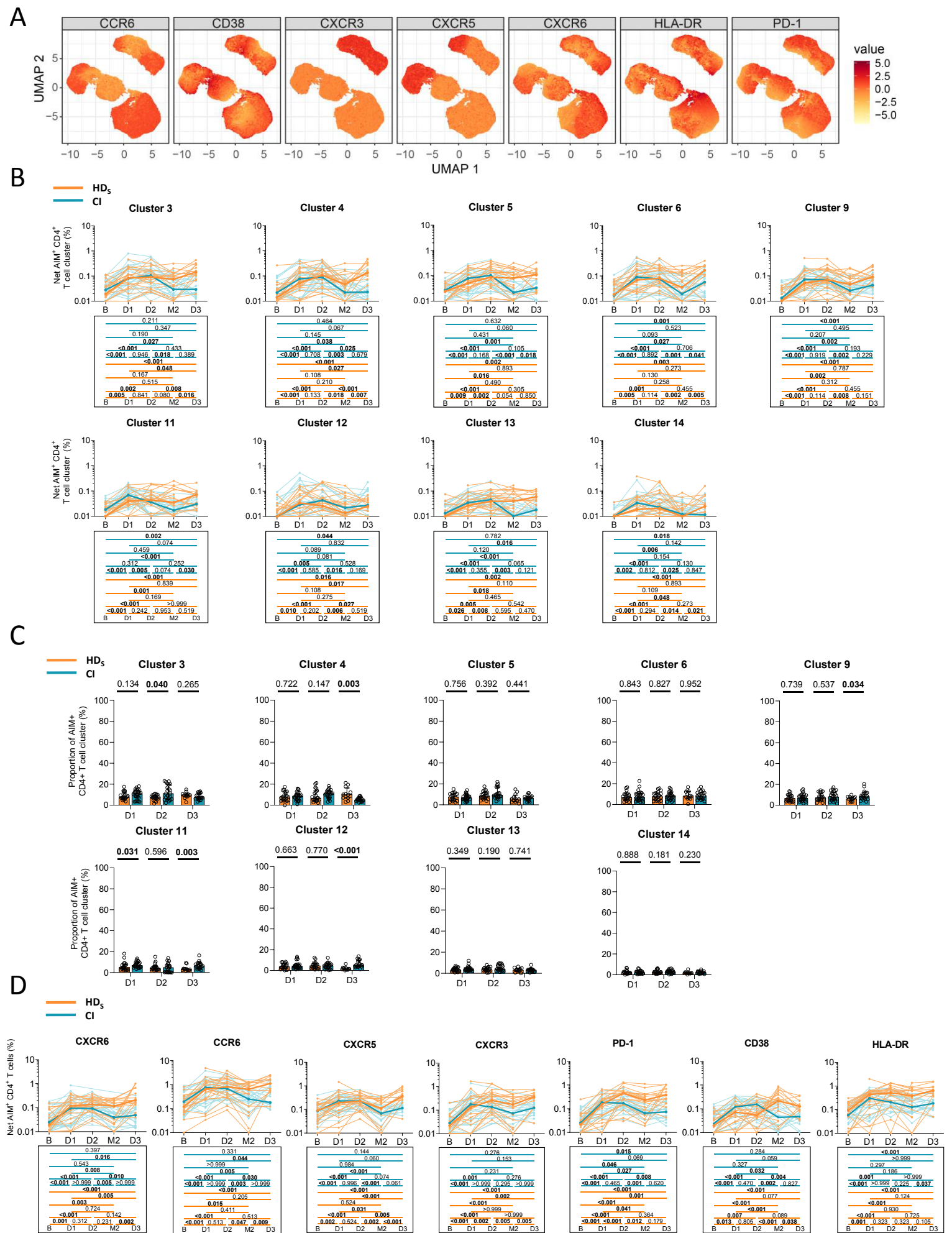
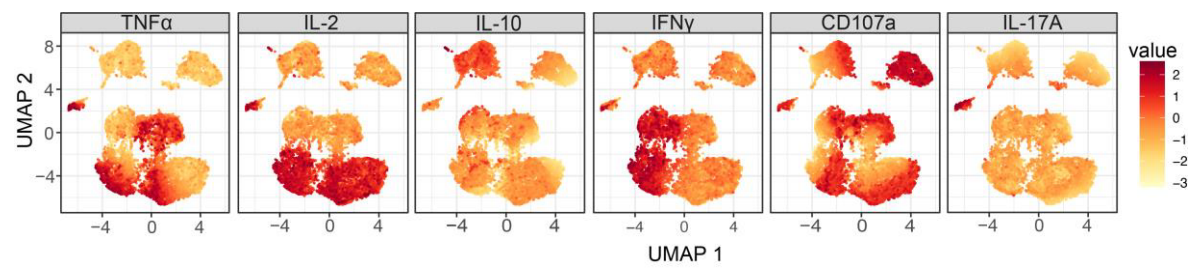


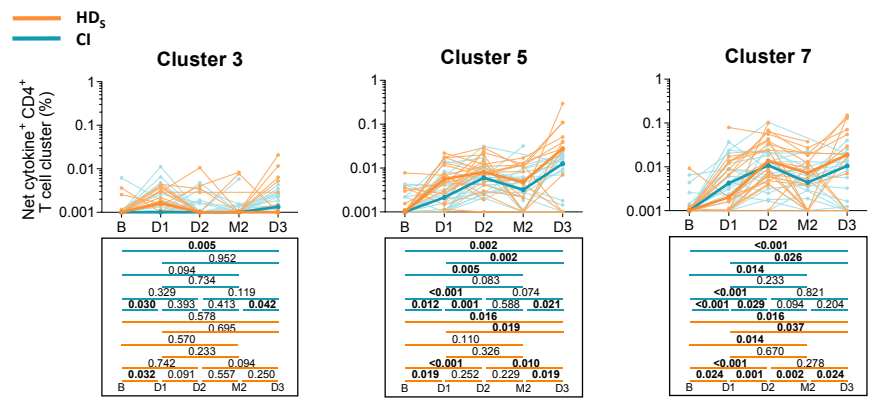
Figure S3. Phenotypic characterization of SARS-CoV-2-specific CD4⁺ T cell responses in hemodialysis patients. Related to Figure 3. (A) Heat map overlaid on the AIM⁺ UMAP showing the gradient of expression for each marker. **(B)** Longitudinal analysis of net AIM⁺ CD4⁺ T cell clusters, regarding clusters 3, 4, 5, 6, 9, 11, 12, 13, and 14 for HD_S (orange, n=20) and CI (blue; n=26) participants. Lines connect data from the same donor. Bold lines represent median values. Wilcoxon tests are shown below for each pairwise comparison. Complement Figure 3E. **(C)** Proportions of AIM⁺ clusters 3, 4, 5, 6, 9, 11, 12, 13 and 14 among AIM⁺ CD4⁺ T cells in HD_S and CI at D1, D2 and D3. Bars represent medians ± interquartile ranges. Mann-Whitey tests are shown. Complement Figure 3F. **(D)** Longitudinal frequencies of CCR6⁺, CXCR5⁺, CXCR3⁺, PD-1⁺, CD38⁺ and HLA-DR⁺ AIM⁺ CD4⁺ T cells in HD_S (orange) and CI (blue). Lines connect data from the same donor. The bold lines represent the median value of each cohort. Statistical comparisons using a linear mixed model.

Figure S4

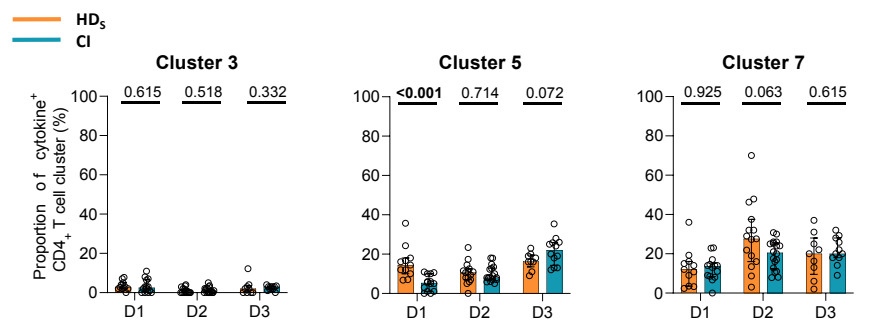
A



B



C



D

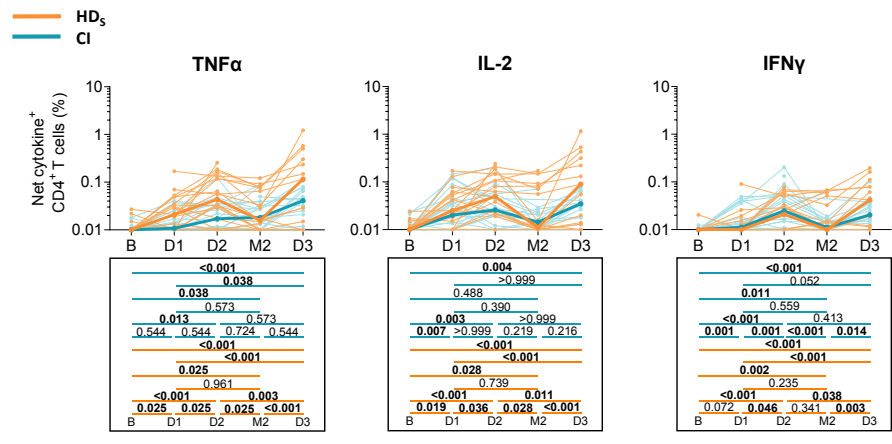


Figure S4. Effector functions profiling of SARS-CoV-2-specific CD4⁺ T cells responses in hemodialysis patients. Related to Figure 4. (A) Heat map overlaid on the cytokine⁺ UMAP showing the gradient of expression for each marker. **(B)** Longitudinal analysis of net cytokine⁺ CD4⁺ T cell clusters, regarding clusters 3, 5 and 7 for HD_s (orange, n=20) and CI (blue; n=26) participants. Lines connect data from the same donor. Bold lines represent median values. Wilcoxon tests are shown below for each pairwise comparison. Complement Figure 4E. **(C)** Proportions of cytokine⁺ clusters 3, 5 and 7 among ICS⁺ CD4⁺ T cells in HD_s and CI at D1, D2 and D3. Bars represent median ± interquartile range. Mann-Whitey tests are shown. Complement Figure 4F. **(D)** Longitudinal frequencies of TNFα⁺, IL-2⁺ and IFNγ⁺ CD4⁺ T cells in HD_s (orange) and CI (blue). Lines connect data from the same donor. The bold line represents the median value of each cohort. Statistical comparisons using a linear mixed model.

Figure S5

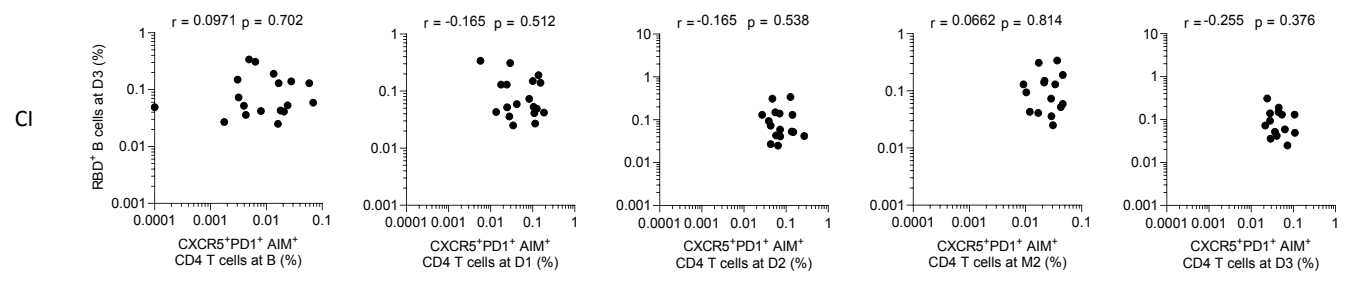
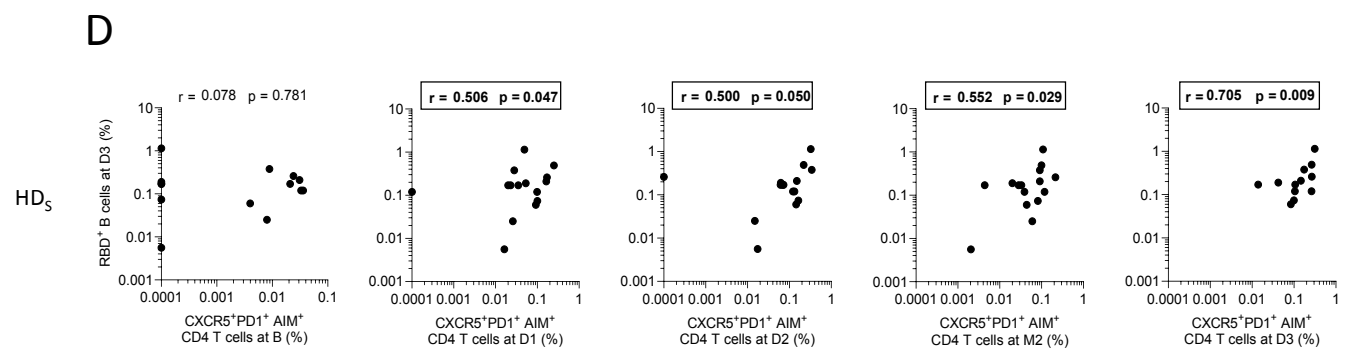
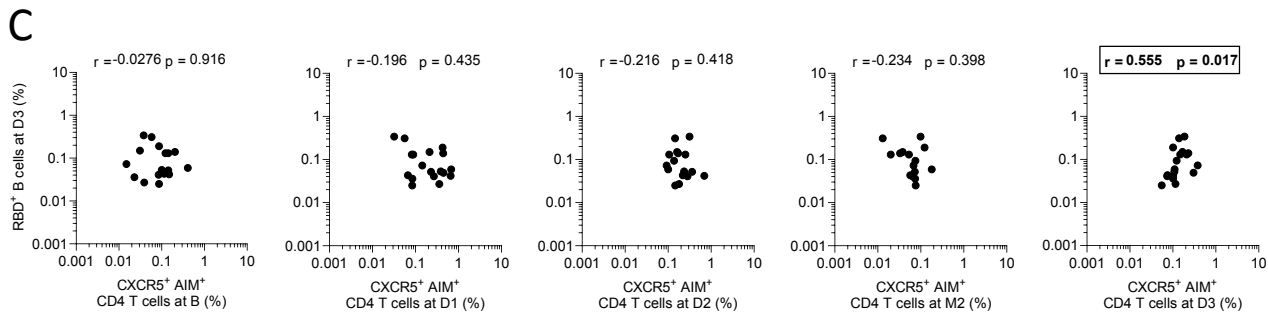
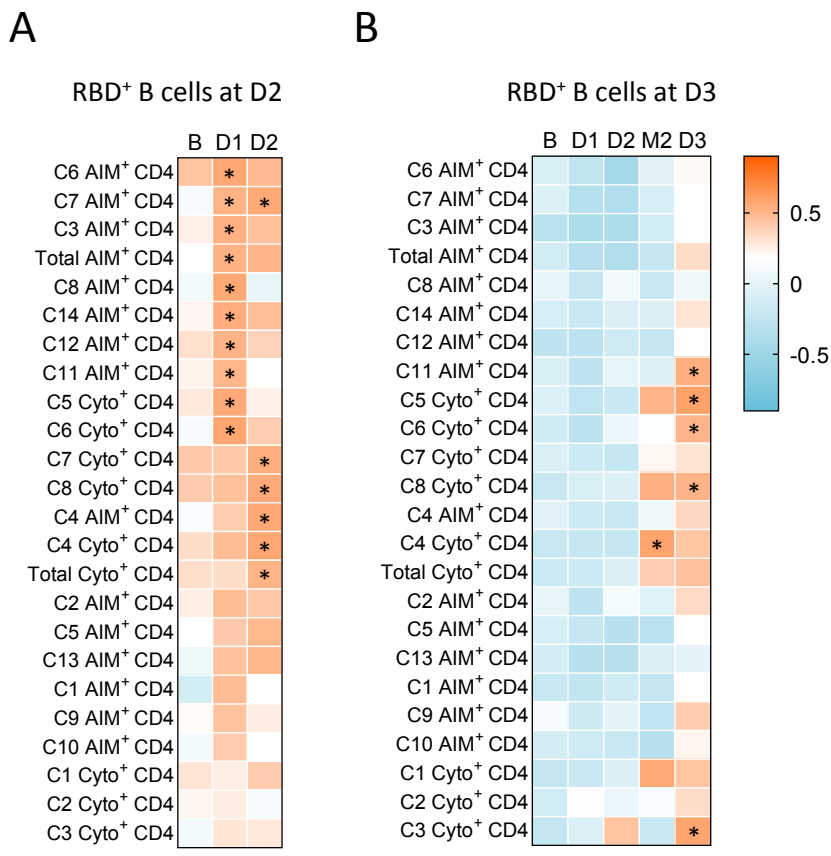


Figure S5. Associations between RBD⁺ B cell and SARS-CoV-2-specific CD4⁺ T cell responses in hemodialysis patients. Related to Figure 5. Temporal relationships between S-specific CD4⁺ T cells and RBD⁺ B cells. **(A)** Correlation between total CD4⁺ T cell frequencies at B-D2 and RBD⁺ B cell frequencies at D2 in CI (n=26). **(B)** Correlation between total CD4⁺ T cell frequencies at B-D3 and RBD⁺ B cell frequencies at D3 in CI (n = 26). Asterisks indicate statistically significant p value from a Spearman test ($p < 0.05$). Colors indicate Spearman r. **(C)** Correlations between frequencies of AIM⁺ CXCR5⁺ CD4⁺ T cells (for cTfh) at the B–D3 visits and RBD⁺ B cell frequencies at D3 in CI. The r and p values from a Spearman test are indicated in each graph. **(D)** Correlations between frequencies of AIM⁺ CXCR5⁺ PD-1⁺ CD4⁺ T cells (for PD-1⁺ cTfh) at the B–D3 visits and RBD⁺ B cell frequencies at D3 in HD_s (top) and CI (bottom). The r and p values from a Spearman test are indicated in each graph.

Table S1. Clinical characteristics of the hemodialysis cohorts[†]. Related to Table 1.

Cohorts	Patients ID	Cause of ESRD	Years on HD	Comorbidities										Immunomodulating characteristics			
				DM	Cancer	CAD	Heart failure	Stroke / TIA	PVD	COPD	HBV	HCV	Cirrhosis	Previous kidney transplant	Immuno-suppressant medication	HIV	
HDs	1072-36	PCKD	15	N	N	N	N	N	N	N	N	N	N	N	Y	Prednisone, Cyclosporine	N
	1072-37	GN	4.3	Y	Y	N	N	N	N	N	N	N	N	N	N	N	N
	1072-38	GN	2.6	N	N	N	N	N	N	N	N	N	N	N	N	N	N
	1072-46	Atypical HUS	14.4	N	N	N	N	N	N	N	N	N	N	N	Y	Prednisone	N
	1072-56	HTN	28.4	N	N	N	N	Y	N	N	N	N	N	N	Y	N	N
	1072-61	GN	13.2	N	N	N	N	N	N	N	N	N	N	N	Y	Prednisone, Tacrolimus	N
	1072-64	DM vs GN	2.7	Y	N	Y	N	N	N	N	N	N	N	N	N	N	N
	1072-66	GN	10.4	N	N	N	N	N	N	N	N	N	N	N	N	N	N
	1072-68	GN	8.2	N	N	N	N	N	N	N	N	Y	N	N	N	N	N
	1072-72	DM	3.7	Y	N	N	N	N	N	N	N	N	N	N	N	N	N
	1072-84	HTN	8.5	N	N	N	N	N	N	N	Y	N	N	N	N	N	N
	1072-86	Alport syndrome	23.4	N	N	N	N	N	N	N	N	N	N	N	Y	Tacrolimus	N
	1072-94	GN	13.4	Y	N	N	N	N	N	N	N	N	N	N	Y	Prednisone, Tacrolimus	N
	1072-103	DM	4.2	Y	N	N	N	N	N	N	Y	Y	N	N	N	N	N
	1072-104	DM	0.9	Y	Y	N	N	N	N	N	N	N	N	N	N	N	N
	1072-105	GN	5.5	Y	Y	N	N	N	N	N	N	N	N	N	Y	Tacrolimus	N
	1072-106	DM	0.4	Y	N	N	N	N	N	N	N	N	N	N	N	N	N
	1072-116	DM & HTN	2.6	Y	N	N	N	N	N	N	N	N	N	N	N	N	N
1072-117	GN	0.2	N	N	N	N	N	N	N	N	N	N	N	N	N	N	
1073-111	DM	0.2	Y	N	Y	Y	N	N	N	N	N	N	N	N	N	N	
Median (Interquartile range)			4.9 (2.6-13.3)	10	2	2	1	1	0	0	2	2	2	7	6	0	
HDL	1071-03	DM	3.9	Y	N	Y	N	Y	N	N	N	N	N	N	N	N	N
	1071-07	DM	6.8	Y	N	N	N	N	N	N	N	N	N	N	N	N	N
	1071-08	DM	6.3	Y	N	N	N	N	N	N	N	N	N	N	N	Prednisone	N
	1071-38	DM	0.6	Y	N	N	N	N	N	N	Y	N	N	N	N	N	N
	1071-42	DM	5.9	Y	N	N	N	N	N	Y	Y	N	N	N	N	N	N
	1071-43	GN	2.0	N	N	N	N	N	N	Y	N	N	N	N	N	N	N
	1071-51	HTN	3.5	N	N	N	N	N	N	N	N	N	N	N	N	N	N
Median (Interquartile range)			3.9 (2.8-6.1)	5	0	1	0	1	0	2	2	0	0	0	1	0	

Sannier, Nicolas et al.

† Values displayed are absolute numbers and percentages for categorical variables.

CAD = Coronary Artery Disease; COPD = Chronic Obstructive Pulmonary Disease; DM = Diabetes Mellitus; GN = Glomerulonephritis; HBV = Hepatitis B Virus; HCV = Hepatitis C Virus; HIV = Human Immunodeficiency Virus; HTN = Hypertension; HUS = Hemolytic Uremic Syndrome; PCKD = Polycystic Kidney Disease; PVD = Perivascular Disease; TIA = Transient Ischemic Attack.

N = No; Y = Yes.

Table S2. Flow cytometry antibody staining panel for B cells characterization. Related to STAR Methods, Main Figure 1, Supplementary Figure 1.

Marker – Fluorophore	Clone	Source	Catalog #
CD3 – BV480	UCHT1	BD Biosciences	566105
CD14 – BV480	M5E2	BD Biosciences	746304
CD16 – BV480	3G8	BD Biosciences	566108
CD19 – BV650	SJ25C1	Biolegend	363026
CD20 – BV711	2H7	Biolegend	563126
CD21 – BV786	B-LY4	BD Biosciences	740969
CD24 – BUV805	ML5	BD Biosciences	742010
CD27 – APC-R700	M-T271	BD Biosciences	565116
CD38 – BB790	HIT2	BD Biosciences	CUSTOM
CD56 – BV480	NCAM16.2	BD Biosciences	566124
CD138 – BUV661	MI15	BD Biosciences	5 749873
CCR10 – BUV395	1B5	BD Biosciences	565322
HLA-DR – BB700	G46-6	BD Biosciences	566480
IgA – PE	IS11-8E10	Miltenyi	130-113-476
IgD – BUV563	IA6-2	BD Biosciences	741394
IgG – BV421	G18-147	BD Biosciences	562581
IgM – BUV737	UCH-B1	Thermo Fisher Scientific	748928
LIVE/DEAD Fixable dead cell	N/A	Thermo Fisher Scientific	L34960

Table S3. Flow cytometry antibody staining panel for activation-induced marker assay. Related to STAR Methods, Main Figure 2 and 3, Supplementary Figure 2 and 3.

Marker – Fluorophore	Clone	Source	Catalog #
CD3 – BUV496	UCHT1	BD Biosciences	612941
CD4 – BB630	SK3	BD Biosciences	624294
CD8 – BV570	RPA-T8	Biolegend	301037
CD14 – BV480	M5E2	BD Biosciences	746304
CD19 – BV480	HIB19	BD Biosciences	746457
CD38 – BB790	HIT2	BD Biosciences	CUSTOM
CD45RA – PerCP Cy5.5	HI100	BD Biosciences	563429
CD69 – BV650	FN50	Biolegend	310934
CD134 (OX40) - APC	ACT35	BD Biosciences	563473
CD137 (4-1BB) – PE-Dazzle 594	4B4-1	Biolegend	309826
CD154 (CD40L) - PE	TRAP1	BD Biosciences	555700
CD183 (CXCR3) – BV605	G025H7	Biolegend	353728
CD185 (CXCR5) – BV421	J25D4	Biolegend	356920
CD186 (CXCR6) – BUV805	13B 1E5	BD Biosciences	748448
CD196 (CCR6) – BUV737	11A9	BD Biosciences	564377
CD279 (PD1) – BV711	EH122H	Biolegend	329928
HLA-DR – FITC	LN3	Biolegend	327005
LIVE/DEAD Fixable dead cell	N/A	Thermo Fisher Scientific	L34960

Table S4. Flow cytometry antibody staining panel for intracellular cytokines staining assay. Related to STAR Methods, Main Figure 2 and 4, Supplementary Figure 2 and 4.

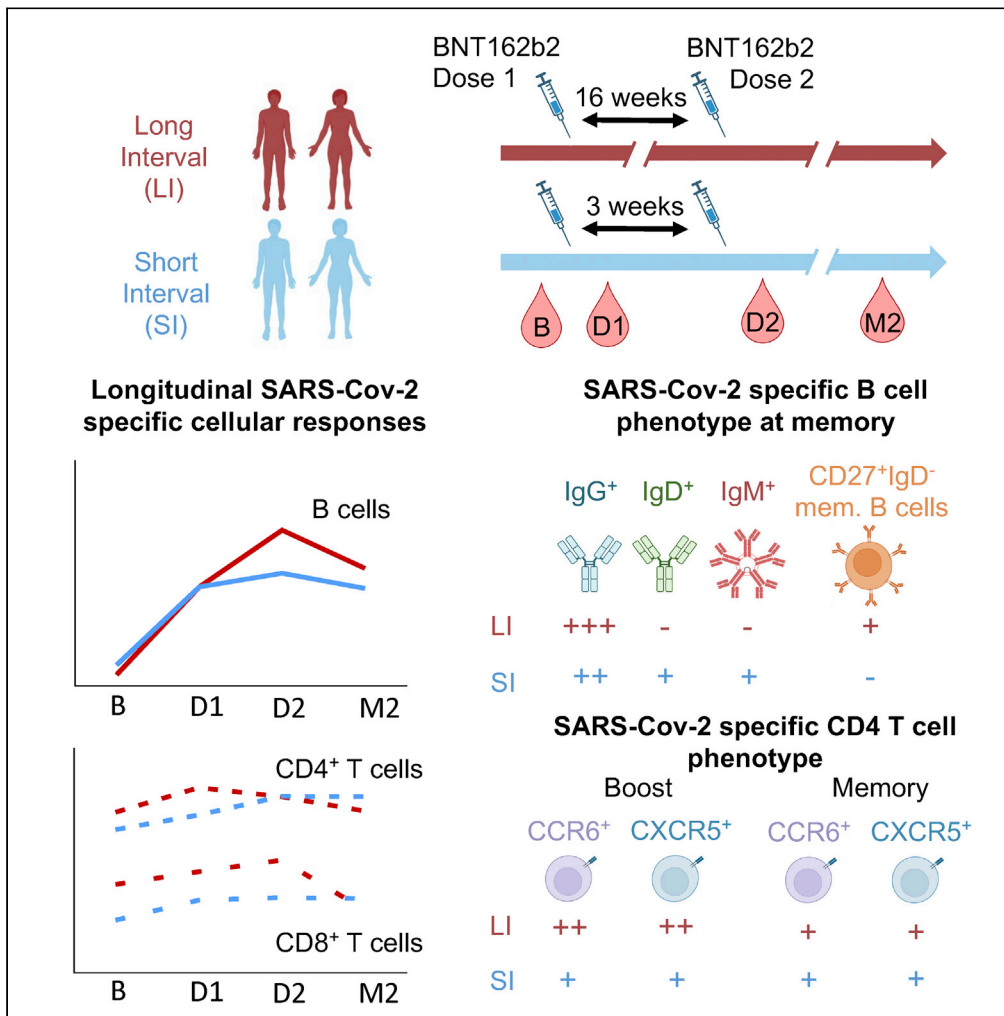
Marker – Fluorophore	Clone	Source	Catalog #
CD3 – BUV395	UCHT1	BD Biosciences	563546
CD4 – BV711	L200	BD Biosciences	563913
CD8 – BV570	RPA-T8	Biolegend	301037
CD14 – BUV805	M5E2	BD Biosciences	612902
CD16 – BV650	3G8	Biolegend	302042
CD19 – APC-eFluor780	HIB19	Thermo Fisher Scientific	47-0199
CD56 – BUV737	NCAM16.2	BD Biosciences	564448
CD69 – PerCP-eFluor710	FN50	Thermo Fisher Scientific	46-0699-42
CD107A – BV786	H4A3	BD Biosciences	563869
IFN- γ – PECy7	B27	BD Biosciences	557643
CD154 (CD40L) – BV421	TRQP1	BD Biosciences	563886
IL-2 – PE-Dazzle 594	MQ1-17H12	Biolegend	500344
IL-10 – PE	JES3-9D7	BD Biosciences	554498
IL-17A – eFluor660	eBio64CAP17	Thermo Fisher Scientific	50-7179-42
TNF- α – Alexa Fluor 488	Mab11	Thermo Fisher Scientific	502915
Granzym B – Alexa Fluor 700	GB11	BD Biosciences	561016
LIVE/DEAD Fixable dead cell	N/A	Thermo Fisher Scientific	L34960

Appendix II.ii: An Extended SARS-CoV-2 mRNA Vaccine Prime-Boost Interval Enhances B Cell Immunity with Limited Impact on T Cells

iScience, 2023

Article

An extended SARS-CoV-2 mRNA vaccine prime-boost interval enhances B cell immunity with limited impact on T cells



Alexandre Nicolas, G eremy Sannier, Mathieu Dub e, ..., Allison R. Greenplate, E. John Wherry, Daniel E. Kaufmann

daniel.kaufmann@chuv.ch

Highlights

A 16-week interval increases B cell response and maturity compared to a 3-week delay

A 16-week interval has limited impact on the magnitude of CD4 and CD8 T cell responses

A long interval is associated with an early increase of specific SARS-CoV-2 cTfh

T cell phenotypes in 16-week versus 3-week regimens converge at late time points

Nicolas et al., iScience 26, 105904
January 20, 2023   2022 The Authors.
<https://doi.org/10.1016/j.isci.2022.105904>



Article

An extended SARS-CoV-2 mRNA vaccine prime-boost interval enhances B cell immunity with limited impact on T cells

Alexandre Nicolas,^{1,2,9} G r my Sannier,^{1,2,9} Mathieu Dub ,¹ Manon Nayrac,^{1,2} Alexandra Tauzin,^{1,2} Mark M. Painter,^{3,4,5} Rishi R. Goel,^{3,4} M lanie Laporte,¹ Gabrielle Gendron-Lepage,¹ Halima Medjahed,¹ Justine C. Williams,⁵ Nathalie Brassard,¹ Julia Niessl,^{1,2,8} Laurie Gokool,¹ Chantal Morrisseau,¹ Pascale Arlotto,¹ C cile Tremblay,^{1,2} Val rie Martel-Laferr re,^{1,2} Andr s Finzi,^{1,2} Allison R. Greenplate,^{3,4} E. John Wherry,^{3,4,5} and Daniel E. Kaufmann^{1,6,7,10,*}

SUMMARY

Spacing the first two doses of SARS-CoV-2 mRNA vaccines beyond 3–4 weeks raised initial concerns about vaccine efficacy. While studies have since shown that long-interval regimens induce robust antibody responses, their impact on B and T cell immunity is poorly known. Here, we compare SARS-CoV-2 naive donors B and T cell responses to two mRNA vaccine doses administered 3–4 versus 16 weeks apart. After boost, the longer interval results in a higher magnitude and a more mature phenotype of RBD-specific B cells. While the two geographically distinct cohorts present quantitative and qualitative differences in T cell responses at baseline and after priming, the second dose led to convergent features with overall similar magnitude, phenotype, and function of CD4⁺ and CD8⁺ T cell responses at post-boost memory time points. Therefore, compared to standard regimens, a 16-week interval has a favorable impact on the B cell compartment but minimally affects T cell immunity.

INTRODUCTION

The standard SARS-CoV-2 mRNA vaccine regimens recommend an interval of 21 days (Pfizer-BioNTech BNT162b2) or 28 days (Moderna mRNA-1273) between vaccine doses. However, the optimal interval has not been determined in controlled trials. In the context of vaccine scarcity and given the significant protection already conferred by the first dose in non-high-risk populations,^{1–3} some public health agencies implemented schedules with longer intervals to rapidly extend population coverage.^{4–6} While such strategies generated concerns given uncertain immunogenicity, a longer period of partial vulnerability to infection, and a hypothetical risk of escape mutant selection, epidemiological evidence supports this approach as a valid alternative in lower-risk populations^{7,8} in which robust T cell and antibody responses are observed after a single dose.⁹ Recent reports suggest that an extended interval between priming and boost procured enhanced humoral responses.^{10–13}

As protective antibodies are associated with vaccine efficacy,^{14,15} there is a need to better understand the generation and maintenance of B cell memory responses elicited by different vaccine modalities. As CD4⁺ T cell help provided by T follicular helper (T_{fh}) is critical for the expansion, affinity maturation, and memory development of B cells,^{16–19} it is also important to determine whether dosing interval affects CD4⁺ and CD8⁺ T cell vaccine responses. Demonstrating a direct protective role of SARS-CoV-2-specific CD4⁺ and CD8⁺ T cells independent of humoral immunity has been more challenging, but a number of studies support the notion that these lymphocyte subsets may contribute to recovery from COVID-19: Th1 cells, which foster development of CD8⁺ T cell memory,²⁰ and Th17 are important for mucosal immunity.²¹ However, T cell subsets show important heterogeneity and plasticity, better fitting with spectra of phenotypes and functions than fully distinct populations.²² Previous studies by our group²¹ and others^{23,24} have demonstrated that SARS-CoV-2-specific CD4⁺ T cells generated after the first vaccine dose predicted the humoral, B cell and CD8⁺ T cell responses at later time points.

¹Centre de Recherche du CHUM, Montr al, QC H2X 0A9 Canada

²D partement de Microbiologie, Infectiologie et Immunologie, Universit  de Montr al, Montr al, QC H2X 0A9, Canada

³Institute for Immunology, University of Pennsylvania Perelman School of Medicine, Philadelphia, PA 19104, USA

⁴Immune Health , University of Pennsylvania Perelman School of Medicine, Philadelphia, PA 19104, USA

⁵Department of Systems Pharmacology and Translational Therapeutics, University of Pennsylvania, Philadelphia, PA 19104, USA

⁶D partement de M decine, Universit  de Montr al, Montr al, QC H3T 1J4, Canada

⁷Division of Infectious Diseases, Department of Medicine, University Hospital of Lausanne and University of Lausanne, Lausanne, Switzerland

⁸Present address: Center for Infectious Medicine, Department of Medicine Huddinge, Karolinska Institutet, Stockholm, 171 77, Sweden

⁹These authors contributed equally

¹⁰Lead contact

*Correspondence: daniel.kaufmann@chuv.ch
<https://doi.org/10.1016/j.isci.2022.105904>



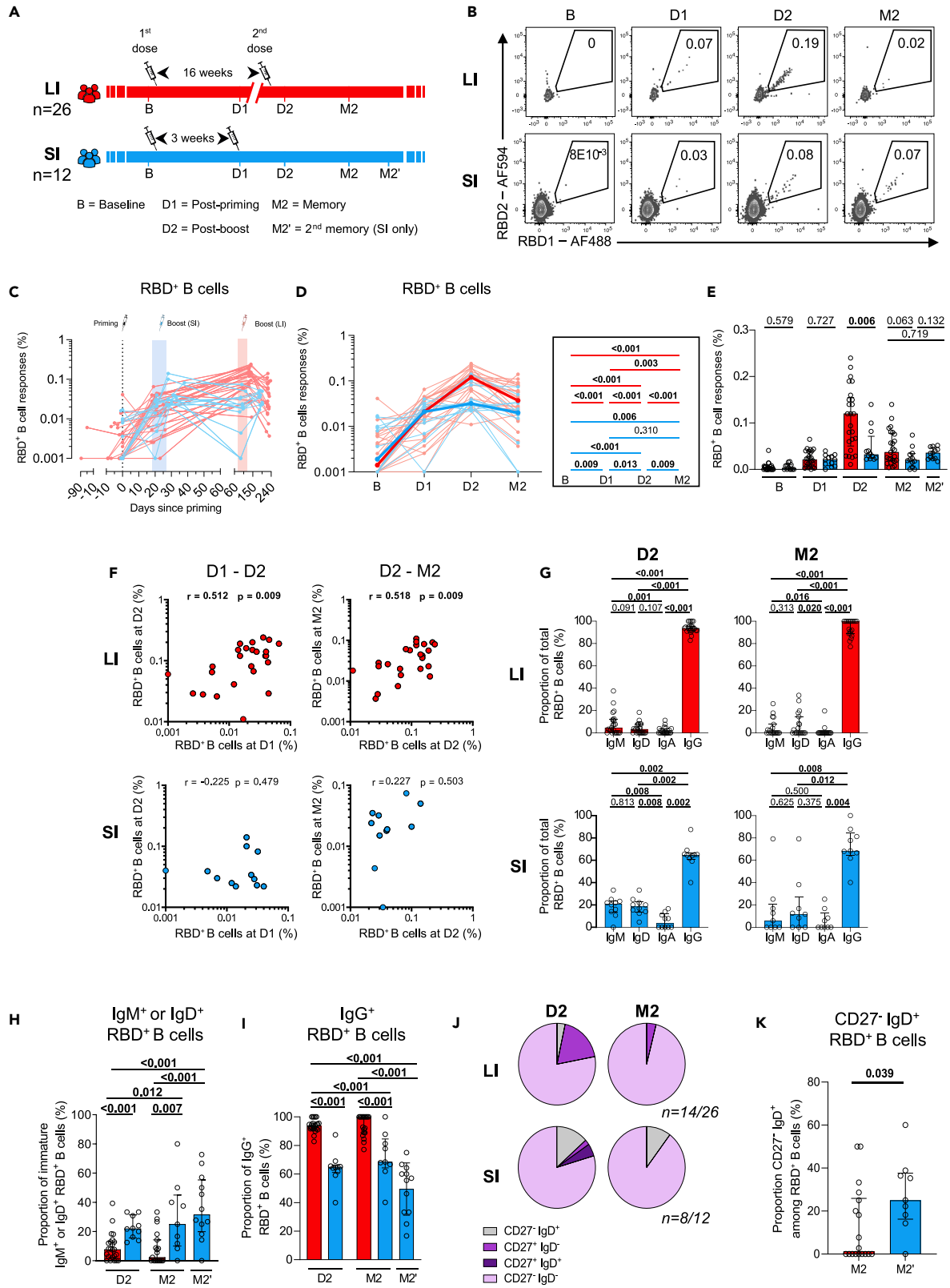


Figure 1. A 16-week delayed boost enhances the magnitude and maturation of B cell responses

- (A) Schematic representation of study design. Blood samples were analyzed at four-time points in the long (red) interval (LI) and short (blue) interval (SI) cohorts: baseline (B); 3 weeks after priming (D1), 1–3 weeks after boost (D2), and 10–16 weeks after boost (M2). For SI participants, a later M2' time point (23 weeks after boost) was also analyzed.
- (B) Representative examples of RBD-specific B cell responses.
- (C–E) Kinetics of RBD-specific B cell responses in LI (red) vs SI (blue) cohorts.
- (C) Individual responses according to time of sampling. Colored background and syringe indicate the time of dose injections. Dots indicate time points examined.
- (D) The bold line represents cohort's median value. Right panel: Wilcoxon tests.
- (E) Inter-cohort comparisons. Bars represent medians \pm interquartile ranges. Mann-Whitney tests are shown.
- (F) Scatterplots showing temporal RBD⁺ B cell correlations in the LI and SI cohorts. *r*: correlation coefficient. Significant correlations by Spearman tests ($p < 0.05$) are shown in bold.
- (G) Frequencies of IgD, IgM, IgA, and IgG-positive cells within RBD-specific B cells within each cohort. Bars represent medians \pm interquartile ranges. Paired comparisons were performed with Wilcoxon tests.
- (H) Proportion of IgM⁺ and IgD⁺ ORgate cells among RBD⁺ B cell cells. Bars represent medians \pm interquartile ranges with Mann-Whitney tests for comparisons between the LI and SI cohorts.
- (I) Proportion of IgG⁺ cells within RBD-specific B cells. Bars represent medians \pm interquartile ranges, with Mann-Whitney tests for comparisons between the LI and SI cohorts.
- (J) Proportion of IgD^{+/−} and CD27^{+/−} populations in RBD-specific B cells.
- (K) Comparison of CD27-IgD⁺ cells within RBD-specific B cells between the LI and SI cohorts. Bars represent medians \pm interquartile ranges, Mann-Whitney tests are shown. In (C–F) $n = 26$ for long-interval (LI), $n = 12$ short-interval (SI). In (G, H, I, and K), $n = 19$ long-interval (LI), $n = 9$ short interval (SI). In (J), only the D2 and M2 time points provided enough events for analysis. $n = 14$ for long-interval (LI), $n = 8$ short-interval (SI). In (F–J), phenotypic analyses include samples for which more than 5 RBD⁺ B cells were measured.

However, in contrast to the important progress made in the understanding of the kinetics of B and T cell responses in short-interval mRNA vaccine schedules,^{23–26} how a long interval between the first two vaccine doses affects B and T cell immunity compared to standard dosing regimens remains poorly known due to the paucity of studies performing side-by-side comparisons with the same cellular immunity assays.^{10,12,27}

Here, we apply standardized high-parameter flow cytometry assays to longitudinally compare the quantitative and qualitative features of vaccine-induced Spike-specific B cells, CD4⁺ T cells, and CD8⁺ T cells in SARS-CoV-2 naive participants enrolled in two cohorts: participants who received the two mRNA vaccine doses administered 16 weeks apart, defined as a long interval regimen; and participants who received the two doses 3–4 weeks apart, defined as a short-interval regimen.

RESULTS

Study participants

We evaluated immune responses in two independent cohorts of health care workers (HCW) that received two doses of mRNA vaccines (Figure 1A). The two cohorts differed by the time interval between the priming and the boosting inoculations, which defined the long interval (LI) cohort (16-week spacing, $n = 26$; Montreal cohort) and the short-interval (SI) cohort (3–4 weeks spacing, $n = 12$; Philadelphia cohort). Blood samples were examined at baseline (B) before vaccination; 3 weeks after the first dose (D1); 1–3 weeks after the second dose (D2), and 10 to 16 weeks after the second dose (M2). A later M2' time point (median 23 weeks (22–25) after the second dose) was also analyzed in SI participants to provide a better comparison to M2 from LI volunteers. Clinical characteristics are shown in Table 1. The median age of the participants in the short-interval cohort was 15-year-old significantly younger (Mann-Whitney $p = 0.019$). Both cohorts significantly differed in the interval between prime and boost, and in the time of sampling D2 (3 weeks post second dose for LI, 1 week for SI) and M2 (16 weeks post second dose for LI, 10 for SI). No other statistical differences were noted.

A 16-week delayed boost enhances the magnitude and maturation of B cell responses

To evaluate SARS-CoV-2-specific B cells, we focused on the Receptor Binding Domain (RBD) of Spike to minimize the inclusion of B cells cross-reactive to endemic coronaviruses.^{28,29} Co-detection of two fluorescently labeled recombinant RBD probes greatly enhances specificity (Figure 1B and³⁰ flow cytometry panel, Table S1; gating strategy, Figure S1A). We examined the magnitude of RBD-specific B cells (defined as RBD1⁺RBD2⁺CD19⁺CD20⁺) in the two cohorts (Figure 1C). Most participants showed no signal at baseline, and clear RBD-specific B cell responses after priming that were very similar between the LI and SI cohorts at the D1 time point, as expected. In the LI cohort, the second dose elicited robust recall responses at D2, followed by a decline at M2. The recall response in SI participants was more modest and plateaued at

Table 1. Clinical characteristics of the study participants^a

	Long Interval (LI) ^b	Short Interval (SI) ^b
Prime-boost interval ^c	16 weeks apart	3 weeks apart
Variable ^c	(n = 26)	(n = 12)
Vaccine regimen		
Pfizer BNT162b2 vaccine (2 doses)	n = 25	n = 11
Heterologous vaccine strategy (Moderna mRNA-1273 and Pfizer BNT162b2)	n = 1	n = 0
Moderna mRNA-1273 vaccine (2 doses)	N = 0	n = 1
Age (years) ^c	51 (41–56)	38 (22–63)
Sex		
Male	11 (42%)	4 (33%)
Female	15 (58%)	8 (66%)
Vaccine dose spacing (days)		
Days between doses 1 and 2 ^c	111 (109–112)	21 (20–28)
Visits for immunological profiling (days)		
B, days before first dose	1 (0–5)	0 (-1–1)
D1, days after first dose	21 (19–26)	21 (20–28)
D1, days before second dose	90 (85–92)	0 (-1–0)
D2, days after first dose ^c	133 (130–139)	29 (27–38)
D2, days after second dose ^c	21 (20–27)	7 (7–12)
M2, days after first dose	224 (222–228)	94 (86–115)
M2, days after second dose ^c	112 (110–119)	70 (65–94)
M2', days after first dose		186 (196–181)
M2', days after second dose		165 (175–153)

^aValues displayed are medians, with IQR: interquartile range in parentheses for continuous variables, or percentages for categorical variables.

^bThe Long-interval (LI) and Short-interval (SI) cohorts were compared by the following statistical tests: for continuous variables, Mann-Whitney test, for categorical variables, Fisher's test.

^cStatistically different values between the LI and SI cohorts ($p < 0.05$).

M2 and M2' (Figures 1C–1E). The LI individuals globally peaked at higher magnitudes of RBD⁺ B cell responses despite being globally older (Figure 1E) but converged with the SI cohort at subsequent memory time points (Figures 1C–1E). In contrast to short-interval participants, where no temporal association could be found between post-prime RBD⁺ B cell responses and post-boost RBD⁺ B cells, a strong and statistically significant positive correlation was observed in the long-interval cohort (Figure 1F). Likewise, RBD⁺ B cell responses at D2 were associated with stronger memory responses in the long-interval cohort (Figure 1F).

We next determined whether the interval between vaccine doses qualitatively impacted the development of antigen-specific B cells by measuring IgM, IgD, IgA, and IgG expression on RBD-specific B cells (Figure S1B). To avoid excessive noise in phenotyping analyses, we only included donors in whom we detected ≥ 5 RBD-specific B cells at every time point. RBD-specific B cells from LI and SI donors were dominated by IgG⁺ at both D2 and M2 time points (Figures 1G and S1C). However, a higher proportion of unswitched IgM⁺ or IgD⁺ RBD-specific B cells was detected at both time points in the SI cohort (Figures 1H and S1D). Consequently, the proportion of IgG⁺ RBD⁺ B cells was lower in the SI than in the LI cohort (Figure 1I). Both the elevated proportion of immature IgM⁺/IgD⁺ RBD-specific B cells (Figure S1E) and decreased proportion of IgG⁺ RBD-specific B cells were observed at the later M2' SI time point (Figure S1F). Thus, when comparing M2' SI with M2 LI, additional maturation time did not mitigate the differences in IgM⁺/IgD⁺ and IgG⁺ RBD-specific B cells proportion between both cohorts (Figures 1H and 1I).

To assess RBD-specific B cell differentiation, we next quantified IgD and CD27 co-expression (Figure S1G). CD27 is predominantly expressed on memory B cells,³¹ and IgD on unswitched B cells.³² An atypical double-negative (DN) IgD⁻CD27⁻ was dominant at both the D2 and M2 time points in both cohorts (Figures 1J

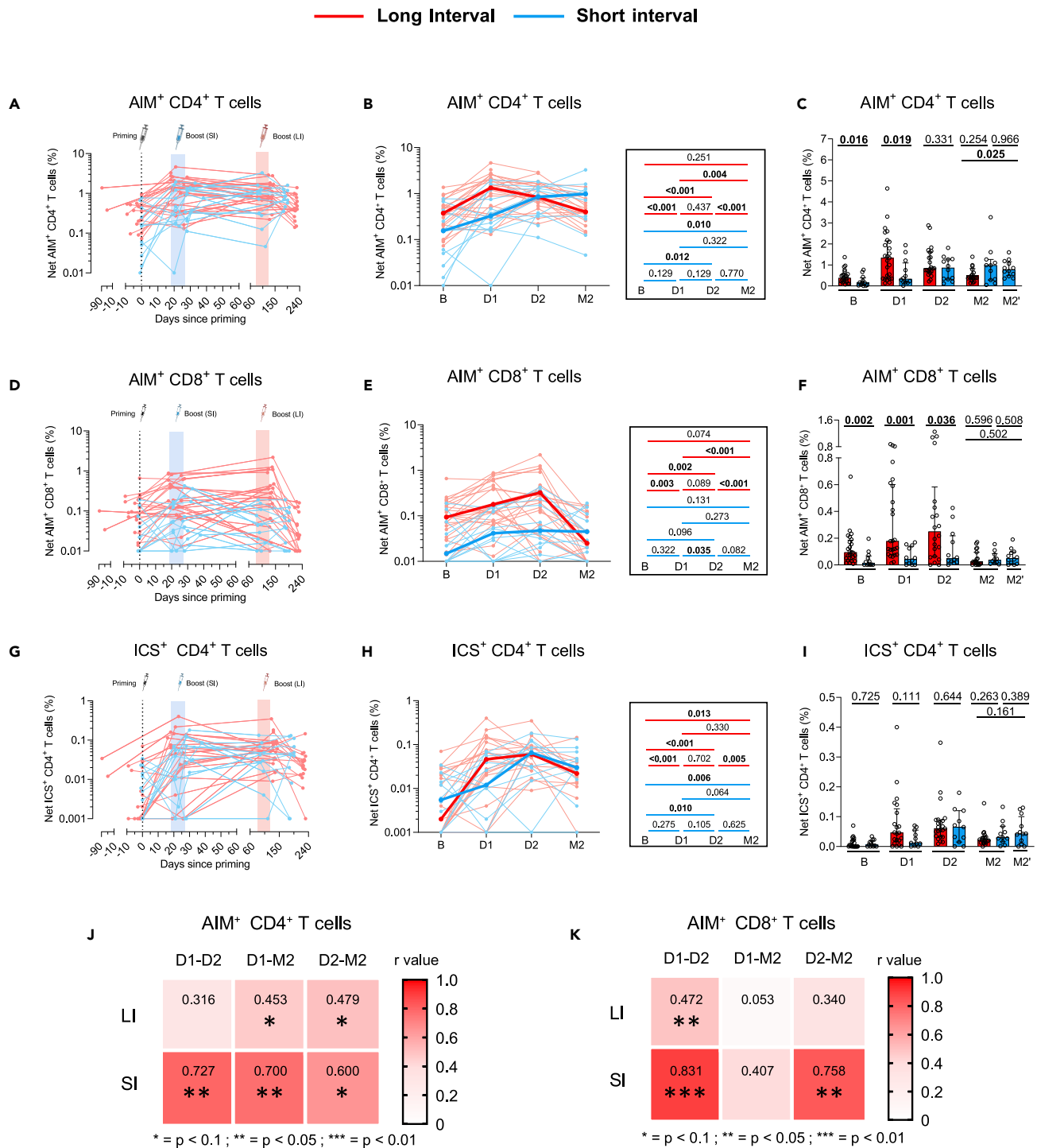


Figure 2. The initial two-dose vaccination series elicits Spike-specific CD4⁺ T cell responses of similar magnitude irrespective of dosing interval
SARS-CoV-2 Spike-specific CD4⁺ and CD8⁺ T cells in long (red) and short (blue) receiving two vaccine doses.
(A–C) Longitudinal (A and B) and inter-cohort (C) analyses of net Spike-specific AIM⁺ CD4⁺ T cell responses.
(D–F) Longitudinal (D and E) and inter-cohort (F) analyses net AIM⁺ CD8⁺ T cell responses.

Figure 2. Continued

(G–I) Longitudinal (G and H) and inter-cohort (I) analyses of the net magnitude of cytokine⁺ CD4⁺ T cell responses. The bold lines in B, E and H represent median values. The bars in C, F and I represent median ± interquartile ranges. In (B, E, H), the right panel shows statistical comparisons using Wilcoxon tests. In (C, F, I), Mann-Whitney tests are shown for inter-cohort comparisons and Wilcoxon tests for intra-cohort comparisons. (J and K) Heatmap showing temporal correlations of (J) AIM⁺ CD4⁺ and (K) AIM⁺ CD8⁺ T cells between the different time points for the two cohorts. The numbers in high square represent the correlation coefficient *r*. Significant Spearman tests results are indicated by stars (*: *p* < 0.1, **: *p* < 0.05, ***: *p* < 0.001). In A–K) LI cohort: *n* = 26, SI cohort: *n* = 12.

and S1H). In the LI cohort, class-switched memory IgD[−]CD27⁺ RBD-specific B cells were present at D2 and subsequently contracted at M2. This more mature subset was negligible at both time points in the SI cohort. Immature IgD⁺CD27[−] were rarely observed in LI participants, contrasting with their sizable proportion at M2 and M2' in the SI cohort (Figures 1J and S1I). There was a trend for a higher proportion of unswitched RBD-specific B cells in SI compared to LI at M2. This difference reached significance when comparing LI M2 with SI M2', time points that are more comparable (Figure 1K).

The SI and LI cohorts studied here represent subsets of cohorts in which we previously studied humoral responses in-depth.¹³ To contextualize our RBD-specific B cells analysis, we plotted the humoral responses against RBD in our cohorts (Figure S1J). We observed no statistically significant differences in the magnitude of RBD-specific antibody responses between the LI and SI cohorts at corresponding time points (Figures S1K and S1L). However, we observed a significantly higher RBD avidity at M2 in the LI cohort (Figure S1M), in agreement with a previous report showing higher RBD avidity in individuals receiving a long interval compared to a short interval.¹³

These data show that compared to the standard short-interval regimen, the second vaccine dose given after a long 16-week interval elicited robust RBD⁺ B cell responses peaking at higher magnitude than a shorter 3-week interval. The longer interval resulted in increased B cell maturity and stronger associations between early post-boost and memory responses.

The initial two-dose vaccination series elicits spike-specific CD4⁺ T cell responses of similar magnitude irrespective of dosing interval

CD4⁺ T cells help play a critical role in the development of B cell and CD8⁺ T cell immunity. We, therefore, measured Spike-specific T-cell responses at the four time points in the two cohorts (Figures 2 and S2). As in our previous work,⁹ we used both a TCR-dependent activation-induced marker (AIM) assay that broadly identifies antigen-specific T cells and intracellular cytokine staining (ICS) to perform functional profiling (flow cytometry panels: Tables S2 and S3).

The AIM assay involved a 15-h incubation of PBMCs with an overlapping peptide pool spanning the Spike coding sequence of the ancestral strain and the measurement of CD69, CD40L, 4-1BB and OX40 upregulation upon stimulation. We used an AND/OR Boolean combination gating to assess the total frequencies of antigen-specific CD4⁺ and CD8⁺ T cells (Figures S2A and S2B).^{9,33} At D2, all individuals had detectable CD4⁺ T cell responses (Figure S2C), and most had measurable CD8⁺ T cell responses (Figure S2D).

AIM CD4⁺ T cell responses in the two cohorts differed at baseline and after the first dose (Figure 2A). An increased plasma antibody binding to the prevalent OC43 betacoronavirus was noted in the LI cohort (Figure S2E). It raises the possibility that the higher AIM responses at baseline of LI are the consequences of previous cross-reactive exposures to common coronaviruses,^{34,35} although pre-exposition to abortive infection without seroconversion is also possible.³⁶ The effect of the second dose in LI was modest, with AIM CD4⁺ T cell responses still higher than at baseline, but lower than the initial responses at D1. In contrast, in SI the second dose further increased after an initially weaker CD4⁺ T cell response. Despite these initial differences, the trajectories converged at D2 (Figures 2B and 2C). In LI participants, the AIM CD4⁺ T cell responses decreased at the memory time points, a decline not yet observed in the SI cohort owing to a comparatively earlier sampling.

The trajectories of AIM⁺ CD8⁺ T responses were heterogeneous (Figure 2D). As reported in our previous study,²¹ LI participants elicited weak but significant responses after priming, a trend for stronger responses after the boost and contraction at M2 (Figure 2E). Consistent with AIM⁺ CD4⁺ T cell responses, AIM⁺ CD8⁺ T cell responses in the SI cohort were lower at baseline and D1 (Figure 2F). AIM⁺ CD8⁺ T responses

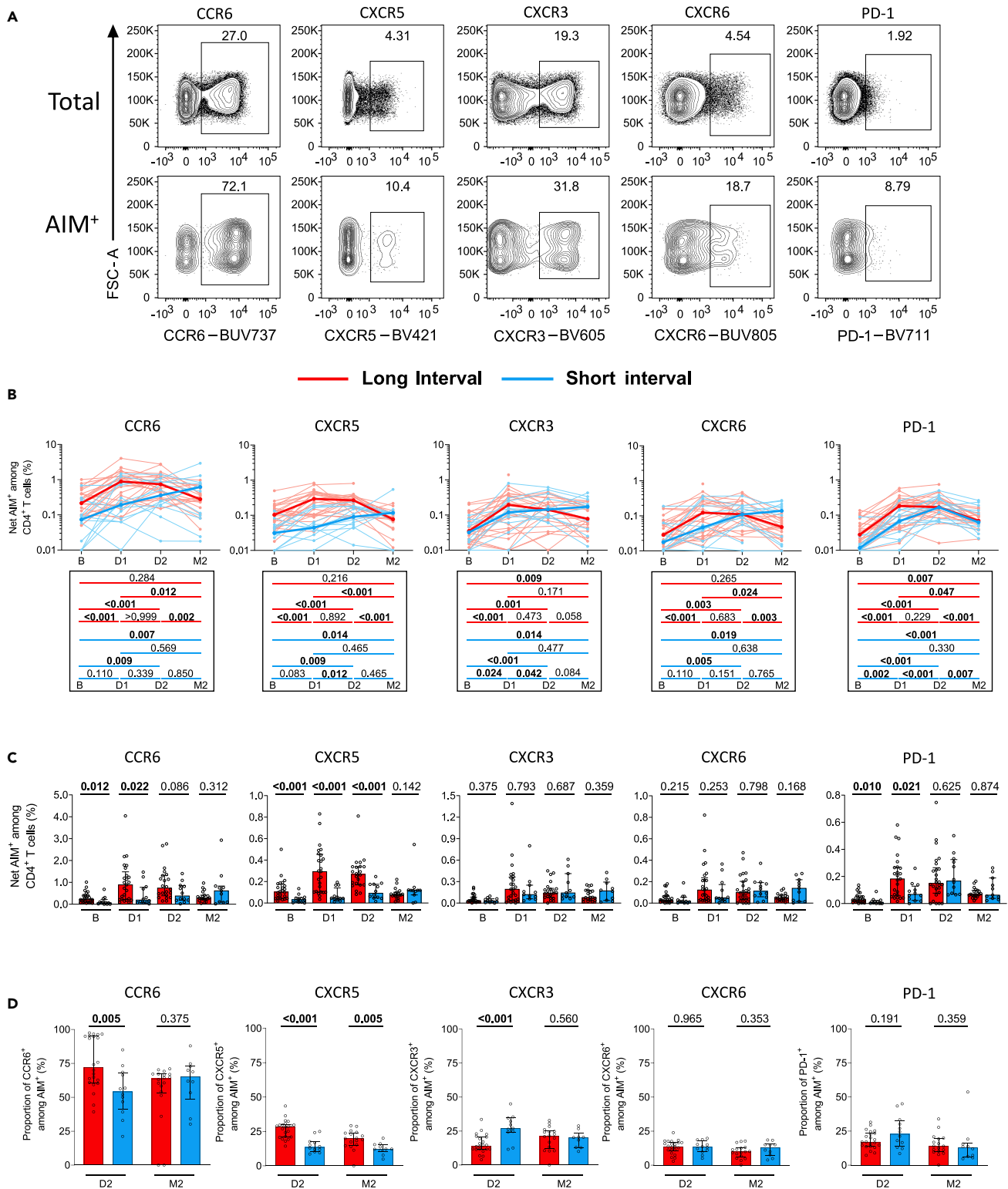


Figure 3. The second dose leads to convergence of some CD4⁺ T helper differentiation features differing early between the LI and SI cohorts
 (A) Representative flow cytometry dot plots for the indicated univariate phenotypic populations.
 (B) Net longitudinal frequencies of each AIM⁺ CD4⁺ T cell subpopulation in LI (red) and SI (blue) cohorts. Bold lines represent cohort's median value. Bottom panel: Wilcoxon tests for each pairwise comparison.

Figure 3. Continued

(C) Cohort comparisons at each time point for the subsets presented in (A). The bars represent median \pm interquartile ranges. Mann-Whitney tests are shown.

(D) Proportion of CXCR5⁺, CXCR3⁺, CCR6⁺, CXCR6⁺ and PD-1⁺ cells in total AIM⁺ CD4⁺ T cells at the D2 and M2 time points following the second dose. Bars represent medians \pm interquartile ranges. Mann-Whitney tests are shown.

(B–D) Phenotypic analyses include only individuals for which the spike-specific signal was ≥ 2 times over the background, with ≥ 5 positive events. (BCD) LI cohort: n = 26, SI cohort: n = 12.

plateaued from D2 up to M2' at levels comparable to the post-attrition levels seen in the LI cohort (Figures 2E and 2F), again indicating a convergence between the two vaccine modalities.

The ICS assay involved a 6-h stimulation with the Spike peptide pool and measurement of the effector molecules IFN- γ , IL-2, TNF- α , IL-17A, IL-10, and CD107a. We defined cytokine⁺CD4⁺ T cell responses by an AND/OR Boolean gating strategy (Figure S2F). Cytokine⁺ CD4⁺ T effector cells were readily detected after vaccination in most participants (Figure S2G). Total cytokine⁺ CD8⁺ T cell responses were weak or undetectable in most participants, precluding their detailed analysis (Figure S2H). The ICS patterns in both cohorts paralleled the AIM assays, albeit at a lower magnitude (Figure 2G). Cytokine responses in SI and LI converged at D2 and remained similar at M2 and M2' (Figures 2H and 2I). In contrast to AIM, however, cytokine⁺ CD4⁺ T cell responses at M2 remained significantly higher than at baseline in both cohorts (Figure 2H), showing longer-term memory poised for exerting effector functions.

As the expansion of previously primed antigen-specific T cells may impact T cell responses to vaccination, we examined correlations across visits (Figures 2J and 2K). We found in the LI cohort weak associations between post-priming AIM⁺ CD4⁺ T cell responses and those measured after boost or at the memory time point, respectively (Figure 2J). These associations were stronger in SI participants. We also found temporal associations for Spike-specific CD8⁺ T responses despite their lower magnitudes (Figure 2K).

These data show that in contrast to B cell responses, the initial differences in the magnitude of Spike-specific CD4⁺ and CD8⁺ T cell responses that we observed between cohorts prior and early after priming disappeared after the second dose. The similar responses at the memory time point suggest that the time interval between the two doses has a limited impact on the emergence and maintenance of Spike-specific CD4⁺ and CD8⁺ T cell immunity.

The second dose leads to convergence of some CD4⁺ T helper differentiation features differing early between the LI and SI cohorts

As the interval had a limited impact on the generation of CD4⁺ T cells but B cell responses remained lower after the second dose, we tested if different intervals could qualitatively affect CD4⁺ T cell responses and compared key CD4⁺ T cell subsets at D2 and M2 (Figure 3). We examined chemokine receptors that are preferentially, but not exclusively, expressed by some lineages and are involved in tissue homing (CXCR5 for Tfh; CXCR3 for Th1; CCR6 for Th17 and Th22 and mucosal homing; CXCR6 for pulmonary mucosal homing,^{37,38} and PD-1 as an inhibitory checkpoint (Figure 3A)), and assessed their longitudinal fluctuations (Figures 3B and 3C).

CCR6⁺ cells were dominant in both cohorts, representing a median of 72% in LI and 54% in SI of all D2 responses, but with a wide inter-individual variation (Figure 3D). Median CXCR5⁺ was 28% (LI) and 14% (SI), median CXCR3⁺ was 14% (LI) and 27% (SI), and PD-1⁺ was 17% (LI) and 23% (SI). CXCR6⁺ cells were the rarest tested polarization, representing 13% (LI) and 14% (SI) of AIM⁺ CD4⁺ T cells. We observed a variable contribution of these T helper subsets to the differences in total magnitude of CD4⁺ T cell responses between the LI and SI cohorts at baseline and after priming (Figures 3B and 3C). The CCR6⁺ and CXCR5⁺ subset showed major differences, with increased frequencies in LI at D2, then convergence at M2, whereas the kinetics of the CXCR3⁺ and CXCR6⁺ subsets showed no significant differences at any time points in the two cohorts (Figures 3B and 3C). The PD-1⁺ subset differed initially but exhibited similar magnitudes after the second dose and at M2 (Figures 3B and 3C). As shown by the relative fraction of each subset in the total AIM⁺ CD4⁺ T cell populations, some qualitative differences were still present shortly after the second dose but mostly waned at the memory time point (Figure 3D).

These results show that although the LI and SI cohorts presented qualitative differences at baseline and after the priming dose, repeat inoculation led to mostly converging features at the memory time point after the second dose despite the interval difference between doses in the two cohorts.

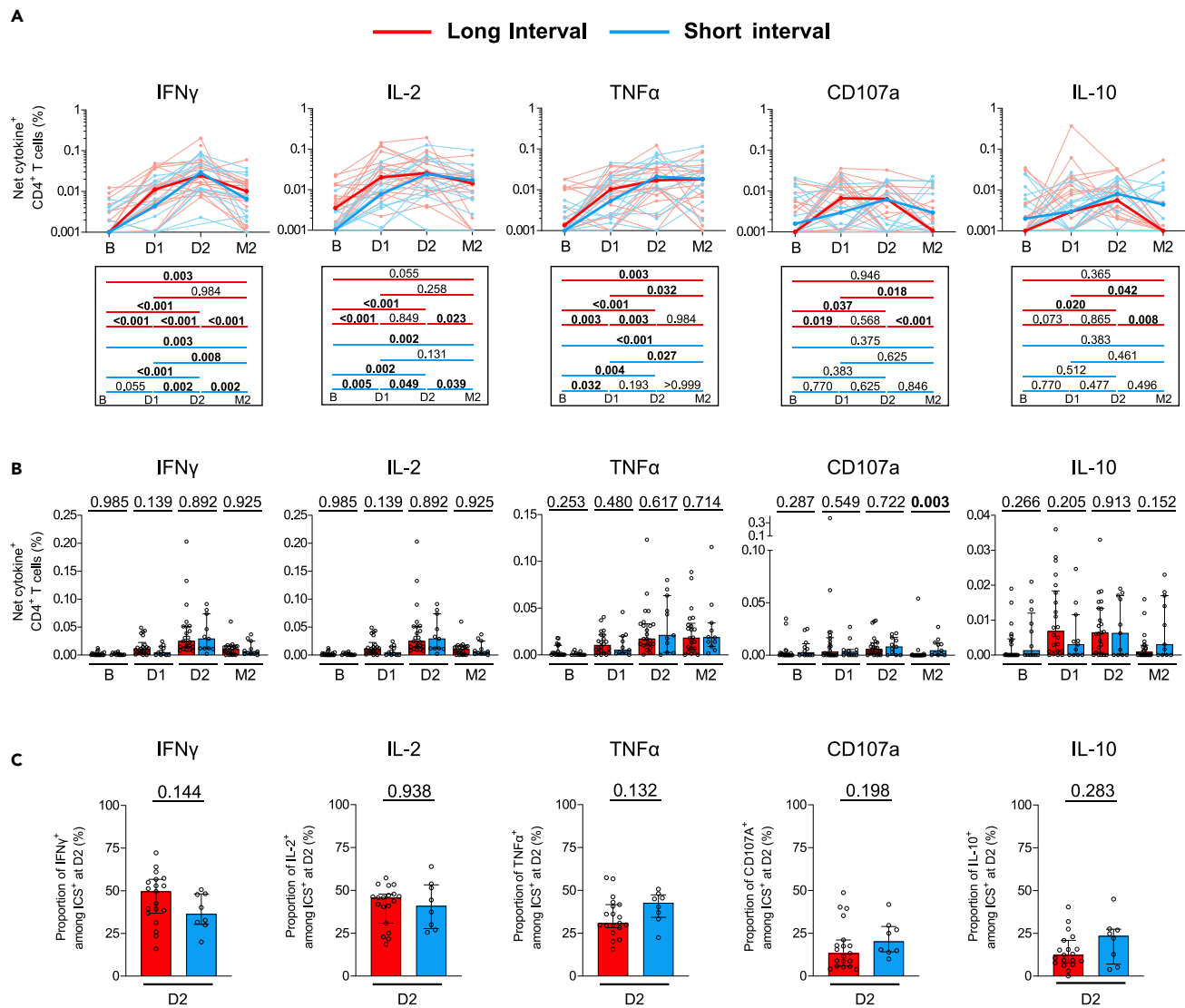


Figure 4. The long and short vaccination regimens elicit largely similar patterns of CD4⁺ T cell effector functions

(A) Longitudinal net frequencies of indicated cytokine⁺ CD4⁺ T cell subpopulations in the LI (red) and SI (blue) cohorts. Bold lines represent cohort's median value. Lower panel: Wilcoxon tests for each pairwise comparison.

(B) Cohort comparisons at each time point for each function represented in (A). The bars represent medians ± interquartile ranges. Mann-Whitney tests are shown.

(C) Proportions of IFN-γ, IL-2, TNF-α, IL-10, and CD107a-expressing cells among total cytokine⁺ CD4⁺ T cells. Bars represent medians ± interquartile ranges. Mann-Whitney tests are shown to compare long and short-interval cohorts.

(A-C) Phenotypic analyses include only individuals for which the spike-specific signal was ≥2 times over the background, with ≥5 positive events. (AB) LI cohort: n = 26, SI cohort: n = 12. (C) LI cohort: n = 19, SI cohort: n = 8.

The long and short vaccination regimens elicit largely similar patterns of CD4⁺ T cell effector functions

We next compared effector functions by ICS at D2 and M2, focusing on IFN-γ, TNF-α, IL-2, IL-10, and CD107a (Figures 4A–4C). IFN-γ⁺ and IL-2⁺ CD4⁺ T cells contracted at M2 in both cohorts, whereas TNF-α remained constant (Figures 4A and 4B). A decline of CD107a⁺ and IL-10⁺ CD4⁺ T cells was also observed at M2 in both cohorts, but was more pronounced in the LI, consistent with the later time of sampling. After the second dose, we did not detect any statistically significant differences in the qualitative functional profile of CD4⁺ T cell responses elicited by the long and short-interval vaccination schedules, as illustrated by the relative fraction of each cytokine in the total ICS response (Figure 4C).

Therefore, a longer interval between the first and second doses does not significantly alter the profile of tested effector CD4⁺ T functions.

DISCUSSION

Several studies have shown that extending the interval between the first two doses of SARS-CoV-2 mRNA vaccines beyond the recommended regimens of 3-4 weeks can lead to stronger antibody responses.¹⁰⁻¹³ These studies have led some public health agencies to modify their vaccination guidelines accordingly (eg., 8 weeks or more between the primary two doses in Quebec³⁹). However, the impact of long-interval regimens on cellular immunity is still poorly known due to the paucity of studies performing side-by-side in-depth comparisons of different dosing regimens with the same assays. Here, we compared the antigen-specific B cell, CD4⁺ T cell, and CD8⁺ T cell responses elicited in SARS-CoV-2 naive participants by a 16-week interval regimen compared to the standard 3-4 weeks schedule. We observed that a long interval increased the magnitude and maturation of RBD-specific B cell responses, while the completion of the primary vaccine series led to quantitatively and qualitatively similar memory CD4⁺ and CD8⁺ T cell memory responses in both regimens.

The RBD-specific B cells responses to the first vaccine dose were very consistent between the two cohorts and did not appear impacted by the age difference between the groups. In contrast, the magnitude of these responses markedly differed after the second dose, with a robust increase in the LI cohort contrasting with a weak gain for the SI cohort. A second dose after a short interval might act like a prolonged antigen delivery rather than a recall of primed responses, thus explaining a more limited benefit. While the sampling time could contribute to differences observed early after the second dose, the differences persisted as a strong trend at M2 before a late convergence at M2' memory time point. The increased B cell responses with a long interval are supporting recent findings showing that a longer interval also increases the peak humoral responses and antibody maturation,^{10-12,40,41} and are consistent with the fact that germinal centers remain active for several weeks after vaccination,⁴² with the continuous evolution of the B cell compartment for several months⁴³ and accumulation of somatic hypermutations.^{18,42,44} Hence, an early second dose likely corresponds to a suboptimal timing in terms of re-exposure to the cognate antigen, while a longer interval allows for a better evolution of the B cell repertoire. In line with these findings, the B cell maturation profile differed between the LI and SI cohorts after the second dose: almost all RBD-specific B cells presented an isotype-switched IgG⁺ phenotype in LI participants, contrasting with sizable IgM⁺ and IgD⁺ cell populations in SI volunteers which, importantly, persisted 23 weeks after boost. The memory differentiation phenotype was also consistent with this profile, with a larger fraction of RBD⁺ B cells with a CD27⁺ IgD⁻ memory phenotype early after boost in the LI participants. As we previously reported²¹ the RBD-specific B cell responses were dominated by the double-negative CD27⁻ IgD⁻ cells, including at the memory time point. This phenotypic subset was described in autoimmune diseases^{45,46} and in response to vaccination.⁴⁷ CD27⁻ IgD⁺ RBD⁺ B cells were absent at baseline and in previously infected individuals,²¹ suggesting recently activated B cells. Taken together, these results suggest that the long-interval regimen is beneficial to the generation and maturation of the B cell compartment, consistent with the higher avidity achieved after the two doses of the long-interval schedule.

We observed that Spike-specific CD4⁺ and CD8⁺ T cell responses at baseline were significantly stronger in the LI compared to the SI cohort. While we cannot exclude that this difference is due to precedent abortive SARS-CoV-2 infection with no seroconversion,³⁶ other studies have shown that cross-reactive immunity to common coronaviruses plays a major role in shaping these pre-existing SARS-CoV-specific CD4⁺ and CD8⁺ T cell responses.⁴⁸⁻⁵¹ Of note, our two cohorts were of geographically distinct locations (LI: Montreal, SI: Philadelphia) and the LI participants were significantly older than the SI volunteers. While the lack of sufficient PBMC samples precluded direct testing of cross-reactivity for CD4 and CD8 T cell responses, the higher antibody recognition of the OC43 Spike by the plasma from the LI cohort supports the possibility that differential previous exposure to endemic coronaviruses contributes to the pre-vaccination differences observed. These differences persisted after the first vaccine dose, consistent with a previously reported association between pre-existing T cell immunity and responses after priming.^{9,49,52,53} Importantly, however, the quantitative and qualitative differences in CD4⁺ and CD8⁺ T cell responses decreased already early after the second vaccine dose and waned almost entirely at the memory time point collected 10 to 16 weeks after the boost. This convergence was present both in phenotypic AIM assays (e.g, for CXCR5⁺ and CCR6⁺ CD4⁺ T cells) and functional ICS assays. IFN- γ ⁺ and IL-2⁺ CD4⁺ T cell responses were

comparable in the two cohorts, consistent with a recent study.¹⁰ Similarly, we did not identify differences in memory responses for TNF- α and IL-10 production. The small difference in CD107a⁺ CD4⁺ T cells frequencies should be interpreted with caution, given the very low magnitude of these responses. At first sight, our IL-2 data differ from another study that reported stronger memory IL-2⁺ CD4 T cell responses in long-interval vaccination.¹² However, the timeline may contribute to these differences. In our study, we assessed memory later after the second dose (10-16 weeks versus 4 weeks in¹²). Therefore, the completion of the primary 2-dose vaccination leads to convergent CD4⁺ and CD8⁺ T cell memory responses irrespective of dosing interval.

While the initial rationale of delaying the second dose was to provide some level of immunity more rapidly to a larger number of people in the context of limited vaccine supply,⁶ our results show that this strategy is beneficial to the generation of B cell responses without negative impact on T cell immunity. The potential immunological benefits of increasing the interval between doses must be weighed against a prolonged window of suboptimal protection, particularly while the virus and its different variants of concern are circulating in the population. Many countries now recommend a third dose, and more, although compliance with additional inoculations is a significant issue. Whether additional inoculations further abrogate the differences in cellular immunity observed between the long and short-interval regimens after the primary vaccination series warrants further investigation.

Limitations of the study

The cohorts were from two different countries that implemented different vaccination policies. As a result, the time points after the second dose were not perfectly matched. To mitigate this, we emphasized the direct comparisons on memory time points, which are less likely to be affected by the difference in the time of sampling.

The LI cohort is globally older than the SI cohort. Because age is associated with immune senescence,^{54,55} we may underestimate the benefit of extending the delay between the two doses. Our global message remains that compared to the standard vaccination schedule, a longer interval provides equivalent or better spike-specific B, CD4, and CD8 T cell responses.

Here, we investigated individuals who were SARS-CoV-2 naive prior to vaccination. However, we did not investigate the impact of long versus short-interval vaccine regimens in previously infected people. Further comparative studies are therefore required to assess the impact of dosing interval on cellular hybrid immunity. Also, we could not measure the impact of pre-exposition to abortive SARS-CoV-2 infection.

The demographically distinct LI and SI cohorts presented differences in T cell responses at baseline that we interpreted as likely reflecting the presence of a pre-existing pool of cross-reactive cells to other coronaviruses. Formal demonstration would require epitope-specific mapping of T cell responses, for which we did not have enough PBMC samples available. Also, in the current study, we could not measure the impact of potential pre-exposition to abortive SARS-CoV-2 infection that might potentiate cellular responses in absence of seroconversion.

We analyzed the cellular responses to ancestral strain antigens corresponding to the mRNA vaccines. The limiting availability in PBMC did not allow to assess the impact of dosing interval on B and T cell responses to variants of concern.

The size of the cohorts investigated here, particularly of the short-interval group, is not sufficient to uncover potential smaller qualitative differences in the T cell responses that might be caused by different intervals. However, the contrasting results obtained for B cell responses compared to T cell responses are clear enough to conclude that modifying the time between vaccine inoculations has a much bigger impact on B cell than T cell immunity.

Our study conducted in a low-risk HCW cohort may not be generalizable to vulnerable groups, particularly immunocompromised or elderly populations, in which the cellular immune responses and the risk/benefit ratio may differ. Future studies will be required to better quantify the immune response over time in these populations.

STAR★METHODS

Detailed methods are provided in the online version of this paper and include the following:

- **KEY RESOURCES TABLE**
- **RESOURCE AVAILABILITY**
 - Lead contact
 - Materials availability
 - Data and code availability
- **EXPERIMENTAL MODEL AND SUBJECT DETAILS**
 - Ethics statement
 - Participants
 - PBMCs collection
 - Plasma and antibodies
 - Cell lines
- **METHOD DETAILS**
 - Protein expression and purification
 - SARS-CoV-2-specific B cells characterization
 - Activation-induced marker (AIM) assay
 - Intracellular cytokine staining (ICS)
 - Enzyme-linked immunosorbent assay (ELISA) and RBD avidity index
 - Cell surface staining and flow cytometry analysis
- **QUANTIFICATION AND STATISTICAL ANALYSIS**
 - Statistical analysis
 - Software scripts and visualization

SUPPLEMENTAL INFORMATION

Supplemental information can be found online at <https://doi.org/10.1016/j.isci.2022.105904>.

ACKNOWLEDGMENTS

The authors are grateful to the study participants. We thank the CRCHUM BSL3 and Flow Cytometry Platforms for technical assistance, Dr. Johanne Poudrier for advice and discussions. This work was supported by an FRQS Merit Research Scholar award to D.E.K, the Fondation du CHUM, the Ministère de l'Économie et de l'Innovation du Québec, Programme de soutien aux organismes de recherche et d'innovation (to A.F), a CIHR operating grant # 178344 (D.E.K and A.F), a foundation grant #352417 (A.F), a CIHR operating Pandemic and Health Emergencies Research grant #177958 (A.F), and an Exceptional Fund COVID-19 from the Canada Foundation for Innovation (CFI) #41027 to A.F and D.E.K. The Symphony flow cytometer was funded by a John R. Evans Leaders Fund Leader Fund from the Canada Foundation for Innovation (# 37521 to D.E.K) and the Fondation Sclérodémie Québec. A.F. is the recipient of Canada Research Chair on Retroviral Entry no. RCHS0235 950-232424. V.M.L. is supported by an FRQS Junior 1 salary award, G.S. is supported by an FRQS doctoral fellowship and by a scholarship from the Department of Microbiology, Infectious Disease, and Immunology of the University of Montreal. A.T. is supported by a Mitacs Accélération postdoctoral fellowship. This work was also supported by NIH funds: grants AI108545, AI155577, AI149680, and U19AI082630 (to E.J.W.), the University of Pennsylvania Perelman School of Medicine COVID Fund (to R.R.G. and E.J.W.); the University of Pennsylvania Perelman School of Medicine 21st Century Scholar Fund (to R.R.G.); and the Paul and Daisy Soros Fellowship for New Americans (to R.R.G). The funders had no role in study design, data collection and analysis, decision to publish, or preparation of the article. Some illustrations were created with [Biorender.com](https://biorender.com).

AUTHOR CONTRIBUTIONS

A.N., G.S., M.D., A.F., and D.E.K. designed the studies. A.N., G.S., M.N., N.B., and M.L. performed B cell and T cell assays. A.N., G.S., and M.D. performed and analyzed the B and T cell experiments. G.G.L. and A.T. performed RBD ELISA, RBD avidity index and OC43 staining. J.N. contributed to the T cell assay design. A.T., H.M., L.G., C.M., P.A., C.T., J.C.W., and V.M.L. secured and processed blood samples. M.M.P., R.R.G., A.R.G., and E.J.W. provided unique reagents. G.G. produced and purified proteins. A.N., G.S., M.D., and D.E.K. wrote the article. Every author has read, edited, and approved the final article.

DECLARATION OF INTERESTS

A.R.G. is a consultant for Relation Therapeutics. E.J.W. is consulting for or is an advisor for Merck, Marengo, Janssen, Related Sciences, Synthekine, and Surface Oncology. E.J.W. is a founder of Surface Oncology, Danger Bio, and Arsenal Biosciences. The other authors have no conflict of interest to declare.

Received: August 8, 2022

Revised: November 10, 2022

Accepted: December 26, 2022

Published: January 20, 2023

REFERENCES

1. Baden, L.R., El Sahly, H.M., Essink, B., Kotloff, K., Frey, S., Novak, R., Diemert, D., Spector, S.A., Rouphael, N., Creech, C.B., et al. (2021). Efficacy and safety of the mRNA-1273 SARS-CoV-2 vaccine. *N. Engl. J. Med.* **384**, 403–416. <https://doi.org/10.1056/NEJMoa2035389>.
2. Skowronski, D.M., and De Serres, G. (2021). Safety and efficacy of the BNT162b2 mRNA Covid-19 vaccine. *N. Engl. J. Med.* **384**, 1576–1577. <https://doi.org/10.1056/NEJMc2036242>.
3. Polack, F.P., Thomas, S.J., Kitchin, N., Absalon, J., Gurtman, A., Lockhart, S., Perez, J.L., Pérez Marc, G., Moreira, E.D., Zerbini, C., et al. (2020). Safety and efficacy of the BNT162b2 mRNA Covid-19 vaccine. *N. Engl. J. Med.* **383**, 2603–2615. <https://doi.org/10.1056/NEJMoa2034577>.
4. Tuite, A.R., Zhu, L., Fisman, D.N., and Salomon, J.A. (2021). Alternative dose allocation strategies to increase benefits from constrained COVID-19 vaccine supply. *Ann. Intern. Med.* **174**, 570–572. <https://doi.org/10.7326/M20-8137>.
5. Paltiel, A.D., Zheng, A., and Schwartz, J.L. (2021). Speed versus efficacy: quantifying potential tradeoffs in COVID-19 vaccine deployment. *Ann. Intern. Med.* **174**, 568–570. <https://doi.org/10.7326/M20-7866>.
6. Rodrigues, C.M.C., and Plotkin, S.A. (2021). The influence of interval between doses on response to vaccines. *Vaccine* **39**, 7123–7127. <https://doi.org/10.1016/j.vaccine.2021.10.050>.
7. Carazo, S., Talbot, D., Boulianne, N., Brisson, M., Gilca, R., Deceuninck, G., Brousseau, N., Drolet, M., Ouakki, M., Sauvageau, C., et al. (2021). Single-dose mRNA vaccine effectiveness against SARS-CoV-2 in healthcare workers extending 16 weeks post-vaccination: a test-negative design from Quebec, Canada. *Clin. Infect. Dis.* **75**, e805–e813. <https://doi.org/10.1093/cid/ciab739>.
8. Skowronski, D.M., Setayeshgar, S., Febriani, Y., Ouakki, M., Zou, M., Talbot, D., Prystajecy, N., Tyson, J.R., Gilca, R., Brousseau, N., et al. (2021). Two-dose SARS-CoV-2 vaccine effectiveness with mixed schedules and extended dosing intervals: test-negative design studies from British Columbia and Quebec, Canada. Preprint at medRxiv. <https://doi.org/10.1101/2021.10.26.21265397>.
9. Tazuin, A., Nayrac, M., Benlarbi, M., Gong, S.Y., Gasser, R., Beaudoin-Bussièrès, G., Brassard, N., Laumaea, A., Vézina, D., Prévost, J., et al. (2021). A single dose of the SARS-CoV-2 vaccine BNT162b2 elicits Fc-mediated antibody effector functions and T cell responses. *Cell Host Microbe* **29**, 1137–1150.e6. <https://doi.org/10.1016/j.chom.2021.06.001>.
10. Hall, V.G., Ferreira, V.H., Wood, H., Ierullo, M., Majchrzak-Kita, B., Manguiat, K., Robinson, A., Kulasingam, V., Humar, A., and Kumar, D. (2022). Delayed-interval BNT162b2 mRNA COVID-19 vaccination enhances humoral immunity and induces robust T cell responses. *Nat. Immunol.* **23**, 380–385. <https://doi.org/10.1038/s41590-021-01126-6>.
11. Grunau, B., Goldfarb, D.M., Asamoah-Boaheng, M., Golding, L., Kirkham, T.L., Demers, P.A., and Lavoie, P.M. (2022). Immunogenicity of extended mRNA SARS-CoV-2 vaccine dosing intervals. *JAMA* **327**, 279–281. <https://doi.org/10.1001/jama.2021.21921>.
12. Payne, R.P., Longuet, S., Austin, J.A., Skelly, D.T., Dejnirattisai, W., Adele, S., Meardon, N., Faustini, S., Al-Taei, S., Moore, S.C., et al. (2021). Immunogenicity of standard and extended dosing intervals of BNT162b2 mRNA vaccine. *Cell* **184**, 5699–5714.e11. <https://doi.org/10.1016/j.cell.2021.10.011>.
13. Tazuin, A., Gong, S.Y., Beaudoin-Bussièrès, G., Vézina, D., Gasser, R., Nault, L., Marchitto, L., Benlarbi, M., Chatterjee, D., Nayrac, M., et al. (2022). Strong humoral immune responses against SARS-CoV-2 Spike after BNT162b2 mRNA vaccination with a 16-week interval between doses. *Cell Host Microbe* **30**, 97–109.e5. <https://doi.org/10.1016/j.chom.2021.12.004>.
14. Gilbert, P.B., Montefiori, D.C., McDermott, A.B., Fong, Y., Benkeser, D., Deng, W., Zhou, H., Houchens, C.R., Martins, K., Jayashankar, L., et al. (2022). Immune correlates analysis of the mRNA-1273 COVID-19 vaccine efficacy clinical trial. *Science* **375**, 43–50.
15. Earle, K.A., Ambrosino, D.M., Fiore-Gartland, A., Goldblatt, D., Gilbert, P.B., Siber, G.R., Dull, P., and Plotkin, S.A. (2021). Evidence for antibody as a protective correlate for COVID-19 vaccines. *Vaccine* **39**, 4423–4428. <https://doi.org/10.1016/j.vaccine.2021.05.063>.
16. Crotty, S. (2019). T follicular helper cell biology: a decade of discovery and diseases. *Immunity* **50**, 1132–1148. <https://doi.org/10.1016/j.immuni.2019.04.011>.
17. Morita, R., Schmitt, N., Bentebibel, S.-E., Ranganathan, R., Bourdery, L., Zurawski, G., Foucat, E., Dullaers, M., Oh, S., Sabzghabaei, N., et al. (2011). Human blood CXCR5+CD4+ T cells are counterparts of T follicular cells and contain specific subsets that differentially support antibody secretion. *Immunity* **34**, 108–121. <https://doi.org/10.1016/j.immuni.2010.12.012>.
18. Kim, W., Zhou, J.Q., Horvath, S.C., Schmitz, A.J., Sturtz, A.J., Lei, T., Liu, Z., Kalaidina, E., Thapa, M., Alsoussi, W.B., et al. (2022). Germinal centre-driven maturation of B cell response to mRNA vaccination. *Nature* **604**, 141–145. <https://doi.org/10.1038/s41586-022-04527-1>.
19. Pardi, N., Hogan, M.J., Naradikian, M.S., Parkhouse, K., Cain, D.W., Jones, L., Moody, M.A., Verkerke, H.P., Myles, A., Willis, E., et al. (2018). Nucleoside-modified mRNA vaccines induce potent T follicular helper and germinal center B cell responses. *J. Exp. Med.* **215**, 1571–1588. <https://doi.org/10.1084/jem.20171450>.
20. Laidlaw, B.J., Craft, J.E., and Kaech, S.M. (2016). The multifaceted role of CD4(+) T cells in CD8(+) T cell memory. *Nat. Rev. Immunol.* **16**, 102–111. <https://doi.org/10.1038/nri.2015.10>.
21. Nayrac, M., Dubé, M., Sannier, G., Nicolas, A., Marchitto, L., Tastet, O., Tazuin, A., Brassard, N., Lima-Barbosa, R., Beaudoin-Bussièrès, G., et al. (2022). Temporal associations of B and T cell immunity with robust vaccine responsiveness in a 16-week interval BNT162b2 regimen. *Cell Rep.* **39**, 111013. <https://doi.org/10.1016/j.celrep.2022.111013>.
22. O’Shea, J.J., and Paul, W.E. (2010). Mechanisms underlying lineage commitment and plasticity of helper CD4+ T cells. *Science* **327**, 1098–1102. <https://doi.org/10.1126/science.1178334>.
23. Rodda, L.B., Morawski, P.A., Pruner, K.B., Fahning, M.L., Howard, C.A., Franko, N., Logue, J., Eggenberger, J., Stokes, C., Golez, I., et al. (2022). Imprinted SARS-CoV-2-specific memory lymphocytes define hybrid immunity. *Cell* **185**, 1588–1601.e14. <https://doi.org/10.1016/j.cell.2022.03.018>.
24. Painter, M.M., Mathew, D., Goel, R.R., Apostolidis, S.A., Pattekar, A., Kuthuru, O.,

- Baxter, A.E., Herati, R.S., Oldridge, D.A., Gouma, S., et al. (2021). Rapid induction of antigen-specific CD4(+) T cells is associated with coordinated humoral and cellular immunity to SARS-CoV-2 mRNA vaccination. *Immunity* 54, 2133–2142.e3. <https://doi.org/10.1016/j.immuni.2021.08.001>.
25. Goel, R.R., Painter, M.M., Apostolidis, S.A., Mathew, D., Meng, W., Rosenfeld, A.M., Lundgreen, K.A., Reynaldi, A., Khoury, D.S., Pattekar, A., et al. (2021). mRNA vaccines induce durable immune memory to SARS-CoV-2 and variants of concern. *Science* 374, eabm0829. <https://doi.org/10.1126/science.abm0829>.
 26. Zollner, A., Watschinger, C., Rössler, A., Farcet, M.R., Penner, A., Böhm, V., Kiechl, S.J., Stampfel, G., Hintenberger, R., Tilg, H., et al. (2021). B and T cell response to SARS-CoV-2 vaccination in health care professionals with and without previous COVID-19. *EBioMedicine* 70, 103539. <https://doi.org/10.1016/j.ebiom.2021.103539>.
 27. Flaxman, A., Marchevsky, N.G., Jenkin, D., Aboagye, J., Aley, P.K., Angus, B., Belj-Rammerstorfer, S., Bibi, S., Bittaye, M., Cappuccini, F., et al. (2021). Reactogenicity and immunogenicity after a late second dose or a third dose of ChAdOx1 nCoV-19 in the UK: a substudy of two randomised controlled trials (COV001 and COV002). *Lancet* 398, 981–990. [https://doi.org/10.1016/s0140-6736\(21\)01699-8](https://doi.org/10.1016/s0140-6736(21)01699-8).
 28. Klumpp-Thomas, C., Kalish, H., Drew, M., Hunsberger, S., Snead, K., Fay, M.P., Mehalko, J., Shunmugavel, A., Wall, V., Frank, P., et al. (2021). Standardization of ELISA protocols for serosurveys of the SARS-CoV-2 pandemic using clinical and at-home blood sampling. *Nat. Commun.* 12, 113. <https://doi.org/10.1038/s41467-020-20383-x>.
 29. Hicks, J., Klumpp-Thomas, C., Kalish, H., Shunmugavel, A., Mehalko, J., Denson, J.P., Snead, K.R., Drew, M., Corbett, K.S., Graham, B.S., et al. (2021). Serologic cross-reactivity of SARS-CoV-2 with endemic and seasonal Betacoronaviruses. *J. Clin. Immunol.* 41, 906–913. <https://doi.org/10.1007/s10875-021-00997-6>.
 30. Anand, S.P., Prevost, J., Nayrac, M., Beaudoin-Bussières, G., Benlarbi, M., Gasser, R., Brassard, N., Laumaea, A., Gong, S.Y., Bourassa, C., et al. (2021). Longitudinal analysis of humoral immunity against SARS-CoV-2 Spike in convalescent individuals up to 8 months post-symptom onset. *Cell reports. Medicine* 2, 100290. <https://doi.org/10.1016/j.xcrn.2021.100290>.
 31. Tangye, S.G., Liu, Y.J., Aversa, G., Phillips, J.H., and de Vries, J.E. (1998). Identification of functional human splenic memory B cells by expression of CD148 and CD27. *J. Exp. Med.* 188, 1691–1703. <https://doi.org/10.1084/jem.188.9.1691>.
 32. Moore, K.W., Rogers, J., Hunkapiller, T., Early, P., Nottenburg, C., Weissman, I., Bazin, H., Wall, R., and Hood, L.E. (1981). Expression of IgD may use both DNA rearrangement and RNA splicing mechanisms. *Proc. Natl. Acad. Sci. USA* 78, 1800–1804. <https://doi.org/10.1073/pnas.78.3.1800>.
 33. Niessl, J., Baxter, A.E., Mendoza, P., Jankovic, M., Cohen, Y.Z., Butler, A.L., Lu, C.L., Dubé, M., Shimeliovich, I., Gruell, H., et al. (2020). Combination anti-HIV-1 antibody therapy is associated with increased virus-specific T cell immunity. *Nat. Med.* 26, 222–227. <https://doi.org/10.1038/s41591-019-0747-1>.
 34. Patrick, D.M., Petric, M., Skowronski, D.M., Guasparini, R., Booth, T.F., Krajden, M., McGeer, P., Bastien, N., Gustafson, L., Dubord, J., et al. (2006). An outbreak of human Coronavirus OC43 infection and serological cross-reactivity with SARS Coronavirus. *Can. J. Infect. Dis. Med. Microbiol.* 17, 330–336. <https://doi.org/10.1155/2006/152612>.
 35. Saib, I., Aleisa, S., Ardah, H., Mahmoud, E., Alharbi, A.O., Alsaedy, A., Aljohani, S., Alshehri, A., Alharbi, N.K., and Bosaeed, M. (2021). Non-SARS non-MERS human coronaviruses: clinical characteristics and outcome. *Pathogens* 10, 1549. <https://doi.org/10.3390/pathogens10121549>.
 36. Swadling, L., Diniz, M.O., Schmidt, N.M., Amin, O.E., Chandran, A., Shaw, E., Pade, C., Gibbons, J.M., Le Bert, N., Tan, A.T., et al. (2022). Pre-existing polymerase-specific T cells expand in abortive seronegative SARS-CoV-2. *Nature* 601, 110–117. <https://doi.org/10.1038/s41586-021-04186-8>.
 37. Morgan, X.C., Kabakchiev, B., Waldron, L., Tyler, A.D., Tickle, T.L., Milgrom, R., Stempak, J.M., Gevers, D., Xavier, R.J., Silverberg, M.S., and Huttenhower, C. (2015). Associations between host gene expression, the mucosal microbiome, and clinical outcome in the pelvic pouch of patients with inflammatory bowel disease. *Genome Biol.* 16, 67. <https://doi.org/10.1186/s13059-015-0637-x>.
 38. Day, C.E., Zhang, S.D., Riley, J., Gant, T., Wardlaw, A.J., and Guillen, C. (2009). A novel method for isolation of human lung T cells from lung resection tissue reveals increased expression of GAPDH and CXCR6. *J. Immunol. Methods* 342, 91–97. <https://doi.org/10.1016/j.jim.2008.12.001>.
 39. Quebec, G.o. (2022). COVID-19 Vaccination Guidelines. <https://www.quebec.ca/en/health/advice-and-prevention/vaccination/covid-19-vaccine>.
 40. Chatterjee, D., Tauzin, A., Marchitto, L., Gong, S.Y., Boutin, M., Bourassa, C., Beaudoin-Bussières, G., Bo, Y., Ding, S., Laumaea, A., et al. (2022). SARS-CoV-2 Omicron Spike recognition by plasma from individuals receiving BNT162b2 mRNA vaccination with a 16-week interval between doses. *Cell Rep.* 38, 110429. <https://doi.org/10.1016/j.celrep.2022.110429>.
 41. Tauzin, A., Gong, S.Y., Painter, M.M., Goel, R.R., Chatterjee, D., Beaudoin-Bussières, G., Marchitto, L., Boutin, M., Laumaea, A., Okeny, J., et al. (2022). A boost with SARS-CoV-2 BNT162b2 mRNA vaccine elicits strong humoral responses independently of the interval between the first two doses. Preprint at medRxiv. <https://doi.org/10.1101/2022.04.18.22273967>.
 42. Turner, J.S., O’Halloran, J.A., Kalaidina, E., Kim, W., Schmitz, A.J., Zhou, J.Q., Lei, T., Thapa, M., Chen, R.E., Case, J.B., et al. (2021). SARS-CoV-2 mRNA vaccines induce persistent human germinal centre responses. *Nature* 596, 109–113. <https://doi.org/10.1038/s41586-021-03738-2>.
 43. Cho, A., Muecksch, F., Schaefer-Babajew, D., Wang, Z., Finkin, S., Gaebler, C., Ramos, V., Cipolla, M., Mendoza, P., Agudelo, M., et al. (2021). Anti-SARS-CoV-2 receptor-binding domain antibody evolution after mRNA vaccination. *Nature* 600, 517–522. <https://doi.org/10.1038/s41586-021-04060-7>.
 44. Paschold, L., Klee, B., Gottschick, C., Willscher, E., Diexer, S., Schultheiß, C., Simnica, D., Sedding, D., Girndt, M., Gekle, M., et al. (2022). Rapid hypermutation B cell trajectory recruits previously primed B cells upon third SARS-CoV-2 mRNA vaccination. *Front. Immunol.* 13, 876306. <https://doi.org/10.3389/fimmu.2022.876306>.
 45. Jenks, S.A., Cashman, K.S., Zumaquero, E., Marigorta, U.M., Patel, A.V., Wang, X., Tomar, D., Woodruff, M.C., Simon, Z., Bugrovsky, R., et al. (2018). Distinct effector B cells induced by unregulated toll-like receptor 7 contribute to pathogenic responses in systemic lupus erythematosus. *Immunity* 49, 725–739.e6. <https://doi.org/10.1016/j.immuni.2018.08.015>.
 46. Wei, C., Anolik, J., Cappione, A., Zheng, B., Pugh-Bernard, A., Brooks, J., Lee, E.H., Milner, E.C.B., and Sanz, I. (2007). A new population of cells lacking expression of CD27 represents a notable component of the B cell memory compartment in systemic lupus erythematosus. *J. Immunol.* 178, 6624–6633. <https://doi.org/10.4049/jimmunol.178.10.6624>.
 47. Ruschil, C., Gabernet, G., Lepenietier, G., Heumos, S., Kaminski, M., Hracsko, Z., Irmeler, M., Beckers, J., Ziemann, U., Nahnsen, S., et al. (2020). Specific induction of double negative B cells during protective and pathogenic immune responses. *Front. Immunol.* 11, 606338. <https://doi.org/10.3389/fimmu.2020.606338>.
 48. Shrock, E., Fujimura, E., Kula, T., Timms, R.T., Lee, I.H., Leng, Y., Robinson, M.L., Sie, B.M., Li, M.Z., Chen, Y., et al. (2020). Viral epitope profiling of COVID-19 patients reveals cross-reactivity and correlates of severity. *Science* 370, eabd4250. <https://doi.org/10.1126/science.abd4250>.
 49. Grifoni, A., Weiskopf, D., Ramirez, S.I., Mateus, J., Dan, J.M., Moderbacher, C.R., Rawlings, S.A., Sutherland, A., Premkumar, L., Jadhav, R.S., et al. (2020). Targets of T Cell responses to SARS-CoV-2 Coronavirus in humans with COVID-19 disease and unexposed individuals. *Cell* 181, 1489–1501.e15. <https://doi.org/10.1016/j.cell.2020.05.015>.
 50. Mateus, J., Grifoni, A., Tarke, A., Sidney, J., Ramirez, S.I., Dan, J.M., Burger, Z.C., Rawlings, S.A., Smith, D.M., Phillips, E., et al. (2020). Selective and cross-reactive SARS-CoV-2 T cell epitopes in unexposed humans. *Science* 370, 89–94. <https://doi.org/10.1126/science.abd3871>.

51. Braun, J., Loyal, L., Frentsch, M., Wendisch, D., Georg, P., Kurth, F., Hippenstiel, S., Dingeldey, M., Kruse, B., Fauchere, F., et al. (2020). SARS-CoV-2-reactive T cells in healthy donors and patients with COVID-19. *Nature* 587, 270–274. <https://doi.org/10.1038/s41586-020-2598-9>.
52. Loyal, L., Braun, J., Henze, L., Kruse, B., Dingeldey, M., Reimer, U., Kern, F., Schwarz, T., Mangold, M., Unger, C., et al. (2021). Cross-reactive CD4(+) T cells enhance SARS-CoV-2 immune responses upon infection and vaccination. *Science* 374, eabh1823. <https://doi.org/10.1126/science.abh1823>.
53. Le Bert, N., Tan, A.T., Kunasegaran, K., Tham, C.Y.L., Hafezi, M., Chia, A., Chng, M.H.Y., Lin, M., Tan, N., Linster, M., et al. (2020). SARS-CoV-2-specific T cell immunity in cases of COVID-19 and SARS, and uninfected controls. *Nature* 584, 457–462. <https://doi.org/10.1038/s41586-020-2550-z>.
54. Kumar, R., and Burns, E.A. (2008). Age-related decline in immunity: implications for vaccine responsiveness. *Expert Rev. Vaccines* 7, 467–479. <https://doi.org/10.1586/14760584.7.4.467>.
55. Müller, L., Andrée, M., Moskorz, W., Drexler, I., Walotka, L., Grothmann, R., Ptok, J., Hillebrandt, J., Ritchie, A., Rabl, D., et al. (2021). Age-dependent immune response to the biontech/pfizer BNT162b2 Coronavirus disease 2019 vaccination. *Clin. Infect. Dis.* 73, 2065–2072. <https://doi.org/10.1093/cid/ciab381>.
56. Prévost, J., Gasser, R., Beaudoin-Bussièrès, G., Richard, J., Duerr, R., Laumaea, A., Anand, S.P., Goyette, G., Benlarbi, M., Ding, S., et al. (2020). Cross-sectional evaluation of humoral responses against SARS-CoV-2 spike. *Cell Rep. Med.* 1, 100126. <https://doi.org/10.1016/j.xcrm.2020.100126>.
57. Beaudoin-Bussièrès, G., Laumaea, A., Anand, S.P., Prévost, J., Gasser, R., Goyette, G., Medjahed, H., Perreault, J., Tremblay, T., Lewin, A., et al. (2020). Decline of humoral responses against SARS-CoV-2 spike in convalescent individuals. *mBio* 11, 02590-20. <https://doi.org/10.1128/mBio.02590-20>.
58. Niessl, J., Baxter, A.E., Morou, A., Brunet-Ratnasingham, E., Sannier, G., Gendron-Lepage, G., Richard, J., Delgado, G.G., Brassard, N., Turcotte, I., et al. (2020). Persistent expansion and Th1-like skewing of HIV-specific circulating T follicular helper cells during antiretroviral therapy. *EBioMedicine* 54, 102727. <https://doi.org/10.1016/j.ebiom.2020.102727>.
59. Morou, A., Brunet-Ratnasingham, E., Dubé, M., Charlebois, R., Mercier, E., Darko, S., Brassard, N., Nganou-Makamdop, K., Arumugam, S., Gendron-Lepage, G., et al. (2019). Altered differentiation is central to HIV-specific CD4(+) T cell dysfunction in progressive disease. *Nat. Immunol.* 20, 1059–1070. <https://doi.org/10.1038/s41590-019-0418-x>.
60. Reiss, S., Baxter, A.E., Cirelli, K.M., Dan, J.M., Morou, A., Daigneault, A., Brassard, N., Silvestri, G., Routy, J.P., Havenar-Daughton, C., et al. (2017). Comparative analysis of activation induced marker (AIM) assays for sensitive identification of antigen-specific CD4 T cells. *PLoS One* 12, e0186998. <https://doi.org/10.1371/journal.pone.0186998>.
61. Roederer, M., Nozzi, J.L., and Nason, M.C. (2011). SPICE: exploration and analysis of post-cytometric complex multivariate datasets. *Cytometry A.* 79, 167–174. <https://doi.org/10.1002/cyto.a.21015>.
62. Tautzin, A., Gendron-Lepage, G., Nayrac, M., Anand, S.P., Bourassa, C., Medjahed, H., Goyette, G., Dubé, M., Bazin, R., Kaufmann, D.E., and Finzi, A. (2022). Evolution of anti-RBD IgG avidity following SARS-CoV-2 infection. *Viruses* 14, 532.

STAR★METHODS

KEY RESOURCES TABLE

REAGENT or RESOURCE	SOURCE	IDENTIFIER
<i>Antibodies</i>		
UCHT1 (BUV395) [Human anti-CD3]	BD Biosciences	Cat#563546; Lot: 9058566; RRID:AB_2744387
1B5 (BUV 395) [Human anti-CCR10]	BD Biosciences	Cat# 565322; Lot: 1198884 RRID:AB_2739181
IA6-2 (BUV 563) [Human anti-IgD]	BD Biosciences	Cat# 741394; Lot: 2048494 RRID:AB_2870889
MI15 (BUV 661) [Human anti-CD138]	BD Biosciences	Cat# 749873; Lot: 1140733 RRID:AB_2874113
UCH-B1 (BUV 737) [Human anti-IgM]	BD Biosciences	Cat# 748928; Lot: 1154015 RRID:AB_2873331
ML5 (BUV 805) [Human anti-CD24]	BD Biosciences	Cat# 742010; Lot: 1154017 RRID:AB_2871308
G18-145 (BV421) [Human anti-IgG]	BD Biosciences	Cat# 562581; Lot: 1033053 RRID:AB_2737665
SJ25C1 (BV650) [Human anti-CD19]	Biologend	Cat# 363026; Lot: B328293 RRID:AB_2564255
2H7 (BV711) [Human anti-CD20]	BD Biosciences	Cat# 563126; Lot: 2032072 RRID:AB_2313579
B-LY4 (BV786) [Human anti-CD21]	BD Biosciences	Cat# 740969; Lot: 1167364 RRID:AB_2740594
G46-6 (BB700) [Human anti-HLADR]	BD Biosciences	Cat# 566480; Lot: 1053189 RRID:AB_2744477
IS11-8E10 (PE) [Human anti-IgA]	Miltenyi	Cat# 130-113-476; Lot: 5210405486 RRID:AB_2733861
M-T271 (APC-R700) [Human anti-CD27]	BD Biosciences	Cat# 565116; Lot: 0262146 RRID:AB_2739074
UCHT1 (BUV496) [Human anti-CD3]	BD Biosciences	Cat#612941; Lot:1022424; RRID:AB_2870222
L200 (BV711) [Human anti-CD4]	BD Biosciences	Cat#563913; Lot:03000025; RRID:AB_2738484
SK3 (BB630) [Human anti-CD4]	BD Biosciences	Cat#624294 CUSTOM; Lot:0289566
RPA-T8 (BV570) [Human anti-CD8]	Biologend	Cat#301037; Lot:B281322; RRID:AB_10933259
M5E2 (BUV805) [Human anti-CD14]	BD Biosciences	Cat#612902; Lot:0262150; RRID:AB_2870189
M5E2 (BV480) [Human anti-CD14]	BD Biosciences	Cat#746304; Lot: 9133961; RRID:AB_2743629

(Continued on next page)

Continued

REAGENT or RESOURCE	SOURCE	IDENTIFIER
3G8 (BV650) [Human anti-CD16]	Biolegend	Cat#302042; Lot:B323847; RRID:AB_2563801
HIB19 (APC-eFluor780) [Human anti-CD19]	Thermo Fisher Scientific	Cat#47-0199; Lot:2145095; RRID:AB_1582231
HIB19 (BV480) [Human anti-CD19]	BD Biosciences	Cat#746457; Lot:1021649; RRID:AB_2743759
HIT2 (BB790) [Human anti-CD38]	BD Biosciences	Cat# 624296 CUSTOM; Lot: 9119974
HI100 (PerCP Cy5.5) [Human anti-CD45RA]	BD Biosciences	Cat#563429; Lot:8332746; RRID:AB_2738199
NCAM16.2 (BUV737) [Human anti-CD56]	BD Biosciences	Cat#564448; Lot:8288818; RRID:AB_2744432
FN50 (PerCP-eFluor710) [Human anti-CD69]	Thermo Fisher Scientific	Cat#46-0699-42; Lot:1920361; RRID:AB_2573694
FN50 (BV650) [Human anti-CD69]	Biolegend	Cat# 310934; Lot:B303462; RRID:AB_2563158
H4A3 (BV786) [Human anti-CD107A]	BD Biosciences	Cat#563869; Lot:8144866; RRID:AB_2738458
ACT35 (APC) [Human anti-CD134 (OX40)]	BD Biosciences	Cat#563473; Lot:1015537; RRID:AB_2738230
4B4-1 (PE-Dazzle 594) [Human anti-CD137 (4-1BB)]	Biolegend	Cat# 309826; Lot:B253152; RRID:AB_2566260
TRAP1 (BV421) [Human anti-CD154 (CD40L)]	BD Biosciences	Cat#563886; Lot:9037850; RRID:AB_2738466
TRAP1 (PE) [Human anti-CD154 (CD40L)]	BD Biosciences	Cat#555700; Lot:7086896; RRID:AB_396050
J25D4 (BV421) [Human anti-CD185 (CXCR5)]	Biolegend	Cat# 356920; Lot:B325837; RRID:AB_2562303
B27 (PECy7) [Human anti-IFN- γ]	BD Biosciences	Cat#557643; Lot:8256597; RRID:AB_396760
MQ1-17H12 (PE-Dazzle594) [Human anti-IL-2]	Biolegend	Cat#500344; Lot:B2261476; RRID:AB_2564091
JES3-9D7 (PE) [Human anti-IL-10]	BD Biosciences	Cat#554498; Lot:8198773; RRID:AB_395434
eBio64CAP17 (eFluor660) [Human anti-IL-17A]	Thermo Fisher Scientific	Cat#50-7179-42; Lot:2151998; RRID:AB_11149126
Mab11 (Alexa Fluor 488) [Human anti-TNF- α]	Biolegend	Cat#502915; Lot:B285221; RRID:AB_493121
LIVE/DEAD Fixable dead cell	Thermo Fisher Scientific	L34960
Mouse monoclonal anti-SARS-CoV-2 Spike (CR3022)	Dr M. Gordon Joyce	RRID: AB_2848080
Goat anti-Human IgG Fc Cross-absorbed Secondary Antibody, HRP	Invitrogen	Cat#31413; RRID: AB_429693
Alexa Fluor 647 AffiniPure Goat Anti-Human IgA + IgG + IgM (H+L)	Jackson ImmunoResearch	Cat#109-605-064; RRID: AB_2337886
Biological samples		
SARS-CoV-2 naïve donor blood samples	This paper	N/A
Chemicals, peptides, and recombinant proteins		
Dulbecco's Modified Eagle's medium (DMEM)	Wisent	Cat#319-005-CL
Roswell Park Memorial Institute (RPMI)	ThermoFischer Scientific	Cat#61870036
Penicillin/Streptomycin	VWR	Cat#450-201-EL
Fetal Bovine Serum (FBS)	VWR	Cat#97068-085
Bovine Serum Albumin	Sigma	Cat#A7638
PepMix™ SARS-CoV-2 (Spike Glycoprotein)	JPT	Cat#PM-WCPV-S-1
Staphylococcal Enterotoxin B (SEB)	Toxin technology	Cat#BT202
Phosphate Buffered Saline (PBS)	ThermoFischer Scientific	Cat#10010023
Tween 20	Sigma	Cat#P9416-100ML
Freestyle 293F expression medium	ThermoFischer Scientific	Cat#12338018
Formaldehyde 37%	ThermoFischer Scientific	Cat#F79-500
ExpiFectamine 293 transfection reagent	ThermoFischer Scientific	Cat#A14525
Westen Lightning Plus-ECL, Enhanced Chemoluminescence Substrate	Perkin Elmer Life Sciences	Cat#NEL105001EA
Experimental models: Cell lines		
HEK293T cells	ATCC	Cat#CRL-3216; RRID: CVCL_0063
FreeStyle 293F cells	ThermoFischer Scientific	Cat#R79007; RRID: CVCL_D603

(Continued on next page)

Continued

REAGENT or RESOURCE	SOURCE	IDENTIFIER
Recombinant DNA		
pCAGGS-OC43 Spike	Prévost et al. ⁵⁶	N/A
Software and algorithms		
Flow Jo v10.8.0	Flow Jo	https://www.flowjo.com
GraphPad Prism v8.4.1	GraphPad	https://www.graphpad.com
R studio v4.1.0	R studio	https://rstudio.com

RESOURCE AVAILABILITY

Lead contact

Further information and requests for resources and reagents should be directed to and will be fulfilled by the lead contact, Daniel E. Kaufmann (daniel.kaufmann@chuv.ch).

Materials availability

All unique reagents generated during this study are available from the [lead contact](#) upon a material transfer agreement (MTA).

Data and code availability

The published article includes all datasets generated and analyzed for this study. This paper does not report any original code. Further information and requests for resources and reagents should be directed to and will be fulfilled by the [lead contact](#) Author (daniel.kaufmann@chuv.ch).

EXPERIMENTAL MODEL AND SUBJECT DETAILS

Ethics statement

All work was conducted in accordance with the Declaration of Helsinki in terms of informed consent and approval by an appropriate institutional board. Blood samples were obtained from donors who consented to participate in this research project at CHUM (19.381). Individuals from the Philadelphia cohort were enrolled in the study with approval from the University of Pennsylvania Institutional Review Board (IRB# 844642). All participants were otherwise healthy and did not report any history of chronic health conditions.

Participants

No specific criteria such as number of patients (sample size), clinical or demographic were used for inclusion, beyond negative PCR confirmation for SARS-CoV-2 infection. The study was conducted in 26 SARS-CoV-2 naïve individuals with a long interval, and 12 with a short interval. All the information is summarized in [Table 1](#).

PBMCs collection

PBMCs were isolated from blood samples by Ficoll density gradient centrifugation and cryopreserved in liquid nitrogen until use.

Plasma and antibodies

Plasma samples were collected, heat-inactivated for 1 hour at 56°C and stored at –80°C until ready to use in subsequent experiments. Plasma samples from uninfected donors collected before the pandemic were used as negative controls and used to calculate the seropositivity threshold in our ELISA assay. The RBD-specific monoclonal antibody CR3022 was used as a positive control in ELISA assays. Horseradish peroxidase (HRP)-conjugated Abs able to detect the Fc region of human IgG (Invitrogen) was used as secondary Abs to detect Ab binding in ELISA experiments. Alexa Fluor-647-conjugated goat anti-human Abs able to detect all Ig isotypes (anti-human IgM+IgG+IgA; Jackson ImmunoResearch Laboratories) were used as secondary Ab to detect plasma binding in flow cytometry experiments.

Cell lines

293T human embryonic kidney cells (obtained from ATCC) were maintained at 37°C under 5% CO₂ in Dulbecco's modified Eagle's medium (DMEM) (Wisent) containing 5% fetal bovine serum (FBS) (VWR) and 100 µg/ml of penicillin-streptomycin (Wisent).

METHOD DETAILS

Protein expression and purification

FreeStyle 293F cells (Thermo Fisher Scientific) were grown in FreeStyle 293F medium (Thermo Fisher Scientific) to a density of 1 × 10⁶ cells/mL at 37°C with 8% CO₂ with regular agitation (150 rpm). Cells were transfected with a plasmid coding for SARS-CoV-2 S RBD using ExpiFectamine 293 transfection reagent, as directed by the manufacturer (Invitrogen).^{56,57} One week later, cells were pelleted and discarded. Supernatants were filtered using a 0.22 µm filter (Thermo Fisher Scientific). The recombinant RBD proteins were purified by nickel affinity columns, as directed by the manufacturer (Thermo Fisher Scientific). The RBD preparations were dialyzed against phosphate-buffered saline (PBS) and stored in aliquots at -80°C until further use. To assess purity, recombinant proteins were loaded on SDS-PAGE gels and stained with Coomassie Blue.

SARS-CoV-2-specific B cells characterization

To detect SARS-CoV-2-specific B cells, we conjugated recombinant RBD proteins with Alexa Fluor 488 or Alexa Fluor 594 (Thermo Fisher Scientific) according to the manufacturer's protocol. 2 × 10⁶ frozen PBMC from SARS-CoV-2 naïve donors were prepared in Falcon® 5ml-round bottom polystyrene tubes at a final concentration of 4 × 10⁶ cells/mL in RPMI 1640 medium (GIBCO) supplemented with 10% of fetal bovine serum (Seradigm), Penicillin-Streptomycin (GIBCO) and HEPES (GIBCO). After a rest of 2h at 37°C and 5% CO₂, cells were stained using LIVE/DEAD Fixable Aqua dead cell (Thermo Fisher Scientific, Waltham, MA) in DPBS (GIBCO) at 4°C for 20min. The detection of SARS-CoV-2-antigen specific B cells was done by adding the RBD probes to the antibody cocktail listed in [Table S1](#). Staining was performed at 4°C for 30min and cells were fixed using 2% paraformaldehyde at 4°C for 15min. Stained PBMC samples were acquired on Symphony cytometer (BD Biosciences) and analyzed using FlowJo v10.8.0 software. To avoid excessive noise in phenotyping analyses, we only included donors in whom we detected ≥ 5 RBD-specific B cells at every time point.

Activation-induced marker (AIM) assay

The AIM assay^{9,33,58,59} was adapted for SARS-CoV-2 specific CD4 and CD8 T cells, as previously described.⁹ PBMCs were thawed and rested for 3h in 96-well flat-bottom plates in RPMI 1640 supplemented with HEPES, penicillin and streptomycin and 10% FBS. PBMCs were then split in 3 conditions of 1.7 × 10⁶ PBMCs each: i) stimulated with an S glycoprotein peptide pool (0.5 µg/ml per peptide, corresponding to the pool of 315 overlapping peptides (15-mers) spanning the complete amino acid sequence of the Spike glycoprotein (JPT), ii) stimulated with *Staphylococcus enterotoxin B* (SEB) (0.5 µg/ml) as positive control and iii) a condition containing the same DMSO concentration as the Spike peptide pool stimulation served as a negative control. Cells were stimulated for 15h at 37°C and 5% CO₂. CXCR3, CCR6, CXCR6 and CXCR5 antibodies were added in culture 15 min before stimulation. Cells were stained using LIVE/DEAD Fixable Aqua dead cell (Thermo Fisher Scientific, Waltham, MA) for 20 min at 4 C then surface markers (30 min, 4°C). Abs used are listed in [Table S2](#). Cells were fixed using 2% paraformaldehyde for 15 min at 4 C before acquisition on Symphony cytometer (BD Biosciences). Analyses were performed using FlowJo v10.8.0 software. To minimize noise and increase specificity in the qualitative phenotypic analysis, we included only samples for which the spike-specific signal was at least 2 times over background with ≥ 5 positive events.^{33,60,61}

Intracellular cytokine staining (ICS)

The ICS assay was adapted to study SARS-CoV-2-specific T cells, as previously described.⁹ PBMCs were thawed and rested for 2 h in RPMI 1640 medium supplemented with 10% FBS, Penicillin-Streptomycin (Thermo Fisher Scientific, Waltham, MA) and HEPES (Thermo Fisher scientific, Waltham, MA). PBMCs were then split in 3 conditions of 1.7 × 10⁶ PBMCs each: i) stimulated with an S glycoprotein peptide pool (0.5 µg/ml per peptide, corresponding to the pool of 315 overlapping peptides (15-mers) spanning the complete amino acid sequence of the Spike glycoprotein (JPT), ii) stimulated with *Staphylococcus enterotoxin B* (SEB) (0.5 µg/ml) as positive control and iii) a condition containing the same DMSO

concentration as the Spike peptide pool stimulation served as a negative control. Cell stimulation was carried out for 6h in the presence of mouse anti-human CD107a, Brefeldin A and monensin (BD Biosciences, San Jose, CA) at 37°C and 5% CO₂. Cells were stained using LIVE/DEAD Fixable Aqua dead cell (Thermo Fisher Scientific, Waltham, MA) for 20 min at 4°C and surface markers (30 min, 4°C), followed by intracellular detection of cytokines using the IC Fixation/Permeabilization kit (Thermo Fisher Scientific, Waltham, MA) according to the manufacturer's protocol before acquisition on a Symphony flow cytometer (BD Biosciences) and analysis using FlowJo v10.8.0 software. Abs used are listed in [Table S3](#).

Characterization of effector functions among total cytokine⁺ cells, defined by our ORgate strategy, was conducted on donors with ≥5 cytokine⁺ cells that represented a two-fold increase over the unstimulated condition to avoid biased phenotyping. Given these criteria, only D2 could be analyzed.

Enzyme-linked immunosorbent assay (ELISA) and RBD avidity index

The SARS-CoV-2 WT RBD ELISA assay used was previously described.^{56,57} Briefly, recombinant SARS-CoV-2 WT RBD proteins (2.5 μg/ml), or bovine serum albumin (BSA) (2.5 μg/ml) as a negative control, were prepared in PBS and were adsorbed to plates (MaxiSorp Nunc) overnight at 4°C. Coated wells were subsequently blocked with blocking buffer (Tris-buffered saline [TBS] containing 0.1% Tween20 and 2% BSA) for 1h at room temperature. Wells were then washed four times with washing buffer (Tris-buffered saline [TBS] containing 0.1% Tween20). CR3022 mAb (50 ng/ml) or a 1/500 dilution of plasma were prepared in a diluted solution of blocking buffer (0.1% BSA) and incubated with the RBD-coated wells for 90 minutes at room temperature. Plates were washed four times with washing buffer followed by incubation with secondary Abs (diluted in a diluted solution of blocking buffer (0.4% BSA)) for 1h at room temperature, followed by four washes. To calculate the RBD-avidity index, we performed in parallel a stringent ELISA, where the plates were washed with a chaotropic agent, 8M of urea, and added to the washing buffer. This assay was previously described.⁶² HRP enzyme activity was determined after the addition of a 1:1 mix of Western Lightning oxidizing and luminol reagents (Perkin Elmer Life Sciences). Light emission was measured with a LB942 TriStar luminometer (Berthold Technologies). The signal obtained with BSA was subtracted for each plasma and was then normalized to the signal obtained with CR3022 present in each plate. The seropositivity threshold was established using the following formula: mean of pre-pandemic SARS-CoV-2 negative plasma + (3 standard deviations of the mean of pre-pandemic SARS-CoV-2 negative plasma).

Cell surface staining and flow cytometry analysis

The plasmid encoding the HCoV-OC43 Spike was previously reported.⁵⁶ 293T cells were co-transfected with a GFP expressor (pIRES2-GFP, Clontech) in combination with a plasmid encoding the full-length HCoV-OC43 Spike. 48h post-transfection, Spike-expressing cells were stained with plasma (1/250 dilution). AlexaFluor-647-conjugated goat anti-human IgM+IgG+IgA Abs (1/800 dilution) were used as secondary Abs. The percentage of transfected cells (GFP+ cells) was determined by gating the living cell population based on viability dye staining (Aqua Vivid, Invitrogen). Samples were acquired on a LSRII cytometer (BD Biosciences) and data analysis was performed using FlowJo v10.7.1 (Tree Star).

QUANTIFICATION AND STATISTICAL ANALYSIS

Statistical analysis

Symbols represent biologically independent samples of HCW from LI and SI cohorts. Lines connect data from the same donor. Thick lines represent median values. Differences in responses for the same patient before and after vaccination were performed using Wilcoxon matched pair tests. Differences in responses between individuals from LI and SI cohorts were measured by Mann-Whitney tests. Wilcoxon and Mann-Whitney tests were generated using GraphPad Prism version 8.4.3 (GraphPad, San Diego, CA).²³ p values <0.05 were considered significant. p values are indicated for each comparison assessed. For descriptive correlations, Spearman's R correlation coefficient was applied. Significant Spearman test results are indicated by stars (*: p < 0.1, **: p < 0.05, ***: p < 0.001). For graphical representation on a log scale (but not for statistical tests), null values were arbitrarily set at the minimum values for each assay.

Software scripts and visualization

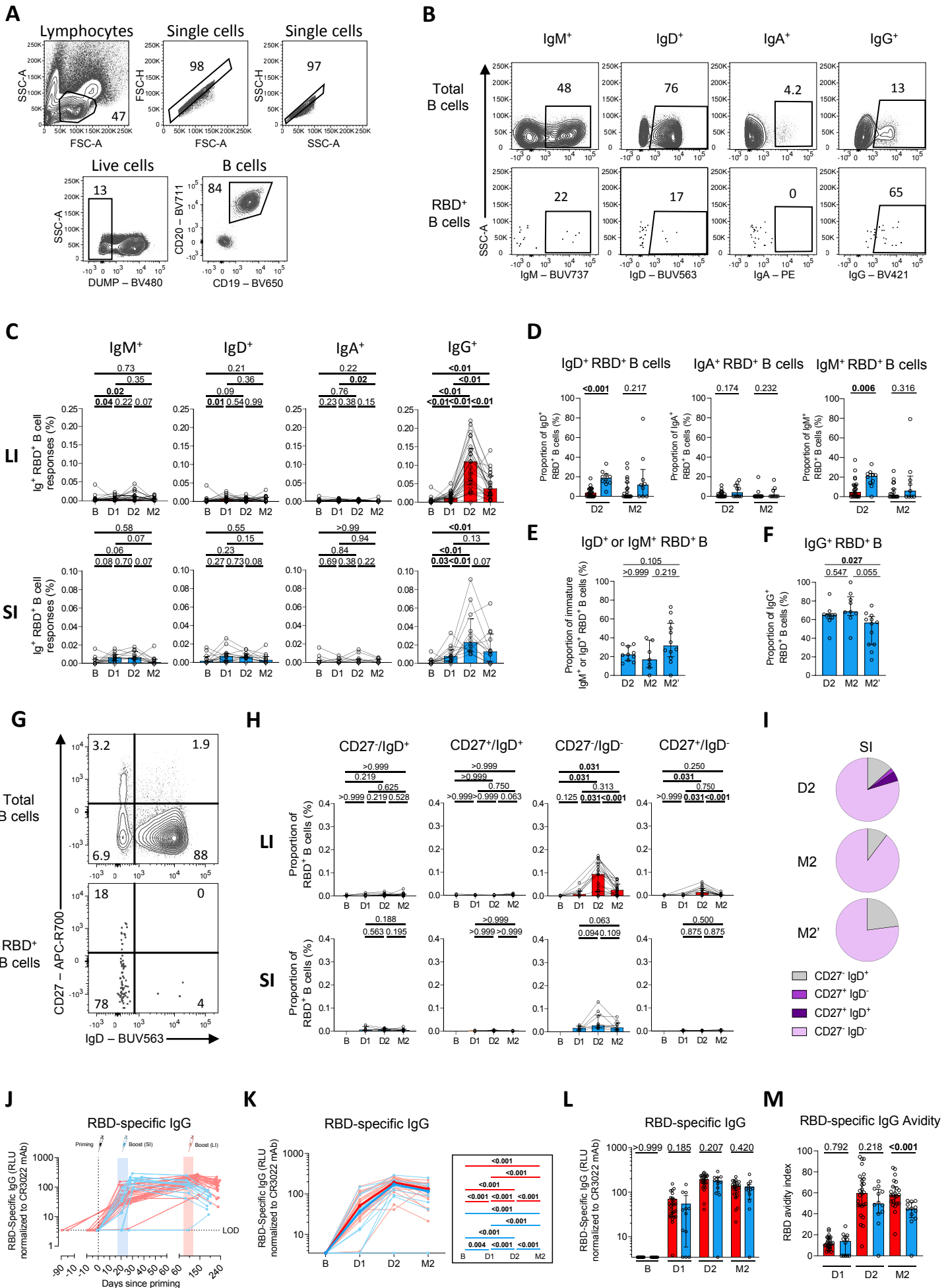
Graphics and pie charts were generated using GraphPad PRISM version 8.4.3 and ggplot2 (v3.3.3) in R (v4.1.0).

Supplemental information

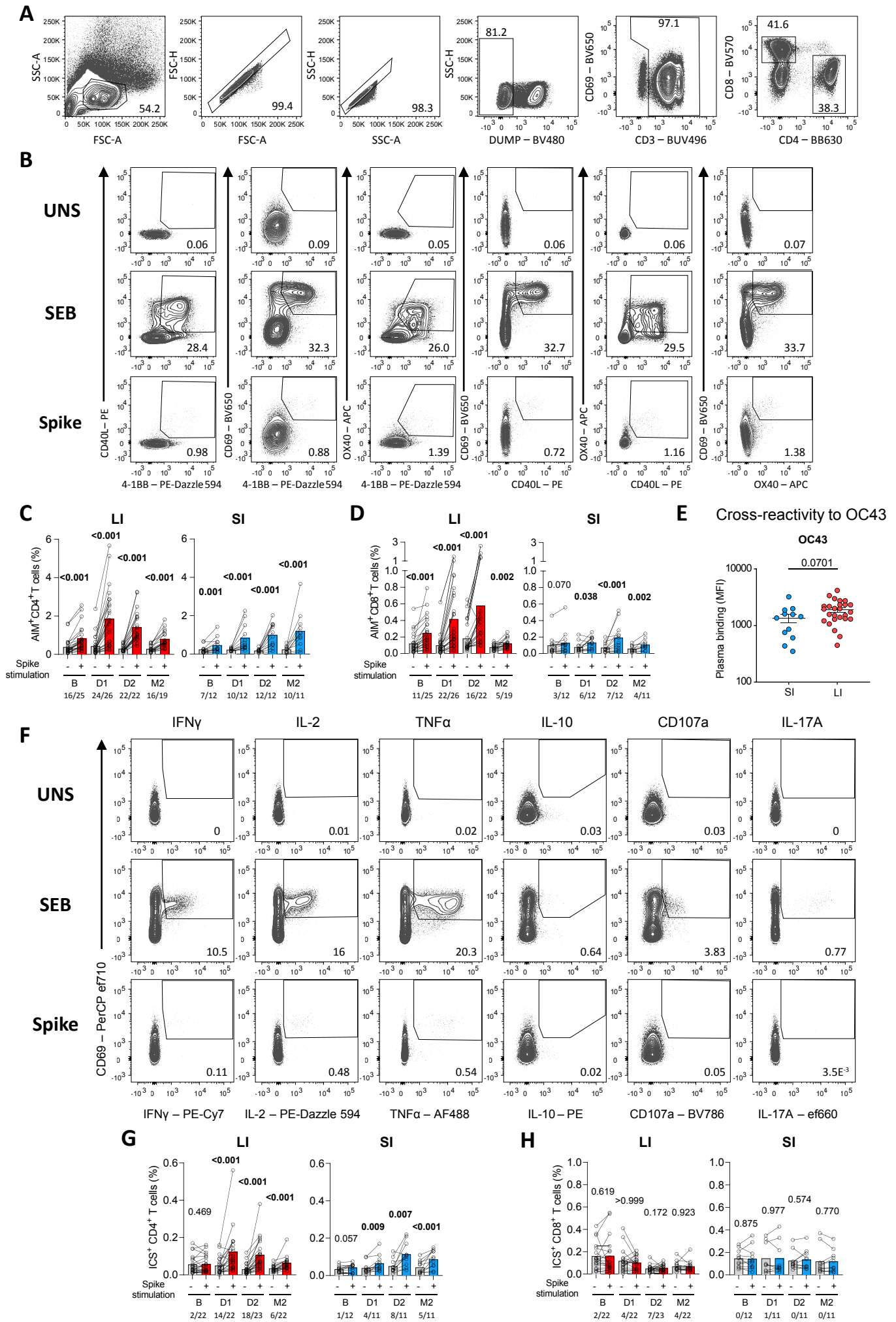
An extended SARS-CoV-2 mRNA vaccine prime-boost interval enhances B cell immunity with limited impact on T cells

Alexandre Nicolas, Gérémy Sannier, Mathieu Dubé, Manon Nayrac, Alexandra Tauzin, Mark M. Painter, Rishi R. Goel, Mélanie Laporte, Gabrielle Gendron-Lepage, Halima Medjahed, Justine C. Williams, Nathalie Brassard, Julia Niessl, Laurie Gokool, Chantal Morriseau, Pascale Arlotto, Cécile Tremblay, Valérie Martel-Laferrère, Andrés Finzi, Allison R. Greenplate, E. John Wherry, and Daniel E. Kaufmann

Supplemental Figure 1



Supplemental Figure 2



SUPPLEMENTARY FIGURE LEGENDS

Figure S1. SARS-CoV-2-specific B cell and antibody responses in the two vaccine schedules. Related to Figure 1. (A) Gating strategy to identify RBD-specific B cell responses. **(B)** Examples of gatings for IgM, IgD, IgA and IgG expression on total CD19⁺CD20⁺ B cells or RBD-specific B cells. **(C)** Longitudinal trajectories of isotype expression frequencies in long interval (LI) (n=26) and short interval (SI) (n=12) participants. Lines connect data points for individual participants. Bars represent medians \pm interquartile ranges. Wilcoxon tests are shown above each panel. **(D)** Proportion of IgD⁺, IgA⁺ and IgM⁺ RBD⁺ B cells at D2 and M2 in LI (red, n=26) and SI (blue, n=12) participants. Bars represent medians \pm interquartile ranges. Mann-Whitney tests are shown. **(E)** Proportion of IgD⁺ or IgM⁺ RBD⁺ B cells in SI participants at D2, M2 and M2' using an ORgate strategy. Bars represent medians \pm interquartile ranges. Wilcoxon tests are shown. **(F)** Proportion of IgG⁺ RBD⁺ B cells in SI participants at D2, M2 and M2'. Bars represent medians \pm interquartile ranges. Wilcoxon tests are shown. **(G)** Example of the gating strategy of IgD and CD27 co-expression on RBD-specific B cells. **(H)** Longitudinal frequency of each IgD and CD27 RBD-B phenotypes in CD19⁺ CD20⁺ B cells for LI (n=26) and SI (n=12) participants. Bars represent medians \pm interquartile ranges. Wilcoxon tests are shown above. **(I)** Proportion of IgD^{+/-} and CD27^{+/-} populations in RBD-specific B cells at D2, M2 and M2' in the short interval (SI) cohort. **(JKL)** Kinetics of RBD-specific IgG responses in the LI (red, n=26) vs SI (blue, n=12) cohorts. **(J)** Individual responses according to time of sampling. Colored background and syringe indicate time of dose injections. Dots indicate time points examined. **(K)** The bold lines represent each cohort's median value. Right panel: Wilcoxon tests. **(L)** Inter-cohort comparisons. Bars represent medians \pm interquartile ranges. Mann-Whitney tests are shown. **(M)** Inter-cohort comparison of RBD-specific IgG avidity between the LI (red, n=26) and SI (blue, n=12) cohorts. Bars represent medians \pm interquartile ranges. Mann-Whitney tests are shown.

Figure S2. SARS-CoV-2-specific T cell responses in the two vaccine schedules. Related to Figure 2. (A) Representative upstream gating and (B) ORgate strategy to identify SARS-CoV-2-specific AIM⁺ T cells. For simplicity, the example focuses on CD4⁺ T cells. (C) Raw frequencies of (C) AIM⁺ CD4⁺ and (D) CD8⁺ T cells following *ex vivo* stimulation of PBMCs with a pool of SARS-CoV-2 Spike peptides. As a control, PBMCs cells were left unstimulated (grey bars). The data for LI (red, n=26) and SI (blue, n=12) individuals are displayed. The bars represent median values. Wilcoxon tests are shown. The number of conditions reaching $\geq 2x$ the no Ag values are shown below each time point. (E) Inter-cohort comparison of cross-reactivity to OC43 at baseline. Mann-Whitney tests are shown above. LI (red, n=26) and SI (blue, n=12). (F) Representative ORgate strategy to identify SARS-CoV-2-specific cytokine-expressing T cells. For simplicity, the example focuses on CD4⁺ T cells. (G) Raw frequencies of cytokine-expressing (G) CD4⁺ and (H) CD8⁺ T cells following *ex vivo* stimulation of PBMCs with a pool of SARS-CoV-2 Spike peptides. As a control, PBMCs cells were left unstimulated (grey bars). The data for LI (red, n=26) and SI (PI; blue, n=12) individuals are displayed. The bars represent median values. Wilcoxon tests are shown. The number of conditions reaching $\geq 2x$ no Ag are shown below each time point.

Table S1. Flow cytometry antibody staining panel for B cells characterization. Related to STAR Methods, Main Figure 1, Supplementary Figure 1.

Marker-Fluorophore	Clone	Source	Catalog #
CD3 – BV480	UCHT1	BD Biosciences	566105
CD14 – BV480	M5E2	BD Biosciences	746304
CD16 – BV480	3G8	BD Biosciences	566108
CD19 – BV650	SJ25C1	Biolegend	363026
CD20 – BV711	2H7	Biolegend	563126
CD21 – BV786	B-LY4	BD Biosciences	740969
CD24 – BUV805	ML5	BD Biosciences	742010
CD27 – APC-R700	M-T271	BD Biosciences	565116
CD38 – BB790	HIT2	BD Biosciences	CUSTOM
CD56 – BV480	NCAM16.2	BD Biosciences	566124
CD138 – BUV661	MI15	BD Biosciences	5 749873
CCR10 – BUV395	1B5	BD Biosciences	565322
HLA-DR – BB700	G46-6	BD Biosciences	566480
IgA - PE	IS11-8E10	Miltenyi	130-113-476
IgD – BUV563	IA6-2	BD Biosciences	741394
IgG – BV421	G18-147	BD Biosciences	562581
IgM – BUV737	UCH-B1	Thermo Fisher Scientific	748928
LIVE/DEAD Fixable dead cell	N/A	Thermo Fisher Scientific	L34960

Table S2. Flow cytometry antibody staining panel for activation-induced marker assay. Related to STAR Methods, Main Figures 2 and 3, Supplementary Figure 2.

Marker-Fluorophore	Clone	Source	Catalog #
CD3 – BUV496	UCHT1	BD	612941
CD4 – BB630	SK3	BD	624294
CD8 – BV570	RPA-T8	Biolegend	301037
CD14 – BV480	M5E2	BD	746304
CD19 – BV480	HIB19	BD	746457
CD38 – BB790	HIT2	BD	CUSTOM
CD45RA – PerCP Cy5.5	HI100	BD	563429
CD69 – BV650	FN50	Biolegend	310934
CD134 (OX40) - APC	ACT35	BD	563473
CD137 (4-1BB) – PE-Dazzle 594	4B4-1	Biolegend	309826
CD154 (CD40L) - PE	TRAP1	BD	555700
CD183 (CXCR3) – BV605	G025H7	Biolegend	353728
CD185 (CXCR5) – BV421	J25D4	Biolegend	356920
CD186 (CXCR6) – BUV805	13B 1E5	BD	748448
CD196 (CCR6) – BUV737	11A9	BD	564377
CD279 (PD1) – BV711	EH122H	Biolegend	329928
HLA-DR - FITC	LN3	Biolegend	327005
LIVE/DEAD Fixable dead cell	N/A	Thermo Fisher Scientific	L34960

Table S3. Flow cytometry antibody staining panel for intracellular cytokines staining assay. Related to STAR Methods, Main Figures 2 and 4, Supplementary Figure 2.

Marker-Fluorophore	Clone	Source	Catalog #
CD3 – BUV395	UCHT1	BD Biosciences	563546
CD4 – BV711	L200	BD Biosciences	563913
CD8 – BV570	RPA-T8	Biolegend	301037
CD14 – BUV805	M5E2	BD Biosciences	612902
CD16 – BV650	3G8	Biolegend	302042
CD19 – APC-eFluor780	HIB19	Thermo Fisher Scientific	47-0199
CD56 – BUV737	NCAM16.2	BD Biosciences	564448
CD69 – PerCP-eFluor710	FN50	Thermo Fisher Scientific	46-0699-42
CD107A – BV786	H4A3	BD Biosciences	563869
IFN- γ – PECy7	B27	BD Biosciences	557643
CD154 (CD40L) – BV421	TRQP1	BD Biosciences	563886
IL-2 – PE-Dazzle 594	MQ1-17H12	Biolegend	500344
IL-10 - PE	JES3-9D7	BD Biosciences	554498
IL-17A – eFluor660	eBio64CAP17	Thermo Fisher Scientific	50-7179-42
TNF- α – Alexa Fluor 488	Mab11	Thermo Fisher Scientific	502915
Granzym B – Alexa Fluor 700	GB11	BD	561016
LIVE/DEAD Fixable dead cell	N/A	Thermo Fisher Scientific	L34960

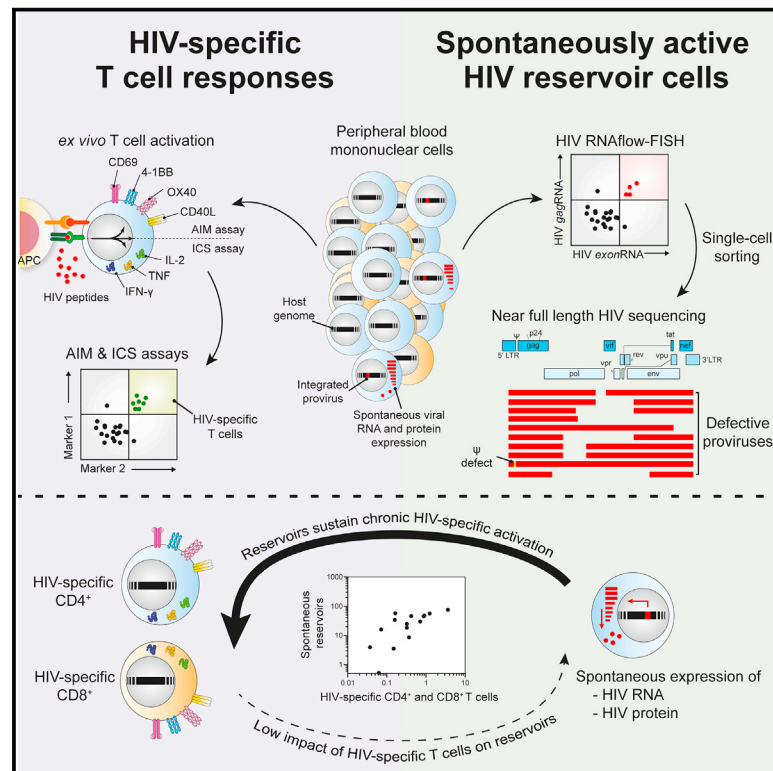
**Appendix II.iii: Spontaneous HIV Expression During Suppressive
ART is Associated with the Magnitude and Function of HIV-
Specific CD4⁺ and CD8⁺ T Cells**

Cell Host & Microbe, 2023

Cell Host & Microbe

Spontaneous HIV expression during suppressive ART is associated with the magnitude and function of HIV-specific CD4⁺ and CD8⁺ T cells

Graphical abstract



Authors

Mathieu Dubé, Olivier Tastet, Caroline Dufour, ..., Rémi Fromentin, Nicolas Chomont, Daniel E. Kaufmann

Correspondence

mathieu.dube.chum@ssss.gouv.qc.ca (M.D.),
daniel.kaufmann@chuv.ch (D.E.K.)

In brief

Dubé et al. identify phenotypically diverse HIV-infected cells that spontaneously express viral RNA, and occasionally protein, during antiretroviral treatment. Despite carrying defective proviruses, active reservoirs correlate with HIV-specific CD4⁺ and CD8⁺ T cell responses. These results suggest that ongoing expression of viral genes maintain HIV-specific immune responses during suppressive ART.

Highlights

- Spontaneously active HIV RNA⁺ and protein^{+/-} reservoirs exist in people with HIV on ART
- These are enriched in central memory and CCR6⁻ and activation-marker-expressing cells
- Proviruses integrated in these active reservoir cells are mostly defective
- Spontaneously active reservoirs correlate with HIV-specific CD4⁺ and CD8⁺ T cells



Article

Spontaneous HIV expression during suppressive ART is associated with the magnitude and function of HIV-specific CD4⁺ and CD8⁺ T cells

Mathieu Dubé,^{1,*} Olivier Tastet,¹ Caroline Dufour,^{1,2} Gérémy Sannier,^{1,2} Nathalie Brassard,¹ Gloria-Gabrielle Delgado,¹ Amélie Pagliuzza,¹ Corentin Richard,¹ Manon Nayrac,¹ Jean-Pierre Routy,^{3,4} Alexandre Prat,^{1,5} Jacob D. Estes,^{6,7} Rémi Fromentin,¹ Nicolas Chomont,^{1,2} and Daniel E. Kaufmann^{1,2,8,9,*}

¹Department of Immunopathology, Research Centre of the Centre Hospitalier de l'Université de Montréal (CRCHUM), Montreal, QC H2X 0A9, Canada

²Department of Microbiology, Infectious Diseases and Immunology, Faculty of Medicine, Université de Montréal, Montreal, QC H3C 3J7, Canada

³Chronic Viral Illnesses Service and Division of Hematology, McGill University Health Centre (CUSM), Montreal, QC H4A 3J1, Canada

⁴Infectious Diseases and Immunity in Global Health Program, Research Institute, McGill University Health Centre, Montreal, QC H4A 3J1, Canada

⁵Department of Neurosciences, Faculty of Medicine, Université de Montréal, Montréal, QC H3C 3J7, Canada

⁶Vaccine and Gene Therapy Institute, Oregon Health & Science University, Beaverton, OR 97006, USA

⁷Oregon National Primate Research Center, Oregon Health & Science University, Beaverton, OR 97006, USA

⁸Division of Infectious Diseases, Department of Medicine, Lausanne University Hospital and University of Lausanne, 1011 Lausanne, Switzerland

⁹Lead contact

*Correspondence: mathieu.dube.chum@ssss.gouv.qc.ca (M.D.), daniel.kaufmann@chuv.ch (D.E.K.)

<https://doi.org/10.1016/j.chom.2023.08.006>

SUMMARY

Spontaneous transcription and translation of HIV can persist during suppressive antiretroviral therapy (ART). The quantity, phenotype, and biological relevance of this spontaneously “active” reservoir remain unclear. Using multiplexed single-cell RNAflow-fluorescence *in situ* hybridization (FISH), we detect active HIV transcription in 14/18 people with HIV on suppressive ART, with a median of 28/million CD4⁺ T cells. While these cells predominantly exhibit abortive transcription, p24-expressing cells are evident in 39% of participants. Phenotypically diverse, active reservoirs are enriched in central memory T cells and CCR6- and activation-marker-expressing cells. The magnitude of the active reservoir positively correlates with total HIV-specific CD4⁺ and CD8⁺ T cell responses and with multiple HIV-specific T cell clusters identified by unsupervised analysis. These associations are particularly strong with p24-expressing active reservoir cells. Single-cell vDNA sequencing shows that active reservoirs are largely dominated by defective proviruses. Our data suggest that these reservoirs maintain HIV-specific CD4⁺ and CD8⁺ T responses during suppressive ART.

INTRODUCTION

The persistence of HIV represents a fundamental challenge to achieving a cure. When antiretroviral therapy (ART) is interrupted in people with HIV (PWH), rare persisting infected cells can fuel viral rebound.¹ Recent advances provided sensitive evaluations of the size of the HIV reservoir.² CD4⁺ T cells bearing HIV genomes^{3,4} are one order of magnitude more abundant than those with the ability to transcribe multiply spliced RNA,^{5,6} themselves another order of magnitude more frequent than those producing p24.^{7–9} These differences may reflect stepwise stages of blocks in viral transcription and translation.^{10,11} Detecting viral reservoirs based on either viral RNA (vRNA) or protein typically involves *ex vivo* stimulation with latency reversal agents (LRAs) that induce viral gene expression. This approach provided valuable information on inducible reservoirs poised for reactivation.

Current antiretroviral therapies do not target HIV transcription nor translation; therefore, spontaneous viral gene transcription^{10,12–17} and translation^{18–20} can persist during ART. The definite quantification, single-cell phenotyping, and biological relevance of these “active” reservoir cells are not established.

CD4⁺ and CD8⁺ T cells are increasingly recognized as essential actors in the control of simian immunodeficiency virus (SIV) and HIV infections.^{21–26} Consequently, anti-HIV immunity is expected to play an important role in cure strategies and to contribute to purging reservoirs, exerting immunosurveillance of residual virus and/or supporting the development of broadly neutralizing HIV-specific antibodies.^{27,28} HIV-specific CD4⁺ and CD8⁺ T cells can be detected during ART, although their magnitude and functions present notable interindividual heterogeneity.^{29–32} The mechanisms involved in the persistence of such HIV-specific immunity during suppressive ART are not



entirely understood but are unlikely to result from ongoing residual viral replication, an actively debated concept.^{33–36} Conversely, active reservoirs that lead to protein expression from a fraction of the largely dominant pool of defective proviruses and low-level virion release from an even smaller proportion of active reservoirs with intact genomes could maintain and shape anti-HIV CD4⁺ and CD8⁺ T cell responses during ART.^{14,37–40}

Herein, we quantified and phenotyped viral reservoirs spontaneously expressing vRNA and the p24 protein in primary clinical samples directly *ex vivo*. We found associations between active reservoirs and HIV-specific CD4⁺ and CD8⁺ T cells, supporting that low-level viral gene expression by spontaneous reservoirs is sufficient to maintain anti-HIV adaptive immunity.

RESULTS

Spontaneous vRNA-expressing reservoirs are detectable in a majority of ART-suppressed PWH

We previously used a multiplexed HIV RNAflow-fluorescence *in situ* hybridization (FISH) assay to characterize viral reservoirs induced *ex vivo*.^{7–9} A previous digital-droplet study on bulk CD4⁺ T cells showed expression during latency of “long-LTR” abortive transcripts.^{10,41} Therefore, to maximize detection of viral reservoir cells that spontaneously express vRNA without *ex vivo* stimulation, termed active reservoir, we adapted our multiplexed vRNA detection strategy and focused on 5′ HIV genes (Figure 1A). As described before,⁹ a first-step analysis provided an inclusive detection of viral transcripts, consisting of an *exonRNA* probe set targeting exon sequences, including a portion of the 5′ long terminal repeat (LTR) region, present on all viral transcripts.⁴² The second step of detection added stringency and ensured specificity. To this end, two additional probe sets were generated: (1) a *gagRNA* probe set, detecting full-length genomic transcripts but also shorter abortive or defective transcripts containing at least a portion of the *gag* gene,⁹ and (2) a *polRNA* detecting transcripts that elongated beyond the gene *gag*. We also stained intracellular p24 to assess viral translation.

We used this adapted HIV RNAflow assay to quantify the viral reservoirs in 18 PWH on ART for >3 years (median = 10 years, see clinical characteristics in Table S1). To reveal inducible viral reservoirs, CD4⁺ T cells isolated from peripheral blood mononuclear cells (PBMCs) were treated 15 h with phorbol myristate acetate (PMA)/ionomycin. To identify viral reservoirs that are able to spontaneously express HIV RNA and/or protein, we left CD4⁺ T cells unstimulated after isolation. We identified HIV-infected cells by Boolean ORgating⁹ and therefore included any cells either *exonRNA*⁺*gagRNA*⁺ or *exonRNA*⁺*polRNA*⁺ or *exonRNA*⁺*p24*⁺ into a single non-overlapping population expressing any combination of the viral genes assessed (henceforth termed vRNA⁺; Figure S1A). CD4⁺ T cells from 6 uninfected donors (UDs) served as specificity controls. We set a positive detection threshold at 7 events/10⁶ CD4⁺ T cells corresponding to the mean detection in UD plus twice the standard deviation, rounded up (mean + 2SD). Based on these criteria, we detected spontaneous reservoirs in 78% (14/18) of PWH on suppressive ART, with a median of 28 active vRNA⁺ cells/10⁶ CD4⁺ (Figure 1B). This level of detection represents a compromise compared to limiting dilution assays with quantitative reverse transcription po-

lymerase chain reaction (RT-qPCR), sacrificing some sensitivity for higher throughput and the ability to maintain phenotyping capability (Figures S1F and S1G). PMA/ionomycin-inducible reservoirs could be detected in 89% (16/18) of participants, with a significantly higher median (79 vRNA⁺/10⁶ CD4⁺). Reservoirs induced by Panobinostat and ingenol-3-angelate (termed LRA) reached an even higher level (325 induced vRNA⁺/10⁶ CD4⁺) (Figure S1B). By comparison, the frequency of CD4⁺ T cells harboring integrated HIV DNA was 12-fold higher than PMA/ionomycin-inducible reservoirs. In contrast, inducible reservoirs were 3-fold more frequent than spontaneous reservoirs (Figure 1C). We calculated that a median of 10% of the CD4⁺ T cells harboring integrated HIV DNA produced viral transcripts upon stimulation, whereas 4% spontaneously expressed vRNA (Figure 1D). Active vRNA⁺ reservoirs correlated with total and integrated HIV DNA (Figures 1E and 1F), whereas PMA/ionomycin-induced reservoirs showed strong trends (Figures S1C and S1D). We found strong associations between reservoir cells with spontaneous viral expression and both PMA/ionomycin (Figure 1G) and LRA-inducible (Figure S1E) reservoirs.

We next tested for associations between integrated HIV DNA, inducible and spontaneously active vRNA⁺ reservoirs, and clinical features (Figure 1H). The time of infection correlated with the size of inducible reservoirs, with a positive trend with the magnitude of the spontaneous reservoir. There was no association between the spontaneous reservoir and time on ART, while there was an association for inducible reservoirs. The level of spontaneous vRNA expression, but not inducibility, was associated with a longer duration of untreated infection. CD4⁺ T cell counts, CD4/CD8 ratios and pre-ART viral loads did not correlate with either inducible or spontaneous reservoirs.

Globally, these data highlighted the existence of spontaneous vRNA⁺ reservoirs in most PWH on suppressive ART. Spontaneous and inducible reservoirs were strongly associated, suggesting a robust relationship.

Spontaneously active reservoirs are enriched in short abortive and defective *gagRNA*⁺ transcripts

We next sought to characterize these active reservoirs based on p24 (Figure 2A), *gagRNA*, and *polRNA* co-expression (Figure 2B). The expression of p24 was used to assess viral protein expression,^{8,9} whereas *gagRNA* and *polRNA* defined the processivity of the transcription. This bilayered analysis created 8 theoretical subpopulations (Figures 2C, S2A, and S2B). Among these, single *exonRNA*⁺ cells could not be interpreted because of the insufficient specificity of single-parameter detection.⁹ The prevalence of the remaining seven theoretical populations is summarized in Figures 2D and S2A. Unstimulated samples from ART-suppressed individuals were homogeneously enriched in p24⁻*gagRNA*⁺*polRNA*⁻ cells (Figure S2C). This population corresponded to short abortive or deleted transcripts (*gagRNA*⁺) described before.^{9,10} PMA/ionomycin-induced reservoirs presented a more heterogeneous profile: although p24⁻*gagRNA*⁺*polRNA*⁻ cells were frequent, other more processive populations could also be detected, such as p24⁻*gagRNA*⁺*polRNA*⁺ (elongated transcripts not sustaining translation, termed vRNA_{DP} for “double *gagRNA*⁺*polRNA*⁺ positive”) > p24⁻*gagRNA*⁻*polRNA*⁺ (likely deleted transcripts, termed *polRNA*⁺) > p24⁺*gagRNA*⁺*polRNA*⁺ (translation-competent reservoirs, termed p24⁺). The

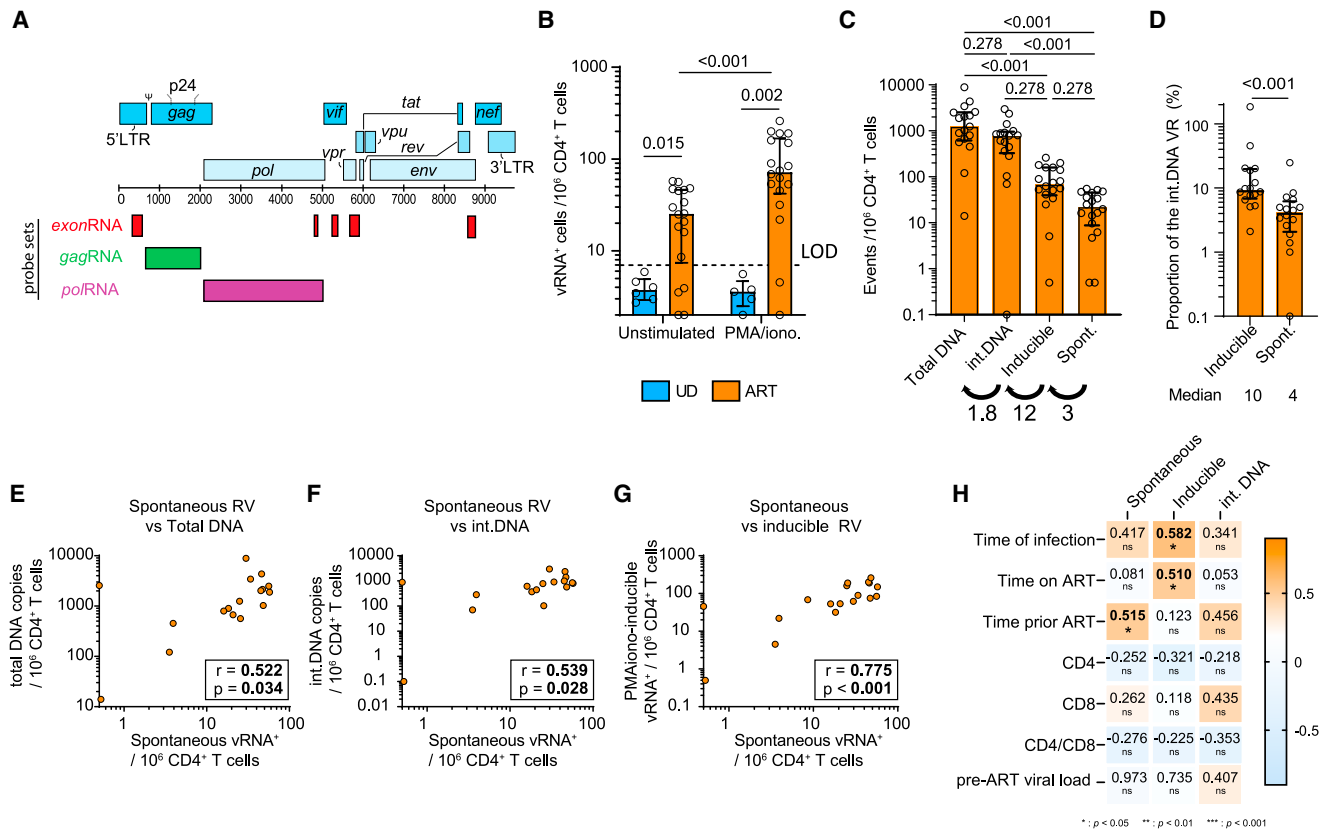


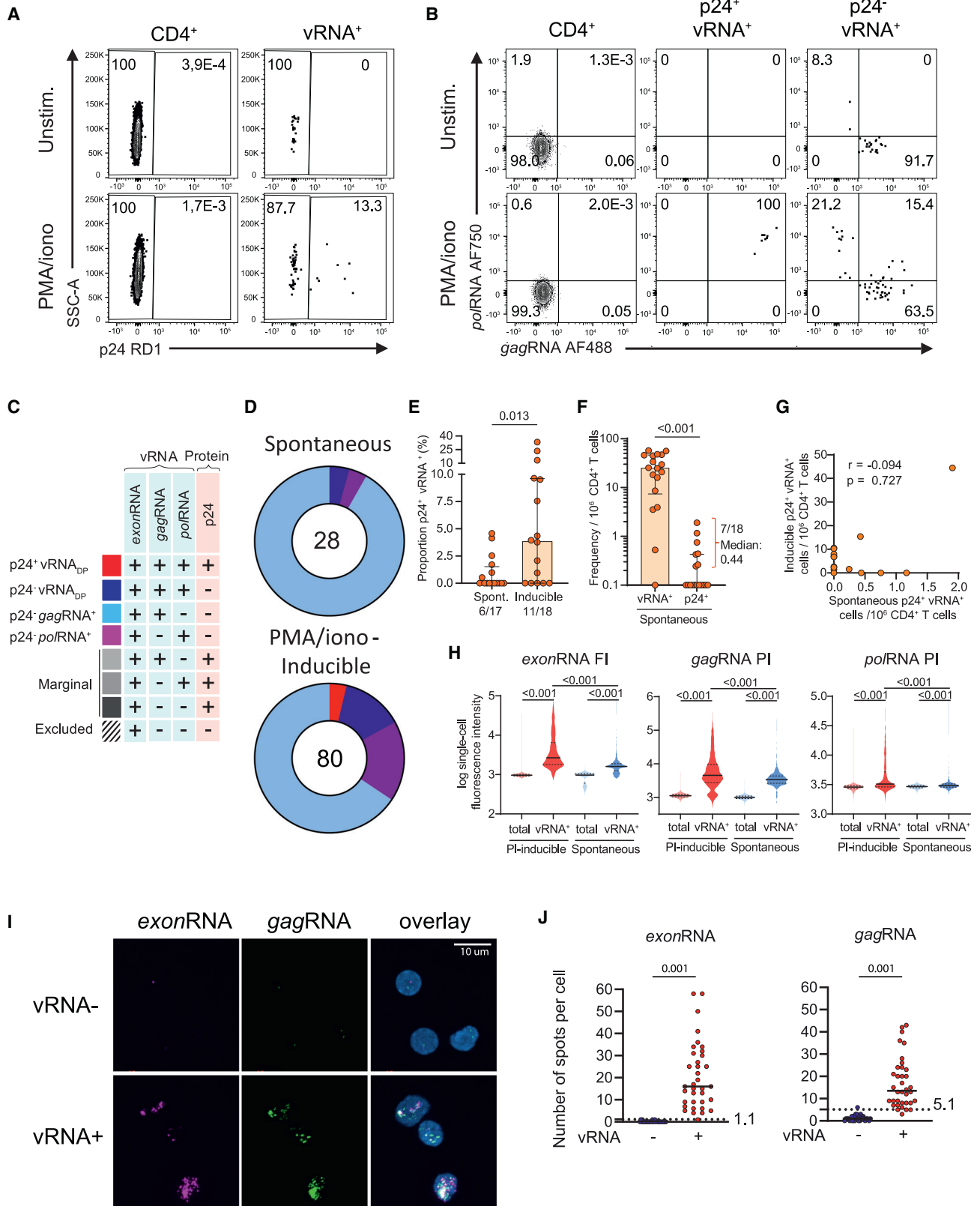
Figure 1. Spontaneous vRNA expression by HIV reservoirs in ART-suppressed PWH

(A) vRNA probe set designs.
 (B) Quantification of vRNA⁺ cells in purified CD4⁺ T cells from ART-treated PWH and uninfected (UD) as controls. Cells were either unstimulated or treated *ex vivo* with PMA/ionomycin for 15 h. Two statistical tests are shown: Mann-Whitney for cohort comparisons and Wilcoxon between stimulations.
 (C) Comparison between four different types of viral reservoir measurements. Numbers below indicate the median fold increase between groups.
 (D) The proportion of inducible and spontaneous vRNA⁺ reservoirs using integrated DNA as denominator. A Wilcoxon test was performed, shown above. Median values are shown below.
 (E–G) Correlations between (E) spontaneous reservoirs and total DNA, (F) spontaneous reservoirs and integrated DNA, (G) spontaneous and inducible reservoirs, with *r* and *p* values from Spearman tests.
 (H) Correlations between reservoir metrics and indicated clinical parameters. CD4 and CD8 stand for CD4⁺ and CD8⁺ T cell clinical counts. Values in the heatmap indicate *r* values, with *p* values underneath: * $p < 0.05$, ** $p < 0.01$, *** $p < 0.001$. The shade of colors indicates the *r* value. Results reaching statistical significance are shown in bold. *n* = 18.
 In (B) and (D), the histograms indicate the median, and the error bars illustrate the interquartile range.

pattern of active reservoirs was similar to combinatory LRA (Panobinostat + ingenol), with strong expression of *gag*RNA and little expression of *pol*RNA and marginal p24 translation (Figures S2A and S2C).^{9,10} In a subset of participants, the *pol*RNA probe set was substituted by a more distal *nef*RNA probe set.⁹ We detected rare *nef*RNA⁺ cells among active reservoirs and none that co-expressed *gag* and *nef* genes (Figure S2B), further suggesting unproductive transcription aborting in the 5' portion of the viral genome. Spontaneous p24-expressing cells represented a rare fraction (Figure 2E). These cells could be detected at low frequencies in 7/18 HIV⁺ participants, with a median frequency of 0.44 p24⁺vRNA⁺ cell/10⁵ CD4⁺ (Figure 2F). These active p24⁺ cells did not correlate with translation-competent reservoirs identified after PMA/ionomycin-stimulation (Figure 2G).

We used cytometric fluorescent intensities (FIs) to obtain a semi-quantitative measurement of RNA copies/cell⁴³ and as-

sessed the viral transcription and translation levels/infected cell. We used this metric to determine whether the level of viral transcription could define the success of viral translation. To avoid biases due to a low number of viral reservoir cells in some PWH, we concatenated all events per condition. Since *exon*RNA is expressed in all vRNA⁺ cells, we used it as a surrogate of global transcriptional activity. In both PMA/ionomycin- or LRA-induced reservoirs, the single-cell *exon*RNA, *gag*RNA, and *pol*RNA expression presented a skewed distribution composed of a low-yield bulky population and a tail spreading about one order of magnitude higher (Figures 2H and S2E). p24-expressing PMA/ionomycin-induced vRNA⁺ cells were almost exclusively found in these tails of high v transcriptional activity (Figure S2F). Consistent with the rare p24 expression in active reservoirs, such a high-yield tail was essentially absent in spontaneous reservoirs. Instead, *exon*RNA and *gag*RNA could be detected at low levels, whereas *pol*RNA expression remained comparably



(legend on next page)

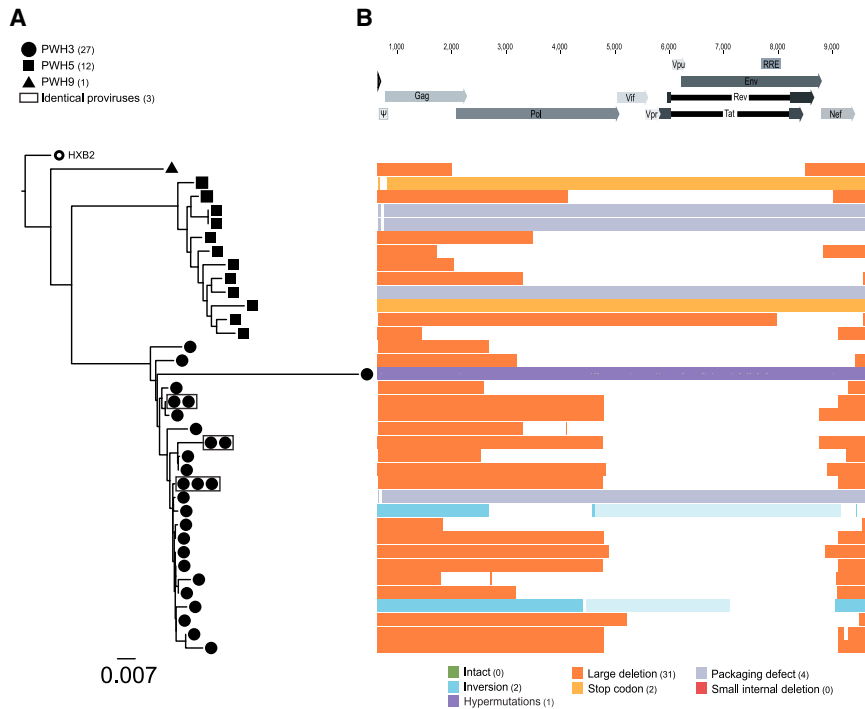


Figure 3. Near full-length single-cell vDNA sequencing of spontaneously active viral reservoirs identifies underlying proviral defects

Purified CD4⁺ T cells from 3 ART-treated participants were co-stained by multiplexed HIV-1 RNAflow-FISH. vRNA⁺ cells were individually sorted for nested PCR amplification and near full-length sequencing.

(A) Phylogenetic trees for the three participants PWH3, PWH5, and PWH9 built from the entire amplified area sequenced based on maximum likelihood. Sequences with 100% identity are boxed in gray.

(B) List of the different defects found in the 36 proviral sequences, aligned on the HxB2 genome. The type of defect is color coded, based on the legend presented below.

marginal (Figure 2H). In contrast to spontaneous p24⁺ cells, the levels of CD4 on the surface of spontaneous vRNA⁺ cells were comparable to vRNA⁻ cells, suggesting suboptimal or no expression of Nef and Vpu proteins (Figure S2G). These data demonstrate the low-yield, unprocessed nature of the active reservoirs.

We next used confocal fluorescence microscopy to count the number of HIV RNA foci per vRNA⁺ cell, as done previously.⁶ We sorted vRNA⁺ and vRNA⁻ cells, imaged and manually enumerated foci per cell (Figures S2H and 2I). The conservative false-positive rates (assuming Gaussian distribution, mean foci/cell in vRNA⁻ cells + 3SD) were established at 1.1 foci/cell for *exonRNA* and 5.1 foci/cell for *gagRNA* (Figure 2J). Conversely, vRNA⁺ cells containing down to 5 foci were clearly detected for both probes, but few vRNA⁺ cells were below this cutoff. The median detection reached 16 foci for *exonRNA* and 14 foci/cell for *gagRNA*, both significantly higher than their respective false-positive rate. *exonRNA*⁺ and *gagRNA*⁺ foci/cell corre-

lated significantly (Figure S2I). Taken together, these results suggest that our approach can reliably identify spontaneously active reservoirs with a cutoff of 5 vRNA copies/cell. To determine the proviral features of spontaneously vRNA⁺ cells, we next performed near full-length sequencing of using a modified full-length individual proviral sequencing (FLIPS) assay^{9,44} (Figure 3). We obtained a total of 40 amplicons from three ART-treated participants. From these 40 amplicons there was 36 distinct viral DNA (vDNA) sequences, and 3 small clones (Figure 3A). Most sequences harbored large deletions spanning the entire *env* region. Deletions in *pol* were also common (Figure 3B). We found two sequences with an inversion. Seven amplicons were near null length: one was hypermutated, two had early stop codons, and two bore packaging signal defects. No intact proviral sequence were found in our limited sampling. This indicates that spontaneous viral transcription is mainly fueled by defective proviruses.

Spontaneously active viral reservoirs are phenotypically diverse

LRA stimulation can alter cell surface marker expression, thus biasing phenotyping.⁹ As measuring spontaneously vRNA⁺ cells

Figure 2. Spontaneously active reservoirs are enriched in short vRNA transcripts

- (A and B) Gating strategy to assess: (A) p24 expression in vRNA⁺ cells and (B) *gagRNA* and *polRNA* co-expression in p24⁻ or p24⁺ vRNA⁺ cells.
- (C) List of the theoretical vRNA⁺ populations.
- (D) Donut charts presenting the median proportions of each vRNA⁺ subpopulation for spontaneous or PMA/ionomycin-induced reservoirs, as colored in (C). Numbers in the donut holes represent the median vRNA⁺/10⁶ CD4⁺.
- (E) The proportion of p24⁺ cells in spontaneous compared with PMA/ionomycin-induced vRNA⁺ reservoirs. The frequency of participants with p24⁺ cell detection is indicated underneath.
- (F) Compared frequencies of spontaneous vRNA⁺ and p24⁺ cells. The median of the 7 participants in which p24 was spontaneously detected is shown.
- (G) Correlation between p24⁺ cells in unstimulated and PMA/ionomycin-induced conditions.
- (H) Violin plots showing total single-cell fluorescence intensities in 18 participants. (E and F) The bars indicate the median. The error bars illustrate the interquartile range. Results from Wilcoxon tests are shown above. n = 18 (excepted for E, where n = 16 because <5 vRNA⁺ events were detected in two participants).
- (I) Representative maximal intensity of confocal microscopy projections from z stacks of vRNA⁻ and vRNA⁺ sorted cells. The scale is represented by the white bar (10 μm).
- (J) Number of spots per cell for *exonRNA* (left) and *gagRNA* (right) probes. The results from a Mann-Whitney test are shown above. False-positive rates are indicated by the dashed lines.

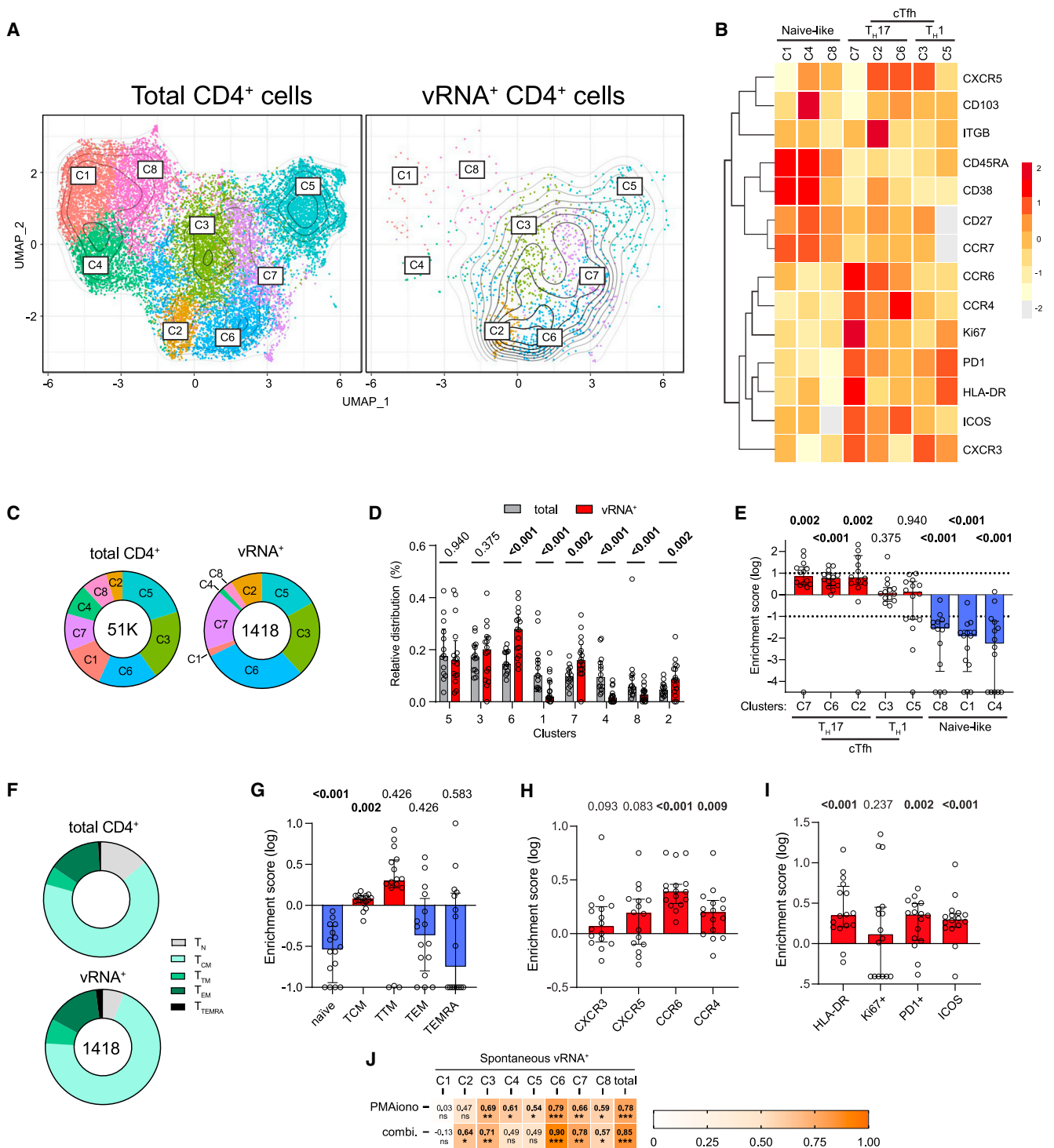


Figure 4. Spontaneously active viral reservoirs are phenotypically diverse

(A) Global uniform manifold approximation and projection (UMAP) for dimension reduction map of all 1,418 vRNA⁺ cells. These cells were embedded among downsampled 3,000 CD4⁺ per donor to help identify stable population clusters. All 8 clusters are identified. Individual CD4⁺ (left) and vRNA⁺ (right) UMAP are shown. Contours show the density of vRNA⁺ cells.

(B) Heatmap showing an unsupervised hierarchical clustering of the 8 clusters, defined by MFI.

(C) The donut charts present the proportion of each cluster for the indicated population, with color matching with (A). The total number of events used to generate the plot are indicated in the donut holes.

(D) The histogram presents the proportion of each cluster, with a side-by-side comparison between CD4⁺ and vRNA⁺ cells. Wilcoxon tests are shown.

(E) The enrichment score for each cluster is calculated as the log of the ratios between vRNA⁺/CD4⁺ cluster proportions.

(legend continued on next page)

does not require an *in vitro* stimulation, the experimental approach used allows reliable phenotyping of viral reservoir cells. We performed unsupervised analyses of high-dimensional flow cytometric phenotyping data to avoid a priori-defined marker combinations (Figure 4). We examined features that were previously found enriched in HIV-infected cells either during ART or during untreated chronic infection (Table S2): chemokine receptors involved in tissue homing ([CXCR5 for Tfh, CXCR3 for Th1, CCR6 for Th17/Th22, and CCR4 for Th2, also expressed on Th17/Th22 and Tregs; reviewed in Strazza and Mor⁴⁵]; gut homing markers [integrin β 7 and CD103, reviewed in Barczyk et al.⁴⁶]; activation markers [CD38, HLA-DR, and ICOS]; cell cycle/proliferation [Ki67]; inhibitory checkpoint [PD-1]; and memory and differentiation markers [CD45RA, CCR7, and CD27]). To avoid excessive background noise in phenotype profiling, we focused the analyses on participants with >5 vRNA⁺ cells and with spontaneous reservoirs above the level of positivity (14/18 participants).

We illustrated the distribution of clustered populations by the uniform manifold approximation and projection (UMAP) algorithm.⁴⁷ To help define clear phenotypic clusters, all identified vRNA⁺ cells were concatenated and downsampled to 3,000 autologous CD4⁺ T cells per participant. Cluster identification was performed using PhenoGraph.⁴⁸ 8 clusters were defined based on distinct profiles of relative marker expression (Figures 4A and 4B and S3A). Active vRNA⁺ reservoir cells were found in all 8 clusters (Figures 4C and 4D). However, compared with total CD4⁺ T cells, vRNA⁺ cells were sparsely found in clusters C1, C4, and C8 (Figures 4A, 4C, and 4D) enriched in CD45RA, CCR7, and CD27, consistent with a naive phenotype (Figure 4B). CCR7 and CD27 expression was moderate in CD45RA-negative clusters C2, C3, C5, C6, and C7, suggesting that these clusters are composed of mixed populations of central memory (T_{CM}), transitional memory (T_{TM}), and effector memory (T_{EM}) cells defined by other phenotypic markers (Figure 4B). We calculated enrichment scores to evaluate the relative over- or under-representation of active vRNA⁺ reservoir cells among the identified clusters (Figure 4E). This analysis confirmed the under-representation of active vRNA⁺ reservoir cells in the naive-like clusters C1, C4, and C8. Univariate analysis relying on CD45RA, CD27, and CCR7 confirmed this finding and further showed a significant enrichment of active vRNA⁺ reservoir cells in T_{CM} and a trend for T_{TM} (Figures 4F, 4G, S3B, and S3C). The paucity of naive active vRNA⁺ reservoir cells is consistent with the significant negative association between the prevalence of naive CD4⁺ T cells and the frequency of active reservoirs (Figure S3D).

Active reservoirs were enriched in clusters C2, C6, and C7 defined by the expression of CCR6 and/or CCR4, suggesting preferential Th17 or Th22 differentiation. C2 and C6 were also enriched in CXCR5 expression, a marker enriched in T follicular helper (Tfh) cells, but this chemokine receptor was not expressed by cells clustering in C7. C7 also included relatively

rare cells with strong features of activation, including higher FI for ICOS, HLA-DR, Ki67, and PD-1 (Figure S3A). Although, we detected frequent active vRNA⁺ reservoir cells in the Th1-like CXCR3-enriched clusters C5 and C3, these subsets were not enriched in infected cells compared with the global CD4⁺ T cell population.

We next analyzed the polarization and integrin and activation marker expression of the active reservoirs through univariate analyses (Figures 4H, 4I, and S3E–S3L). We focused these analyses on CD45RA[−] vRNA⁺ cells to avoid biasing our phenotyping given the near complete absence of vRNA⁺ cells in naive populations. Active vRNA⁺ reservoirs could express any of the four chemokine receptors tested (Figure S3E), with no clear dominance for one over another (Figure S3F). Confirming the previous unsupervised findings, significant enrichments were observed for CCR6⁺ and CCR4⁺ cells, with trends for CXCR5 and CXCR3 (Figures 4H and S3G). CCR6 stood out as the most consistently enriched chemokine receptor among all tested participants (increase in all 16/18 participants). A trend for enrichment of vRNA⁺ events in β 7-integrin⁺ cells was observed, but not in CD103⁺ cells, nor CD32a, another marker previously associated with viral transcription⁴⁹ (Figures S3H–S3J). HLA-DR and Ki67 expression was infrequent in vRNA⁺ cells (2%–15%) (Figures S3K and S3L). ICOS and PD-1 expression was more heterogeneous, with frequencies reaching a much higher level in some participants (2%–43%). Irrespective of their range, all these activation markers except for Ki67, appeared significantly enriched in active vRNA⁺ reservoir cells compared with the global CD4⁺ T cells (Figure 4I).

We next tested whether the magnitude of the inducible reservoir correlated with specific spontaneous vRNA⁺ reservoir clusters (Figure 4J). Several correlations were observed at varying degrees. The connections appeared particularly strong and significant with C3, C6, and C7, which corresponded to the enriched CCR6⁺/CCR4⁺ vRNA⁺ active reservoirs. Because inducible reservoirs could not be reliably phenotyped, we could not relate active reservoirs to inducible reservoir subsets.

These multivariate and univariate analyses provide complementary portraits of peripheral blood active vRNA⁺ cell phenotypes. These cells tend to be memory CD4⁺ T cells, particularly T_{CM}. Compared with other memory CD4⁺ T cells, they are polarized, with a consistent enrichment for CCR6, a marker associated with Th17 and Th22 differentiation, and are more frequently activated than the global CD4⁺ T cell population.

Spontaneously active reservoirs are associated with HIV-specific CD4⁺ and CD8⁺ T cell responses

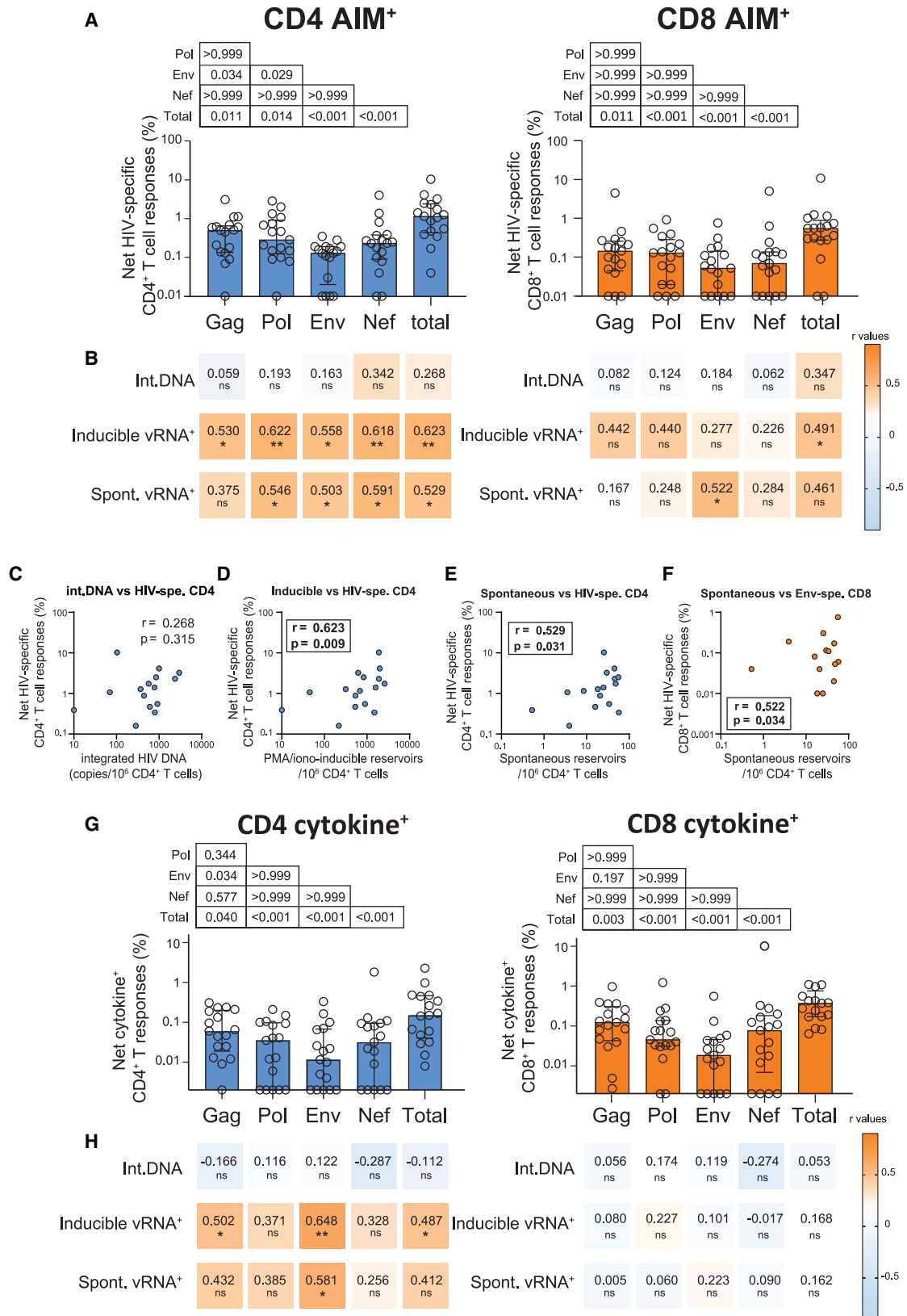
We next tested whether infected cells spontaneously expressing vRNA⁺ could fuel adaptive cellular immunity against HIV during ART. We used a T cell receptor (TCR)-dependent activation-induced marker (AIM) assay that broadly identifies antigen-specific T cells^{29,50,51} (Table S3). We complemented these data with functional profiling by intracellular cytokine staining (ICS) (flow

(F) Donut charts presenting the median proportions of each memory vRNA⁺ subpopulation for spontaneous or PMA/ionomycin-induced reservoirs.

(G–I) Enrichment scores for univariate analysis of (H) memory, (I) polarization, and (J) activation subsets. The enrichment scores were calculated as in (E).

(J) Correlations between PMA/ionomycin- or Panobinostat + ingenol-inducible reservoirs and each active vRNA⁺ cluster. Values and the shade of color indicate r values. p values are shown underneath: *p < 0.05, **p < 0.01, ***p < 0.001.

In (D), (E), and (G)–(I), the histograms indicate the median, and the error bars illustrate the interquartile range and bold values indicate statistical significance.



(legend on next page)

cytometry panels: Table S4). The AIM assay was previous shown to allow a broader capture of antigenic responses than standard ICS, even in the context of CD4⁺ T cell dysfunction.^{29,50}

The AIM assay involved a 15-h incubation of autologous PBMCs with an overlapping peptide pool spanning the coding sequences of either Gag, Pol, Env, or Nef. In CD4⁺ T cells, specificity for these peptides was inferred by the upregulation of CD69, CD40L, 4-1BB, and OX-40 upon stimulation, compared with unstimulated controls, whereas CD69 and 4-1BB co-expression was used for CD8⁺ T cells. We used an AND/OR Boolean combination gating to assess the total frequencies of antigen-specific CD4⁺ and CD8⁺ T cells^{50–52} (Figure S4A). Cells co-expressing at least one pair of AIM were deemed HIV-specific. The significant increases compared with unstimulated conditions confirmed the assay's specificity (Figure S4B).

Effector CD4⁺ and CD8⁺ T cell functions were measured by a 6-h ICS using the same stimulation conditions as for the AIM assays. We focused on interferon-gamma (IFN- γ), interleukin-2 (IL-2), and tumor necrosis factor (TNF) expression. We also defined total cytokine⁺CD4⁺, and cytokine⁺CD8⁺ T cell responses by an OR Boolean gating strategy (Figure S4C). Most participants showed cytokine⁺CD4⁺ and cytokine⁺CD8⁺ T cell responses, although cytokine⁺ CD8⁺ T responses were smaller and more frequently undetectable (Figure S4D).

Gag, Pol, Env, and Nef responses were all readily detectable (Figure 5A). We used the sum of the net responses to each peptide pool to quantify “total” HIV responses. We next correlated total HIV, Gag, Pol, Env, and Nef responses to cells harboring integrated HIV DNA, PMA/ionomycin-inducible, and spontaneously active reservoirs (Figure 5B). There was no significant correlation between AIM⁺ CD4⁺ and CD8⁺ T cell responses and integrated DNA (Figures 5B and 5C). In contrast, inducible reservoirs were strongly associated with total HIV-specific CD4⁺ T cell responses defined by AIM (Figures 5B and 5D). Similar association existed when considering Gag, Pol, Env, and Nef-specific CD4⁺ T cells. A strong correlation was also found between the magnitude of the spontaneous reservoir and total HIV-specific CD4⁺ T cell responses (Figures 5B and 5E). The correlation with Nef was particularly strong ($r = 0.591$), whereas the correlation with Gag ($r = 0.375$) was the weakest. The association between active reservoir cells and total HIV-specific CD8⁺ T cell responses was weaker than with CD4, yet there was a trend. Individual peptide analyses revealed a significant correlation of the active reservoir cells with Env-specific CD8⁺ T cell responses (Figures 5B and 5F, $r = 0.522$). Correlations with Gag, Pol, or Nef-specific CD8⁺ T cell responses were weaker and did not reach significance.

Cytokine⁺ Gag-specific responses were also slightly higher for CD4⁺ and CD8⁺ T cell responses (Figure 5G). The correlation between reservoir metrics and ICS was weaker than with AIM (Figure 5H), possibly due to the lower sensitivity of functional assays. Total HIV-specific CD4⁺ T cells correlated with inducible reservoirs, and a strong trend was observed with active reservoirs. For both inducible and active reservoirs, strong correlations were observed with Env-specific cytokine⁺ CD4⁺ T cells (Figure 5H). The other correlations were weaker and only Gag-specific cytokine⁺ CD4⁺ T cells, for inducible reservoirs, reached significance. No correlation was observed with CD8⁺ T cell effector functions (Figure 5H). These data suggest that active reservoirs and HIV-specific immune responses, particularly Thelper responses, are connected.

A subset of active reservoirs displays stronger links to HIV-specific CD4⁺ and CD8⁺ T cell responses

Next, we performed an unsupervised analysis to characterize HIV-specific CD4⁺ T cells. To account for the inherent phenotypic diversity of circulating CD4⁺ T cells and avoid a-priori-defined marker combinations, we performed an unsupervised analysis of the high-dimensional flow cytometric phenotyping data including total (Gag + Pol + Env + Nef) HIV-specific CD4⁺ T cells. We used chemokine receptors, activation markers and a key immune checkpoint (CXCR5, CXCR3, CCR6, CD38 and HLA-DR, and PD-1). The various clusters were represented using UMAP, and clusters were identified by PhenoGraph. 15 clusters were identified (Figure 6A) based on distinct profiles of relative marker expression (Figures S5A and S5B). Each of these clusters represented 3%–12% of total responses, with the largest C2 and C4 clusters representing no more than 13% of the total population examined (Figure 6B). To simplify the analysis, we grouped these clusters into 6 “superclusters” defined by the expression of chemokine receptors (Figures 6A, 6B, and S5B). The superclusters, ranked by decreasing frequencies, were characterized by the expression of (1) CCR6, (2) none of the tested chemokine receptor, (3) CXCR3, (4) CXCR3 and CCR6, (5) CXCR5, and (6) CXCR5 and CXCR3. Based on previous studies,^{53,54} these superclusters would correspond respectively to (1) T_H17, (2) unpolarized cells, (3) T_H1, (4) non-conventional T_H1 (T_H1*), (5) cTfh, and (6) a T_H1-like subset of cTfh. The frequencies of HIV-specific superclusters in total CD4⁺ T cells showed great variability among participants (Figure S5C), indicating that HIV-specific CD4⁺ T cell responses can adopt very different profiles during ART.

As our results showed relationships between active reservoirs and immune responses, we next examined how associations

Figure 5. Associations between spontaneously active reservoirs and HIV-specific CD4⁺ and CD8⁺ T cell responses

- (A) Net magnitude of HIV-specific CD4⁺ and CD8⁺ T cells by AIM assay.
 (B) Heatmap reporting the associations between AIM⁺ CD4⁺ and CD8⁺ T responses and integrated DNA, inducible and spontaneously active reservoirs.
 (C–E) Correlations between net AIM⁺ CD4⁺ responses and (C) integrated DNA, (D) inducible reservoirs, and (E) spontaneous reservoirs.
 (F) Correlation between net AIM⁺ CD8⁺ T cell responses and spontaneous reservoirs.
 (G) Net magnitude of HIV-specific CD4⁺ and CD8⁺ T cells defined by the ICS.
 (H) Heatmap reporting the associations between cytokine⁺ CD4⁺ and cytokine⁺ CD8⁺ T responses and integrated DNA, inducible and spontaneously active reservoirs.

In (A), (B), (G), and (H), peptide pools used to stimulate PBMCs are indicated. “HIV” responses were inferred by the sum of Gag, Pol, Env, and Nef net responses. In (A) and (G), net magnitudes after background subtraction are shown. The bars indicate the median, and the error bars illustrate the interquartile range. The results from a Friedman test are shown above. In (B) and (H), r and p (Spearman) values are shown. $p < 0.05$, $**p < 0.01$, $***p < 0.001$. $n = 16$ (1 participant had <5 vRNA⁺ cells, therefore could not be phenotyped).

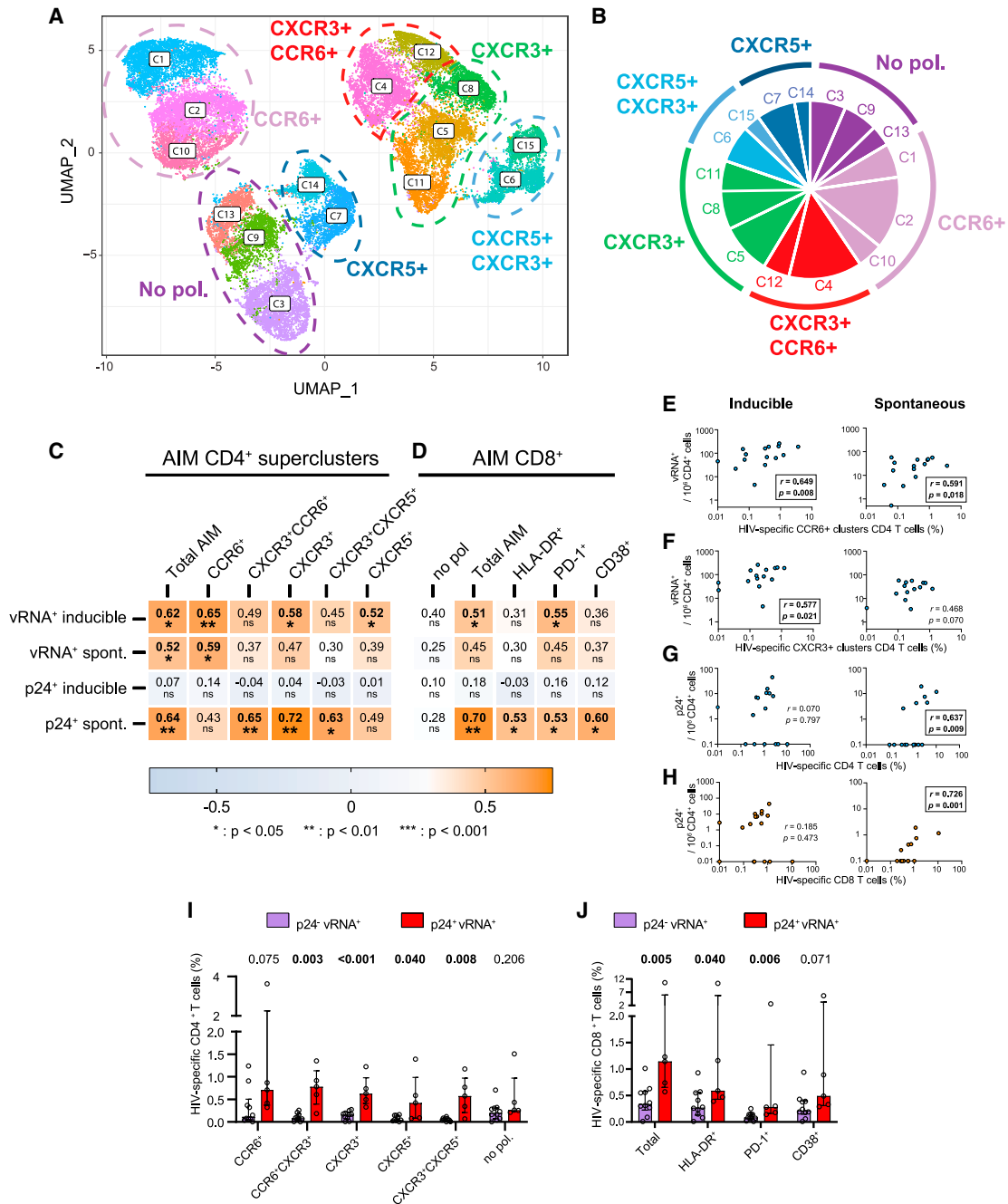


Figure 6. A subset of active reservoirs display strong links to HIV-specific CD4⁺ and CD8⁺ T cell responses

(A) Global uniform manifold approximation and projection (UMAP) for dimension reduction of HIV-specific AIM⁺ CD4⁺ T cells. 15 clusters were identified and regrouped in 6 superclusters.

(B) Median proportions of each cluster, regrouped by superclusters.

(C and D) Heatmap showing correlations between (C) vRNA⁺ cluster frequencies and net magnitudes of AIM⁺ CD4⁺, regrouped by superclusters, or (D) vRNA⁺ cluster frequencies and net magnitudes of AIM⁺ CD8⁺ T cells. p values from Spearman test are shown, with significance underneath. *p < 0.05, **p < 0.01, ***p < 0.001.

(E and F) Correlations between the inducible or spontaneous vRNA⁺ reservoir and the magnitude of cells in (E) AIM⁺ HIV-specific CCR6⁺ CD4⁺ T cell supercluster and (F) AIM⁺ HIV-specific CXCR3⁺ CD4⁺ T cell supercluster.

(G and H) Correlations between the inducible or spontaneous p24⁺ reservoir and the magnitude of cells in (G) total AIM⁺ HIV-specific CD4⁺ and (H) total AIM⁺ HIV-specific CD8⁺ T cells. Spearman tests were performed. r and p values are shown.

(I and J) Histogram comparing median HIV-specific AIM⁺ (I) CD4⁺ and (J) CD8⁺ T cell responses in people where p24⁺ cells were detectable in peripheral blood (n = 5) or were not (n = 11). Mann-Whitney tests are shown above. Error bars indicate the interquartile range. n = 16 (1 participant had <5 vRNA⁺ cells, therefore could not be phenotyped).

varied between types of viral reservoirs and subpopulations of HIV-specific AIM⁺ CD4⁺ and CD8⁺ T cells. Our first layer of analysis focused on total HIV-specific CD4⁺ T cell superclusters (Figure 6C). We found a strong correlation between the magnitude of both inducible or spontaneous vRNA⁺ cells and total AIM⁺ CD4⁺ T cell responses (Figure 6C). For the spontaneous reservoirs, correlations with CCR6⁺ AIM⁺ CD4⁺ T cell responses was particularly strong (Figures 6C and 6E), and showed a trend with CXCR3⁺ AIM⁺ CD4⁺ T cell responses (Figures 6C and 6F). Inducible vRNA⁺ cells showed significant correlations with total and PD1⁺ AIM⁺ CD8⁺ T cell responses (Figure 6D). The correlations between spontaneous vRNA⁺ cells and total and PD1⁺ AIM⁺ CD8⁺ T cell responses showed trends. Associations with HLA-DR⁺ and CD38⁺ responses were weaker.

We observed a significant correlation between active p24⁺ reservoirs and total AIM⁺ specific CD4⁺ T cells (Figures 6C and 6G). The *r* value (*r* = 0.720) was particularly strong for the CXCR3⁺ supercluster (Figure 6C). We also noted strong correlations of total and activated AIM⁺ specific CD8 T cells with active p24⁺ reservoirs (Figures 6D and 6H). Correlations were lost with PMA/ionomycin-induced p24⁺ reservoirs, indicating that, critically, only spontaneously p24-expressing cells can shape HIV-specific CD4⁺ and CD8⁺ T cell responses. We divided our cohort based on whether p24⁺ could or could not be detected among vRNA⁺ cells (Figure 2F). HIV-specific CD4⁺ and CD8⁺ T cell responses were significantly higher in the p24⁺ group (Figures 6I and 6J). There were marked differences between the two groups for CXCR3⁺ and CXCR3⁺ CXCR5⁺ superclusters, suggesting that protein expression is a prerequisite for their maintenance.

Together, these results demonstrate important relationships between spontaneous vRNA⁺ and—especially—p24-expressing viral reservoirs and magnitude and function of HIV-specific CD4⁺ and CD8⁺ T cell responses.

DISCUSSION

In this study, we characterized HIV reservoirs spontaneously expressing viral transcripts, as detected at the single-cell level by RNAflow-FISH. We identified these active reservoir cells in most PWH investigated, at a frequency only 3-fold lower than the PMA/ionomycin-inducible reservoirs. We phenotyped these active reservoirs without the confounding impact of LRAs. Integrated analyses demonstrated the heterogeneous nature of active vRNA⁺ reservoirs. Certain features were enriched, such as high expression of CCR6, a marker of Th17 and Th22 cells. We found associations between active viral reservoirs and HIV-specific CD4⁺ and CD8⁺ T cell responses during suppressive ART. CCR6⁺ HIV-specific CD4⁺ T cells seemed particularly connected to various active reservoirs. HIV-specific CD4⁺ and CD8⁺ T cell responses were higher in the few participants in which active p24⁺ reservoir cells could be detected, suggesting that maintaining those immune responses requires spontaneous viral translation.

We and others previously showed how the RNAflow-FISH assay could identify reactivated viral reservoirs at the single-cell level.^{8,9,55} By adapting a multigene HIV-specific probe set design, we detected viral reservoirs with great sensitivity and resolution without *ex vivo* latency reversal. Spontaneous and inducible vRNA⁺ reservoirs correlated. One possible explanation

for this relationship is that they represent two facets of the same cell: latency reversal could exacerbate pre-existing, very low-yield transcriptional activity possibly missed by our experimental technique. These cells may be poised for higher transcriptional activity upon induction, as suggested by the higher median fluorescence intensity (MFI) for the vRNA signal in induced vs spontaneously active cells. The low transcriptional activity may be due to (1) suboptimal Tat-mediated transactivation during latency,⁵⁶ (2) the shortness of the abortive transcripts, consistent with data previously obtained by digital-droplet PCR,^{10,41} that may make them less sensitive to detection by a branched DNA amplification technique, and (3) the requirement for staining with two HIV RNA probe sets can reduce sensitivity of detection. Alternatively, a portion of the PMA/ionomycin-inducible reservoirs may have been in a deeper state of latency and fully silent prior to stimulation,^{57–59} therefore only revealed after pharmacological reactivation. Spontaneous viral gene expression was also characterized by a shorter transcription and rare translation of Gag. These observations are consistent with previous reports and suggest transcriptional¹⁰ and post-transcription blocks⁶⁰ to viral gene expression.

Another notable finding of our study is that active reservoirs are not confined to any specific CD4⁺ T subset. This finding is consistent with recent reports correlating viral transcriptomic and genomic properties.^{60,61} All CD4⁺ clusters we analyzed were populated to some degree with vRNA⁺ reservoirs. Yet, compared with total peripheral CD4⁺ T cells, active reservoir cells profiles were (1) rarely naive and mostly T_{CM}, (2) enriched in CCR6, suggesting a preferential Th17 and Th22 polarization, (3) enriched in activation and exhaustion markers such as HLA-DR, ICOS, and PD-1, and (4) enriched with cell proliferation marker Ki67. Although modest, enrichment in activation/exhaustion and proliferation markers is consistent with homeostatic^{62–64} and antigen-driven proliferation reported during ART.^{34,65} Although we observed some enrichment of activation markers in active reservoirs, the vast majority of spontaneous reservoir cells were still found in cells that did not express activation markers, indicating that T cell activation is not a prerequisite for spontaneous viral gene expression. The enrichment of HIV-infected cells we have observed in T_{CM}, CCR6, and to a lesser extent, CXCR5 and CXCR3 are consistent with previous reports using univariate analyses.^{62,66–71} These enrichments may reflect preferential replication of HIV-1 in specific anatomic compartments before ART initiation, such as the intestinal mucosa (hence the enrichment in the gut homing and Th17 marker CCR6)^{8,72,73} and germinal centers of lymph nodes (hence the enrichment in the Tfh marker CXCR5).^{8,72,73} Some tissues and microenvironments (e.g., gastrointestinal tract) may also be more permissive to viral transcription,^{74,75} and this would be mirrored in the circulation when these cells egress from tissues into the blood. We cannot exclude that residual replication occurs in tissues where penetration of antivirals may be suboptimal. However, to date, no direct evidence has shown that ongoing viral replication contributes to viral reservoir persistence in PWH receiving suppressive ART.^{33,35,36}

An association was previously reported between cytotoxic Nef-specific CD8⁺ T cell responses and HIV DNA and RNA.⁷⁶ Using single-cell approaches, we now find multiple strong positive correlations between active reservoirs and the magnitude of Pol,

Env, Nef, and to a lesser extent, Gag-specific CD4⁺ and CD8⁺ T cell responses, indicating a broader relationship than initially anticipated. The correlations were always stronger with HIV RNA than with HIV DNA, suggesting that some gene expression is necessary to reveal these relationships. Detailed analyses showed that the strength of these correlations varied among the pairs of viral and immune clusters assessed, suggesting that viral reservoirs do not all influence anti-HIV immune responses equally. HIV-specific CCR6⁺ CD4⁺ clusters were particularly well correlated with active reservoir cells. While this correlation suggests tissue-specific interface between active reservoirs and HIV-specific T cells, putatively the gut, further investigations will be necessary to deeply decipher connections between reservoirs and HIV-specific immune responses.

The positivity of the relationship suggests that spontaneous reservoirs are sustaining HIV-specific CD4⁺ and CD8⁺ T cells rather than HIV-specific cells controlling the reservoirs. In this later case, a negative association would have been expected. However, spontaneously active reservoirs that still persist after >3 post-ART initiation and reservoir selection by the immune system are likely inherently more resistant to cell death. Consistent with this, recent studies showed that persistent reservoirs adopt a pro-survival gene expression profile.^{60,77,78} How viral transcription may drive immune responses remains a key question. The magnitude of HIV-specific CD4⁺ and CD8⁺ T cell responses were lower in participants with no spontaneous p24-expressing active reservoir. In contrast, these responses were robust in participants in which p24-expressing vRNA⁺ reservoir cells could be detected. These findings suggest that viral protein expression, although rare, is the driving force keeping HIV reservoirs and HIV-specific immune responses closely related. It will be important to determine whether spontaneous expression of Gag and other HIV proteins is more frequent in specific tissues, possibly the gut due to proinflammatory microenvironment more favorable for provirus activation or in anatomic compartments harboring a weaker immune surveillance.⁷⁹ Alternatively, sporadic Gag expression in peripheral blood, perhaps during transient challenges such as acute illnesses could possibly contribute to the antigen-stimulated maintenance of HIV-specific immunity. If this is the case, active vRNA⁺ reservoir cells in the circulation may mirror tissue reservoir cells that are prone to produce proteins and subsequently cognate peptides presented by major histocompatibility complex (MHC) molecules to T cells.

Inducible proviruses can bear not only minor,^{9,17} but extensive defects predicted to prevent viral replication. We showed here that spontaneously active reservoirs are mostly defective as well. Yet, reservoirs expressing transcripts from these defective proviruses may still allow some translation,^{37,38,80} depending on where the defect is located. Our work supports that such defective proviruses can also maintain HIV-specific CD4⁺ and CD8⁺ T cell responses in a chronic state of expansion, activation, and exhaustion during ART.

Our study has some limitations. Only Caucasian males were included mostly due to the epidemiology of the PWH population in Montreal and, to some extent, the more frequent difficulties for peripheral vein access to perform leukaphereses in females. It will be important to conduct such studies in women and in other ethnicities, as immune responses may vary with sex and genetic background. ART was initiated in most participant's years after

HIV acquisition; investigations of PWH who initiated therapy early would provide valuable complementary information. While the assay used allows high-parameter profiling of active reservoir cells, our conservative detection limit (about 5 vRNA copies/cell)^{8,43} missed the lowest levels of gene transcription. Other approaches indeed indicated even higher magnitudes of spontaneous reservoirs.⁸¹ Studies of gut and other lymphoid tissues will be important to gain a deeper understanding of the immunovirological dynamics involved. The relatively small size of the cohort studied did not allow us to reliably rank the strength of the associations between active reservoir clusters and HIV-specific T cell superclusters.

Finally, our study may have notable implications for HIV cure strategies. Approaches considered include Env-specific broadly neutralizing antibodies. The fraction of active reservoirs that are competent for Env expression will impact the potential effectiveness of such therapies to eliminate these cells. While the replication-competent HIV reservoir is the primary target of HIV cure, our data highlight the pathophysiologic relevance of other fractions of the HIV reservoirs, likely contributing to the deleterious effect of immune activation. Research efforts should also consider the putatively negative impact of spontaneously active reservoirs in the design of interventions aiming at clinical benefit for PWH on suppressive ART.

STAR METHODS

Detailed methods are provided in the online version of this paper and include the following:

- **KEY RESOURCES TABLE**
- **RESOURCE AVAILABILITY**
 - Lead contact
 - Materials availability
 - Data and code availability
- **EXPERIMENTAL MODEL AND SUBJECT DETAILS**
 - Ethics Statement
 - Participants and Samples
- **METHOD DETAILS**
 - Total and integrated DNA measures
 - CD4⁺ T cell preparation for HIV reservoir profiling
 - HIV-1 RNAflow-FISH assay
 - Limiting Dilution Assay
 - Microscopy
 - Single-cell near full-length PCR
 - Activation-induced marker (AIM) assay
 - Intracellular Cytokine Staining (ICS)
- **QUANTIFICATION AND STATISTICAL ANALYSIS**
 - Statistical analysis
 - Software scripts and visualization

SUPPLEMENTAL INFORMATION

Supplemental information can be found online at <https://doi.org/10.1016/j.chom.2023.08.006>.

ACKNOWLEDGMENTS

We thank Josée Girouard, Angie Massicotte (CUSM), and all study participants for their invaluable role in this project; Dr. Dominique Gauchat, Dr. Gaël

Dulude, Philippe St-Onge, and the CRCHUM Flow Cytometry Platform; Dr. Olfa Debbeche and the CRCHUM BSL3 platform; and Aurélie Cleret-Buhot and the Microscopy platform. The following reagents were obtained through the NIH HIV Reagent Program, Division of AIDS, NIAID: Maraviroc (ARP-11580), Raltegravir (ARP-11680), Tenofovir (ARP-10199), and Emtricitabine (ARP-10071). Funding: this study was supported by the Canadian Institutes for Health Research (CIHR grant #152977 to D.E.K.), the US National Institutes of Health (R01AI14341 to J.D.E., N.C., and D.E.K.), and the Réseau Fonds de la recherche Québec-Santé (FRQS) SIDA & Maladies infectieuses and thérapies cellulaires. D.E.K. is an FRQS Merit Research Scholar. N.C. is an FRQS Research Scholar awardee. G.S. is supported by an FRQS doctorate fellowship and by a scholarship from the Department of Microbiology, Infectious Disease, and Immunology of the University of Montreal. J.D.E. is supported by the Oregon National Primate Research Center grant award P51OD011092. The Symphony flow cytometer was funded by a John R. Evans Leaders Fund Leader Fund from the Canada Foundation for Innovation (fund #37521 to D.E.K.) and the Fondation Sclérodermie Québec.

AUTHOR CONTRIBUTIONS

Conceptualization and supervision, M.D. and D.E.K.; methodology, M.D., G.S., and N.B.; software, O.T.; investigation and validation, G.-G.D., M.D., N.B., G.S., M.N., and A. Pagliuzza; formal analysis, M.D., O.T., C.D., C.R., and R.F. J.-P.R. ensured recruitment and clinical assessments. Data curation, C.R. and M.D.; interpretation, M.D., O.T., A. Pagliuzza, R.F., J.D.E., N.C., and D.E.K. J.D.E. and A. Prat provided intellectual input. Writing – original draft, M.D. and D.E.K.; review & editing, all co-authors; visualization, M.D., C.D., and O.T.; project administration, M.D.; funding acquisition, D.E.K., N.C., and J.D.E.

DECLARATION OF INTERESTS

The authors declare no competing interests.

Received: January 24, 2023

Revised: June 1, 2023

Accepted: August 11, 2023

Published: September 13, 2023

REFERENCES

1. Davey, R.T., Jr., Bhat, N., Yoder, C., Chun, T.W., Metcalf, J.A., Dewar, R., Natarajan, V., Lempicki, R.A., Adelsberger, J.W., Miller, K.D., et al. (1999). HIV-1 and T cell dynamics after interruption of highly active antiretroviral therapy (HAART) in patients with a history of sustained viral suppression. *Proc. Natl. Acad. Sci. USA* *96*, 15109–15114. <https://doi.org/10.1073/pnas.96.26.15109>.
2. Baxter, A.E., O'Doherty, U., and Kaufmann, D.E. (2018). Beyond the replication-competent HIV reservoir: transcription and translation-competent reservoirs. *Retrovirology* *15*, 18. <https://doi.org/10.1186/s12977-018-0392-7>.
3. Gaebler, C., Lorenzi, J.C.C., Oliveira, T.Y., Nogueira, L., Ramos, V., Lu, C.-L., Pai, J.A., Mendoza, P., Jankovic, M., Caskey, M., and Nussenzweig, M.C. (2019). Combination of quadruplex qPCR and next-generation sequencing for qualitative and quantitative analysis of the HIV-1 latent reservoir. *J. Exp. Med.* *216*, 2253–2264. <https://doi.org/10.1084/jem.20190896>.
4. Bruner, K.M., Wang, Z., Simonetti, F.R., Bender, A.M., Kwon, K.J., SenGupta, S., Fray, E.J., Beg, S.A., Antar, A.A.R., Jenike, K.M., et al. (2019). A quantitative approach for measuring the reservoir of latent HIV-1 proviruses. *Nature* *566*, 120–125. <https://doi.org/10.1038/s41586-019-0898-8>.
5. Procopio, F.A., Fromentin, R., Kulpa, D.A., Brehm, J.H., Bebin, A.G., Strain, M.C., Richman, D.D., O'Doherty, U., Palmer, S., Hecht, F.M., et al. (2015). A novel assay to measure the magnitude of the inducible viral reservoir in HIV-infected individuals. *EBioMedicine* *2*, 874–883. <https://doi.org/10.1016/j.ebiom.2015.06.019>.
6. Pasternak, A.O., and Berkhout, B. (2018). What do we measure when we measure cell-associated HIV RNA. *Retrovirology* *15*, 13. <https://doi.org/10.1186/s12977-018-0397-2>.
7. Pardons, M., Baxter, A.E., Massanella, M., Pagliuzza, A., Fromentin, R., Dufour, C., Leyre, L., Routy, J.P., Kaufmann, D.E., and Chomont, N. (2019). Single-cell characterization and quantification of translation-competent viral reservoirs in treated and untreated HIV infection. *PLoS Pathog.* *15*, e1007619. <https://doi.org/10.1371/journal.ppat.1007619>.
8. Baxter, A.E., Niessl, J., Fromentin, R., Richard, J., Porichis, F., Charlebois, R., Massanella, M., Brassard, N., Alshafi, N., Delgado, G.-G., et al. (2016). Single-cell characterization of viral translation-competent reservoirs in HIV-infected individuals. *Cell Host Microbe* *20*, 368–380. <https://doi.org/10.1016/j.chom.2016.07.015>.
9. Sannier, G., Dubé, M., Dufour, C., Richard, C., Brassard, N., Delgado, G.G., Pagliuzza, A., Baxter, A.E., Niessl, J., Brunet-Ratnasingham, E., et al. (2021). Combined single-cell transcriptional, translational, and genomic profiling reveals HIV-1 reservoir diversity. *Cell Rep.* *36*, 109643. <https://doi.org/10.1016/j.celrep.2021.109643>.
10. Yukl, S.A., Kaiser, P., Kim, P., Telwate, S., Joshi, S.K., Vu, M., Lampiris, H., and Wong, J.K. (2018). HIV latency in isolated patient CD4⁺ T cells may be due to blocks in HIV transcriptional elongation, completion, and splicing. *Sci. Transl. Med.* *10*, eaap9927. <https://doi.org/10.1126/scitranslmed.aap9927>.
11. Mohammadi, P., di Iulio, J., Muñoz, M., Martinez, R., Bartha, I., Cavassini, M., Thorball, C., Fellay, J., Beerenwinkel, N., Ciuffi, A., and Telenti, A. (2014). Dynamics of HIV latency and reactivation in a primary CD4⁺ T cell model. *PLoS Pathog.* *10*, e1004156. <https://doi.org/10.1371/journal.ppat.1004156>.
12. Dornadula, G., Zhang, H., VanUitert, B., Stern, J., Livornese, L., Jr., Ingeman, M.J., Witek, J., Kedanis, R.J., Natkin, J., DeSimone, J., and Pomerantz, R.J. (1999). Residual HIV-1 RNA in blood plasma of patients taking suppressive highly active antiretroviral therapy. *JAMA* *282*, 1627–1632. <https://doi.org/10.1001/jama.282.17.1627>.
13. Günthard, H.F., Havlir, D.V., Fiscus, S., Zhang, Z.-Q., Eron, J., Mellors, J., Gulick, R., Frost, S.D., Brown, A.J., Schleif, W., et al. (2001). Residual human immunodeficiency virus (HIV) type 1 RNA and DNA in lymph nodes and HIV RNA in genital secretions and in cerebrospinal fluid after suppression of viremia for 2 years. *J. Infect. Dis.* *183*, 1318–1327. <https://doi.org/10.1086/319864>.
14. Halvas, E.K., Joseph, K.W., Brandt, L.D., Guo, S., Sobolewski, M.D., Jacobs, J.L., Tumiottio, C., Bui, J.K., Cyktor, J.C., Keele, B.F., et al. (2020). HIV-1 viremia not suppressible by antiretroviral therapy can originate from large T cell clones producing infectious virus. *J. Clin. Invest.* *130*, 5847–5857. <https://doi.org/10.1172/JCI138099>.
15. Ishizaka, A., Sato, H., Nakamura, H., Koga, M., Kikuchi, T., Hosoya, N., Koibuchi, T., Nomoto, A., Kawana-Tachikawa, A., and Mizutani, T. (2016). Short intracellular HIV-1 transcripts as biomarkers of residual immune activation in patients on antiretroviral therapy. *J. Virol.* *90*, 5665–5676. <https://doi.org/10.1128/JVI.03158-15>.
16. Fischer, M., Günthard, H.F., Opravil, M., Joos, B., Huber, W., Bisset, L.R., Ott, P., Böni, J., Weber, R., and Cone, R.W. (2000). Residual HIV-RNA levels persist for up to 2.5 years in peripheral blood mononuclear cells of patients on potent antiretroviral therapy. *AIDS Res. Hum. Retroviruses* *16*, 1135–1140. <https://doi.org/10.1089/088922200414974>.
17. White, J.A., Wu, F., Yasin, S., Moskovljevic, M., Varriale, J., Dragoni, F., Camilo-Contreras, A., Duan, J., Zheng, M.Y., Tadzong, N.F., et al. (2023). Clonally expanded HIV-1 proviruses with 5'-Leader defects can give rise to nonsuppressible residual viremia. *J. Clin. Invest.* *133*, e165245. <https://doi.org/10.1172/JCI165245>.
18. Ferdin, J., Goričar, K., Dolžan, V., Plemenitas, A., Martin, J.N., Peterlin, B.M., Deeks, S.G., and Lenassi, M. (2018). Viral protein Nef is detected in plasma of half of HIV-infected adults with undetectable plasma HIV RNA. *PLoS ONE* *13*, e0191613. <https://doi.org/10.1371/journal.pone.0191613>.

19. Passaes, C., Delagrèverie, H.M., Avettand-Fenoel, V., David, A., Monceaux, V., Essat, A., Müller-Trutwin, M., Duffy, D., De Castro, N., Wittkop, L., et al. (2021). Ultrasensitive detection of p24 in plasma samples from people with primary and chronic HIV-1 infection. *J. Virol.* *95*, e0001621. <https://doi.org/10.1128/JVI.00016-21>.
20. Wu, G., Zuck, P., Goh, S.L., Milush, J.M., Vohra, P., Wong, J.K., Somsouk, M., Yukl, S.A., Shacklett, B.L., Chomont, N., et al. (2021). Gag p24 is a marker of human immunodeficiency virus expression in tissues and correlates with immune response. *J. Infect. Dis.* *224*, 1593–1598. <https://doi.org/10.1093/infdis/jiab121>.
21. Cartwright, E.K., Spicer, L., Smith, S.A., Lee, D., Fast, R., Paganini, S., Lawson, B.O., Nega, M., Easley, K., Schmitz, J.E., et al. (2016). CD8(+) lymphocytes are required for maintaining viral suppression in SIV-infected macaques treated with short-term antiretroviral therapy. *Immunity* *45*, 656–668. <https://doi.org/10.1016/j.immuni.2016.08.018>.
22. Chevalier, M.F., Jülg, B., Pyo, A., Flanders, M., Ransinghe, S., Soghoian, D.Z., Kwon, D.S., Rychert, J., Lian, J., Muller, M.I., et al. (2011). HIV-1-specific interleukin-21+ CD4+ T cell responses contribute to durable viral control through the modulation of HIV-specific CD8+ T cell function. *J. Virol.* *85*, 733–741. <https://doi.org/10.1128/JVI.02030-10>.
23. Gray, G.E., Huang, Y., Grunenberg, N., Laher, F., Roux, S., Andersen-Nissen, E., De Rosa, S.C., Flach, B., Randhawa, A.K., Jensen, R., et al. (2019). Immune correlates of the Thai RV144 HIV vaccine regimen in South Africa. *Sci. Transl. Med.* *11*, eaax1880. <https://doi.org/10.1126/scitranslmed.aax1880>.
24. Tebas, P., Jadlowsky, J.K., Shaw, P.A., Tian, L., Esparza, E., Brennan, A.L., Kim, S., Naing, S.Y., Richardson, M.W., Vogel, A.N., et al. (2021). CCR5-edited CD4+ T cells augment HIV-specific immunity to enable post-rebound control of HIV replication. *J. Clin. Invest.* *131*, e144486. <https://doi.org/10.1172/JCI144486>.
25. Tuyishime, S., Haut, L.H., Kurupati, R.K., Billingsley, J.M., Carnathan, D., Gangahara, S., Styles, T.M., Xiang, Z., Li, Y., Zopfs, M., et al. (2018). Correlates of protection against SIV_{mac251} infection in rhesus macaques immunized with chimpanzee-derived adenovirus vectors. *EBioMedicine* *31*, 25–35. <https://doi.org/10.1016/j.ebiom.2018.02.025>.
26. International HIV Controllers Study, Pereyra, F., Jia, X., McLaren, P.J., Telenti, A., de Bakker, P.I., Walker, B.D., Ripke, S., Brumme, C.J., Pulit, S.L., et al. (2010). The major genetic determinants of HIV-1 control affect HLA class I peptide presentation. *Science* *330*, 1551–1557. <https://doi.org/10.1126/science.1195271>.
27. Moysi, E., Petrovas, C., and Koup, R.A. (2018). The role of follicular helper CD4 T cells in the development of HIV-1 specific broadly neutralizing antibody responses. *Retrovirology* *15*, 54. <https://doi.org/10.1186/s12977-018-0437-y>.
28. Trautmann, L. (2016). Kill: boosting HIV-specific immune responses. *Curr. Opin. HIV AIDS* *11*, 409–416. <https://doi.org/10.1097/COH.0000000000000286>.
29. Niessl, J., Baxter, A.E., Morou, A., Brunet-Ratnasingham, E., Sannier, G., Gendron-Lepage, G., Richard, J., Delgado, G.-G., Brassard, N., Turcotte, I., et al. (2020). Persistent expansion and Th1-like skewing of HIV-specific circulating T follicular helper cells during antiretroviral therapy. *EBioMedicine* *54*, 102727. <https://doi.org/10.1016/j.ebiom.2020.102727>.
30. Reiss, S., Baxter, A.E., Cirelli, K.M., Dan, J.M., Morou, A., Daigneault, A., Brassard, N., Silvestri, G., Routy, J.P., Havenar-Daughton, C., et al. (2017). Comparative analysis of activation induced marker (AIM) assays for sensitive identification of antigen-specific CD4 T cells. *PLoS ONE* *12*, e0186998. <https://doi.org/10.1371/journal.pone.0186998>.
31. Warren, J.A., Zhou, S., Xu, Y., Moeser, M.J., MacMillan, D.R., Council, O., Kirchherr, J., Sung, J.M., Roan, N.R., Adimora, A.A., et al. (2020). The HIV-1 latent reservoir is largely sensitive to circulating T cells. *eLife* *9*, e57246. <https://doi.org/10.7554/eLife.57246>.
32. Thomas, A.S., Jones, K.L., Gandhi, R.T., McMahon, D.K., Cyktor, J.C., Chan, D., Huang, S.-H., Truong, R., Bosque, A., Macedo, A.B., et al. (2017). T-cell responses targeting HIV Nef uniquely correlate with infected cell frequencies after long-term antiretroviral therapy. *PLoS Pathog.* *13*, e1006629. <https://doi.org/10.1371/journal.ppat.1006629>.
33. Mok, H.P., Norton, N.J., Hirst, J.C., Fun, A., Bandara, M., Wills, M.R., and Lever, A.M.L. (2018). No evidence of ongoing evolution in replication competent latent HIV-1 in a patient followed up for two years. *Sci. Rep.* *8*, 2639. <https://doi.org/10.1038/s41598-018-20682-w>.
34. Simonetti, F.R., Sobolewski, M.D., Fyne, E., Shao, W., Spindler, J., Hattori, J., Anderson, E.M., Watters, S.A., Hill, S., Wu, X., et al. (2016). Clonally expanded CD4+ T cells can produce infectious HIV-1 in vivo. *Proc. Natl. Acad. Sci. USA* *113*, 1883–1888. <https://doi.org/10.1073/pnas.1522675113>.
35. Van Zyl, G.U., Katusiime, M.G., Wiegand, A., McManus, W.R., Bale, M.J., Halvas, E.K., Luke, B., Boltz, V.F., Spindler, J., Laughton, B., et al. (2017). No evidence of HIV replication in children on antiretroviral therapy. *J. Clin. Invest.* *127*, 3827–3834. <https://doi.org/10.1172/JCI94582>.
36. Vancollie, L., Hebberecht, L., Dauwe, K., Demecheleer, E., Dinakis, S., Vaneechoutte, D., Mortier, V., and Verhofstede, C. (2017). Longitudinal sequencing of HIV-1 infected patients with low-level viremia for years while on ART shows no indications for genetic evolution of the virus. *Virology* *510*, 185–193. <https://doi.org/10.1016/j.virol.2017.07.010>.
37. Imamichi, H., Smith, M., Adelsberger, J.W., Izumi, T., Scrimieri, F., Sherman, B.T., Rehm, C.A., Imamichi, T., Pau, A., Catalfamo, M., et al. (2020). Defective HIV-1 proviruses produce viral proteins. *Proc. Natl. Acad. Sci. USA* *117*, 3704–3710. <https://doi.org/10.1073/pnas.1917876117>.
38. Pollack, R.A., Jones, R.B., Perteau, M., Bruner, K.M., Martin, A.R., Thomas, A.S., Capoferri, A.A., Beg, S.A., Huang, S.-H., Karandish, S., et al. (2017). Defective HIV-1 proviruses are expressed and can be recognized by cytotoxic T lymphocytes, which shape the proviral landscape. *Cell Host Microbe* *21*, 494–506.e4. <https://doi.org/10.1016/j.chom.2017.03.008>.
39. Simonetti, F.R., Zhang, H., Soroosh, G.P., Duan, J., Rhodehouse, K., Hill, A.L., Beg, S.A., McCormick, K., Raymond, H.E., Nobles, C.L., et al. (2021). Antigen-driven clonal selection shapes the persistence of HIV-1-infected CD4+ T cells in vivo. *J. Clin. Invest.* *131*, e145254. <https://doi.org/10.1172/JCI145254>.
40. Wiegand, A., Spindler, J., Hong, F.F., Shao, W., Cyktor, J.C., Cillo, A.R., Halvas, E.K., Coffin, J.M., Mellors, J.W., and Kearney, M.F. (2017). Single-cell analysis of HIV-1 transcriptional activity reveals expression of proviruses in expanded clones during ART. *Proc. Natl. Acad. Sci. USA* *114*, E3659–E3668. <https://doi.org/10.1073/pnas.1617961114>.
41. Moron-Lopez, S., Xie, G., Kim, P., Siegel, D.A., Lee, S., Wong, J.K., Price, J.C., Elnachef, N., Greenblatt, R.M., Tien, P.C., et al. (2021). Tissue-specific differences in HIV DNA levels and mechanisms that govern HIV transcription in blood, gut, genital tract and liver in ART-treated women. *J. Int. AIDS Soc.* *24*, e25738. <https://doi.org/10.1002/jia2.25738>.
42. Karn, J., and Stoltzfus, C.M. (2012). Transcriptional and posttranscriptional regulation of HIV-1 gene expression. *Cold Spring Harb. Perspect. Med.* *2*, a006916. <https://doi.org/10.1101/cshperspect.a006916>.
43. Porichis, F., Hart, M.G., Griesbeck, M., Everett, H.L., Hassan, M., Baxter, A.E., Lindqvist, M., Miller, S.M., Soghoian, D.Z., Kavanagh, D.G., et al. (2014). High-throughput detection of miRNAs and gene-specific mRNA at the single-cell level by flow cytometry. *Nat. Commun.* *5*, 5641. <https://doi.org/10.1038/ncomms6641>.
44. Dufour, C., Richard, C., Pardons, M., Massanella, M., Ackaoui, A., Murrell, B., Routy, B., Thomas, R., Routy, J.P., Fromentin, R., and Chomont, N. (2023). Phenotypic characterization of single CD4+ T cells harboring genetically intact and inducible HIV genomes. *Nat. Commun.* *14*, 1115. <https://doi.org/10.1038/s41467-023-36772-x>.
45. Strazza, M., and Mor, A. (2017). Consider the chemokines: a review of the interplay between chemokines and T cell subset function. *Discov. Med.* *24*, 31–39.
46. Barczyk, M., Carracedo, S., and Gullberg, D. (2010). Integrins. *Cell Tissue Res.* *339*, 269–280. <https://doi.org/10.1007/s00441-009-0834-6>.
47. Becht, E., McInnes, L., Healy, J., Dutertre, C.-A., Kwok, I.W.H., Ng, L.G., Ginhoux, F., and Newell, E.W. (2018). Dimensionality reduction for

- visualizing single-cell data using UMAP. *Nat. Biotechnol.* **37**, 38–44. <https://doi.org/10.1038/nbt.4314>.
48. Levine, J.H., Simonds, E.F., Bendall, S.C., Davis, K.L., Amir el, A.D., Tadmor, M.D., Litvin, O., Fienberg, H.G., Jager, A., Zunder, E.R., et al. (2015). Data-driven phenotypic dissection of AML reveals progenitor-like cells that correlate with prognosis. *Cell* **162**, 184–197. <https://doi.org/10.1016/j.cell.2015.05.047>.
 49. Abdel-Mohsen, M., Kuri-Cervantes, L., Grau-Exposito, J., Spivak, A.M., Nell, R.A., Tomescu, C., Vadrevu, S.K., Giron, L.B., Serra-Peinado, C., Genescà, M., et al. (2018). CD32 is expressed on cells with transcriptionally active HIV but does not enrich for HIV DNA in resting T cells. *Sci. Transl. Med.* **10**, eaar6759. <https://doi.org/10.1126/scitranslmed.aa6759>.
 50. Morou, A., Brunet-Ratnasingham, E., Dubé, M., Charlebois, R., Mercier, E., Darko, S., Brassard, N., Nganou-Makamdop, K., Arumugam, S., Gendron-Lepage, G., et al. (2019). Altered differentiation is central to HIV-specific CD4⁺ T cell dysfunction in progressive disease. *Nat. Immunol.* **20**, 1059–1070. <https://doi.org/10.1038/s41590-019-0418-x>.
 51. Niessi, J., Baxter, A.E., Mendoza, P., Jankovic, M., Cohen, Y.Z., Butler, A.L., Lu, C.-L., Dubé, M., Shimeliovich, I., Gruell, H., et al. (2020). Combination anti-HIV-1 antibody therapy is associated with increased virus-specific T cell immunity. *Nat. Med.* **26**, 222–227. <https://doi.org/10.1038/s41591-019-0747-1>.
 52. Nayrac, M., Dubé, M., Sannier, G., Nicolas, A., Marchitto, L., Tastet, O., Tauzin, A., Brassard, N., Lima-Barbosa, R., Beaudoin-Bussièrès, G., et al. (2022). Temporal associations of B and T cell immunity with robust vaccine responsiveness in a 16-week interval BNT162b2 regimen. *Cell Rep.* **39**, 111013. <https://doi.org/10.1016/j.celrep.2022.111013>.
 53. Becattini, S., Latorre, D., Mele, F., Foglierini, M., De Gregorio, C., Cassotta, A., Fernandez, B., Kelderman, S., Schumacher, T.N., Corti, D., et al. (2015). T cell immunity. Functional heterogeneity of human memory CD4⁺ T cell clones primed by pathogens or vaccines. *Science* **347**, 400–406. <https://doi.org/10.1126/science.1260668>.
 54. Morita, R., Schmitt, N., Bentebibel, S.-E., Ranganathan, R., Bourdery, L., Zurawski, G., Foucat, E., Dullaers, M., Oh, S., Sabzghabaei, N., et al. (2011). Human blood CXCR5(+)CD4(+) T cells are counterparts of T follicular cells and contain specific subsets that differentially support antibody secretion. *Immunity* **34**, 108–121. <https://doi.org/10.1016/j.immuni.2010.12.012>.
 55. Grau-Expósito, J., Luque-Ballesteros, L., Navarro, J., Curran, A., Burgos, J., Ribera, E., Torrella, A., Planas, B., Badía, R., Martin-Castillo, M., et al. (2019). Latency reversal agents affect differently the latent reservoir present in distinct CD4⁺ T subpopulations. *PLoS Pathog.* **15**, e1007991. <https://doi.org/10.1371/journal.ppat.1007991>.
 56. Sodroski, J., Rosen, C., Wong-Staal, F., Salahuddin, S.Z., Popovic, M., Arya, S., Gallo, R.C., and Haseltine, W.A. (1985). trans-acting transcriptional regulation of human T-cell leukemia virus type III long terminal repeat. *Science* **227**, 171–173. <https://doi.org/10.1126/science.2981427>.
 57. Ho, Y.C., Shan, L., Hosmane, N.N., Wang, J., Laskey, S.B., Rosenbloom, D.I., Lai, J., Blankson, J.N., Siliciano, J.D., and Siliciano, R.F. (2013). Replication-competent noninduced proviruses in the latent reservoir increase barrier to HIV-1 cure. *Cell* **155**, 540–551. <https://doi.org/10.1016/j.cell.2013.09.020>.
 58. Einkauf, K.B., Lee, G.Q., Gao, C., Sharaf, R., Sun, X., Hua, S., Chen, S.M., Jiang, C., Lian, X., Chowdhury, F.Z., et al. (2019). Intact HIV-1 proviruses accumulate at distinct chromosomal positions during prolonged antiretroviral therapy. *J. Clin. Invest.* **129**, 988–998. <https://doi.org/10.1172/JCI124291>.
 59. Kwon, K.J., Timmons, A.E., SenGupta, S., Simonetti, F.R., Zhang, H., Hoh, R., Deeks, S.G., Siliciano, J.D., and Siliciano, R.F. (2020). Different human resting memory CD4⁺ T cell subsets show similar low inducibility of latent HIV-1 proviruses. *Sci. Transl. Med.* **12**, eaax6795. <https://doi.org/10.1126/scitranslmed.aax6795>.
 60. Clark, I.C., Mudvari, P., Thaploo, S., Smith, S., Abu-Laban, M., Hamouda, M., Theberge, M., Shah, S., Ko, S.H., Pérez, L., et al. (2023). HIV silencing and cell survival signatures in infected T cell reservoirs. *Nature* **614**, 318–325. <https://doi.org/10.1038/s41586-022-05556-6>.
 61. Sun, W., Gao, C., Hartana, C.A., Osborn, M.R., Einkauf, K.B., Lian, X., Bone, B., Bonheur, N., Chun, T.W., Rosenberg, E.S., et al. (2023). Phenotypic signatures of immune selection in HIV-1 reservoir cells. *Nature* **614**, 309–317. <https://doi.org/10.1038/s41586-022-05538-8>.
 62. Chomont, N., El-Far, M., Ancuta, P., Trautmann, L., Procopio, F.A., Yassine-Diab, B., Boucher, G., Boulassel, M.R., Ghattas, G., Brechley, J.M., et al. (2009). HIV reservoir size and persistence are driven by T cell survival and homeostatic proliferation. *Nat. Med.* **15**, 893–900. <https://doi.org/10.1038/nm.1972>.
 63. Wang, Z., Gurule, E.E., Brennan, T.P., Gerold, J.M., Kwon, K.J., Hosmane, N.N., Kumar, M.R., Beg, S.A., Capoferri, A.A., Ray, S.C., et al. (2018). Expanded cellular clones carrying replication-competent HIV-1 persist, wax, and wane. *Proc. Natl. Acad. Sci. USA* **115**, E2575–E2584. <https://doi.org/10.1073/pnas.1720665115>.
 64. Hosmane, N.N., Kwon, K.J., Bruner, K.M., Capoferri, A.A., Beg, S., Rosenbloom, D.I., Keele, B.F., Ho, Y.-C., Siliciano, J.D., and Siliciano, R.F. (2017). Proliferation of latently infected CD4⁺ T cells carrying replication-competent HIV-1: potential role in latent reservoir dynamics. *J. Exp. Med.* **214**, 959–972. <https://doi.org/10.1084/jem.20170193>.
 65. Mendoza, P., Jackson, J.R., Oliveira, T.Y., Gaebler, C., Ramos, V., Caskey, M., Jankovic, M., Nussenzweig, M.C., and Cohn, L.B. (2020). Antigen-responsive CD4⁺ T cell clones contribute to the HIV-1 latent reservoir. *J. Exp. Med.* **217**, e20200051. <https://doi.org/10.1084/jem.20200051>.
 66. Buzon, M.J., Sun, H., Li, C., Shaw, A., Seiss, K., Ouyang, Z., Martin-Gayo, E., Leng, J., Henrich, T.J., Li, J.Z., et al. (2014). HIV-1 persistence in CD4⁺ T cells with stem cell-like properties. *Nat. Med.* **20**, 139–142. <https://doi.org/10.1038/nm.3445>.
 67. Lee, G.Q., Orlova-Fink, N., Einkauf, K., Chowdhury, F.Z., Sun, X., Harrington, S., Kuo, H.-H., Hua, S., Chen, H.-R., Ouyang, Z., et al. (2017). Clonal expansion of genome-intact HIV-1 in functionally polarized Th1 CD4⁺ T cells. *J. Clin. Invest.* **127**, 2689–2696. <https://doi.org/10.1172/JCI93289>.
 68. Jaafoura, S., de Goër de Herve, M.G., Hernandez-Vargas, E.A., Hendel-Chavez, H., Abdoh, M., Mateo, M.C., Krzysiek, R., Merad, M., Seng, R., Tardieu, M., et al. (2014). Progressive contraction of the latent HIV reservoir around a core of less-differentiated CD4⁺ memory T cells. *Nat. Commun.* **5**, 5407. <https://doi.org/10.1038/ncomms6407>.
 69. Gosselin, A., Wiche Salinas, T.R., Planas, D., Wacleche, V.S., Zhang, Y., Fromentin, R., Chomont, N., Cohen, É.A., Shacklett, B., Mehraj, V., et al. (2017). HIV persists in CCR6+CD4⁺ T cells from colon and blood during antiretroviral therapy. *AIDS* **31**, 35–48. <https://doi.org/10.1097/QAD.0000000000001309>.
 70. Pardons, M., Fromentin, R., Pagliuzza, A., Routy, J.P., and Chomont, N. (2019). Latency-reversing agents induce differential responses in distinct memory CD4⁺ T cell subsets in individuals on antiretroviral therapy. *Cell Rep.* **29**, 2783–2795.e5. <https://doi.org/10.1016/j.celrep.2019.10.101>.
 71. Banga, R., Procopio, F.A., Ruggiero, A., Noto, A., Ohmiti, K., Cavassini, M., Corpataux, J.-M., Paxton, W.A., Pollakis, G., and Perreau, M. (2018). Blood CXCR3⁺ CD4⁺ T cells are enriched in inducible replication competent HIV in aviremic antiretroviral therapy-treated individuals. *Front. Immunol.* **9**, 144. <https://doi.org/10.3389/fimmu.2018.00144>.
 72. Perreau, M., Savoye, A.L., De Crignis, E., Corpataux, J.M., Cubas, R., Haddad, E.K., De Leval, L., Graziosi, C., and Pantaleo, G. (2013). Follicular helper T cells serve as the major CD4⁺ T cell compartment for HIV-1 infection, replication, and production. *J. Exp. Med.* **210**, 143–156. <https://doi.org/10.1084/jem.20121932>.
 73. Monteiro, P., Gosselin, A., Wacleche, V.S., El-Far, M., Said, E.A., Kared, H., Grandvaux, N., Boulassel, M.R., Routy, J.-P., and Ancuta, P. (2011). Memory CCR6+CD4⁺ T cells are preferential targets for productive HIV type 1 infection regardless of their expression of integrin β7. *J. Immunol.* **186**, 4618–4630. <https://doi.org/10.4049/jimmunol.1004151>.

74. Estes, J.D., Kityo, C., Ssali, F., Swainson, L., Makamdop, K.N., Del Prete, G.Q., Deeks, S.G., Luciw, P.A., Chipman, J.G., Beilman, G.J., et al. (2017). Defining total-body AIDS-virus burden with implications for curative strategies. *Nat. Med.* **23**, 1271–1276. <https://doi.org/10.1038/nm.4411>.
75. Telwatte, S., Lee, S., Somsouk, M., Hatano, H., Baker, C., Kaiser, P., Kim, P., Chen, T.H., Milush, J., Hunt, P.W., et al. (2018). Gut and blood differ in constitutive blocks to HIV transcription, suggesting tissue-specific differences in the mechanisms that govern HIV latency. *PLoS Pathog.* **14**, e1007357. <https://doi.org/10.1371/journal.ppat.1007357>.
76. Stevenson, E.M., Ward, A.R., Truong, R., Thomas, A.S., Huang, S.-H., Dilling, T.R., Terry, S., Bui, J.K., Mota, T.M., Danesh, A., et al. (2021). HIV-specific T cell responses reflect substantive in vivo interactions with antigen despite long-term therapy. *JCI Insight* **6**, e142640. <https://doi.org/10.1172/jci.insight.142640>.
77. Huang, S.H., Ren, Y., Thomas, A.S., Chan, D., Mueller, S., Ward, A.R., Patel, S., Bollard, C.M., Cruz, C.R., Karandish, S., et al. (2018). Latent HIV reservoirs exhibit inherent resistance to elimination by CD8+ T cells. *J. Clin. Invest.* **128**, 876–889. <https://doi.org/10.1172/JCI97555>.
78. Ren, Y., Huang, S.H., Patel, S., Alberto, W.D.C., Magat, D., Ahimovic, D., Macedo, A.B., Durga, R., Chan, D., Zale, E., et al. (2020). BCL-2 antagonism sensitizes cytotoxic T cell-resistant HIV reservoirs to elimination ex vivo. *J. Clin. Invest.* **130**, 2542–2559. <https://doi.org/10.1172/JCI132374>.
79. Jiang, S., Chan, C.N., Rovira-Clavé, X., Chen, H., Bai, Y., Zhu, B., McCaffrey, E., Greenwald, N.F., Liu, C., Barlow, G.L., et al. (2022). Combined protein and nucleic acid imaging reveals virus-dependent B cell and macrophage immunosuppression of tissue microenvironments. *Immunity* **55**, 1118–1134.e8. <https://doi.org/10.1016/j.immuni.2022.03.020>.
80. Imamichi, H., Dewar, R.L., Adelsberger, J.W., Rehm, C.A., O'Doherty, U., Paxinos, E.E., Fauci, A.S., and Lane, H.C. (2016). Defective HIV-1 proviruses produce novel protein-coding RNA species in HIV-infected patients on combination antiretroviral therapy. *Proc. Natl. Acad. Sci. USA* **113**, 8783–8788. <https://doi.org/10.1073/pnas.1609057113>.
81. Einkauf, K.B., Osborn, M.R., Gao, C., Sun, W., Sun, X., Lian, X., Parsons, E.M., Gladkov, G.T., Seiger, K.W., Blackmer, J.E., et al. (2022). Parallel analysis of transcription, integration, and sequence of single HIV-1 proviruses. *Cell* **185**, 266–282.e15. <https://doi.org/10.1016/j.cell.2021.12.011>.
82. Vandergeeten, C., Fromentin, R., Merlini, E., Lawani, M.B., DaFonseca, S., Bakeman, W., McNulty, A., Ramgopal, M., Michael, N., Kim, J.H., et al. (2014). Cross-clade ultrasensitive PCR-based assays to measure HIV persistence in large-cohort studies. *J. Virol.* **88**, 12385–12396. <https://doi.org/10.1128/JVI.00609-14>.
83. Baxter, A.E., Niessl, J., Morou, A., and Kaufmann, D.E. (2017). RNA flow cytometric FISH for investigations into HIV immunology, vaccination and cure strategies. *AIDS Res. Ther.* **14**, 40. <https://doi.org/10.1186/s12981-017-0171-x>.
84. Dubé, M., and Kaufmann, D.E. (2022). Single-cell multiparametric analysis of rare HIV-infected cells identified by duplexed RNAflow-FISH. *Methods Mol. Biol.* **2407**, 291–313. https://doi.org/10.1007/978-1-0716-1871-4_20.
85. Brunet-Ratnasingham, E., Morou, A., Dubé, M., Niessl, J., Baxter, A.E., Tastet, O., Brassard, N., Ortega-Delgado, G., Charlebois, R., Freeman, G.J., et al. (2022). Immune checkpoint expression on HIV-specific CD4+ T cells and response to their blockade are dependent on lineage and function. *EBioMedicine* **84**, 104254. <https://doi.org/10.1016/j.ebiom.2022.104254>.
86. Quintelier, K., Couckuyt, A., Emmaneel, A., Aerts, J., Saeys, Y., and Van Gassen, S. (2021). Analyzing high-dimensional cytometry data using FlowSOM. *Nat. Protoc.* **16**, 3775–3801. <https://doi.org/10.1038/s41596-021-00550-0>.

STAR★METHODS

KEY RESOURCES TABLE

REAGENT or RESOURCE	SOURCE	IDENTIFIER
Antibodies		
UCHT1 (BUV395) [Human anti-CD3]	BD Biosciences	Cat#563546; Lot:9058566; RRID:AB_2744387
UCHT1 (BUV496) [Human anti-CD3]	BD Biosciences	Cat#612941; Lot:1022424; RRID:AB_2870222
L200 (BV711) [Human anti-CD4]	BD Biosciences	Cat#563913; Lot:03000025; RRID:AB_2738484
SK3 (BB630) [Human anti-CD4]	BD Biosciences	Cat#624294 CUSTOM; Lot:0289566
RPA-T8 (BV570) [Human anti-CD8]	Biolegend	Cat#301037; Lot:B281322; RRID:AB_10933259
M5E2 (BUV805) [Human anti-CD14]	BD Biosciences	Cat#612902; Lot:0262150; RRID:AB_2870189
M5E2 (BV480) [Human anti-CD14]	BD Biosciences	Cat#746304; Lot : 9133961; RRID:AB_2743629
3G8 (BV650) [Human anti-CD16]	Biolegend	Cat#302042; Lot:B323847; RRID:AB_2563801
HIB19 (APC-eFluor780) [Human anti-CD19]	Thermo Fisher Scientific	Cat#47-0199; Lot:2145095; RRID:AB_1582231
HIB19 (BV480) [Human anti-CD19]	BD Biosciences	Cat#746457; Lot:1021649; RRID:AB_2743759
HI100 (PerCP Cy5.5) [Human anti-CD45RA]	BD Biosciences	Cat#563429; Lot:8332746; RRID:AB_2738199
NCAM16.2 (BUV737) [Human anti-CD56]	BD Biosciences	Cat#564448; Lot:8288818; RRID:AB_2744432
FN50 (PerCP-eFluor710) [Human anti-CD69]	Thermo Fisher Scientific	Cat#46-0699-42; Lot:1920361; RRID:AB_2573694
FN50 (BV650) [Human anti-CD69]	Biolegend	Cat# 310934; Lot:B303462; RRID:AB_2563158
H4A3 (BV786) [Human anti-CD107A]	BD Biosciences	Cat#563869; Lot:8144866; RRID:AB_2738458
ACT35 (APC) [Human anti-CD134 (OX40)]	BD Biosciences	Cat#563473; Lot:1015537; RRID:AB_2738230
4B4-1 (PE-Dazzle 594) [Human anti-CD137 (4-1BB)]	Biolegend	Cat# 309826; Lot:B253152; RRID:AB_2566260
TRAP1 (BV421) [Human anti-CD154 (CD40L)]	BD Biosciences	Cat#563886; Lot:9037850; RRID:AB_2738466
TRAP1 (PE) [Human anti-CD154 (CD40L)]	BD Biosciences	Cat#555700; Lot:7086896; RRID:AB_396050
J25D4 (BV421) [Human anti-CD185 (CXCR5)]	Biolegend	Cat# 356920; Lot:B325837; RRID:AB_2562303
B27 (PECy7) [Human anti-IFN- γ]	BD Biosciences	Cat#557643; Lot:8256597; RRID:AB_396760
MQ1-17H12 (PE-Dazzle594) [Human anti-IL-2]	Biolegend	Cat#500344; Lot:B2261476; RRID:AB_2564091
JES3-9D7 (PE) [Human anti-IL-10]	BD Biosciences	Cat#554498; Lot:8198773; RRID:AB_395434
eBio64CAP17 (eFluor660) [Human anti-IL-17A]	Thermo Fisher Scientific	Cat#50-7179-42; Lot:2151998; RRID:AB_11149126
Mab11 (Alexa Fluor 488) [Human anti-TNF- α]	Biolegend	Cat#502915; Lot:B285221; RRID:AB_493121
Mab11 (APC) [Human anti-TNF- α]	BD Biosciences	Cat#562084 Lot: 0350627 RRID:AB_10893226
LIVE/DEAD Fixable dead cell	Thermo Fisher Scientific	L34960
Biological samples		
SARS-CoV-2 naïve donor blood samples	N/A	N/A
SARS-CoV-2 prior infection donor blood samples	N/A	N/A
Chemicals, peptides, and recombinant proteins		
PepMix™ SARS-CoV-2 (Spike Glycoprotein)	JPT	Cat#PM-WCPV-S-1
Staphylococcal Enterotoxin B (SEB)	Toxin technology	Cat#BT202
Software and algorithms		
Flow Jo v10.8.0	Flow Jo	https://www.flowjo.com
GraphPad Prism v8.4.1	GraphPad	https://www.graphpad.com
R studio v4.1.0	R studio	https://rstudio.com
R codes scripted	Github	https://github.com/otastet/Nayrac_et_al
Deposited data		
Sequence number		GenBank accession number
PWH9_L3p1_A2_C0_434		GenBank : OR105517

(Continued on next page)

Continued

REAGENT or RESOURCE	SOURCE	IDENTIFIER
PWH5_L2p3_A9_PCR2_G9_C0_455		GenBank : OR105518
PWH5_L2p2_F6_C0_290		GenBank : OR105519
PWH5_L2p2_E10_C0_386		GenBank : OR105520
PWH5_L2p2_E9_PCR2_E9_C0_454		GenBank : OR105521
PWH5_L2p2_E3_C0_463		GenBank : OR105522
PWH5_L2p2_D10_C0_432		GenBank : OR105523
PWH5_L2p1_C12_PCR2_C12_C0_440		GenBank : OR105524
PWH5_L2p1_C10_C0_473		GenBank : OR105525
PWH5_L2p1_C6_PCR2_C6_C0_474		GenBank : OR105526
PWH5_L2p1_B7_C0_325		GenBank : OR105527
PWH5_L2p1_B4_C0_391		GenBank : OR105528
PWH5_L2p1_A10_C0_341		GenBank : OR105529
PWH3_L1p3_B11_C0_402		GenBank : OR105530
PWH3_L1p3_A5_C0_417		GenBank : OR105531
PWH3_L1p3_A3_C0_418		GenBank : OR105532
PWH3_L1p2_H12_C0_390		GenBank : OR105533
PWH3_L1p2_H4_C0_378		GenBank : OR105534
PWH3_L1p2_G5_C0_392		GenBank : OR105535
PWH3_L1p2_F2_C0_412		GenBank : OR105536
PWH3_L1p2_D12_C0_394		GenBank : OR105537
PWH3_L1p2_D3_C0_399		GenBank : OR105538
PWH3_L1p2_C11_C0_329		GenBank : OR105539
PWH3_L1p2_C8_C0_432		GenBank : OR105540
PWH3_L1p2_C2_C0_366		GenBank : OR105541
PWH3_L1p2_B10_C0_371		GenBank : OR105542
PWH3_L1p2_A10_C0_42		GenBank : OR105543
PWH3_L1p1_H7_C0_263		GenBank : OR105544
PWH3_L1p1_G3_C0_365_inversion		GenBank : OR105545
PWH3_L1p1_G1_C0_430		GenBank : OR105546
PWH3_L1p1_F7_C0_350		GenBank : OR105547
PWH3_L1p1_F3_C0_418_inversion		GenBank : OR105548
PWH3_L1p1_E12_C0_413		GenBank : OR105549
PWH3_L1p1_E10_C0_430		GenBank : OR105550
PWH3_L1p1_D9_C0_436		GenBank : OR105551
PWH3_L1p1_D8_C0_366		GenBank : OR105552
PWH3_L1p1_C6_C0_390		GenBank : OR105553
PWH3_L1p1_B5_C0_422		GenBank : OR105554
PWH3_L1p1_B4_C0_392		GenBank : OR105555
PWH3_L1p1_A6_C0_433		GenBank : OR105556

RESOURCE AVAILABILITY

Lead contact

Further information and requests for resources and reagents should be directed to and fulfilled by the lead contact, Daniel E. Kaufmann (daniel.kaufmann@chuv.ch).

Materials availability

All unique reagents generated during this study are available from the [lead contact](#) upon a material transfer agreement (MTA).

Data and code availability

- The published article includes all datasets generated and analyzed for this study.

- We developed R codes scripted to perform unsupervised analysis of B and T cells from SARS-CoV-2 naive and previously infected individuals. All original codes have been deposited at Github and are publicly available as of publication. URL link is listed in the [key resources table](#).
- Gen Bank accession codes for single-cell HIV sequences are provided in [Table S5](#).
- Any additional information required to reanalyze the data reported in this paper is available from the [lead contact](#) Author upon request (daniel.kaufmann@chuv.ch).

EXPERIMENTAL MODEL AND SUBJECT DETAILS

Ethics Statement

All work was conducted following the Declaration of Helsinki regarding informed consent and approval by an appropriate institutional board. Blood samples were obtained from donors who consented to participate in this research project at CHUM (CE13.019).

Participants and Samples

Leukaphereses were obtained from study participants at the McGill University Health Centre, Montreal, Quebec, Canada, and at Centre Hospitalier de l'Université de Montréal (CHUM), Quebec, Canada. The study was approved by the respective IRBs, and written informed consent was obtained from all participants before enrolment. Uninfected donors (UD) are free of HIV-1 infection. Treated subjects (ART) were on antiretrovirals with controlled viremia (<40 vRNA copies/mL). Participants' characteristics are summarized in [Table S1](#). PBMCs were isolated by the Ficoll density gradient method and stored in liquid nitrogen until use.

METHOD DETAILS

Total and integrated DNA measures

The quantifications of total and integrated HIV-1 DNA were determined as previously described.⁸²

CD4⁺ T cell preparation for HIV reservoir profiling

Frozen PBMCs were thawed in cold heat-inactivated Fetal Calf Serum (FCS; Seradigm) before CD4⁺ T-cells isolation. CD4⁺ T-cells were isolated by negative magnetic bead selection (StemCell). Purified CD4⁺ T cells were resuspended at 2x10⁶/mL in RPMI (Gibco by Life Technologies) supplemented with penicillin/streptomycin (Gibco by Life Technologies), 10% heat-inactivated FCS, and ARV (Maraviroc [10μM] + Raltegravir [0.2μM] + Tenofovir [5μM] + Emtricitabine [10μM] and seeded into 24-well plates (all obtained through the NIH AIDS Reagent Program). After a rest of 2h at 37°C, 5% CO₂, the cells were either left unstimulated or stimulated with PMA/ionomycin (162 nM PMA, 705 nM Ionomycin, Sigma) for 15-h. Alternatively, cells were either left unstimulated or stimulated with 30nM panobinostat (Selleck Chem) complemented with 25nM ingenol-3-angelate (Sigma). 10-15x10⁶ purified CD4⁺ T-cells were used per condition.

HIV-1 RNAflow-FISH assay

The HIV-1 RNAflow-FISH assay was performed as previously described and per the manufacturer's instructions.^{8,9,83,84} All buffers and fixation reagents were provided with the kit, except flow cytometry staining (1% FCS/PBS). Briefly, negatively purified CD4⁺ T cells were harvested after stimulation and stained first with Fixable Viability Dye (20 min, 4°C, Fixable LiveDead, eBioscience), FcR blocked, followed by a mix containing a brilliant stain buffer (BD Biosciences) and the surface markers for memory (CD45RA) and gut homing (integrin β7, CD103) phenotype, activation markers (HLA-DR, ICOS) and inhibitory checkpoint (PD-1) as well as for CD4⁺ T-cells detection (CD3 and CD4) and CD8/NK/B cells and macrophages exclusions (CD8, CD56, CD14, CD19, CD16) (30 min, 4°C). Anti-CXCR5, CCR6, CCR4, CXCR3, CCR7 and CD27 were added at 37°C 15 min before stimulation to stain chemokine receptors. Samples were fixed, permeabilized, and labeled intracellularly for the activation marker Ki67 and the structural HIV-1 p24 protein with the anti-p24 clone KC57 antibody (30 min RT followed by 30 min 4°C, Beckman Coulter). HIV-1 RNA probing was performed using the PrimeFlow RNA Assay (ThermoFisher). HIV-1 RNA was labeled using HIV-1 *gag*RNA (20 pairs of "ZZ" probes), HIV-1 exonRNA (21 pairs of "ZZ" probes), and HIV-1 *pol*RNA (6 pairs of "ZZ" probes) probe sets, all designed based on a consensus B HIV sequence. The probes were diluted 1:5 in diluent and hybridized to the target mRNAs for 2 hrs at 40°C. Samples were washed to remove excess probes and stored overnight in the presence of RNAsin. Signal amplification was achieved by sequential 1.5 hr at 40°C incubations with the pre-amplification and amplification mix. Amplified mRNAs were labeled with fluorescently tagged probes for 1h at 40°C. The complete list of antibodies used is presented in [Table S2](#) for the panel. Samples were acquired on a FACSymphony™ (BD Biosciences) and analyzed using FlowJo (BD, V10.8.0). Unspecific binding of the fluorescent-labeled branched probe in the multiplex kit can lead to a low level of false-positive background noise, which, if present, is detected across all the four channels corresponding to the types of labeled probes (AF488, AF594, AF647, AF750). To decrease background noise, we thus left the AF594 channel vacant and excluded false-positive events based on fluorescence in this channel before further gating. Gates were set on the HIV-uninfected donor control or unstimulated control where appropriate (See gating strategy, [Figure S1](#)). Because HIV

infection can downregulate CD4, and because RNAflow-FISH was performed on negatively purified CD4⁺ T cells, no CD4 gating was applied during the analysis. To calculate the frequency of vRNA⁺ cells per 10⁶, we directly used as the denominator the counts of cells after the dump exclusion gating.

Limiting Dilution Assay

CD4⁺ T cells were isolated from PBMC by negative selection using magnetic beads (StemCell). After 18h hours of resting, the cells were distributed in limiting dilutions in a 96-well plate, with 11 replicates for each of the following dilutions: 100000, 50000, 16667, 5556 cells per well. The plate was spun at 300xg for 5 min, and the cell pellets were resuspended in Lysis/Binding solution (Magmax 96 Total RNA Isolation Kit, Life Technologies). Ca-RNA was extracted in plate using Magmax 96 Total RNA Isolation Kit (Life Technologies) following manufacturer's instructions. A nested RT-qPCR was performed to amplify LTRgag caRNA for all the replicates of each dilution. A 1-step RT and pre-amplification step was carried out by adding 9uL of extracted RNA (corresponding to 18000, 9000, 3000 and 1000 cell-equivalent depending on the dilution) to a mix of 6.25uL of Taq-1-Path master mix (Applied Biosystems) and 800 nM of LTRgag specific primers.⁸² The PCR cycles were as follow: 15 min at 53°C, 2 min at 95°C, and 18 cycles of 15 s at 95°C and 2 min at 60°C. The pre-amplified product was used to perform a real-time PCR as previously described.⁸² Positive wells at each dilution were counted and the maximum likelihood method was used to calculate the frequency of cells with LTRgag RNA (<http://bioinf.wehi.edu.au/software/elda>).

Microscopy

CD4⁺ T cells from one uninfected and one ART-treated PWH were isolated, rested 2h and reactivated with LRA (30nM panobinostat (Selleck Chem) and 25nM ingenol-3-angelate (Sigma) for 15h. Cells were collected and stained with a viability dye (Fixable Live/Dead (eF780, eBioscience) and with antibodies against surface CD8, CD14 and CD19 (BV510). mRNA Flow FISH was performed as described above and sorted with a BD FACS Aria. Single, CD8/14/19- T cells were sorted into two populations based on *exonRNA* AF647 and *gagRNA* AF488 staining (Figure S2H). Prior to microscopy analysis, nuclei were stained (DAPI, 1ng/ml, 2 min RT), directly loaded in ibidi μ -Slide VI 0.4 microscopy chambers and imaged using a Zeiss Axio Observer.Z1 inverted spinning disk confocal microscope coupled to an Evolve camera (EMCCD, 512x512, 16bit, 1.2x adapter) and ZEN blue software (version 2012). Images were acquired with an alpha Plan-Apochromat 100x/1.46 Oil DIC (UV) M27 objective. Excitation was performed with a 639nm, a 488nm and a 405nm solid state lasers for AF647, AF488 and DAPI respectively. Emission was collected through Chroma filters: DBP 527/54 + 645/60 for AF488 and AF647 and a DBP 460/30 + 590/30 for DAPI. Z-stacks were performed to image whole cells with a step size of 0.220 μ m. Final resolution is 0.133 μ m x 0.133 μ m x 0.220 μ m in xyz. Brightfield images were acquired with the same modalities but with a LED white light illumination, no filter and without Zstack. Fiji was used for all image analysis and facilitate counting. DAPI staining was used to define the nuclear compartment and the "Find Maxima" command was used to identify and count HIV RNA foci.

Single-cell near full-length PCR

Unstimulated CD4⁺ T-cells from 3 ART-treated donors were stained in HIV-1 RNAflow-FISH assays using HIV-1 *gagRNA*, *exonRNA*, and *polRNA* probes. Single vRNA⁺ cells were sorted in 12-wells PCR strips containing 8 μ L of DirectPCR Lysis Reagent (Viagen Biotech) with 0.4mg/mL proteinase K. The PCR strips were subsequently incubated at 55°C for 1h for cell lysis followed by 15 min at 85°C to inactivate proteinase K. Single sorted cells were subjected to near full-length amplification using a modified FLIPS assay.^{9,44} HIV-1 genomes were pre-amplified using Invitrogen Platinum SuperFi II MasterMix with 0.2 μ M of each primer.⁴⁴ 30 μ L of PCR mix was added directly to the lysed cells for a 25 cycles 3-steps PCR protocol as recommended by the manufacturer. The pre-amplified products were diluted 1:3 with Tris-HCl 0.5 μ M pH 8.0 and subjected to a nested PCR with 5 μ L of pre-amplified product, 2X of Platinum SuperFi II PCR Mix and 0.2 μ M of each primer in a 30 μ L final volume.⁴⁴ This second amplification consists in 30 cycles and follows the manufacturer's instructions. The length of the sequences obtained were verified on a 0.8% agarose gel and the amplicons were individually barcoded for PacBio Sequel II sequencing (DNA Link, South Korea). The demultiplex barcodes analysis was powered by the Lima PacBio software v2.0.0. High-quality phased consensus sequences representing near full HIV-1 genome sequences with high fidelity and without reconstruction have been generated with the LAA PacBio algorithm v2.4.2. For each individual, sequences obtained were aligned using Multiple Alignment using Fast Fourier Transform (MAFFT) with strategy E-INS-i and Scoring matrix for nucleotide sequences of 1PAM/ k=2 (online <https://mafft.cbrc.jp/alignment/server/> or with Geneious Prime (v2021.1.1) plugging). Trees were built with iqtree2 using Maximum-Likelihood tree GTR+I+G model, with 1000 bootstraps, and then visualized with Figtree (v1.4.4). Clonality was evaluated with diversity of sequences in Geneious Prime, and sequences with 0 nucleotide difference were considered clonal. Integrity was assessed using both HIVDatabase QCtool (<https://www.hiv.lanl.gov/content/sequence/QC/index.html>) and ProseqIT (https://psd.cancer.gov/tools/pvs_annot.php). Finally, Psi defects were confirmed manually by visualization in Geneious Prime of this portion of the sequence. Genbank accession numbers for single-cell sequences are provided in Table S5.

Activation-induced marker (AIM) assay

The AIM assay was reported before.^{29,30,50,51} PBMCs were thawed and rested for 3h in 96-well flat-bottom plates in RPMI 1640 supplemented with HEPES, penicillin and streptomycin and 10% FBS. 2x10⁶ PBMCs and stimulated with Gag or Pol or Env or Nef peptide 15-mers pools (0.5 μ g/ml per peptide) spanning the complete amino acid sequence of each HIV protein (JPT) for 15h at 37 °C and 5% CO₂. CD40-blocking antibody was added to prevent CD40L downregulation following activation. In addition,

CXCR3, CCR6, and CXCR5 antibodies were added to the culture 15 min before stimulation. A DMSO-treated condition served as a negative control and *Staphylococcus enterotoxin B* SEB-treated condition (0.5 $\mu\text{g}/\text{ml}$) as a positive control. Cells were stained for viability dye for 20 min at 4 °C, FcR receptors were blocked using an FcR block antibody, and then surface markers (CD3, CD4, CD8, CD45RA, CD69, OX40, 41BB, CD40L, PD1, HLA-DR) (30 min, 4 °C). Abs used are listed in the [Table S3](#). Cells were fixed using 2% paraformaldehyde for 15 min at 4 °C before acquisition on Symphony cytometer (BD Biosciences). Analyses were performed using FlowJo v10.8.0 software.

Intracellular Cytokine Staining (ICS)

The previously described ICS assay was adapted to study HIV-specific T cells.^{29,51,85} PBMCs were thawed and rested for 2-h in RPMI 1640 medium supplemented with 10% FBS, Penicillin-Streptomycin (Thermo Fisher Scientific, Waltham, MA), and HEPES (Thermo Fisher Scientific, Waltham, MA). 1.7×10^6 PBMCs were stimulated with Gag or Pol or Env or Nef peptide pools (0.5 $\mu\text{g}/\text{ml}$ per peptide; JPT) for 15h at 37 °C and 5% CO₂. Cell stimulation was carried out for 6h at 5% CO₂ at 37 °C. Brefeldin A and monensin (BD Biosciences, San Jose, CA) was added 1h after stimulation. DMSO-treated cells served as a negative control and SEB as a positive control. Cells were stained for Aquavid viability marker (Thermo Fisher Scientific, Waltham, MA) for 20 min at 4 °C, then surface markers (CD4, CD3, CD8, CD14, CD19; 30 min, 4 °C), followed by intracellular Detection of cytokines (IFN γ , Il-2, and TNF- α) using the IC Fixation/Permeabilization kit (Thermo Fisher Scientific, Waltham, MA) according to the manufacturer's protocol before acquisition on a LSRII flow cytometer (BD Biosciences). Analysis was performed using FlowJo v10.8.0 software. Abs used are listed in [Table S4](#).

QUANTIFICATION AND STATISTICAL ANALYSIS

Statistical analysis

Symbols represent biologically independent samples from uninfected and HIV-infected under suppressive ART. Wilcoxon, Mann-Whitney, and Friedman with Dunn's post-test were generated using GraphPad Prism version 8.4.3 (GraphPad, San Diego, CA). P values <0.05 were considered significant. P values are indicated for each comparison assessed. Fold differences were calculated per participant, then median of these fold differences was calculated. Median values were used to generate donut charts. Each median value was normalized to obtain a total of 100%. For descriptive correlations, Spearman's R correlation coefficient was applied. For graphical representation on a log scale (but not for statistical tests), null values were arbitrarily set at the minimum values for each assay.

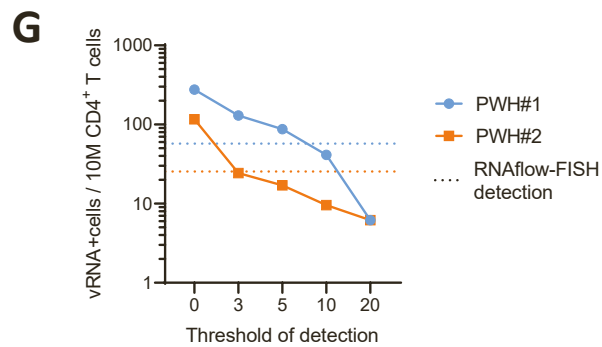
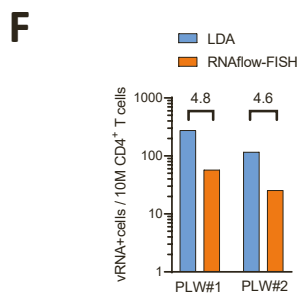
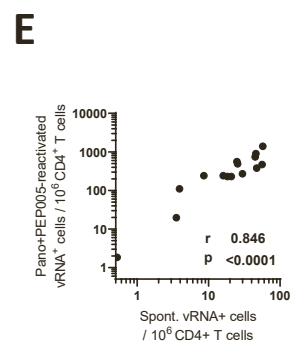
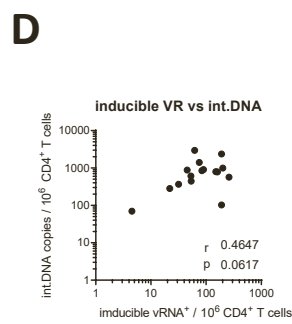
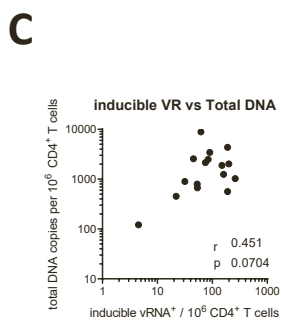
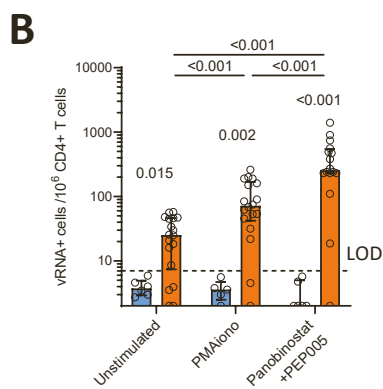
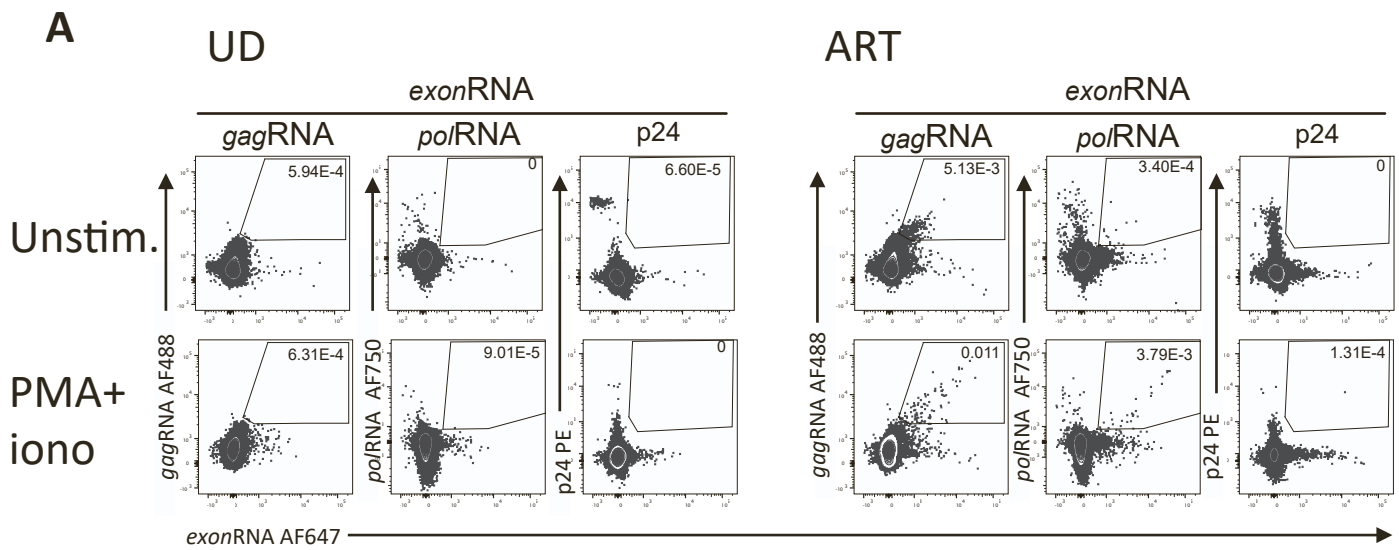
Software scripts and visualization

Graphics and pie charts were generated using GraphPad PRISM version 8.4.1 and ggplot2 (v3.3.3) in R (v4.1.0). Heat maps were generated in GraphPad PRISM version 8.4.1. Uniform manifold approximation and projection (UMAP) was performed using package M3C (v1.14.0) on gated FCS files loaded through the flowCore package (v2.4.0). For reservoir phenotyping, all vRNA⁺ events were loaded along with 3000 downsampled autologous CD4⁺ T cells per participant, for a total of 1,418 vRNA⁺ cells + 51,000 autologous CD4⁺ T cells. For the AIM analysis, samples were downsampled to a comparable 300 cells per peptide (Gag, Pol, Env and Pol) pool tested, therefore 1200 peptide-specific cells per participant, and a grand total of 20,400 HIV-specific cells. This number was chosen to avoid biases due to larger responses in certain participants. Scaling and logicle transformation of the flow cytometry data were applied using the FlowSOM⁸⁶ R package (v2.0.0). Clustering was achieved using Phenograph (v0.99.1) with the hyperparameter k (number of nearest neighbors) set to 150). R code scripted for this paper was adapted from https://github.com/otastet/Nayrac_et_al with the parameters described above. We obtained an initial 18 AIM⁺ clusters. After careful examination, we regrouped these clusters into 6 larger superclusters based on similar chemokine receptor expression. For vRNA⁺ and CD4⁺ T cell phenotyping, only participants with >5 events were analyzed.

Supplemental information

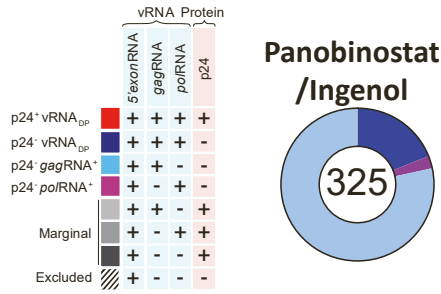
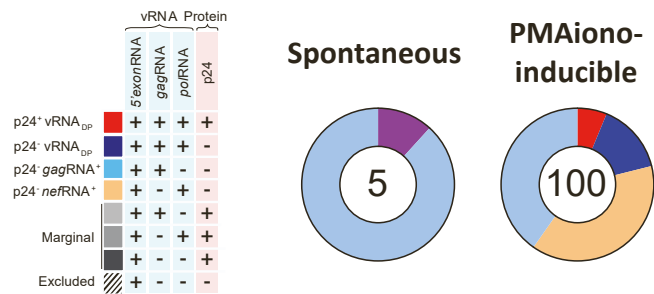
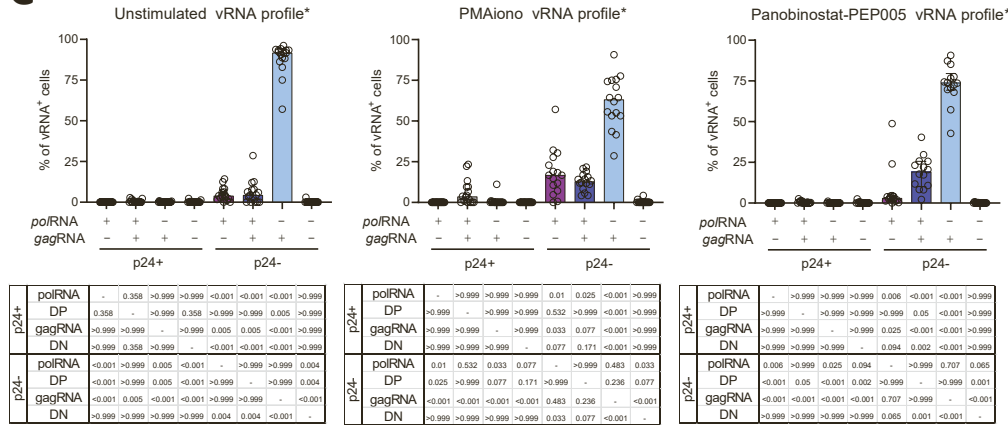
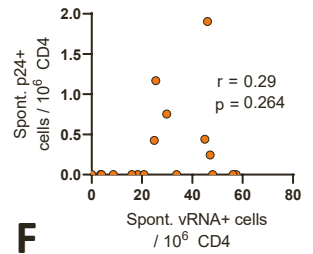
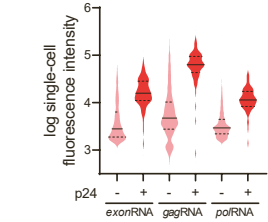
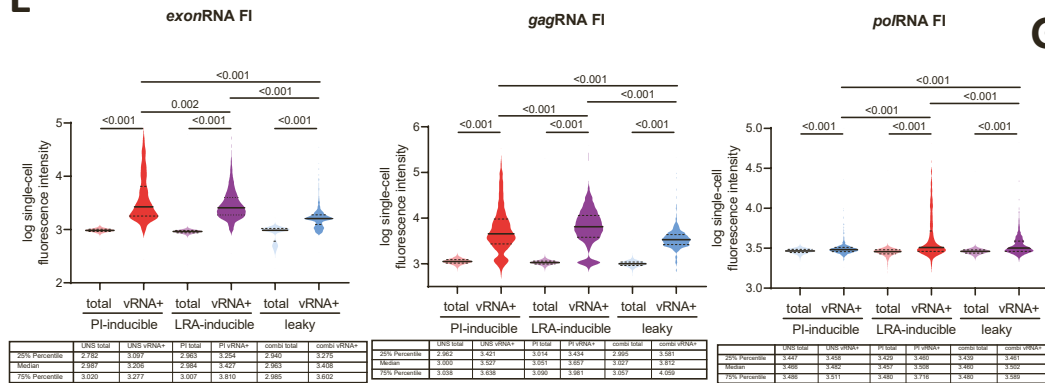
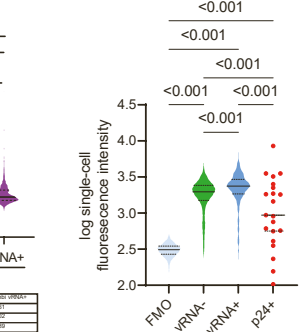
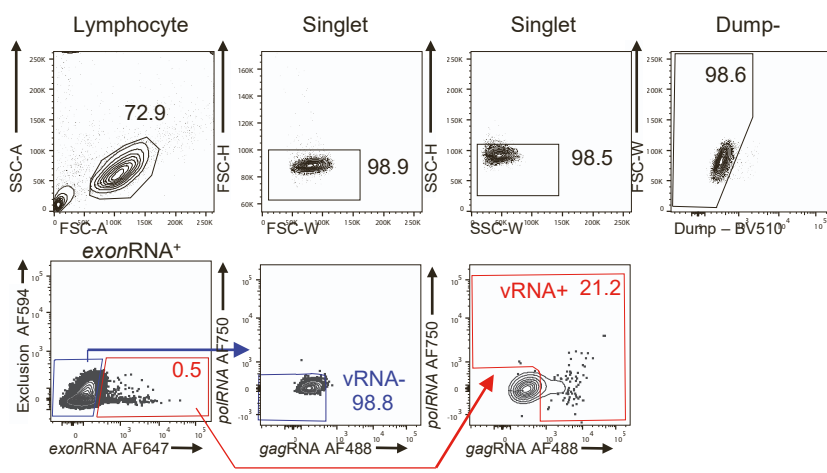
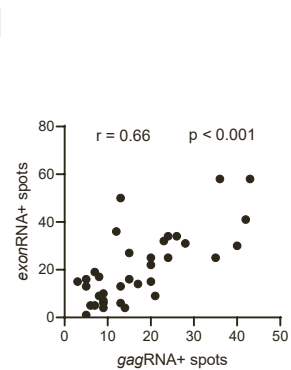
**Spontaneous HIV expression during suppressive ART
is associated with the magnitude and function
of HIV-specific CD4⁺ and CD8⁺ T cells**

Mathieu Dubé, Olivier Tastet, Caroline Dufour, Gérémy Sannier, Nathalie Brassard, Gloria-Gabrielle Delgado, Amélie Pagliuzza, Corentin Richard, Manon Nayrac, Jean-Pierre Routy, Alexandre Prat, Jacob D. Estes, Rémi Fromentin, Nicolas Chomont, and Daniel E. Kaufmann



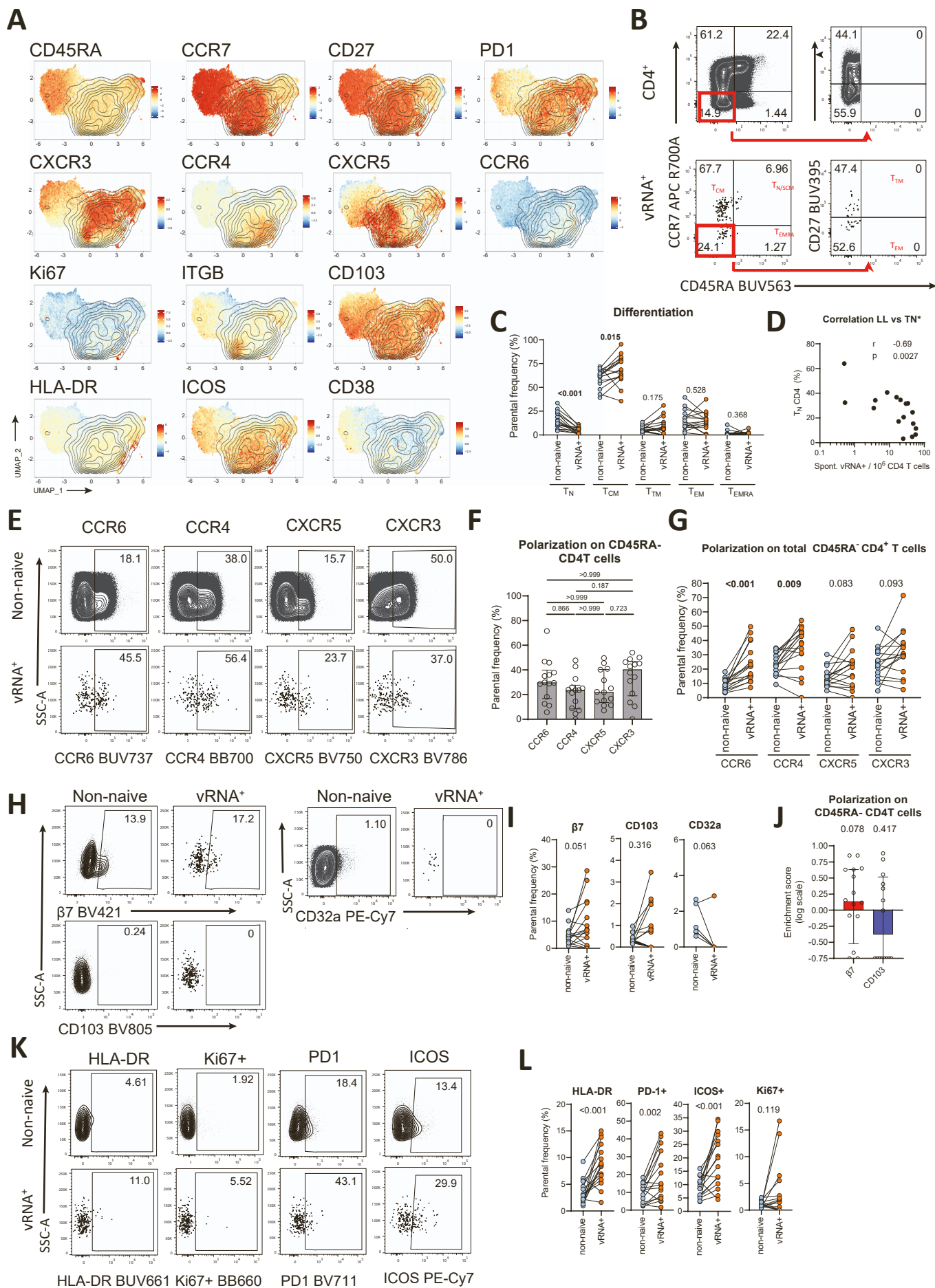
Supplemental Figure 1: Detection of vRNA expression in purified CD4⁺ T cells from participants on ART. Related to Figure 1.

Figure S1: Detection of vRNA expression in purified CD4⁺ T cells from participants on ART. Related to Figure 1. (A) Gating strategy identifying vRNA⁺ cells. **(B)** Complete quantification of vRNA⁺ cells from UD and ART participants, i) without stimulation or ii) stimulated with PMAionomycin or iii) a combination of Panobinostat and Ingenol. Two statistical tests are shown: Mann-Whitney to cohort comparisons and Wilcoxon to compare unstimulated vs. PMAionomycin induction. The bars indicate the median, and the error bars illustrate the interquartile range. **(C-E)** Correlations between **(C)** total DNA vs. PMAionomycin-induced, **(D)** integrated DNA vs. PMAionomycin-induced, and **(E)** Panobinostat+Ingenol-induced vs. spontaneously active reservoir. R and p values from Spearman tests are indicated. N =18. **(F)** Compared quantifications of vRNA⁺ cells using a limiting dilution RT-qPCR assay and the HIV RNAflow-FISH assay in two PWH. **(G)** Quantification of the RT-qPCR with different threshold of detection. The dash bar correspond to paired HIV RNAflow-FISH detection. The error bars represent standard deviation of 11 technical replicates.

A**B****C****D****F****E****G****H****I**

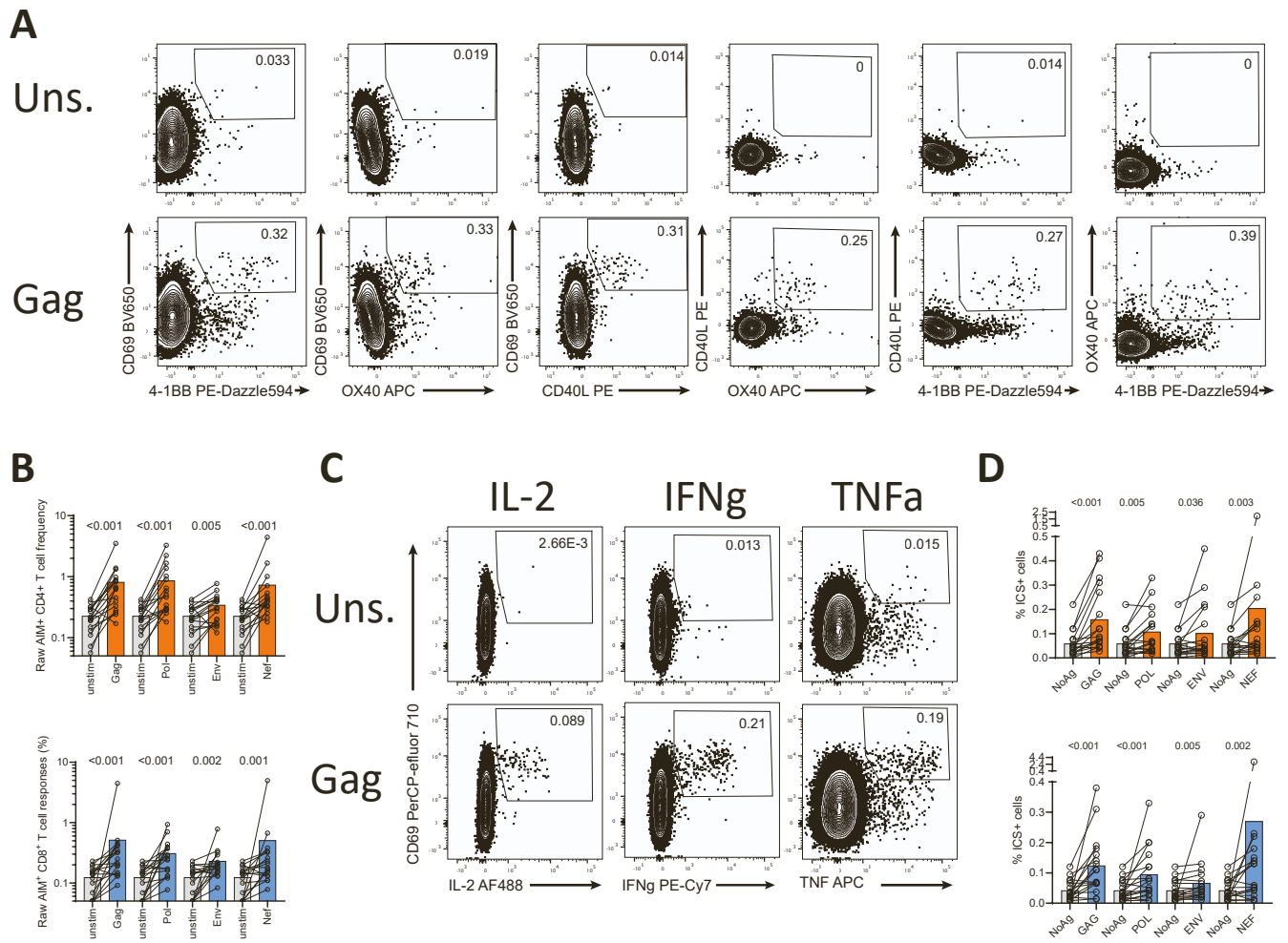
Supplemental Figure 2: Details of the viral gene expression in vRNA+ cells. Related to Figure 2.

Figure S2: Details of the viral gene expression in vRNA⁺ cells. Related to Figure 2. (A) A legend listing the different theoretical vRNA⁺ populations defined by *exon*RNA, *gag*RNA, and *pol*RNA probesets is shown on the left. Donut charts presenting the median proportions of each vRNA⁺ subpopulation for the combinatory Panobinostat+Ingenol stimulation are shown on the right. (B) Legend listing the different theoretical vRNA⁺ populations using *exon*RNA, *gag*RNA, and *nef*RNA probesets. Donut charts presenting the median proportions of each vRNA⁺ subpopulation for the spontaneously active or PMAionomycin-induced reservoirs. In **AB**, the numbers in the donut hole represent the median vRNA⁺ cells per 10⁶ CD4 T cells. (C) The histograms report the proportions of each vRNA⁺ subpopulation for spontaneously active, PMAionomycin, or Panobinostat+Ingenol-induced reservoirs, supporting Figures 2D and S2A. The bars represent median values. All results from a Friedman test are shown underneath. (D) Correlations between spontaneously active p24⁺ and vRNA⁺ cells. R and p values are indicated. (E) Violin plots showing single-cell fluorescence intensities for all vRNA⁺ cells detected in 17 participants, including Panobinostat+Ingenol stimulation. (F) Single-cell fluorescence intensities of *exon*RNA, *gag*RNA and *pol*RNA in translation-competent vRNA⁺p24⁺ cells upon induction by PMAionomycin. For the sake of comparison, the total vRNA⁺ population is also represented. N=17. (G) Violin plots showing single-cell CD4 fluorescence intensities in vRNA⁺ versus vRNA⁻ cells, without stimulation. FMO levels are also indicated. The results from Wilcoxon tests are shown above. N=17 (1 participant with no active vRNA was excluded to maintain a side-by-side comparison). (H) Gating strategy for vRNA⁻ and vRNA⁺ cell sorting, prior to study by confocal fluorescence microscopy. (I) Correlation between the number of *exon*RNA⁺ and *gag*RNA⁺ spots per cell.



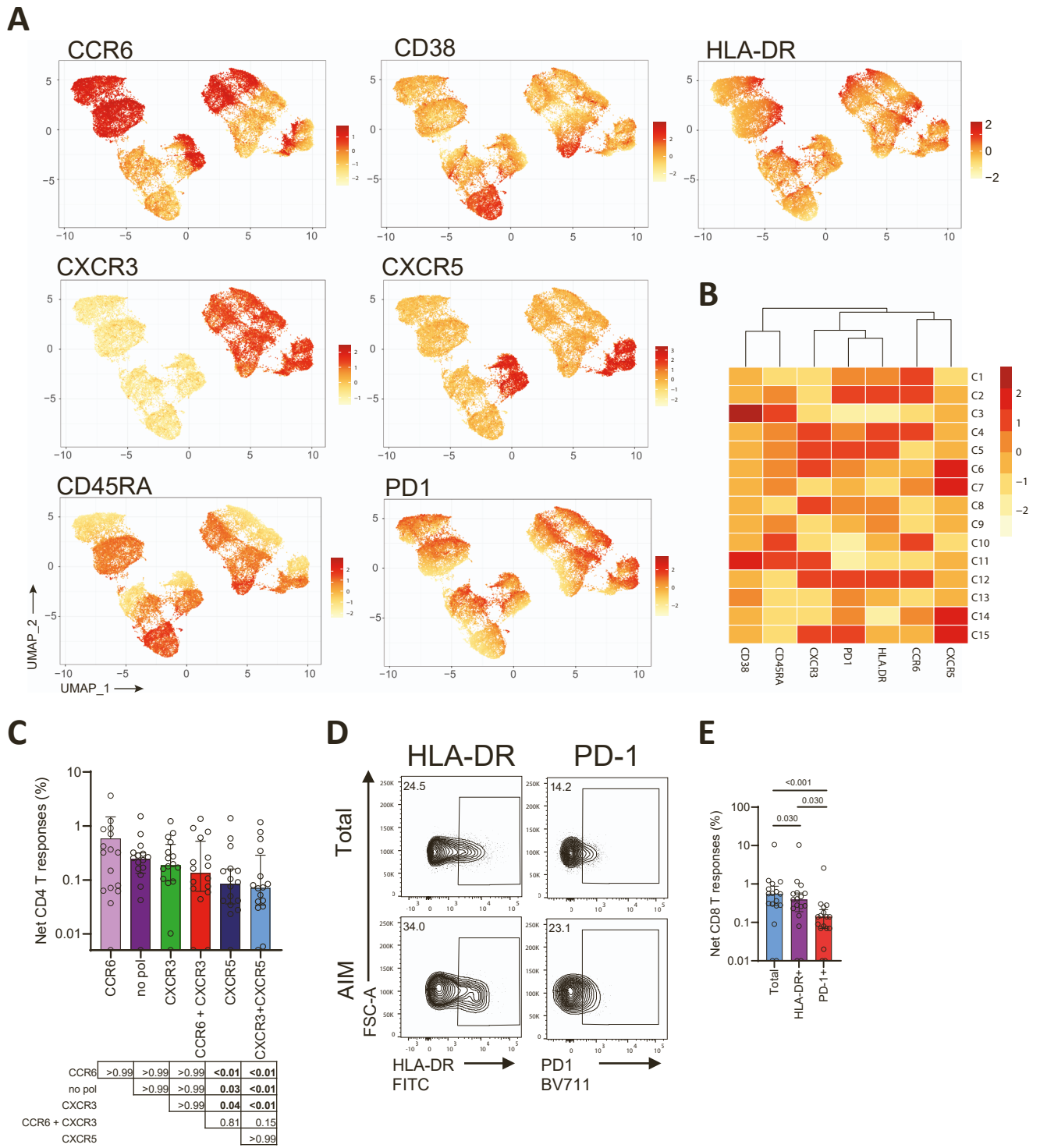
Supplemental Figure 3: Phenotyping of spontaneously active reservoirs. Related to Figure 3.

Figure S3: Phenotyping of spontaneously active reservoirs. Related to Figure 3. (A) Multiple iterations of the UMAP representation from Figure 3 where the expression level of each loaded parameter was individually layered. Warm colors indicate high expression, and cold colors are for lower expression. Each feature was subject to scaling to ease the comparison. (BC) Univariate CD4⁺ T memory analysis. (B) Representative gating strategy. (C) Relative enrichment of vRNA⁺ cells compared to the parental CD4 T cell population. The enrichment is shown for the indicated CD4 T memory subsets, including T naïve. Wilcoxon tests are shown above. (D) Correlation between total CD4⁺ T_N and active vRNA⁺ cells. N=17. (EFG) Univariate analyses of vRNA⁺ cell polarization. (E) Representative gating strategy. (F) Median frequencies of each single total HIV-specific CD45RA⁻ CD4⁺ T cell polarization. The bars represent the median and the error bars, the interquartile range. (G) Relative enrichment of vRNA⁺ cells compared to the parental CD4⁺ T cell population for each tested polarization marker. Wilcoxon tests are shown above. (HIJ) Univariate analyses of β7 and CD103 expression on vRNA⁺ cells. (H) Representative gating strategy. (I) Relative enrichment of vRNA⁺ cells compared to the parental CD4⁺ T cell population for each tested marker. Wilcoxon tests are shown above. (J) Enrichment score. (KL) Univariate analyses of activation markers on vRNA⁺ cells. (K) Representative gating strategy. (L) Relative enrichment of vRNA⁺ cells compared to the parental CD4⁺ T cell population for each tested activation marker. Wilcoxon tests are shown above. (A-C, E-L) N=16 (2 participants had <5 vRNA⁺ cells, our threshold for phenotyping).



Supplemental Figure 4: AIM and ICS assays. Related to Figure 4.

Figure S4: AIM and ICS assays. Related to Figure 4. (A) Representative gating of each AIM pair was used for the ORgate analysis of Gag-specific CD4⁺ T cell responses. The same gating was applied for Pol, Env, and Nef-specific CD4⁺ T cells. (B) Raw CD4⁺ (top) and CD8⁺ (down) T cell responses, comparing the unstimulated vs. peptide-stimulated conditions. The bars indicate the median, and the error bars illustrate the interquartile range. The results from Wilcoxon tests are shown above the histograms. (C) Representative gating of each cytokine used for the ORgate analysis of Gag-specific effector CD4⁺ T cell responses. The same gating was applied for Pol, Env, and Nef-specific CD4⁺ T cells. (D) Raw CD4⁺ (top) and CD8⁺ (down) T cell responses compared the unstimulated vs. peptide-stimulated conditions. The bars indicate the median, and the error bars illustrate the interquartile range. The results from Wilcoxon tests are shown above the histograms. N=16 (1 participant had < 5 vRNA+ cells, therefore could not be phenotyped).



Supplemental Figure 5: Cell markers distribution in the AIM+ UMAP representation. Related to Figure 5.

Figure S5: Cell markers distribution in the AIM⁺ UMAP representation. Related to Figure 5. (A) Multiple iterations of the same UMAP representation from Figure 6 where the expression level of each loaded parameter was individually layered. Warm colors indicate high expression, cold is for lower expression. Each feature was subject to scaling to ease comparison. **(B)** Heat map showing an unsupervised clustering of the 15 clusters defined by the MFI of each loaded parameter. N = 17. **(C)** Histogram showing the magnitudes of net HIV-specific AIM⁺ CD4⁺ T cell responses per superclusters. The bars indicate median values, and the error bars represent the interquartile range. Stats shown underneath are results for a Friedman test with multiple comparisons, with Dunn correction. N=17 **(D)** Representative examples of HLA-DR and PD1 AIM⁺ CD8⁺ T cell gatings. **(E)** Histogram showing the magnitudes of net HIV-specific AIM⁺ CD8⁺ T cell responses. The bars indicate median values, and the error bars represent the interquartile range. Stats shown underneath are results for a Friedman test with multiple comparisons, with Dunn correction. N=17

Table S1. Clinical characteristics of the study participants. Related to Figures 1 to 6. †

	PLWH on ART n = 18	Uninfected controls n = 6
Age (year old)	55 (51-58)	51 (42-56)
Sex	100% male	50% male 50% female
Duration of infection (y)	19.6 (12.9-24.1)	NA
Time before ART (y)	3.9 (1.3-11.9)	NA
Time on ART (y)	10.8 (6.6-26.9)	NA
CD4 counts	619 (436-813)	582 (531-703)
CD8 counts	1179 (565-1373)	298 (252-359)
CD4/CD8 ratio	0.52 (0.34-1.15)	2.14 (1.99-2.28)
Log Pre-ART VL	4.41 (4.21-4.94)	-

† Values displayed in bold are medians. Interquartile ranges are shown in parentheses for continuous variables. Percentages were used for categorical variables.

Table S2. Flow cytometry antibody staining panel for viral reservoir characterization. Related to the STAR Methods section.

Marker-Fluorophore	Clone	Vendor	Catalog #
In culture			
CCR4 – BB700	1G1	BD Biosciences	566475
CCR7 – APC R700	2-L1-A	BD Biosciences	566767
CXCR5 – BV750	RF8B2	BD Biosciences	747111
CXCR3 – BV786	G025H7	BioLegend	353738
CCR6 – BUV737	11A9	BD Biosciences	564377
CD103 – BUV805	Ber-ACT8	BD Biosciences	748501
Surface staining			
CD4 – BB630	SK3	BD Biosciences	CUSTOM
CD38 – BB790	HIT2	BD Biosciences	CUSTOM
β 7-integrin – BV421	Fib504	BD Biosciences	564283
CD8 – BV480	RPA-T8	BD Biosciences	566121
CD14 – BV480	M5E2	BD Biosciences	746304
CD16 – BV480	3G8	BD Biosciences	566108
CD19 – BV480	HIB19	BD Biosciences	746457
CD56 – BV480	NCAM16.2	BD Biosciences	566124
PD1 – BV711	EH12.2H7	BioLegend	329928
CD27 – BUV395	L128	BD Biosciences	563815
CD3 – BUV496	UCHT1	BD Biosciences	612941
CD45RA – BUV563	HI100	BD Biosciences	612926
HLA-DR – BUV661	G46-6	BD Biosciences	612980
ICOS – PE-Cy7	ISA-3	eBiosciences	25-9948-42
Intracellular staining			
p24 – PE	KC57	Beckman Coulter	6604667
Ki67 – BB660	B56	BD Biosciences	624295
RNAflow-FISH probeset			
<i>exon</i> RNA probe – AF647	NA	Thermofisher	VF1-6000978-210
<i>gag</i> RNA probe – AF488	NA	Thermofisher	VFKA3CY-210
<i>pol</i> RNA probe – AF750	NA	Thermofisher	VF6-18315
Dye			
LIVE/DEAD Fixable dead cell eFluor506	NA	Thermofisher	65-0866-14

Table S3. Flow cytometry antibody staining panel for activation-induced marker assay. Related to the STAR Methods section.

Marker-Fluorophore	Clone	Vendor	Catalog #
In culture			
CD183 (CXCR3) – BV605	G025H7	Biolegend	353728
CD185 (CXCR5) – BV421	J25D4	Biolegend	356920
CD196 (CCR6) – BUV737	11A9	BD	564377
Surface			
CD3 – BUV496	UCHT1	BD	612941
CD4 – BB630	SK3	BD	624294
CD8 – BV570	RPA-T8	Biolegend	301037
CD14 – BV480	M5E2	BD	746304
CD19 – BV480	HIB19	BD	746457
CD38 – BB790	HIT2	BD	CUSTOM
CD45RA – PerCP Cy5.5	HI100	BD	563429
CD69 – BV650	FN50	Biolegend	310934
CD134 (OX40) - APC	ACT35	BD	563473
CD137 (4-1BB) – PE-Dazzle 594	4B4-1	Biolegend	309826
CD154 (CD40L) - PE	TRAP1	BD	555700
CD279 (PD1) – BV711	EH122H	Biolegend	329928
HLA-DR - FITC	LN3	Biolegend	327005
Dye			
LIVE/DEAD Fixable dead cell	N/A	Thermo Fisher Scientific	L34960

Table S4. Flow cytometry antibody staining panel for intracellular detection. Related to the STAR Methods section.

Marker-Fluorophore	Clone	Vendor	Catalog #
Surface			
CD3 – BV650	UCHT1	BD Biosciences	563852
CD4 – BV605	RPA-T4	BD Biosciences	562658
CD8 – APCeFluor780	SK1	eBioscience	47-0087-42
CD14 – V500	M5E2	BD Biosciences	561391
CD19 – V500	H1B189	BD Biosciences	561121
CD69 – PerCP-eFluor710	FN50	eBioscience	46-0699-42
CD107A – BV785	H4A3	BD Biosciences	563869
PD-1 – BV421	EH12.2H7	Biolegend	329920
Intracellular			
IFN- γ – PE-Cy7	B27	BD Biosciences	557643
CD154 (CD40L) – PE	TRAP1	BD Biosciences	555700
IL-2 – AF488	MQ1-17H12	Biolegend	500314
TNF - APC	Mab11	BD Biosciences	562084
Dye			
Aquavidid	NA	Invitrogen	L34966

Table S5: Single-cell vRNA+ sequences accession numbers. Related to Figure 3.

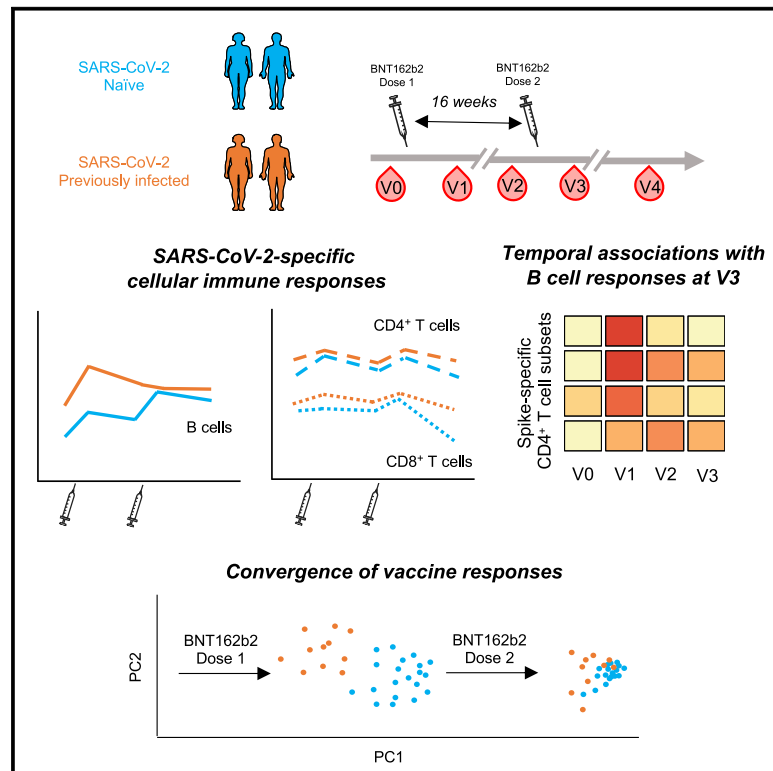
Sequence number	GenBank accession number
PWH9_L3p1_A2_C0_434	OR105517
PWH5_L2p3_A9_PCR2_G9_C0_455	OR105518
PWH5_L2p2_F6_C0_290	OR105519
PWH5_L2p2_E10_C0_386	OR105520
PWH5_L2p2_E9_PCR2_E9_C0_454	OR105521
PWH5_L2p2_E3_C0_463	OR105522
PWH5_L2p2_D10_C0_432	OR105523
PWH5_L2p1_C12_PCR2_C12_C0_440	OR105524
PWH5_L2p1_C10_C0_473	OR105525
PWH5_L2p1_C6_PCR2_C6_C0_474	OR105526
PWH5_L2p1_B7_C0_325	OR105527
PWH5_L2p1_B4_C0_391	OR105528
PWH5_L2p1_A10_C0_341	OR105529
PWH3_L1p3_B11_C0_402	OR105530
PWH3_L1p3_A5_C0_417	OR105531
PWH3_L1p3_A3_C0_418	OR105532
PWH3_L1p2_H12_C0_390	OR105533
PWH3_L1p2_H4_C0_378	OR105534
PWH3_L1p2_G5_C0_392	OR105535
PWH3_L1p2_F2_C0_412	OR105536
PWH3_L1p2_D12_C0_394	OR105537
PWH3_L1p2_D3_C0_399	OR105538
PWH3_L1p2_C11_C0_329	OR105539
PWH3_L1p2_C8_C0_432	OR105540
PWH3_L1p2_C2_C0_366	OR105541
PWH3_L1p2_B10_C0_371	OR105542
PWH3_L1p2_A10_C0_42	OR105543
PWH3_L1p1_H7_C0_263	OR105544
PWH3_L1p1_G3_C0_365_inversion	OR105545
PWH3_L1p1_G1_C0_430	OR105546
PWH3_L1p1_F7_C0_350	OR105547
PWH3_L1p1_F3_C0_418_inversion	OR105548
PWH3_L1p1_E12_C0_413	OR105549
PWH3_L1p1_E10_C0_430	OR105550
PWH3_L1p1_D9_C0_436	OR105551
PWH3_L1p1_D8_C0_366	OR105552
PWH3_L1p1_C6_C0_390	OR105553
PWH3_L1p1_B5_C0_422	OR105554
PWH3_L1p1_B4_C0_392	OR105555
PWH3_L1p1_A6_C0_433	OR105556

**Appendix II.iv: Temporal Associations of B and T Cell Immunity
with Robust Vaccine Responsiveness in a 16-Week Interval
BNT162b2 Regimen**

Cell Reports, 2022

Temporal associations of B and T cell immunity with robust vaccine responsiveness in a 16-week interval BNT162b2 regimen

Graphical abstract



Authors

Manon Nayrac, Mathieu Dubé,
Gérémy Sannier, ...,
Valérie Martel-Laferrrière, Andrés Finzi,
Daniel E. Kaufmann

Correspondence

andres.finzi@umontreal.ca (A.F.),
daniel.kaufmann@umontreal.ca (D.E.K.)

In brief

Nayrac et al., show that a 16-week interval BNT162b2 regimen elicits robust SARS-CoV-2-specific B and T cell responses in SARS-CoV-2 naive and previously infected individuals. Immune response kinetics differs after the first dose between cohorts but converges after boosting, which elicits a multifaceted cellular recall response and functional memory.

Highlights

- A 16-week interval BNT162b2 regimen generates strong and diverse immune responses
- Features of responses in SARS-CoV-2 naive versus PI donors converge after boost
- The 16-week interval BNT162b2 vaccination leads to development of immune memory
- There are contemporaneous and temporal associations between B and T cell responses



Article

Temporal associations of B and T cell immunity with robust vaccine responsiveness in a 16-week interval BNT162b2 regimen

Manon Nayrac,^{1,2,9} Mathieu Dubé,^{1,9} Gérémy Sannier,^{1,2,10} Alexandre Nicolas,^{1,2,10} Lorie Marchitto,^{1,2} Olivier Tastet,¹ Alexandra Tauzin,^{1,2} Nathalie Brassard,¹ Raphaël Lima-Barbosa,^{3,7} Guillaume Beaudoin-Bussièrès,^{1,2} Dani Vézina,¹ Shang Yu Gong,^{1,4} Mehdi Benlarbi,¹ Romain Gasser,^{1,2} Annemarie Laumaea,^{1,2} Jérémie Prévost,^{1,2} Catherine Bourassa,¹ Gabrielle Gendron-Lepage,¹ Halima Medjahed,¹ Guillaume Goyette,¹ Gloria-Gabrielle Ortega-Delgado,¹ Mélanie Laporte,¹ Julia Niessl,^{1,2,8} Laurie Gokool,¹ Chantal Morrissette,¹ Pascale Arlotto,¹ Jonathan Richard,^{1,2} Justin Bélair,^{3,7} Alexandre Prat,^{1,5} Cécile Tremblay,^{1,2} Valérie Martel-Laferrrière,^{1,2} Andrés Finzi,^{1,2,4,*} and Daniel E. Kaufmann^{1,2,6,11,*}

¹Centre de Recherche du CHUM, Montréal, QC H2X 0A9, Canada

²Département de Microbiologie, Infectiologie et Immunologie, Université de Montréal, Montréal, QC H2X 0A9, Canada

³Université de Montréal, Montréal, QC H3T 1J4, Canada

⁴Department of Microbiology and Immunology, McGill University, Montréal, QC H3A 2B4, Canada

⁵Département de Neurosciences, Faculty of Medicine, Université de Montréal, Montréal, QC, Canada

⁶Département de Médecine, Université de Montréal, Montréal, QC H3T 1J4, Canada

⁷Present address: Independent data scientist

⁸Present address: Center for Infectious Medicine, Department of Medicine Huddinge, Karolinska Institutet, Stockholm 171 77, Sweden

⁹These authors contributed equally

¹⁰These authors contributed equally

¹¹Lead contact

*Correspondence: andres.finzi@umontreal.ca (A.F.), daniel.kaufmann@umontreal.ca (D.E.K.)

<https://doi.org/10.1016/j.celrep.2022.111013>

SUMMARY

Spacing of BNT162b2 mRNA doses beyond 3 weeks raises concerns about vaccine efficacy. We longitudinally analyze B cell, T cell, and humoral responses to two BNT162b2 mRNA doses administered 16 weeks apart in 53 SARS-CoV-2 naive and previously infected donors. This regimen elicits robust RBD-specific B cell responses whose kinetics differs between cohorts, the second dose leading to increased magnitude in naive participants only. While boosting does not increase magnitude of CD4⁺ T cell responses further compared with the first dose, unsupervised clustering of single-cell features reveals phenotypic and functional shifts over time and between cohorts. Integrated analysis shows longitudinal immune component-specific associations, with early T helper responses post first dose correlating with B cell responses after the second dose, and memory T helper generated between doses correlating with CD8 T cell responses after boosting. Therefore, boosting elicits a robust cellular recall response after the 16-week interval, indicating functional immune memory.

INTRODUCTION

The coronavirus disease 19 (COVID-19) pandemic caused a race for prophylactic vaccines against SARS-CoV-2 (Krammer, 2020), including mRNA-based technologies (Baden et al., 2021; Dickerman et al., 2021; Skowronski and De Serres, 2021; Thomas et al., 2021). These mRNA vaccines target the trimeric Spike glycoprotein that facilitates SARS-CoV-2 entry into host cells via its receptor-binding domain (RBD) (Hoffmann et al., 2020; Walls et al., 2020). Antibody responses are associated with protection for most licensed vaccines and the generation of Spike-specific antibodies, particularly of neutralizing RBD-specific antibodies, is considered critical for SARS-CoV-2 vaccine efficacy. Protective antibody responses are being iden-

tified (Earle et al., 2021; Gilbert et al., 2021) but there is a need for a better understanding of B cell memory responses in the context of different vaccine modalities. CD4⁺ T cell help is critical for development and maintenance of antibody immunity. SARS-CoV-2-specific CD4⁺ and CD8⁺ T cells may contribute to recovery from COVID-19 (Bange et al., 2021; Wurm et al., 2020). mRNA vaccines elicit CD4⁺ T cell responses (Anderson et al., 2020; Lederer et al., 2020; Painter et al., 2021; Prendecki et al., 2021; Rodda et al., 2022; Sahin et al., 2020) that are likely important determinants of vaccine efficacy. CD4⁺ T subsets include T follicular helper (Tfh) cells that are critical for the expansion, affinity maturation, and memory development of B cells (Crotty, 2019), and T helper 1 (Th1) cells, which foster development of CD8⁺ T cell memory (Laidlaw et al., 2016). However, T cell



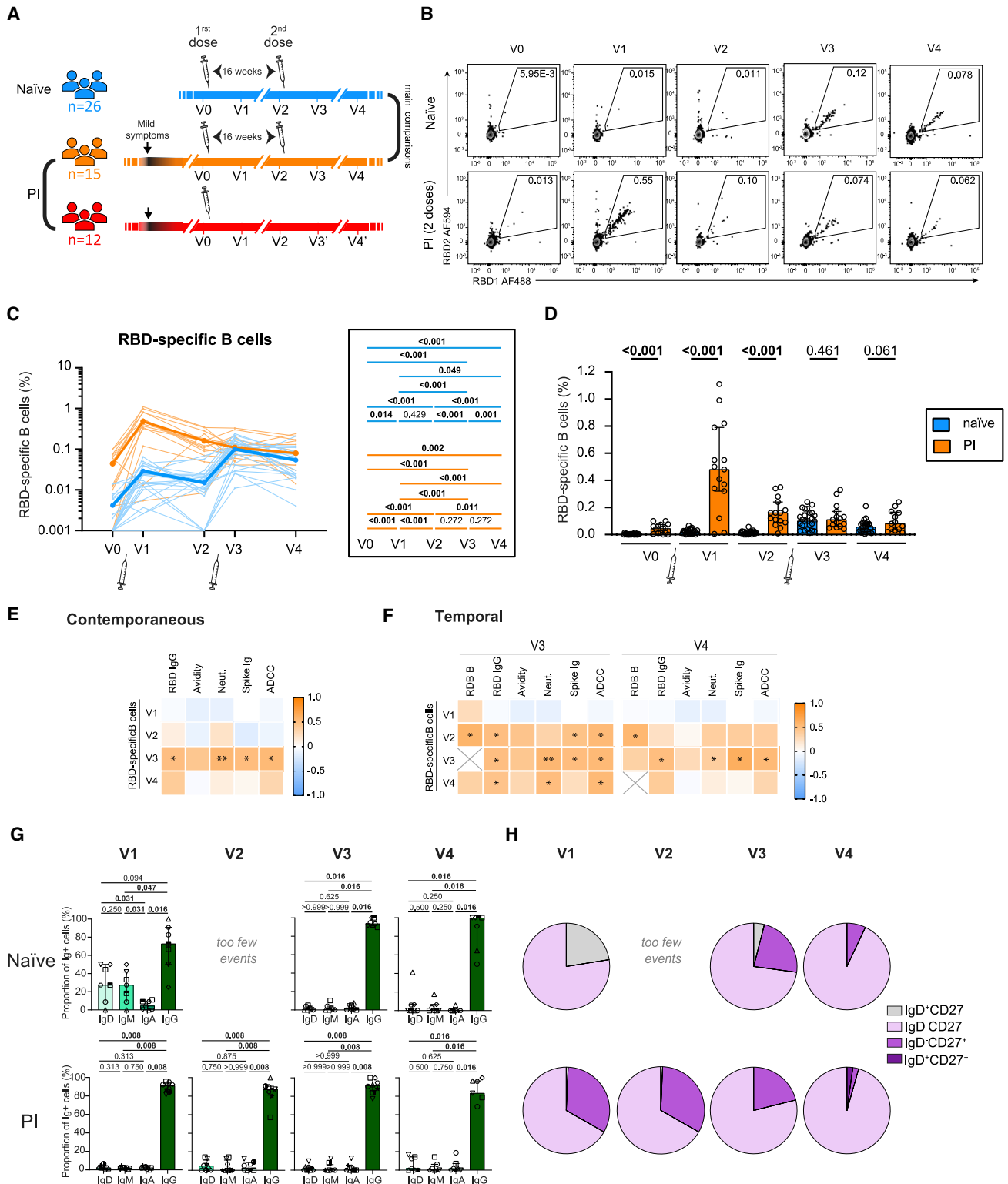


Figure 1. Marked differences in B cell responses to the first BNT162b2 dose between naive and pre-infected participants contrast with convergent features after boosting

(A) Schematic representation of study design. Blood samples were collected at five time points (summarized in Table 1): baseline (V0); 3 weeks (V1) or 12 weeks (V2) after dose 1; 3 weeks (V3) or 16 weeks (V4) after dose 2. For participants receiving a single dose, V3' was sampled 19 weeks after dose 1 and V4' 16 weeks after V3'. Dose administrations are indicated by a syringe.

(legend continued on next page)

subsets show important heterogeneity and plasticity, better fitting with spectra of phenotypes and functions than fully distinct populations (O'Shea and Paul, 2010). Unequivocal lineage characterization is therefore challenging, and unsupervised clustering analytical approaches are increasingly used to identify T cell subsets more specifically associated with immunological outcomes (Apostolidis et al., 2021; Maucourant et al., 2020).

The standard BNT162b2 immunization regimen recommends a 21-day interval between vaccine doses, and inoculation of two doses irrespective of prior SARS-CoV-2 infection status. However, the optimal interval has not been determined in controlled trials. In the context of vaccine scarcity and given the significant protection already conferred by the first dose in non-high-risk populations (Baden et al., 2021; Polack et al., 2020; Skowronski and De Serres, 2021), some public health agencies implemented schedules with longer intervals to rapidly extend population coverage (Paltiel et al., 2021; Tuite et al., 2021) and recommended a single dose for previously infected immunocompetent people. Longer delays between doses also frequently occur in real-life settings. While such strategies generated concerns given uncertain immunogenicity, a longer period of partial vulnerability to infection, and a hypothetical risk of escape mutant selection, epidemiological evidence supports this approach as a valid alternative in lower-risk populations (Carazo et al., 2021; Skowronski et al., 2021) in which robust T cell and antibody responses are observed after a single dose (Tauzin et al., 2021b), and stronger and broader antibody immunity induced after the second dose (Grunau et al., 2021; Tauzin et al., 2021a). While significant progress has been made in the understanding of the kinetics of B and T cell responses in short-interval mRNA vaccine schedules (Goel et al., 2021; Painter et al., 2021; Rodda et al., 2022; Zollner et al., 2021), the immunological implications of widely spaced vaccination regimens remain poorly known.

Here, we define the trajectories, differentiation state, and interplay of vaccine-induced Spike-specific B cells, CD4⁺ T cells, CD8⁺ T cells, and antibody responses in SARS-CoV-2 naive or previously infected individuals who received two mRNA vaccine doses administered 16 weeks apart, and in a third group of previously infected individuals who received a single vaccine dose.

RESULTS

Study participants

We evaluated immune responses in three cohorts of health care workers (HCW) (Figure 1A): 26 SARS-CoV-2 naive and 15 previously infected (PI) donors who received a two-dose BNT162b2 regimen spaced by 16 weeks; and 12 PI individuals who received a single dose. Blood samples were collected at five time points:

at baseline (V0); 3 weeks after the first dose (V1); 12 weeks after the first dose (V2); 3 weeks after the second dose for participants receiving two doses (V3) or 19 weeks after the first dose for the single-dose PI participants (V3'); and 16 weeks after the second dose (V4). Clinical characteristics (Table 1) did not statistically differ between cohorts, except for the numbers of days between V0 and the first dose and for time between the first dose and V2.

Marked differences in B cell responses to the first BNT162b2 dose between naive and PI participants contrast with convergent features after boosting

To evaluate SARS-CoV-2-specific B cells, we focused on RBD to minimize inclusion of B cells cross-reactive to endemic coronaviruses (Hicks et al., 2021; Klumpp-Thomas et al., 2021). Co-detection of two fluorescently labeled recombinant RBD probes greatly enhances specificity (Figure 1B and Anand et al., 2021; flow cytometry panel, Table S1; gating strategy, Figure S1A). We examined the magnitude of RBD-specific B cells (defined as RBD1⁺RBD2⁺CD19⁺CD20⁺) in the two-dose cohorts (Figures 1C and 1D). In naive individuals, most participants showed no baseline signal. Priming induced significant RBD-specific B cell responses at V1. The second dose elicited a homogeneous brisk recall response at V3 in all participants. Responses subsequently declined at V4 yet remained significantly higher than at pre-boost time points. The pattern markedly differed in PI (Figures 1C and 1D). Consistent with previous SARS-CoV-2 exposure, RBD-specific B cells were already present at V0. This response increased sharply at V1, followed by attrition at V2. We observed no boosting effect after the second dose and no significant decline at V4. The response to the first BNT162b2 dose in PI (V1) differed in magnitude from the second dose in naive (V3) (Figure S1B). Therefore, the RBD-specific B cell kinetics between the two cohorts markedly differed after the first dose, converged after the second dose, and remained close after the subsequent decline observed at V4 (Figure 1D). In single-dose PI, we observed stable B cell responses at V3' and V4' compared with V2, comparable with what we observed in two-dose PI, consistent with a steady memory B cell pool after an initial decline between V1 and V2 (Figures S1C and S1D).

We next investigated the relationships between RBD-specific B cell frequencies at the different time points and antibody responses in naive participants: RBD-specific immunoglobulin G (IgG) antibody levels, anti-RBD IgG avidity, neutralization activity, cell-binding ELISA (CBE) antibody levels, and antibody-dependent cellular cytotoxicity (ADCC) (Figures 1E and 1F). RBD-specific B cell responses positively correlated with contemporaneous antibody levels at V3, but not at V1 (Figure 1E). Contemporaneous correlations were lost at V4. Early V1 B cell

(B) Representative RBD-specific B cell gating.

(C and D) Kinetics of RBD-specific B cell responses in previously naive (blue) or pre-infected (PI; orange) participants receiving two doses. (C) Bold line represents the cohort's median value. Right: statistical comparisons using a linear mixed model. (D) Intercohort comparisons. Bars represent median \pm interquartile range. Intercohort statistical comparisons using a linear mixed model are shown.

(E and F) Heatmap showing (E) contemporaneous or (F) temporal correlations of RBD-specific B cells versus the indicated antibody responses ($n = 22$). Significant correlations by Spearman tests are shown (* $p < 0.05$, ** $p < 0.01$).

(G) Frequencies of IgD⁻, IgM⁻, IgA⁻, and IgG⁺ cells in RBD-specific memory B cells in naive and PI donors, with Wilcoxon tests. Bars represent median \pm interquartile range.

(H) Proportion of IgD^{+/+} and CD27^{+/+} populations in RBD-specific memory B cells in naive and PI donors.

In (G) and (H), V2 for naive participants could not be analyzed because of low number of events. In (C) and (D), $n = 26$ naive and $n = 15$ PI; in (E), $n = 26$ naive; in (G) and (H), $n = 7$ naive and $n = 8$ PI.

Table 1. Clinical characteristics of the study participants^a

Variable	Previously naive cohort	Previously infected (PI) cohort		
	Two doses ^b (n = 26)	Two doses ^b (n = 15)	Single dose ^c (n = 12)	Entire (PI) cohort (n = 27)
BNT162b2 vaccine				
Variable				
Age	51 (41–56)	47 (43–56)	51 (34–62)	48 (39–59)
Sex				
Male	11 (42%)	10 (66%)	4 (33%)	14 (52%)
Female	15 (58%)	5 (34%)	8 (66%)	13 (48%)
Previous SARS-CoV-2 infection				
Days between day of symptom onset and first vaccine dose	NA	274 (258–307)	287 (227–306)	281 (250–307)
Vaccine dose spacing				
Days between doses 1 and 2	111 (109–112)	110 (110–112)	NA	NA
Visits for immunological profiling				
V0, days before first dose	1 (0–5)	24 (6–43)	18 (7–45)	23 (6–43)
V1, days after first dose	21 (19–26)	20 (19–21)	20 (18–21)	20 (18–21)
V2, days after first dose	83 (82–84)	89 (86–93)	90 (87–94)	89 (86–93)
V2, days before second dose	28 (26–29)	23 (18–28)	NA	NA
V3, days after first dose	133 (130–139)	138 (132–142)	132 (130–138)	136 (131–141)
V3, days after second dose	21 (20–27)	22 (18–28)	NA	NA
V4, days after first dose	224 (222–228)	224 (222–227)	227 (223–237)	NA
V4, days after second dose	112 (110–119)	113 (110–117)	NA	NA

^aValues displayed are medians, with interquartile range in parentheses for continuous variables or percentages for categorical variables.

^bThe previously naive cohort and previously infected cohort that also received two vaccine doses were compared by the following statistical tests: for continuous variables, Mann-Whitney U test; for categorical variables, Fisher's test. Values in bold are statistically different between the pre-infected naive and pre-infected cohorts. No statistical difference was found between the two pre-infected subcohorts, except between naive and pre-infected for days before V0 and days after V2.

^cThe previously infected cohort with one dose was likewise compared with the previously infected cohort that received two doses. No significant differences were observed between the two cohorts.

responses were not associated with subsequent V3 and V4 antibody responses, but significant correlations were found between RBD-specific B cells at V2 and RBD IgG, total Spike antibody, cell binding, and ADCC at V3 (Figure 1F). Similarly, V3 RBD-specific B cell responses correlated significantly with V4 RBD-specific IgG, total anti-Spike antibody levels, and ADCC, suggesting that the B cell pool post boost conditioned the long-term quantity and quality of the humoral response.

To determine how B cell populations qualitatively evolved, we measured IgD, IgM, IgG, and IgA expression in RBD-specific B cells. In the naive cohort, we detected subpopulations of IgD⁺, IgM⁺, and IgA⁺ cells at V1, whose proportion decreased at V3 and V4 visits. In contrast, RBD-specific memory B cells in PI donors were almost entirely IgG⁺ at all time points (Figures 1G, S1E, and S1F). To assess B cell differentiation, we quantified IgD and CD27 co-expression (Figure S1G). CD27 is predominantly expressed on memory B cells (Tangye et al., 1998), and IgD on unswitched B cells (Moore et al., 1981). In the naive cohort, IgD⁺CD27⁻ RBD-specific B cells present at V1 disappeared at V3, while IgD⁻CD27⁺ RBD-specific B cells emerged (Figure 1H), consistent with isotype-switched memory B cells. This subset contracted at V4. In PI, IgD⁻CD27⁺ cells already present at baseline expanded after priming and remained stable at V2. Boosting did not further expand this subset.

Instead, it gradually declined at V3 and V4. A class-switched IgG⁺ DN population dominated at all time points (Figures 1H, S1H, and S1I).

These data show that despite the long 16-week interval and the divergent RBD-specific B cell trajectories after the first dose, boosting in naive subjects induced robust recall responses with a mature phenotype that converged with those observed in PI individuals.

The first and delayed second vaccine doses elicit Spike-specific CD4⁺ T cell responses of similar magnitude

CD4⁺ T cells help play a critical role in development of B cell and CD8⁺ T cell immunity. We measured Spike-specific T cell responses at the V0–V4 time points in the three cohorts (Figures 2 and S2). As in our previous work (Tauzin et al., 2021b), we used a T cell receptor-dependent activation-induced marker (AIM) assay that broadly identifies antigen-specific T cells and functional profiling by intracellular cytokine staining (ICS) (for flow cytometry panels, see Tables S2 and S3).

The AIM assay involved a 15-h incubation of peripheral blood mononuclear cells (PBMCs) with an overlapping peptide pool spanning the Spike coding sequence and the upregulation of CD69, CD40L, 4-1BB, and OX-40 upon stimulation. We used an AND/OR Boolean combination gating to assess total

frequencies of antigen-specific CD4⁺ and CD8⁺ T cells (Figures S2A and S2B) (Niessi et al., 2020a). At V3, all individuals had CD4⁺ T cell responses (Figure S2C), and most had CD8⁺ T cell responses (Figure S2D).

In contrast to B cell responses, the kinetics of Spike-specific AIM⁺CD4⁺ T cell responses was similar between naive and PI individuals (Figure 2A). Several naive participants had detectable AIM⁺CD4⁺ T cell responses at baseline, probably due to cross-reactivity with other coronaviruses (Mateus et al., 2020). The significant increase at V1 was followed by a moderate attrition at the V2 memory time point. The second dose significantly boosted the responses at V3 in naive, whereas the increase was non-significant in PI. No significant differences in median magnitude of AIM⁺CD4⁺ T cell responses were observed at V1 and V3 between naive and PI, although a faster decay in naive created a significant difference at V4 (Figure 2B).

The ICS assay involved a 6-h stimulation with the Spike peptide pool and measurement of effector molecules interferon- γ (IFN- γ), interleukin-2 (IL-2), tumor necrosis factor α (TNF- α), IL-17A, IL-10, and CD107a. We defined cytokine⁺CD4⁺ T cell responses by an AND/OR Boolean gating strategy (Figure S2E). The ICS patterns in both cohorts paralleled the AIM assays, albeit at a lower magnitude (Figures 2C, 2D, and S2F). Consistent with the lower ability of ICS to detect memory cells compared with recently primed or reactivated cells (da Silva Antunes et al., 2018), the relative increase in cytokine⁺CD4⁺ T cells was stronger at V1 versus V0 and V3 versus V2. Cytokine⁺CD4⁺ T cell responses at V4 remained significantly higher than at baseline, showing longer-term memory, but without significant gain compared with V2.

The magnitude of Spike-specific AIM⁺ T cell responses was globally lower in CD8⁺ than in CD4⁺ T cells (Figures 2E, 2F, and S2G). The trajectories of AIM⁺CD8⁺ T responses were heterogeneous. Naive participants elicited weak but significant responses after priming, and a trend for stronger responses after the boost. There was higher heterogeneity in PI, consistent with variable pre-existing responses before vaccination. Several PI showed robust responses after the priming and boosting inoculations, although the increase did not reach statistical significance (Figure 2E). AIM⁺CD8⁺ T cell responses declined significantly at V4 for naive participants while the decrease was slower for the PI cohort. Total cytokine⁺CD8⁺ T cell responses were weak or undetectable in most participants, precluding their detailed analysis (Figure S2H).

To define the evolution of T cell responses in the absence of boosting, we examined the single-dose PI cohort. In these participants, the magnitude of AIM⁺CD4⁺ (Figure S2I), AIM⁺CD8⁺ (Figure S2J), and cytokine⁺CD4⁺ (Figure S2K) T cell responses did not further decline at V3', suggesting stable early memory. We did not observe significant differences in AIM⁺CD4⁺ and CD8⁺ T cell responses between this V3' time point in the single-dose PI cohort compared with the V3 post boost in the two-dose PI cohort, while we saw stronger cytokine⁺CD4⁺ T cell responses in the two-dose PI cohort. The boost helped maintain higher T cell responses at the V4 late memory time point, with a significant difference for the AIM⁺CD4⁺ T responses (Figures S2L–S2N).

As expansion of previously primed antigen-specific T cells may impact T cell responses to vaccination, we examined corre-

lations across visits (Figure 2G) and found a significant association or a strong trend between CD4⁺ T cell responses at V0 and the post-first-dose time points V1 and V2, but not after the second dose. Similar to CD4⁺ T cells, we observed that pre-existing CD8⁺ T cell responses at V0 significantly correlated with responses to the first dose at V1, and that this association disappeared after the second dose (Figure 2H). Therefore, the second vaccine dose reduced the heterogeneity in magnitude of T cell responses and its link to pre-vaccination immunity.

These data show that a single dose of the BNT162b2 is sufficient to induce CD4 Th and CD8⁺ T cell responses in most participants. After a 16-week interval, the second dose boosts CD4⁺ and CD8⁺ T cell responses back to the peak magnitudes reached soon after priming. Pre-vaccination T cell immunity is associated with the BNT162b2-induced CD4⁺ and CD8⁺ T cell responses to the first vaccination, but this correlation is lost after boosting.

The 16-week interval BNT162b2 regimen elicits phenotypically diverse CD4⁺ T helper subsets

We next profiled the qualitative heterogeneity and evolution of Spike-specific AIM⁺CD4⁺ T cells. To avoid a priori defined marker combinations, we performed unsupervised analyses of the high-dimensional flow cytometric phenotyping data (Figure 3). We examined chemokine receptors that are preferentially, but not exclusively, expressed by some lineages and involved in tissue homing (CXCR5 for Tfh; CXCR3 for Th1; CCR6 for Th17/Th22 and mucosal homing; CXCR6 for pulmonary mucosal homing [Day et al., 2009; Morgan et al., 2015]), CD38 and HLA-DR as activation markers, and PD-1 as inhibitory checkpoint.

We illustrated the distribution of clustered populations by the uniform manifold approximation and projection (UMAP) algorithm (Becht et al., 2018). Cluster identity was performed using Phenograph (Levine et al., 2015), resulting in the identification of ten clusters (Figures 3A and 3B) based on distinct profiles of relative marker expression (Figures 3C and S3A). All ten clusters were detectable at V0 and persisted at all time points. The relative frequencies of each cluster did not show major differences across visits (Figure 3D), but there were fluctuations and inter-individual variations within cohorts (Figures 3E and S3B). We did not observe emergence of new Th clusters after the second inoculation. While variability and relatively small cohort size precluded definitive conclusions about the behavior of individual clusters, some general trends were observed. In naive, most clusters showed either a significant increase or a trend for increase after the second dose (Figure 3E), except C4 (Figure S3B). These included clusters enriched in CXCR5 (C3 and C5) and CXCR3 (C2, C3, and C10). In contrast, the qualitative response to the second in PI was more constrained (Figures 3D and S4C). Consistent with the analysis of total AIM⁺CD4⁺ cells, all naive participant clusters declined at V4, except C4 (Figures 3E and S3B). Although some clusters also showed a trend for decline in PI (C5, C6, C9, and C10), most did not (C1, C2, C3, C4, C7, and C8).

We next performed univariate analyses of chemokine receptor expression (Figures 3F–3K and S3D–S3I). CXCR5⁺AIM⁺CD4⁺ T cells increased after both doses in naive individuals, but only after the first dose in PI (Figure 3F). Trajectories did not

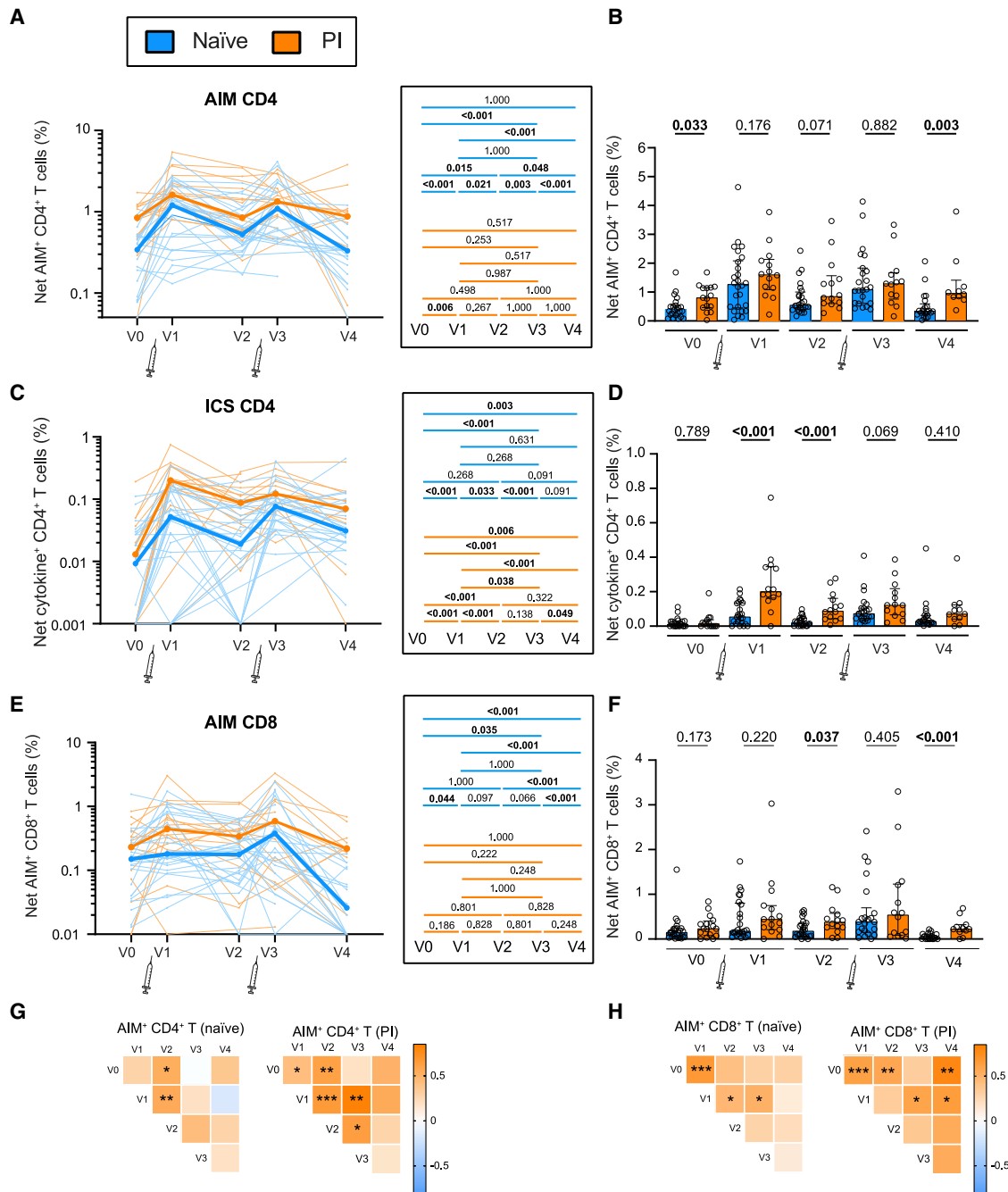


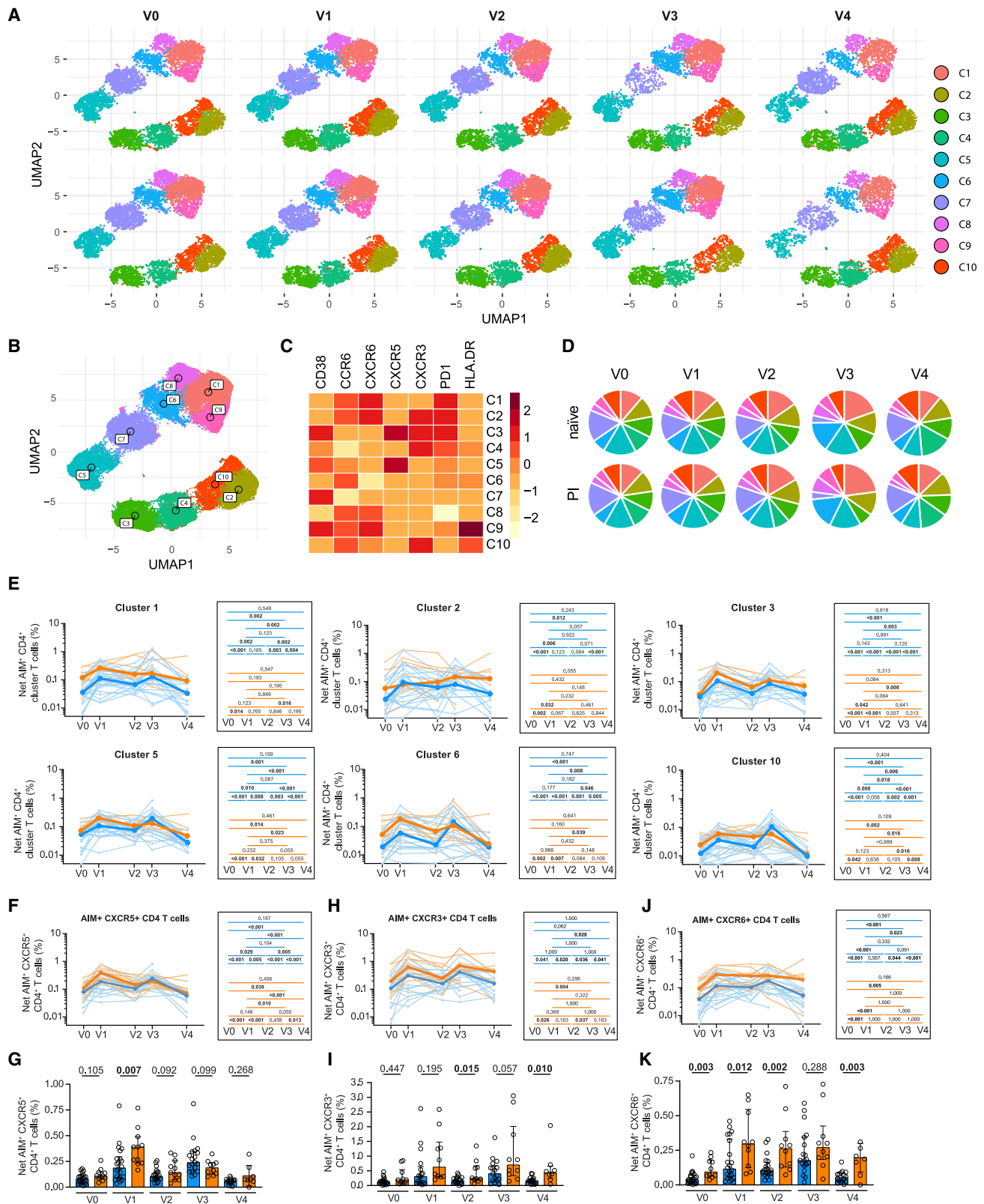
Figure 2. The first and delayed second vaccine doses elicit Spike-specific CD4⁺ T cell responses of similar magnitude

SARS-CoV-2 Spike-specific CD4⁺ and CD8⁺ T cells in naive (blue) and PI (orange) receiving two vaccine doses.

(A–F) (A and B) Longitudinal (A) and intercohort (B) analyses of net Spike-specific AIM⁺CD4⁺ T cell responses. Right: statistical comparisons. (C and D) Longitudinal (C) and intercohort (D) analyses of the net magnitude of cytokine⁺CD4⁺ T cell responses. (E and F) Longitudinal (E) and intercohort (F) analyses net AIM⁺CD8⁺ T cell responses. The bold lines in (A), (C), and (E) represent median values. The bars in (B), (D), and (F) represent median ± interquartile range. In (A), (C), and (E), the syringe indicates vaccine dose inoculation and the right-hand panels show statistical comparisons. Pairwise (A, C, E) and intercohort (B, D, F) statistical analyses were performed using a linear mixed model.

(G and H) Heatmap showing temporal correlations of (G) AIM⁺CD4⁺ and (H) AIM⁺CD8⁺ T cells between the different time points for naive and PI participants. Significant Spearman test results are indicated (*p < 0.05, **p < 0.01, ***p < 0.001).

In (A) to (F), n = 26 naive and n = 15 PI; in (G) and (H), n = 26 naive and n = 27 PI (comparisons at time points V0, V1, and V2), and n = 15 PI (comparisons at time points V3 and V4).



(legend on next page)

statistically differ between cohorts past V1 (Figure 3G). CXCR3⁺AIM⁺CD4⁺ T cells increased similarly after either dose, with significant decline post first inoculation (Figure 3H). This pattern was similar in naive and PI, but the CXCR3⁺ subset was more abundant in PI (Figure 3I). CXCR6⁺AIM⁺ (Figures 3J and 3K) and CCR6⁺AIM⁺CD4⁺ T cells (Figures S3H and S3I) remained persistently elevated after priming in PI, while in naive they were weaker at early time points but responsive to the second dose at V3. However, they declined at the late memory time point V4 in this cohort.

Therefore, the first vaccine dose already elicits phenotypically diverse Th clusters that do not necessarily fit with canonical lineages. The second vaccine dose variably impacted these subsets but did not elicit new clusters. Th phenotype in PI was enriched in markers, suggestive of prior mucosal priming.

The delayed second BNT162b2 dose leads to partially convergent functional profiles in naive and PI participants

We next applied the same unsupervised analysis pipeline to Spike-specific cytokine⁺CD4⁺ T cells for the six functions measured, identifying 11 clusters (Figures 4A–4C and S4A) that were present at all time points (Figures 4A and 4D), with notable interindividual differences within each cohort (Figures 4E and S4B). However, we observed clearer functional differences between cohorts and between doses when compared with phenotypic analysis. Most clusters increased after both doses in naive, whereas they expanded only after the first dose in PI (Figures 4E and S4B). Individual clusters followed different trajectories depending on pre-infection status (Figures 4E and S4C). The evolution of the IL-2 enriched C1, the most abundant cluster, was similar in the PI and naive cohorts, except for significant contraction at V4 in naive only. In contrast, the C2 and C3 clusters, characterized by high IFN- γ expression, were markedly larger in PI after the first dose, but responded more to the second dose in naive. Consequently, the responses of C2 and C3 partially converged at V3 compared with V1; they significantly contracted at V4. The polyfunctional cluster C5, enriched in IFN- γ , IL-2, TNF- α , and CD107a, showed yet another pattern: it was expanded in PI compared with naive at all time points, and showed excellent long-term stability in both cohorts.

Single-parameter analyses (Figures 4F–4K) showed that in naive participants the first dose significantly increased IFN- γ ⁺ and IL-2⁺ CD4⁺ T cell responses, with a strong trend for an increase in TNF- α ⁺ responses. The increase in ICS responses was greater in PI. The second dose significantly boosted these responses in naive only, contrasting with little effect in PI. These

differential trajectories led to partially convergent CD4⁺ T cell functions after repeated antigenic challenges in naive and PI at V3. However, consistent with AIM measurements, weaker responses in naive at V4 led to re-emergence of significant differences at this late memory time point.

These analyses show that pre-infection status is associated with significant differences in the functional profile elicited by the first BNT162b2 dose. Preferential expansion of Th1-cytokine-enriched subsets after boosting in naive participants contrasting with stable responses in PI leads to partial, and possibly transient, convergence of Th functions between cohorts after full vaccination. The unsupervised analysis reveals a polyfunctional cluster of CD4⁺ T cells stably maintained at the late memory time point.

Temporal relationships between antigen-specific CD4⁺ T cell, B cell, and CD8⁺ T cell responses

As CD4⁺ T cell help is essential for optimal adaptive B cell and CD8⁺ T cell immunity, we next examined the temporal associations between these immune components (Figure 5). We considered the total Spike-specific AIM⁺CD4⁺ T cells, the AIM⁺C1-C10 clusters, the total Spike-specific cytokine⁺CD4⁺ T cells, and the ICS (cyto⁺C1–C11) clusters at time points V0–V3. We applied unsupervised clustering analyses to determine the longitudinal relationships between these Th subsets and RBD-specific B cell (Figure 5A) and AIM⁺CD8 T cell (Figure 5B) responses, measured at V3 after completing the vaccination regimen.

We observed significant positive correlations between all AIM⁺CD4⁺ T cell subsets elicited at V1 and the B cell responses at V3 after the second dose (Figure 5A). This contrasted with the weaker correlations between V2–V3 cytokine⁺ Th responses and RBD-specific B cells at V3. Some of the positively correlated clusters (AIM⁺C3, AIM⁺C5) were enriched in CXCR5⁺ cells. Consistently, CXCR5⁺AIM⁺CD4⁺ T cell responses at V1 strongly correlated with B cell responses at V3, but this association weakened for V2 and disappeared at V3 (Figure 5C). Similar patterns were seen with total AIM⁺CD4⁺ T cells (Figure S5A) and for some non-circulating Tfh (cTfh) subsets, but we did not have the statistical power to rank the strength of the correlations.

We next examined the temporal associations between longitudinal Th subsets and AIM⁺CD8⁺ T cells at V3 (Figure 5B). Th responses at V1 showed no significant correlation with AIM⁺CD8⁺ T cells at V3. However, we found significant correlations between cytokine⁺CD4⁺ T cell subsets at the pre-boost V2 memory time point or at the contemporaneous V3 and the AIM⁺CD8⁺ T cell responses at V3, and IFN- γ ⁺CD4⁺ T cells at V2 correlated with AIM⁺CD8⁺ T cells at V3 (Figure 5D), as did total cytokine⁺CD4⁺ T cell responses (Figure S5B).

Figure 3. The 16-week interval BNT162b2 regimen elicits phenotypically diverse CD4⁺ T helper subsets

(A) Multiparametric UMAP representation of Spike-specific AIM⁺CD4⁺ T cells at each time point, with aggregated data for the two-dose naive and PI cohorts. The colors identify ten populations clustered by unsupervised analysis.

(B) Clusters are labeled on the global UMAP.

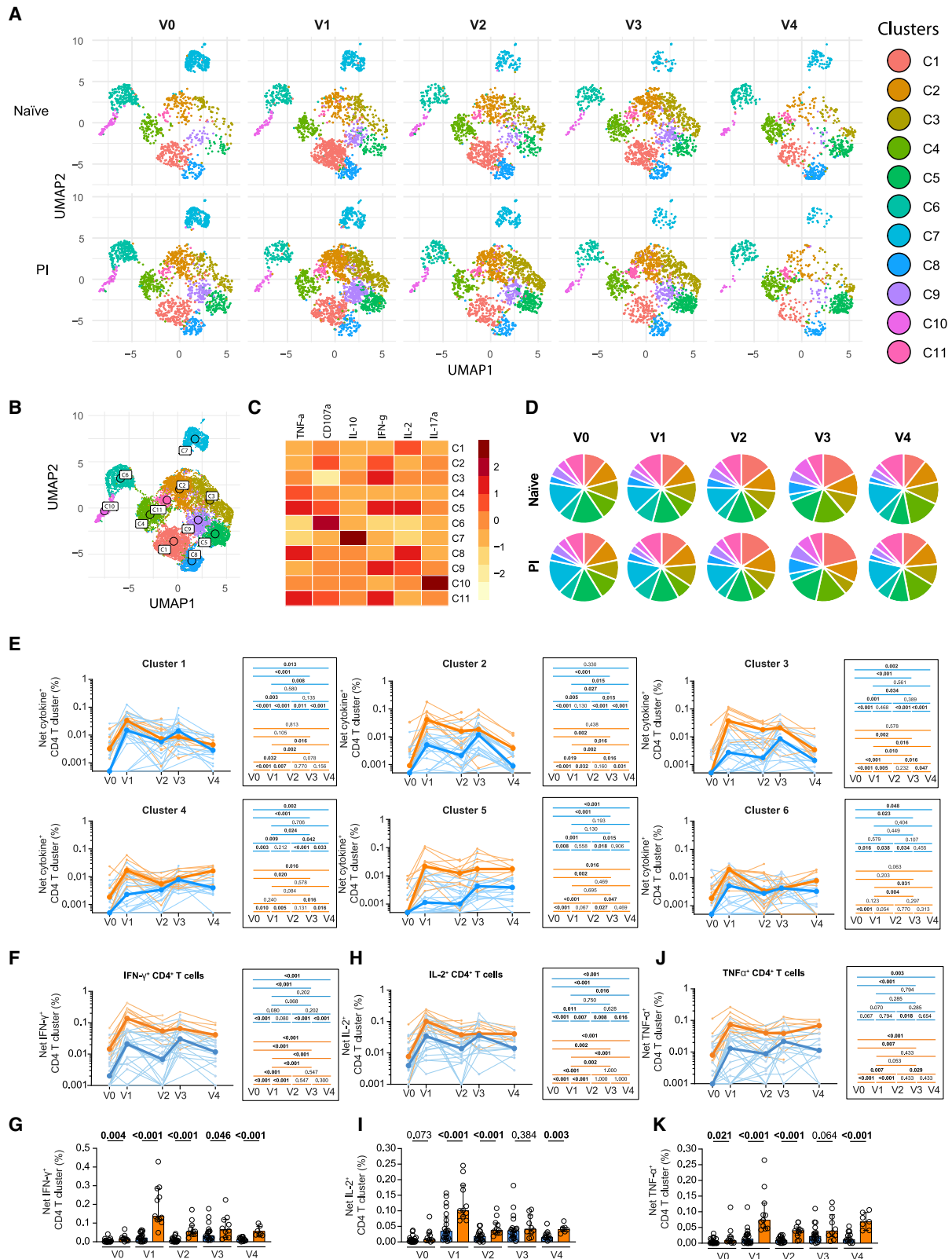
(C) Heatmap summarizing mean fluorescence intensity of each loaded parameter.

(D) Pie charts depicting the proportion of each identified cluster within total AIM⁺CD4⁺ T cells.

(E, F, H, and J) Longitudinal frequencies of selected AIM⁺CD4⁺ T cell (E) clusters and (F) CXCR5-expressing, (G) CXCR6-expressing, and (H) CXCR3-expressing AIM⁺CD4⁺ T cells. Bold lines represent cohort's median value. Right: Wilcoxon tests for each pairwise comparison.

(G, I, and K) Cohort comparisons at each time point for (G) CXCR5-expressing, (I) CXCR3-expressing, and (K) CXCR6-expressing AIM⁺CD4⁺ T cells. Bars represent median \pm interquartile range.

In (A) to (K), n = 22 naive and n = 11 PI.



(legend on next page)

The differential temporal associations between antigen-specific CD4⁺ T cell, B cell, and CD8⁺ T cell immunity suggest different requirements for the coordination of these responses.

Immune profile kinetics in naive and PI vaccinees shows only partial, and transient, convergence after the delayed second dose

Our data suggest that the relationships between the different immune parameters after the first vaccine dose were strongly influenced by prior infection history, while its impact decreased, but did not disappear, after the second dose. We performed an integrated analysis of 34 features of antibody, B cell CD4⁺ T cell, and CD8⁺ T cell responses (Figure 6A). V1–V4 time points were first loaded altogether (Figure 6B), then from this master principal component analysis (PCA) we depicted each time point separately (Figure 6C). The two cohorts clustered apart at V1 due to a significant difference in principal component 1 (PC1) (Figure 6D). The distance between groups decreased upon attrition of the responses (V2). No statistical difference between naive and PI PC1 was observed at V3, showing convergence of the immune features. Importantly, however, the PC1-driven distinction between naive and PI re-emerged at the late memory time point V4.

We sought to identify the features underlying the group clustering at V1 using the same approach focused on AIM⁺CD4⁺ and cytokine⁺CD4⁺ T cell responses. The correlation between the immune features and PC1 identified anti-RBD IgG levels, memory RBD-specific B cells, and IFN- γ -enriched Spike-specific CD4⁺ T cell clusters with little contribution of AIM⁺CD4⁺ T cells. A PCA analysis performed using AIM⁺CD4⁺ T cell features confirmed the limited contribution of these features to cohort clustering (Figure S6A), in contrast to the cytokine⁺CD4⁺ T cells (Figure S6B).

Therefore, unsupervised integrated analysis shows that pre-infection status shapes a vaccine-induced hybrid immunity after the first dose, while its influence largely wanes in the short-term response to the second dose but subsequently becomes more manifest again 8 months after initial inoculation.

DISCUSSION

The decision to extend intervals between doses of the BNT162b2 mRNA vaccine led to concerns about vaccine immunogenicity and efficacy. Here, we profiled the B cell, CD4⁺ T cell, CD8⁺ T cell, and antibody responses in SARS-CoV-2 naive and PI individuals who received the two vaccine doses 16 weeks apart. We longitudinally followed these immune features from

baseline over an 8-month period to determine the characteristics and temporal associations of the immune features elicited by this wide-interval immunization regimen.

We observed that in naive participants, the priming dose elicited RBD-specific responses of low magnitude, a strong increase after the second dose administered after 16 weeks, and a moderate contraction in the following months. These robust B cell responses were associated with the development of strong and broad humoral responses, as we reported (Tauzin et al., 2021a). The phenotypic changes were consistent with B cell maturation. However, while we observed the expansion of a CD27⁺IgD⁻ memory subset after the second dose compared with the first dose, a majority of double-negative (CD27⁻IgD⁻) cells was measured at all time points. This phenotypic subset was described in autoimmune diseases (Jenks et al., 2018; Wei et al., 2007) and in response to vaccination (Ruschil et al., 2020). Their transcriptional program is distinct from canonical switched memory cells and naive cells (Jenks et al., 2018). They may be associated with an extrafollicular maturation pathway (Ruschil et al., 2020). In our study, the long-lasting persistence of these cells and their expression of RBD-specific IgG may suggest an atypical switched memory subset. These data are consistent with development of functional memory B cells with robust recall potential, alleviate the concern that an extended-interval regimen would lead to poor antibody immunity, and are in line with recent findings (Parry et al., 2021; Payne et al., 2021).

The kinetics of B cell responses differed in PI and naive individuals: the first vaccine dose elicited a brisk expansion of RBD-specific B cells in PI, with subsequent partial attrition before the delayed boost that did not expand them further. Consequently, B cell responses were similar in naive and PI participants post boost. The responses observed after the first dose are consistent with results from other studies (Efrati et al., 2021; Stamatatos et al., 2021; Tauzin et al., 2021b; Urbanowicz et al., 2021). A previous short-interval regimen study showed a profound impact of the second dose on antigen-specific B cell responses in naive participants, but a limited one in PI, with convergent trajectories between the groups (Goel et al., 2021). Our results demonstrate that this holds true after an extended 16-week interval, consistent with the limited quantitative and qualitative enhancement of humoral immunity we previously reported (Tauzin et al., 2021a). It further suggests that pre-infection can accelerate the generation of stable memory RBD-specific B cell responses.

CD4⁺ T cell responses were already quantitatively robust after the first dose. Although variable in magnitude, they were induced

Figure 4. The delayed second BNT162b2 dose leads to partially convergent functional profiles in naive and PI participants

(A) Multiparametric UMAP representation of Spike-specific ICS cytokine⁺CD4⁺ T cells at each time point, with aggregated data for the two-dose naive and PI cohorts. The colors identify 11 populations clustered by unsupervised analysis. (B) Each cluster is labeled on the global UMAP. (C) Heatmap summarizing the mean fluorescence intensity of each loaded parameter. (D) Pie charts depicting the proportion of each cluster within total cytokine⁺CD4⁺ T cells. (E, F, H, and J) Longitudinal frequencies of selected cytokine⁺CD4⁺ T cell (E) clusters and (F) IFN- γ ⁺, (H) IL-2⁺, and (J) TNF- α ⁺ single functions in naive (blue) and PI (orange) participants. Bold lines represent the cohort's median value. Right: Wilcoxon tests for each pairwise comparison. (G, I, and K) Cohort comparisons at each time point for (G) IFN- γ ⁺, (I) IL-2⁺, and (K) TNF- α ⁺ single functions. Bars represent median \pm interquartile range. In (A) to (K), n = 22 naive and n = 11 PI.

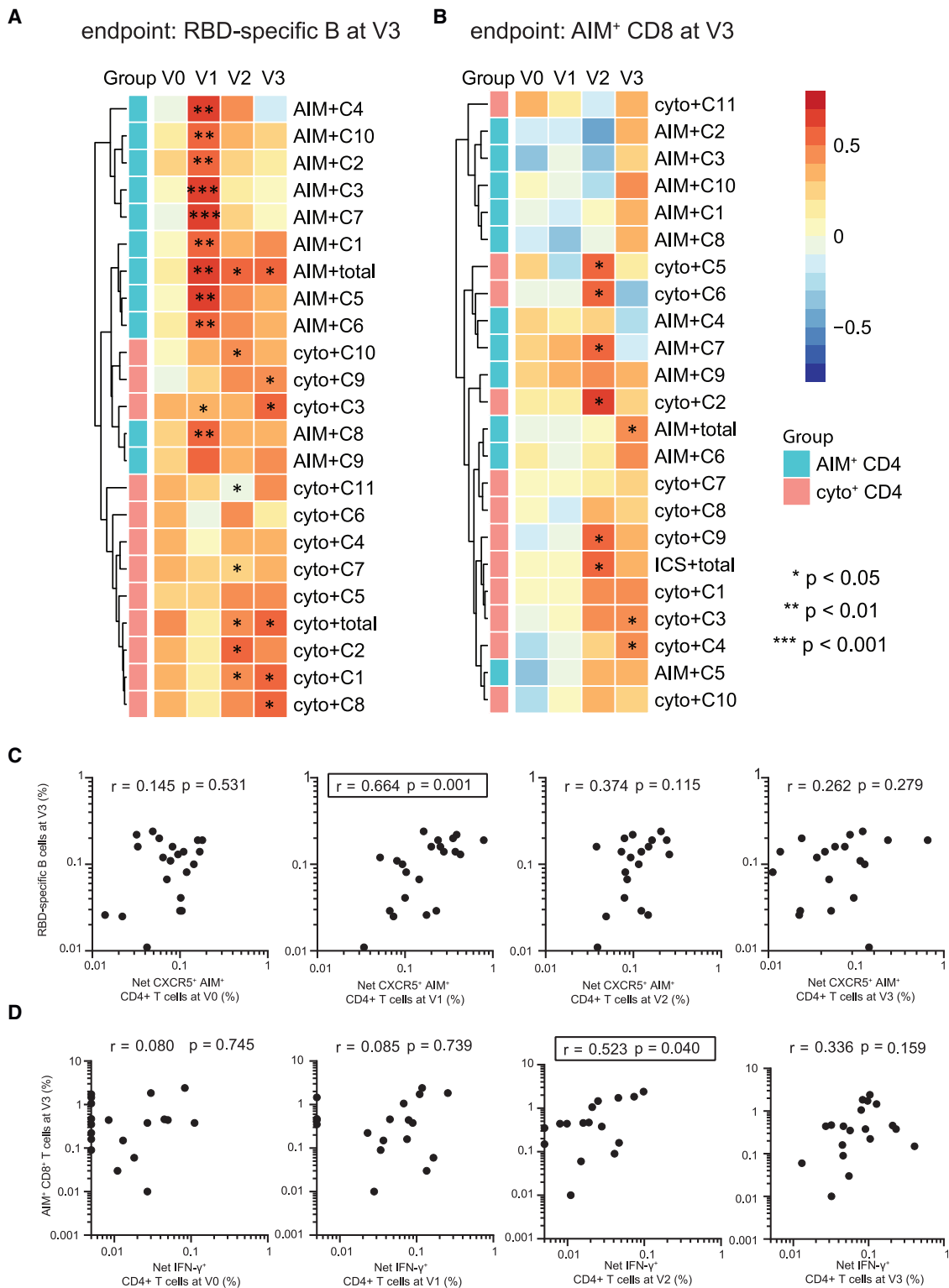


Figure 5. Temporal relationships between antigen-specific CD4⁺ T cell, B cell, and CD8⁺ T cell responses in naive participants (A and B) Heatmaps displaying temporal correlations between the different subsets of Spike-specific CD4⁺ T cells measured by AIM or ICS assays at the V0, V1, V2, and V3 time points and: (A) RBD-specific B cell frequencies measured at V3; (B) AIM⁺CD8⁺ T cell frequencies measured at V3. Asterisks indicate significance (*p < 0.05, **p < 0.01, ***p < 0.001). The CD4⁺ T cell clusters were stratified by assay (cyan, AIM; light red, ICS).

(legend continued on next page)

in all individuals examined. Mirroring the B cell findings, CD4⁺ T cell responses decreased moderately before boosting, a contraction to memory that does not have the time to occur in the standard 3-week interval schedule. The second dose reinvigorated Spike-specific CD4⁺ T responses without surpassing those elicited by the first dose. These trajectories are consistent with short-interval studies (Oberhardt et al., 2021; Painter et al., 2021).

Our unsupervised and supervised analyses demonstrated that the BNT162b2 vaccine elicits a highly diversified CD4⁺ T cell response, which is maintained over time with no novel distinct subset after the boost. This is consistent with a recent short-delay vaccination study (Rodda et al., 2022). Some qualitative Th features differed between the naive and PI cohorts, and evolved between time points within cohorts. We observed higher frequencies of CXCR6 Th cells in PI than in naive. As CXCR6, the CXCL16 ligand, is a homing molecule to the respiratory mucosa (Day et al., 2009; Morgan et al., 2015), these results are consistent with prior priming of CD4⁺ T cells at this anatomic site during SARS-CoV-2 infection in PI participants, resulting in differences in their differentiation program, compared with intramuscular vaccine injection. We observed a similar pattern for CCR6, a marker of Th17 and Th22 cells that play an important role in maintaining mucosal barriers and contribute to pathogen clearance at mucosal surfaces (Aujla et al., 2008; Khader et al., 2007). Functional CD4⁺ T cell subsets also presented differential kinetics between naive and PI individuals but in both cohorts, we identified a polyfunctional Th1 cell subset with excellent temporal stability. An analogous population has been associated with vaccine protection in a murine *Leishmania* model (Darrach et al., 2007). Previous studies reported robust Th1 and Tfh responses after short-delay vaccinations (Goel et al., 2021; Oberhardt et al., 2021; Painter et al., 2021; Sahin et al., 2020). Our unsupervised analyses are consistent with these findings, as such responses defined the bulk of our Spike-specific clusters. Recent unsupervised analyses conducted in short-delay vaccination samples reported that hybrid immunization combining natural and vaccinal challenges imprints partially distinct functional features on SARS-CoV-2-specific CD4⁺ T cells (Rodda et al., 2022). These imprints attenuated after a third dose. Our data globally suggest that evolution over time contributes to partial convergence between vaccinal and hybrid immunities. Some hybrid immunity imprints were maintained, as we detected a higher frequency of IFN- γ - and TNF- α -rich clusters in PI compared with naive participants at late memory time points.

The hybrid immunity elicited in PI was associated with a more durable immune memory up to 8 months after the first dose. The pattern was particularly pronounced for AIM⁺CD8⁺ T cells. Besides loss of cytotoxic T lymphocyte (CTL) responses, there are other possible explanations: the measurements in peripheral blood may not reflect persistent tissue-resident memory populations in other anatomic compartments; and the activation-

induced markers used may be insensitive to identifying some antigen-specific T cell subsets.

We identified strong temporal associations between several subsets of early vaccine-induced cTfh, a lineage critical for B cell help, and other CD4⁺ T cell subsets with B cell responses measured several months after the boost, but these correlations were lost at later time points. While the observed disconnect in peripheral blood measurements at the late time points might be related to compartmentalization in lymphoid tissues (rather than major changes in CD4-B cell interplay), they suggest that the early antigen-specific CD4⁺ T cell responses critically shape the B cell pool, which will later respond to the delayed boosting. Despite the difference in dosing intervals, these results are thus consistent with the immune dynamics observed in the standard regimen (Oberhardt et al., 2021; Painter et al., 2021; Rodda et al., 2022). In contrast, Th1 features identified at the early memory time point were better associated with the CTL responses after full vaccination, and we noted contemporaneous correlations as well. While this might suggest that the responsiveness of CD8⁺ T cells to boosting benefit from the pre-existing memory Th pool, mechanistic studies in murine models have shown that CD4⁺ T cell help is key at the time of CTL priming (Laidlaw et al., 2016), although they still play important roles later (Nakanishi et al., 2009). Our observational study does not allow us to delineate causation due to other factors.

While the initial rationale of delaying the second dose was to provide some level of immunity more rapidly to a larger number of people in the context of limiting vaccine supply, our results suggest that this strategy provides strong, multifaceted B and T cell immunity. The potential immunological benefits of increasing the interval between doses must be weighed against a prolonged period of good but still suboptimal protection, particularly while the virus and its different variants of concern are still circulating in the population at epidemic levels. Many countries now recommend a third dose, usually at least 6 months after the second dose. The benefit of a third dose in the context of a 16-week interval between the first and second dose will warrant further investigation.

Limitations of the study

Many individuals in the naive cohort had detectable AIM⁺ and cytokine⁺ T cell responses at baseline. We interpreted this as likely reflecting the presence of a pre-existing pool of cross-reactive cells to other coronaviruses (Grifoni et al., 2020; Shrock et al., 2020; Mateus et al., 2020; Loyal et al., 2021). Formal demonstration in our cohort would require epitope-specific mapping of T cell responses, for which we did not have enough PBMC samples available.

Whether the long interval between doses and/or the pre-infection status affects the differentiation of T cell responses, particularly of vaccine-induced CD8⁺ T cells, is a question that may impact the efficacy of these responses. We did not address this issue, which will require further studies.

(C) Correlations between frequencies of AIM⁺CXCR5⁺ CD4⁺ T cells (for cTfh) at the V0–V3 visits and RBD-specific B cell frequencies at V3.

(D) Correlations between frequencies of IFN- γ ⁺ (as Th1 function) at the V0–V3 visits and AIM⁺CD8⁺ T cell at V3. The r and p values from a Spearman test are indicated in each graph.

In (A) and (C), n = 21 naive; in (B) and (D), n = 19 naive.

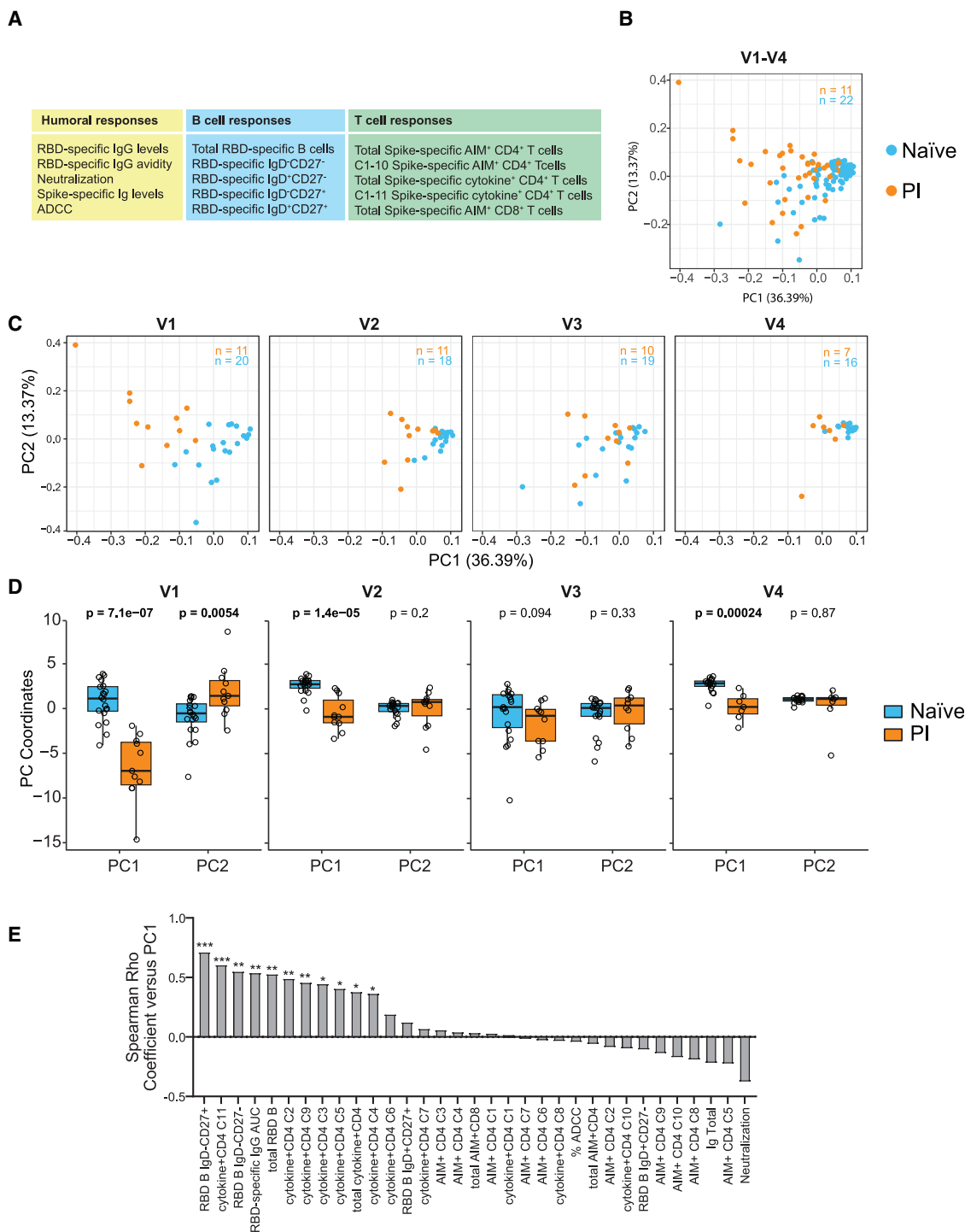


Figure 6. Immune profile kinetics between naïve and PI vaccinees shows only partial, and transient, convergence after the delayed second dose

Integrated PCA analysis combining various immune features to compare evolution of vaccine responses in the two-dose naïve and PI cohorts.

(A) List of the 34 antigen-specific immune magnitudes included in the PCA analysis.

(B) Global PCA analysis. The percentage on the x and y axes presents the variance attributed to PC1 and PC2, respectively.

(legend continued on next page)

The goal of our study was to provide an in-depth characterization of SARS-CoV-2 vaccine responses. The size of the cohorts investigated here, particularly of the one-dose and two-dose PI cohorts, is not sufficient to robustly prove the benefit of hybrid immunity. However, this question has also been addressed in other reports, with results consistent with our study (Goel et al., 2021; Painter et al., 2021; Rodda et al., 2022).

We did not provide a direct side-by-side comparison of cellular immunity in the long- versus short-interval vaccine regimens. However, in another study, we investigated the impact of dose spacing on antibody responses and demonstrated that the delayed boosting facilitates antibody maturation, resulting in enhanced recognition breadth and neutralization against SARS-CoV-2 variants (Chatterjee et al., 2022).

Our study conducted in a low-risk HCW cohort may not be generalizable to vulnerable groups, particularly immunocompromised or elderly populations, in which the immune responses and the risk/benefit ratio may differ. Future studies will be required to better quantify the immune response over time in these populations.

STAR★METHODS

Detailed methods are provided in the online version of this paper and include the following:

- **KEY RESOURCES TABLE**
- **RESOURCE AVAILABILITY**
 - Lead contact
 - Materials availability
 - Data and code availability
- **EXPERIMENTAL MODEL AND SUBJECT DETAILS**
 - Ethics statement
 - Participants
 - PBMCs and plasma collection
 - Cell lines
- **METHOD DETAILS**
 - Protein expression and purification
 - RBD-specific IgG levels and avidity measured by enzyme-linked immunosorbent assay (ELISA)
 - Spike IgG levels measured by cell-based ELISA (CBE)
 - ADCC assay
 - Virus neutralization assay
 - SARS-CoV-2-specific B cells characterization
 - Activation-induced marker (AIM) assay
 - Intracellular cytokine staining (ICS)
- **QUANTIFICATION AND STATISTICAL ANALYSIS**
 - Statistical analysis
 - Software scripts and visualization

SUPPLEMENTAL INFORMATION

Supplemental information can be found online at <https://doi.org/10.1016/j.celrep.2022.111013>.

ACKNOWLEDGMENTS

The authors are grateful to the study participants. We thank the CRCHUM BSL3 and Flow Cytometry platforms for technical assistance, Dr. Johanne Poudrier for advices and discussions, Dr. Stefan Pöhlmann (Georg-August University, Germany) for the plasmid coding for SARS-CoV-2 S glycoproteins, and Dr. M. Gordon Joyce (U.S. MHRP) for the monoclonal antibody CR3022. This work was supported by an FRQS Merit Research Scholar award to D.E.K., the Fondation du CHUM, le Ministère de l'Économie et de l'Innovation du Québec, Program de soutien aux organismes de recherche et d'innovation (to A.F.), a CIHR operating grant #178344 (D.E.K. and A.F.), a foundation grant #352417 (A.F.), a CIHR operating Pandemic and Health Emergencies Research grant #177958(A.F.), and an Exceptional Fund COVID-19 from the Canada Foundation for Innovation (CFI) #41027 to A.F. and D.E.K. The Symphony flow cytometer was funded by a John R. Evans Leaders Fund Leader Fund from the Canada Foundation for Innovation (#37521 to D.E.K.) and the Fondation Sclérodémie Québec. A.F. is the recipient of Canada Research Chair on Retroviral Entry no. RCHS0235 950-232424. A.P. holds a Canada Research Chair in Multiple Sclerosis and the Power Corporation of Canada Chair of Université de Montréal. V.M.L. is supported by an FRQS Junior 1 salary award, G.S. by a scholarship from the Department of Microbiology, Infectious Disease and Immunology of the University of Montréal, G.B.B. by an FRQS doctoral fellowship, R.G. and A.L. by a MITACS Accélération postdoctoral fellowship, and J.P. by a CIHR doctoral fellowship. The funders had no role in study design, data collection and analysis, decision to publish, or preparation of the manuscript.

AUTHOR CONTRIBUTIONS

M.N., M.D., A.F., and D.E.K. designed the studies. M.N., G.S., A.N., N.B., and M.L. performed B cell and T cell assays. J.P. generated the B cell probes. M.N., M.D., G.S., A.N., and O.T. performed and analyzed the B and T cell experiments. J.N. contributed to the T cell assay design. O.T. performed unsupervised clustering analyses. L.M., A.T., G.B.-B., D.V., S.Y.G., M.B., R.G., J.P., C.B., G.G.-L., and J.R. performed ELISA, ADCC, flow cytometry, avidity, and neutralization assays. A.L., C.B., G.G.-L., H.M., L.G., C.M., P.A., G.-G.O.-D., C.T., and V.M.-L. secured and processed blood samples. G.G. produced and purified proteins. A.P. provided intellectual input. J.B. and R.L.-B. generated and applied the linear mixed models for statistical comparison. M.N., M.D., and D.E.K. wrote the manuscript. Every author has read, edited, and approved the final manuscript.

DECLARATION OF INTERESTS

The authors declare no competing interests.

Received: January 4, 2022

Revised: April 27, 2022

Accepted: June 6, 2022

Published: June 28, 2022

REFERENCES

- Anand, S.P., Prévost, J., Nayrac, M., Beaudoin-Bussièrès, G., Benlarbi, M., Gasser, R., Brassard, N., Laumaea, A., Gong, S.Y., Bourassa, C., et al. (2021). Longitudinal analysis of humoral immunity against SARS-CoV-2 Spike in convalescent individuals up to 8 months post-symptom onset. *Medicine* 2, 100290. <https://doi.org/10.1016/j.xcrm.2021.100290>.
- Anderson, E.J., Roupheal, N.G., Widge, A.T., Jackson, L.A., Roberts, P.C., Makhene, M., Chappell, J.D., Denison, M.R., Stevens, L.J., Pruijssers, A.J., et al. (2020). Safety and immunogenicity of SARS-CoV-2 mRNA-1273 vaccine

(C) PCA subanalyses divided by time points. Only complete datasets could be loaded in the PCA analysis. The numbers of participants by PCA are shown in each plot.

(D) Box-and-whisker plots of the PC1 and PC2 between group are shown with Mann-Whitney tests.

(E) Spearman correlations between each individual immune feature and PC1 (*p < 0.05, **p < 0.01, ***p < 0.001).

- in older adults. *N. Engl. J. Med.* 383, 2427–2438. <https://doi.org/10.1056/NEJMoa2028436>.
- Apostolidis, S.A., Kakara, M., Painter, M.M., Goel, R.R., Mathew, D., Lenzi, K., Rezk, A., Patterson, K.R., Espinoza, D.A., Kadri, J.C., et al. (2021). Cellular and humoral immune responses following SARS-CoV-2 mRNA vaccination in patients with multiple sclerosis on anti-CD20 therapy. *Nature medicine* 27, 1990–2001. <https://doi.org/10.1038/s41591-021-01507-2>.
- Aujla, S.J., Chan, Y.R., Zheng, M., Fei, M., Askew, D.J., Pociask, D.A., Reinhart, T.A., McAllister, F., Edeal, J., Gaus, K., et al. (2008). IL-22 mediates mucosal host defense against Gram-negative bacterial pneumonia. *Nature medicine* 14, 275–281. <https://doi.org/10.1038/nm1710>.
- Baden, L.R., El Sahly, H.M., Essink, B., Kotloff, K., Frey, S., Novak, R., Diemert, D., Spector, S.A., Roupael, N., Creech, C.B., et al. (2021). Efficacy and safety of the mRNA-1273 SARS-CoV-2 vaccine. *N. Engl. J. Med.* 384, 403–416. <https://doi.org/10.1056/NEJMoa2035389>.
- Bange, E.M., Han, N.A., Wileyto, P., Kim, J.Y., Gouma, S., Robinson, J., Greenplate, A.R., Hwee, M.A., Porterfield, F., Owoyemi, O., et al. (2021). CD8(+) T cells contribute to survival in patients with COVID-19 and hematologic cancer. *Nature medicine* 27, 1280–1289. <https://doi.org/10.1038/s41591-021-01386-7>.
- Beaudoin-Bussi eres, G., Laumaea, A., Anand, S.P., Pr evost, J., Gasser, R., Goyette, G., Medjahed, H., Perreault, J., Tremblay, T., Lewin, A., et al. (2020). Decline of humoral responses against SARS-CoV-2 Spike in convalescent individuals. *mBio* 11. <https://doi.org/10.1128/mBio.02590-20>.
- Becht, E., McInnes, L., Healy, J., Dutertre, C.A., Kwok, I.W.H., Ng, L.G., Ginhoux, F., and Newell, E.W. (2018). Dimensionality reduction for visualizing single-cell data using UMAP. *Nat. Biotechnol.* 37, 38–44. <https://doi.org/10.1038/nbt.4314>.
- Carazo, S., Talbot, D., Boulianne, N., Brisson, M., Gilca, R., Deceuninck, G., Brousseau, N., Drolet, M., Ouakki, M., Sauvageau, C., et al. (2021). Single-dose mRNA vaccine effectiveness against SARS-CoV-2 in healthcare workers extending 16 weeks post-vaccination: a test-negative design from Quebec, Canada. *Clin. Infect. Dis.* 74 (11), ciab739, an official publication of the Infectious Diseases Society of America. <https://doi.org/10.1093/cid/ciab739>.
- Chatterjee, D., Tauzin, A., Marchitto, L., Gong, S.Y., Boutin, M., Bourassa, C., Beaudoin-Bussi eres, G., Bo, Y., Ding, S., Laumaea, A., et al. (2022). SARS-CoV-2 Omicron Spike recognition by plasma from individuals receiving BNT162b2 mRNA vaccination with a 16-week interval between doses. *Cell Rep.* 38, 110429. <https://doi.org/10.1016/j.celrep.2022.110429>.
- Crotty, S. (2019). T follicular helper cell biology: a decade of discovery and diseases. *Immunity* 50, 1132–1148. <https://doi.org/10.1016/j.immuni.2019.04.011>.
- da Silva Antunes, R., Babor, M., Carpenter, C., Khalil, N., Cortese, M., Mentzer, A.J., Seumo, G., Petro, C.D., Purcell, L.A., Vijayanand, P., et al. (2018). Th1/Th17 polarization persists following whole-cell pertussis vaccination despite repeated acellular boosters. *J. Clin. Invest.* 128, 3853–3865. <https://doi.org/10.1172/JCI121309>.
- Darrah, P.A., Patel, D.T., De Luca, P.M., Lindsay, R.W.B., Davey, D.F., Flynn, B.J., Hoff, S.T., Andersen, P., Reed, S.G., Morris, S.L., et al. (2007). Multifunctional TH1 cells define a correlate of vaccine-mediated protection against *Leishmania major*. *Nature medicine* 13, 843–850. <https://doi.org/10.1038/nm1592>.
- Day, C.E., Zhang, S.D., Riley, J., Gant, T., Wardlaw, A.J., and Guillen, C. (2009). A novel method for isolation of human lung T cells from lung resection tissue reveals increased expression of GAPDH and CXCR6. *J. Immunol. Methods* 342, 91–97. <https://doi.org/10.1016/j.jim.2008.12.001>.
- Dickerman, B.A., Gerlovin, H., Madenci, A.L., Kurgansky, K.E., Ferolito, B.R., Figueroa Mu niz, M.J., Gagnon, D.R., Gaziano, J.M., Cho, K., Casas, J.P., and Hern an, M.A. (2022). Comparative effectiveness of BNT162b2 and mRNA-1273 vaccines in U.S. Veterans. *N. Engl. J. Med.* 386, 105–115. <https://doi.org/10.1056/NEJMoa2115463>.
- Earle, K.A., Ambrosino, D.M., Fiore-Gartland, A., Goldblatt, D., Gilbert, P.B., Siber, G.R., Dull, P., and Plotkin, S.A. (2021). Evidence for antibody as a protective correlate for COVID-19 vaccines. *Vaccine* 39, 4423–4428. <https://doi.org/10.1016/j.vaccine.2021.05.063>.
- Efrati, S., Catalogna, M., Abu Hamad, R., Hadanny, A., Bar-Chaim, A., Benveniste-Levkovitz, P., and Levtzion-Korach, O. (2021). Safety and humoral responses to BNT162b2 mRNA vaccination of SARS-CoV-2 previously infected and naive populations. *Sci. Rep.* 11, 16543. <https://doi.org/10.1038/s41598-021-96129-6>.
- Gilbert, P.B., Montefiori, D.C., McDermott, A.B., Fong, Y., Benkeser, D., Deng, W., Zhou, H., Houchens, C.R., Martins, K., Jayashankar, L., et al. (2022). Immune correlates analysis of the mRNA-1273 COVID-19 vaccine efficacy clinical trial. *Science* 375, 43–50. <https://doi.org/10.1126/science.abm3425>.
- Goel, R.R., Painter, M.M., Apostolidis, S.A., Mathew, D., Meng, W., Rosenfeld, A.M., Lundgreen, K.A., Reynaldi, A., Khoury, D.S., Pattekar, A., et al. (2021). mRNA vaccines induce durable immune memory to SARS-CoV-2 and variants of concern. *Science* 374, eabm0829. <https://doi.org/10.1126/science.abm0829>.
- Grifoni, A., Weiskopf, D., Ramirez, S.I., Mateus, J., Dan, J.M., Moderbacher, C.R., Rawlings, S.A., Sutherland, A., Premkumar, L., Jazi, R.S., et al. (2020). Targets of T Cell Responses to SARS-CoV-2 Coronavirus in Humans with COVID-19 Disease and Unexposed Individuals. *Cell* 181, 1489–1501, e1415. <https://doi.org/10.1016/j.cell.2020.05.015>.
- Grunau, B., Goldfarb, D.M., Asamoah-Boaheng, M., Golding, L., Kirkham, T.L., Demers, P.A., and Lavoie, P.M. (2022). Immunogenicity of extended mRNA SARS-CoV-2 vaccine dosing intervals. *JAMA* 327, 279–281. <https://doi.org/10.1001/jama.2021.21921>.
- Hicks, J., Klumpp-Thomas, C., Kalish, H., Shunmugavel, A., Mehalko, J., Denison, J.P., Snead, K.R., Drew, M., Corbett, K.S., Graham, B.S., et al. (2021). Serologic cross-reactivity of SARS-CoV-2 with endemic and seasonal betacoronaviruses. *J. Clin. Immunol.* 41, 906–913. <https://doi.org/10.1007/s10875-021-00997-6>.
- Hoffmann, M., Kleine-Weber, H., Schroeder, S., Kr uger, N., Herrler, T., Erichsen, S., Schiergens, T.S., Herrler, G., Wu, N.H., Nitsche, A., et al. (2020). SARS-CoV-2 cell entry depends on ACE2 and TMPRSS2 and is blocked by a clinically proven protease inhibitor. *Cell* 181, 271–280.e8, e278. <https://doi.org/10.1016/j.cell.2020.02.052>.
- Jenks, S.A., Cashman, K.S., Zumaquero, E., Marigorta, U.M., Patel, A.V., Wang, X., Tomar, D., Woodruff, M.C., Simon, Z., Bugrovsky, R., et al. (2018). Distinct effector B cells induced by unregulated toll-like receptor 7 contribute to pathogenic responses in systemic lupus erythematosus. *Immunity* 49, 725–739.e6, e726. <https://doi.org/10.1016/j.immuni.2018.08.015>.
- Khader, S.A., Bell, G.K., Pearl, J.E., Fountain, J.J., Rangel-Moreno, J., Cilley, G.E., Shen, F., Eaton, S.M., Gaffen, S.L., Swain, S.L., et al. (2007). IL-23 and IL-17 in the establishment of protective pulmonary CD4+ T cell responses after vaccination and during *Mycobacterium tuberculosis* challenge. *Nat. Immunol.* 8, 369–377. <https://doi.org/10.1038/ni1449>.
- Klumpp-Thomas, C., Kalish, H., Drew, M., Hunsberger, S., Snead, K., Fay, M.P., Mehalko, J., Shunmugavel, A., Wall, V., Frank, P., et al. (2021). Standardization of ELISA protocols for serosurveys of the SARS-CoV-2 pandemic using clinical and at-home blood sampling. *Nat. Commun.* 12, 113. <https://doi.org/10.1038/s41467-020-20383-x>.
- Krammer, F. (2020). SARS-CoV-2 vaccines in development. *Nature* 586, 516–527. <https://doi.org/10.1038/s41586-020-2798-3>.
- Laidlaw, B.J., Craft, J.E., and Kaeck, S.M. (2016). The multifaceted role of CD4(+) T cells in CD8(+) T cell memory. *Nat. Rev. Immunol.* 16, 102–111. <https://doi.org/10.1038/nri.2015.10>.
- Lederer, K., Casta o, D., G omez Atria, D., Oguin, T.H., 3rd, Wang, S., Manzoni, T.B., Muramatsu, H., Hogan, M.J., Amanat, F., Cherubin, P., et al. (2020). SARS-CoV-2 mRNA vaccines foster potent antigen-specific germinal center responses associated with neutralizing antibody generation. *Immunity* 53, 1281–1295.e5, e1285. <https://doi.org/10.1016/j.immuni.2020.11.009>.
- Levine, J.H., Simonds, E.F., Bendall, S.C., Davis, K.L., Amir, E.a., Amir el, A.D., Tadmor, M.D., Litvin, O., Fienberg, H.G., Jager, A., et al. (2015). Data-driven phenotypic dissection of AML reveals progenitor-like cells that correlate with prognosis. *Cell* 162, 184–197. <https://doi.org/10.1016/j.cell.2015.05.047>.

- Loyal, L., Braun, J., Henze, L., Kruse, B., Dingeldey, M., Reimer, U., Kern, F., Schwarz, T., Mangold, M., Unger, C., et al. (2021). Cross-reactive CD4(+) T cells enhance SARS-CoV-2 immune responses upon infection and vaccination. *Science* 374, eabh1823. <https://doi.org/10.1126/science.abh1823>.
- Mateus, J., Grifoni, A., Tarke, A., Sidney, J., Ramirez, S.I., Dan, J.M., Burger, Z.C., Rawlings, S.A., Smith, D.M., Phillips, E., et al. (2020). Selective and cross-reactive SARS-CoV-2 T cell epitopes in unexposed humans. *Science* 370, 89–94. <https://doi.org/10.1126/science.abd3871>.
- Maucourant, C., Filipovic, I., Ponzetta, A., Aleman, S., Cornillet, M., Hertwig, L., Strunz, B., Lentini, A., Reinius, B., Brownlie, D., et al. (2020). Natural killer cell immunotypes related to COVID-19 disease severity. *Science immunology* 5, eabd6832. <https://doi.org/10.1126/sciimmunol.abd6832>.
- Moore, K.W., Rogers, J., Hunkapiller, T., Early, P., Nottenburg, C., Weissman, I., Bazin, H., Wall, R., and Hood, L.E. (1981). Expression of IgD may use both DNA rearrangement and RNA splicing mechanisms. *Proc. Natl. Acad. Sci. U. S. A.* 78, 1800–1804. <https://doi.org/10.1073/pnas.78.3.1800>.
- Morgan, X.C., Kabakchiev, B., Waldron, L., Tyler, A.D., Tickle, T.L., Milgrom, R., Stempak, J.M., Gevers, D., Xavier, R.J., Silverberg, M.S., and Huttenhower, C. (2015). Associations between host gene expression, the mucosal microbiome, and clinical outcome in the pelvic pouch of patients with inflammatory bowel disease. *Genome Biol.* 16, 67. <https://doi.org/10.1186/s13059-015-0637-x>.
- Morou, A., Brunet-Ratnasingham, E., Dubé, M., Charlebois, R., Mercier, E., Darko, S., Brassard, N., Nganou-Makamdop, K., Arumugam, S., Gendron-Lepage, G., et al. (2019). Altered differentiation is central to HIV-specific CD4(+) T cell dysfunction in progressive disease. *Nat. Immunol.* 20, 1059–1070. <https://doi.org/10.1038/s41590-019-0418-x>.
- Nakanishi, Y., Lu, B., Gerard, C., and Iwasaki, A. (2009). CD8(+) T lymphocyte mobilization to virus-infected tissue requires CD4(+) T-cell help. *Nature* 462, 510–513. <https://doi.org/10.1038/nature08511>.
- Niessl, J., Baxter, A.E., Mendoza, P., Jankovic, M., Cohen, Y.Z., Butler, A.L., Lu, C.L., Dubé, M., Shimeliovich, I., Gruell, H., et al. (2020a). Combination anti-HIV-1 antibody therapy is associated with increased virus-specific T cell immunity. *Nature medicine* 26, 222–227. <https://doi.org/10.1038/s41591-019-0747-1>.
- Niessl, J., Baxter, A.E., Morou, A., Brunet-Ratnasingham, E., Sannier, G., Gendron-Lepage, G., Richard, J., Delgado, G.G., Brassard, N., Turcotte, I., et al. (2020b). Persistent expansion and Th1-like skewing of HIV-specific circulating T follicular helper cells during antiretroviral therapy. *EBioMedicine* 54, 102727. <https://doi.org/10.1016/j.ebiom.2020.102727>.
- O’Shea, J.J., and Paul, W.E. (2010). Mechanisms underlying lineage commitment and plasticity of helper CD4+ T cells. *Science* 327, 1098–1102. <https://doi.org/10.1126/science.1178334>.
- Oberhardt, V., Luxenburger, H., Kemming, J., Schullien, I., Ciminski, K., Giese, S., Csernalabics, B., Lang-Meli, J., Janowska, I., Staniek, J., et al. (2021). Rapid and stable mobilization of CD8(+) T cells by SARS-CoV-2 mRNA vaccine. *Nature* 597, 268–273. <https://doi.org/10.1038/s41586-021-03841-4>.
- Painter, M.M., Mathew, D., Goel, R.R., Apostolidis, S.A., Pattekar, A., Kuthuru, O., Baxter, A.E., Herati, R.S., Oldridge, D.A., Gouma, S., et al. (2021). Rapid induction of antigen-specific CD4(+) T cells is associated with coordinated humoral and cellular immunity to SARS-CoV-2 mRNA vaccination. *Immunity* 54, 2133–2142.e3, e2133. <https://doi.org/10.1016/j.immuni.2021.08.001>.
- Paltiel, A.D., Zheng, A., and Schwartz, J.L. (2021). Speed versus efficacy: quantifying potential tradeoffs in COVID-19 vaccine deployment. *Ann. Intern. Med.* 174, 568–570. <https://doi.org/10.7326/M20-7866>.
- Parry, H., Bruton, R., Stephens, C., Brown, K., Amirhalingam, G., Otter, A., Hallis, B., Zuo, J., and Moss, P. (2021). Differential immunogenicity of BNT162b2 or ChAdOx1 vaccines after extended-interval homologous dual vaccination in older people. *Immun. Ageing: I & A* 18, 34. <https://doi.org/10.1186/s12979-021-00246-9>.
- Payne, R.P., Longet, S., Austin, J.A., Skelly, D.T., Dejnirattaisai, W., Adele, S., Meardon, N., Faustini, S., Al-Taei, S., Moore, S.C., et al. (2021). Immunogenicity of standard and extended dosing intervals of BNT162b2 mRNA vaccine. *Cell* 184, 5699–5714.e11, e5611. <https://doi.org/10.1016/j.cell.2021.10.011>.
- Polack, F.P., Thomas, S.J., Kitchin, N., Absalon, J., Gurtman, A., Lockhart, S., Perez, J.L., Pérez Marc, G., Moreira, E.D., Zerbini, C., et al. (2020). Safety and efficacy of the BNT162b2 mRNA Covid-19 vaccine. *N. Engl. J. Med.* 383, 2603–2615. <https://doi.org/10.1056/NEJMoa2034577>.
- Prendecki, M., Clarke, C., Brown, J., Cox, A., Gleeson, S., Guckian, M., Randell, P., Pria, A.D., Lightstone, L., Xu, X.N., et al. (2021). Effect of previous SARS-CoV-2 infection on humoral and T-cell responses to single-dose BNT162b2 vaccine. *Lancet* 397, 1178–1181. [https://doi.org/10.1016/S0140-6736\(21\)00502-X](https://doi.org/10.1016/S0140-6736(21)00502-X).
- Prevost, J., Gasser, R., Beaudoin-Bussières, G., Richard, J., Duerr, R., Laumaea, A., Anand, S.P., Goyette, G., Benlarbi, M., Ding, S., et al. (2020). Cross-sectional evaluation of humoral responses against SARS-CoV-2 Spike. Preprint at bioRxiv, the preprint server for biology. <https://doi.org/10.1101/2020.06.08.140244>.
- Quintelier, K., Couckuyt, A., Emmaneel, A., Aerts, J., Saeys, Y., and Van Gassen, S. (2021). Analyzing high-dimensional cytometry data using FlowSOM. *Nat. Protoc.* 16, 3775–3801. <https://doi.org/10.1038/s41596-021-00550-0>.
- Rodda, L.B., Morawski, P.A., Pruner, K.B., Fahning, M.L., Howard, C.A., Franko, N., Logue, J., Eggenberger, J., Stokes, C., Golez, I., et al. (2022). Imprinted SARS-CoV-2-specific memory lymphocytes define hybrid immunity. *Cell* 185, 1588–1601.e14. <https://doi.org/10.1016/j.cell.2022.03.018>.
- Ruschil, C., Gabernet, G., Lepennetier, G., Heumos, S., Kaminski, M., Hracsko, Z., Irmir, M., Beckers, J., Ziemann, U., Nahnsen, S., et al. (2020). Specific induction of double negative B cells during protective and pathogenic immune responses. *Front. Immunol.* 11, 606338. <https://doi.org/10.3389/fimmu.2020.606338>.
- Sahin, U., Muik, A., Derhovanessian, E., Vogler, I., Kranz, L.M., Vormehr, M., Baum, A., Pascal, K., Quandt, J., Maurus, D., et al. (2020). COVID-19 vaccine BNT162b1 elicits human antibody and TH1 T cell responses. *Nature* 586, 594–599. <https://doi.org/10.1038/s41586-020-2814-7>.
- Shrock, E., Fujimura, E., Kula, T., Timms, R.T., Lee, I.H., Leng, Y., Robinson, M.L., Sie, B.M., Li, M.Z., Chen, Y., et al. (2020). Viral epitope profiling of COVID-19 patients reveals cross-reactivity and correlates of severity. *Science* 370. <https://doi.org/10.1126/science.abd4250>.
- Skowronski, D.M., and De Serres, G. (2021). Safety and efficacy of the BNT162b2 mRNA Covid-19 vaccine. *N. Engl. J. Med.* 384, 1576–1577. <https://doi.org/10.1056/NEJMc2036242>.
- Skowronski, D.M., Setayeshgar, S., Febriani, Y., Ouakki, M., Zou, M., Talbot, D., Prystajeky, N., Tyson, J.R., Gilca, R., Brousseau, N., et al. (2021). Two-dose SARS-CoV-2 vaccine effectiveness with mixed schedules and extended dosing intervals: test-negative design studies from British Columbia and Quebec, Canada. Preprint at medRxiv, the preprint server for health sciences. <https://doi.org/10.1101/2021.10.26.21265397>.
- Stamatatos, L., Czartoski, J., Wan, Y.H., Homad, L.J., Rubin, V., Glantz, H., Neradilek, M., Seydoux, E., Jennewein, M.F., MacCamy, A.J., et al. (2021). mRNA vaccination boosts cross-variant neutralizing antibodies elicited by SARS-CoV-2 infection. *Science* 372 (6549), eabg9175. <https://doi.org/10.1126/science.abg9175>.
- Tangye, S.G., Liu, Y.J., Aversa, G., Phillips, J.H., and de Vries, J.E. (1998). Identification of functional human splenic memory B cells by expression of CD148 and CD27. *J. Exp. Med.* 188, 1691–1703. <https://doi.org/10.1084/jem.188.9.1691>.
- Tauzin, A., Gong, S.Y., Beaudoin-Bussières, G., Vézina, D., Gasser, R., Nault, L., Marchitto, L., Benlarbi, M., Chatterjee, D., Nayrac, M., et al. (2022). Strong humoral immune responses against SARS-CoV-2 Spike after BNT162b2 mRNA vaccination with a 16-week interval between doses. *Cell host & microbe* 30, 97–109.e5. <https://doi.org/10.1016/j.chom.2021.12.004>.
- Tauzin, A., Nayrac, M., Benlarbi, M., Gong, S.Y., Gasser, R., Beaudoin-Bussières, G., Brassard, N., Laumaea, A., Vézina, D., Prévost, J., et al. (2021b). A single dose of the SARS-CoV-2 vaccine BNT162b2 elicits Fc-mediated antibody effector functions and T cell responses. *Cell host & microbe* 29, 1137–1150.e6, e1136. <https://doi.org/10.1016/j.chom.2021.06.001>.
- Thomas, S.J., Moreira, E.D., Jr., Kitchin, N., Absalon, J., Gurtman, A., Lockhart, S., Perez, J.L., Pérez Marc, G., Polack, F.P., Zerbini, C., et al. (2021).

Safety and efficacy of the BNT162b2 mRNA Covid-19 vaccine through 6 months. *N. Engl. J. Med.* 385, 1761–1773. <https://doi.org/10.1056/NEJMoa2110345>.

Tuite, A.R., Zhu, L., Fisman, D.N., and Salomon, J.A. (2021). Alternative dose allocation strategies to increase benefits from constrained COVID-19 vaccine supply. *Ann. Intern. Med.* 174, 570–572. <https://doi.org/10.7326/M20-8137>.

Urbanowicz, R.A., Tsoleridis, T., Jackson, H.J., Cusin, L., Duncan, J.D., Chappell, J.G., Tarr, A.W., Nightingale, J., Norrish, A.R., Ikram, A., et al. (2021). Two doses of the SARS-CoV-2 BNT162b2 vaccine enhance antibody responses to variants in individuals with prior SARS-CoV-2 infection. *Sci. Transl. Med.* 13, eabj0847. <https://doi.org/10.1126/scitranslmed.abj0847>.

Walls, A.C., Park, Y.J., Tortorici, M.A., Wall, A., McGuire, A.T., and Velesler, D. (2020). Structure, function, and antigenicity of the SARS-CoV-2 Spike glycoprotein. *Cell* 181, 281–292.e6, e286. <https://doi.org/10.1016/j.cell.2020.02.058>.

Wei, C., Anolik, J., Cappione, A., Zheng, B., Pugh-Bernard, A., Brooks, J., Lee, E.H., Milner, E.C.B., and Sanz, I. (2007). A new population of cells lacking expression of CD27 represents a notable component of the B cell memory compartment in systemic lupus erythematosus. *J. Immunol.* 178, 6624–6633. <https://doi.org/10.4049/jimmunol.178.10.6624>.

Wurm, H., Attfield, K., Iversen, A.K., Gold, R., Fugger, L., and Haghikia, A. (2020). Recovery from COVID-19 in a B-cell-depleted multiple sclerosis patient. *Mult. Scler.* 26, 1261–1264. <https://doi.org/10.1177/1352458520943791>.

Zollner, A., Watschinger, C., Rössler, A., Farcet, M.R., Penner, A., Böhm, V., Kiechl, S.J., Stampfel, G., Hintenberger, R., Tilg, H., et al. (2021). B and T cell response to SARS-CoV-2 vaccination in health care professionals with and without previous COVID-19. *EBioMedicine* 70, 103539. <https://doi.org/10.1016/j.ebiom.2021.103539>.

STAR★METHODS

KEY RESOURCES TABLE

REAGENT or RESOURCE	SOURCE	IDENTIFIER
Antibodies		
UCHT1 (BUV395) [Human anti-CD3]	BD Biosciences	Cat#563546 ; Lot:9058566 ; RRID:AB_2744387
UCHT1 (BUV496) [Human anti-CD3]	BD Biosciences	Cat#612941 ; Lot:1022424 ; RRID:AB_2870222
L200 (BV711) [Human anti-CD4]	BD Biosciences	Cat#563913 ; Lot:03000025 ; RRID:AB_2738484
SK3 (BB630) [Human anti-CD4]	BD Biosciences	Cat#624294 CUSTOM ; Lot:0289566
RPA-T8 (BV570) [Human anti-CD8]	Biolegend	Cat#301037 ; Lot:B281322 ; RRI- D:AB_10933259
M5E2 (BUV805) [Human anti-CD14]	BD Biosciences	Cat#612902 ; Lot:0262150 ; RRID:AB_2870189
M5E2 (BV480) [Human anti-CD14]	BD Biosciences	Cat#746304 ; Lot : 9133961 ; RRID:AB_2743629
3G8 (BV650) [Human anti-CD16]	Biolegend	Cat#302042 ; Lot:B323847 ; RRI- D:AB_2563801
HIB19 (APC-eFluor780) [Human anti-CD19]	Thermo Fisher Scientific	Cat#47-0199 ; Lot:2145095 ; RRID:AB_1582231
HIB19 (BV480) [Human anti-CD19]	BD Biosciences	Cat#746457 ; Lot:1021649 ; RRID:AB_2743759
HI100 (PerCP Cy5.5) [Human anti-CD45RA]	BD Biosciences	Cat#563429 ; Lot:8332746 ; RRID:AB_2738199
NCAM16.2 (BUV737) [Human anti-CD56]	BD Biosciences	Cat#564448 ; Lot:8288818 ; RRID:AB_2744432
FN50 (PerCP-eFluor710) [Human anti- CD69]	Thermo Fisher Scientific	Cat#46-0699-42 ; Lot:1920361 ; RRID:AB_2573694
FN50 (BV650) [Human anti-CD69]	Biolegend	Cat# 310934 ; Lot:B303462 ; RRI- D:AB_2563158
H4A3 (BV786) [Human anti-CD107A]	BD Biosciences	Cat#563869 ; Lot:8144866 ; RRID:AB_2738458
ACT35 (APC) [Human anti-CD134 (OX40)]	BD Biosciences	Cat#563473 ; Lot:1015537 ; RRID:AB_2738230
4B4-1 (PE-Dazzle 594) [Human anti-CD137 (4-1BB)]	Biolegend	Cat# 309826 ; Lot:B253152 ; RRI- D:AB_2566260
TRAP1 (BV421) [Human anti-CD154 (CD40L)]	BD Biosciences	Cat#563886 ; Lot:9037850 ; RRID:AB_2738466
TRAP1 (PE) [Human anti-CD154 (CD40L)]	BD Biosciences	Cat#555700 ; Lot:7086896 ; RRID:AB_396050
J25D4 (BV421) [Human anti-CD185 (CXCR5)]	Biolegend	Cat# 356920 ; Lot:B325837 ; RRI- D:AB_2562303
B27 (PECy7) [Human anti-IFN- γ]	BD Biosciences	Cat#557643 ; Lot:8256597 ; RRID:AB_396760
MQ1-17H12 (PE-Dazzle594) [Human anti- IL-2]	Biolegend	Cat#500344 ; Lot:B2261476 ; RRI- D:AB_2564091
JES3-9D7 (PE) [Human anti-IL-10]	BD Biosciences	Cat#554498 ; Lot:8198773 ; RRID:AB_395434
eBio64CAP17 (eFluor660) [Human anti-IL- 17A]	Thermo Fisher Scientific	Cat#50-7179-42 ; Lot:2151998 ; RRID:AB_11149126

(Continued on next page)

Continued		
REAGENT or RESOURCE	SOURCE	IDENTIFIER
Mab11 (Alexa Fluor 488) [Human anti-TNF- α]	Biologend	Cat#502915 ; Lot:B285221 ; RRI-D:AB_493121
LIVE/DEAD Fixable dead cell	Thermo Fisher Scientific	L34960
Biological samples		
SARS-CoV-2 naive donor blood samples	N/A	
SARS-CoV-2 prior infection donor blood samples	N/A	
Chemicals, peptides, and recombinant proteins		
PepMix™ SARS-CoV-2 (Spike Glycoprotein)	JPT	Cat#PM-WCPV-S-1
Staphylococcal Enterotoxin B (SEB)	Toxin technology	Cat#BT202
Software and algorithms		
Flow Jo v10.8.0	Flow Jo	https://www.flowjo.com
GraphPad Prism v8.4.1	GraphPad	https://www.graphpad.com
R studio v4.1.0	R studio	https://rstudio.com
R codes scripted	Github	https://github.com/otastet/Nayrac_et_al
Deposited data		
Table S4	Mendeley database: DOI: 10.17632/d5mg48z55p.1	

RESOURCE AVAILABILITY

Lead contact

Further information and requests for resources and reagents should be directed to and will be fulfilled by the lead contact, Daniel E. Kaufmann (daniel.kaufmann@umontreal.ca).

Materials availability

All unique reagents generated during this study are available from the [lead contact](#) upon a material transfer agreement (MTA).

Data and code availability

The published article includes all datasets generated and analyzed for this study. All datasets are also available at Mendeley Data: <https://doi.org/10.17632/d5mg48z55p.1>. Further information and requests for resources and reagents should be directed to and will be fulfilled by the [Lead Contact](#) Author (daniel.kaufmann@umontreal.ca).

We adapted R codes scripted to perform unsupervised analyzes on B and T cells from SARS-CoV-2 naive and previously-infected individuals. All original codes have been deposited at Github and are publicly available as of the date of publication. URL link is listed in the [key resources table](#).

Any additional information required to reanalyze the data reported in this paper is available from the [Lead Contact](#) Author upon request (daniel.kaufmann@umontreal.ca).

EXPERIMENTAL MODEL AND SUBJECT DETAILS

Ethics statement

All work was conducted in accordance with the Declaration of Helsinki in terms of informed consent and approval by an appropriate institutional board. Blood samples were obtained from donors who consented to participate in this research project at the CHUM (19.381). Plasma and PBMCs were isolated by centrifugation and Ficoll gradient, and samples stored at -80°C and in liquid nitrogen, respectively, until use.

Participants

No specific criteria such as number of patients (sample size), clinical or demographic were used for inclusion, beyond PCR confirmed SARS-CoV-2 infection in adults enrolled in the previously infected cohorts. Clinical data are summarized in [Table 1](#).

PBMCs and plasma collection

PBMCs were isolated from blood samples by Ficoll density gradient centrifugation and cryopreserved in liquid nitrogen until use. Plasma was collected, heat-inactivated for 1 h at 56°C and stored at -80°C until ready to use in subsequent experiments. Plasma

from uninfected donors collected before the pandemic were used as negative controls and used to calculate the seropositivity threshold in our ELISA and ADCC assays.

Cell lines

293T human embryonic kidney and HOS cells (obtained from ATCC) were maintained at 37°C under 5% CO₂ in Dulbecco's modified Eagle's medium (DMEM) (Wisent) containing 5% fetal bovine serum (FBS) (VWR) and 100 µg/mL of penicillin-streptomycin (Wisent). CEM.NKr CCR5+ cells (NIH AIDS reagent program) were maintained at 37°C under 5% CO₂ in Roswell Park Memorial Institute (RPMI) 1,640 medium (Gibco) containing 10% FBS and 100 µg/mL of penicillin-streptomycin. 293T-ACE2 cell line was previously reported (Prevost et al., 2020). HOS and CEM.NKr CCR5+ cells stably expressing the SARS-CoV-2 S glycoproteins (CEM.NKr.Spike cells) were previously reported (Anand et al., 2021).

METHOD DETAILS

Protein expression and purification

FreeStyle 293F cells (Thermo Fisher Scientific) were grown in FreeStyle 293F medium (Thermo Fisher Scientific) to a density of 1×10^6 cells/mL at 37°C with 8% CO₂ with regular agitation (150 rpm). Cells were transfected with a plasmid coding for SARS-CoV-2 S RBD using ExpiFectamine 293 transfection reagent, as directed by the manufacturer (Invitrogen) (Beaudoin-Bussières et al., 2020; Prevost et al., 2020). One week later, cells were pelleted and discarded. Supernatants were filtered using a 0.22 µm filter (Thermo Fisher Scientific). The recombinant RBD proteins were purified by nickel affinity columns, as directed by the manufacturer (Thermo Fisher Scientific). The RBD preparations were dialyzed against phosphate-buffered saline (PBS) and stored in aliquots at –80°C until further use. To assess purity, recombinant proteins were loaded on SDS-PAGE gels and stained with Coomassie Blue.

RBD-specific IgG levels and avidity measured by enzyme-linked immunosorbent assay (ELISA)

The SARS-CoV-2 RBD ELISA assay was used to measure the level of RBD-specific IgG, as previously described (Beaudoin-Bussières et al., 2020; Prevost et al., 2020). Briefly, recombinant SARS-CoV-2 RBD protein was prepared in PBS (2.5 µg/mL) and adsorbed to plates overnight at 4°C. Coated wells were subsequently blocked with blocking buffer then washed. CR3022 monoclonal Ab (50 ng/mL) at 1/250, 1/500, 1/1,250, 1/2,500, 1/5,000, 1/10,000, 1/20,000 dilutions of plasma from SARS-CoV-2-naive or previously infected donors were prepared in a diluted solution of blocking buffer and incubated with the RBD-coated wells. Plates were washed followed by incubation with the respective secondary Abs. Area Under the Curve (AUC) was calculated by using GraphPad. To calculate the RBD-avidity index, we performed a stringent ELISA where the plate was washed with washing buffer supplemented 8M urea. The binding of CR3022 IgG and plasma was quantified with HRP-conjugated antibodies specific for the Fc region of human IgG. HRP enzyme activity was determined after the addition of a 1:1 mix of Western Lightning oxidizing and luminol reagents (Perkin Elmer Life Sciences). Light emission was measured with a LB942 TriStar luminometer (Berthold Technologies).

Spike IgG levels measured by cell-based ELISA (CBE)

Detection of the trimeric SARS-CoV-2 S at the surface of HOS cells was performed by a previously described cell-based enzyme-linked immunosorbent assay (ELISA) (Anand et al., 2021). Briefly, parental HOS cells or HOS-Spike cells by Spike specific IgG were seeded in 96-well plates (6×10^4 cells per well) overnight. Cells were blocked with blocking buffer (10 mg/mL nonfat dry milk, 1.8 mM CaCl₂, 1 mM MgCl₂, 25 mM Tris [pH 7.5], and 140 mM NaCl) for 30 min. CR3022 mAb (1 µg/mL) or plasma (at a dilution of 1/250) were prepared in blocking buffer and incubated with the cells for 1 h at room temperature. Respective HRP-conjugated anti-human IgG Fc secondary Abs were then incubated with the samples for 45 min at room temperature. For all conditions, cells were washed 6 times with blocking buffer and 6 times with washing buffer (1.8 mM CaCl₂, 1 mM MgCl₂, 25 mM Tris [pH 7.5], and 140 mM NaCl). HRP enzyme activity was determined after the addition of a 1:1 mix of Western Lightning oxidizing and luminol reagents (PerkinElmer Life Sciences). Light emission was measured with an LB942 TriStar luminometer (Berthold Technologies). Signal obtained with parental HOS was subtracted for each plasma and was then normalized to the signal obtained with CR3022 mAb present in each plate. The seropositivity threshold was established using the following formula: mean of all SARS-CoV-2 negative plasma + (3 standard deviation of the mean of all SARS-CoV-2 negative plasma).

ADCC assay

The SARS-CoV-2 ADCC assay used was previously described (Anand et al., 2021; Beaudoin-Bussières et al., 2020; Prevost et al., 2020). Briefly, parental CEM.NKr CCR5+ cells were mixed at a 1:1 ratio with CEM.NKr.Spike cells and were stained for viability (Aquavid: Thermo Fisher Scientific) and a cellular dye (cell proliferation dye eFluor670; Thermo Fisher Scientific) to be used as target cells. Overnight rested PBMCs were stained with another cellular dye (cell proliferation dye eFluor450; Thermo Fisher Scientific), then used as effector cells. Stained target and effector cells were mixed at a ratio of 1:10 in 96-well V-bottom plates. Plasma from SARS-CoV-2 naive or PI individuals (1/500 dilution) or monoclonal antibody CR3022 (1 µg/mL) were added to the appropriate wells. The plates were subsequently centrifuged and incubated at 37°C, 5% CO₂ for 5 h before being fixed in a 2% PBS-formaldehyde solution. All samples were acquired on an LSRII cytometer (BD Biosciences) and data analysis was performed using FlowJo v10.7.1 (Tree Star).

Virus neutralization assay

The SARS-CoV-2 virus neutralization assay used was previously (Prevost et al., 2020). Briefly, 293T cells were transfected with the lentiviral vector pNL4.3 R-E- Luc plasmid (NIH AIDS Reagent Program) and a plasmid encoding for the full-length SARS-CoV-2 Spike D614G glycoprotein (Beaudoin-Bussieres et al., 2020; Prevost et al., 2020) at a ratio of 10:1. Two days post-transfection, cell supernatants were harvested and stored at -80°C until use. Pseudoviral particles were incubated with the indicated plasma dilutions (1/50; 1/250; 1/1,250; 1/6,250; 1/31,250) for 1 h at 37°C and were then added to the 293T-ACE2 target cells followed by incubation for 48 h at 37°C . Then, cells were lysed and followed by one freeze-thaw cycle. An LB942 TriStar luminometer (Berthold Technologies) was used to measure the luciferase activity. The neutralization half-maximal inhibitory dilution (ID_{50}) represents the plasma dilution to inhibit 50% of the infection of 293T-ACE2 cells by SARS-CoV-2 pseudoviruses.

SARS-CoV-2-specific B cells characterization

To detect SARS-CoV-2-specific B cells, we conjugated recombinant RBD proteins with Alexa Fluor 488 or Alexa Fluor 594 (Thermo Fisher Scientific) according to the manufacturer's protocol. 2×10^6 frozen PBMC from SARS-CoV-2 naive and previously-infected donors were prepared in Falcon® 5mL-round bottom polystyrene tubes at a final concentration of 4×10^6 cells/mL in RPMI 1640 medium (GIBCO) supplemented with 10% of fetal bovine serum (Seradigm), Penicillin- Streptomycin (GIBCO) and HEPES (GIBCO). After a rest of 2 h at 37°C and 5% CO_2 , cells were stained using Aquavid viability marker (GIBCO) in DPBS (GIBCO) at 4°C for 20 min. The detection of SARS-CoV-2-antigen specific B cells was done by adding the RBD probes to the antibody cocktail listed in Table S1. Staining was performed at 4°C for 30 min and cells were fixed using 2% paraformaldehyde at 4°C for 15 min. Stained PBMC samples were acquired on Symphony cytometer (BD Biosciences) and analyzed using FlowJo v10.8.0 software.

Activation-induced marker (AIM) assay

The AIM assay (Morou et al., 2019; Niessl et al., 2020a, 2020b) was adapted for SARS-CoV-2 specific CD4 and CD8 T cells, as previously described (Tauzin et al., 2021b). PBMCs were thawed and rested for 3 h in 96-well flat-bottom plates in RPMI 1640 supplemented with HEPES, penicillin and streptomycin and 10% FBS. 1.7×10^6 PBMCs were stimulated with a S glycoprotein peptide pool (0.5 $\mu\text{g}/\text{mL}$ per peptide, corresponding to the pool of 315 overlapping peptides (15-mers) spanning the complete amino acid sequence of the Spike glycoprotein (JPT) for 15 h at 37°C and 5% CO_2 . CXCR3, CCR6, CXCR6 and CXCR5 antibodies were added in culture 15 min before stimulation. A DMSO-treated condition served as a negative control and *Staphylococcus enterotoxin B* SEB-treated condition (0.5 $\mu\text{g}/\text{mL}$) as positive control. Cells were stained for viability dye for 20 min at 4°C then surface markers (30 min, 4°C). Abs used are listed in the Table S2. Cells were fixed using 2% paraformaldehyde for 15 min at 4°C before acquisition on Symphony cytometer (BD Biosciences). Analyses were performed using FlowJo v10.8.0 software.

Intracellular cytokine staining (ICS)

The ICS assay adapted to study SARS-CoV-2-specific T cells was previously described (Tauzin et al., 2021b). PBMCs were thawed and rested for 2 h in RPMI 1640 medium supplemented with 10% FBS, Penicillin-Streptomycin (Thermo Fisher scientific, Waltham, MA) and HEPES (Thermo Fisher scientific, Waltham, MA). 1.7×10^6 PBMCs were stimulated with a S glycoprotein peptide pool (0.5 $\mu\text{g}/\text{mL}$ per peptide from JPT, Berlin, Germany) corresponding to the pool of 315 overlapping peptides (15-mers) spanning the complete amino acid sequence of the S glycoprotein.

Cell stimulation was carried out for 6 h in the presence of mouse anti-human CD107a, Brefeldin A and monensin (BD Biosciences, San Jose, CA) at 37°C and 5% CO_2 . DMSO-treated cells served as a negative control, and SEB as positive control. Cells were stained for Aquavid viability marker (Thermo Fisher scientific, Waltham, MA) for 20 min at 4°C and surface markers (30 min, 4°C), followed by intracellular detection of cytokines using the IC Fixation/Permeabilization kit (Thermo Fisher scientific, Waltham, MA) according to the manufacturer's protocol before acquisition on a Symphony flow cytometer (BD Biosciences) and analysis using FlowJo v10.8.0 software. Abs used are listed in the Table S3.

QUANTIFICATION AND STATISTICAL ANALYSIS

Statistical analysis

Symbols represent biologically independent samples from SARS-CoV-2 naive individuals and SARS-CoV-2 PI individuals. Lines connect data from the same donor. Thick lines represent median values.

Linear mixed models fitting cell frequencies in terms of cohort, time point and their interaction were run using R and the package "nlme". Model diagnostics were performed, checking for heteroscedasticity and normality among residuals. Variance-covariance matrices were estimated using different weights for each time point, accounting for heteroscedasticity. All retained models used a square-root transform on the response variable, which helped in reducing the impact of outliers. Post-hoc contrasts across all pairwise comparisons of factor levels were obtained with the package "emmeans", correcting the p values by the method of Holm-Bonferroni where applicable. An important caveat of the square-root transform is that the reported contrast estimates and their confidence intervals remain on this scale, making their interpretation tricky. This was not deemed too great an obstacle, as qualitative statements on significant contrasts could be made based on p-values. Fifteen linear mixed models were retained, those being RBD B, AIM CD4, ICS CD4, AIM CD8, CXCR3, CXCR5, CXCR6, IFNg, IL-2, TNFa and CCR6 being compared between naive and PI co-

horts. There were also comparisons of PI donors receiving 1 dose vs 2 doses for RBD B, AIM CD4, ICS CD4 and AIM CD8. Models without satisfactory diagnostics were abandoned in favor of non-parametric methods. Differences in responses for the same patient before and after vaccination were performed using Wilcoxon matched pair tests. Differences in responses between naive and PI individuals were measured by Mann-Whitney tests. Wilcoxon and Mann-Whitney tests were generated using GraphPad Prism version 8.4.3 (GraphPad, San Diego, CA) (Rodda et al., 2022).

p values <0.05 were considered significant. p values are indicated for each comparison assessed. For descriptive correlations, Spearman's R correlation coefficient was applied. For graphical representation on a log scale (but not for statistical tests), null values were arbitrarily set at the minimal values for each assay. Complete statistical tests are centralized in the [Table S4](#).

Software scripts and visualization

Graphics and pie charts were generated using GraphPad PRISM version 8.4.1 and ggplot2 (v3.3.3) in R (v4.1.0). Heat maps were generated in R (v4.1.0) using the pheatmap package (v1.0.12). Principal component analyses were performed with the prcomp function (R). Uniform manifold approximation and projection (UMAP) was performed using package M3C (v1.14.0) on gated FCS files loaded through the flowCore package (v2.4.0). Samples were down-sampled to a comparable number of events (300 cells for AIM, 100 cells for ICS). Scaling and logicle transformation of the flow cytometry data was applied using the FlowSOM (Quintelier et al., 2021) R package (v2.0.0). All samples from naive and PI at all time points were loaded. Clustering was achieved using Phenograph (v0.99.1) with the hyperparameter k (number of nearest-neighbors) set to 150). R codes scripted for this paper are provided as https://github.com/otastet/Nayrac_et_al. We obtained an initial 15 AIM+ and 11 cyto + clusters. After careful examination, five low-abundance AIM + clusters were merged based on proximity on the UMAP, phenotypic similarities and concomitant longitudinal trajectories. This resulted in a final 10 AIM + clusters. None of the 11 cyto + clusters were merged. For B and CD4+ T cell phenotyping, only participants with >5 RBD + B events across all depicted time points were analyzed.

Supplemental information

Temporal associations of B and T cell immunity with robust vaccine responsiveness in a 16-week interval BNT162b2 regimen

Manon Nayrac, Mathieu Dubé, Gérémy Sannier, Alexandre Nicolas, Lorie Marchitto, Olivier Tastet, Alexandra Tauzin, Nathalie Brassard, Raphaël Lima-Barbosa, Guillaume Beaudoin-Bussières, Dani Vézina, Shang Yu Gong, Mehdi Benlarbi, Romain Gasser, Annemarie Laumaea, Jérémie Prévost, Catherine Bourassa, Gabrielle Gendron-Lepage, Halima Medjahed, Guillaume Goyette, Gloria-Gabrielle Ortega-Delgado, Mélanie Laporte, Julia Niessl, Laurie Gokool, Chantal Morriseau, Pascale Arlotto, Jonathan Richard, Justin Bélair, Alexandre Prat, Cécile Tremblay, Valérie Martel-Laferrrière, Andrés Finzi, and Daniel E. Kaufmann

Figure S1

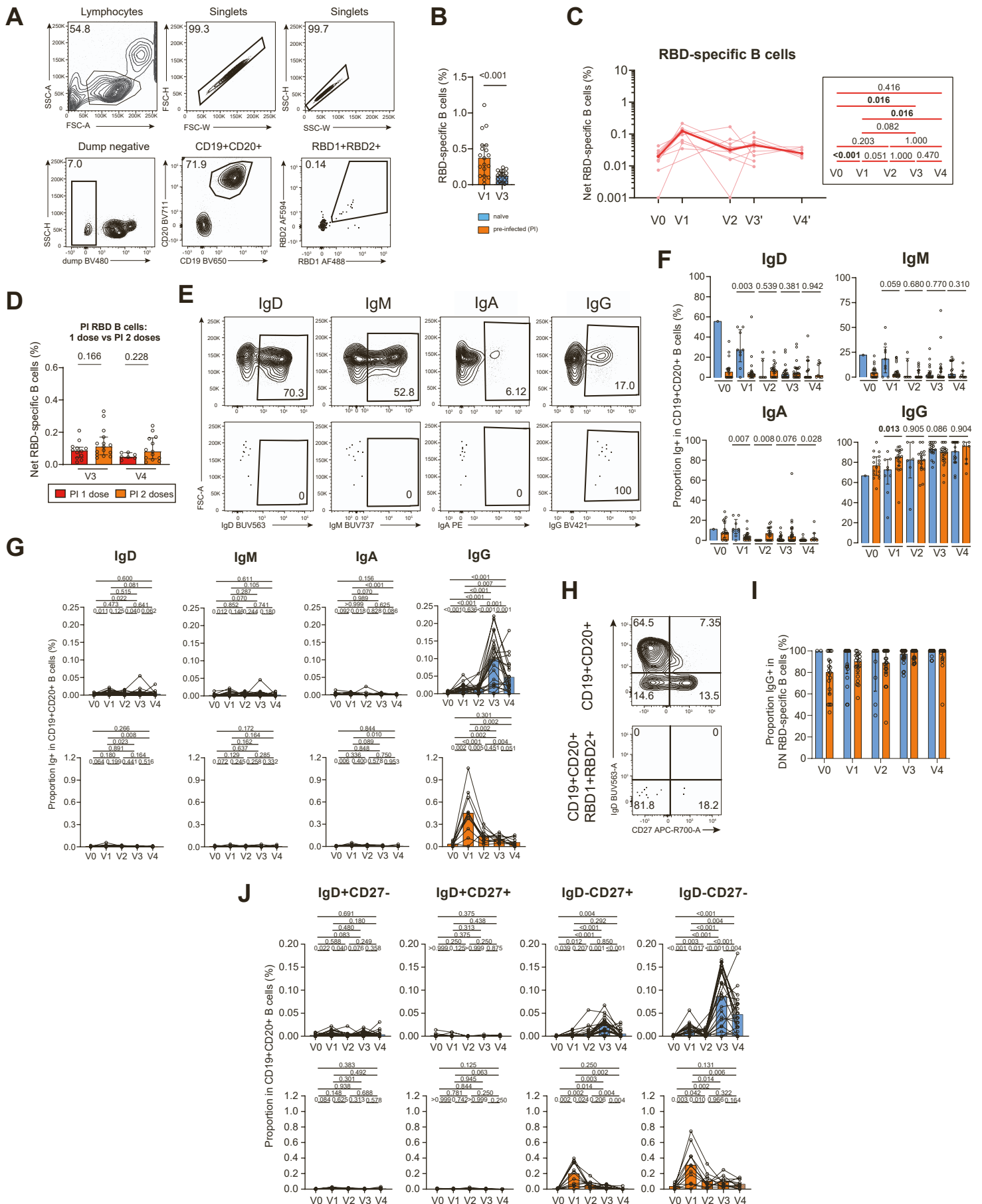


Figure S1. RBD-specific B cell responses. Related to figure 1. (A) Gating strategy to identify RBD-specific B cell responses. (B) Comparisons between RBD-B cell responses at the V1 timepoint for PI and at the V3 timepoint for naïve participants. A Mann-Whitney test is indicated above the graph. Data repre-

sented naïve (blue; n=22) and SARS-CoV-2 pre-infected (PI) individuals (orange, n=21). A Mann-Whitney test is shown. (C) Longitudinal RBD-specific B cell responses in pre-infected (PI) participants that did not receive a second dose after V2 (n=12). (D) Comparisons between RBD-specific B cell responses in pre-infected (PI) participants that receive one dose vs. two doses at V3 and V4. Lines connect data from the same donor. The bold line represents the median value of each cohort. Linear mixed models were used for pairwise comparisons shown on the right panel. (E) Examples of gatings for IgD, IgM, IgA and IgG expression on total CD19+CD20+ B cells or RBD-specific B cells. (F) Histograms quantifying the frequency of IgD+, IgM+, IgA+ and IgG+ RBD-specific B cells at different timepoints, comparing naïve (n=22) vs PI participants (n=11). Only datapoints with more than 5 events were analyzed. Mann-Whitney test are shown. (G) Longitudinal trajectories of isotype expression frequencies in naïve (n=22) and PI (n=11) participants. Lines connect data points for individual participants. Wilcoxon tests are shown above each panel. (H) Example of the gating strategy of IgD and CD27 co-expression on RBD-specific B cells. In support to the pie charts displayed in Figure 1H. (I) Histograms showing the proportion of IgG+ in IgD-CD27- RBD+ B cells. (J) Histograms reporting the longitudinal frequency of each IgD and CD27 RBD-B phenotypes in CD19+CD20+ B cells for naïve (n=22) and PI (n=11) participants. In support to the pie charts displayed in Figure 1H. Wilcoxon tests are shown above. In (F,I), only datapoints with more than 5 events were analyzed.

Figure S2

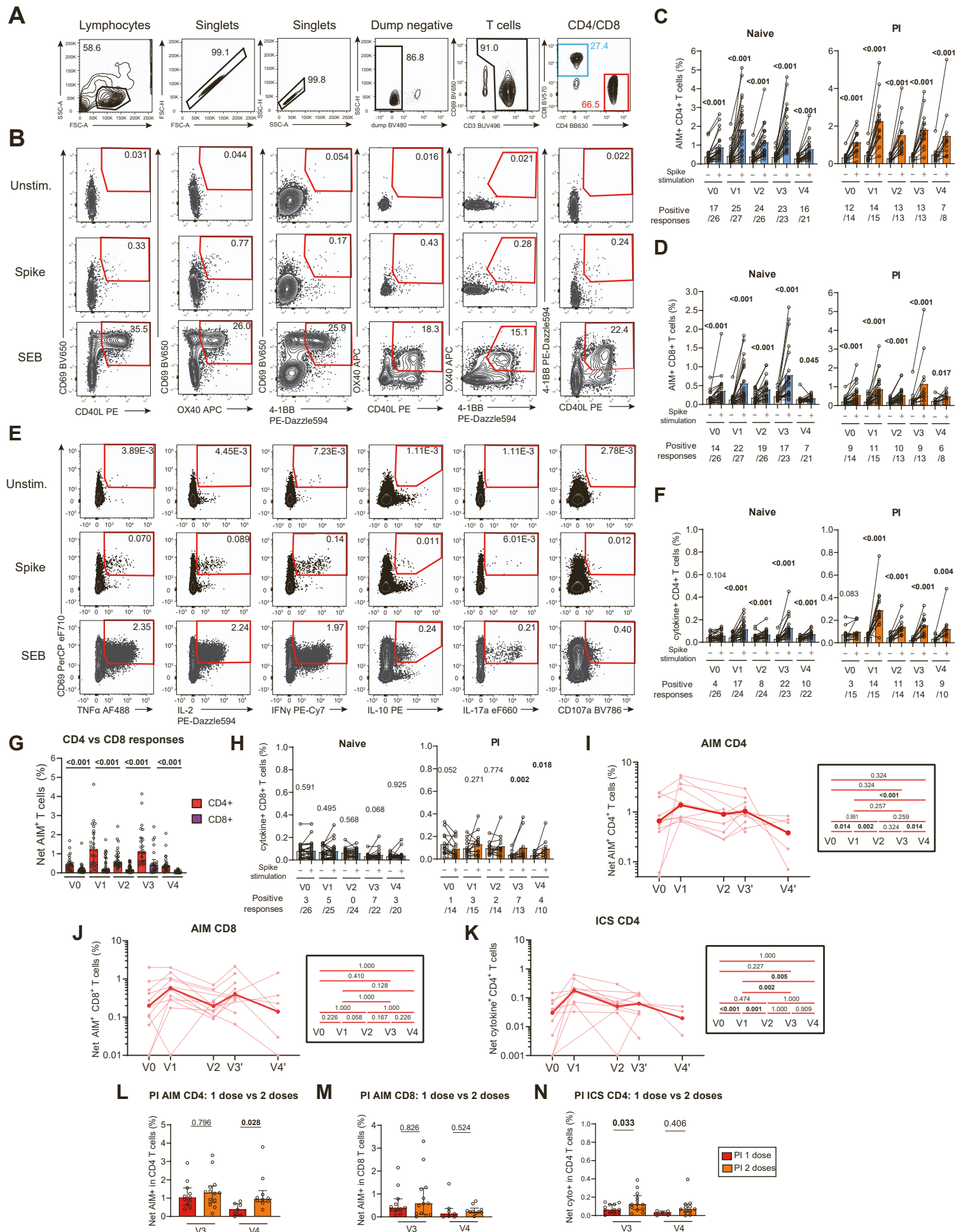


Figure S2: SARS-CoV-2-specific CD4 and CD8 T cell responses. Related to figure 2. (A) Represent-

tative upstream generic gating and (B) ORgate strategy to identify SARS-CoV-2-specific AIM+ T cells. For simplicity, the example focuses on CD4+ T cells. (C) Raw frequencies of AIM+ CD4+ and (D) CD8+ T cells following ex vivo stimulation of PBMCs with a pool of SARS-CoV-2 Spike peptides. As a control, PBMCs cells were left unstimulated (grey bars). The data for naïve (blue, n=26) and pre-infected (PI; orange, n=27) individuals are displayed. The bars represent median values. Wilcoxon tests are shown. The number of conditions reaching >2x no Ag are shown below each timepoint. (E) Representative ORgate strategy to identify SARS-CoV-2-specific cytokine-expressing T cells. For simplicity, the example focuses on CD4+ T cells. (F) Raw frequencies of cytokine-expressing CD4+ T cells following ex vivo stimulation of PBMCs with a pool of SARS-CoV-2 Spike peptides. As a control, PBMCs cells were left unstimulated (grey bars). The data for naïve (blue, n=26) and pre-infected (PI; orange, n=27) individuals are displayed. The bars represent median values. Wilcoxon tests are shown. The number of conditions reaching >2x no Ag are shown below each time point. (G) Comparisons between AIM+CD4+ (red) and AIM+CD8+ (purple) T cell responses. Median and interquartile range are shown, with Wilcoxon tests. (H) Raw frequencies of cytokine-expressing CD8+ T cells following ex vivo stimulation of PBMCs with a pool of SARS-CoV-2 Spike peptides. As a control, PBMCs cells were left unstimulated (grey bars). The data for naïve (blue, n=26) and pre-infected (PI; orange, n=27) individuals are displayed. The bars represent median values. Wilcoxon tests are shown. The number of conditions reaching >2x no Ag are shown below each timepoint. (IJK) Longitudinal (I) AIM+CD4+, (J) CD8+ and (K) cytokine+ CD4+ T cell responses in pre-infected (PI) participants that did not receive a second dose after V2 (n=12). Lines connect data from the same donor. The bold line represents the median value of each cohort. Linear mixed models were used to generate statistics for each pairwise comparison, shown on the right panels. (LMN) Comparisons of (L) AIM+ CD4+, (M) CD8+ and (N) cytokine+ CD4+ T cell responses between one dose vs. two doses PI at V3 and V4. Median and interquartile range are shown, with results from linear mixed models.

Figure S3

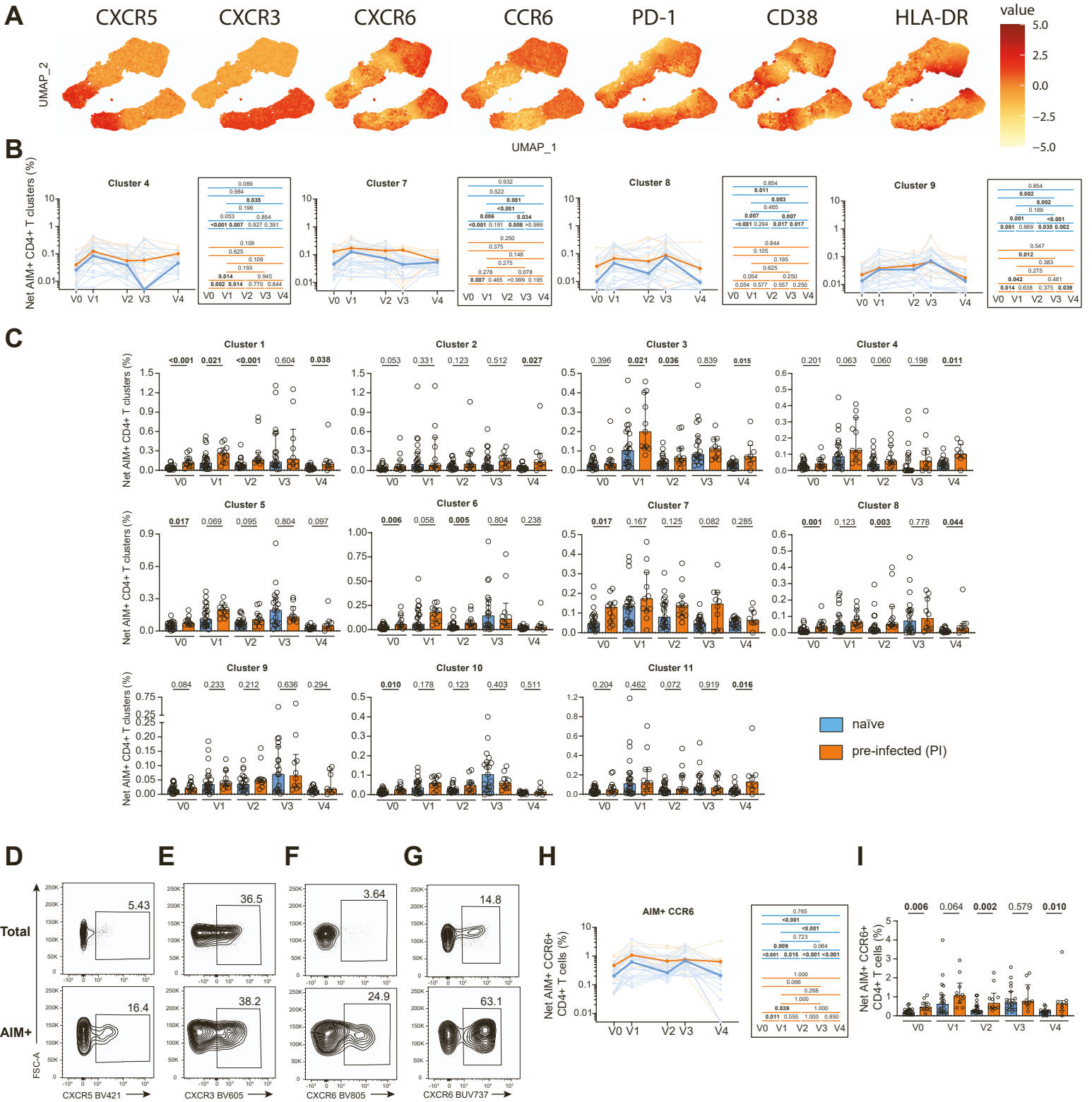


Figure S3: Unsupervised phenotype analysis of SARS-CoV-2-specific CD4+ T cell responses. Related to figure 3. (A-C) Multivariate analysis. (A) Heat map overlaid on the AIM+ UMAP showing the gradient of expression for each marker. (B) The longitudinal net frequency of AIM+ in CD4+ T cells for clusters 4, 7, 8 and 9 for naïve (blue, n=22) and PI (orange; n=11) participants. Wilcoxon tests are shown beside for each pairwise comparison. Complement Figure 3D. (C) Cohort comparisons, with Mann-Whitney tests. (C-F) Univariate analyses. Example of (D) CXCR5+, (E) CXCR3+, (F) CXCR6+ and (G) CCR6+ gating on total and AIM+ populations for univariate analyses. (H) Net frequencies of AIM+CCR6+CD4+ T cells. (H) Longitudinal analysis presenting both naïve and PI are overlaid. Wilcoxon tests are shown besides each panel. Lines connect data from the same donor. Bold lines represent median values. (I) Histogram comparing naïve and PI participants. (HI) Linear mixed model tests are shown.

Figure S4

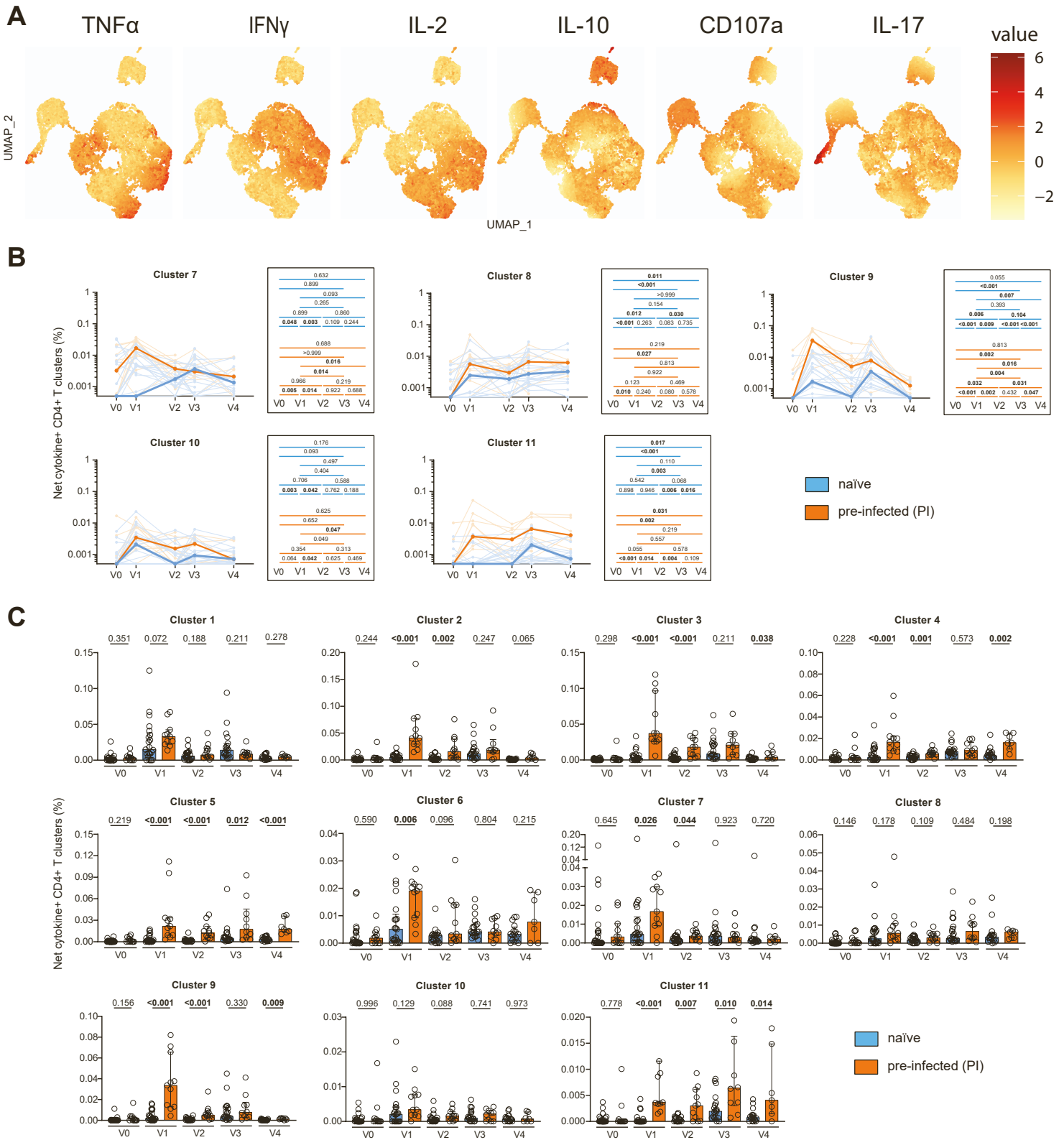


Figure S4: Unsupervised cytokine analysis of SARS-CoV-2 specific CD4+ T cells. Related to Figure 4. (A-C) Multivariate analysis. (A) Heat map overlaid on the cytokine+ UMAP showing the gradient of expression for each marker. (B) Longitudinal net frequencies of cytokine+CD4+ T cells for clusters 7, 8, 9, 10 and 11 for naïve (blue, n=22) and PI (orange; n=11) participants. Wilcoxon tests are shown for each pairwise comparison. Support figure 4D. (C) Cohort comparison with Mann-Whitney tests.

Figure S5

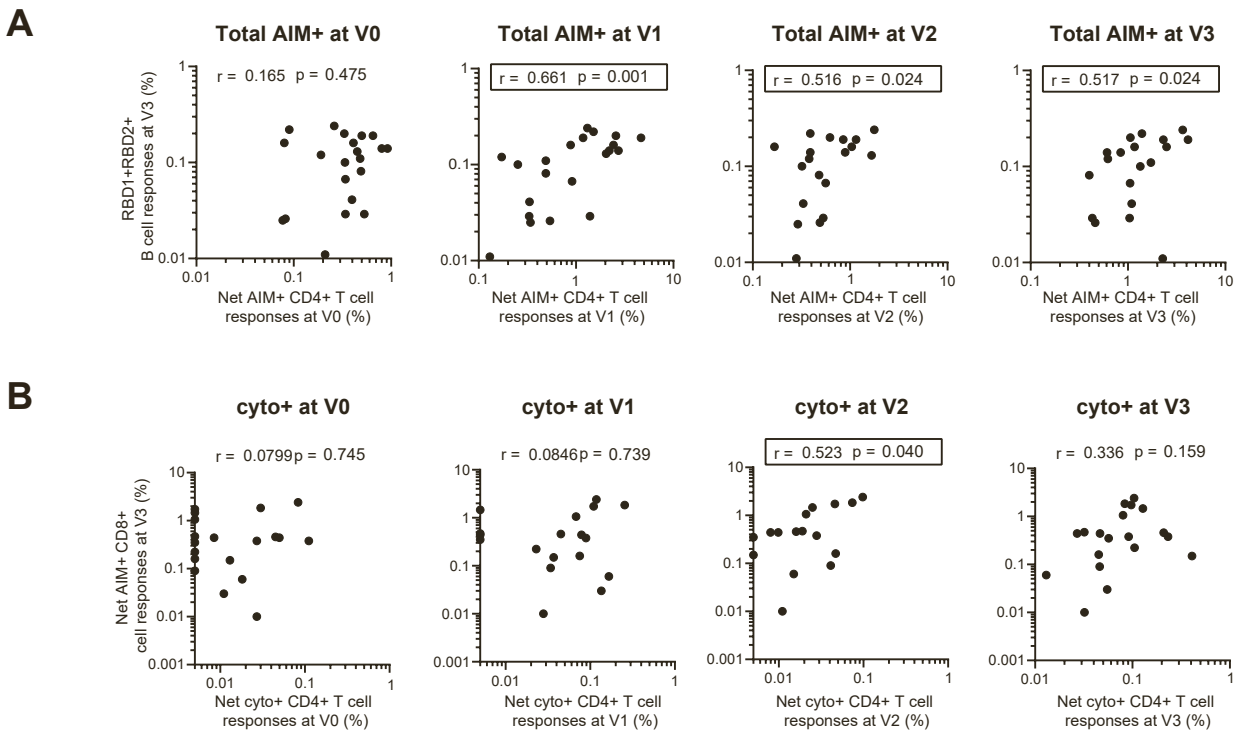
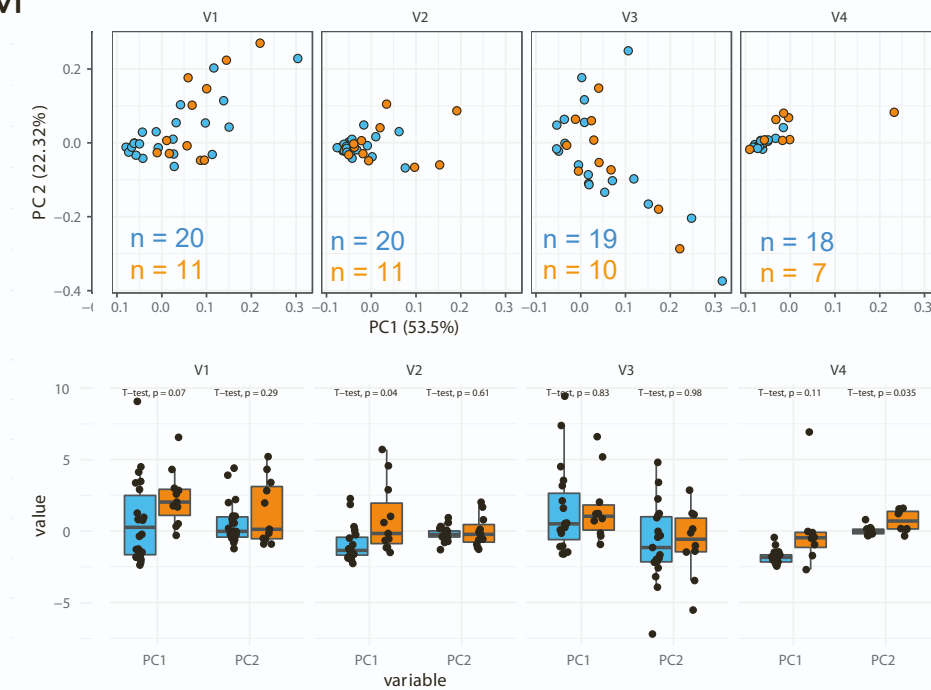


Figure S5: Univariate correlations for validation. Related to Figure 5. (A) Correlation between total AIM+CD4+ T cell frequencies at V0-V3 and RBD-specific B cell frequencies at V3 (n=21). (B) Correlation between total cytokine+CD4+ T cell frequencies at V0-V3 and AIM+CD8+ T cell frequencies at V3 (n = 19). (C) The r and p values from a Spearman test are indicated in each graph.

Figure S6

A AIM⁺



B Cytokine⁺

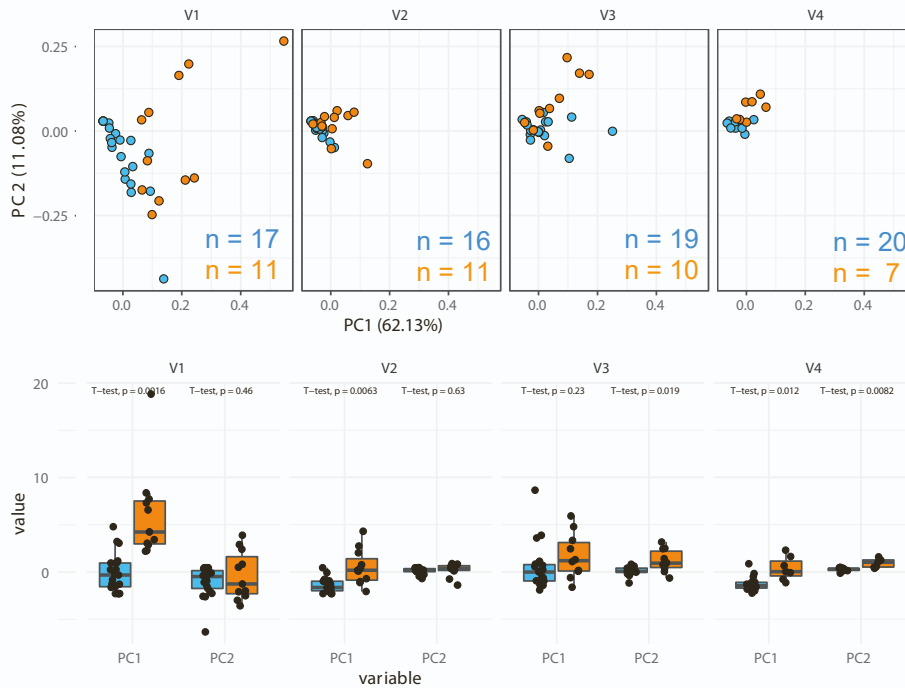


Figure S6: PCA analysis of AIM⁺ and cytokine⁺ CD4⁺ T cell responses. Related to Figure 6. AIM⁺ (A) and cytokine⁺ (B) CD4⁺ T cell sub-PCA analyses. The PC coordinates were set based on the primary PCA combining all timepoints. PC coordinates were then plotted by timepoints for clarity. (A) The top panels present the PCA plots. The proportion of the variance attributed to PC1 and PC2 are indicated on the axes. The numbers of participants analyzed in each PCA plot are indicated in each plot. Box and whisker plots of the PC1 and PC2 between group are presented below, with Mann-Whitney tests. In BC, blue is representing naïve participants and orange, PI.

Table S1. Flow cytometry antibody staining panel for B cells characterization. Related to the STAR Methods section.

Marker-Fluorophore	Clone	Vendor	Catalog #
CD3 – BV480	UCHT1	BD Biosciences	566105
CD14 – BV480	M5E2	BD Biosciences	746304
CD16 – BV480	3G8	BD Biosciences	566108
CD19 – BV650	SJ25C1	Biolegend	363026
CD20 – BV711	2H7	Biolegend	563126
CD21 – BV786	B-LY4	BD Biosciences	740969
CD24 – BUV805	ML5	BD Biosciences	742010
CD27 – APC-R700	M-T271	BD Biosciences	565116
CD38 – BB790	HIT2	BD Biosciences	CUSTOM
CD56 – BV480	NCAM16.2	BD Biosciences	566124
CD138 – BUV661	MI15	BD Biosciences	5 749873
CCR10 – BUV395	1B5	BD Biosciences	565322
HLA-DR – BB700	G46-6	BD Biosciences	566480
IgA - PE	IS11-8E10	Miltenyi	130-113-476
IgD – BUV563	IA6-2	BD Biosciences	741394
IgG – BV421	G18-147	BD Biosciences	562581
IgM – BUV737	UCH-B1	Thermo Fisher Scientific	748928
LIVE/DEAD Fixable dead cell	N/A	Thermo Fisher Scientific	L34960

Table S2. Flow cytometry antibody staining panel for activation-induced marker assay. Related to the STAR Methods section.

Marker-Fluorophore	Clone	Vendor	Catalog #
CD3 – BUV496	UCHT1	BD	612941
CD4 – BB630	SK3	BD	624294
CD8 – BV570	RPA-T8	Biolegend	301037
CD14 – BV480	M5E2	BD	746304
CD19 – BV480	HIB19	BD	746457
CD38 – BB790	HIT2	BD	CUSTOM
CD45RA – PerCP Cy5.5	HI100	BD	563429
CD69 – BV650	FN50	Biolegend	310934
CD134 (OX40) - APC	ACT35	BD	563473
CD137 (4-1BB) – PE-Dazzle 594	4B4-1	Biolegend	309826
CD154 (CD40L) - PE	TRAP1	BD	555700
CD183 (CXCR3) – BV605	G025H7	Biolegend	353728
CD185 (CXCR5) – BV421	J25D4	Biolegend	356920
CD186 (CXCR6) – BUV805	13B 1E5	BD	748448
CD196 (CCR6) – BUV737	11A9	BD	564377
CD279 (PD1) – BV711	EH122H	Biolegend	329928
HLA-DR - FITC	LN3	Biolegend	327005
LIVE/DEAD Fixable dead cell	N/A	Thermo Fisher Scientific	L34960

Table S3. Flow cytometry antibody staining panel for intracellular detection. Related to the STAR Methods section.

Marker-Fluorophore	Clone	Vendor	Catalog #
CD3 – BUV395	UCHT1	BD Biosciences	563546
CD4 – BV711	L200	BD Biosciences	563913
CD8 – BV570	RPA-T8	Biolegend	301037
CD14 – BUV805	M5E2	BD Biosciences	612902
CD16 – BV650	3G8	Biolegend	302042
CD19 – APC-eFluor780	HIB19	Thermo Fisher Scientific	47-0199
CD56 – BUV737	NCAM16.2	BD Biosciences	564448
CD69 – PerCP-eFluor710	FN50	Thermo Fisher Scientific	46-0699-42
CD107A – BV786	H4A3	BD Biosciences	563869
IFN- γ – PECy7	B27	BD Biosciences	557643
CD154 (CD40L) – BV421	TRQP1	BD Biosciences	563886
IL-2 – PE-Dazzle 594	MQ1-17H12	Biolegend	500344
IL-10 - PE	JES3-9D7	BD Biosciences	554498
IL-17A – eFluor660	eBio64CAP17	Thermo Fisher Scientific	50-7179-42
TNF- α – Alexa Fluor 488	Mab11	Thermo Fisher Scientific	502915
Granzym B – Alexa Fluor 700	GB11	BD	561016
LIVE/DEAD Fixable dead cell	N/A	Thermo Fisher Scientific	L34960

Appendix II.iv: Single-Cell Technologies Applied to HIV-1

Research: Reaching Maturity

Frontiers in Microbiology, 2020



Single-Cell Technologies Applied to HIV-1 Research: Reaching Maturity

Gérémy Sannier^{1,2†}, Mathieu Dubé^{1†} and Daniel E. Kaufmann^{1,3,4*}

¹ Research Centre of the Centre Hospitalier de l'Université de Montréal (CRCHUM), Montreal, QC, Canada, ² Department of Microbiology, Infectiology and Immunology, Université de Montréal, Montreal, QC, Canada, ³ Department of Medicine, Université de Montréal, Montreal, QC, Canada, ⁴ Consortium for HIV/AIDS Vaccine Development (Scripps CHAVD), La Jolla, CA, United States

OPEN ACCESS

Edited by:

Fatah Kashanchi,
George Mason University,
United States

Reviewed by:

Kei Sato,
The University of Tokyo, Japan
Ed Browne,
The University of North Carolina
at Chapel Hill, United States

*Correspondence:

Daniel E. Kaufmann
daniel.kaufmann@umontreal.ca

† These authors have contributed
equally to this work

Specialty section:

This article was submitted to
Virology,
a section of the journal
Frontiers in Microbiology

Received: 31 October 2019

Accepted: 10 February 2020

Published: 04 March 2020

Citation:

Sannier G, Dubé M and
Kaufmann DE (2020) Single-Cell
Technologies Applied to HIV-1
Research: Reaching Maturity.
Front. Microbiol. 11:297.
doi: 10.3389/fmicb.2020.00297

The need for definitive answers probably explains our natural tendency to seek simplicity. The reductionist “bulk” approach, in which a mean behavior is attributed to a heterogeneous cell population, fulfills this need by considerably helping the conceptualization of complex biological processes. However, the limits of this methodology are becoming increasingly clear as models seek to explain biological events occurring *in vivo*, where heterogeneity is the rule. Research in the HIV-1 field is no exception: the challenges encountered in the development of preventive and curative anti-HIV-1 strategies may well originate in part from inadequate assumptions built on bulk technologies, highlighting the need for new perspectives. The emergence of diverse single-cell technologies set the stage for potential breakthrough discoveries, as heterogeneous processes can now be investigated with an unprecedented depth in topics as diverse as HIV-1 tropism, dynamics of the replication cycle, latency, viral reservoirs and immune control. In this review, we summarize recent advances in the HIV-1 field made possible by single-cell technologies, and contextualize their importance.

Keywords: HIV-1, single-cell technologies, pathogenesis, cure, vaccine, single-cell omics, fluorescence *in situ* DNA and RNA hybridization, mass cytometry (CyTOF)

INTRODUCTION

HIV-1 remains a major public health problem around the world. Although ART succeeds in suppressing viral replication and has had a tremendously positive impact for people living with HIV-1, it fails to eradicate the virus and restore effective anti-HIV-1 immunity: the virus persists in long-lived reservoirs, and viral rebound occurs almost invariably after cessation of therapy. HIV-1 pathogenesis is complex and diverse at multiple levels. In the absence of therapy, steady-state viremia and disease progression rate are highly variable, depending on both host and pathogen factors; the enormous diversity of circulating viral strains is a major hurdle for the development of effective vaccination and cure strategies (Ho et al., 2013). This intricacy is also important with regard to immunovirological features within an HIV-1-infected individual. HIV-1 infects or interacts with a wide variety of immune cells that harbor considerable heterogeneity in term of phenotype and functions (Chomont et al., 2009).

Fast evolution, diversification and coordination are core traits allowing immune cells to keep up with the threat of remarkably diverse pathogens. Elucidating this complex interconnected cellular network is a formidable task only achievable through high dimensional tools. Despite the increasing availability of these approaches, single-cell studies on HIV-1 infection remains few relative to other immunology fields. Studying HIV-1-infected cells at the single-cell level remains

particularly challenging for various reasons: (1) The extremely low frequency of HIV-1⁺ CD4⁺ T cells, in particular in ART-suppressed individuals (Baxter et al., 2016); the large cell number needed to overcome rare event sampling errors (predicted by the Poisson distribution) and the assay specificity required are often beyond the capacity of many single-cell methods. (2) A large fraction of the integrated HIV-1 DNA proviruses are latent (Ho et al., 2013); currently, no known viral protein or unambiguous cellular surface marker allows their detection in quiescent cells. (3) Secondary lymphoid tissues, which are the main sites of HIV-1 replication and persistence and therefore key for pathogenesis and cure studies, are difficult to sample in humans, thus limiting downstream analyses (Estes et al., 2017). (4) Biosafety issues can make some studies difficult to achieve. Fixation can affect yield and resolution in certain single-cell systems and cutting-edge equipment is not always available in containment labs to work on unfixed samples.

Despite these hurdles, great strides were nonetheless made using more standard methods that could be considered conceptual predecessors of newer single-cell technologies, including limiting dilutions, subpopulation partitioning by population cell sorting, digital droplet PCR (ddPCR), immunohistochemistry, conventional confocal microscopy and flow cytometry etc. While these technologies remain major research tools, their low dimensionality, poor resolution, laboriousness or low-throughput are all good reasons to complement them with newer single-cell techniques. Single-cell “multiomic” technologies play a dominant role in the “single-cell revolution,” but other cutting-edge approaches must not be overlooked. In this review, we broadly define “single-cell technologies” as any approach providing quantitative analyses reaching single-cell resolution. For convenience, we grouped these technologies in four global categories based on their key contribution to the field (Table 1).

Single-Cell Detection of Rare Events

Identification of HIV-1⁺ cells is typically achieved by the detection of viral RNA (vRNA), viral DNA (vDNA) or expression of the structural protein p24. Several direct single-cell virus detection imaging methods with signal amplification were developed in the past years, including *in situ* PCR (Bagasra et al., 1993), tyramide amplification (Soontornniyomkij et al., 1999), and the tunable rolling circle amplification (Frei et al., 2016; Duckworth et al., 2019). All these methods relied on sensitive RNA or DNA fluorescence detection through signal amplification, but at the cost of low reproducibility and high false detection rate due to high background. New methods with higher signal-to-noise ratio combined with dual parametric detection strategies now allow stringent and reliable detection at single-cell resolution (Table 1). The nature of the viral parameters selected for detection impacts data interpretation. CD4 downregulation indirectly provides information about Nef or Vpu expression in the fiber-optic array scanning technology (FAST) assay (DeMaster et al., 2015). Dual non-competitive anti-p24 antibodies (HIVflow) is a convenient way to get insight on p24 translation. The multiplexable branching technology provided the opportunity to use vRNA or vDNA as a co-parameter of detection in fluorescence *in situ* hybridization (FISH) techniques, including RNAflow-FISH (flow cytometry)

and DNA/RNAscope (microscopy) assays (Baxter et al., 2016, 2017a,b; Deleage et al., 2016; Estes et al., 2017). This technology takes advantage of the high signal-to-noise ratios of branching RNA or DNA (Figure 1) to achieve high specificity and sensitivity, rapidity and easiness in the structural analysis of HIV-1 reservoirs.

Single-Cell Genetic Profiling

By partitioning single cells, capturing their transcripts, and generating sequencing libraries in which the transcripts are mapped to individual cells, single-cell RNA sequencing (scRNA-Seq) and its DNA equivalent (scDNA-Seq) represent unequaled “omic” opportunities. All single-cell sequencing technologies follow the same basic principles. Cells must first be individualized by fluidic technologies, limiting dilutions or single-cell sorting flow cytometry (Figure 2). Single cells are then lysed, and RNA or DNA molecules are amplified to generate a library for deep full-genome sequencing (Rato et al., 2017; Bradley et al., 2018; Golumbeanu et al., 2018; de Armas et al., 2019). Epigenetic profiling at the single-cell level is also possible. The assay for transposase-accessible chromatin using sequencing (ATAC-Seq) enables single-cell epigenomic profiling by taking advantage of the insertion of sequencing adapters by a hyperactive Tn5 transposase mutant to map transcriptionally active chromatin regions (Figure 3; Buggert et al., 2018). Subsequent deep sequencing reveals the degree of transcriptional activity throughout the genome. These methods are increasingly used to study HIV-1 at the single-cell level (Table 1).

Single-Cell High Dimensional Phenotyping

High-throughput cell phenotyping for protein markers is most frequently performed by polychromatic flow cytometry or mass cytometry (or cytometry by time-of-flight, CyTOF). In addition to antibodies, polychromatic flow cytometry allows detection of fluorescent dyes and benefits from a large pool of commercially available reagents. However, overlapping fluorescence spectra are a recurrent problem that requires complex compensation. Conversely, mass spectrometry by time-of-flight relies on metal-conjugated antibodies requiring essentially no compensation. Limitations of this technology includes fewer available reagents and a lower acquisition throughput than fluorescent cytometry. Current high-end platforms are designed to achieve high dimensionality (up to >30 parameters for cytometers and >40 parameters for CyTOF, accordingly to manufacturers). While technical considerations usually slightly reduce the number of channels useable simultaneously compared to the limit of parameters available, the depth of single-cell profiling achieved is still remarkable (Cavrois et al., 2017; Bengsch et al., 2018a; Buggert et al., 2018; Bekele et al., 2019). For both technologies analytical tools, rather than instrument performance, can still be bottlenecks preventing full exploitation of the data.

Single-Cell Imaging of Subcellular Molecular Dynamics

Microscopy is often overlooked as a single-cell technology probably because of its traditionally low throughput and

TABLE 1 | Some examples of studies providing single-cell insight into HIV-1 biology or pathogenesis.

	Approaches	Description	Few examples of application
Detection of rare events	Branched DNA signal amplification (RNA or DNA)	Flow cytometric or microscopic detection of RNAs or DNAs, compatible with protein co-detection	Compare latency reversal in different cell subsets (Baxter et al., 2016; Grau-Exposito et al., 2019) Quantify and phenotype the viral reservoirs <i>ex vivo</i> (Baxter et al., 2016; Grau-Exposito et al., 2017) Interrogate viral reservoirs in tissues (Deleage et al., 2016) and estimate whole body viral burden (Estes et al., 2017) Identify HIV ⁺ cells in tissue-resident cells, including non-T cells (Vasquez et al., 2018)
	Dual protein detection	Co-detection of viral proteins by flow cytometry	Study translation-competent viral reservoirs (DeMaster et al., 2015; Pardons et al., 2019)
Genetic profiling	Targeted PCR for viral genes	Quantification of RNA or DNA targets	Correlate residual HIV-1 transcription to sites of integrated proviruses (Wiegand et al., 2017) Quantify HIV-1 splicing upon latency reversal (Yucha et al., 2017) Assess gene expression in different stages of SIV replication (Bolton et al., 2017) Identify biomarkers of HIV-1 permissiveness (Rato et al., 2017)
	Unsupervised sequencing (RNAseq, DNaseq, and ATAC-seq)	Unbiased assessment of transcriptional and epigenetic landscapes	Define quiescent HIV-1 infected cells (Bradley et al., 2018; Golumbeanu et al., 2018), B cell profile post-vaccination (de Armas et al., 2019) Establish an epigenetic signature of resident memory T cells during HIV infection (Buggert et al., 2018)
	BCR and TCR sequencing	Profiling of the B cell and T cell repertoires	Analysis of BCR repertoire post-immunization (Scheid et al., 2009; Sundling et al., 2014)
	Integration sequencing	Mapping of integrated vDNA	Study T cell clonal expansion <i>in vivo</i> in the context of HIV infection (Wendel et al., 2018) Map HIV-1 integration sites in the CD4 ⁺ T cell genome of primary samples (Cohn et al., 2015)
	Virus barcoding	Engineered viruses with degenerate unique barcodes	Examine the transcriptional potential of integrations sites by correlating barcodes in integrated DNA and vRNA (Chen et al., 2017)
High dimensional phenotyping	Mass cytometry (CyTOF)	Time-of-flight cytometry based on heavy ion metal tags with minimal spectral overlap	Evaluate the susceptibility of CD4 ⁺ T subsets to productive HIV-1 infection (Cavrois et al., 2017) Define the phenotypic landscape of exhausted T cells (Bengsch et al., 2018a; Bekele et al., 2019) Link new CD8 ⁺ T cell subsets to HIV-1 pathogenesis (Buggert et al., 2018)
Imaging of subcellular molecular dynamics	Fluorescent tags	Temporal interrogation of bioengineered fluorescently tagged proteins of interest in primary cells	Dissect, in live cells viral entry (Miyachi et al., 2009), uncoating (Arhel et al., 2006; Mamede et al., 2017; Francis and Melikyan, 2018b), nuclear import (Chin et al., 2015), and assembly (Ivanchenko et al., 2009) Estimate the timeline of gene expression (Holmes et al., 2015)
	Branched DNA signal amplification for RNA/DNA single-cell microscopy Imaging of integrated DNA	Snapshots of selected RNAs, vDNA and proteins sub-localization SCIP Detection of CRISPR-Cas9-cleaved integrated provirus	Study the nuclear import of vDNA (Chin et al., 2015) Locate integration sites of native proviruses in primary cells (Marini et al., 2015) Study the uncoating of native viruses (Puray-Chavez et al., 2017) Investigate the spatial localization of HIV-1 integration sites in live cells (Di Primio et al., 2013) Assess HIV-1 integration in real-time in live cells (Ma et al., 2017)

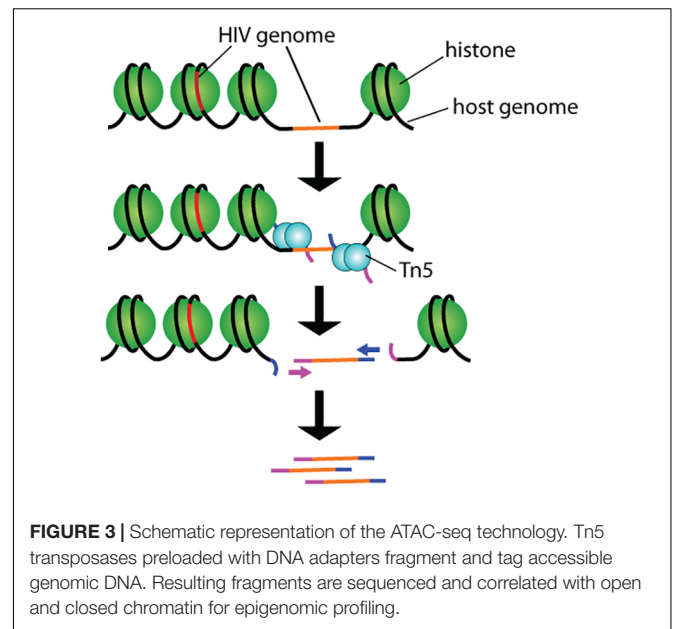
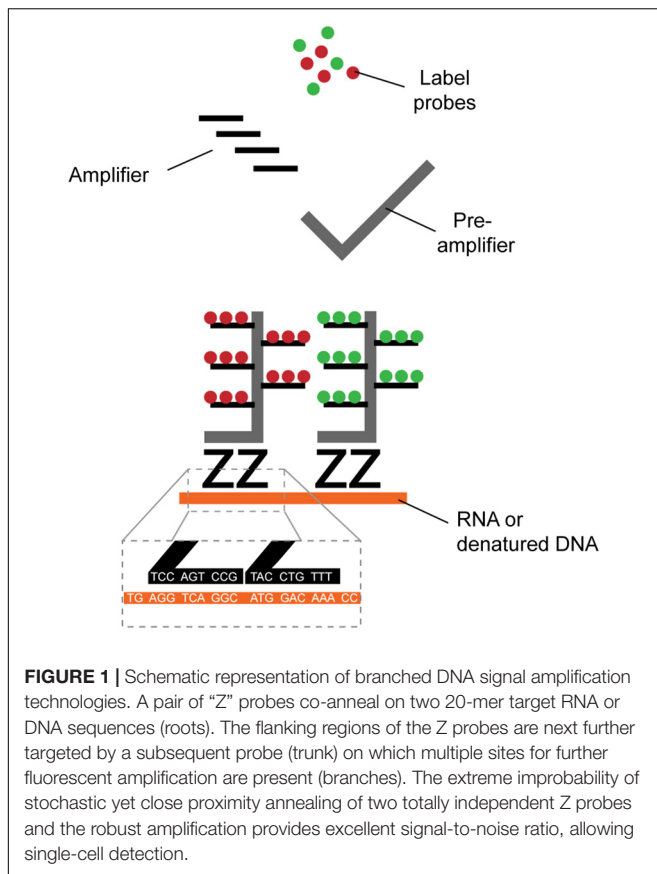
semi-quantitative nature. High-resolution time-lapse imaging technologies now provide unprecedented spatial information of unique HIV-1 infected cells in near real-time (**Table 1**). Automated acquisition and quantification platforms allow unbiased data acquisition, correcting the typical caveat of microscopy. The preservation of the 3D architecture grants access to information impossible to obtain by other single-cell methods.

These recent developments helped the HIV-1 field take the leap toward single-cell technologies. Here, we discuss the contribution of these various new single-cell technologies in

the context of HIV-1 research and review concrete examples of their applications.

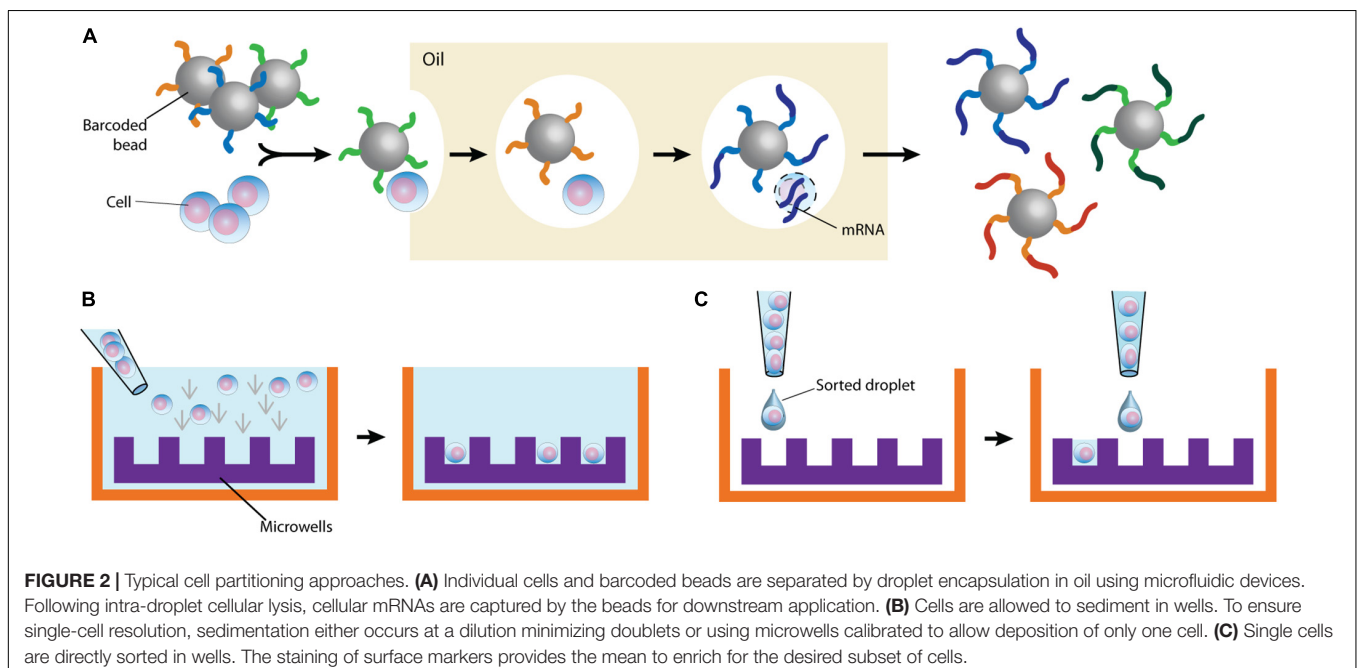
HIV-1 TROPISM AND HOST CELL REMODELING

Better defining the nature of HIV-1 infected cells has been an active topic of research since the discovery of the virus. CD4⁺ T cells were quickly found to be primary targets during productive infection. The evolution of molecular biology and flow cytometry tools came with more precise characterization of cells targeted by



HIV-1. The ever-improving capacity to divide cell populations into more and more refined subsets by cell sorting or column enrichment enabled the *in vitro* interrogation of various immune

cells for either their susceptibility to HIV-1 infection or the presence of vDNA by ultrasensitive PCR methods. These approaches provided a wealth of data, with at times conflicting results that may be mostly due to technical considerations. Numerous studies identified several cell populations with high susceptibility to infection, including central memory CD4⁺ T cells (T_{CM}) (Chomont et al., 2009; Jaafoura et al., 2014; Boritz et al., 2016), CD4⁺ T memory stem (T_{SCM}) cells (Buzon et al., 2014), regulatory T (T_{REG}) cells (Oswald-Richter et al., 2004; Tran et al., 2008; Moreno-Fernandez et al., 2009; McGary et al., 2017); T_H17 cells (Gosselin et al., 2010, 2017),



T follicular helper cells (T_{FH}) (Perreau et al., 2013; Banga et al., 2016). All these subsets are defined by sets of phenotypic features broadly accepted at the time of experimentation. However, these labels are not set in stone and are frequently updated based on more refined characterizations. High dimensional single-cell technologies can address these categorizing issues by system biology rather than knowledge-based approaches. For example, unsupervised scRNA-Seq experiments on primary $CD4^+$ T cells infected *in vitro* identified novel biomarkers of HIV-1 permissiveness such as CD25, CD298 (ATP1B3), CD63, and CD317 (BST-2) that all correlated with T cell activation (Rato et al., 2017). Activation-induced proteins were not equally predictive of HIV-1 permissiveness, however, suggesting that there are more to permissibility than just cell activation.

Studies of viral permissibility performed *in vitro* must be interpreted with caution. Cultured $CD4^+$ T cells drift from their original transcriptional program, especially when exogenous biologically active molecules are applied to maintain survival (ex: IL-2) or promote infection (ex: $CD4^+$ T cell activation by PHA or CD3/CD28 crosslinking). Such models are often a reasonable and necessary compromise because of the rarity of infected cells in people living with HIV-1. This bias can now be avoided to some extent by direct *ex vivo* detection of infected cells using dual HIV-1 detection by flow cytometry, as described above. Both HIVflow and RNAflow-FISH showed remarkable consistency in providing *ex vivo* validation of previous bulk observations such as HIV-1 enrichment in cells (1) expressing the activation-associated proteins CD25, HLA-DR, Ki67 and the inhibitory receptors TIGIT, PD-1 or CTLA-4 (Baxter et al., 2016; Pardons et al., 2019); (2) transitional memory $CD4^+$ T (T_{TM}) cells rather than in central and effector memory (T_{CM} and T_{EM} , respectively); (3) in cells of T_{H17} , T_{FH} and T_{REG} polarizations (Pardons et al., 2019). Unfortunately, detection of HIV-1 infected cells implies experimental procedures that tend not to preserve well RNA integrity, often precluding downstream RNA-Seq analysis. However, high dimensional protein profiling of infected cells is now doable by flow cytometry and while some obstacles remain, these strategies are adaptable to mass cytometry. These single-cell technologies enable studying the permissibility of subsets to sub-viral processes like entry and gene expression using engineered reporter viruses. In a recent mass cytometry study (Cavrois et al., 2017), cells undergoing viral fusion, as detected by the fluorescent CCF2 substrate in response to the release of the chimeric BlaM-Vpr protein, were sorted and compared in parallel to cells expressing the virally encoded, mass cytometry-compatible murine heat-stable antigen (HSA) marking productively infected cells. The comparison of these two independent single-cell datasets drew an atlas of $CD4^+$ T cell phenotypic features contrasting entry and productive infection. Tonsillar T cells with features of memory, T_{H2} , T_{H17} and T_{REG} subsets were thus found prone to viral entry in sharp contrast to naïve T cells whereas T_{H17} and T_{FH} were found predominant productively infected cells.

HIV-1 does not exclusively infect $CD4^+$ T cells. Myeloid cells could also represent targets and/or facilitate viral dissemination although definitive *in vivo* confirmation of productive infection is still lacking. The best current technologies to detect HIV-1⁺

cells by flow cytometry call for a large number of cells difficult to obtain from blood, typically a poor source of mature myeloid cells. Microscopy studies using DNA/RNA FISH techniques are therefore better suited to address this detection challenge (Wang et al., 2012; Deleage et al., 2016; Estes et al., 2017). DNA/RNA FISH preserves tissue integrity and allows spatial interrogation of the microenvironment. This approach was used in a recent study (Estes et al., 2017) of multiple anatomic compartments in SIV and HIV-1 infection, further confirming that more than 98% of infected cells in primates would originate from lymphoid organs, a proportion likely similar in humans. A similar multiplex ISH microscopy method (mFISH) has led to the identification of rare HIV-1⁺ $CD21^+$ follicular dendritic cells (FDCs) and $CD68^+/CD163^+$ macrophages in lymph nodes of a viremic donor (Vasquez et al., 2018). Consistent with these results, confocal microscopy studies demonstrated that FDCs retain infectious HIV-1 in cycling endosomes through the complement receptor CD21 (Heesters et al., 2015) and multispectral flow cytometry (ImageStream) showed *in vitro* infection of macrophages via selective capture of HIV-1-infected $CD4^+$ T cells (Baxter et al., 2014). While very powerful, microscopy imaging also has some drawbacks, including labor intensiveness, relatively low throughput, limited number of parameters on most instruments, and in most cases reliance on solid tissues that are hard to sample from human participants.

HIV-1 REPLICATION CYCLE

The HIV-1 replication cycle has been studied for decades. Through the use of bulk methods, the processes governing viral replication were detailed to reach a canonical model (Engelman and Cherepanov, 2012). Single-cell technologies now reveal critical cell-to-cell disparities.

Viral Entry

An innovative dually fluorescent viral platform combining lipophilic dyes staining viral membrane, and a cleavable GFP-Gag chimeric protein as a fluid-phase marker present inside the virion was developed to study HIV-1 entry (Miyachi et al., 2009). This platform provided evidence that frequently occurring plasma membrane-fusion events were in fact dead-ends and suggested that only endosomal fusion is productive.

Pre-integration Events

Co-detection of vRNA and vDNA by FISH-based technologies now enables detection of ongoing reverse transcription by high resolution microscopy, confirming its initiation in the cytoplasm (Puray-Chavez et al., 2017). Reverse transcription consistently culminated within a range of 10-14h post-entry in cell lines (Hulme et al., 2011; Holmes et al., 2015; Puray-Chavez et al., 2017). Several approaches enabled the visualization of the ill-characterized HIV-1 uncoating process: IN-TC/FLAsh (Arhel et al., 2006), A3F-YFP or IN-YFP (Burdick et al., 2017), or 5-ethynyl-2-deoxyuridine-labeled vDNA (EdU), GagiGFP, or CypA-DsRed/CA, with INsfGFP (Peng et al., 2014; Francis

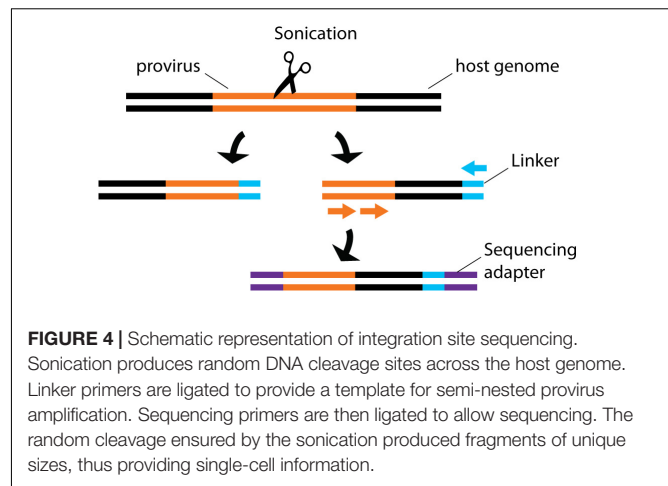
et al., 2016; Mamede et al., 2017; Francis and Melikyan, 2018a). Productive infection, attributed to only $\approx 2\%$ of cell-bound-viruses (Burdick et al., 2017; Francis and Melikyan, 2018a), was characterized by tracking the intact or partially uncoated cores toward the nucleus where uncoating is completed in the vicinity of nuclear pores (Arhel et al., 2006; Francis et al., 2016; Mamede et al., 2017). While live-cell imaging of native viruses has not yet been achieved, snapshots of native virus egress in single primary cells are possible. Probing of the negative strand of the vDNA with a branching amplification technique along with protein staining enabled visualization of the nuclear import of native vDNA 12h post-infection confirmed the essential role of nuclear pore complex subunits (Chin et al., 2015).

Integration

By sequencing genomic vDNA from cell populations calculated to contain a single-infected cell, the frequency of HIV-1⁺ cells bearing a single integrated provirus was estimated at 85-90%, suggesting that only a minority of infected cells can sustain recombination, an important mechanism for viral evolution (Josefsson et al., 2011, 2013). To draw a landscape of HIV-1 integration sites in primary cells, the translocation-capture sequencing (TC-Seq) initially designed to study chromosomal rearrangements in B lymphocytes (Klein et al., 2011) was adapted in the integration sequencing assay (Cohn et al., 2015; **Figure 4**). Consistently with previous bulk population results (Schroder et al., 2002), this method detected globally more frequent integration events in intragenic regions of the genome with high transcriptional activity. Integration in genes with lower transcription activity occurred more frequently in treated individual with latent infection. While single-cell sequencing is a powerful way to map integrated vDNA in the genome, several imaging techniques were designed to assess its spatial location in the nucleus. They revealed that HIV-1 preferentially integrates in the chromatin found close to the nuclear membrane (Di Primio et al., 2013). Three-dimensional immuno-DNA FISH localized in *in vitro* infected primary CD4⁺ T cells both HIV-1 recurrent integration genes (RIGs) and integrated HIV-1 proviruses close to nuclear pores (Marini et al., 2015). More recently, a single-cell CRISPR imaging method was developed to assess integration in real-time. In this system, a guide DNA targeting the U3-LTR region triggers the co-localization of exogenous Cas9 proteins conjugated with two different quantum-dot fluorophores (Ma et al., 2017). This stringent dual-parametric detection provided an estimation of 1.6 ± 0.4 integrated events per HIV-1⁺ cell. This estimation was remarkably consistent with the data inferred by single-sorted cell sequencing results (Josefsson et al., 2011, 2013). Although initially applied to a cell line as a proof-of-concept, its compatibility with primary cell studies could provide physiological insight into vDNA integration.

Assembly and Release

A key challenge in studying HIV-1 assembly and release is the inability to totally synchronize infection in target cells, underlining the need for single-cell technologies to conduct fine analyses. Total internal reflection fluorescence microscopy (TIRFM) enabled the visualization in adherent



cell lines of clusters of mixed native and fluorescently tagged Gag proteins corresponding to single virions. Combined with photoconvertible fluorescence technology, it showed the nucleation of recently membrane-associated Gag proteins rather than the existence of long-lived stable platforms (Ivanchenko et al., 2009). Assembly was timed as fast as within 4-10 min after nucleation (Jouvenet et al., 2008; Ivanchenko et al., 2009), with an extra 25-min delay to achieve budding (Ivanchenko et al., 2009). The high resolution achieved by TIRFM or stochastic optical reconstruction microscopy (STORM) lead to the detection of ESCRT factors lattices co-localization with HIV-1 assembly sites (Baumgartel et al., 2011; Prescher et al., 2015). Other technologies enabling imaging of native virions on primary cells will be required to extend our knowledge of assemble/release in physiological context.

Interplay With Host Cell Factors

More discovery-oriented approaches are required to understand the dynamics of the viral cycle in host cells *in vivo*, given the heterogeneity of immune cells. One strategy involves taking transcriptional snapshots of thousands of unsynchronized single cells and reconstitute the dynamic pattern of gene expression. This approach implies a compromise as the data produced only infer temporality to allow assessment of primary cells infected with native viruses. Using RT-qPCR on single-sorted cells, investigators were able to subdivide SIV replication cycle in various stages defined by the relative presence of multiply spliced versus unspliced vRNAs (Bolton et al., 2017; Tokarev et al., 2018). Simultaneous assessment of cellular gene expression revealed distinct transcriptional patterns associated with SIV infection, which could further be indexed to phenotypic data acquired during the single-cell flow cytometry sorting. This approach also provided some of the rare documented *ex vivo* evidence of SIV/HIV-1-mediated cellular protein downregulation. While in most cells progressive infection was associated with post-transcriptional downregulation of the CD4 protein, surface MHC class I expression was surprisingly largely maintained, in contradiction with previous reports suggesting maintenance of Nef-mediated MHC-I downregulation *in vivo* through selective

pressure (Munch et al., 2001; Swigut et al., 2004). The same approach can in principle be further expanded to downstream unsupervised scRNA-Seq.

REGULATION OF HIV-1 EXPRESSION

High resolution information is now available on the temporal regulation of viral gene expression. Live cell imaging studies of viruses encoding a fluorescent marker in place of the early gene *nef* or in frame within the late gene *gag* determined that as much as 42h can be necessary to complete a single replication cycle. This timespan varies considerably from one cell to another, suggesting the existence of cellular specificities that may temporally modulate viral egress (Holmes et al., 2015). Multiple well-tuned delays were noticed, including a 3-h delay between the onset of early and late gene translation followed by an overshadowing 6-12-h delay until viral assembly and release. These “programmed” delays would allow viruses to carry out pre-requisite processes that may be cell-specific. In independent studies, ddPCR provided *ex vivo* evidence of multiple blocks through transcription preventing initiation, elongation and termination of viral transcripts in CD4⁺ T cells (Yukl et al., 2018). Accumulation of multiply spliced variants sustaining only expression of the early Tat, Rev or Nef genes was also reported in some cells (Yukl et al., 2018). However, whether the transcriptional blocks and the well-tuned delays are related processes remain unclear because ddPCR does not preserve single-cell information and natively infected primary CD4⁺ T cells cannot be adequately interrogated with the currently available imaging methods. Indeed, single-cell PCR methods have the best potential to test this relation in physiological context.

A fine balance in the expression of the HIV-1 transactivator Tat protein is necessary to sustain adequate viral gene expression. As Tat is self-regulated, its downmodulation creates a transcriptional contraction that can lead to latency, a reversible state characterized by low or absent viral transcription. The dynamics of HIV-1 latency is complex and calls for high-dimensional tools (Kok et al., 2017). A time-lapse single-molecule mRNA fluorescence *in situ* hybridization (smFISH) method brought molecular evidence that Tat can act as a molecular switch. By following the relative expression of dual reporters of spliced and unspliced vRNA, a novel post-transcriptional mechanism of noise suppression stabilizing the commitment of HIV-1 to its active gene expression state was discovered (Hansen et al., 2018). The accumulation of unspliced transcripts reduced the relative level of Tat and Rev-coding spliced transcripts, creating a negative-feedback loop of noise suppression. Transcriptional noise would hinder fate commitment to the active state, thus promoting latency. A similar pattern of spliced/unspliced transcript temporal dynamics was observed in another single-cell study using a dual cherry/GFP reporter construct (Holmes et al., 2015).

While not all infected CD4⁺ T cells have the potential to become latent reservoirs, defining the determinants of this transition has been challenging in spite of intense investigation. The paucity of latent reservoirs persisting on suppressive ART

in vivo and their difficult identification are major hurdles in the field. A number of latency models were used to circumvent this limitation (reviewed in Whitney and Brad Jones, 2018). While such models have enabled significant progress, they still face major questions regarding their representativity of actual events occurring *in vivo* and present notable discrepancies (Spina et al., 2013). The location of provirus integration was suggested as a key determinant for establishment of latency (Jordan et al., 2001; Sherrill-Mix et al., 2013). In that regards, barcoded HIV-1 Ensembles (B-HIVE) proved very informative. This technology involves insertion of a barcode into the viral genome. Because multiple viruses sharing the same degenerate 20 nucleotides-long barcode are extremely improbable, each barcode is statistically indicative of a single provirus providing single-cell resolution. After sequencing, vRNA can be connected to integrated vDNA sharing the same unique barcode, thus giving a robust examination of the transcriptional potential of each integration site (Chen et al., 2017, 2018). Using B-HIVE, latent proviruses were found integrated far from active host promoters or enhancers (Chen et al., 2017). This is consistent with integration sequencing data demonstrating that latent cells are more likely to bear vDNA in intergenic regions or in genes with low or no level of transcriptional activity than active reservoir cells. Proviruses inserted into active regions of the genome were found selected against probably due to virus-mediated toxicity, thus precluding the expansion of the clones bearing vRNA with the strongest transcriptional potential (Cohn et al., 2015).

Why would an unfavorable site of integration forcing latency would suddenly become good enough to fuel viral rebound? The regulation of viral gene expression by the intracellular environment can explain this apparent paradox. This notion is supported by the finding that timely infection of activated cells in the process of becoming quiescent promotes latency (Shan et al., 2017). Two recent scRNA-Seq studies using post-activation latency models drew transcriptional landscapes of quiescent HIV-1 infected cells (Bradley et al., 2018; Golumbeanu et al., 2018). Globally, latently infected cells clustered close to uninfected cells, suggesting that latent infection does not extensively remodel host cells (Bradley et al., 2018). Consistent with integration sequencing data, poor HIV-1 gene transcription was also associated with increase proliferative capabilities and cell survival (Bradley et al., 2018). A superficial resting state prone to HIV-1 reactivation could be discriminated from a deeper hardly reactivable latency by their higher expression level of genes associated with metabolism, gene expression, disease, immune system and DNA repair, giving rise to a 134-gene-specific transcriptional signature of inducible latent cells (Golumbeanu et al., 2018). Although powerful and informative with regard to the gene profile and mechanisms behind latency, these studies still rely on latency models with engineered laboratory-adapted viral strains which may not express all viral genes adequately, thus having an impact on the overall transcriptional landscape. As such, the extent at which the aforementioned findings can be transposed to *in vivo* latency is still unclear. Nevertheless, combined multi-faceted single-cell studies can lead to an elegant model of latency. Integration in intergenic

regions far from enhancers or promoters results in a dead-end deep latency state. Inversely, integration in intragenic regions close to active enhancers or promoters leads to robust gene expression and selection against by cell-mediated cytotoxicity or virus-mediated apoptosis. Proviruses integrating in the perfect sweet-spot between those two extremes can become reversibly latent and undergo homeostatic expansion once the global transcriptional activity of its host decreases toward quiescence. It is still unclear if the distance of the integrated provirus from the nuclear membrane may also influence latency. The single-cell imaging tools to address this question are there however, and further investigations will certainly be informative in this regard.

Latency is not a permanent state. This is a central problem in HIV-1 pathogenesis and clinical care as the virus almost always spontaneously rebounds after treatment interruption. However, this problem can also become an opportunity: upon reactivation of latent reservoirs, the immune system can much better detect infected cells and destroy them. Therapeutically inducing reservoir reactivation to facilitate its elimination, also termed a “shock and kill” approach, is thus considered as potential strategy for HIV-1 cure. TCR cross-linking and PMA/ionomycin are well known to reactivate latent reservoirs *in vitro*, but their pleiotropic effects prohibit their use *in vivo*. A growing list of pharmaceutical compounds are now known as latency reversal agents (LRA) (reviewed in Kim et al., 2018). A microfluidic single-cell-in droplet PCR (scdPCR) assay in which single cells are partitioned in lipid droplets for individualized PCR allowed enumeration of CD4⁺ T cells that produce unspliced (us)RNA and multiply spliced (ms)RNA upon LRA stimulation of primary CD4⁺ T cells from ART participants (Yucha et al., 2017). It revealed that reactivation induced by TCR cross-linking or the LRA Romidepsin is asymmetrical at the single-cell level and is variable amongst donors. These results highlighted a fact that bulk analysis could not identify: latency reversal can be the result of a robust viral expression in a few cells or a modest induction in many (Yucha et al., 2017). The B-HIVE assay further shed light on latency reversal: cells responding to Vorinostat harbored integrated proviruses closer to enhancers than PHA did (Chen et al., 2017). The insertion context defined at the single-cell level thus carries some predictive value about the potential response of a provirus to LRAs.

Flow cytometric RNA FISH assays, thanks to their ability to simultaneously monitor at the single-cell level vRNA and HIV-1 protein expression upon LRA reactivation, are powerful approaches in latency reversal studies (Baxter et al., 2016, 2018; Grau-Exposito et al., 2017, 2019). For example, while Romidepsin increased frequencies of vRNA⁺ cells, this LRA was a poor inducer of Gag protein expression in these reactivated cells compared to PMA/ionomycin (Grau-Exposito et al., 2017). The kinetics of latency reversal at the transcriptional and translational level could also be monitored using this method (Martrus et al., 2016). As detection of HIV-1⁺ cells can be combined with multiparametric phenotyping for cellular markers, RNAflow-FISH approaches can distinguish subsets of CD4⁺ T cells able to respond to LRAs in primary clinical samples. For example, the protein kinase C (PKC) agonist Bryostatins-1 preferentially

reactivated T_{EM} reservoirs whereas the PEP005 showed broader activity, including on T_{CM} cells (Baxter et al., 2016) and stem-cell memory T cells were found to be more refractory to reactivation (Grau-Exposito et al., 2019). These are early studies for these technologies that suggest they have potential as advanced monitoring tools for clinical trials.

VIRAL RESERVOIRS

Determining the size of HIV-1 reservoir during ART is challenging, as long-lived latently infected cells are largely transcriptionally silent. Early methods applied to bulk populations relied on the direct detection of total or integrated HIV DNA. Few DNA-based detection methods can accurately distinguish the rare cells bearing an intact, potentially replicative-competent provirus from the vastly more numerous HIV-1⁺ cells bearing integrated proviruses containing lethal defects. Intact proviruses were found enriched in cell refractory to standard *in vitro* stimulation with frequencies in the few percent range of total vDNA (Ho et al., 2013). While the potential of these viruses to reactivate *in vivo* is unknown, they may constitute a higher barrier to cure. Conversely, the quantitative viral outgrowth assay (Q-VOA), in which single infected-cell are seeded in limiting dilutions among reporter cells to allow the amplification of p24, gives a minimal estimation of the size of replication-competent reservoirs. These methods offer the highest and lowest estimates of “total” and “replication-competent” viral reservoirs. New highly sensitive and specific flow cytometry-based methods based on detection of viral products (viral RNA and/or proteins) provide additional information on the competence of the reservoirs at the single-cell resolution required to associate viral or cellular features to the quantified reservoirs, with estimated VR sizes that are intermediate between standard DNA and Q-VOA quantification (DeMaster et al., 2015; Baxter et al., 2016, 2018; Grau-Exposito et al., 2017; Zhang et al., 2018; Pardons et al., 2019). In these studies, translation-competent reservoirs were determined by the expression of p24 (Baxter et al., 2016, 2017a; Pardons et al., 2019) whereas production of viral RNAs such as *gagpol* defined transcription-competent reservoirs (Baxter et al., 2016; Grau-Exposito et al., 2017). To isolate live reservoir cells, dual staining with broadly neutralizing antibodies (bNAbs) has also been successfully applied (Cohn et al., 2018). These methods are well adapted to assess HIV-1⁺ events in blood, where reservoir cells are rare but cell numbers is not limiting. Probing lymphoid tissues, the primary viral sanctuaries during ART, is more difficult because of limited sample availability. While cytometry can be performed on extracted cells, *in situ* microscopy is frequently the method of choice to perform those measurements in tissues. Signal amplification technologies have been developed to allow simultaneous single-cell detection of proviral vDNA and vRNA, giving valuable information both on DNA integration and viral gene expression without altering tissue structure (Deleage et al., 2018). Coupled with automated imaging of multiple tissues, these approaches have allowed rigorous assessment of anatomical compartmentalization and total body burden of SIV and HIV-1 reservoirs (Deleage et al.,

2016; Estes et al., 2017, 2018). A variant of this method enabled detection of spliced viral RNA using probes specific for the *tat-rev* splice junctions, thus increasing the likelihood of detecting viral RNA⁺ cells *in situ* associated with replication-competent viruses (Deleage et al., 2018). Applied to flow cytometry, this approach distinguished spliced and unspliced vRNA and was sufficiently sensitive to capture the delayed export from the nucleus to the cytoplasm of unspliced vRNA compared to the spliced variant (Puray-Chavez et al., 2017). Determining if residual vRNA⁺ cells can represent a primary source of viral rebound upon treatment interruption necessitates single-cell analysis because expanded clones cannot be recognized as such in bulk analyses. The cell-associated HIV-1 RNA and DNA, single-genome sequence assay (CARD-SGS) can connect residual HIV-1 transcriptional activity to proviruses in ART-treated donors (Wiegand et al., 2017). Single-cell resolution of sequencing is achieved through statistical assumption of the dilution required to obtain single HIV-1⁺ cells. On ART, vRNA sequences were found less diverse than vDNA, further suggesting that few HIV-1⁺ cells actually contribute to the viral diversity *in vivo* (Wiegand et al., 2017). The extent of the contribution of expanded vRNA⁺ clones to viral rebound is still debated, as there are notable discrepancies between reported observations (Cohn et al., 2015; Barton et al., 2016; Boritz et al., 2016; Kearney et al., 2016). Nevertheless, all these studies are consistent with a very limited pool of HIV-1⁺ cells fueling viremia or viral rebound. These findings emphasize the importance of studying proviral sequences at the single-cell level to discriminate the cells susceptible to fuel viremia from the numerically superior ones that cannot.

IMMUNE RESPONSE

HIV-1 pathogenesis is determined by complex interactions between the virus and the host immune system. While the study of the anti-HIV-1 immune response quickly became a major field of research in the perspective of developing effective cure strategies and prophylactic vaccines, it is only relatively recently that single-cell technologies have been exploited and have yielded major results in this area.

Immune Response and Immune Dysfunction

Multiple arms of the immune responses are dysregulated in HIV-1 infection. Hypergammaglobulinemia is frequent, contrasting with qualitative defects of humoral immunity such as lower titers and less durable B cell responses to seasonal influenza vaccine (Tebas et al., 2010; Crum-Cianflone et al., 2011; de Armas et al., 2019). The extreme diversity of the B cell receptor (BCR) repertoire and complex differentiation patterns of B cell subsets limit the insight gained from bulk population studies. To overcome these limitations, transcriptional profiling was recently performed by scRNA-Seq on post-vaccination Influenza-specific memory B cell in virally suppressed HIV-1-infected individuals (de Armas et al., 2019). In this approach, fluorescent probes identifying HA-specific B cells allowed single-cell sorting and downstream scRNA-Seq. The high-dimensional

data thus generated contrasted transcriptional differences in cells otherwise indistinguishable by conventional flow cytometry. *PTEN*, a gene associated with hampered BCR signaling through inhibition of the PI3K signaling pathway, was found elevated in influenza-specific B cells from HIV-1-infected individuals. Other studies attributed B cell dysfunction to inefficient help provided from germinal center follicular T cells (GC T_{FH}) (Cubas et al., 2013, 2015; Boswell et al., 2014). The analysis of lymph node samples from untreated HIV-1⁺ donors by combined high dimensional mass cytometry and TCR repertoire single-cell sequencing shed light on the fine structure of these T_{FH} responses (Wendel et al., 2018), revealing that HIV-1-specific T_{FH} expand but become functionally skewed with limited TCR diversity, features that correlate with B cell dysregulation in the same lymph node.

T cell dysfunction is a hallmark of chronic infections, and is in part an adaptive compromise required for the host by antigen persistence, as it balances some partially effective immunity with reduction of immunopathology. While this immune impairment was initially conceptualized as a state of chronic loss of function, a number of studies have highlighted T cell “exhaustion” as being a distinct differentiation program, which itself presents important cellular heterogeneity among subsets of exhausted cells (e.g., CD4⁺ vs CD8⁺ T cells, McLane et al., 2019). High dimensional single-cell analyses can now provide a better understanding of this complexity. Rather than relying on a limited set of parameters to identify exhausted T cells in HIV-1 infected humans, investigators used an epigenomic-guided mass cytometry approach (Bengsch et al., 2018b) and identified up to 12 exhausted CD8⁺ T cell clusters with considerable heterogeneity in inhibitory co-receptor and transcription factor co-expression. Some clusters of severely exhausted CD8⁺ T cells were found similarly enriched in people afflicted with lung cancer whereas others were differentially represented, suggesting that a common core biology of T cell exhaustion across diseases exists along with more disease-specific defects (Bengsch et al., 2018b). The extent to which these findings also apply to CD4⁺ T cells remains to be determined, and single-cell technologies applied to CD4⁺ T cell biology will be informative. Mass cytometry data revealed a complex network of CD4⁺ T cell clusters that correlated with functional decline and was associated with late ART initiation (Bekele et al., 2019). Most high-dimensional studies on T cell dysfunction in HIV infection have thus far been focused on T cell subsets, not HIV-specific T cells, a step required to delineate antigen-specific immune dysfunction from broader dysregulation in the context of HIV-1 infection and associated chronic immune activation.

While epitope-specific tetramers of good quality and broad HLA Class I diversity are easily accessible for human CD8⁺ T cell studies and can also be used for high-dimensional flow cytometry or mass cytometry studies (Newell et al., 2013), accessibility to reliable human Class II multimers remains limited. Several groups have thus established sensitive methods based on upregulation of activation-induced markers (AIM) to detect virus-specific CD4⁺ T cells after cognate antigen stimulation (Zaunders et al., 2009; Havenar-Daughton et al.,

2016; Reiss et al., 2017). A major advantage of this approach is the possibility to live-sort HIV-1-specific CD4⁺ T cells for downstream analyses such as -omics studies, including single-cell technologies. This was recently illustrated by a genome-wide transcriptome profiling study of HIV-1-specific CD4⁺ T cell responses pre- and post-ART (Morou et al., 2019). Expression patterns of selected genes and their association with cell phenotypes was confirmed at the single-cell level by multiplexed RNAflow-FISH, providing an experimental pipeline for detailed HIV-1-specific CD4⁺ T cell studies. Compared to Thelper responses identified in HIV-1 elite controllers, ART did not fully reverse the dysregulated transcriptional program identified in viremic progressors before initiation of therapy (Morou et al., 2019). This is consistent with mass cytometry studies of the total CD8⁺ and CD4⁺ T cell subsets conducted on other HIV-1⁺ cohorts, which showed incomplete restoration of clusters of exhausted T cells on suppressive ART (Bensch et al., 2018b; Bekele et al., 2019). A precise map of the corrected versus persistently altered gene modules will be key to understand residual T cell dysfunction in people living with HIV-1.

Single-cell technologies can also facilitate in-depth studies of anatomic compartments for which sampling is quite limiting in humans. Until recently, the paradigms of protection against HIV-1 largely relied on peripheral blood studies, although virus replication occurs mainly in lymphoid tissues. An approach combining high dimensional mass cytometry, scRNA-Seq, and ATAC-Seq enabled transcriptional and epigenetic-profiling of a novel extrafollicular LN-resident CD69⁺ virus-specific CD8⁺ T cell subset (Buggert et al., 2018), with notable transcriptional and functional differences observed compared to blood HIV-1-specific CD8⁺ T cells. Central nervous system (CNS) studies exemplify the challenges of human studies as well as the potential to make optimal use of the rare cell populations isolated from precious clinical samples. CNS involvement remains a significant issue, as neurocognitive disorders occur in spite of highly effective ART and as the CNS can serve as immune sanctuary. A recent study used scRNA-Seq to define the immune cell landscape in the cerebrospinal fluid (CSF) of virologically suppressed individuals (Farhadian et al., 2018). They found a rare subset of myeloid cells whose gene signature overlapped with neurodegenerative disease-associated microglia. These findings suggest that an immunopathogenic subset of myeloid cells may perpetuate neuronal insults during HIV-1 infection, thus providing physiological evidence of myeloid dysfunction. Unsupervised analytical approaches have the benefits of identifying new subsets of rare dysregulated cells, better assessing immune cell dysfunction *in vivo* and identifying factors with direct contribution to residual immune impairment. Clearly, further investigations will be needed to establish the extent of myeloid dysfunction during HIV-1 infection.

Vaccine Development and Immunomonitoring

The best hope to control the HIV-1 pandemic probably resides in prophylactic vaccines. Although none of the attempted

vaccine trials led to a definitive breakthrough, correlates of protection could be identified in human studies (reviewed in Corey et al., 2015). Broadly neutralizing Abs (bNAbs) targeting Env epitopes from many HIV-1 strains exist in a small proportion of chronically infected individuals (reviewed in Klein et al., 2013; Kwong et al., 2013; Burton and Mascola, 2015). However, how to elicit bNAb-producing B cells by vaccination strategies remains unclear because the ontogeny of this atypical B cell response is not yet fully elucidated, and may be very challenging to elicit by a vaccination strategy. Indeed, bNAbs originate from rare clones diluted in the vastly heterogeneous B cell populations, which precludes the use of bulk analytic approaches. The B cell repertoire was studied by combining image-based on-chip cytometry and micro engraving (Ogunniyi et al., 2014; **Figure 4**). Thousands of independent cells loaded into microwells were labeled with antibodies, then subjected to RT-PCR and sequencing, thus yielding single-cell phenotypic information and sequencing data in the same system. RT-PCR on single-sorted B cells emerged as an essential tool to understand the features of bNAb generation (Scheid et al., 2009; Sundling et al., 2012, 2014; Wang et al., 2016). In contrast to bulk population PCR, this approach readily identified unique Env-specific B cell clones and provided the matched heavy and light V(D)J sequences for subsequent cloning, thus allowing the functional characterization of key monoclonal antibodies *in vitro* (Sundling et al., 2012, 2014). This approach is used to conduct preclinical assessment of vaccine candidates in non-human primates (NHPs) (Scheid et al., 2009; Sundling et al., 2012, 2014; Wang et al., 2016), and to explore the pathways toward bNAb development in humanized mouse models upon sequential immunization (Escolano et al., 2016). Furthermore, single-cell BCR sequencing of naïve B cells in HIV-uninfected human donors has been successfully used to estimate the frequencies of germline precursors that would have the potential to develop into a given bNAb lineage, provided that an optimal vaccination strategy could lead them along this path (Jardine et al., 2016). Deployment of such advanced single-cell technologies in Phase I clinical trials of new immunogens should help select the most promising vaccination strategies for further development.

Single-cell transcriptomics and epigenomics strategies, in some cases combined with TCR sequencing, have also been successfully applied to study the T cell response in human diseases (Buggert et al., 2018; Jerby-Aron et al., 2018). Although the conduct of such single CD4⁺ or CD8⁺ T cell studies currently appear to lag behind in the HIV field compared to B cell studies and to investigations of cellular immunity in other diseases, the conceptual and technical frameworks now appear to be mature for such cutting-edge investigations in advanced HIV-1 vaccine immunomonitoring.

Standard biostatistical approaches often failed to appreciate differences in the quality of the immune vaccine response because they rely on expected biological outcome and consequently fail to grasp the inherent complexity of the multi-component nature of immunity. Single-cell technologies have been used to provide high throughput multi-dimensional data, but the lack of computational tools has in many instances led to suboptimal exploitation of the wealth of data generated.

To overcome these limitations, analytical frameworks harnessing the full extent of single-cell technologies were tested on multidimensional datasets (Finak et al., 2014; Lin et al., 2015). For example, combinatorial polyfunctionality analysis of antigen-specific T cell subsets (COMPASS) models enable identification of cell subsets and select those most likely to have antigen-specific responses using a Bayesian hierarchical framework, thus allowing to correlate the quality of an individual response with clinical outcome. COMPASS identified CD4⁺ T cell polyfunctionality as a new correlate of vaccine efficacy in the RV144 HIV vaccine trial and delineated qualitative differences in CD4⁺ T cell responses between different HIV-1 vaccine regimens (Lin et al., 2015). These findings support the hypothesis that the general quality of response is more important to determine the outcome of vaccination, and perhaps infection, than magnitude on single-parameter responses (Lin et al., 2015). Such studies further support combining single-cell technologies with multivariate computational analyses to adequately interpret the complex immune network at play during infection or vaccination.

PERSPECTIVES

Single-cell analysis is not a novel concept. However, recently developed technologies are now bringing the resolution and

depth of single-cell investigations to the next level in every field of biology. Immunology and cancer are fields that pioneered the use of these new tools. HIV-1 research contributed to the development of many technologies in the past, for example single-cell microscopy applied to investigation of the viral replication cycle. Yet, compared to other areas of biomedical research, the field appears to currently lag behind in fully adopting newer high throughput single-cell technologies, this despite the fact that the very nature of HIV-1 biology would extensively benefit from these tools. The ball is now in the HIV-1 researchers' court.

AUTHOR CONTRIBUTIONS

GS and MD performed the literature review and wrote the manuscript. DK edited the manuscript and provided supervision. All authors read and approved the final version of the manuscript.

FUNDING

DK is supported by a FRQS Merit Award (# 268471), CIHR #377124, CIHR # 416148, CIHR # 426495, NIH UM1-AI-144462 (CHAVID), and NIH R01-AI-143411.

REFERENCES

- Arhel, N., Genovesio, A., Kim, K. A., Miko, S., Perret, E., Olivo-Marín, J. C., et al. (2006). Quantitative four-dimensional tracking of cytoplasmic and nuclear HIV-1 complexes. *Nat. Methods* 3, 817–824. doi: 10.1038/nmeth928
- Bagasra, O., Seshamma, T., and Pomerantz, R. J. (1993). Polymerase chain reaction in situ: intracellular amplification and detection of HIV-1 proviral DNA and other specific genes. *J. Immunol. Methods* 158, 131–145. doi: 10.1016/0022-1759(93)90265-9
- Banga, R., Procopio, F. A., Noto, A., Pollakis, G., Cavassini, M., Ohmiti, K., et al. (2016). PD-1(+) and follicular helper T cells are responsible for persistent HIV-1 transcription in treated aviremic individuals. *Nat. Med.* 22, 754–761. doi: 10.1038/nm.4113
- Barton, K., Hiener, B., Winckelmann, A., Rasmussen, T. A., Shao, W., Byth, K., et al. (2016). Broad activation of latent HIV-1 in vivo. *Nat. Commun.* 7:12731. doi: 10.1038/ncomms12731
- Baumgartel, V., Ivanchenko, S., Dupont, A., Sergeev, M., Wiseman, P. W., Krausslich, H. G., et al. (2011). Live-cell visualization of dynamics of HIV budding site interactions with an ESCRT component. *Nat. Cell Biol.* 13, 469–474. doi: 10.1038/ncb2215
- Baxter, A. E., Niessl, J., Fromentin, R., Richard, J., Porichis, F., Charlebois, R., et al. (2016). Single-Cell characterization of viral translation-competent reservoirs in HIV-infected individuals. *Cell Host Microbe* 20, 368–380. doi: 10.1016/j.chom.2016.07.015
- Baxter, A. E., Niessl, J., Fromentin, R., Richard, J., Porichis, F., Massanella, M., et al. (2017a). Multiparametric characterization of rare HIV-infected cells using an RNA-flow FISH technique. *Nat. Protoc.* 12, 2029–2049. doi: 10.1038/nprot.2017.079
- Baxter, A. E., Niessl, J., Morou, A., and Kaufmann, D. E. (2017b). RNA flow cytometric FISH for investigations into HIV immunology, vaccination and cure strategies. *AIDS Res. Ther.* 14:40. doi: 10.1186/s12981-017-0171-x
- Baxter, A. E., O'doherty, U., and Kaufmann, D. E. (2018). Beyond the replication-competent HIV reservoir: transcription and translation-competent reservoirs. *Retrovirology* 15:18. doi: 10.1186/s12977-018-0392-7
- Baxter, A. E., Russell, R. A., Duncan, C. J., Moore, M. D., Willberg, C. B., Pablos, J. L., et al. (2014). Macrophage infection via selective capture of HIV-1-infected CD4⁺ T cells. *Cell Host Microbe* 16, 711–721. doi: 10.1016/j.chom.2014.10.010
- Bekele, Y., Lakshmikanth, T., Chen, Y., Mikes, J., Nasi, A., Petkov, S., et al. (2019). Mass cytometry identifies distinct CD4⁺ T cell clusters distinguishing HIV-1-infected patients according to antiretroviral therapy initiation. *JCI Insight* 4:e125442. doi: 10.1172/jci.insight.125442
- Bengsch, B., Ohtani, T., Herati, R. S., Bovenschen, N., Chang, K. M., and Wherry, E. J. (2018a). Deep immune profiling by mass cytometry links human T and NK cell differentiation and cytotoxic molecule expression patterns. *J. Immunol. Methods* 453, 3–10. doi: 10.1016/j.jim.2017.03.009
- Bengsch, B., Ohtani, T., Khan, O., Setty, M., Manne, S., O'brien, S., et al. (2018b). Epigenomic-guided mass cytometry profiling reveals disease-specific features of exhausted CD8 T cells. *Immunity* 48, 1029.e5–1045.e5. doi: 10.1016/j.immuni.2018.04.026
- Bolton, D. L., Mcginnis, K., Finak, G., Chattopadhyay, P., Gottardo, R., and Roederer, M. (2017). Combined single-cell quantitation of host and SIV genes and proteins ex vivo reveals host-pathogen interactions in individual cells. *PLoS Pathog.* 13:e1006445. doi: 10.1371/journal.ppat.1006445
- Boritz, E. A., Darko, S., Swaszek, L., Wolf, G., Wells, D., Wu, X., et al. (2016). Multiple origins of virus persistence during natural control of HIV infection. *Cell* 166, 1004–1015. doi: 10.1016/j.cell.2016.06.039
- Boswell, K. L., Paris, R., Boritz, E., Ambrozak, D., Yamamoto, T., Darko, S., et al. (2014). Loss of circulating CD4 T cells with B cell helper function during chronic HIV infection. *PLoS Pathog.* 10:e1003853. doi: 10.1371/journal.ppat.1003853
- Bradley, T., Ferrari, G., Haynes, B. F., Margolis, D. M., and Browne, E. P. (2018). Single-cell analysis of quiescent HIV infection reveals host transcriptional profiles that regulate proviral latency. *Cell Rep.* 25, 107.e3–117.3e. doi: 10.1016/j.celrep.2018.09.020
- Buggert, M., Nguyen, S., Salgado-Montes De Oca, G., Bengsch, B., Darko, S., Ransier, A., et al. (2018). Identification and characterization of HIV-specific resident memory CD8(+) T cells in human lymphoid tissue. *Sci. Immunol.* 3:eaar4526. doi: 10.1126/sciimmunol.aar4526

- Burdick, R. C., Delviks-Frankenberry, K. A., Chen, J., Janaka, S. K., Sastri, J., Hu, W. S., et al. (2017). Dynamics and regulation of nuclear import and nuclear movements of HIV-1 complexes. *PLoS Pathog* 13:e1006570. doi: 10.1371/journal.ppat.1006570
- Burton, D. R., and Mascola, J. R. (2015). Antibody responses to envelope glycoproteins in HIV-1 infection. *Nat. Immunol.* 16, 571–576. doi: 10.1038/ni.3158
- Buzon, M. J., Sun, H., Li, C., Shaw, A., Seiss, K., Ouyang, Z., et al. (2014). HIV-1 persistence in CD4+ T cells with stem cell-like properties. *Nat. Med.* 20, 139–142. doi: 10.1038/nm.3445
- Cavrois, M., Banerjee, T., Mukherjee, G., Raman, N., Hussien, R., Rodriguez, B. A., et al. (2017). Mass Cytometric analysis of HIV entry, replication, and remodeling in tissue CD4+ T Cells. *Cell Rep.* 20, 984–998. doi: 10.1016/j.celrep.2017.06.087
- Chen, H. C., Martinez, J. P., Zorita, E., Meyerhans, A., and Filion, G. J. (2017). Position effects influence HIV latency reversal. *Nat. Struct. Mol. Biol.* 24, 47–54. doi: 10.1038/nsmb.3328
- Chen, H. C., Zorita, E., and Filion, G. J. (2018). Using barcoded HIV ensembles (B-HIVE) for single provirus transcriptomics. *Curr. Protoc. Mol. Biol.* 122:e56. doi: 10.1002/cpmb.56
- Chin, C. R., Perreira, J. M., Savidis, G., Portmann, J. M., Aker, A. M., Feeley, E. M., et al. (2015). Direct visualization of HIV-1 replication intermediates shows that capsid and F6 modulate HIV-1 intra-nuclear invasion and integration. *Cell Rep.* 13, 1717–1731. doi: 10.1016/j.celrep.2015.10.036
- Chomont, N., El-Far, M., Ancuta, P., Trautmann, L., Procopio, F. A., Yassine-Diab, B., et al. (2009). HIV reservoir size and persistence are driven by T cell survival and homeostatic proliferation. *Nat. Med.* 15, 893–900. doi: 10.1038/nm.1972
- Cohn, L. B., Da Silva, I. T., Valieris, R., Huang, A. S., Lorenzi, J. C. C., Cohen, Y. Z., et al. (2018). Clonal CD4(+) T cells in the HIV-1 latent reservoir display a distinct gene profile upon reactivation. *Nat. Med.* 24, 604–609. doi: 10.1038/s41591-018-0017-7
- Cohn, L. B., Silva, I. T., Oliveira, T. Y., Rosales, R. A., Parrish, E. H., Learn, G. H., et al. (2015). HIV-1 integration landscape during latent and active infection. *Cell* 160, 420–432. doi: 10.1016/j.cell.2015.01.020
- Corey, L., Gilbert, P. B., Tomaras, G. D., Haynes, B. F., Pantaleo, G., and Fauci, A. S. (2015). Immune correlates of vaccine protection against HIV-1 acquisition. *Sci. Transl. Med.* 7:310rv317.
- Crum-Cianflone, N. F., Iverson, E., Defang, G., Blair, P. J., Eberly, L. E., Maguire, J., et al. (2011). Durability of antibody responses after receipt of the monovalent 2009 pandemic influenza A (H1N1) vaccine among HIV-infected and HIV-uninfected adults. *Vaccine* 29, 3183–3191. doi: 10.1016/j.vaccine.2011.02.040
- Cubas, R., Van Grevenynghe, J., Wills, S., Kardava, L., Santich, B. H., Buckner, C. M., et al. (2015). Reversible reprogramming of circulating memory T follicular helper cell function during chronic HIV infection. *J. Immunol.* 195, 5625–5636. doi: 10.4049/jimmunol.1501524
- Cubas, R. A., Mudd, J. C., Savoye, A. L., Perreau, M., Van Grevenynghe, J., Metcalf, T., et al. (2013). Inadequate T follicular cell help impairs B cell immunity during HIV infection. *Nat. Med.* 19, 494–499. doi: 10.1038/nm.3109
- de Armas, L. R., Pallikkuth, S., Pan, L., Rinaldi, S., Cotugno, N., Andrews, S., et al. (2019). Single cell profiling reveals PTEN overexpression in influenza-specific B cells in aging HIV-infected individuals on anti-retroviral therapy. *Sci. Rep.* 9:2482. doi: 10.1038/s41598-019-38906-y
- Deleage, C., Chan, C. N., Busman-Sahay, K., and Estes, J. D. (2018). Next-generation in situ hybridization approaches to define and quantify HIV and SIV reservoirs in tissue microenvironments. *Retrovirology* 15:4. doi: 10.1186/s12977-017-0387-9
- Deleage, C., Wietgreffe, S. W., Del Prete, G., Morcock, D. R., Hao, X. P., Piatak, M., et al. (2016). Defining HIV and SIV reservoirs in lymphoid tissues. *Pathog. Immun.* 1, 68–106.
- DeMaster, L. K., Liu, X., Vanbelzen, D. J., Trinite, B., Zheng, L., Agosto, L. M., et al. (2015). A Subset of CD4/CD8 double-negative T cells expresses HIV proteins in patients on antiretroviral therapy. *J. Virol.* 90, 2165–2179. doi: 10.1128/JVI.01913-15
- Di Primio, C., Quercioli, V., Allouch, A., Gijbbers, R., Christ, F., Debyser, Z., et al. (2013). Single-cell imaging of HIV-1 provirus (SCIP). *Proc. Natl. Acad. Sci. U.S.A.* 110, 5636–5641. doi: 10.1073/pnas.1216254110
- Duckworth, A. D., Gherardini, P. F., Sykorova, M., Yasin, F., Nolan, G. P., Slupsky, J. R., et al. (2019). Multiplexed profiling of RNA and protein expression signatures in individual cells using flow or mass cytometry. *Nat. Protoc.* 14, 901–920. doi: 10.1038/s41596-018-0120-8
- Engelman, A., and Cherepanov, P. (2012). The structural biology of HIV-1: mechanistic and therapeutic insights. *Nat. Rev. Microbiol.* 10, 279–290. doi: 10.1038/nrmicro2747
- Escolano, A., Steichen, J. M., Dosenovic, P., Kulp, D. W., Golijanin, J., Sok, D., et al. (2016). Sequential immunization elicits broadly neutralizing Anti-HIV-1 antibodies in Ig knockin mice. *Cell* 166:e1412. doi: 10.1016/j.cell.2016.07.030
- Estes, J. D., Kityo, C., Ssali, F., Swainson, L., Makamdop, K. N., Del Prete, G. Q., et al. (2017). Defining total-body AIDS-virus burden with implications for curative strategies. *Nat. Med.* 23, 1271–1276. doi: 10.1038/nm.4411
- Estes, J. D., Legrand, R., and Petrovas, C. (2018). Visualizing the immune system: providing key insights into HIV/SIV infections. *Front. Immunol.* 9:423. doi: 10.3389/fimmu.2018.00423
- Farhadian, S. F., Mehta, S. S., Zografou, C., Robertson, K., Price, R. W., Pappalardo, J., et al. (2018). Single-cell RNA sequencing reveals microglia-like cells in cerebrospinal fluid during virologically suppressed HIV. *JCI Insight* 3:121718. doi: 10.1172/jci.insight.121718
- Finak, G., Mcdavid, A., Chattopadhyay, P., Dominguez, M., De Rosa, S., Roederer, M., et al. (2014). Mixture models for single-cell assays with applications to vaccine studies. *Biostatistics* 15, 87–101. doi: 10.1093/biostatistics/kxt024
- Francis, A. C., Marin, M., Shi, J., Aiken, C., and Melikyan, G. B. (2016). Time-Resolved Imaging of Single HIV-1 Uncoating In Vitro and in Living Cells. *PLoS Pathog* 12:e1005709. doi: 10.1371/journal.ppat.1005709
- Francis, A. C., and Melikyan, G. B. (2018a). Live-cell imaging of early steps of single HIV-1 infection. *Viruses* 10:275. doi: 10.3390/v10050275
- Francis, A. C., and Melikyan, G. B. (2018b). Single HIV-1 imaging reveals progression of infection through CA-dependent steps of docking at the nuclear pore, uncoating, and nuclear transport. *Cell Host Microbe* 23, 536.e6–548.e6. doi: 10.1016/j.chom.2018.03.009
- Frei, A. P., Bava, F. A., Zunder, E. R., Hsieh, E. W., Chen, S. Y., Nolan, G. P., et al. (2016). Highly multiplexed simultaneous detection of RNAs and proteins in single cells. *Nat. Methods* 13, 269–275. doi: 10.1038/nmeth.3742
- Golumbeanu, M., Cristinelli, S., Rato, S., Munoz, M., Cavassini, M., Beerenwinkel, N., et al. (2018). Single-cell RNA-Seq reveals transcriptional heterogeneity in latent and reactivated HIV-infected cells. *Cell Rep.* 23, 942–950. doi: 10.1016/j.celrep.2018.03.102
- Gosselin, A., Monteiro, P., Chomont, N., Diaz-Griffero, F., Said, E. A., Fonseca, S., et al. (2010). Peripheral blood CCR4+CCR6+ and CXCR3+CCR6+CD4+ T cells are highly permissive to HIV-1 infection. *J. Immunol.* 184, 1604–1616. doi: 10.4049/jimmunol.0903058
- Gosselin, A., Wiche Salinas, T. R., Planas, D., Wacleche, V. S., Zhang, Y., Fromentin, R., et al. (2017). HIV persists in CCR6+CD4+ T cells from colon and blood during antiretroviral therapy. *AIDS* 31, 35–48. doi: 10.1097/qad.0000000000001309
- Grau-Exposito, J., Serra-Peinado, C., Miguel, L., Navarro, J., Curran, A., Burgos, J., et al. (2017). A novel single-cell FISH-Flow assay identifies effector memory CD4(+) T cells as a major niche for HIV-1 transcription in HIV-Infected patients. *MBio* 8:e00876-17. doi: 10.1128/mBio.00876-17
- Grau-Exposito, J., Luque-Ballesteros, L., Navarro, J., Curran, A., Burgos, J., Ribera, E., et al. (2019). Latency reversal agents affect differently the latent reservoir present in distinct CD4+ T subpopulations. *PLoS Pathog* 15:e1007991. doi: 10.1371/journal.ppat.1007991
- Hansen, M. M. K., Wen, W. Y., Ingerman, E., Razoooky, B. S., Thompson, C. E., Dar, R. D., et al. (2018). A Post-transcriptional feedback mechanism for noise suppression and fate stabilization. *Cell* 173, 1609.e15–1621.e15. doi: 10.1016/j.cell.2018.04.005
- Havenar-Daughton, C., Reiss, S. M., Carnathan, D. G., Wu, J. E., Kendric, K., Torrents De La Pena, A., et al. (2016). Cytokine-independent detection of antigen-specific germinal center T follicular helper cells in immunized nonhuman primates using a live cell activation-induced marker technique. *J. Immunol.* 197, 994–1002. doi: 10.4049/jimmunol.1600320
- Heesters, B. A., Lindqvist, M., Vagefi, P. A., Scully, E. P., Schildberg, F. A., Altfeld, M., et al. (2015). Follicular dendritic cells retain infectious HIV in cycling endosomes. *PLoS Pathog* 11:e1005285. doi: 10.1371/journal.ppat.1005285
- Ho, Y. C., Shan, L., Hosmane, N. N., Wang, J., Laskey, S. B., Rosenbloom, D. I., et al. (2013). Replication-competent noninduced proviruses in the latent reservoir

- increase barrier to HIV-1 cure. *Cell* 155, 540–551. doi: 10.1016/j.cell.2013.09.020
- Holmes, M., Zhang, F., and Bieniasz, P. D. (2015). Single-cell and single-cycle analysis of HIV-1 replication. *PLoS Pathog.* 11:e1004961. doi: 10.1371/journal.ppat.1004961
- Hulme, A. E., Perez, O., and Hope, T. J. (2011). Complementary assays reveal a relationship between HIV-1 uncoating and reverse transcription. *Proc. Natl. Acad. Sci. U.S.A.* 108, 9975–9980. doi: 10.1073/pnas.1014522108
- Ivanchenko, S., Godinez, W. J., Lampe, M., Krausslich, H. G., Eils, R., Rohr, K., et al. (2009). Dynamics of HIV-1 assembly and release. *PLoS Pathog.* 5:e1000652. doi: 10.1371/journal.ppat.1000652
- Jaafoura, S., De Goer De Herve, M. G., Hernandez-Vargas, E. A., Hendel-Chavez, H., Abdoh, M., Mateo, M. C., et al. (2014). Progressive contraction of the latent HIV reservoir around a core of less-differentiated CD4(+) memory T Cells. *Nat. Commun.* 5:5407. doi: 10.1038/ncomms6407
- Jardine, J. G., Sok, D., Julien, J. P., Briney, B., Sarkar, A., Liang, C. H., et al. (2016). Minimally mutated HIV-1 broadly neutralizing antibodies to guide reductionist vaccine design. *PLoS Pathog.* 12:e1005815. doi: 10.1371/journal.ppat.1005815
- Jerby-Arnon, L., Shah, P., Cuoco, M. S., Rodman, C., Su, M. J., Melms, J. C., et al. (2018). A cancer cell program promotes T cell exclusion and resistance to checkpoint blockade. *Cell* 175, 984.e24–997.e24. doi: 10.1016/j.cell.2018.09.006
- Jordan, A., Defechereux, P., and Verdin, E. (2001). The site of HIV-1 integration in the human genome determines basal transcriptional activity and response to Tat transactivation. *EMBO J.* 20, 1726–1738. doi: 10.1093/emboj/20.7.1726
- Josefsson, L., King, M. S., Makitalo, B., Brannstrom, J., Shao, W., Maldarelli, F., et al. (2011). Majority of CD4+ T cells from peripheral blood of HIV-1-infected individuals contain only one HIV DNA molecule. *Proc. Natl. Acad. Sci. U.S.A.* 108, 11199–11204. doi: 10.1073/pnas.1107729108
- Josefsson, L., Palmer, S., Faria, N. R., Lemey, P., Casazza, J., Ambrozak, D., et al. (2013). Single cell analysis of lymph node tissue from HIV-1 infected patients reveals that the majority of CD4+ T-cells contain one HIV-1 DNA molecule. *PLoS Pathog.* 9:e1003432. doi: 10.1371/journal.ppat.1003432
- Jouvenet, N., Bieniasz, P. D., and Simon, S. M. (2008). Imaging the biogenesis of individual HIV-1 virions in live cells. *Nature* 454, 236–240. doi: 10.1038/nature06998
- Kearney, M. F., Wiegand, A., Shao, W., Coffin, J. M., Mellors, J. W., Lederman, M., et al. (2016). Origin of rebound plasma HIV includes cells with identical proviruses that are transcriptionally active before stopping of antiretroviral therapy. *J. Virol.* 90, 1369–1376. doi: 10.1128/JVI.02139-15
- Kim, Y., Anderson, J. L., and Lewin, S. R. (2018). Getting the “Kill” into “Shock and Kill”: strategies to eliminate latent HIV. *Cell Host Microbe* 23, 14–26. doi: 10.1016/j.chom.2017.12.004
- Klein, F., Diskin, R., Scheid, J. F., Gaebler, C., Mouquet, H., Georgiev, I. S., et al. (2013). Somatic mutations of the immunoglobulin framework are generally required for broad and potent HIV-1 neutralization. *Cell* 153, 126–138. doi: 10.1016/j.cell.2013.03.018
- Klein, I. A., Resch, W., Jankovic, M., Oliveira, T., Yamane, A., Nakahashi, H., et al. (2011). Translocation-capture sequencing reveals the extent and nature of chromosomal rearrangements in B lymphocytes. *Cell* 147, 95–106. doi: 10.1016/j.cell.2011.07.048
- Kok, Y. L., Ciuffi, A., and Metzner, K. J. (2017). Unravelling HIV-1 Latency. One cell at a time. *Trends Microbiol.* 25, 932–941. doi: 10.1016/j.tim.2017.06.002
- Kwong, P. D., Mascola, J. R., and Nabel, G. J. (2013). Broadly neutralizing antibodies and the search for an HIV-1 vaccine: the end of the beginning. *Nat. Rev. Immunol.* 13, 693–701. doi: 10.1038/nri3516
- Lin, L., Finak, G., Ushey, K., Seshadri, C., Hawn, T. R., Frahm, N., et al. (2015). COMPASS identifies T-cell subsets correlated with clinical outcomes. *Nat. Biotechnol.* 33, 610–616. doi: 10.1038/nbt3187
- Ma, Y., Wang, M., Li, W., Zhang, Z., Zhang, X., Wu, G., et al. (2017). Live visualization of HIV-1 proviral DNA using a dual-color-labeled CRISPR system. *Anal. Chem.* 89, 12896–12901. doi: 10.1021/acs.analchem.7b03584
- Mamede, J. I., Cianci, G. C., Anderson, M. R., and Hope, T. J. (2017). Early cytoplasmic uncoating is associated with infectivity of HIV-1. *Proc. Natl. Acad. Sci. U.S.A.* 114, E7169–E7178. doi: 10.1073/pnas.1706245114
- Marini, B., Kertesz-Farkas, A., Ali, H., Lucic, B., Lisek, K., Manganaro, L., et al. (2015). Nuclear architecture dictates HIV-1 integration site selection. *Nature* 521, 227–231. doi: 10.1038/nature14226
- Martus, G., Niehrs, A., Cornelis, R., Rechtiën, A., Garcia-Beltran, W., Lutgehetmann, M., et al. (2016). Kinetics of HIV-1 latency reversal quantified on the single-cell level using a novel flow-based technique. *J. Virol.* 90, 9018–9028. doi: 10.1128/JVI.01448-16
- McGary, C. S., Deleage, C., Harper, J., Micci, L., Ribeiro, S. P., Paganini, S., et al. (2017). CTLA-4(+)PD-1(-) memory CD4(+) T cells critically contribute to viral persistence in antiretroviral therapy-suppressed, SIV-infected rhesus macaques. *Immunity* 47, 776.e5–788.e5. doi: 10.1016/j.immuni.2017.09.018
- McLane, L. M., Abdel-Hakeem, M. S., and Wherry, E. J. (2019). CD8 T cell exhaustion during chronic viral infection and cancer. *Annu. Rev. Immunol.* 37, 457–495. doi: 10.1146/annurev-immunol-041015-055318
- Miyauchi, K., Kim, Y., Latinovic, O., Morozov, V., and Melikyan, G. B. (2009). HIV enters cells via endocytosis and dynamin-dependent fusion with endosomes. *Cell* 137, 433–444. doi: 10.1016/j.cell.2009.02.046
- Moreno-Fernandez, M. E., Zapata, W., Blackard, J. T., Franchini, G., and Chougnet, C. A. (2009). Human regulatory T cells are targets for human immunodeficiency Virus (HIV) infection, and their susceptibility differs depending on the HIV type 1 strain. *J. Virol.* 83, 12925–12933. doi: 10.1128/JVI.01352-09
- Morou, A., Brunet-Ratnasingham, E., Dube, M., Charlebois, R., Mercier, E., Darko, S., et al. (2019). Altered differentiation is central to HIV-specific CD4(+) T cell dysfunction in progressive disease. *Nat. Immunol.* 20, 1059–1070. doi: 10.1038/s41590-019-0418-x
- Munch, J., Stolte, N., Fuchs, D., Stahl-Hennig, C., and Kirchhoff, F. (2001). Efficient class I major histocompatibility complex down-regulation by simian immunodeficiency virus Nef is associated with a strong selective advantage in infected rhesus macaques. *J. Virol.* 75, 10532–10536. doi: 10.1128/jvi.75.21.10532-10536.2001
- Newell, E. W., Sigal, N., Nair, N., Kidd, B. A., Greenberg, H. B., and Davis, M. M. (2013). Combinatorial tetramer staining and mass cytometry analysis facilitate T-cell epitope mapping and characterization. *Nat. Biotechnol.* 31, 623–629. doi: 10.1038/nbt.2593
- Ogunniyi, A. O., Thomas, B. A., Politano, T. J., Varadarajan, N., Landais, E., Poignard, P., et al. (2014). Profiling human antibody responses by integrated single-cell analysis. *Vaccine* 32, 2866–2873. doi: 10.1016/j.vaccine.2014.02.020
- Oswald-Richter, K., Grill, S. M., Shariat, N., Leelawong, M., Sundrud, M. S., Haas, D. W., et al. (2004). HIV infection of naturally occurring and genetically programmed human regulatory T-cells. *PLoS Biol.* 2:E198. doi: 10.1371/journal.pbio.0020198
- Pardons, M., Baxter, A. E., Massanella, M., Pagliuzza, A., Fromentin, R., Dufour, C., et al. (2019). Single-cell characterization and quantification of translation-competent viral reservoirs in treated and untreated HIV infection. *PLoS Pathog.* 15:e1007619. doi: 10.1371/journal.ppat.1007619
- Peng, K., Muranyi, W., Glass, B., Laketa, V., Yant, S. R., Tsai, L., et al. (2014). Quantitative microscopy of functional HIV post-entry complexes reveals association of replication with the viral capsid. *elife* 3:e04114. doi: 10.7554/eLife.04114
- Perreau, M., Savoye, A. L., De Crignis, E., Corpataux, J. M., Cubas, R., Haddad, E. K., et al. (2013). Follicular helper T cells serve as the major CD4 T cell compartment for HIV-1 infection, replication, and production. *J. Exp. Med.* 210, 143–156. doi: 10.1084/jem.20121932
- Prescher, J., Baumgartel, V., Ivanchenko, S., Torrano, A. A., Brauchle, C., Muller, B., et al. (2015). Super-resolution imaging of ESCRT-proteins at HIV-1 assembly sites. *PLoS Pathog.* 11:e1004677. doi: 10.1371/journal.ppat.1004677
- Puray-Chavez, M., Tedbury, P. R., Huber, A. D., Ukah, O. B., Yap, V., Liu, D., et al. (2017). Multiplex single-cell visualization of nucleic acids and protein during HIV infection. *Nat. Commun.* 8:1882. doi: 10.1038/s41467-017-01693-z
- Rato, S., Rausell, A., Munoz, M., Telenti, A., and Ciuffi, A. (2017). Single-cell analysis identifies cellular markers of the HIV permissive cell. *PLoS Pathog.* 13:e1006678. doi: 10.1371/journal.ppat.1006678
- Reiss, S., Baxter, A. E., Cirelli, K. M., Dan, J. M., Morou, A., Daigneault, A., et al. (2017). Comparative analysis of activation induced marker (AIM) assays for sensitive identification of antigen-specific CD4 T cells. *PLoS One* 12:e0186998. doi: 10.1371/journal.pone.0186998
- Scheid, J. F., Mouquet, H., Feldhahn, N., Seaman, M. S., Velinzon, K., Pietzsch, J., et al. (2009). Broad diversity of neutralizing antibodies isolated from memory B cells in HIV-infected individuals. *Nature* 458, 636–640. doi: 10.1038/nature07930

- Schroder, A. R., Shinn, P., Chen, H., Berry, C., Ecker, J. R., and Bushman, F. (2002). HIV-1 integration in the human genome favors active genes and local hotspots. *Cell* 110, 521–529. doi: 10.1016/s0092-8674(02)00864-4
- Shan, L., Deng, K., Gao, H., Xing, S., Capoferri, A. A., Durand, C. M., et al. (2017). Transcriptional reprogramming during effector-to-memory transition renders CD4(+) T cells permissive for latent HIV-1 infection. *Immunity* 47, 766.e3–775.e3. doi: 10.1016/j.immuni.2017.09.014
- Sherrill-Mix, S., Lewinski, M. K., Famiglietti, M., Bosque, A., Malani, N., Ocwieja, K. E., et al. (2013). HIV latency and integration site placement in five cell-based models. *Retrovirology* 10:90. doi: 10.1186/1742-4690-10-90
- Soontornniyomkij, V., Wang, G., Pittman, C. A., Hamilton, R. L., Wiley, C. A., and Achim, C. L. (1999). Absence of brain-derived neurotrophic factor and trkB receptor immunoreactivity in glia of Alzheimer's disease. *Acta Neuropathol.* 98, 345–348. doi: 10.1007/s004010051092
- Spina, C. A., Anderson, J., Archin, N. M., Bosque, A., Chan, J., Famiglietti, M., et al. (2013). An in-depth comparison of latent HIV-1 reactivation in multiple cell model systems and resting CD4+ T cells from aviremic patients. *PLoS Pathog.* 9:e1003834. doi: 10.1371/journal.ppat.1003834
- Sundling, C., Li, Y., Huynh, N., Poulsen, C., Wilson, R., O'dell, S., et al. (2012). High-resolution definition of vaccine-elicited B cell responses against the HIV primary receptor binding site. *Sci. Transl. Med.* 4:142ra196. doi: 10.1126/scitranslmed.3003752
- Sundling, C., Zhang, Z., Phad, G. E., Sheng, Z., Wang, Y., Mascola, J. R., et al. (2014). Single-cell and deep sequencing of IgG-switched macaque B cells reveal a diverse Ig repertoire following immunization. *J. Immunol.* 192, 3637–3644. doi: 10.4049/jimmunol.1303334
- Swigut, T., Alexander, L., Morgan, J., Lifson, J., Mansfield, K. G., Lang, S., et al. (2004). Impact of Nef-mediated downregulation of major histocompatibility complex class I on immune response to simian immunodeficiency virus. *J. Virol.* 78, 13335–13344. doi: 10.1128/jvi.78.23.13335-13344.2004
- Tebas, P., Frank, I., Lewis, M., Quinn, J., Zifchak, L., Thomas, A., et al. (2010). Poor immunogenicity of the H1N1 2009 vaccine in well controlled HIV-infected individuals. *AIDS* 24, 2187–2192. doi: 10.1097/QAD.0b013e32833c6d5c
- Tokarev, A., Cregan, M., Eller, M. A., Roederer, M., and Bolton, D. L. (2018). Single-cell quantitation of mRNA and surface protein expression in simian immunodeficiency virus-infected CD4+ T cells isolated from rhesus macaques. *J. Vis. Exp.* 2018:57776. doi: 10.3791/57776
- Tran, T. A., De Goer De Herve, M. G., Hendel-Chavez, H., Dembele, B., Le Nevot, E., Abbed, K., et al. (2008). Resting regulatory CD4 T cells: a site of HIV persistence in patients on long-term effective antiretroviral therapy. *PLoS One* 3:e3305. doi: 10.1371/journal.pone.0003305
- Vasquez, J. J., Hussien, R., Aguilar-Rodriguez, B., Junger, H., Dobi, D., Henrich, T. J., et al. (2018). Elucidating the burden of HIV in tissues using multiplexed immunofluorescence and in situ hybridization: methods for the single-cell phenotypic characterization of cells harboring HIV in situ. *J. Histochem. Cytochem.* 66, 427–446. doi: 10.1369/0022155418756848
- Wang, F., Flanagan, J., Su, N., Wang, L. C., Bui, S., Nielson, A., et al. (2012). RNAscope: a novel in situ RNA analysis platform for formalin-fixed, paraffin-embedded tissues. *J. Mol. Diagn.* 14, 22–29. doi: 10.1016/j.jmoldx.2011.08.002
- Wang, Y., Sundling, C., Wilson, R., O'dell, S., Chen, Y., Dai, K., et al. (2016). High-resolution longitudinal study of HIV-1 Env vaccine-elicited B cell responses to the virus primary receptor binding site reveals affinity maturation and clonal persistence. *J. Immunol.* 196, 3729–3743. doi: 10.4049/jimmunol.1502543
- Wendel, B. S., Del Alcazar, D., He, C., Del Rio-Estrada, P. M., Aiamkitsumrit, B., Ablanedo-Terrazas, Y., et al. (2018). The receptor repertoire and functional profile of follicular T cells in HIV-infected lymph nodes. *Sci. Immunol.* 3:eaa8884. doi: 10.1126/sciimmunol.aan8884
- Whitney, J. B., and Brad Jones, R. (2018). In vitro and in vivo models of HIV latency. *Adv. Exp. Med. Biol.* 1075, 241–263. doi: 10.1007/978-981-13-0484-2_10
- Wiegand, A., Spindler, J., Hong, F. F., Shao, W., Cyktor, J. C., Cillo, A. R., et al. (2017). Single-cell analysis of HIV-1 transcriptional activity reveals expression of proviruses in expanded clones during ART. *Proc. Natl. Acad. Sci. U.S.A.* 114, E3659–E3668. doi: 10.1073/pnas.1617961114
- Yucha, R. W., Hobbs, K. S., Hanhauser, E., Hogan, L. E., Nieves, W., Ozen, M. O., et al. (2017). High-throughput characterization of HIV-1 reservoir reactivation using a single-cell-in-droplet PCR assay. *EBio Med.* 20, 217–229. doi: 10.1016/j.ebiom.2017.05.006
- Yukl, S. A., Kaiser, P., Kim, P., Telwate, S., Joshi, S. K., Vu, M., et al. (2018). HIV latency in isolated patient CD4(+) T cells may be due to blocks in HIV transcriptional elongation, completion, and splicing. *Sci. Transl. Med.* 10:eaa9927. doi: 10.1126/scitranslmed.aap9927
- Zaunders, J. J., Munier, M. L., Seddiki, N., Pett, S., Ip, S., Bailey, M., et al. (2009). High levels of human antigen-specific CD4+ T cells in peripheral blood revealed by stimulated coexpression of CD25 and CD134 (OX40). *J. Immunol.* 183, 2827–2836. doi: 10.4049/jimmunol.0803548
- Zhang, W., Svensson Akusjarvi, S., Sonnerborg, A., and Neogi, U. (2018). Characterization of inducible transcription and translation-competent HIV-1 Using the RNAscope ISH technology at a single-cell resolution. *Front. Microbiol.* 9:2358. doi: 10.3389/fmicb.2018.02358

Conflict of Interest: The authors declare that the research was conducted in the absence of any commercial or financial relationships that could be construed as a potential conflict of interest.

Copyright © 2020 Sannier, Dubé and Kaufmann. This is an open-access article distributed under the terms of the Creative Commons Attribution License (CC BY). The use, distribution or reproduction in other forums is permitted, provided the original author(s) and the copyright owner(s) are credited and that the original publication in this journal is cited, in accordance with accepted academic practice. No use, distribution or reproduction is permitted which does not comply with these terms.

Curriculum Vitae

Education

January 2018 – November 2023

Ph.D. in Virology and Immunology

Faculté de Médecine

Université de Montréal

September 2015 – July 2017

M.Sc. with honors in Immunology

Faculté des Sciences

Université Paris-Saclay

September 2012 – July 2015

B.Sc. in Biology-Health

Faculté des Sciences

Université Paris-Sud 11

Distinctions, honors, and awards

2022 – 2023

FRQS Doctoral Scholarship

Fonds de Recherche en santé
du Québec

2020 – 2022

Bourse de doctorat

Département de Microbiologie,
Infectiologie et Immunologie,
Université de Montréal

2021

Young investigator award

Conference on Retroviruses and
Opportunistic Infection (CROI)

Publications

First author publications:

G. Sannier, G.G Delgado, R. Cloutier, M. Benlarbi, A. Pagliuzza, M. Duchesne, C. Bourassa, G. Gendron-Lepage, N. Brassard, J-P. Routy, N. Chomont, A. Finzi, M. Dubé[#], D.E. Kaufmann[#];

Single-Cell Relationships Between HIV-1-Specific Immune Responses in Untreated Individuals and Viral Transcription and Translation

In preparation.

G. Sannier*, A. Nicolas*, M. Dubé, L. Marchitto, M. Nayrac, O. Tastet, D. Chatterjee, A. Tauzin, R. Lima-Barbosa, M. Laporte, R. Cloutier, A.M. Sreng Flores, M. Boutin, S.Y. Gong, M. Benlarbi, S. Ding, C. Bourassa, G. Gendron-Lepage, H. Medjahed, G. Goyette, N. Brassard, G.G Delgado, J. Niessl, L. Gokool, C. Morrissette, P. Arlotto, N. Rios, C. Tremblay, V. Martel-Laferrrière, A. Prat, J. Bélair, W. Beaubien-Souligny, R. Goupil, A.C. Nadeau-Fredette, C. Lamarche, A. Finzi[#], R.S. Suri[#], D.E. Kaufmann[#];

A third SARS-CoV-2 mRNA vaccine dose in people receiving hemodialysis overcomes B cell defects but elicits a skewed CD4+ T cell profile

Cell Reports Medicine. 2023 Mar 21;4(3):100955. doi: 10.1016/j.xcrm.2023.100955.

A. Nicolas*, **G. Sannier***, M. Dubé, M. Nayrac, A. Tauzin, M.M. Painter, R.R. Goel, M. Laporte, G. Gendron-Lepage, H. Medjahed, J.C. Williams, N. Brassard, J. Niessl, L. Gokool, C. Morrissette, P. Arlotto, C. Tremblay, V. Martel-Laferrrière, A. Finzi, A.R. Greenplate, E.J. Wherry, D.E. Kaufmann;

An extended SARS-CoV-2 mRNA vaccine prime-boost interval enhances B cell immunity with limited impact on T cells

iScience. 2023 Jan 20;26(1):105904. doi: 10.1016/j.isci.2022.105904.

G. Sannier*, M. Dubé*, C. Dufour, C. Richard, N. Brassard, G.G. Delgado, A. Pagliuzza, A.E. Baxter, J. Niessl, E. Brunet-Ratnasingham, R. Charlebois, B. Routy, J-P. Routy, R. Fromentin, N. Chomont, D.E. Kaufmann;

Combined Single-Cell Transcriptional, Translational, and Genomic Profiling Reveals HIV-1 Reservoir Diversity

Cell Reports. 2021 Aug 31;36(9):109643. doi: 10.1016/j.celrep.2021.109643.

G. Sannier*, M. Dubé*, D.E. Kaufmann;

Single-Cell Technologies Applied to HIV-1 Research: Reaching Maturity

Frontiers in Microbiology. 2020 Mar 4;11:297. doi: 10.3389/fmicb.2020.00297.

A. Charbonnier*, **G. Sannier***, S. Dupré*;

Mission phagocytosis: how to fit the weapons to the target size

Medecine/Sciences. 2016 Jun-Jul;31(6-7):587-9. doi: 10.1051/medsci/20163206021.

Co-author publications:

M. Dubé, O. Tastet, C. Dufour, **G. Sannier**, N. Brassard, G.G Delgado, A. Pagliuzza, C. Richard, M. Nayrac, J-P. Routy, A. Prat, J.E. Estes, R. Fromentin, N. Chomont, D.E. Kaufmann;

Spontaneous HIV expression during suppressive ART is associated with the magnitude and function of HIV-specific CD4+ and CD8+ T cells

Cell Host & Microbe. 2023 Sep 13;31(9):1507-1522.e5. doi: 10.1016/j.chom.2023.08.006.

S.W. Wietgreffe, L. Duan, J. Anderson, G. Marqués, M. Sanders, N.W. Cummins, A.D. Badley, C. Dobrowolski, J. Karn, A. Pagliuzza, N. Chomont, **G. Sannier**, M. Dubé, D.E. Kaufmann, P. Zuck, G. Wu, B.J. Howell, C. Reilly, A. Herschhorn, T.W. Schacker, A.T. Haase;

Detecting Sources of Immune Activation and Viral Rebound in HIV Infection

Journal of Virology. 2022 Aug 10;96(15):e0088522. doi: 10.1128/jvi.00885-22.

M. Nayrac*, M. Dubé*, **G. Sannier**[#], A. Nicolas[#], L. Marchitto, O. Tastet, A. Tauzin, N. Brassard, R. Lima-Barbosa, G. Beaudoin-Bussièrès, D. Vézina, S.Y. Gong, M. Benlarbi, R. Gasser, A. Laumaea, J. Prévost, C. Bourassa, G. Gendron-Lepage, H. Medjahed, G. Goyette, G.G Delgado, M. Laporte, J. Niessl, L. Gokool, C. Morrissette, P. Arlotto, J. Richard, J. Bélair, A. Prat, C. Tremblay, V. Martel-Laferrière, A. Finzi**, D.E. Kaufmann**;

Temporal associations of B and T cell immunity with robust vaccine responsiveness in a 16-week interval BNT162b2 regimen

Cell Reports. 2022 Jun 28;39(13):111013. doi: 10.1016/j.celrep.2022.111013.

A. Tauzin, S.Y. Gong, G. Beaudoin-Bussièrès, D. Vézina, R. Gasser, L. Nault, L. Marchitto, M. Benlarbi, D. Chatterjee, M. Nayrac, A. Laumaea, J. Prévost, M. Boutin, **G. Sannier**, A. Nicolas, C. Bourassa, G. Gendron-Lepage, H. Medjahed, G. Goyette, Y. Bo, J. Perreault, L. Gokool, C. Morrissette, P. Arlotto, R. Bazin, M. Dubé, G. De Serres, N. Brousseau, J. Richard, R. Rovito, M. Côté, C. Tremblay, G.C. Marchetti, R. Duerr, V. Martel-Laferrière*, D.E. Kaufmann*, A. Finzi*;

Strong humoral immune responses against SARS-CoV-2 Spike after BNT162b2 mRNA vaccination with a 16-week interval between doses

Cell Host & Microbe. 2022 Jan 12;30(1):97-109.e5. doi: 10.1016/j.chom.2021.12.004.

E. Brunet-Ratnasingham*, S.P. Anand*, P. Gantner*, A. Dyachenko, G. Moquin-Beaudry, N. Brassard, G. Beaudoin-Bussi eres, A. Pagliuzza, R. Gasser, M. Benlarbi, F. Point, J. Pr evost, A. Laumaea, J. Niessl, M. Nayrac, **G. Sannier**, C. Orban, M. Messier-Peet, G. Butler-Laporte, D.R. Morrison, S. Zhou, T. Nakanishi, M. Boutin, J. Desc oteaux-Dinelle, G. Gendron-Lepage, G. Goyette, C. Bourassa, H. Medjahed, L. Laurent, R-M R ebillard, J. Richard, M. Dub e, R. Fromentin, N. Arbour, A. Prat, C. Larochelle, M. Durand, J.B. Richards, M. Chass e, M. T etreault, N. Chomont#, A. Finzi#, D.E. Kaufmann#;

Integrated immunovirological profiling validates plasma SARS-CoV-2 RNA as an early predictor of COVID-19 mortality

Science Advances. 2021 Nov 26;7(48):eabj5629. doi: 10.1126/sciadv.abj5629.

J. Niessl, A.E. Baxter, E. Brunet-Ratnasingham, **G. Sannier**, G. Gendron-Lepage, J. Richard, G.G Delgado, N. Brassard, I. Turcotte, R. Fromentin, N.F. Bernard, N. Chomont, J-P. Routy, M. Dub e, A. Finzi, D.E. Kaufmann;

Persistent expansion and Th1-like skewing of HIV-specific circulating T follicular helper cells during antiretroviral therapy

EBioMedicine. 2020 Apr;54:102727. doi: 10.1016/j.ebiom.2020.102727.

F. Real, C. Capron, A. Sennepin, R. Arrigucci, A. Zhu, **G. Sannier**, J. Zheng, L. Xu, J-M. Mass e, S. Greffe, M. Cazabat, M. Donoso, P. Delobel, J. Izopet, E. Eugenin, M.L. Gennaro, E. Rouveix, E. Cramer Bord e, M. Bomsel;

Platelets from HIV-infected individuals on antiretroviral drug therapy with poor CD4+ T cell recovery can harbor replication-competent HIV despite viral suppression

Science Translational Medicine. 2020 Mar 18;12(535):eaat6263.

doi: 10.1126/scitranslmed.aat6263

Presentations

Oral presentations:

G. Sannier, M. Dubé, C. Dufour, C. Richard, N. Brassard, G.G. Delgado, A. Pagliuzza, A.E. Baxter, J. Niessl, E. Brunet-Ratnasingham, R. Charlebois, B. Routy, J-P. Routy, R. Fromentin, N. Chomont, D.E. Kaufmann;

Combined Single-Cell Transcriptional, Translational and Genomic Profiling Reveals HIV-1 Reservoir Diversity

Keystone EK43: HIV Pathogenesis and Cure, Keystone (USA) online, 2021

G. Sannier, M. Dubé, N. Brassard, G.G. Delgado, A.E. Baxter, J-P. Routy, N. Chomont, D.E. Kaufmann;

Single-Cell Multiplexed RNAflow-FISH Analyses of Primary Human Samples Reveals Distinct VR Reactivation Profiles Among LRA Classes and Curtailed VR by HDAC Inhibitors

Keystone X5: HIV Pathogenesis and Cure, Keystone (USA), 2020

Canceled due to CoVID19 pandemic

Poster presentations:

G. Sannier, A. Nicolas, L. Marchitto, M. Dubé, M. Nayrac, O. Tastet, S. Ding, A. Tauzin, R. Goupil, W. Beaubien-Souligny, A. Finzi, R.S. Suri, D.E. Kaufmann;

mRNA vaccine elicits delayed B cell and CD8 T cell responses associated with a skewed Th1 CD4 T cell profile in patients receiving hemodialysis

Keystone RJ3: Viral Immunity: Basic Mechanisms and Therapeutic Applications, Keystone (USA), 2022

G. Sannier, M. Dubé, C. Dufour, C. Richard, N. Brassard, G.G. Delgado, A. Pagliuzza, A.E. Baxter, J. Niessl, E. Brunet-Ratnasingham, R. Charlebois, B. Routy, J-P. Routy, R. Fromentin, N. Chomont, D.E. Kaufmann;

Combined Single-Cell Transcriptional, Translational and Genomic Profiling Reveals HIV-1 Reservoir Diversity

Keystone EK43: HIV Pathogenesis and Cure, Keystone (USA) online, 2021

G. Sannier, M. Dubé, C. Dufour, N. Brassard, G.G. Delgado, A.E. Baxter, J. Niessl, R. Charlebois, A. Pagliuzza, R. Fromentin, J-P. Routy, N. Chomont, D.E. Kaufmann;

Distinct Transcriptional Responses to LRAs Characterized by Single-Cell RNAflow-FISH CROI (Conference on Retroviruses and Opportunistic Infections), Chicago (USA), 2021

G. Sannier, M. Dubé, N. Brassard, G.G. Delgado, A.E. Baxter, J-P. Routy, N. Chomont, D.E. Kaufmann;

Single-Cell Multiplexed RNAflow-FISH Analyses of Primary Human Samples Reveals Distinct VR Reactivation Profiles Among LRA Classes and Curtailed VR by HDAC Inhibitors

Keystone X5: HIV Pathogenesis and Cure, Keystone (USA), 2020

Canceled due to CoVID19 pandemic

G. Sannier, M. Dubé, N. Brassard, G.G. Delgado, A.E. Baxter, J-P. Routy, N. Chomont, D.E. Kaufmann;

Multiplexed RNA flow cytometric FISH Allows Single-Cell Viral Transcriptional Profiling of Reactivated Translation-Incompetent HIV Reservoirs

CAHR (Canadian Association for HIV Research), Québec (Canada) 2020

Canceled due to CoVID19 pandemic

G. Sannier, M. Dubé, N. Brassard, G.G. Delgado, A.E. Baxter, J-P. Routy, N. Chomont, D.E. Kaufmann;

Single-Cell Multiplexed RNAflow-FISH Analyses of Primary Human Samples Reveals Distinct VR Reactivation Profiles Among LRA Classes and Curtailed VR transcriptional and Translational Reactivation Patterns by HDAC Inhibitors

9th HIV Persistence during Therapy, Miami (USA), 2019

Technical expertise and training

- **Immunological techniques:** Multiparameter flow cytometry for detection of surface or intracellular proteins, or mRNA (RNAflow-FISH) (spectral unmixing and compensation workflows), proliferation assay (CFSE), cytotoxic assay, ELISA, Luminex, Olink
- **Cell biology technique:** Isolation and culture of T and B cells from human blood or tissues samples, generation of MDMs from tissues and peripheral blood monocytes, work with infectious material in BSL2 and BSL3 conditions
- **Molecular biology techniques:** Real-time PCR, qPCR, Near-Full length PCR
- **Imaging:** Electron, confocal, and two-photon excitation microscopy
- **Computer software:** FlowJo, GraphPad Prism, RStudio, Geneious Prime, Spice, Adobe Illustrator